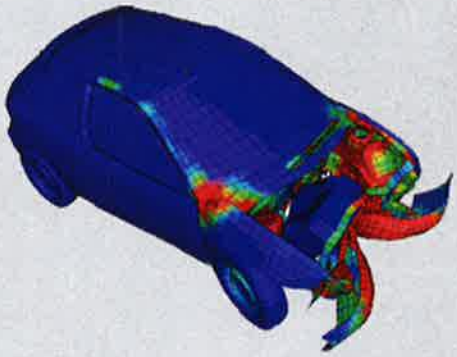


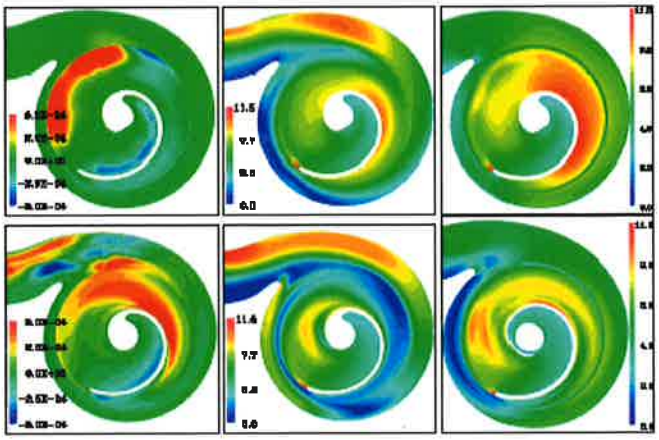
Raimo von Hertzen ja Tapani Halme (toim.)

PROCEEDINGS OF THE IX FINNISH MECHANICS DAYS

IX Suomen Mekaniikkapäivät

Lappeenrannan teknillinen yliopisto
13.-14. kesäkuuta 2006

1. Kokouspäivän esitelmät



LAPPEENRANTA
UNIVERSITY OF TECHNOLOGY

LAPPEENRANNAN TEKNILLINEN YLIOPISTO
KONETEKNIIKAN OSASTO

LAPPEENRANTA UNIVERSITY OF TECHNOLOGY
DEPARTMENT OF MECHANICAL ENGINEERING

RAPORTTI 17
REPORT

Raportti 17
Report 17

Proceedings of the IX Finnish Mechanics Days
IX Suomen Mekaniikkapäivät
Lappeenrannan teknillinen yliopisto
13.-14. kesäkuuta 2006

Nide 1

1. kokouspäivän esitelmät

Toimittajat

Raimo von Hertzen

Tapani Halme

ISBN 952-214-227-1
ISSN 1459-2924

Lappeenrannan teknillinen yliopisto
Konetekniikan osasto/Koneensuunnittelun laitos
Rakenne- ja lujuustekniikan laboratorio
PL 20, FIN-53851 Lappeenranta
puh. 05-62 111

LTY digipaino 2006

Tieteellinen neuvosto

Tapani Halme	Lappeenrannan teknillinen yliopisto
Heikki Handroos	Lappeenrannan teknillinen yliopisto
Raimo von Hertzen	Lappeenrannan teknillinen yliopisto
Juhani Koski	Tampereen teknillinen yliopisto
Gary Marquis	Lappeenrannan teknillinen yliopisto
Aki Mikkola	Lappeenrannan teknillinen yliopisto
Timo Nykänen	Lappeenrannan teknillinen yliopisto
Rolf Stenberg	Teknillinen korkeakoulu
Stig-Göran Sjölind	Oulun yliopisto

Järjestelytoimikunta

Tapani Halme
Sami Heinilä
Raimo von Hertzen
Lauri Huhtala
Matti Koskimäki
Janne Lepistö
Ilkka Poutiainen
Riitta Ruokonen
Kaija Tammelin
Pasi Tanskanen

Lappeenrannan teknillinen yliopisto
Konetekniikan osasto
Rakenne- ja lujuustekniikan laboratorio
PL 20
53851 LAPPEENRANTA

Puh. (05) 621 2436
Fax. (05) 621 2499

ISBN 952-214-227-1
ISSN 1459-2924

ESIPUHE

Suomen mekaniikkapäivät on järjestetty vuodesta 1982 lähtien kolmen vuoden välein. Vuonna 2006 järjestysvuorossa oli Lappeenranta, jossa IX Suomen Mekaniikkapäivät pidettiin 13.-14. kesäkuuta. Päivien käytännön järjestelyistä vastasi Lappeenrannan teknillinen yliopisto. Mekaniikkapäivien tarkoituksena on saattaa yhteen tutkijoita, opiskelijoita ja teollisuuden asiantuntijoita, joiden mielenkiinto kohdistuu mekaniikkaan, siihen liittyvään matematiikkaan ja tieteelliseen laskentaan.

Kutsuttuina esitelmöitsijöinä olivat professorit **Giancarlo Genta**, Politecnico di Torino; **Arne Johansson**, Kungliga Tekniska Högskolan; **Franz X. Tanner**, Michigan Technological University; **Darrell Socie**, University of Illinois; **Kim Wallin**, Valtion teknillinen tutkimuskeskus; ja **Károly Jármai**, University of Miskolc. Tämän lisäksi päivillä esitettiin tarjottuja esitelmiä yhteensä 66 kappaletta. Esitelmiin liittyvät artikkelit on koottu tähän konferenssijulkaisuun.

Haluamme lopuksi lämpimästi kiittää kaikkia niitä, jotka ovat tavalla tai toisella myötävaikuttaneet päivien onnistumiseen: osallistujia, artikkelien kirjoittajia ja esitelmöitsijöitä, tieteellistä neuvostoa ja ennen muuta kaikkia niitä henkilöitä, jotka ovat osallistuneet järjestelytyöhön.

Raimo von Hertzen
Tapani Halme

FOREWORD

The IX Finnish Mechanics Days were held in Lappeenranta at Lappeenranta University of Technology during 13-14th June, 2006. The aim of the Finnish Mechanics Days is to bring together researchers, doctoral students and industrial specialists whose interest lies in mechanics, mathematics associated with it, and scientific computing.

The invited speakers were professors **Giancarlo Genta**, Politecnico di Torino; **Arne Johansson**, Royal Institute of Technology; **Franz X. Tanner**, Michigan Technological University; **Darrell Socie**, University of Illinois; **Kim Wallin**, Technical Research Centre of Finland; and **Károly Jármai**, University of Miskolc. Also 66 contributed papers were presented. These two volumes contain the Proceedings of the IX Finnish Mechanics Days.

SISÄLLYSLUETTELO

Esipuhe

Foreword

NIDE 1

Kutsutut esitelmät

G. Genta
Vibration Control of Rotors: Tradeoff Between Active, Semiactive and Passive Solutions 1

A. Johansson
Recent Developments in Measurement, Modelling and Simulation of Turbulent Flows 16

F. Tanner
Computational Engine Research 17

Numeeriset menetelmät I

A. Niemi ja J. Pitkäranta
Matala-asteiset kuorielementit yleisellä nelikulmioverkolla 18

J. Mäkipelto
Advantages of T-splines in Shape Optimization 30

J. Mäkinen ja H. Marjamäki
Monikappalemekaniikan mallintaminen parametrisoimalla sidosmonisto 38

Materiaalien käyttäytyminen I

T. Manninen, R. Kouhia, E. Turunen and S.-P. Hannula
Microcrack Closure Effect on Indentation Testing of Thermally Sprayed Materials 50

T. Saksala
Kiven särkymisen numeerinen mallinnus iskumaisessa kuormituksessa 61

S. Holopainen
Treatment of the Tangent Modulus of Nonlinear Continua 72

Dynamiikka ja värähtelyt I

V.-M. Järvenpää
Dynamical Time Domain Simulation of Roll Contact 84

A. Laiho and P. Klinge
Modal Model Approach to Electromechanical Interaction in Rotordynamics of Electrical Machines 92

H. Marjamäki ja J. Mäkinen
Puomin nostoliikkeen mallinnuksesta 102

Rakenteiden mekaniikka I

J. Kovanen, P. Pykäläinen, M. Tanttu, M. Kemppinen and A. Nylen
Crash Safe, Energy Absorbing Composite Lighting Column 113

A. Borovkov, O. Klyavin, A. Michailov, M. Kemppinen and M. Kajatsalo
The Impact Simulation of Crash Safe Composite Lighting Columns 120

M. Kajatsalo, T. Karttunen, J. Kovanen ja M. Kemppinen
Kevytrakenteisten ontelopalkkien laskenta ja testaus 131

T. Brander, K. Lumppio ja O. Muttilainen
Teräksen ja muovikomposiittien väliset liimaliitokset konepajasovellutuksissa 143

Virtausmekaniikka I

J. Saloranta and A. Hellsten
Verification of a Reynolds-Averaged Navier-Stokes Solver for Direct Numerical Simulation of Turbulent Flow 155

M. Auvinen, J. Ala-Juusela and T. Siikonen
CFD Modeling of a Single-Blade Pump 167

F. Bergström, J. Åkerholm, R. Hansson and R. Möller
Web Drying Simulations Based on Computational Fluid Dynamics 179

A. Karvinen and H. Ahlstedt
Comparison of Turbulence Models in a Case of Slanted Jets in Crossflow 189

Kokeellinen mekaniikka

S. Moilanen ja J. Tervokoski
Raskaan kranaatinheittimen laukauspaineen mittausmenetelmien vertailu 201

M. Hokka, V.-T. Kuokkala and T. Vuoristo
Mechanical Testing of Materials with the Hopkinson Split Bar Technique 214

A.-J. Vuotikka and S.-G. Sjölind
Palosuojalisäaineen vaikutus polyesterihartsin materiaaliominaisuuksiin 226

J. Aalto, P. Hassinen, M. Reivinen ja J. Valtonen
Tavaravaunujonon pysäyttäminen kitkan avulla 238

Rakenteiden mekaniikka II

E. Eloranta
Kontinuumimekaniikka osana geofysiikan kenttäteorian opetusta 246

K. Ärölä and R. von Hertzen
Large Deformation Analysis of Wound Roll Stresses 257

P. Kere and M. Lyly
On the Effect of Geometric Imperfection on the Numerical Prediction of Cylindrical Composite Shell Post-Buckling Behaviour 270

Fluidin ja rakenteen vuorovaikutus

M. Kurki and J. Åkerholm
Analysis of Strongly Coupled Fluid-Structure Interaction Problem Using Optimization Principle 280

M. Reivinen and E.-M.Salonen
Surface Tension Problems, Virtual Work and Free Boundary 291

Optimointi

K. Mela, J. Koski ja R. Silvennoinen
Monitavoitteisen epälineaarisen sekalukuoptimointitehtävän Pareto-optimien ratkaisualgoritmi 302

J. Ojala ja J. Jalkanen
Kaupallisen FEM-ohjelman käyttö kantavien rakenteiden optimoinnissa 314

A. Niemistö, K. Hiltunen, J. Korpijärvi and H. Tuomola
Efficient Multiphysics Simulations and Optimizations Using Commercial Simulation Tools 326

J. Jalkanen
Cost Optimization of Welded Steel Structures 327

Rakenteiden mekaniikka III

J. Paavilainen
Modelling of Beams in Discrete Element Simulations 339

Väsyminen ja murtuminen I

M. Savolainen and B.R. Rabb
Fatigue Strength Analysis of a Crankshaft by Using Multibody Dynamic Simulation 347

T. Nykänen, G. Marquis and T. Björk
Effect of Local Geometrical Variations on the Fatigue Strength of Fillet Welded Joints 359

I. Poutiainen and G. Marquis
Comparison of Local Approaches in Fatigue Analysis of Welded Structures 378

J. S. Lepistö
Fatigue Assessment of a Notched Nodular Cast Iron Component Subjected to Multiaxial Loading 392

L. Huhtala and V.-M. Lihavainen
Fatigue Strength of Cold-Formed Tubular X- and T-Joints 404

NIDE 2

Kutsutut esitelmät

Darrell Socie
Smart Sensors for Railcar Monitoring 417

Kim Wallin
Transitiolämpötilakriteerien tausta ja merkitys haurasmurtumismitoituksen kannalta 418

Károly Jármai
Design of Economic Steel Structures 419

Numeeriset menetelmät II

C. Lovadina, R. Stenberg and M. Rüter
Error-Controlled Adaptive Mixed Finite Element Methods for Second-Order Elliptic Equations 434

R. Kouhia and M. Rüter
An Adaptive Integration Scheme in Computational Inelasticity 442

A. Hannukainen
A Posteriori Error Control in Terms of Linear Functionals for Elliptic Problems: Estimation and Mesh Adaptivity 452

M. Juntunen ja R. Stenberg
Epäjatkuva Galerkinin menetelmä sekaelementtitehtävälle 464

S. Korotov
A Posteriori Estimates for Computational Error Control in Terms of Linear Functionals for Linear Elasticity Problems 476

Virtausmekaniikka II

J. Heikkinen, M. Honkanen, J. Korpijärvi, P. Saarenrinne and T. Kilpiö
Validation of CFD Simulations in a Mixing Tank with Stereo-PIV Experiments 488

P. Råback, M. Malinen, A. Pursula ja T. Veijola
Vaihtoehtoisia menetelmiä mikrosysteemien vaimennusominaisuuksien laskemiseen 500

A. Hellsten
Effect of Parallel System Rotation on Heat Transfer in Laminar Pipe Flow 509

T. Karvinen
Volume Flow Rate Oscillation in Tapered Channels 518

T. Zwinger, O. Gagliardini, J. Ruokolainen, M. Lyly and P. Råback
Finite Element Techniques Applied to Glaciological Problems 529

Dynamiikka ja värähtelyt II

J. Toivola
Nippikontaktin värähtelyjen syntymekanismista kumilla pinnoitetun telan yhteydessä 538

L. Yuan
Vibration Analysis of Nonlinear Model for Nip Contact 549

T. Frondelius
Coupling Between Longitudinal Vibrations of an Axially Moving Web and Rotational Vibrations of Rolls with Time Dependent Parameters 559

Mekaniikan erityisongelmia

M.A. Ranta ja R. von Hertzen
Navigointia pallolla 560

J. Freund
The Force Capacity and Fatigue of Muscle 572

Rakenteiden mekaniikka IV

J. Paavola and E.-M. Salonen
Buckling Analysis Through Equilibrium Equations of Curved Structures 582

T. Halme and S. Heinilä
Stress and Displacement Analysis of a Monorail Beam Including the Distortion of the Cross-Section 591

P. Varpasuo
Experimental Set-Up and Numerical Simulation of Soft Missile Impact Small Scale Tests 604

J. Aalto, P. Hassinen and I. Kotsionis
Stresses of Insulating Glass Units 616

A.-J. Romppanen and E. Keskinen
Analysis of Line Load Determination by Influence Coefficient Method 631

Materiaalien käyttäytyminen II

A. Polojärvi and J. Tuhkuri
Combined Finite-Discrete Element Method for Applications in Ice Mechanics 642

S. Fortino, J. Hartikainen, K. Kolari, R. Kouhia and T. Manninen
A Constitutive Model for Strain-Rate Dependent Ductile-to-Brittle Transition 652

A. Vuotikka, S.-G. Sjölind ja T. Jämsä
Muistimetalli-implanttien mallintaminen lääketieteellisissä sovelluksissa 663

A. Belahcen, K. Fonteyn, S. Fortino and R. Kouhia
A Coupled Magnetoelastic Model for Ferromagnetic Materials 673

J. Hartikainen, R. Kouhia and T. Manninen
A Model for Concrete at High Temperatures 683

Väsyminen ja murtuminen II

J. Toivola ja S. Moilanen
Aseen tuliputken lujuusteknisen mitoituksen ohjelmointi 692

T. Björk, S. Heinilä and G. Marquis
Fracture and J-Integral Assessment of a Welded CFSHS K-Joint Tested at -40 ° C 699

M. Kajatsalo, T. Karttunen ja J. Kovanen
Lujitemuovien väsytystestaus: menetelmät, ongelmia ja esimerkkitapaus 711

S. Heinilä, G. Marquis and T. Björk
Fracture Mechanics Assessment of Mixed Mode Fatigue Cracks in CFRHS Beams 721

T.Björk
Hitsin laadun määrityksestä 732

VIBRATION CONTROL OF ROTORS: TRADEOFF BETWEEN ACTIVE, SEMIACTIVE AND PASSIVE SOLUTIONS

G. GENTA, N. AMATI, S. CARABELLI, P. MACCHI, F. NICOLOTTI, M. SILVAGNI, A. TONOLI, M. VISCONTI

Mechatronics Laboratory
Politecnico di Torino
C. Duca degli Abruzzi 24
TORINO, ITALY

ABSTRACT

The trend towards higher rotational speeds shown by rotating machinery in the last 150 years was made possible by a deeper and more detailed understanding of their dynamic behaviour. In the last decades several devices aimed not only at damping but also controlling their vibration have been proposed and applied in many experimental devices and are now entering the application phase. The aim of the present paper is that of describing various devices studied in a project aimed at build a 'more electric turbojet engine' and to compare their performances. The results are however more general and can supply some guidelines in the choice between passive, semiactive and active rotor vibration control devices.

1. INTRODUCTION

The first papers dealing with the dynamics of rotating shafts were published at the middle of the XIX century [1] but the first successful attempts to built high speed rotating machines, requiring a throughout understanding of rotordynamics, date back to the end of that century. The rotational speed of these machines was far higher than those common in other fields of mechanical engineering and the peculiar dynamic problems encountered had to be dealt with to produce a successful design. Although the concept of critical speed was introduced earlier, in connection with flexible transmission shafts, it is significant that De Laval, during his design of a steam turbine, had to understand the behavior of a rotor in supercritical conditions [2].

While the first turbine rotors were very simple and could be dealt with using highly idealized models of the type now widely known as 'Jeffcott rotor' [3], more complicated machines required a more detailed and complex modeling. Actually, while this simplified approach can explain qualitatively many important features of real-life rotors, like selfcentring in supercritical conditions and the different roles of the damping of the rotor and of the nonrotating parts of the machine, it fails to explain other features, like the dependence of the natural frequencies on the rotational speed and above all does not allow to obtain a precise quantitative analysis of the dynamic behavior of complex systems.

Increasingly complex models and procedures had to be developed. Graphical computation schemes can be found in books and papers of the first quarter of the XX century, as the books by Belluzzo and Stodola [4, 5], and became the basic instrument for the dynamic analysis of turbine rotors. By including gyroscopic moments and centrifugal stiffening, the natural frequencies of rotors were found to be functions of the rotational speed. The analytical [6] and experimental [7] work on rotating membranes clarified this issue, leading to a graphical representation of the frequencies as functions of the speed which is today known as the Campbell diagram.

Later on, also owing to the availability of electromechanical calculators, tabular procedures were developed, mainly based on the transfer matrices approach. In particular, Myklestadt-Prohl [8] method was (and still is) widely used to compute the critical speeds of turbine rotors. These methods were immediately automatised when digital computers become available.

More recently the wide diffusion of the finite element method (FEM) deeply influenced also the field of rotordynamics. Usual general purpose FEM codes cannot be used for rotordynamic analysis owing to the lack of consideration of gyroscopic effects. It is true that a gyroscopic matrix can be forced in the conventional formulation and that several Companies used commercial FEM codes as NASTRAN or ANSYS to perform rotordynamic analysis, but rotordynamics is one of the fields where purposely written, specialized FEM codes can give their best. FEM modeling allows to study the dynamic behavior of machines containing high speed rotors in greater detail, obtaining quantitative predictions with an unprecedented degree of accuracy.

No modern high speed rotating machine can be designed without performing rotordynamic analysis. Generally speaking accurate dynamic analysis is useful

- at the design stage, to predict possible dynamic problems and to take the needed countermeasures, allowing to obtain higher performances (power/weight ratio, specific consumption, cost containment, etc.) with confidence, without jeopardizing safety;
- during testing, to compare the experimental results with a 'theoretical behavior', allowing to gain a better insight on how the machine works. Even more important, numerical results suggest what to look for, where to locate probes and help to plan the experiments. The cost and time needed for this stage of the development of the machine is so greatly reduced;
- allows to simplify flexible-rotor balancing procedures, owing to the knowledge of the mode shapes corresponding to the critical speeds, both whether influence coefficients method or modal balancing is used. Moreover, the field of diagnostics of rotating machinery, whose importance is growing, is deeply indebted to rotordynamics.

2. OPEN PROBLEMS

In spite of the progress made in recent years in the application of concepts which are well established since decades, there are still areas in which research work is needed.

A first point is linked with stability analysis. It is well known that any rotor operating in the supercritical range may develop stability problems owing to several causes, some of which have been deeply investigated in the past while others are still less well known. Often it is necessary to resort to extensive experimentation, finding sometimes unexpected results. One of the main problems here is that the stability of the rotor is linked to damping of both the nonrotating and rotating parts of the machine or to the behavior of the fluids in lubricated bearings, seals and other narrow gaps between the stator and the rotor. In the first case damping is not easily assessed, partly due to the internal damping of the material, known with ample uncertainty margins, and partly to phenomena like dry friction between the parts constituting the rotor. The latter is intrinsically nonlinear and can be accommodated into the basic mathematical models only up to a certain limit and with approximations whose validity may be questionable. Fluid-related phenomena are easier to study, accepting some common assumptions, but for a detailed analysis, the fluid-structure interaction and even elastohydrodynamic conditions must be dealt with.

A second problem is linked with deviations from linearity. Rotordynamic analysis is typically linearised and many of the concepts, from critical speeds to modal or influence-coefficients balancing, are valid only within the limits imposed by linearity. While rotors are often linear within ample margins, at least in their nominal conditions, other components like bearings, dampers or seals may display a severe nonlinear behavior. The alternatives of considering these

elements as rigid (e.g. in the case of bearings), neglecting them (e.g. seals) or linearising their behavior (e.g. using the eight coefficient approach) are very common but in many cases the results obtained in this way may be unsatisfactory. Another possible cause of nonlinearity can be the presence of a crack in some structural element, which causes a difference between local tensile and compressive characteristics. If nonlinearities are not neglected, the analysis must be performed in ways quite different from those of classical rotordynamics: Campbell diagrams and critical speed analysis lose their meaning and the attention must be concentrated on the unbalance response and on the spectral analysis of the vibration records. But this is only one aspect of the problem: when a system is highly nonlinear new phenomena can arise, particularly those related with chaotic vibrations. Chaotic motion has been found in both numerical simulations on simple mathematical rotor models and test results on actual rotating machinery.

A further aspect that needs more research work is the dynamic behavior of rotors in nonstationary conditions. If the spin speed is not constant or if some other working parameter changes abruptly, no analytical solution to the problem is known, or at least is practical, and the analysis is best performed by numerical simulation. This is the case when studying the acceleration through a critical speed or the behavior of a rotor when a blade detaches from a disc (blade-loss conditions).

The stator-rotor interaction, and in particular the detailed modeling of bearings, dampers and seals, is another field of research. Numerical modeling, mainly using the FEM, of the oil film allows a detailed study of the behavior of hydrodynamic bearings, but if this is extended to nonstationary conditions the complexities to be faced are large. Moreover, bearings like air bearings or magnetic bearings are now used as alternatives to classical hydrodynamic and rolling element bearings.

Finally, classical rotordynamics deals only with the lateral behavior of rotors, assuming a complete uncoupling between lateral, axial and torsional behavior. A significant example of this is the dynamic analysis of reciprocating machinery: in spite of the fact that all vibration of crankshaft is at the same time torsional, flexural and axial, the usual mathematical models are based on uncoupling, an approximation dictated by the complexity of the coupled analysis.

3. FROM ROTORDYNAMICS TO ROTOR VIBRATION CONTROL

Rotordynamic analysis allows predicting the dynamic behavior of rotors and is essential in the design of any rotating machine, particularly if operating at high speed. If this is intended as 'operating in the supercritical range', provisions to insure a safe crossing of the critical speed (or of a few critical speeds) and to grant stability in the supercritical range must be accurately studied.

Very often these requirements can be fulfilled by contrasting measures and a trade-off must be done. As an example, fast turbines operate in the supercritical range and to cross the rigid-body critical speed low support stiffness is expedient. At the same time, the need of low clearance between stator and rotor, particularly at the tip of the blades, dictated by the need of obtaining high efficiency, results in high support stiffness. Operation in the high supercritical regime allows to exploit self-centering, but at the same time makes more difficult to achieve the required stability.

In the various applications of high speed rotating machines specific design practices were developed, often with much success. Some of these fields are very specialized and have peculiar problems that compelled designers to develop technologies that are distinctive; in other cases it was just a matter of applying general rules leading to a sound design.

In general the provisions that can be taken to keep rotor vibrations under control may be subdivided in two different lines, namely either adapting the stiffness properties of the system or providing a suitable amount of damping. These provisions influence what is generally regarded as the free behavior of the system, with the understanding that if the system is linear enough the free and the forced behavior can be studied and acted upon separately. Another line is that of reducing the forcing actions on the rotor, above all, but not exclusively, those linked with unbalance.

Clearly a better balancing has no effect on critical speeds (assuming that the system is linear) but makes it easier to get through them and to reach supercritical conditions. However improving balance condition has no effect whatsoever on supercritical stability, and there are cases in which, owing to nonlinear effects, might even make stability problems worse.

Acting on the system stiffness allows changing the natural frequencies and, as a consequence, the values of the critical speeds. Usually the point is to reduce the stiffness to obtain lower natural frequencies and critical speeds, making their crossing and reaching self-centered conditions easier. As already said, this not always is possible and a trade-off is usually required.

Damping has a more subtle effect. It is well known that the damping of the non rotating parts of the machine is always favorable to stability and increasing it is very often the basic method to improve stability and to make it easier to cross critical speeds. Rotating damping (i.e. the damping associated to rotating parts of the machine) has a similar effects in the whole subcritical field, in spite of some incorrect statements forwarded even recently [9]. In the supercritical field rotating damping may be a cause of instability. This consideration must not however be intended in an absolute sense: the effect of damping of a certain element of the machine depends on how it participates to the various modes of vibration. A typical example is that of the dampers applied to turbine blades, that may be stabilizing even at supercritical speeds, since the blades' vibratory modes are displaced to higher speeds by centrifugal stiffening [10, 11].

What actually matters in distinguishing between rotating and non rotating damping is whether the element where energy is dissipated rotates or not. Rotating damping is usually synchronous, i.e. the element dissipating energy rotates at the speed of the rotor, but there are cases of nonsynchonous, or even counter-rotating, damping; the most important one being that of the oil film in hydrodynamic bearings. Oil, where energy is dissipated, rotates at a speed slightly lower than half the rotation speed of the rotor, destabilizing modes occurring at a frequency lower than half (or slightly less than half) the spin speed.

The traditional way of controlling rotor vibration in the supercritical range is adding dampers, usually of the squeeze film type (SFD, squeeze film dampers), or, particularly in low cost machines, elastomeric dampers. SFDs and elastomeric dampers are connected to the rotor via a bearing, usually of the rolling element type, so that energy is dissipated in a stationary element. Elastomeric dampers supply damping as well as a restoring force while SFDs are pure dampers, even if they display also a dynamic stiffness component and a spring can be placed in parallel to constitute a damped support. In some cases, mainly in twin-spool turbines, squeeze film dampers are located between the shafts, and oil rotates at the speed of one of the two rotors. A sort of nonsynchronous rotating damping is so obtained and its effects are stabilizing on some modes and unstabilizing on others.

Advances in electronics and control theory allowed to build active magnetic bearings (AMB), that promised a much more complete and flexible control of rotor vibration. They are controlled systems, and then through their sensors, actuators and controller, possibly digital, allow a complete active vibration control. The sensors needed for control tasks can be used also for real-time monitoring on the rotordynamic behavior of the machine and to perform diagnostic studies even from a remote location through the internet.

However AMBs didn't gain that widespread diffusion someone predicted a decade ago, in spite of their many advantages, while remaining confined to some niche applications, like turbomolecular vacuum pumps, where the absence of lubricating fluids contaminating the vacuum is the deciding factor. For many applications, particularly where the mass of the rotor is not small, the loads on the bearings are large or high stiffness is needed for reasons linked with the tasks the rotor has to fulfill, the drawbacks of magnetic bearings in terms of mass and bulk of the actuators and high current drain can be strong disadvantages. It is often not so much a problem of performances or of

power required to achieve levitation, but of a number of practical disadvantages and the need of bulky, heavy and costly components that discourage their application.

But to perform an active vibration control there is no need to resort to fully active AMBs. Active rotor vibration control can be achieved in a number of ways that are promising to be simpler and less costly. As a simple way to overcome the limitations of viscoelastic and fluid film dampers, electro-hydraulic active or semi-active systems have been developed to allow some forms of online tuning or adaptive behavior (see Table 1 for a classification of rotor vibration control devices). More recently electrorheological [12, 13] and magnetorheological semi-active damping systems have shown attractive potentialities for adapting damping forces according to the operating conditions. However, electro-hydraulic, electrorheological, and magnetorheological devices cannot avoid some drawbacks related to the ageing of the fluid and to the tuning required for the compensation of temperature and frequency effects.

Electromechanical dampers seem to be a valid alternative to viscoelastic and hydraulic ones due to, among other reasons,

1) absence of all fatigue and tribology issues motivated by the absence of contact,
2) small sensitivity to operating conditions,
3) wide possibility of tuning even during operation, and
4) predictability of their behavior.

The attractive potentialities of electromechanical damping devices motivated a considerable research effort during the past decade. The target applications range from the field of rotating machinery to that of vehicle suspensions. The damping force density that can be supplied by such devices is the main issue to be investigated. Preliminary analysis performed in the field of rotordynamics [14] and vehicle suspensions [15] underline how the weight and size are the main drawbacks. Even if this drawback could be a limiting factor in practical applications, the above listed advantages motivate a more detailed analysis. Following the experience accumulated in magnetic suspensions, Kasarda *et al.* [16] proposed a mixed active-passive strategy to control vibration: active magnetic bearings in conjunction with conventional supports to damp lateral vibration of rotors contained in gear boxes to reduce the noise emission. The same authors perform a preliminary investigation on the use of active magnetic dampers to minimize flexural vibration of aero-engines shafts. However, their medium term applications suffer the lack of a consolidated design practice and of the availability of low cost power and signal electronics.

Passive	Elastomeric	Temperature dependent
	SFD (squeeze film)	
	Permanent magnet MEMD (motional electro-magnetic)	
Semi-active	Magnetoreologic	Fluid different from lubricant
	Electroreologic	
	MEMD (motional electro-magnetic)	
	TEMD (transformer electro-magnetic)	
Active	Controlled fluid-dynamic (geometry control)	Temp. dependant
	Piezoelectric active dampers	
	AMD (active magnetic dampers)	
	AMB (active magnetic bearings)	High forces

Table 1: Devices for vibration control of rotors. Passive: not requiring power or control. Semi-active: requiring power but only slow, open-loop control to adapt the device characteristics. Active: requiring power and closed-loop control. Note that the list includes only the most commonly considered devices. In the last column some drawbacks are listed.

Passive or semi-active electromagnetic (eddy current) dampers seem to be an interesting alternative in the near future. Compared to active closed loop devices, eddy current dampers have

a simpler architecture thanks to the absence of power electronics and position sensors and are intrinsically unaffected by instability problems due to the absence of a fast feedback loop. The simplified architecture guarantees higher reliability and lower cost, but allows less flexibility and adaptability to working conditions. Eddy current dampers are based on the magnetic interaction due to variations of the magnetic flux linked to a conductor [17, 18]. Such a variation may be generated using two different strategies:

- Moving a conductor in a stationary magnetic field that is variable along the direction of motion (motional electro-magnetic dampers);
- Changing the reluctance of a magnetic circuit whose flux is linked with the conductor (transformer electro-magnet dampers).

The eddy currents in the conductor interact with the magnetic field and generate Lorenz forces proportional to the relative velocity of the conductor itself in the first case. Graves *et al.* [19] define this kind of damper as "motional" or "Lorentz" type. In the second case the variation of the reluctance of the magnetic circuit produces a time variation of the magnetic flux. The flux variation induces a current in the voltage driven coil and, therefore, a dissipation of energy. This kind of dampers is defined in [20] as "transformer", or "reluctance" devices.

The literature on eddy current dampers is mainly focused on the analysis of "motional" devices. Nagaya in [21, 22] introduced an analytical approach to describe how damping forces can be exploited using monolithic plane conductors of various shapes. Karnopp and Margolis [23, 24] describe how "Lorentz" type eddy current dampers could be used as semi-active shock absorbers in automotive suspensions. The application of the same type of eddy current damper in the field of rotordynamics is described in [25, 26]. Additionally, a dedicated research activity [20] has been devoted to model the effects of the electric circuit dynamics on the damping performances and therefore on the design procedure of eddy current dampers.

Being usually less efficient than *Lorentz* type, *transformer* eddy current dampers are less common in industrial applications. However they may be preferred in some areas for their flexibility and construction simplicity. If driven with a constant voltage they operate in passive mode while if current driven they become force actuators to be used in active configurations. Transformer eddy current dampers seem to be promising as non rotating damping system in the support of aero-engines rotors. They are meant to be used in parallel with a flexible support connecting a rolling bearing with the casing. To the authors' knowledge, a design methodology of *transformer* dampers taking the system dynamic behavior into account has not been presented yet in the literature. In a previous paper [27] the authors describe the modeling of the this type of eddy current dampers studying the effects of the design parameters. The models have been validated experimentally on two dedicated test rigs, developed at the Mechatronics Laboratory of the Politecnico di Torino to simulate in laboratory conditions the dynamics of aircraft engine rotors and to test devices alternative to traditional squeeze film dampers.

Note that here only devices aimed to controlling rotor motions by applying forces between the rotor and the stator of the machine are considered. Another approach is using dampers in the suspension of the machine, i.e. between the stator and the 'ground'. In general, the first ones control the generation of vibration, while the latter control the transmission of vibration to the surroundings, often making things worse for the rotor itself, like when soft supports are used to cut the transmission of high-frequency disturbances. This second approach will not be dealt with here.

4. ACTIVE MAGNETIC DAMPER (AMD)

Active magnetic dampers (AMD, Fig. 1a) work in the same way as active magnetic bearings, with the only difference that in this case the force generated by the actuator is not aimed at supporting the rotor, but just at supplying damping. It might be said that in the former the controller works in

a derivative mode, while in the second one in a proportional mode. The force each coil of the actuator exerts on the rotor is

$$F = \frac{\mu_0 N^2 A}{4}\left(\frac{i(t)}{q_0 + q(t)}\right)^2 \tag{1}$$

where N is the number of turns of each winding, A is the area of the magnetic circuit at the air gap, μ_0 is the magnetic permeability of vacuum, i is the current q_0 is the air gap and q is the displacement.

The force needed to supply damping is much smaller than that needed to support the rotor and this explains the advantages of AMD over AMB. An AMD can be integrated in one of the supports of the rotor and in this case a bearing, e.g. a rolling elements bearing, connected to the housing with springs providing the required stiffness, is present (Fig. 1b). The stiffness is then that of the mechanical structure (spring) with the bearing in series, and the damping is due to the AMD that can be easily tuned operating on the control law.

The stiffness of the spring must be high enough to overcome the open loop negative stiffness of a typical AMB, but nevertheless there is no guarantee that the system is stable. Like with all active systems, stability must be assessed by properly designing the control law. Sensors and a controller are required, and the latter must be able to deal with frequencies higher than the rotation frequency and this, together with the fact that the actuator is a low resistance, high inductance, load, increases power dissipations. However, power dissipation in AMBs and AMDs mostly depends on the type of power amplifiers and can be strongly reduced by properly designing the electronics. The advantages here are the absence of eddy current losses since the actuator exerts a force on a nonrotating part, the possibility of using sensors that are not contactless and above all the much lower forces actuators must exert.

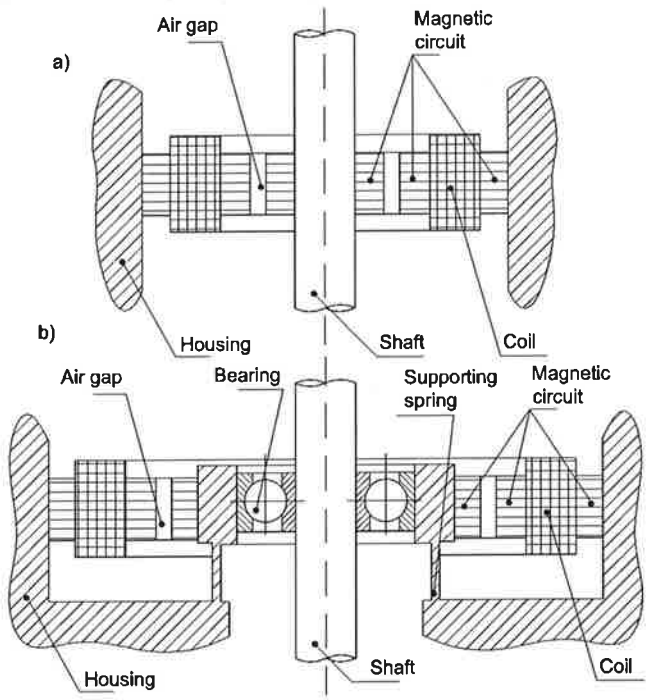


Fig. 1. Sketch of an active magnetic bearing or damper (a) and of an active magnetic damper (b) operating also as an elastic support.

5. EDDY CURRENT DAMPERS

5.1. Transformer type (TEMD)

A "transformer" eddy current damper may use the same configuration as AMDs with the difference that now the coils, supplied with constant voltage, generate the magnetic field linked to the moving element (anchor). Both configurations of Fig. 1 a) and b) can be used, but the second one can be preferred since the magnetic flux does not cross rotating parts, avoiding eddy currents and energy dissipation due to rotation.

The displacement with speed $\dot{q}$ of the anchor changes the reluctance of the magnetic circuit and produces a variation of the flux linkage so generating a back electromotive force and ultimately eddy currents in the coils. The current in the coils has two contributions: a fixed one due to the voltage supply, and a variable one induced by the back electromotive force. The first contribution generates a force increasing with decreasing air-gap, thus producing a negative stiffness. The damping force is generated by the second contribution, acting against the speed of the moving element. It is then a semiactive device, since it requires some power to generate the magnetic field and may be controlled in the sense that the current in the coil may be changed to change its performance, but it doesn't need to be controlled in closed loop and hence may have no sensors. However, it may supply information on the dynamic behavior of the rotor, since the current in the coil can be monitored. Energy dissipations take place in the stator, so that the device supplies nonrotating damping.

The transfer function between the speed v and the electromagnetic force F shows a first order dynamics with pole frequency ω_{RL} due to the R-L nature of each circuit

$$\frac{F}{\dot{q}} = \frac{1}{s}\frac{K_{em}}{\left(1+s/\omega_{RL}\right)}, \tag{2}$$

where $K_{em} = -\dfrac{2V^2/R}{q_0^2\omega_{RL}}$, $\omega_{RL} = \dfrac{R}{L_0}$, $L_0 = \dfrac{\mu_0 N^2 A}{2q_0}$.

Due to the factor $1/s$, and the negative value of K_{em}, the mechanical impedance is that of a band limited negative stiffness. The value of the negative stiffness is proportional to the electrical power (V^2/R) dissipated at steady state by the electromagnet.

For given values of the number of turns of the windings (N), of the air gap area (A), and clearance (q_0), the mechanical impedance and the pole frequency are functions of the voltage supply V and the resistance R.

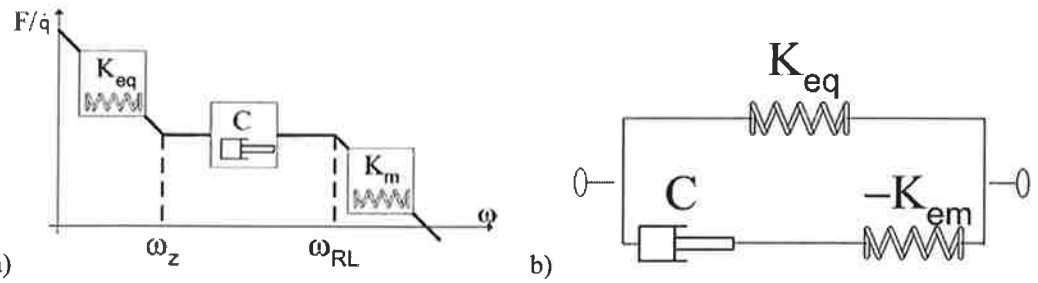


Fig. 2: "Transformer" eddy current damper. a) Mechanical impedance of a transformer damper in parallel to a spring of stiffness K_m and b) mechanical equivalent.

The negative stiffness prevents the use of the electromagnet as support of a mechanical structure unless the excitation voltage is driven by an active feedback that compensates it. A very simple alternative to the active feedback is to put a mechanical spring in parallel to the electromagnet. The stiffness K_m of the added spring has to be larger than the negative electromechanical stiffness of the damper in order to avoid the static instability ($K_m \geq -K_{em}$). In the case of an already supported structure the mechanical stiffness could be that of the structure, alternatively, in case of a structure supported by the dampers themselves, the springs have to be installed in parallel to them. As a matter of fact, the mechanical spring in parallel to the transformer damper can be considered as part of the damper, and in the following the parallel will be referred to as "transformer electromechanical damper" (TEMD).

Due to the essential role of that spring, the impedance is not very helpful in understanding the consequences of including a transformer damper in a mechanical structure. Instead, a better insight can be obtained by studying the mechanical impedance of the damper in parallel with the mechanical spring, i.e. of the TEMD:

$$\frac{F}{\dot{q}} = \frac{1}{s}\left(\frac{K_{em}}{(1+s/\omega_{RL})} + K_m\right) = \frac{K_{eq}}{s}\frac{1+s/\omega_z}{1+s/\omega_{RL}} \tag{3}$$

where $K_{eq} = K_m + K_{em}$; $\omega_z = \omega_{RL}\frac{K_{eq}}{K_m}$.

Apart from the pole at null frequency, the impedance shows a zero-pole behavior. Since to ensure stability $0 < -K_{em} < K_m$, the zero frequency (ω_z) results to be smaller than the pole frequency ($0 < \omega_z < \omega_{RL}$).

As shown in Fig. 2a, it is possible to identify three different frequency ranges:

- Equivalent stiffness range $\omega << \omega_z < \omega_{RL}$: the system behaves as a spring of stiffness $K_{eq} > 0$.
- Damping range $\omega_z < \omega < \omega_{RL}$: the system behaves as a viscous damper with coefficient

$$C = \frac{K_m}{\omega_{RL}} \tag{4}$$

- Mechanical stiffness range $\omega_z < \omega_{RL} << \omega$: the transformer damper contribution vanishes and the only contribution is that of the mechanical spring (K_m).

5.2. Motional type (MEMD)

The sketch of a MEMD is shown in Fig. 3. In the figure the magnetic field is generated by a permanent magnet, and a passive damper is obtained. If the field is generated by a coil a semi-active, controllable device is obtained. Eddy currents are generated in a conductor that follows the rotor in its whirling motion owing to the rolling elements bearings, but does not rotate, so that nonrotating damping is supplied. Note that in this case a bearing is needed, because if the conductor is attached to the rotor, unstabilizing rotating damping would result. The solid conductor may be substituted by a coil, in which case it is possible to close the circuit on a resistor, a RLC circuit or a more complex circuit to obtain various forms of uncontrolled or controlled device.

The basic difference between a TEMD and a MEMD is that in the former eddy currents flow in the same coil generating the field, while in the latter the field is generated by a coil or a permanent magnet, while eddy currents flow in a different element, be it a solid conductor, a coil or a more complex circuit.

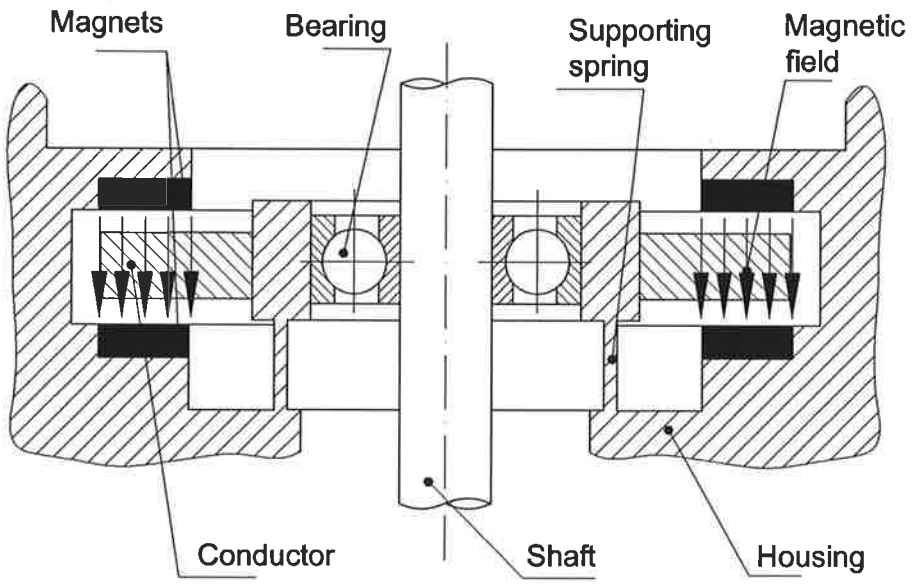


Fig. 3. Sketch of a motional active magnetic damper (MEMD)

6. ROTOR TEST RIG CHARACTERISTICS

Figure 4a shows the *Engine-like Rotordynamics Test Rig* (RTR), a general purpose rotordynamic equipment designed and built at the Mechatronics Laboratory of the Politecnico di Torino. The rig is intended to work at speeds up to 7000 rpm. The main requirement was for the stator dynamic behaviour not to interact with that of the rotor up to the 2X component of the vibration. Since the maximum design spin speed is 7000 rpm, the first natural frequency of the stator had to be higher than $2 \cdot 7000$ rpm $\approx$ 234 Hz. Such a requirement was fulfilled by designing a very stiff structure based on four columns and thick end plates. The rig was designed to accommodate various types of rotors and bearings, in various configurations and allows to place the probes wherever needed along the rotor structure. The intermediate plates supporting both transducers and possible other bearings can be adjusted along the structure. The rig was designed for these main tasks:

- Implementation and testing of data acquisition systems for monitoring and control,
- Experimental validation of on line monitoring techniques ([28]),
- Implementation and testing of active control systems to reduce the lateral vibration of flexible rotors,
- Experimental verification of new non rotating damping devices as alternative to traditional squeeze film dampers.

Here the rig is shown as used to reproduce the lateral dynamics of an aircraft engine to study alternative electromagnetic non rotating damping systems. The study is focused on the low pressure (LP) shaft which is more critical from the dynamic point of view. To take the main dynamic effects of the rotor into account, the low pressure turbine (LPT) and the low pressure compressor (LPC) are modelled using two disks (1 and 6 in Fig. 4b) connected by a small diameter hollow shaft (7) supported by a roller (2) and a ball bearing (5) on the turbine and compressor side respectively. Both supports are connected to the stator by two sets of four bars (3 and 4) subject to bending when the rotor moves laterally. A similar support configuration was already proposed by Holmes and Sykes [29] to test the lateral vibration of aero engines rotors equipped with squeeze film dampers. The inertia and stiffness properties are set to reproduce the main dynamic behaviour of the low pressure shaft taking into account the rotational speed limitation (Ω_{max}=7000 rpm) and

the dimensional constraints (max axial length=700 mm, max diameter of the disks=200 mm). The lateral dynamics of the full size low pressure shaft is characterized by the first two critical speeds in the operating speed range while the vibrations occurring at the third critical speed should not affect the lateral motion of the rotor in the working range. This means that the first two critical speeds (ω_{cr1}, ω_{cr2}) of the reduced size rotating machine may occur at about 2500 rpm and 4800 rpm while the third critical speed (ω_{cr3}) should be out of the speed range (about twice the max rotational speed) to avoid the contribution of higher order harmonics in the working range. Moreover, the first and the second critical speeds may be characterized by the bouncing of the LPC and LPT supports respectively. Additionally, the vibration amplitude cannot be higher than 0.7 mm in the whole speed range being in the present case lower than 1 mm the allowed radial displacement of the turbine and compressor blade arrays. This means that the vibration motion at the first and second critical speeds should be damped in order to satisfy such a requirement.

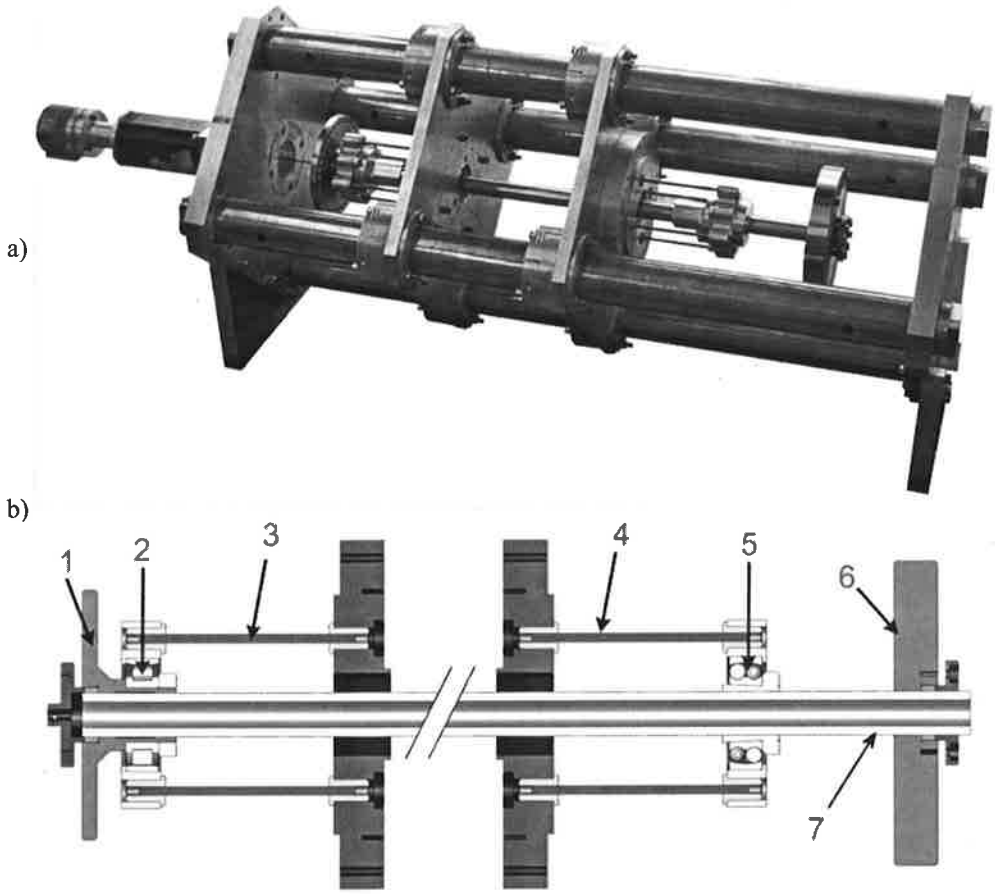


Figure 4: Rotordynamics test rig. (a) picture; (b) section view of the rotor of the machine and of the elastic supports. (1) Low pressure turbine (LPT) disk, (2) LPT roller bearing, (3) LPT beam support, (4) Low pressure compressor (LPC) beam support, (5) LPC ball bearing, (6) LPC disk, (7) hollow shaft.

Following the above mentioned specifications, the design leads to a rotor with a total mass of 4.15 kg and a polar/transverse moment of inertia ratio of 1/27. The required stiffness of 300 kN/m at both the supports is provided by a set of four bars having a length of 75 mm and a diameter of 4

mm. To satisfy the limitation of the vibration amplitude at $\omega_{cr1}, \omega_{cr2}$, an equivalent viscous damping of 50 and 20 Ns/m is required at the LPC and LPT support respectively.

The trade off analysis of the dimensional specifications and of the rotor lateral dynamic behaviour has been carried out with the support of DYNROT, a FE code specific for rotordynamics.

7. DESIGN OF THE DAMPERS

The design criterion for AMD was based on the force it should be able to supply, assuming the force generated by the damper should counteract the unbalance force. To justify this statement consider a Jeffcott rotor. Its equation of motion in complex coordinates is [11]

$$m\ddot{z} + c\dot{z} + kz = m\varepsilon\Omega^2 e^{i\Omega t} \tag{5}$$

Only nonrotating damping has been included in the equation, since only synchronous whirling will be considered. During critical speed crossing, elastic and inertia forces balance with each other and then damping forces must counteract unbalance forces. Note that the larger the damping coefficient is, the smaller is the velocity needed to supply the required force and, since the frequency is known, the amplitude of whirling. While in an AMB the bearing must supply a force large enough to support all forces acting on the rotor (static and dynamic loads), in AMD electromagnetic forces must, in the worst situation, counteract only the unbalance force $m\varepsilon\Omega^2$ while crossing the critical speeds.

Eq. (5) holds only for a Jeffcott rotor, but this reasoning can be generalized for multi d.o.f. rotors considering each mode: the modal forces due to the dampers must counteract modal unbalance forces for each mode at the crossing of the relevant critical speed. This implies that dampers must act in locations where the amplitude at the relevant modes is not too small or, in other words, damper must not be close to the nodes of the mode shapes.

The forces at the LPT and LPC supports of the RTR, computed using an unbalance grade of 6.3, are respectively of 4.3 N and 11.1 N at the maximum speed. The most conservative condition is verified when the unbalance has 180° phase shift between LPT and LPC. Since TEMDs should provide the required damping in order to limit vibration amplitude within the required range while crossing the critical speed, a preliminary investigation was performed to identify the damping ratio ζ to have a maximum displacement of 0.7mm with an actuator airgap of 1mm. The results are ζ = 0.00434 and ζ = 0.0052 for the LPT and LPC respectively. The electromagnetic dampers were then accordingly designed.

8. DESIGN RESULTS AND TRADE-OFF

A set of AMB, AMD and TEMD were designed for the test rig. The main parameters of the dampers are reported in Tables 2 and 3. In all cases heteropolar configurations were chosen. The overall geometry of the bearings and of the dampers was that of an 8-poles electric motor. In the case of the dampers the low force generated by the actuators suggests a copper mass optimization instead of the typical optimization for the maximum magnetic flux.

The total actuator masses for the RTR are: AMB 1.393 kg, AMD 0.487 kg, TEMD 0.476 kg.

9. CONCLUSIONS

The literature review of the damping devices used in rotating machines and in particular in aero engines as alternative to traditional squeeze film dampers underline how a large effort has been devoted to study and develop electrorelogical and magnetorelogical squeeze film dampers even if they cannot avoid some drawbacks (ageing, wear, fine control of the performances) which are

intrinsic in fluid film devices. The results of almost two decades of research work are not so satisfactory for industrial applications.

		LPT AMD	LPC AMD
Required Force	[N]	4.3	11.1
Actuator Force	[N]	4.4	11.7
Teeth Width	[mm]	2	2
Teeth Axial Length	[mm]	11	15
Copper Turns	-	180	252
Maximum Current	[A]	4.42	4.42
Actuator External Diameter	[mm]	62	70
Iron mass (each axis)	[kg]	0.011	0.017
Copper mass (each axis)	[kg]	0.035	0.058
Total Actuator Mass	[kg]	0.186	0.303
Estimated Coil Resistance	[Ohm]	0.36	0.60
Estimated Power Dissipation	[W]	7.1	11.7

Table 2. Main design parameters for the RTR AMDs.

		LPT TEMD	LPC TEMD
Actuator AirGap	[mm]	1.00	1.00
Maximum Displacement	[mm]	0.70	0.70
Required Zita	[--]	0.0043	0.0052
Related Critical Speed	[rad/s]	493	260
Effective Zita	[--]	0.0046	0.0052
Effective Critical Speed	[rad/s]	N/A	N/A
Effective Electrical Pole	[rad/s]	599	412
Required Power	[W]	1.50	1.45
Effective Spring Stiffness	[N/m]	305000	307000
Supply Voltage	[V]	1.50	1.50
Resistance (Total)	[Ohm]	1.50	1.552
Inductance	[mH]	0.00250	0.00377
Effective Induction (B)	[T]	0.74	0.70
Teeth Width	[mm]	4	5
Teeth Axial Length	[mm]	8	10
Nr. of Turns	[-]	352.44	345.78
Wire Diameter	[mm]	0.5	0.55
Current	[A]	1.00	0.97
Current Density	[A/mm^2]	5.09	4.07
Actuator Ext. Diameter	[mm]	68	76
Iron Mass	[kg]	0.019	0.033
Coil Mass	[kg]	0.029	0.039
Total Actuator Mass	[kg]	0.190	0.287
Estimated Coil Resistance	[Ohm]	1.50	1.37

Table 3. Main design parameters for the RTR TEMDs.

Since the beginning of the new century, the interest in electromechanical actuators has grown. The results of preliminary analysis of both active and on semi-active devices are promising. Further work is needed to investigate the actual potential of such devices in terms of force density, even if

the main effort may be devoted to study electromagnetic actuators related to the effective dynamic requirements of aero engines. This medium term goal is within the aim of building what is usually referred to as a 'more electric engine', i.e. a turbojet that relies less and less on lubricated devices like gearboxes to drive ancillary equipment (using instead electric transmission) or squeeze film dampers. A more distant goal is the construction of an 'all electric' engine, that is completely free from lubricated devices and uses a total magnetic suspension of the spools.

A research line at the Mechatronics Laboratory of the Politecnico di Torino is devoted to the study and development of electromagnetic actuators to supply non rotating damping in rotating machines. The preliminary results on the modeling of transformer eddy current dampers and on the definition of a design procedure to exploit the effective force density of these actuators are here reported. They seem to be more powerful than motional configurations in the field of aero engines as they can be used in active mode to supply additional forces during critical maneuvering conditions. Preliminary results on a laboratory test bench are promising even if a deep trade off analysis is required to evaluate the effective applicability to industrial applications. This topic will be investigated in future works.

As predicted, AMD and TEMD configurations are much less bulky and heavy than AMBs. Another interesting conclusion is that the AMD and TEMD strategies lead to similar results, showing that in rotating machines TEMDs offer advantages over the more common MEMDs.

Absence of lubrication, with the connected ancillary euipment, lower temperature dependence, higher flexibility and the possibility of working with different strategies make semiactive electromagnetic dampers, particularly of the transformer type a very interesting altermative to the traditional squeeze film and elastomeric dampers in rotating machinery applications.

10. ACKNOWLEDGMENTS

The present research has been carried on within the ADVACT project supported by the sixth research framework program of the European Union.

11. REFERENCES

1. Rankine W.J. Centrifugal Whirling of Shafts, *Engineer*, XXVI (Apr. 9, 1869).
2. Föppl A., Das Problem Der Laval'shen Turbinewelle, *Civilingenieur*, 41, (1895), 332-342.
3. Jeffcott H.H., Lateral Vibration of Loaded Shafts in the Neighbourhood of a Whirling Speed – the Effect of Want of Balance, *Phil. Mag.*, 37, (1919), 304-314.
4. Belluzzo G., *Le turbine a vapore ed a gas*, Hoepli, Milano, 1905.
5. Stodola A., *Dampf- und Gas-turbinen*, Springer, Berlin, 1924.
6. Lamb H. Southwell R.V., The vibrations of a spinning disk, *Proceedings of the Royal Society of London*, 99 (1291), 272-280.
7. Campbell W., Protection of Steam Turbine Disk Wheels from Axial Vibration, *Trans. ASME*, 46, (1924), 31-160.
8. Prohl M.A., A General Method for Calculating Critical Speeds of Flexible Rotors, *Journal Appl. Mech*, (1945).
9. Genta G., On a Persisting Misunderstanding on the Role of Hysteretic Damping in Rotordynamics, *Journal of Vibration and Acoustics*, Vol. 126, July 2004, 469-471.
10. Genta G., On the Stability of Rotating Blade Arrays, *Journal of Sound and Vibration*, 273, 2004, pp. 805-836.
11. Genta G., *Dynamics of Rotating Systems*, Springer, New York, 2005.
12. Ahn Y.K., Yang B. , Morishita S., Directional Controllable Squeeze Film Damper Using Electro-Rheological Fluid, *ASME Journal of Vibration and Acoustics*, Vol. 124, pp. 105-109.

13. Vance, J. M., Ying, D., 2000, Experimental Measurements of Actively Controlled Bearing Damping with an Electrorheological fluid, *ASME Journal of Engineering for Gas Turbines and Power*, Vol. 122, pp 337, 344..
14. Vance, J. M., Ying, D., Nikolajsen, J. L., 2000, Actively Controlled Bearing Dampers for Aircraft Engine Applications, *Journal of Engineering for Gas Turbines and Power*-Transaction of the ASME, vol. 122, pp. 466-472.
15. Tonoli, A., Carabelli, S., Amati, N., 2003, Design of semiactive vibration dampers for automotive applications, *Proceedings of the International Workshop Robotics and Mems for Vehicle Systems*, Roma, pp. 99-116.
16. Kasarda M., Johnson M., Imlach J., Mendoza H., Kirk G., Bash T., Applications of a Magnetic Bearing Acting as an Actuator In Conjunction with Conventional Support Bearings *Proceedings of the 9th Int. Symposium on Magnetic Bearings.*
17. Crandall, S. H., Karnopp, D. C., Kurtz, E. F., Pridmore-Brown, E. C., 1968, *Dynamics of Mechanical and Electromechanical Systems*, New York: McGraw-Hill.
18. Meisel, J., 1984, *Principles of Electromechanical Energy Conversion* Malabar, Florida: Robert Krieger.
19. Graves, K. E., Toncich, D., Iovenitti, P. G., 2000, Theoretical comparison of the motional and transformer EMF device damping efficiency, *Journal of Sound and Vibration*, Vol. 233, No. 3, pp 441-453.
20. Tonoli, A., Amati, N., Padovani M., 2003, Progetto di smorzatori e giunti elettromagnetici per alberi a gomiti, *Proc. of the XXIII AIAS Conf.*, Salerno, 3-6.
21. Nagaya, K., 1984, On a Magnetic Damper Consisting of a Circular Magnetic Flux and a Conductor of Arbitrary Shape. Part I: Derivation of the Damping Coefficients, *Journal of Dynamic Systems, Meas. and Control*, vol. 106, pp. 46-51.
22. Nagaya, K., Karube, Y., 1989, A Rotary Magnetic Damper or Brake Consisting of a Number of Sector Magnets and a Circular Conductor, *Journal of Dynamic Systems Measurement and Control*, Vol. 111, pp. 97-104.
23. Karnopp, D., 1989, Permanent magnets linear motors used as variable mechanical damper for vehicle suspension, *Vehicle System Dynamics*, Vol. 18, pp. 187-200.
24. Karnopp, D. C., Margolis, D. L., Rosenberg, R. C., 1990, *System dynamics: a unified approach*, J. Wiley & Sons.
25. Kligerman Y., Gottlieb O., 1998, Dynamics of a Rotating System with a Nonlinear Eddy-Current Damper, *Journal of Vibration and Acoustics*, Transaction of the ASME, Vol. 120, pp. 848-853.
26. Kligerman Y., Grushkevich A., Darlow M.S., 1998, Analytical and experimental evaluation of instability in rotordynamics system with electromagnetic eddy-current damper, *Journal of Vibration and Acoustics*, Transaction of the ASME, Vol. 120, pp. 272-278.
27. Amati N., Carabelli S., Macchi P., Silvagni M., Tonoli A., 2006, Transformer Eddy Current Dampers for the Vibration Control of Rotatine Machines, submitted to the *8th Biennial ASME Conference on Engineering System Design and Analysis*, Torino.
28. Carabelli S., Macchi P., Silvani M., Tonoli A., Visconti M., 2005, Rotordynamics signature for embedded systems, *ISCORMA 3*, Cleveland, Ohio.
29. Holmes R., Sykes J.E.H., 1996, The Vibration of an aero-engine rotor incorporating two squeeze-film dampers, Proceedings of the Institution of Mechanical Engineers, Part G: Journal of Aerospace Engineering, vol. 210, pp. 39-51.

RECENT DEVELOPMENTS IN MEASUREMENT, MODELLING AND SIMULATION OF TURBULENT FLOWS

ARNE V. JOHANSSON
Department of Mechanics, KTH
SE-100 44 Stockholm, SWEDEN

The present talk will give a brief overview of four different topics in turbulence research that are studied in various projects in our turbulence research group at the department of mechanics at KTH in Stockholm. Two of the topics are experimental and two concern direct numerical simulation of turbulent flows.

We have studied turbulent separation and its control in a plane asymmetric diffuser by use of extensive PIV and LDV measurements. This has also been combined with some computational work based on recently developed turbulence models. Vortex generators have been used in the experiments for separation control. This was also studied by use of time-dependent (quasi-steady) model computations where a detailed computational model for the vortex generators was developed and used to illustrate the difference in timescales for the establishment of the separation bubble after control was removed compared to that for the corresponding removal of the separation after insertion of the vortex generators.

In a collaboration with prof Y. Tsuji, Univ. of Nagoya, the first measurements of pressure fluctuation statistics in high Reynolds turbulent boundary layers were achieved recently in the MTL wind-tunnel at KTH. The results comprise both pressure fluctuation intensities and spectra of pressure fluctuations from positions inside the turbulent boundary layer.

In an ongoing project we study the effects of rapid system rotation on wall bounded turbulence through direct numerical simulation (DNS) of plane turbulent channel flow subject to system rotation around the spanwise axis. A characteristic feature of this flow case is the damping of the turbulence on the stabilized side along with an enhanced vertical mixing on the destabilized side of the channel. By varying the rate of system rotation we have been able to illustrate many of the characteristic features of rotational effects on turbulence. We have also shown that the entire flow becomes laminar for very high rates of rotation. This limit for absolute stability is identified and the entire range of rotation numbers are covered by simulations.

In a Swedish national collaboration program on combustion research we have contributed with a DNS study of near-wall mixing in a plane wall jet. The code used for this case is fully compressible, but so far the computational studies have been restricted to studies of mixing of a passive scalar in the flow at a Mach number of 0,5. Velocity statistics have been compared to experiments and e.g. scalar fluxes, scalar fluctuation intensities, and scalar dissipation rate have been determined.

IX Finnish Mechanics Days
Lappeenranta University of Technology, 13 – 14 June, 2006

COMPUTATIONAL ENGINE RESEARCH

Franz X. Tanner

Computational Science and Engineering Research Institute
Michigan Technological University
Houghton, MI 49931-1295, U.S.A.

E-mail: tanner@mtu.edu
http://www.math.mtu.edu/~tanner

ABSTRACT

Environmental concerns, health issues and the limited resources of fossil fuels are the main driving forces behind today's engine research. The objectives of this research include the understanding and description of the flow, spray and combustion processes in order to determine their influence on fuel efficiency, power output and pollution formation. Computer simulations are an expedient and economical way to contribute to the realization of these goals. In this talk, the mathematical formulation of dispersed multiphase flows used in engine simulations will be outlined, followed by a discussion of some of the author's modeling and simulation activities.

The gas phase is described by the Reynolds/Favre averaged conservation equations for mass, species, momentum and energy, and includes a k-ε-based turbulence model. The liquid phase is model by means of a stochastic discrete droplet method which is coupled to the gas phase via source terms. In addition, there are several reaction mechanisms which describe the heat release and the emissions formation. The discussion of the author's model developments focus on the Cascade Atomization and Drop Breakup (CAB) model and the Least Squares Fitted Ignition Transport (LIT) model. In addition, applications of these models to engine simulations will be discussed.

Also, a recently developed optimization method will be presented where engine operating conditions are sought which minimize the fuel consumption while meeting legislative emission mandates. The optimization is performed by a steepest decent method utilizing an adaptive cost function together with a backtracking algorithm for the line search. The adaptive cost function is based on the penalty method where the penalty parameter is updated before every line search depending on the distance of the current emissions from the target values. The optimization is performed over a normalized parameter space which is defined by the parameters to be optimized. This optimization has lead to a new injection concept, the asynchronous fuel injection. In this method, the fuel is injected through multiple nozzle orifices, each orifice having its own injection geometry and injection timing. This asynchronous fuel injection can achieve a low fuel consumption while meeting the desired emission standards.

MATALA-ASTEISET KUORIELEMENTIT YLEISELLÄ NELIKULMIOVERKOLLA

A. NIEMI ja J. PITKÄRANTA

Matematiikan laitos
PL 1100
02015 Teknillinen korkeakoulu
sähköposti: antti.h.niemi@tkk.fi

TIIVISTELMÄ

Eräs laskennallisen mekaniikan vanhimmista haasteista on konstruoida matala-asteinen kuorielementti, joka välttäisi niin kutsutun lukkiutumisilmiön ohuen kuoren tapauksessa ja olisi muutenkin luotettava. Tunnetuimpia tällaisista yrityksistä lienevät ADINA-ohjelmiston MITC4 sekä NASTRAN-ohjelmiston QUAD4. Elementtien suorakulmaiset versiot ovatkin osoittautuneet sekä käytännössä että teoriassa melko hyvin toimiviksi. Tässä työssä pyrimme selvittämään, missä määrin menestys perustuu elementin suorakaidemuotoon ja mitä on tehtävissä yleisellä isoparametrisella nelikulmioverkolla. Tilannetta voidaan analysoida matemaattisesti yksinkertaistetun matalan kuoren mallin avulla, joka on analoginen Reissnerin ja Mindlinin laattamallin kanssa. Lähtökohdaksi otetaan tällöin kaksiulotteisen kuorimallin tavallinen bilineaarinen elementtiapproksimaatio, johon liittyviä venymiä muokataan numeerisesti lukkiutumisen välttämiseksi. Analyysi perustuu energianormissa mitatun virheen jakoon kahteen ortogonaaliseen komponenttiin, approksimaatio- ja konsistenssivirheeseen.

1 JOHDANTO

Yleisten kuorirakenteiden analysointiin liittyvät vaikeudet ovat saaneet aikaan sekaannusta ongelman parissa työskentelevien matemaatikkojen ja insinöörien keskuudessa. Hankaluuksia on aiheuttanut erityisesti numeerisen mallin taustalla olevan kuorimallin valinta. Käytännön kuorielementit nimittäin yleensä "degeneroidaan" kiinteistä kolmiulotteisista elementeistä kuoren paksuussuunnassa tehtävien kinemaattisten oletusten avulla, kun taas matemaattinen virheanalyysi on toistaiseksi onnistunut ainoastaan elementtiapproksimaatioille, jotka perustuvat klassisiin kaksiulotteisiin kuorimalleihin. Vaikuttaisi kuitenkin siltä, että viime aikona nämä kaksi koulukuntaa ovat lähentyneet toisiaan, kun eri mallien välistä suhdetta on tutkittu ja kiinnostus dimensionaalisesti redusoituja malleja kohtaan on kasvanut, katso erityisesti [2].

Otamme lähtökohdaksi Reissnerin ja Naghdin mukaan nimetyn yksinkertaistetun matalan kuoren mallin, joka huomioi kuoren poikittaiset leikkausmuodonmuutokset kalvo- ja taipumamuodonmuutosten ohella. Tarkastelemme kuorimallin bilineaarisia elementtiapproksimaatioita perustuen tavanomaiseen energiaperiaatteeseen ja muokattuihin venymälausekkeisiin. Elementin leikkauslukkiutuminen voidaan välttää luontevasti muokkaamalla leikkausvenymiä, kuten analogisessa MITC4-elementissä. Kalvo- eli membraanilukkiutumisen

välttäminen ei sen sijaan ole läheskään yhtä suoraviivaista paitsi suorakulmaisen elementin tapauksessa, jolloin MITC4:ään liittyvä kuoren geometrian isoparametrinen bilineaarinen approksimaatio vastaa tarkkojen kalvovenymien sopivaa keskiarvoistamista kussakin elementissä [6, 7]. Yleisellä nelikulmioverkolla MITC4:n tulkinta on tällä hetkellä epäselvä. Tässä artikkelissa tarkastelemme kahta isoparametrista elementtiskeemaa matalalle kuorelle saadaksemme teoreettisen käsityksen tilanteesta, mistä voi olla hyötyä myös käytännössä.

Seuraavassa luvussa esittelemme tutkimuksen lähtökohtana olevan kuorimallin. Tarkasteltavat elementtialgoritmit määritellään luvussa 3 ja virheanalyysin periaatteet käsitellään luvussa 4. Yksinkertaisen malliongelman avulla saatuja numeerisia tuloksia esitellään luvussa 5.

2 KUORIMALLI

Tarkastelemme matalaa kuorta, jonka keskipinta koordinaateissa x, y ilmaistuna on alue $\Omega \subset \mathbb{R}^2$ ja joka koostuu homogeenisesta materiaalista (kimmokerroin E, Poissonin luku ν). Keskipinnan siirtymävektorikenttä $\mathbf{u}$ voidaan kirjoittaa muodossa

$$\mathbf{u}(x,y) = (u(x,y), v(x,y), w(x,y), \theta(x,y), \psi(x,y)) \quad (x,y) \in \Omega,$$

missä u, v edustavat siirtymiä koordinaattien x, y suunnissa, w on keskipinnan poikittaissiirtymä ja $\boldsymbol{\theta} = (\theta, \psi)$ on keskipinnan normaalin rotaatiovektori.

Käytämme samoja lyhennysmerkintöjä $(\cdot,\cdot)$ ja $\|\cdot\|$ sekä vektori- että tensoriarvoisten funktioiden $L_2(\Omega)$-sisätulolle ja normille eli

$$(\boldsymbol{\sigma}, \boldsymbol{\varepsilon}) = \int_\Omega \boldsymbol{\sigma} : \boldsymbol{\varepsilon}\, dxdy = \int_\Omega \sum_{i,j=1}^{2} \sigma_{ij}\epsilon_{ij}\, dxdy, \quad \|\boldsymbol{\sigma}\| = (\boldsymbol{\sigma}, \boldsymbol{\sigma})^{1/2}$$

tensoriarvoisille funktioille $\boldsymbol{\sigma}, \boldsymbol{\varepsilon}$ ja

$$(\boldsymbol{\eta}, \boldsymbol{\rho}) = \int_\Omega \boldsymbol{\eta} \cdot \boldsymbol{\rho}\, dxdy = \int_\Omega \sum_{i=1}^{2} \eta_i\rho_i\, dxdy, \quad \|\boldsymbol{\eta}\| = (\boldsymbol{\eta}, \boldsymbol{\eta})^{1/2}$$

vektoriarvoisille funktioille $\boldsymbol{\eta}, \boldsymbol{\rho}$ vastaavasti. Klassisen Reissnerin ja Naghdin mallin mukaan kuoren venymäenergia määräytyy kvadraattisena funktionaalina

$$\mathcal{A}(\mathbf{u},\mathbf{u}) = D\left(\mathcal{C}\boldsymbol{\beta}(\mathbf{u}), \boldsymbol{\beta}(\mathbf{u})\right) + kD\left(\boldsymbol{\rho}(\mathbf{u}), \boldsymbol{\rho}(\mathbf{u})\right) + \frac{Dt^2}{12}\left(\mathcal{C}\boldsymbol{\kappa}(\mathbf{u}), \boldsymbol{\kappa}(\mathbf{u})\right), \tag{1}$$

missä tensorit $\boldsymbol{\beta} = (\beta_{ij})$, $\boldsymbol{\kappa} = (\kappa_{ij})$, $i,j = 1,2$ kuvaavat kalvo- ja taipumavenymiä vektorin $\boldsymbol{\rho} = (\rho_i)$, $i = 1,2$ kuvatessa leikkausvenymiä. Parametri t on kuorenpaksuus, joka oletetaan pieneksi verrattuna alueen Ω halkaisijaan. Lisäksi $D = Et/(1-\nu^2)$ ja $k = \gamma(1-\nu)/2$, missä γ on nk. leikkauskorjaustekijä. Isotrooppisen materiaalin tapauksessa kalvo- ja taipumajännitysten konstitutiiviset yhtälöt voidaan kirjoittaa muodossa

$$\mathcal{C}\boldsymbol{\beta} = \nu\,\mathrm{tr}(\boldsymbol{\beta})\mathbf{I} + (1-\nu)\boldsymbol{\beta} \quad \text{ja} \quad \mathcal{C}\boldsymbol{\kappa} = \nu\,\mathrm{tr}(\boldsymbol{\kappa})\mathbf{I} + (1-\nu)\boldsymbol{\kappa}.$$

Tarkastelemme yksinkertaistettua matalan kuoren mallia, jossa venymien ja siirtymien välinen yhteys ilmaistaan muodossa

$$\begin{aligned}
&\beta_{11} = \frac{\partial u}{\partial x} + aw, \quad \beta_{22} = \frac{\partial v}{\partial y} + bw, \quad \beta_{12} = \frac{1}{2}\left(\frac{\partial u}{\partial y} + \frac{\partial v}{\partial x}\right) + cw,\\
&\rho_1 = \theta - \frac{\partial w}{\partial x}, \qquad \rho_2 = \psi - \frac{\partial w}{\partial y},\\
&\kappa_{11} = \frac{\partial \theta}{\partial x}, \qquad \kappa_{22} = \frac{\partial \psi}{\partial y}, \qquad \kappa_{12} = \frac{1}{2}\left(\frac{\partial \theta}{\partial y} + \frac{\partial \psi}{\partial x}\right),
\end{aligned} \tag{2}$$

joka on yksinkertaisin mahdollinen tässä yhteydessä [11].

Kuoren geometria kuvataan kalvovenymissä esiintyvillä kolmella vakioparametrilla a, b, c, kun taas leikkaus- ja taipumavenymät määritellään itse asiassa samoin kuin Reissnerin ja Mindlinin laattamallissa. Parametrit $a = b_{11}$, $b = b_{22}$, ja $c = b_{12} = b_{21}$ ovat keskipinnan kaarevuustensorin komponentit.

Jos $\mathcal{L}$ on lineaarinen funktionaali vastaten keskipinnalla Ω vaikuttavaa ulkoista kuormaa, niin kuoriongelma on minimoida

$$\mathcal{F}(\mathbf{u}) = \frac{1}{2}\mathcal{A}(\mathbf{u}, \mathbf{u}) - \mathcal{L}(\mathbf{u})$$

energia-avaruudessa $\mathbf{u} \in \mathcal{U}$. Kun jäykän kappaleen liikettä vastaavat siirtymät on eliminoitu esimerkiksi alueen Ω reunalla $\partial\Omega$ asetettujen kinemaattisten rajoitusehtojen avulla, on $\mathcal{U}$ Hilbertin avaruus sisätulona $\mathbf{u}, \mathbf{v} \to \mathcal{A}(\mathbf{u}, \mathbf{v})$ vastaten energianormia

$$\|\mathbf{u}\| = \sqrt{\mathcal{A}(\mathbf{u}, \mathbf{u})}. \tag{3}$$

Kuoren muodonmuutoksen asymptoottinen luonne rajalla $t \to 0$ riippuu pääasiassa puhtaista taipumakentistä koostuvasta avaruudesta

$$\mathcal{W} = \{\mathbf{u} \in \mathcal{U} \mid \boldsymbol{\beta}(\mathbf{u}) = \mathbf{0} \;\&\; \boldsymbol{\rho}(\mathbf{u}) = \mathbf{0}\}. \tag{4}$$

Kuoriongelma voidaan tällöin luokitella taipumadominoiduksi, jos kuorma kykenee virittämään puhtaita taipumamoodeja eli $\mathcal{L}(\mathbf{v}) \neq 0$ ainakin yhdellä $\mathbf{v} \in \mathcal{W}$. Tarkastelemme myös käytännön sovellutusten kannalta yleisempää tilannetta, jossa kuoren puhdas taipuminen on estetty kinemaattisilla rajoitusehdoilla. Tyypillisiä näille (koville) kalvodominoiduille muodonmuutostiloille ovat voimakkaat reunahäiriöt lähellä reunaa $\partial\Omega$. Reunahäiriöiden systemaattinen tutkimus on aloitettu artikkelissa [11], ja niihin liittyviä numeerisia lukkiutumisilmiöitä on hiljattain tarkasteltu artikkelissa [8]. Tässä työssä keskitymme kuitenkin sileiden taipuma- ja kalvodominoitujen muodonmuutostilojen elementtiapproksimaatioihin.

3 ELEMENTTIAPPROKSIMAATIO

Olkoon $\mathcal{T}_h$ (monikulmio)alueen Ω jako konvekseihin erillisiin nelikulmioihin, joiden halkaisija on enintään h. Tavanomaisista oletuksista koskien jaon $\mathcal{T}_h$ säännöllisyyttä seuraa, että jokaisella $K \in \mathcal{T}_h$ on olemassa kääntyvä bilineaarikuvaus $\mathbf{F}_K : \hat{K} \to K$, missä $\hat{K} = [-1, 1] \times [-1, 1]$ on referenssineliö. Käytämme jatkossa kuvauksen $\mathbf{F}_K$ Jacobin matriisille $\mathbf{J}_{\mathbf{F}_K}$ merkintää

$$\mathbf{J}_{\mathbf{F}_K} = \begin{bmatrix} \dfrac{\partial x}{\partial \hat{x}} & \dfrac{\partial x}{\partial \hat{y}} \\ \dfrac{\partial y}{\partial \hat{x}} & \dfrac{\partial y}{\partial \hat{y}} \end{bmatrix}.$$

Tarkastelemme tästä eteenpäin matalan kuoren numeerisia malleja, joissa kutakin siirtymäkomponenttia approksimoidaan tavanomaisilla isoparametrisilla bilineaarielementeillä. Jos $Q_1(\hat{K})$ on bilineaarisista kantafunktioista koostuva referenssiavaruus, niin globaali elementtiavaruus määritellään muodossa $\mathcal{U}_h = \mathcal{V}_h^5 \cap \mathcal{U}$, missä

$$\mathcal{V}_h = \left\{ v : \Omega \to \mathbb{R} \mid v|_K = \hat{v} \circ \mathbf{F}_K^{-1},\ \hat{v} \in Q_1(\hat{K}) \text{ jokaisella } K \in \mathcal{T}_h \right\}.$$

Lukkiutumisilmiön välttämiseksi tutkimme kuoren venymäenergian (1) elementtiverkosta $\mathcal{T}_h$ riippuvia modifikaatioita

$$\mathcal{A}(\mathbf{u}, \mathbf{u}) \hookrightarrow \mathcal{A}_h(\mathbf{u}, \mathbf{u})$$

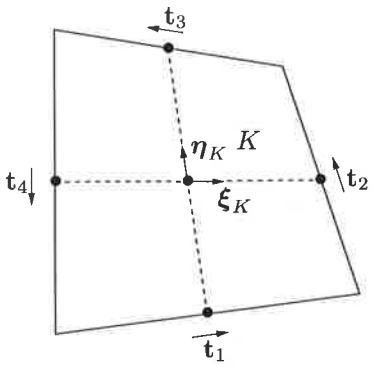
elementtiavaruuden $\mathcal{U}_h$ jäädessä kuitenkin ennalleen. Modifikaatiot perustuvat numeerisiin reduktio-operaattoreihin $\mathbf{\Pi}_h, \mathbf{\Lambda}_h$, jotka kohdistuvat kalvo- ja leikkausvenymiin muodossa

$$\boldsymbol{\beta} \hookrightarrow \mathbf{\Pi}_h \boldsymbol{\beta} \quad \text{ja} \quad \boldsymbol{\rho} \hookrightarrow \mathbf{\Lambda}_h \boldsymbol{\rho}, \tag{5}$$

kun taas taipumavenymiä ei muuteta. Algoritmeissa $\mathbf{\Pi}_h$ ja $\mathbf{\Lambda}_h$ määritellään interpolaatio-operaattoreina, jotka liittyvät seuraaviin (globaaleihin) vapausasteisiin:

$$\begin{cases} \text{arvot } \mathbf{t}_e^T \boldsymbol{\beta} \mathbf{t}_e \text{ ja } \mathbf{t}_e^T \boldsymbol{\rho} \text{ kunkin sivun } e \in \mathcal{T}_h \text{ keskipisteessä,} \\ \text{arvot } \boldsymbol{\xi}_K^T \boldsymbol{\beta} \boldsymbol{\eta}_K \text{ kunkin nelikulmion } K \in \mathcal{T}_h \text{ keskiössä,} \end{cases} \tag{6}$$

missä $\mathbf{t}_e$ on sivun e yksikkötangenttivektori ja $\boldsymbol{\xi}_K, \boldsymbol{\eta}_K$ ovat kunkin elementin K keskiössä, kuvauksen $\mathbf{F}_K$ avulla määriteltyjä yksikkövektoreita (kuva 1).



Kuva 1: Muokattujen kalvo- ja leikkausvenymien paikalliset vapausasteet elementissä $K \in \mathcal{T}_h$.

Tutkimme kaikkiaan kolmea erilaista formulaatiota:

3.1 Q4

Valinta $\mathbf{\Pi}_h = \mathbf{I}, \mathbf{\Lambda}_h = \mathbf{I}$ johtaa tavanomaiseen elementtimenetelmään, jossa energia minimoidaan sellaisenaan. Tämä menetelmä toimii vertailukohtana modifioiduille elementtialgoritmeille.

3.2 Q4-TC

Perustuen MITC-lähestymistapaan määrittelemme kussakin $K \in \mathcal{T}_h$ vektorielementtiavaruuden muotoa

$$\mathbf{S}(K) = \left\{ \boldsymbol{\eta} = \mathbf{J}^T_{\mathbf{F}_K^{-1}} \left(\hat{\boldsymbol{\eta}} \circ \mathbf{F}_K^{-1} \right) \doteqdot \mathcal{S}(\hat{\boldsymbol{\eta}}),\ \hat{\boldsymbol{\eta}} \in \mathbf{S}(\hat{K}) \right\} \tag{7}$$

ja tensorielementtiavaruuden muotoa

$$\mathbf{M}(K) = \left\{ \boldsymbol{\sigma} = \mathbf{J}^T_{\mathbf{F}_K^{-1}} \left(\hat{\boldsymbol{\sigma}} \circ \mathbf{F}_K^{-1} \right) \mathbf{J}_{\mathbf{F}_K^{-1}} \doteqdot \mathcal{M}(\hat{\boldsymbol{\sigma}}),\ \hat{\boldsymbol{\sigma}} \in \mathbf{M}(\hat{K}) \right\}. \tag{8}$$

Redusoitujen leikkausvenymien referenssiavaruus voidaan määritellä muodossa

$$\mathbf{S}(\hat{K}) = \{ \hat{\boldsymbol{\eta}} = (c_1 + c_2 \hat{y}, c_3 + c_4 \hat{x}),\ c_i \in \mathbb{R} \}, \tag{9}$$

vertaa [5, 1]. Vastaavasti luonnollinen referenssiavaruus redusoiduille kalvovenymille on muotoa

$$\mathbf{M}(\hat{K}) = \left\{ \hat{\boldsymbol{\sigma}} = \begin{bmatrix} c_1 + c_2\hat{y} & c_3 \\ c_3 & c_4 + c_5\hat{x} \end{bmatrix},\ c_i \in \mathbb{R} \right\}, \tag{10}$$

katso [9].

Reduktio-operaattorit $\boldsymbol{\Pi}_h, \boldsymbol{\Lambda}_h$ voidaan nyt konstruoida seuraavasti: Olkoot $\hat{\boldsymbol{\sigma}}$ ja $\hat{\boldsymbol{\eta}}$ referenssielementillä $\hat{K}$ määriteltyjä tensori- ja vektorikenttiä, jolloin vapausasteet (6) määräävät yksikäsitteisesti redusoidut kentät $\boldsymbol{\Pi}_{\hat{K}}\hat{\boldsymbol{\sigma}} \in \mathbf{M}(\hat{K})$ ja $\boldsymbol{\Lambda}_{\hat{K}}\hat{\boldsymbol{\eta}} \in \mathbf{S}(\hat{K})$. Tämän jälkeen vastaavat lokaalit projektiot $\boldsymbol{\Pi}_K, \boldsymbol{\Lambda}_K$ mielivaltaiselle elementille $K \in \mathcal{T}_h$ määräytyvät muunnoskaavojen (7),(8) avulla muodossa

$$\boldsymbol{\Pi}_K = \mathcal{M}_K \circ \boldsymbol{\Pi}_{\hat{K}} \circ \mathcal{M}_K^{-1} \quad \text{ja} \quad \boldsymbol{\Lambda}_K = \mathcal{S}_K \circ \boldsymbol{\Lambda}_{\hat{K}} \circ \mathcal{S}_K^{-1}.$$

Nämä voidaan ilmaista myös kommutoivana kaaviona:

$$\begin{array}{ccc} \hat{\boldsymbol{\sigma}}, \hat{\boldsymbol{\eta}} & \xrightarrow{\boldsymbol{\Pi}_{\hat{K}}, \boldsymbol{\Lambda}_{\hat{K}}} & \boldsymbol{\Pi}_{\hat{K}}\hat{\boldsymbol{\sigma}}, \boldsymbol{\Lambda}_{\hat{K}}\hat{\boldsymbol{\eta}} \\ {\scriptstyle \mathcal{M}_K, \mathcal{S}_K}\downarrow & & \downarrow{\scriptstyle \mathcal{M}_K, \mathcal{S}_K} \\ \boldsymbol{\sigma}, \boldsymbol{\eta} & \xrightarrow[\boldsymbol{\Pi}_K, \boldsymbol{\Lambda}_K]{} & \boldsymbol{\Pi}_K\boldsymbol{\sigma}, \boldsymbol{\Lambda}_K\boldsymbol{\eta} \end{array}$$

Globaalit operaattorit $\boldsymbol{\Pi}_h, \boldsymbol{\Lambda}_h$ määritellään tavanomaisesti:

$$(\boldsymbol{\Pi}_h\boldsymbol{\beta})\,|_K = \boldsymbol{\Pi}_K(\boldsymbol{\beta}\,|_K) \quad \text{ja} \quad (\boldsymbol{\Lambda}_h\boldsymbol{\rho})\,|_K = \boldsymbol{\Lambda}_K(\boldsymbol{\rho}\,|_K) \quad \text{jokaisella } K \in \mathcal{T}_h.$$

Huomautamme, että poikittaiset leikkausmuodonmuutokset käsitellään tässä, kuten analogisessa MITC4-laattaelementissä. Erityisesti vakioleikkausmuodonmuutostilat esitetään tarkasti, varmistaen että approksimaatio-ominaisuus

$$\|\boldsymbol{\rho} - \boldsymbol{\Lambda}_h\boldsymbol{\rho}\| \leq Ch|\boldsymbol{\rho}|_1 \tag{11}$$

on voimassa. Tässä $|\boldsymbol{\rho}|_1$ määritellään muodossa

$$|\boldsymbol{\rho}|_1 = \left\{ \sum_{i=1}^{2} \|\nabla\rho_i\|^2 \right\}^{1/2}. \tag{12}$$

Lisäksi on voimassa

$$\boldsymbol{\Lambda}_h\nabla w = \nabla w \quad \forall w \in \mathcal{V}_h, \tag{13}$$

koska isoparametriselle bilineaariselle funktiolle w pätee että $\nabla(w \circ \mathbf{F}_K) = \mathbf{J}_{\mathbf{F}_K}^{-T}\hat{\nabla}\hat{w}$ sekä $\hat{\nabla}\hat{w} \in S(\hat{K})$, jolloin $\nabla w\,|_K \in \mathbf{S}(K)$. Nämä ovat tärkeitä ominaisuuksia menetelmän stabiilisuuden kannalta.

Toisaalta voimme todeta, että $\boldsymbol{\Pi}_h\widetilde{\boldsymbol{\beta}} = \widetilde{\boldsymbol{\beta}}$ vakiokalvomuodonmuutostilalle $\boldsymbol{\beta} = \widetilde{\boldsymbol{\beta}}$ ainoastaan suunnikkaista koostuvilla elementtiverkoilla. Toinen ongelma yleisillä verkoilla syntyy derivaattatermien muokkaamisesta komponenteissa β_{11}, β_{22}, koska menetelmän stabiilisuus suorakaideverkoilla perustuu olennaisesti näiden termin säilyttämiseen ennallaan [10, 4].

3.3 Q4-R

Päästäksemme eroon edellisen menetelmän selvistä heikkouksista tarkastelemme suorempaa lähestymistapaa paikallisten elementtiavaruksien $\mathbf{M}(K)$ ja $\mathbf{S}(K)$ määrittelemiseksi. Olkoon $\mathbf{M}(K)$ muotoa

$$\mathbf{M}(K) = \mathbf{P}_0(K) \oplus \mathbf{V}(K), \tag{14}$$

missä $\mathbf{P}_0(K)$ koostuu symmetrisistä vakiotensoreista ja $\mathbf{V}(K)$ valitaan seuraavasti. Olkoon $\Xi_K = \Xi_K(x,y)$ isoparametrinen bilineaarinen funktio elementillä K, joka häviää elementin kunkin sivun keskipisteessä ja saa arvon ± 1 elementin kärjissä eli

$$\Xi_K(x,y) = \hat{x}\hat{y} \circ \mathbf{F}_K^{-1}.$$

Asetamme

$$\mathbf{V}(K) = \text{span}\left\{ \begin{bmatrix} \dfrac{\partial \Xi_K}{\partial x} & \dfrac{1}{2}\dfrac{\partial \Xi_K}{\partial y} \\ \dfrac{1}{2}\dfrac{\partial \Xi_K}{\partial y} & 0 \end{bmatrix}, \begin{bmatrix} 0 & \dfrac{1}{2}\dfrac{\partial \Xi_K}{\partial x} \\ \dfrac{1}{2}\dfrac{\partial \Xi_K}{\partial x} & \dfrac{\partial \Xi_K}{\partial y} \end{bmatrix} \right\}, \tag{15}$$

jolloin $\dim \mathbf{M}(K) = 5$, ja huomaamme, että *kaikki* derivaattatermit tensorissa $\boldsymbol{\beta}$ säilyvät ennallaan tällä valinnalla. Kalvovenymätensori voidaan nimittäin kirjoittaa muodossa

$$\boldsymbol{\beta}(\mathbf{U}, w) = \boldsymbol{\varepsilon}(\mathbf{U}) + \mathbf{b}w, \tag{16}$$

missä $\mathbf{U} = (u, v)$ ja $\boldsymbol{\varepsilon}(\mathbf{U})$ on $\mathbf{U}$:n gradientin symmetrinen osa. Näemme, että jos $u, v \in \mathcal{V}_h$, niin $\boldsymbol{\varepsilon}(\mathbf{U})\,|_K \in \mathbf{M}(K)$ ja siis

$$\boldsymbol{\Pi}_h \boldsymbol{\varepsilon}(\mathbf{U}) = \boldsymbol{\varepsilon}(\mathbf{U}) \quad \forall u, v \in \mathcal{V}_h. \tag{17}$$

Ominaisuus $\mathbf{P}_0(K) \subset \mathbf{M}(K)$ määritelmässä (14) tarvitaan takaamaan approksimaatio-ominaisuus

$$\|\boldsymbol{\beta} - \boldsymbol{\Pi}_h \boldsymbol{\beta}\| \leq Ch|\boldsymbol{\beta}|_1, \tag{18}$$

missä

$$|\boldsymbol{\beta}|_1 = \left\{ \sum_{i,j=1}^{2} \|\nabla \beta_{ij}\|^2 \right\}^{1/2}$$

kuten kaavoissa (11) ja (12).

Redusoitujen leikkausvenymien avaruus $\mathbf{S}(K)$ voidaan määritellä vastaavalla tavalla, mutta kuten olettaa sopii, lopputulos on sama kuin määrittelyillä (7) ja (9).

4 VIRHEANALYYSI

Modifikaatioiden (5) tarkoitus on suurentaa avaruutta

$$\mathcal{W}_h = \{\mathbf{u}_h \in \mathcal{U}_h \mid \boldsymbol{\beta}(\mathbf{u}_h) = \mathbf{0} \;\&\; \boldsymbol{\rho}(\mathbf{u}_h) = \mathbf{0}\}$$

numeerisesti lukkiutumisen välttämiseksi taipumadominoiduissa kuoren muodonmuutostiloissa. Toisin sanoen päämääränä on heikentää energianormia (3) siten, että puhtaita taipumamoodeja voitaisin approksimoida riittävän tarkasti. Toisaalta muunnetun energianormin

$$\|\mathbf{u}\|_h = \sqrt{\mathcal{A}_h(\mathbf{u}, \mathbf{u})}, \quad \mathbf{u} \in \mathcal{U} \tag{19}$$

tulee olla riittävän vahva, jotta menetelmä olisi stabiili myös kalvodominoiduissa muodonmuutostiloissa. Minimaalinen stabiilisuusehto on että

$$\mathbf{u} \in \mathcal{U}_h \;\&\; \|\mathbf{u}\|_h = 0 \quad \Rightarrow \quad \mathbf{u} = \mathbf{0}$$

eli että $\|\cdot\|_h$ todella määrittelee normin elementtiavaruudessa $\mathcal{U}_h$. Menetelmän Q4-R suoraviivainen stabiilisuusanalyysi osoittaa, että

$$\|\mathbf{u}_h\|_h \geq ct\|\mathbf{u}_h\| \quad \forall \mathbf{u}_h \in \mathcal{U}_h. \tag{20}$$

Vastaava tulos on todennäköisesti voimassa myös menetelmälle Q4-TC, mikä tarkoittaa, että $\|\cdot\|_h$ on yleisesti ottaen melko heikko normi elementtiavaruudessa $\mathcal{U}_h$.

Aloitamme kvantitatiivisemman virheanalyysin määrittelemällä virheindikaattorin

$$e = \frac{\|\mathbf{u} - \mathbf{u}_h\|_h}{\|\mathbf{u}\|} \tag{21}$$

ja artikkelia [10] jäljitellen jakamalla kokonaisvirheen kahteen osaan, approksimaatio- ja konsistenssivirheeseen. Tällöin

$$e^2 = e_a^2 + e_c^2, \tag{22}$$

missä approksimaatiovirhe e_a voidaan kirjoittaa muodossa

$$e_a = \frac{\|\mathbf{u} - \tilde{\mathbf{u}}_h\|_h}{\|\mathbf{u}\|} = \min_{\mathbf{v}\in\mathcal{U}_h} \frac{\|\mathbf{u} - \mathbf{v}\|_h}{\|\mathbf{u}\|} \tag{23}$$

ja konsistenssivirhe e_c muodossa

$$e_c = \frac{\|\mathbf{z}_h\|_h}{\|\mathbf{u}\|} = \sup_{\mathbf{v}\in\mathcal{U}_h, \|\mathbf{v}\|_h\neq 0} \frac{\mathcal{L}_h(\mathbf{v})}{\|\mathbf{u}\|\|\mathbf{v}\|_h}. \tag{24}$$

Bilineaarista kuorielementtiä voidaan tässä yhteydessä pitää lukkiutumattomana, jos

$$e_a, e_c \sim Ch, \tag{25}$$

missä vakio C on tasaisesti rajoitettu kuorenpaksuuden t suhteen kaikissa kuoren muodonmuutostiloissa. Taipumadominoidussa tapauksessa ratkaisevaa on, pystyvätkö algoritmien Q4-TC ja Q4-R numeeriset modifikaatiot parantamaan tavallisen bilineaarielementin Q4 approksimaatiokykyä, jolle pätee arvio $e_a = \mathcal{O}(h/t)$. Koska molemmat formulaatiot käyttävät samoja vapausasteita redusoiduille venymille, voidaan päätellä, että niiden approksimaatioominaisuudet ovat käytännössä yhtenevät, koska $\mathcal{W}_h^{\text{Q4-TC}} = \mathcal{W}_h^{\text{Q4-R}}$. Toisaalta eroja todennäköisesti syntyy kalvodominoiduissa muodonmuutoksissa, jolloin konsistenssivirheestä muodostuu dominoiva virhetermi. Yleistetyn kuormafunktionaalin $\mathcal{L}_h$ suuruus kaavassa (24) riippuu nimittäin pääasiassa venymien muodoista.

Algoritmin Q4-R konsistenssivirhefunktionaali voidaan kirjoittaa auki yhtälöitä (13) ja (17) hyväksi käyttäen muodossa

$$\mathcal{L}_h(\mathbf{v}) = \mathcal{G}_h^1(\mathbf{v}) + \mathcal{G}_h^2(\mathbf{v}) + \mathcal{G}_h^3(\mathbf{v}) + \mathcal{G}_h^4(\mathbf{v}) \tag{26}$$

kaikilla $\mathbf{v} = (\tilde{u}, \tilde{v}, \tilde{w}, \boldsymbol{\phi}) \in \mathcal{U}_h$, missä

$$\begin{aligned}
\mathcal{G}_h^1(\mathbf{v}) &= (\mathbf{T} - \boldsymbol{\Pi}_h\mathbf{T}, \boldsymbol{\Pi}_h\boldsymbol{\beta}(\mathbf{v}))\,, \\
\mathcal{G}_h^2(\mathbf{v}) &= (\mathbf{T}, \mathbf{b}\tilde{w} - \boldsymbol{\Pi}_h(\mathbf{b}\tilde{w}))\,, \\
\mathcal{G}_h^3(\mathbf{v}) &= (\mathbf{q} - \boldsymbol{\Lambda}_h\mathbf{q}, \boldsymbol{\Lambda}_h\boldsymbol{\rho}(\mathbf{v}))\,, \\
\mathcal{G}_h^4(\mathbf{v}) &= (\mathbf{q}, \boldsymbol{\phi} - \boldsymbol{\Lambda}_h\boldsymbol{\phi})\,,
\end{aligned} \tag{27}$$

ja missä edelleen $\mathbf{T} = \mathcal{C}\boldsymbol{\beta}(\mathbf{u})$ ja $\mathbf{q} = k\boldsymbol{\rho}(\mathbf{u})$ ovat tarkan ratkaisun kalvo- ja leikkausjännitys.

Käyttäen aluksi Cauchyn ja Schwarzin epäyhtälöä ja ominaisuutta (18) voidaan $\mathcal{G}_h^1$ rajoittaa muodossa

$$|\mathcal{G}_h^1(\mathbf{v})| \leq \|\mathbf{T} - \boldsymbol{\Pi}_h\mathbf{T}\|\|\boldsymbol{\Pi}_h\boldsymbol{\beta}(\mathbf{v})\| \leq Ch|\mathbf{T}|_1\|\mathbf{v}\|_h.$$

Kolmannelle termille saadaan vastaava arvio ominaisuuden (11) avulla,

$$|\mathcal{G}_h^3(\mathbf{v})| \leq Ch|\mathbf{q}|_1\|\mathbf{v}\|_h,$$

mutta kahdelle jäljelle jäänelle termille saamme ainoastaan ylärajat

$$|\mathcal{G}_h^2(\mathbf{v})| \leq Ch|\tilde{w}|_1\|\mathbf{T}\| \leq C\frac{h}{t}\|\mathbf{T}\|\|\mathbf{v}\|_h, \tag{28}$$

ja

$$|\mathcal{G}_h^4(\mathbf{v})| \leq C\frac{h}{t}\|\mathbf{q}\|\|\mathbf{v}\|_h \tag{29}$$

heikon stabiilisuuden (20) takia.

Yhdistämällä tulokset saadaan konsistenssivirheelle arvio

$$e_c \leq C_1(\mathbf{u})h + C_2(\mathbf{u})\frac{h}{t}, \tag{30}$$

missä

$$C_1(\mathbf{u}) = C\frac{|\mathbf{T}|_1 + |\mathbf{q}|_1}{\|\mathbf{u}\|} \quad \text{ja} \quad C_2(\mathbf{u}) = C\frac{\|\mathbf{T}\| + \|\mathbf{q}\|}{\|\mathbf{u}\|}.$$

Koska leikkausvenymät ovat tyypillisesti merkityksettömiä, kun t on pieni, voidaan päätellä, että konsistenssivirheen dominoiva osa syntyy termistä $\mathcal{G}_h^2$ hajotelmassa (26).

Verrattuna optimaaliseen konvergenssinopeuteen (25) ylläoleva virhearvio ennustaa pahaa konsistenssivirheen vahvistumista menetelmälle Q4-R, kun $t \to 0$. Oletettavasti menetelmä Q4-TC toimii vielä huonommin, katso kommentit luvun 3.2 lopussa. Suorakaideverkolla tilanne kuitenkin muuttuu, koska menetelmät ovat tällöin keskenään lähes ekvivalentteja. Itseasiassa Q4-TC redusoituu artikkelissa [9] tarkastelluksi menetelmäksi, jota on tutkittu hiljattain esimerkiksi artikkeleissa [3, 4, 8].

Menetelmän Q4-R virhearviota (30) voidaan parantaa olettamalla ainoastaan elementtien suorakaidemuoto. Reduktio-operaattorilla $\mathbf{\Pi}_K$ on nimittäin tällöin ominaisuus

$$\int_K \mathbf{\Pi}_K\boldsymbol{\sigma}\, dxdy = \int_K \boldsymbol{\sigma}\, dxdy$$

jokaisella bilineaarisella tensorikentällä $\boldsymbol{\sigma}$ ja suorakaiteella $K \in \mathcal{T}_h$.

Näin ollen $(\mathbf{I}-\mathbf{\Pi}_h)(\mathbf{b}\tilde{w})$ on ortogonaalinen sellaisia alueen Ω tensorikenttiä vastaan, jotka ovat paloittain vakioita, ja voimme kirjoittaa funktionaalin $\mathcal{G}_h^2$ kehitelmässä (27) muodossa

$$\mathcal{G}_h^2(\mathbf{v}) = \left(\mathbf{T} - \mathbf{R}_h\mathbf{T}, \mathbf{b}\tilde{w} - \mathbf{\Pi}_h(\mathbf{b}\tilde{w})\right),$$

missä $\mathbf{R}_h$ on ortogonaalinen L_2-projektio paloittain vakioille. Koska $\mathbf{R}_h\mathbf{T}$ on $\mathbf{T}$:n paras approksimaatio paloittaisilla vakioilla, saadaan $\mathcal{G}_h^2$:lle arvio

$$|\mathcal{G}_h^2(\mathbf{v})| \leq C\frac{h^2}{t}|\mathbf{T}|_1\|\mathbf{v}\|_h$$

kaavan (28) sijaan. Koska termille $\mathcal{G}_h^4$ saadaan vastaava yläraja samanlaisella päättelyllä, tulee menetelmän Q4-R konsistenssivirheeksi suorakaideverkolla

$$e_c \leq C(\mathbf{u})\left(h + \frac{h^2}{t}\right), \tag{31}$$

missä nyt

$$C(\mathbf{u}) = C\frac{|\mathbf{T}|_1 + |\mathbf{q}|_1}{\|\mathbf{u}\|}.$$

5 NUMEERISET TULOKSET

Demonstroimme edellä esiteltyjen kuorielementtien suorituskykyä yksinkertaisen malliongelman avulla, jossa $\Omega = (0, 2\pi) \times (0, 2\pi)$ ja reunaehdot ovat kummassakin suunnassa periodiset. Ulkoinen kuormitus on kuoren keskipintaa vasten kohtisuora painejakauma

$$f(x, y) = \cos(2x)\cos(2y)$$

vastaten kuormafunktionaalia $\mathcal{L}(\mathbf{u}) = (f, w)$. Olettaen, että x, y ovat pääkaarevuuskoordinaatit eli että $c = 0$, tehtävän ratkaisu $\mathbf{u}$ on muotoa

$$\mathbf{u}(x, y) = \begin{bmatrix} U\sin(2x)\cos(2y) \\ V\cos(2x)\sin(2y) \\ W\cos(2x)\cos(2y) \\ \Theta\sin(2x)\cos(2y) \\ \Psi\cos(2x)\sin(2y) \end{bmatrix}, \tag{32}$$

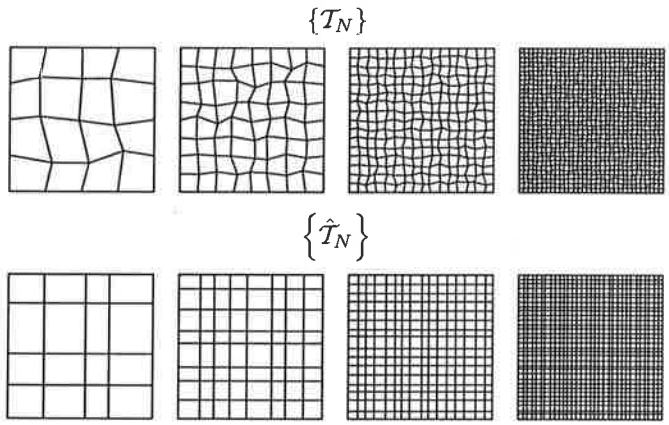
missä kertoimet U, V, W, Θ, Ψ määräytyvät energiaperiaatteesta.

Tarkastelemme kahta seuraavaa esimerkkiongelmaa, jotka edustavat erilaisia kuoren geometrioita:

A Tarkastellaan hyperbolista kuorta, missä $a = 1, b = -1$. Tämä ongelma on hyvä lukkiutumistesti, koska osoittautuu, että syntyvä muodonmuutos on taipumadominoitu.

B Tarkastellaan parabolista (sylinteri)kuorta, missä $a = 0, b = 1$. Syntyvä muodonmuutos on kalvodominoitu, joten tämä ongelman avulla voidaan tutkia menetelmien Q4-TC ja Q4-R stabiilisuutta sekä konsistenssivirhettä.

Valitsemme laskennalliseksi alueeksi neliön $\omega = (0, \pi/4) \times (0, \pi/4)$ ja huomioimme ratkaisun muodosta (32) seuraavat symmetria/antisymmetriaehdot oleellisina reunaehtoina reunalla $\partial\omega$. Käytämme laskennassa suorakaiteista koostuvia elementtiverkkoja $\{\hat{\mathcal{T}}_N\}$ ja yleisemmistä nelikulmioista koostuvia elementtiverkkoja $\{\mathcal{T}_N\}$, missä verkkoindeksi N saa molemmissa tapauksissa arvot $N = 4, 8, 16, 32$. Tässä N^2 on elementtien lukumäärä kussakin verkossa (kuva 2).



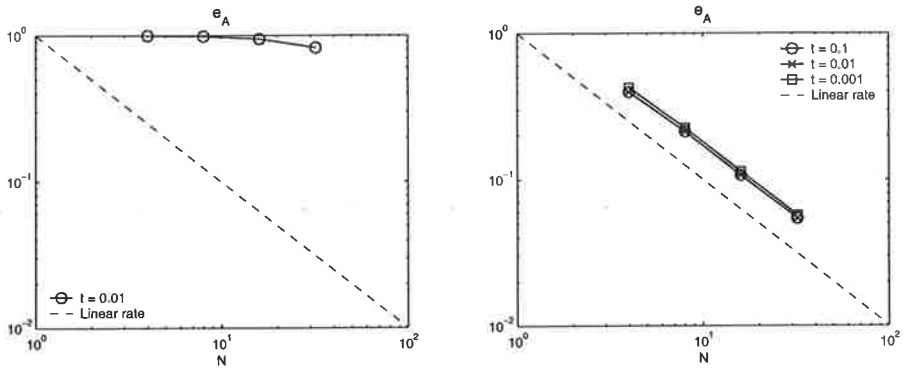
Kuva 2: Käytettävät elementtiverkot.

Asetamme Poissonin luvuksi $\nu = 0.3$, valitsemme $\gamma = 1$ ja D:n energiayksiköksi. Evaluoimme termit e_a ja e_c kokonaisvirheen hajotelmassa (22) eri ongelmissa käyttäen kuorenpaksuudelle arvoja 0.1, 0.01, ja 0.001.

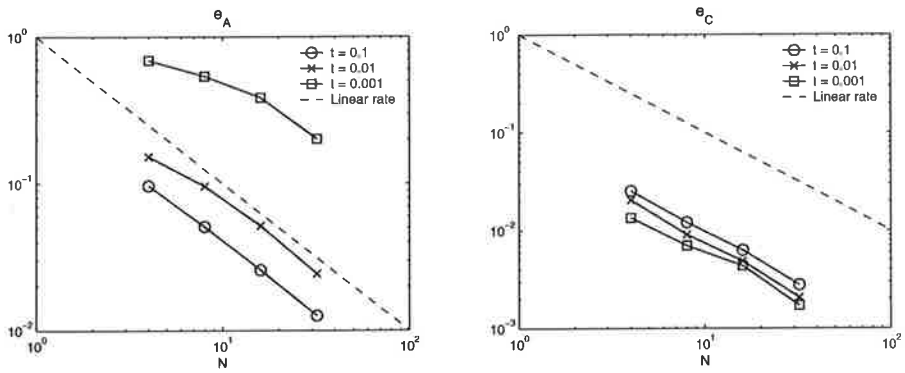
Kuvassa 3 on esitetty tavallisen elementtiapproksimaation Q4 virhe kummassakin malliongelmassa (nyt $e_c \equiv 0$). Kuten olettaa sopii suhteellinen virhe on lähes 100% taipumadominoidussa tapauksessa jo kuorenpaksuudella $t = 0.01$, kun taas menetelmän suorituskyky on optimaalinen kalvodominoidussa ongelmassa.

Algoritmit Q4-TC ja Q4-R sen sijaan osoittautuvat ekvivalenteiksi ongelmassa A, kuten ennustimme luvussa 4. Kuvassa 4 on esitetty Q4-R:n tulokset epäsäännöllisellä verkolla ja kuvassa 5 suorakaideverkolla. Parannus tavalliseen elementtimenetelmään verrattuna on selkeä. Suorakaideverkolla tulokset ovat erinomaisia, mutta yleisellä verkolla approksimaatiovirheen e_a konvergenssi huononee selvästi, kun $t \to 0$. Konsistenssivirhe on tässä esimerkissä merkityksetön.

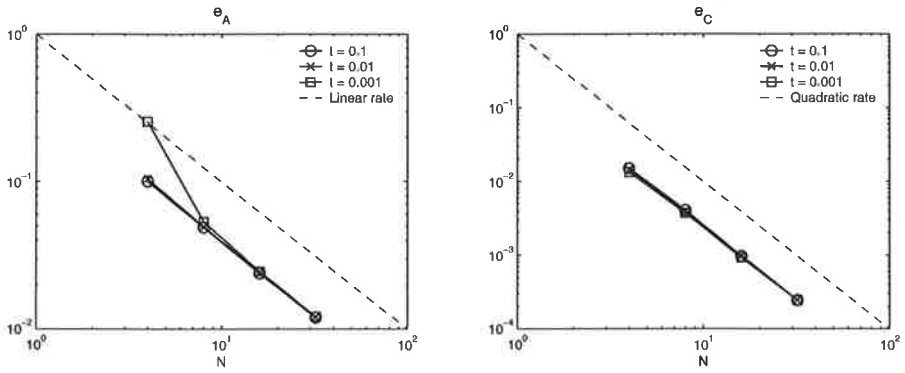
Menetelmien Q4-TC ja Q4-R ero yleisellä nelikulmioverkolla tulee selkeästi esiin toisessa esimerkissä. Q4-TC:n konsistenssivirhe pysyy käytännössä vakiotasolla kuvassa 6 riippumatta elementtien lukumäärästä N, kun taas Q4-R toimii karkeasti virhearvion (30) mukaisesti (kuva 7). Suorakaideverkolla konsistenssivirheen suppenemisnopeus näyttää kvadraattiselta (kuvat 5 ja 8), mikä on hyvin sopusoinnussa parannetun virhearvion (31) kanssa.



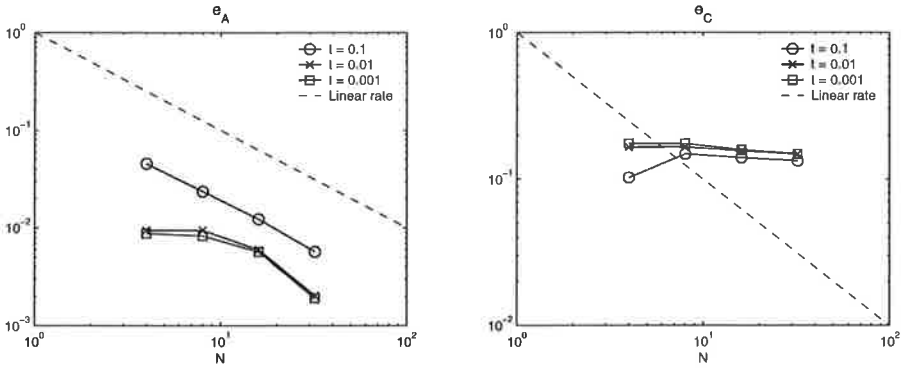
Kuva 3: Q4: approksimaatiovirhe testiongelmissa A ja B.



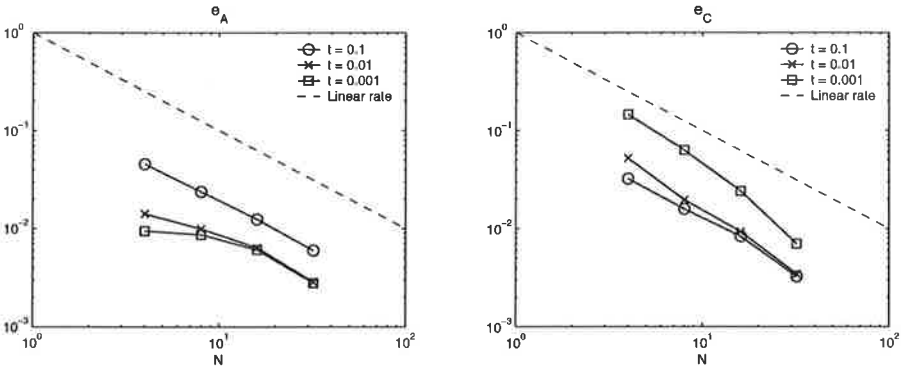
Kuva 4: Q4-R ongelmassa A: approksimaatio- ja konsistenssivirhe epäsäännöllisellä verkolla.



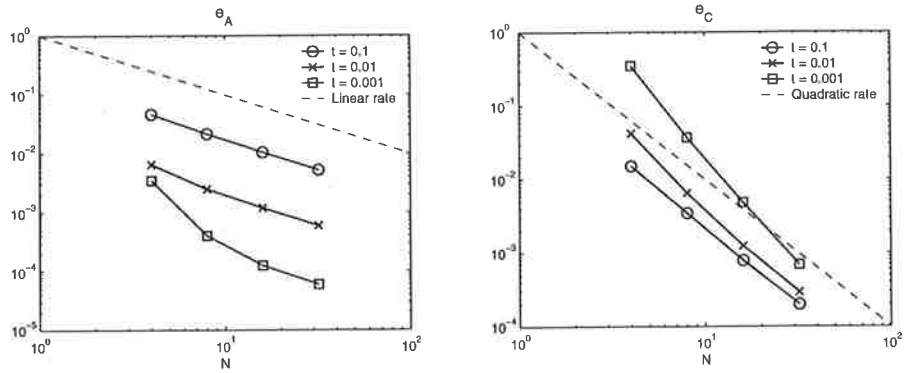
Kuva 5: Q4-R ongelmassa A: approksimaatio- ja konsistenssivirhe suorakaideverkolla.



Kuva 6: Q4-TC ongelmassa B: approksimaatio- ja konsistenssivirhe epäsäännöllisellä verkolla.



Kuva 7: Q4-R ongelmassa B: approksimaatio- ja konsistenssivirhe epäsäännöllisellä verkolla.



Kuva 8: Q4-R ongelmassa B: approksimaatio- ja konsistenssivirhe suorakaideverkolla.

VIITTEET

[1] BATHE, K.-J., AND DVORKIN, E. N. A four-node plate bending element based on Mindlin/Reissner plate theory and a mixed interpolation. *Int. J. Numer. Meth. Engng 21* (1985), 367–383.

[2] CHAPELLE, D., OLIVEIRA, D., AND BUCALEM, M. MITC elements for a classical shell model. *Computers & Structures 81* (2003), 523–533.

[3] HAVU, V., AND PITKÄRANTA, J. Analysis of a bilinear finite element for shallow shells I: Approximation of inextensional deformations. *Math. Comp. 71* (2002), 923–943.

[4] HAVU, V., AND PITKÄRANTA, J. Analysis of a bilinear finite element for shallow shells II: Consistency error. *Math. Comp. 72* (2003), 1635–1653.

[5] HUGHES, T. J. R., AND TEZDUYAR, T. E. Finite Elements Based Upon Mindlin Plate Theory With Particular Reference to the Four-Node Bilinear Isoparametric Element. *J. Appl. Mech. 48* (1981), 587–596.

[6] MALINEN, M. On the classical shell model underlying bilinear degenerated shell finite elements. *Int. J. Numer. Meth. Engng 52* (2001), 389–416.

[7] MALINEN, M. On the classical shell model underlying bilinear degenerated shell finite elements: general shell geometry. *Int. J. Numer. Meth. Engng 55* (2002), 629–652.

[8] NIEMI, A., PITKÄRANTA, J., AND HAKULA, H. Benchmark computations on point-loaded shallow shells: Fourier vs. FEM. *To appear in Comput. Methods Appl. Mech. Engrg.*.

[9] PITKÄRANTA, J. The problem of membrane locking in finite element analysis of cylindrical shells. *Numer. Math. 61* (1992), 523–542.

[10] PITKÄRANTA, J. The first locking-free plane-elastic finite element: historia mathematica. *Comput. Methods Appl. Mech. Engrg. 190* (2000), 1323–1366.

[11] PITKÄRANTA, J., MATACHE, A.-M., AND SCHWAB, C. Fourier mode analysis of layers in shallow shell deformations. *Comput. Methods Appl. Mech. Engrg. 190* (2001), 2943–2975.

ADVANTAGES OF T-SPLINES IN SHAPE OPTIMIZATION

J. MÄKIPELTO

Institute of Applied Mechanics and Optimization
Tampere University of Technology
P.O. Box 589, FIN-33101 Tampere, Finland
e-mail: juha.makipelto@tut.fi

ABSTRACT

This paper compares T-spline surfaces to non-uniform rational B-spline (NURBS) surfaces with emphasis on the applications in shape optimization. NURBS surfaces are a de facto standard in computer aided geometric design and have been utilized in shape optimization, too. However, NURBS surfaces have some drawbacks, which T-spline surfaces seem to overcome.

1 INTRODUCTION

Most softwares of computer aided geometric design describe the geometry of the objects with NURBS surfaces, which have the favorable capability of precisely representing quadric surfaces, as well as free-form surfaces. A NURBS surface is defined by bivariate piecewise rational basis functions and a control net of weighted control points. The control net is bidirectional and it must be regular, so that in either of the directions each row of the control net has equal number of control points. Therefore, a typical NURBS surface has a large percentage of superfluous control points.

A generalization of NURBS surfaces, called T-splines [1], are capable of significantly reducing the number of superfluous control points. T-junctions, the origin of the term T-spline, are permitted in a control net, which means that rows of control points need not traverse the entire control net. In other words, a T-spline control net does not have to be topologically rectangular. Therefore, one and the same T-spline can have more control points in regions where precise control over shape is required, without excessive number of control points in less interesting regions. This property is especially beneficial in shape optimization, where each extraordinary control point in variable surface inflicts one or more extraordinary design variables, which hinder both the creation of the optimization model and the solution of the optimization problem.

T-splines support true local refinement, i.e., a single control point can be inserted into the control net without propagating an entire row of control points. Thus modification of shape optimization model is straightforward; control points can be readily added and removed locally. Another convenient feature of T-splines is that several surfaces can be merged into a single T-spline with desired continuity, and hence the geometry model for the problem of finding optimal fillet shape between two separate surfaces is effortless to create.

Section 2 gives a very brief description of NURBS surfaces, and Section 3 introduces

point based surfaces called PB-splines. Section 4 defines T-splines in a slightly more general setting than in [1]. Examples in Section 5 show that T-spline surfaces are worth examining in shape optimization.

2 NURBS SURFACES

In this section we briefly present NURBS surfaces, an interested reader is referred to the exhaustive book of Piegl and Tiller [2]. A NURBS surface of degree p in the parameter u direction and degree q in the parameter v direction is defined as

$$\mathbf{N}(u,v) = \frac{\sum_{i=0}^{n}\sum_{j=0}^{m}\mathcal{N}_{ip}(u)\mathcal{N}_{jq}(v)w_{ij}\mathbf{p}_{ij}}{\sum_{i=0}^{n}\sum_{j=0}^{m}\mathcal{N}_{ip}(u)\mathcal{N}_{jq}(v)w_{ij}} \qquad \begin{matrix} u_p \le u \le u_{r-p} \\ v_q \le v \le v_{s-q}, \end{matrix} \tag{1}$$

which is a bivariate vector-valued piecewise rational function. The $\mathcal{N}_{ip}(u)$ and $\mathcal{N}_{jq}(v)$ are the ith p-degree and jth q-degree polynomial B-spline basis functions defined on the knot vectors $U = \{u_0, u_1, \ldots, u_r\}$ and $V = \{v_0, v_1, \ldots, v_s\}$. The control points $\mathbf{p}_{ij}$ and their weights w_{ij} form a bidirectional weighted control net, which has $n+1$ and $m+1$ control points in the u and v directions respectively. In both of the parameter directions, the number of control points (or equally the number of basis functions), the number of knots, and the degree of the surface are related such that

$$\begin{aligned} r &= n + p + 1 \\ s &= m + q + 1. \end{aligned} \tag{2}$$

The bidirectional control net formed by the control points must be topologically rectangular, which means that the number of control points in each row of the net is equal. Consequently, each column of the net has equal number of control points.

In computer aided geometric design and optimization the definition (1) would be very inconvenient to use. Fortunately, rational curves and surfaces have an elegant geometric interpretation which enables efficient processes and compact data storage. The idea is based on *homogeneous coordinates*, which represent a rational surface in n-dimensional space as a polynomial surface in $(n+1)$-dimensional space. First we consider a control point in three-dimensional space $\mathbf{p} = (x, y, z)$ and its nonzero weight w, which are written in four-dimensional space as $\mathbf{p}^w = (wx, wy, wz, w) = (X, Y, Z, W)$. Now the original $\mathbf{p}$ can be extracted from $\mathbf{p}^w$ by dividing the first three coordinates by the fourth coordinate W. This is the same as perspective mapping from the origin to the hyperplane $W = 1$, denoted here by H

$$\mathbf{p} = H(\mathbf{p}^w) = H((X, Y, Z, W)) = \left(\frac{X}{W}, \frac{Y}{W}, \frac{Z}{W}\right). \tag{3}$$

The NURBS surface (1) has a counterpart given by

$$\mathbf{N}^w(u,v) = \sum_{i=0}^{n}\sum_{j=0}^{m}\mathcal{N}_{ip}(u)\mathcal{N}_{jq}(v)\mathbf{p}_{ij}^w \qquad \begin{matrix} u_p \le u \le u_{r-p} \\ v_q \le v \le v_{s-q}, \end{matrix} \tag{4}$$

where $\mathbf{p}_{ij}^w = (w_{ij}x_{ij}, w_{ij}y_{ij}, w_{ij}z_{ij}, w_{ij})$ are the four-dimensional control points. $\mathbf{N}^w(u,v)$ is a piecewise polynomial surface in four-dimensional space, from which the mapping (3) yields the three-dimensional NURBS surface, hence $\mathbf{N}(u,v) = H(\mathbf{N}^w(u,v))$.

3 PB-SPLINES

Tensor product B-spline surfaces, such as NURBS surfaces, use a topologically rectangular net of control points. The goal of Sederberg et al. [1] was to generalize B-spline surface to allow partial rows or columns of control points and they began by describing a surface whose control points are totally independent of each other. This surface is *point based* instead of grid based and therefore referred to as *PB-spline* . A PB-spline surface is defined over domain D by

$$\mathbf{P}(u,v) = \frac{\sum_{i=1}^{n} \mathcal{B}_i(u,v) w_i \mathbf{p}_i}{\sum_{i=1}^{n} \mathcal{B}_i(u,v) w_i} \qquad (u,v) \in D, \tag{5}$$

where the $\mathbf{p}_i$ constitute a set of control points. Contrary to the equation given in [1], the control points of the PB-spline (5) are weighted by the $w_i > 0$. The two restrictions on the domain D are that

$$\sum_{i=1}^{n} \mathcal{B}_i(u,v) > 0 \qquad \forall (u,v) \in D, \tag{6}$$

and D must be a single connected component. The blending functions $\mathcal{B}_i(u,v)$ are given by

$$\mathcal{B}_i(u,v) = \mathcal{N}^i_{0p}(u) \mathcal{N}^i_{0q}(v), \tag{7}$$

where the $\mathcal{N}^i_{0p}(u)$ and $\mathcal{N}^i_{0q}(v)$ are the first (and the only) pth and qth degree polynomial B-spline basis functions defined on the knot vectors $U^i = \{u^i_0, u^i_1, \ldots, u^i_{p+1}\}$ and $V^i = \{v^i_0, v^i_1, \ldots, v^i_{q+1}\}$ respectively. Hence, to specify a PB-spline, one must provide a set of control points and a pair of knot vectors for each control point.

The B-spline basis functions have local support, i.e., the ith p-degree basis function $\mathcal{N}_{ip}(u)$ is positive only on a restricted interval $u \in [u_i, u_{i+p+1}]$ and zero elsewhere. Consequently, $\mathcal{B}_i(u,v)$ is positive only on its influence domain $D_i = [u^i_0, u^i_{p+1}] \times [v^i_0, v^i_{q+1}]$ and zero elsewhere. Furthermore, if we define rational blending functions as

$$\mathcal{R}_i(u,v) = \frac{\mathcal{B}_i(u,v) w_i}{\sum_{i=1}^{n} \mathcal{B}_i(u,v) w_i} \qquad (u,v) \in D, \tag{8}$$

they are nonnegative and partition the unity

$$\mathcal{R}_i(u,v) \geq 0 \qquad \sum_{i=1}^{n} \mathcal{R}_i(u,v) \equiv 1 \qquad (u,v) \in D. \tag{9}$$

The PB-spline (5) can now be written as

$$\mathbf{P}(u,v) = \sum_{i=1}^{n} \mathcal{R}_i(u,v) \mathbf{p}_i \qquad (u,v) \in D. \tag{10}$$

On the basis of Equations (9) and (10) it is clear that PB-splines have the important convex hull property; $\mathbf{P}(u,v)$ lies in the convex hull of its control points $\mathbf{p}_i$.

The requirement (6) placed on the definition domain of PB-spline implies that $D \subset \{D_1 \cup D_2 \cup \ldots \cup D_n\}$, but D does not need to be rectangular. If $(u,v) \in D$ lies only in a

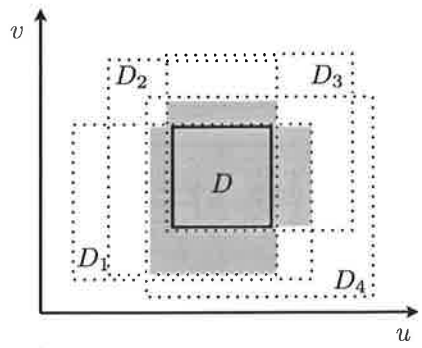


Figure 1: Influence domains of individual control points are marked with dotted line. The domain influenced by at least three control points is shaded with light gray. A possible choice for the definition domain D is marked with solid line.

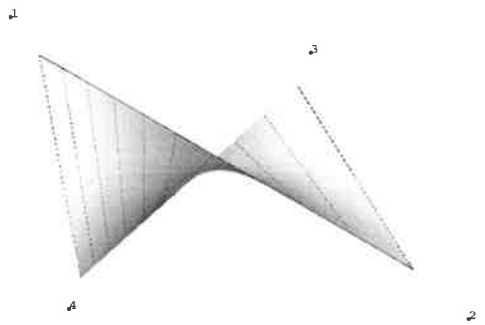


Figure 2: A PB-spline surface defined on four control points and their influence domains shown in Figure 1.

single influence domain D_i, then $\mathbf{P}(u,v) = \mathbf{p}_i$ due to the convex hull property. Similarly, if $(u,v) \in D$ lies only in three influence domains D_i, D_j, and D_k, then $\mathbf{P}(u,v)$ lies on the triangular face determined by $\mathbf{p}_i$, $\mathbf{p}_j$, and $\mathbf{p}_k$. Since PB-splines are typically employed in surface modeling, it is therefore recommended to have each $(u,v) \in D$ lie in at least three influence domains D_i. Figure 1 shows an example of influence domains for a PB-spline with four control points. Although all the D_i in Figure 1 are axis-aligned, generally influence domains do not have to be axis-aligned.

In the same way as with NURBS surfaces, homogeneous coordinates offer a convenient way of handling PB-spline surfaces. The control points $\mathbf{p}_i^w = (w_i x_i, w_i y_i, w_i z_i, w_i)$ define a PB-spline in four-dimensional space as

$$\mathbf{P}^w(u,v) = \sum_{i=1}^{n} \mathcal{B}_i(u,v)\mathbf{p}_i^w \qquad (u,v) \in D, \tag{11}$$

from which a point on the surface in three-dimensional coordinates is obtained by the mapping (3) as $\mathbf{P}(u,v) = H(\mathbf{P}^w(u,v))$.

4 T-SPLINES

A T-spline is a PB-spline for which the two knot vectors U^i and V^i for each control point $\mathbf{p}_i$ are derived from a rectangular control grid called T-mesh, which consists of vertices and edges. Each vertex in a T-mesh corresponds to a control point, and therefore we identify the vertices with the control points $\mathbf{p}_i$. Figure 3 shows an example of a T-mesh, where the vertices are marked with small circles and the edges are drawn as solid line segments. Edges are either horizontal or vertical, and they mostly lie between two vertices; those edges that have no vertices at the ends define boundary conditions for the T-spline. The term T-mesh stems from T-junctions that are allowed also in the interior of the grid, and herein a T-junction is a vertex shared by one horizontal and two vertical edges, or by one vertical and two horizontal edges. For example, in Figure 3 $\mathbf{p}_2$ is a T-junction, but $\mathbf{p}_3$ is not since it lies on the boundary of the T-mesh. If there are no T-junctions in a T-mesh, the T-spline reduces to a NURBS.

In addition to having a corresponding control point, every vertex has two knot values,

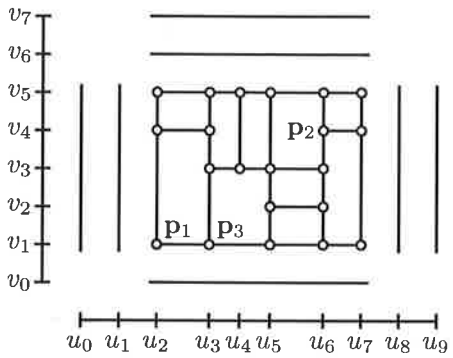


Figure 3: A T-mesh for a T-spline of third-degree in the u-direction and second-degree in the v-direction.

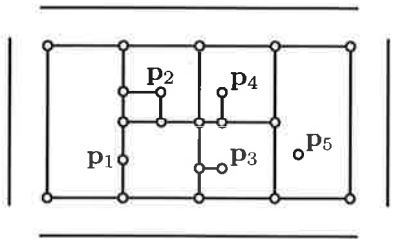


Figure 4: A T-mesh with an I-junction, an L-junction, two dead end vertices, and an isolated vertex.

one for surface parameter u and one for v. For example, in Figure 3 the vertex $\mathbf{p}_1$ has knots u_2 and v_1, and the $\mathbf{p}_2$ has knots u_6 and v_4. Similarly, every edge has three knot values; for example, the edge between $\mathbf{p}_1$ and $\mathbf{p}_3$ has the knot value v_1 in the knot interval $u \in [u_2, u_3]$.

Next we explain how the knot vectors for each vertex (and further for each control point) $\mathbf{p}_i$ are inferred from the T-mesh. Sederberg et al. [1] restrict their discussion to cubic T-splines, but we let the T-spline be of degree p in the u-direction. Then the knot vector is of the form $U^i = \{u_0^i, u_1^i, \ldots, u_{p+1}^i\}$, and the knot in the middle $u_{\lceil p/2 \rceil}^i$ is simply the knot value of the $\mathbf{p}_i$. Next consider a horizontal ray going from the $\mathbf{p}_i$ to the right; the knots following the middle knot $u_{\lceil p/2 \rceil}^i$ in U^i are given by the first vertical edges intersected by the ray. The other knots in U^i and V^i are found in the same way. For example, in Figure 3 the vertex $\mathbf{p}_1$ has knot vectors $U^1 = \{u_0, u_1, u_2, u_3, u_5\}$ and $V^1 = \{v_0, v_1, v_4, v_5\}$. $\mathbf{p}_2$ has knot vectors $U^2 = \{u_4, u_5, u_6, u_7, u_8\}$ and $V^2 = \{v_3, v_4, v_5, v_6\}$, and $\mathbf{p}_3$ has $U^3 = \{u_1, u_2, u_3, u_5, u_6\}$ and $V^3 = \{v_0, v_1, v_3, v_4\}$.

In their first paper on T-splines Sederberg et al. [1] restricted T-meshes to have only regular junctions (a vertex connecting four edges) and T-junctions. The way the knot vectors for each each vertex are obtained from the T-mesh does not necessitate such a restriction, and so in the follow-up paper [3] new junction types, which could be called I-junction and L-junction, are used. For example, in Figure 4 the vertex $\mathbf{p}_1$ is an I-junction and $\mathbf{p}_2$ an L-junction. In addition to T-, I-, and L-junctions used in [3], we have successfully used the two obvious vertex types still left in the repertoire. The first type could be called dead end vertex, see the vertices $\mathbf{p}_3$ and $\mathbf{p}_4$ in Figure 4 for example. The second type is a vertex isolated from edges, as the $\mathbf{p}_5$ in Figure 4.

Since a T-spline is basically a PB-spline, the properties introduced in Section 3 for PB-splines hold true for T-splines also. Therefore, T-spline basis functions are nonnegative and partition the unity, and consequently T-spline surfaces have the convex hull property. Furthermore, T-splines can be conveniently handled using the homogeneous coordinates and the four-dimensional form (11).

With respect to the relation between T-splines and NURBS, T-spline surfaces are a proper superset of NURBS surfaces, i.e., every NURBS is a special case of a T-spline, but not all T-splines are NURBS. However, every T-spline can be exactly converted into a *collection* of NURBS surfaces, and so there is an important forward-backward compatibility between T-spline and NURBS surfaces.

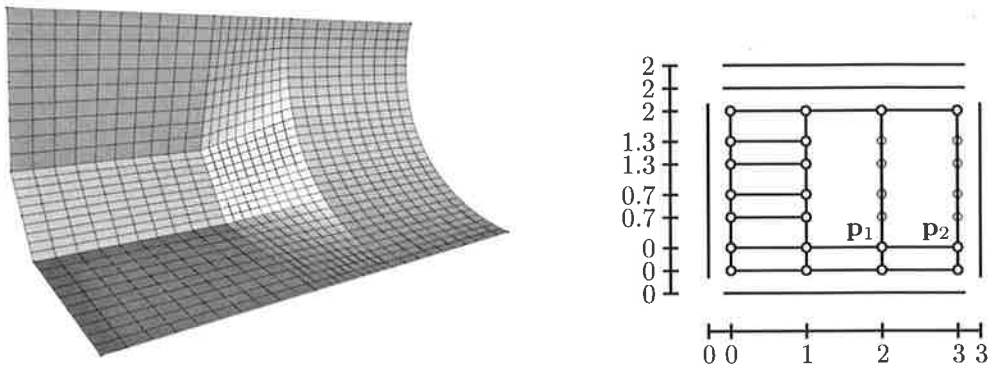


Figure 5: A linear × quadratic T-spline surface and its T-mesh. The same surface modeled as a NURBS surface would require eight more control points, which are drawn with light gray in the T-mesh.

5 EXAMPLES

In this section we give some examples that demonstrate the potential of the T-spline surfaces, especially in shape optimization. Figure 5 shows a T-spline surface and its T-mesh. The T-spline, linear in u-direction and quadratic in v-direction, joins a facet and a rounding surface. If this kind of transitional surface was modeled with a NURBS, it would require eight more control points. In addition to the burden of just having these extra control points in the model, their positioning and weighting in such a way that the round surface is exactly circular would be very laborious. Besides that, if for example the shape of the rounded part was to be optimized, the extra control point locations would have to be used as extra design variables in the optimization model. This would require more effort in both the model creation stage and the problem solution stage.

Figure 6 shows from two different angles a T-spline surface that is quadratic in both parameter directions. The T-spline forms a kind of pipe, which is circular in the left end and triangular in the right end. T-splines facilitate creation of sharp and smooth features in the same surface, and Figure 6 depicts how the transition between the features is fluent. Since T-splines take care of the transition zone more or less automatically, in optimization

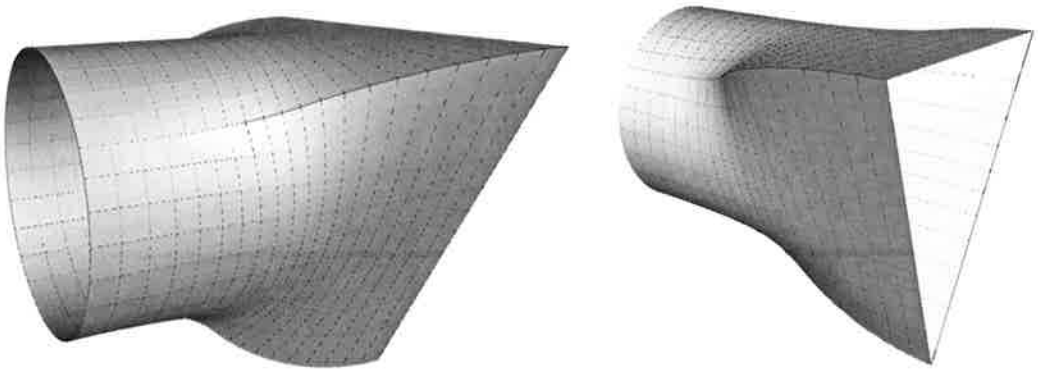


Figure 6: A quadratic × quadratic T-spline surface with sharp and smooth features fluently joined.

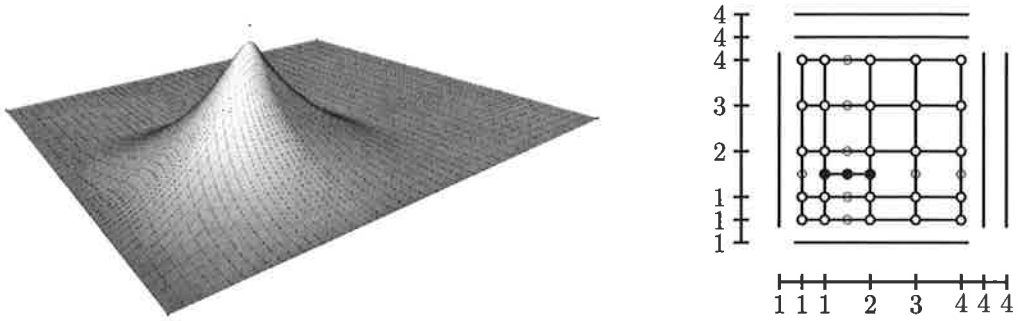


Figure 7: Adding a control point to a quadratic × quadratic T-spline surface.

we can concentrate on the shape of the features.

Figure 7 shows how easily a control point can be added to a T-spline. The original T-mesh with 25 vertices is marked with black circles, and the three vertices added to the T-mesh are marked with filled black circles. If the surface was a NURBS, we would have to add eight more vertices, and thereby eight more control points. These extra vertices are the light gray ones in Figure 7. Further, if we added into the T-mesh a single isolated vertex discussed in Section 4, the ratio of additional control points of T-spline to NURBS would be even more drastic 1/11. This example illustrates the ease of increasing local shape control over a T-spline, which in shape optimization applications is a desirable property. On the

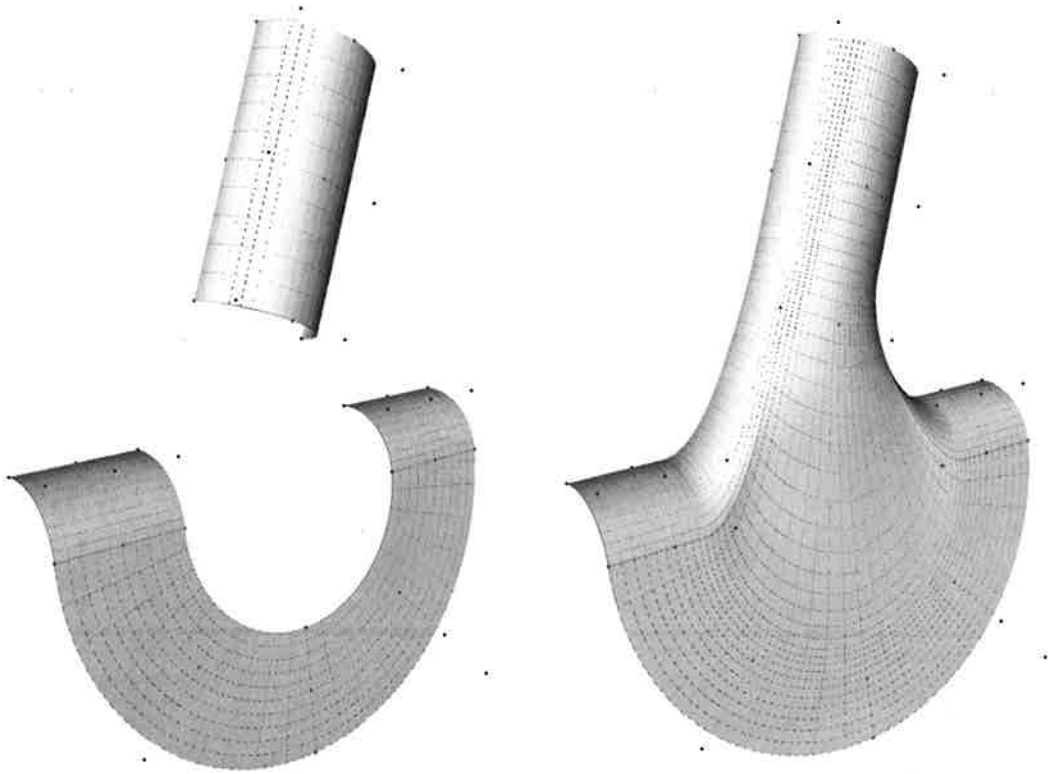


Figure 8: Two NURBS surfaces to be joined and a T-spline surface combining them.

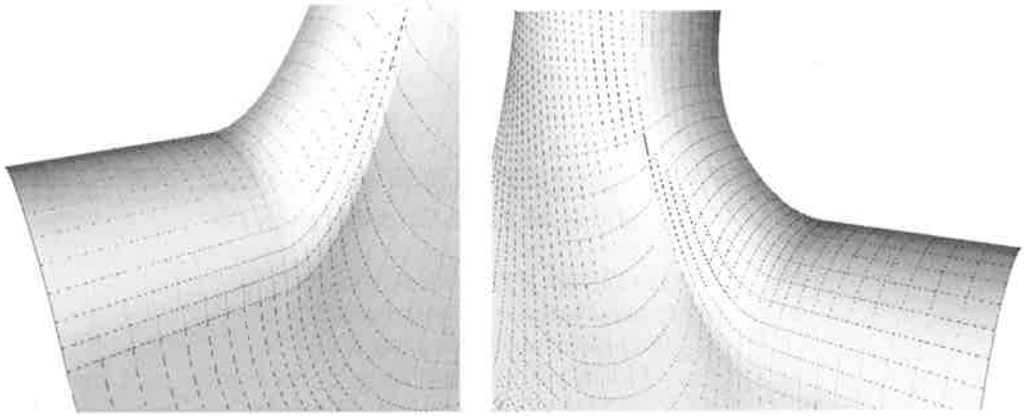


Figure 9: Closeups to the joining T-spline of Figure 8 show that the surface is very smooth.

other hand, also *decreasing* the shape control over a certain part of a T-spline is equally simple, i.e., unwanted control points and design variables possibly related to them can be just removed. Finally, it should be noted that a plain addition or deletion of a control point naturally alters the shape of a T-spline, but if the goal is to continue the shape optimization process with the modified model, this is not an issue.

A problem often faced in the design of structures is to find a best possible shape to connect two or more fixed shapes. As an example, the left part of Figure 8 shows two NURBS surfaces, which should be joined such that the shape of their external boundary curves does not change. The right part of Figure 8 shows a T-spline that combines the two NURBS surfaces into a one surface while preserving the outer boundaries. If the composite surface was a NURBS, it would require 12 fruitless additional control points around the upper cylindrical surface, only to achieve a regular control net. With the T-spline, the design process could be continued by first adding a few control points to the intermediate surface and then optimizing the shape. The T-spline is a good starting point for shape optimization, since it is throughout very smooth, as Figure 9 shows.

6 CONCLUSION

This paper presents the benefits that T-spline surfaces have when compared to NURBS surfaces. The main focus is on applying T-spline surfaces in shape optimization. Several examples show that T-splines have indeed potential, and actually employing them in shape optimization would be a natural continuation of the present study.

REFERENCES

[1] Thomas W. Sederberg, Jianmin Zheng, Almaz Bakenov, and Ahmad Nasri. T-splines and T-NURCCs. *ACM Transactions on Graphics*, 22(3):477–484, July 2003. DOI: `http://doi.acm.org/10.1145/882262.882295`.

[2] Les A. Piegl and Wayne Tiller. *The NURBS Book*. Monographs in Visual Communication Series. Springer-Verlag, Berlin, second edition, 1997.

[3] Thomas W. Sederberg, David L. Cardon, G. Thomas Finnigan, Nicholas S. North, Jianmin Zheng, and Tom Lyche. T-spline simplification and local refinement. *ACM Transactions on Graphics*, 23(3):276–283, August 2004. DOI: `http://doi.acm.org/10.1145/1015706.1015715`.

MONIKAPPALEMEKANIIKAN MALLINTAMINEN PARAMETRISOIMALLA SIDOSMONISTO

J. MÄKINEN & H. MARJAMÄKI
Teknillisen mekaniikan ja optimoinnin laitos
Tampereen teknillinen yliopisto
PL 589, 33101 TAMPERE

TIIVISTELMÄ

Tässä esityksessä kuvataan lyhyesti erästä monikappalemekaniikan mallinnustapaa, jossa holonomisten sidosehtojen muodostama sidosmonisto parametrisoidaan. Parametrisoimalla sidosmonisto päädytään liikeyhtälöihin, joissa sidosehtoja ei ole laisinkaan näkyvillä, vaan sidokset on upotettu sidosmoniston parametrisointikuvaukseen. Monikappalemekaniikan useimmat holonomiset sidokset, kuten erilaiset nivelet ja luistit, voidaan varsin yksinkertaisella tavalla parametrisoida. Tällä mallinnustavalla saavutetaan merkittäviä etuja: muuttujia liikeyhtälössä on minimimäärä sekä vältytään rajoiteyhtälöformulaatioden numeerisilta häiriöherkkyyksiltä, jolloin aikaintegroinnissa voidaan käyttää pidempää aika-askelta.

1 SIDOSMONISTO

Monikappalemekaniikassa kappaleiden väliset erilaiset liitokset ja nivelet sekä reunaehdot synnyttävät sidosehtoja. Erilaiset nivelet kuten kiertymänivel ja prismaattinen nivel ovat esimerkkejä pistemäisistä kinemaattisista sidoksista, jotka voidaan esittää geometrisesti puhtaasti siirtymävapausasteiden avulla. Tämänkaltaisia sidoksia, jotka voidaan esittää siirtymävapausasteiden avulla, kutsutaan holonomisiksi sidoksiksi.

Määritelmä 1: Holonominen sidosvektori (n-d kappaletta sidoksia) voidaan määritellä vektoriarvoisena kuvauksena $\mathbf{h}$: $\mathbb{R}\times\mathbb{E}^n \rightarrow \mathbb{E}^{n-d}$ $(d<n)$

$$\mathbf{h}(t,\mathbf{x})=\mathbf{0},$$

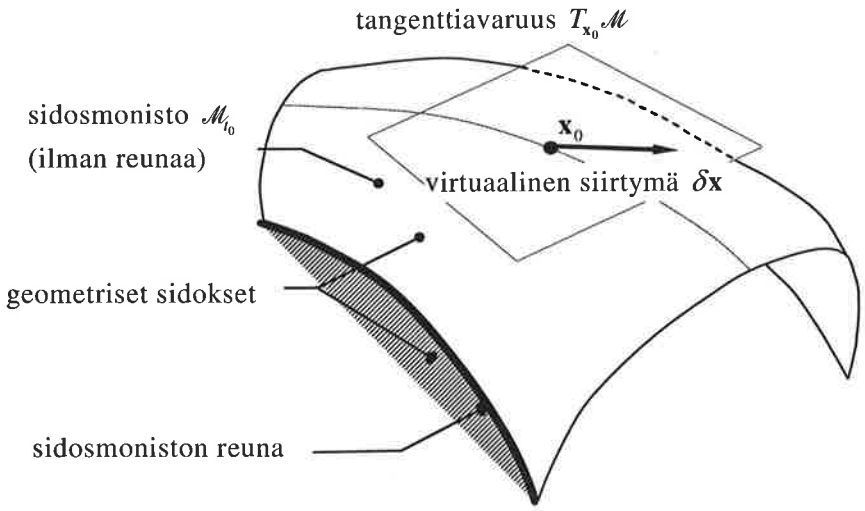
missä t on aikaparametri ja $\mathbf{x}(t)\in\mathbb{E}^n$ on yleistetty paikkavektori.

Mikäli sidoksia ei voi esittää edes integroituna määritelmän *1* mukaisella tavalla, sidoksia kutsutaan epäholonomisiksi. Esimerkiksi kosketusepäyhtälöitä ei voida esittää määritelmän mukaisella sidosyhtälöllä, vaikka itse sidosvektori riippuukin vain siirtymämuuttujista.

Määritelmä 2: Holonomisten sidosehtojen (määr. *1*) synnyttämä sidosmonisto määritellään

$$\mathcal{M}:=\left\{t\times\mathbf{x}\in\mathbb{R}\times\mathbb{E}^n \,\middle|\, \mathbf{h}(t,\mathbf{x})=\mathbf{0}\in\mathbb{E}^{n-d}\right\}.$$

Sidosmonisto $\mathcal{M}$ on d-ulotteinen sileä monisto eli d-monisto, jossa aika on parametrina. Sidosmonisto $\mathcal{M}$ kiinnitetyllä ajanhetkellä $t=t_0$ merkitään $\mathcal{M}_{t_0}$:llä.



Kuva 1 Geometrinen tulkinta kinemaattisista sidoksista

Holonomisten sidosehtojen muodostamalla monistolla (määr. 2) ei ole reunaa, sillä reunallisten monistojen syntyminen edellyttää epäyhtälörajoitteita. Seuraavaksi tutkitaan pistemäisiä holonomisia sidoksia, jotka siis muodostavat reunattoman moniston yleiseen paikka-avaruuteen. Holonomisilla sidoksilla kyetään mallintamaan suuri joukko kappaleitten välisiä kinemaattisia sidosehtoja, kuten erilaisia niveliä. Virtuaalinen siirtymä liittyy läheisesti sidosmonistoon, sillä virtuaalinen siirtymä ei saa rikkoa sidosehtoja. Toisin sanoen virtuaalisen siirtymän tulee olla kinemaattisesti käypä siirtymä, kuva 1.

Määritelmä 3: Sidosmoniston tangenttiavaruus, toimintapisteessä $\mathbf{x}_0 = \mathbf{x}(t_0)$ kiinnitetyllä ajanhetkellä $t = t_0$, määritellään virtuaalisen siirtymän $\delta\mathbf{x}$ avulla

$$T_{\mathbf{x}_0}\mathcal{M} := \left\{ \delta\mathbf{x} \in \mathbb{E}^n \,\middle|\, \mathbf{x}_0 \in \mathcal{M}_{t_0},\ \mathrm{D}_{\mathbf{x}}\mathbf{h}(t_0, \mathbf{x}_0)\cdot\delta\mathbf{x} = \mathbf{0},\ \ \mathrm{D}_{\mathbf{x}}\mathbf{h} \text{ on surjektio} \right\},$$

missä $\mathrm{D}_{\mathbf{x}}\mathbf{h}$ on holonomisten sidosten derivaatta paikkavektorin $\mathbf{x}$ suhteen.

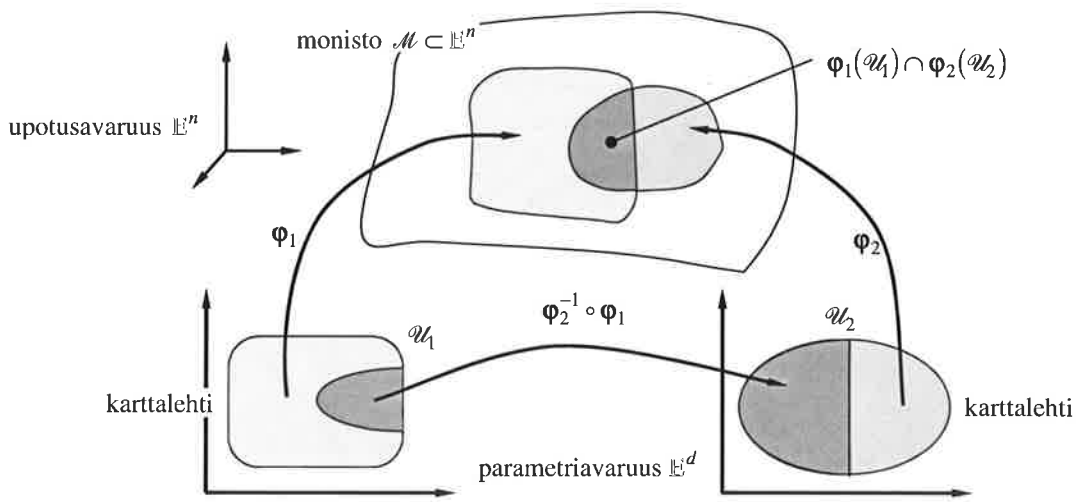
Määritelmä *3* rajaa pois moniston epäsäännölliset pisteet, sillä derivaattamatriisi oletetaan surjektiiviseksi, ts. matriisin ranki on täysi. Näin ollen sidosmoniston $\mathcal{M}$ dimensio ei muutu. Geometrisesti määritelmä tarkoittaa sitä, että käypä virtuaalinen siirtymä sijaitsee sidosmoniston senhetkisen toimintapisteen tangenttiavaruudessa, kuva 1.

2 SIDOSMONISTON PARAMETRISOINTI

Tavallisimmat monikappalejärjestelmän geometriset nivelet kuten pallo-, kiertymä- sylinteri-, kardaani- ja ruuvinivelet sekä erilaiset johteet voidaan esittää holonomisten sidosehtojen avulla, jotka siis riippuvat vain siirtymävapausasteista. Kaikki nämä sidokset synnyttävät sidosmoniston, joka voidaan parametrisoida. Tämä parametrisointi on tavallisesti mahdollista vain paikallisesti mutta useammalla karttalehdellä voidaan kuvata sidosmonisto kokonaisuudessaan, kuva 2.

Newtonin liikeyhtälö kappalejärjestelmälle, jossa siirtymämuuttujia on n kappaletta, voidaan kirjoittaa muodossa

$$\mathbf{f}(\mathbf{q}, \dot{\mathbf{q}}) - \mathbf{M}\cdot\ddot{\mathbf{q}} = \mathbf{0}, \tag{1}$$



Kuva 2 Sidosmoniston $\mathcal{M}$ parametrisointi kahden karttalehden avulla, kun $n = 3$ ja $d = 2$

missä $\mathbf{f}(\mathbf{q}, \dot{\mathbf{q}})$ on siirtymistä ja nopeuksista riippuva yleistetty voimavektori, $\mathbf{M}$ on massatensori ja $\ddot{\mathbf{q}}$ on kiihtyvyysvektori. Vaaditaan lisäksi, että järjestämän tulee toteuttaa holonomiset sidokset $\mathbf{h}: \mathbb{E}^n \to \mathbb{E}^{n-d}$, jotka tuottavat d -moniston $\mathbb{E}^n$:ssä

$$\mathcal{M} := \left\{ t \in \mathbb{R}, \mathbf{q} \in \mathbb{E}^n \,\middle|\, \mathbf{h}(t, \mathbf{q}) = \mathbf{0} \in \mathbb{E}^{n-d} \right\}. \tag{2}$$

Oletetaan myös, että sidosmonisto $\mathcal{M}$ on säännöllinen kaikkialla, jolloin sidosten derivaatta $\mathrm{D}_{\mathbf{q}}\mathbf{h}$ on surjektiivinen sidosmoniston jokaisessa pisteessä.

Nyt virtuaalisen työn periaate ongelmalle (1) sidosmonistolla (2) on

$$\delta W = \left(\mathbf{f}(\mathbf{q}, \dot{\mathbf{q}}) - \mathbf{M} \cdot \ddot{\mathbf{q}} \right) \cdot \delta \mathbf{q} = 0. \tag{3}$$

Yleistetty voimavektori $\mathbf{f}$ voidaan jakaa annettuihin voimiin $\mathbf{f}^{\text{appl}} \in T_{\mathbf{q}_0}\mathcal{M}$ ja sidosvoimiin $\mathbf{f}^{\text{con}} \in T_{\mathbf{q}_0}\mathcal{M}^{\perp}$, joiden virtuaalinen työ häviää. Virtuaalinen siirtymä $\delta\mathbf{q}$ kuuluu sidosmoniston tangenttiavaruuteen $T_{\mathbf{q}_0}\mathcal{M}$, mikä voidaan antaa muodossa

$$T_{\mathbf{q}_0}\mathcal{M} = \left\{ \delta\mathbf{q} \in \mathbb{E}^n \,\middle|\, \mathrm{D}_{\mathbf{q}}\mathbf{h}(t_0, \mathbf{q}_0) \cdot \delta\mathbf{q} = \mathbf{0} \right\}. \tag{4}$$

Oletetaan, että siirtymävektori $\mathbf{q} \in \mathbb{E}^n$ voidaan jakaa isäntäsiirtymävektoriksi $\mathbf{q}_{\text{mr}} \in \mathbb{E}^d$ ja orjasiirtymävektoriksi $\mathbf{q}_{\text{s}} \in \mathbb{E}^{n-d}$ siten, että derivaattamatriisilla $\mathrm{D}_{\mathbf{q}_{\text{s}}}\mathbf{h}(t, \mathbf{q}_{\text{mr}}, \mathbf{q}_{\text{s}})$, mikä on neliömatriisi, on olemassa käänteismatriisi. Implisiittifunktiolauseen nojalla on olemassa kuvaus $\boldsymbol{\phi}(t, \mathbf{q}_{\text{mr}}): \mathbb{R} \times \mathbb{E}^d \to \mathbb{E}^{n-d}$ toimintapisteen ympäristössä siten, että

$$\hat{\mathbf{h}}(t, \mathbf{q}_{\text{mr}}) := \mathbf{h}(t, \mathbf{q}_{\text{mr}}, \boldsymbol{\phi}(t, \mathbf{q}_{\text{mr}})) = \mathbf{0}. \tag{5}$$

Näin ollen orjasiirtymävektori $\mathbf{q}_{\text{s}} \in \mathbb{E}^{n-d}$ voidaan esittää isäntäsiirtymävektorin $\mathbf{q}_{\text{mr}} \in \mathbb{E}^d$ avulla, ts. $\mathbf{q}_{\text{s}} = \boldsymbol{\phi}(t, \mathbf{q}_{\text{mr}})$. Lisäksi sidosmoniston $\mathcal{M}$ parametrisointi voidaan kirjoittaa nyt suoraan ku-

vauksen $\boldsymbol{\phi}(t,\mathbf{q}_{mr})$ avulla

$$\boldsymbol{\varphi}:\mathbb{R}\times\mathbb{E}^d \to \mathcal{M} \quad (t,\mathbf{q}_{mr}) \mapsto \boldsymbol{\varphi}(t,\mathbf{q}_{mr}) := \left(\mathbf{q}_{mr}, \boldsymbol{\phi}(t,\mathbf{q}_{mr})\right). \tag{6}$$

Parametrisointikuvaus $\boldsymbol{\varphi}$ toteuttaa sidokset $\mathbf{h}(t,\boldsymbol{\varphi}(t,\mathbf{q}_{mr})) = \mathbf{0}$ kaavan (5) perusteella. Toisinaan sidokset voidaan antaa ajasta riippumattomassa muodossa $\mathbf{h}(\mathbf{q}_{mr},\mathbf{q}_s) := \mathbf{q}_s - \boldsymbol{\phi}(\mathbf{q}_{mr}) = \mathbf{0}$, mikä antaa luonnollisen sidosmoniston $\mathcal{M}$ parametrisoinnin, sillä $\mathrm{D}_{\mathbf{q}_s}\mathbf{h}(t,\mathbf{q}_{mr},\mathbf{q}_s) = \mathbf{I}$.

Tarkastellaan seuraavaksi ajasta riippumatonta sidosmoniston $\mathcal{M}$ parametrisointikuvausta $\boldsymbol{\varphi}:\mathbb{E}^d \to \mathcal{M} \subset \mathbb{E}^n$

$$\mathbf{q} = \boldsymbol{\varphi}(\mathbf{q}_{mr}). \tag{7}$$

Siirtymävektorin $\mathbf{q} \in \mathcal{M}$ variaatio isäntäsiirtymävektorin $\mathbf{q}_{mr} \in \mathbb{E}^d$ avulla lausuttuna on

$$\begin{aligned} \delta\mathbf{q} &= \mathbf{B}\cdot\delta\mathbf{q}_{mr}, \\ \mathbf{B} &:= \mathrm{D}_{\mathbf{q}_{mr}}\boldsymbol{\varphi}(\mathbf{q}_{mr}), \end{aligned} \tag{8}$$

missä $\mathbf{B}$ kinemaattinen operaattori $\mathbf{B}:T_{\mathbf{q}_{mr}}\mathbb{E}^d = \mathbb{E}^d \to T_{\mathbf{q}}\mathcal{M} \subset \mathbb{E}^n$ tangenttiavaruuksien välillä. Siirtymävektorin aikaderivaatat ovat vastaavasti

$$\begin{aligned} \dot{\mathbf{q}} &= \mathbf{B}\cdot\dot{\mathbf{q}}_{mr} \quad \in T_{\mathbf{q}}\mathcal{M}, \\ \ddot{\mathbf{q}} &= \mathbf{B}\cdot\ddot{\mathbf{q}}_{mr} + \dot{\mathbf{B}}\cdot\dot{\mathbf{q}}_{mr} \quad \in T_{\mathbf{q}}\mathcal{M}, \end{aligned} \tag{9}$$

missä kinemaattisen operaattorin aikaderivaatta $\dot{\mathbf{B}}$ yleensä epälineaarisesti isäntäsiirtymävektorista $\mathbf{q}_{mr}$ ja lineaarisesti nopeusvektorista $\dot{\mathbf{q}}_{mr}$. Tämä nähdään yhteydestä

$$\begin{aligned} \dot{\mathbf{B}} &= \mathrm{D}_{\mathbf{q}_{mr}}\mathbf{B}\cdot\dot{\mathbf{q}}_{mr}, \\ \dot{\mathbf{B}}\cdot\dot{\mathbf{q}}_{mr} &= \mathrm{D}^2_{\mathbf{q}_{mr}}\boldsymbol{\varphi}(\mathbf{q}_{mr}):(\dot{\mathbf{q}}_{mr}\otimes\dot{\mathbf{q}}_{mr}), \end{aligned} \tag{10}$$

missä jälkimmäinen yhtälö esittää neliöllistä riippuvuutta nopeusvektorista $\dot{\mathbf{q}}_{mr}$.

Nyt virtuaalisen työn periaate (3) sidosmonistolla $\mathcal{M}$ voidaan kirjoittaa parametriavaruudessa $\mathbb{E}^d$ yhteyksien (7-9) avulla

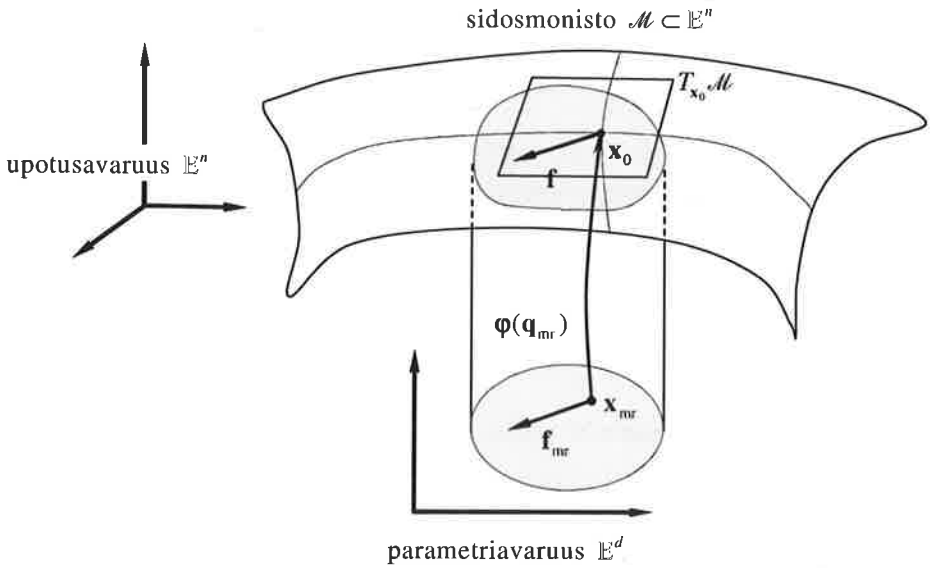
$$\delta\mathbf{q}_{mr}\cdot\mathbf{B}^{\mathrm{T}}\left(\mathbf{f}(\mathbf{q}_{mr},\dot{\mathbf{q}}_{mr}) - \mathbf{M}\mathbf{B}\ddot{\mathbf{q}}_{mr} - \mathbf{M}\dot{\mathbf{B}}\dot{\mathbf{q}}_{mr}\right) = 0, \qquad \forall\delta\mathbf{q}_{mr} \in \mathbb{E}^d, \tag{11}$$

missä sidokset (2) toteutuvat automaattisesti parametrisoinnin (7) ansiosta. Toisin sanoen holonomiset sidokset on nyt upotettu virtuaalisen työn periaatteeseen (11), jolloin saatu liikeyhtälö riippuu vain isäntäsiirtymävektorista $\mathbf{q}_{mr}$ ja sen aikaderivaatoista.

Virtuaalisen työn (11) linearisointi ajanhetkellä $t = t_0$ toimintapisteen ympäristössä $(\mathbf{q}_{mr0},\dot{\mathbf{q}}_{mr0}) \in \mathbb{E}^d \times \mathbb{E}^d$ suuntaan $(\Delta\mathbf{q}_{mr},\Delta\dot{\mathbf{q}}_{mr})$ antaa tuloksen

$$\delta\mathbf{q}_{mr}\cdot\left(\mathbf{f}_{mr0} - \mathbf{M}_{mr}\ddot{\mathbf{q}}_{mr} - \mathbf{C}_{mr}\cdot\Delta\dot{\mathbf{q}}_{mr} - \mathbf{K}_{mr}\cdot\Delta\mathbf{q}_{mr}\right) = 0, \qquad \forall\delta\mathbf{q}_{mr} \in \mathbb{E}^d, \tag{12}$$

missä yleistetty isäntävoimavektori $\mathbf{f}_{mr0}$, jäykkyys-, vaimennus- ja massatensorit ovat vastaavasti



Kuva 3 Yleistetyn voimavektorin kuvaus upotusavaruudesta parametriavaruuteen

$$
\begin{aligned}
\mathbf{f}_{mr0} &:= \mathbf{B}^T\left(\mathbf{f}(\mathbf{q}_{mr0}, \dot{\mathbf{q}}_{mr0}) - \mathbf{M}\dot{\mathbf{B}}\dot{\mathbf{q}}_{mr0}\right) \quad \in \mathbb{E}^d, \\
\mathbf{K}_{mr} &:= \mathrm{D}_{\mathbf{q}_{mr}}\left(\mathbf{B}^T(-\mathbf{f}(\mathbf{q}_{mr}, \dot{\mathbf{q}}_{mr}) + \mathbf{M}\mathbf{B}\ddot{\mathbf{q}}_{mr} + \mathbf{M}\dot{\mathbf{B}}\dot{\mathbf{q}}_{mr})\right) \quad \in \mathbb{E}^{d\times d}, \\
\mathbf{C}_{mr} &:= \mathrm{D}_{\dot{\mathbf{q}}_{mr}}\left(\mathbf{B}^T(-\mathbf{f}(\mathbf{q}_{mr}, \dot{\mathbf{q}}_{mr}) + \mathbf{M}\dot{\mathbf{B}}\dot{\mathbf{q}}_{mr})\right) \quad \in \mathbb{E}^{d\times d}, \\
\mathbf{M}_{mr} &:= \mathbf{B}^T\mathbf{M}\mathbf{B} \quad \in \mathbb{E}^{d\times d}.
\end{aligned}
\tag{13}
$$

Yllä olevien yhtälöiden avulla voidaan johtaa parametriavaruuden voimavektorin sekä tangenttitensorit ja massatensorin, kun parametrisointikuvaus: $\varphi: \mathbb{E}^d \to \mathcal{M}$ on olemassa. Tavallisesti orjasiirtymävektori $\mathbf{q}_s$ osataan lausua isäntäsiirtymävektorin $\mathbf{q}_{ms}$ avulla, jolloin orjakuvaus $\mathbf{q}_s = \boldsymbol{\phi}(\mathbf{q}_{mr})$ tunnetaan. Tällöin parametrisointikuvaus φ seuraa suoraan yhtälöstä (6).

Yleistetty voimavektori $\mathbf{f}$ Newtonin liikeyhtälössä (1) sisältää sekä kuormituksesta johtuvan ulkoisen voimavektorin, sisäisen voimavektori että nopeudesta riippuvan kiihtyvyysvoimavektorin

$$
\mathbf{f}(\mathbf{q}, \dot{\mathbf{q}}) = \mathbf{f}^{\mathrm{ext}}(\mathbf{q}) - \mathbf{f}^{\mathrm{int}}(\mathbf{q}, \dot{\mathbf{q}}) - \mathbf{f}^{\mathrm{accB}}(\mathbf{q}, \dot{\mathbf{q}}), \quad \in \mathbb{E}^n, \tag{14}
$$

missä $\mathbf{f}^{\mathrm{ext}}$, $\mathbf{f}^{\mathrm{int}}$ and $\mathbf{f}^{\mathrm{accB}}$ ovat ulkoinen ja sisäinen voimavektori sekä nopeudesta riippuva kiihtyvyysvoimavektori. Upotusavaruuden siirtymävektori tunnetaan parametrisointikuvauksen $\mathbf{q} = \boldsymbol{\varphi}(\mathbf{q}_{mr})$ avulla.

Upotusavaruudessa $\mathbb{E}^{n\times n}$ voidaan määritellä seuraavat tangenttitensorit

$$
\begin{aligned}
&\mathbf{K} := \mathrm{D}_{\mathbf{q}}\mathbf{f}^{\mathrm{int}}(\mathbf{q}, \dot{\mathbf{q}}), \quad \mathbf{C} := \mathrm{D}_{\dot{\mathbf{q}}}\mathbf{f}^{\mathrm{int}}(\mathbf{q}, \dot{\mathbf{q}}), \\
&\mathbf{K}_{\mathrm{load}} := \mathrm{D}_{\mathbf{q}}\mathbf{f}^{\mathrm{ext}}(\mathbf{q}), \\
&\mathbf{K}_{\mathrm{cent}} := \mathrm{D}_{\mathbf{q}}\mathbf{f}^{\mathrm{acc}}(\mathbf{q}, \dot{\mathbf{q}}, \ddot{\mathbf{q}}), \quad \mathbf{C}_{\mathrm{gyro}} := \mathrm{D}_{\dot{\mathbf{q}}}\mathbf{f}^{\mathrm{acc}}(\mathbf{q}, \dot{\mathbf{q}}, \ddot{\mathbf{q}}).
\end{aligned}
\tag{15}
$$

Sijoittamalla yhteydet (14-15) yhtälöön (13) saadaan

$$
\begin{aligned}
\mathbf{f}_{\mathrm{mr0}} &:= \mathbf{B}^{\mathrm{T}}\left(\mathbf{f}^{\mathrm{ext}}(\mathbf{q}_{\mathrm{mr}}) - \mathbf{f}^{\mathrm{int}}(\mathbf{q}_{\mathrm{mr}}, \dot{\mathbf{q}}_{\mathrm{mr}}) - \mathbf{f}^{\mathrm{accB}}(\mathbf{q}_{\mathrm{mr}}, \dot{\mathbf{q}}_{\mathrm{mr}}) - \mathbf{M}\dot{\mathbf{B}}\dot{\mathbf{q}}_{\mathrm{mr0}}\right) \quad \in \mathbb{E}^{d}, \\
\mathbf{K}_{\mathrm{mr}} &:= \mathbf{B}^{\mathrm{T}}\left((-\mathbf{K}_{\mathrm{load}} + \mathbf{K} + \mathbf{K}_{\mathrm{cent}})\mathbf{B} + (\mathbf{C} + \mathbf{C}_{\mathrm{gyro}})\dot{\mathbf{B}} + \mathbf{M}\ddot{\mathbf{B}}\right) + \mathbf{K}_{\sigma\mathrm{mr}}(-\mathbf{f}^{\mathrm{ext}} + \mathbf{f}^{\mathrm{int}} + \mathbf{f}^{\mathrm{acc}}) \quad \in \mathbb{E}^{d\times d}, \\
\mathbf{C}_{\mathrm{mr}} &:= \mathbf{B}^{\mathrm{T}}\left((\mathbf{C} + \mathbf{C}_{\mathrm{gyro}})\mathbf{B} + 2\mathbf{M}\dot{\mathbf{B}}\right) \quad \in \mathbb{E}^{d\times d}, \\
\mathbf{M}_{\mathrm{mr}} &:= \mathbf{B}^{\mathrm{T}}\mathbf{M}\mathbf{B} \quad \in \mathbb{E}^{d\times d},
\end{aligned}
\tag{16}
$$

missä kiihtyvyysvektori $\mathbf{f}^{\mathrm{acc}} = \mathbf{f}^{\mathrm{accA}} + \mathbf{f}^{\mathrm{accB}} \in \mathbb{E}^{n}$, ja geometrinen jäykkyystensori $\mathbf{K}_{\sigma\mathrm{mr}}$ määritellään

$$
\mathbf{K}_{\sigma\mathrm{mr}}(\mathbf{f}) := \mathrm{D}_{\mathbf{q}_{\mathrm{mr}}}(\mathbf{B}^{\mathrm{T}}\bar{\mathbf{f}}),
\tag{17}
$$

missä vektoria $\mathbf{f}$ pidetään derivoinnissa vakioina; merkinnällä $\bar{\mathbf{f}}$. Geometrinen jäykkyystensori $\mathbf{K}_{\sigma\mathrm{mr}}$ on symmetrinen tensori, sillä kaavan (8b) mukaan $\mathbf{K}_{\sigma\mathrm{mr}}(\mathbf{f}) = \mathrm{D}^{2}_{\mathbf{q}_{\mathrm{mr}}}(\boldsymbol{\varphi}\cdot\bar{\mathbf{f}})$. Ts. geometrinen jäykkyystensori on skalaarifunktion toinen derivaatta isäntäsiirtymävektorin suhteen.

Yhtälöiden (16) avuilla voidaan johtaa parametriavaruuden $\mathbb{E}^{d}$ yleistetyn voimavektorin ja tangenttitensorit sekä massatensorin, kun vastaavat suureet upotusavaruudessa $\mathbb{E}^{n}$ ja kinemaattinen operaattori $\mathbf{B}$ sekä sen aikaderivaatat tunnetaan. Ainoastaan geometrinen jäykkyystensori $\mathbf{K}_{\sigma\mathrm{mr}}$, kaava (17), on hieman vaikeammin laskettavissa.

3 ERITYISIÄ PALKKIELEMENTTEJÄ

Tässä kappaleessa esitellään pari erikoiselementtiä, jotka sisältävät holonomisen sidosehdon. Sidosmonisto parametrisoidaan ja yleistetty voimavektori sekä tensorit esitetään sidosmoniston parametriavaruudessa. Saatuja erityiselementtejä voidaan käyttää elementtimenetelmässä tavanomaisten elementtien tapaan eikä tällöin liikeyhtälössä ole tällöin lainkaan sidosehtoja näkyvissä, vaan ne ovat upotettuina parametrisointikuvaukseen $\mathbf{q} = \boldsymbol{\varphi}(\mathbf{q}_{\mathrm{mr}})$.

3.1 Komplementaarinen palkkielementti

Kuten tunnettua ei ole olemassa kiertymisoperaattorin parametrisointia, joka olisi samalla sekä globaali että ei-singulaarinen. Esimerkiksi kaikilla kiertymisoperaattorin Eulerin kulmaesitysmuodoilla on olemassa toimintapiste, jossa parametrisointi on singulaarinen. Seuraavaksi esitellään komplementaarinen palkkielementti, jossa kiertymisoperaattori kuvataan kahdella karttalehdellä. Tällä menettelyllä vältytään singulaarisuusongelmista.

Mikä tahansa kiertymisoperaattori $\mathbf{R}$ voidaan esittää kiertymävektorin $\boldsymbol{\Psi}$ avulla, joka määritellään

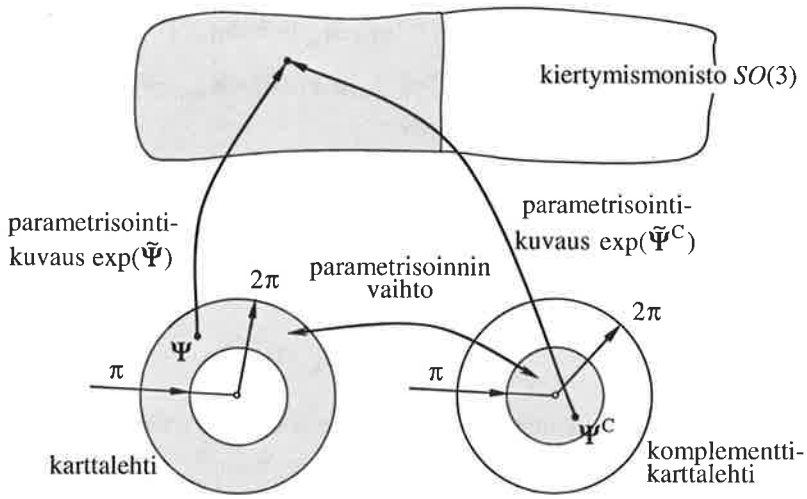
$$
\boldsymbol{\Psi} := \psi\mathbf{n}, \qquad \mathbf{n} \in \mathbb{E}^{3}, \psi \in \mathbb{R}_{+},
\tag{18}
$$

missä $\mathbf{n}$ on kiertymisakselin ykkösvektori $\|\mathbf{n}\| = 1$ ja ψ on positiivinen kiertymiskulma. Kiertymävektorin $\boldsymbol{\Psi}$ ja kiertymisoperaattorin $\mathbf{R}$ välillä on yhteys

$$
\mathbf{R} := \mathbf{I} + \frac{\sin\psi}{\psi}\tilde{\boldsymbol{\Psi}} + \frac{1-\cos\psi}{\psi^{2}}\tilde{\boldsymbol{\Psi}}^{2} = \exp\left(\tilde{\boldsymbol{\Psi}}\right), \qquad \psi = \|\boldsymbol{\Psi}\|,
\tag{19}
$$

missä vinosymmetrinen tensori $\tilde{\boldsymbol{\Psi}}$ määritellään kaavalla

$$
\tilde{\boldsymbol{\Psi}}\mathbf{h} = \boldsymbol{\Psi}\times\mathbf{h}, \qquad \forall\mathbf{h} \in \mathbb{E}^{3}.
\tag{20}
$$



Kuva 4 Kiertymismoniston kaksi parametrisointia kiertymävektorin ja sen komplementtivektorin avulla

Toisin sanoen $\tilde{\Psi}$ on akselivektoria Ψ vastaava vinosymmetrinen tensori. Kuvassa 4 on esitetty kiertymismoniston ja sen parametrisoinnin geometrinen tulkinta. Kiertymävektori Ψ on kiertymisoperaattorin parametrisointi, jossa tämän parametrisointikuvaus φ on nyt matriisieksponenttikuvaus $\exp(\tilde{\Psi})$. Kiertymävektoriesitysmuoto on singulaarinen kiertymiskulman arvolla $\psi = 2\pi$. Tällöin nollakiertymisvektori sekä kiertymisvektori, jonka pituus on 2π kuvautuvat samaksi pisteeksi, identiteetiksi $\mathbf{I}$.

Kiertymisoperaattoreiden muodostavat kiertymismoniston $SO(3)$ joka voidaan määritellä kaavalla

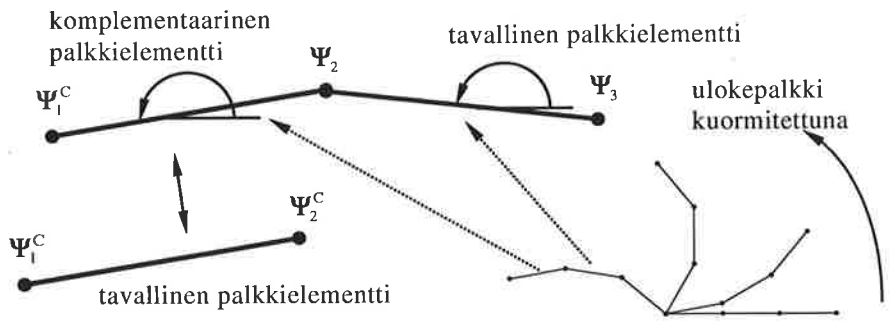
$$SO(3) := \left\{ \mathbf{R} : \mathbb{E}^3 \to \mathbb{E}^3 \text{ lineaarinen} \,\middle|\, \mathbf{R}^T\mathbf{R} = \mathbf{I},\ \det \mathbf{R} = +1 \right\}. \tag{21}$$

Kiertymisoperaattori $\mathbf{R}$ on siis ortogonaalinen operaattori, joka säilyttää kuvauksessa alkuperäisen kätisyyden. Kaava määrittää epäsuorasti derivoituvan moniston, jossa ortogonaalisuusehto asettaa kuusi toisistaan riippumatonta sidosehtoa kiertymisoperaattorille, jolloin kiertymisoperaattoreiden joukko $SO(3)$ muodostaa 3-uloitteisen pinnan, tai oikeammin 3-moniston, 9-ulotteiseen avaruuteen. Kiertymismonisto voidaan parametrisoida vain paikallisesti, mutta jo kahdella karttalehdellä tämä parametrisointi voidaan suorittaa täysin peittävästi.

Kiertymisvektorin esitysmuodon singulaarisuusongelmat – kiertymäkulman arvolla $\psi = 2\pi$ – voidaan välttää määrittelemällä myös toinen karttalehti, joka parametrisoi täydentävästi kiertymismonistoa. Komplementtikiertymävektori Ψ^C määritellään kaavalla

$$\Psi^C := \Psi - \frac{2\pi}{\psi}\Psi \quad (= \phi(\mathbf{q})), \qquad \psi = \|\Psi\|, \tag{22}$$

Kiertymävektori kuvataan komplementtikiertymävektoriksi, kun kiertymiskulma ylittää oikokulman, ts. $\psi > \pi$. Tällöin komplementtikiertymäkulma $\psi^C = 2\pi - \psi$, joka on siis pienempi kuin oikokulma, ts. $\psi^C < \pi$. Kuvassa 4 on esitetty parametrisoinnin vaihdot alkuperäisestä kiertymävektoriparametrisoinnista komplementaariseen kiertymävektoriparametrisointiin. Näillä kahdella karttalehdellä mikä tahansa kiertymisliike voidaan kuvata kattavasti.



Kuva 5 Tilanne jolloin komplementaarista palkkielementtiä tarvitaan

Dynamiikan laskennassa suurilla kiertymillä joudutaan usein tilanteisiin, jossa kaksisolmuisen palkkielementin toinen solmun kiertymävektori esitetään komplementtikarttalehdellä ja toinen kiertymävektori primäärisellä karttalehdellä. Tällöin interpolointi solmujen välillä ei ole voimassa. Kuvassa 5 on esitetty tilanne, jolloin tämänkaltaista erityiselementtiä kaivataan. Kuvassa solmun 1 kiertymävektori esitetään komplementtivektorina $\boldsymbol{\Psi}_1^C$, sillä kiertymäkulma on ylittänyt arvon π, ja solmussa 2 kiertymävektori esitetään primäärisellä karttalehdellä $\boldsymbol{\Psi}_2$, sillä solmun kiertymäkulma on pienempi kuin oikokulma. Interpolointiongelma voidaan ratkaista isäntä-orjatekniikkaa käyttäen.

Nyt komplementtikiertymävektori $\boldsymbol{\Psi}_2^C$ vastaa orjasiirtymävektoria $\mathbf{q}_s \in \mathbb{E}^3$, ja kuvan 5 vasemmanpuoleisen palkin solmusiirtymävektori on $(\mathbf{d}_1, \boldsymbol{\Psi}_1^C, \mathbf{d}_2, \boldsymbol{\Psi}_2)$, missä $\mathbf{d}_i$ on solmun i translaatiosiirtymä, vastaa isäntäsiirtymävektoria $\mathbf{q}_{mr} \in \mathbb{E}^{12}$.

Orjakuvaus $\mathbf{q}_s = \boldsymbol{\phi}(\mathbf{q}_{mr})$ on suoraan kaavan (22) mukainen kuvaus, jonka variaatio ja aikaderivaatat ovat

$$\begin{aligned}
\delta\boldsymbol{\Psi}_2^C &= \mathbf{B}_s \cdot \delta\boldsymbol{\Psi}_2, \\
\dot{\boldsymbol{\Psi}}_2^C &= \mathbf{B}_s \cdot \dot{\boldsymbol{\Psi}}_2, \\
\ddot{\boldsymbol{\Psi}}_2^C &= \mathbf{B}_s \cdot \ddot{\boldsymbol{\Psi}}_2 + \dot{\mathbf{B}}_s \cdot \dot{\boldsymbol{\Psi}}_2,
\end{aligned} \tag{23}$$

missä orjasiirtymän kinemaattinen operaattori $\mathbf{B}_s = \mathbf{B}_s(\boldsymbol{\Psi}_2)$ ja sen ajan suhteen lasketut derivaatat $\dot{\mathbf{B}}_s = \dot{\mathbf{B}}_s(\boldsymbol{\Psi}_2, \dot{\boldsymbol{\Psi}}_2)$ ja $\ddot{\mathbf{B}}_s = \ddot{\mathbf{B}}_s(\boldsymbol{\Psi}_2, \dot{\boldsymbol{\Psi}}_2, \ddot{\boldsymbol{\Psi}}_2)$ ovat

$$\begin{aligned}
\mathbf{B}_s &= (1 - \frac{2\pi}{\psi})\mathbf{I} + \frac{2\pi}{\psi}\mathbf{e}\otimes\mathbf{e} \in \mathbb{E}^{3\times3}, \\
\dot{\mathbf{B}}_s &= \frac{2\pi}{\psi^2}\left[(\mathbf{e}\cdot\dot{\boldsymbol{\Psi}})\mathbf{I} + (\dot{\boldsymbol{\Psi}}\otimes\mathbf{e} + \mathbf{e}\otimes\dot{\boldsymbol{\Psi}}) - 3(\mathbf{e}\cdot\dot{\boldsymbol{\Psi}})\mathbf{e}\otimes\mathbf{e}\right] \in \mathbb{E}^{3\times3}, \\
\ddot{\mathbf{B}}_s &= \frac{2\pi}{\psi^2}\left[\left((\mathbf{e}\cdot\ddot{\boldsymbol{\Psi}}) + (\dot{\mathbf{e}}\cdot\dot{\boldsymbol{\Psi}})\right)\mathbf{I} + \ddot{\boldsymbol{\Psi}}\otimes\mathbf{e} + \mathbf{e}\otimes\ddot{\boldsymbol{\Psi}} + \dot{\boldsymbol{\Psi}}\otimes\dot{\mathbf{e}} + \dot{\mathbf{e}}\otimes\dot{\boldsymbol{\Psi}}\right] + \\
&\quad - \frac{6\pi}{\psi^2}\left[\left((\mathbf{e}\cdot\ddot{\boldsymbol{\Psi}}) + (\dot{\mathbf{e}}\cdot\dot{\boldsymbol{\Psi}})\right)\mathbf{e}\otimes\mathbf{e} + (\mathbf{e}\cdot\dot{\boldsymbol{\Psi}})(\dot{\mathbf{e}}\otimes\mathbf{e} + \mathbf{e}\otimes\dot{\mathbf{e}})\right] - \frac{2}{\psi}(\mathbf{e}\cdot\dot{\boldsymbol{\Psi}})\dot{\mathbf{B}}_s .
\end{aligned} \tag{24}$$

missä kiertymisakseli $\mathbf{e} = \boldsymbol{\Psi}/\psi$. Upotusavaruuden siirtymävektori $\mathbf{q}$ $\mathbb{E}^{15}$:ssä, isäntäsiirtymävektori $\mathbf{q}_{mr}$ ja orjasiirtymävektori $\mathbf{q}_s$ ovat

$$\mathbf{q} := \begin{pmatrix} \mathbf{q}_{mr} \\ \mathbf{q}_s \end{pmatrix} = \begin{pmatrix} \mathbf{d}_1 \\ \boldsymbol{\Psi}_1^C \\ \mathbf{d}_2 \\ \boldsymbol{\Psi}_2 \\ \boldsymbol{\Psi}_2^C \end{pmatrix} \in \mathbb{E}^{15}. \tag{25}$$

Kaavassa (24) on annettu orjakuvauksen $\mathbf{q}_s = \boldsymbol{\phi}(\mathbf{q}_{mr})$ kinemaattinen operaattori. Parametrisointikuvauksen $\mathbf{q} = \boldsymbol{\varphi}(\mathbf{q}_{mr})$ kinemaattinen operaattori $\mathbf{B}$ ja sen aikaderivaatat ovat vastaavasti

$$\mathbf{B} = \begin{pmatrix} \mathbf{I}_{12\times 12} \\ (\mathbf{O}_{3\times 9} \quad \mathbf{B}_s) \end{pmatrix} \in \mathbb{E}^{15\times 12}, \quad \dot{\mathbf{B}} = \begin{pmatrix} \mathbf{O}_{12\times 12} \\ (\mathbf{O}_{3\times 9} \quad \dot{\mathbf{B}}_s) \end{pmatrix}, \quad \ddot{\mathbf{B}} = \begin{pmatrix} \mathbf{O}_{12\times 12} \\ (\mathbf{O}_{3\times 9} \quad \ddot{\mathbf{B}}_s) \end{pmatrix}, \tag{26}$$

Kaavojen mukaiset (16) voimavektori $\mathbf{f}_{mr0}$ ja tensorit $\mathbf{K}_{mr}$, $\mathbf{C}_{mr}$ ja $\mathbf{M}_{mr}$ parametriavaruudessa $\mathbb{E}^{12}$ voidaan laskea suoraan, kun vielä kaavan (17) geometrinen jäykkyystensori $\mathbf{K}_{\sigma mr}$ lasketaan:

$$\begin{aligned} \mathbf{K}_{\sigma mr_S} &= \begin{pmatrix} \mathbf{O}_{9\times 9} & \mathbf{O}_{9\times 3} \\ \mathbf{O}_{3\times 9} & \mathbf{K}_{\sigma s} \end{pmatrix} \in \mathbb{E}^{12\times 12}, \\ \mathbf{K}_{\sigma s} &= \frac{2\pi}{\psi^2}\left[(\mathbf{f}_s \cdot \mathbf{e})\mathbf{I} + \mathbf{f}_s \otimes \mathbf{e} + \mathbf{e} \otimes \mathbf{f}_s - 3(\mathbf{f}_s \cdot \mathbf{e})\mathbf{e} \otimes \mathbf{e}\right] \in \mathbb{E}^{3\times 3}, \end{aligned} \tag{27}$$

missä orjavoimavektorin $\mathbf{f}_s \in \mathbb{E}^3$ vapausasteet vastaavat orjasiirtymävektoria $\boldsymbol{\Psi}_2^C$.

Voimavektori $\mathbf{f}_{mr0}$, tangenttitensorit $\mathbf{K}_{mr}$, $\mathbf{C}_{mr}$ ja massatensori $\mathbf{M}_{mr}$ parametriavaruudessa $\mathbb{E}^{12}$ saadaan kaavojen (16) avulla, kun upotusavaruuden $\mathbb{E}^{15}$ voimavektori $\mathbf{f}$, tangenttitensorit $\mathbf{K}_{load}, \mathbf{K}, \mathbf{K}_{cent}, \mathbf{C}_{gyro}$ ja massatensori $\mathbf{M}$ on laskettu. Nämä upotusavaruuden suureet tunnetaan, sillä elementin solmusiirtymävektori $(\mathbf{d}_1, \boldsymbol{\Psi}_1^C, \mathbf{d}_2, \boldsymbol{\Psi}_2^C)$ on osa upotusavaruuden siirtymävektoria $\mathbf{q}$, kaavan (25) perusteella.

3.2 Kiertymänivelelementti

Tässä kappaleessa esitetään erikoispalkkielementti, joka pitää sisällään kiertymis- eli sarananivelen. Kiertymisnivelelle pätee kinemaattinen yhteys kiertymisoperaattoreiden välillä

$$\mathbf{R}_s = \mathbf{R}_m \mathbf{R}_j, \tag{28}$$

missä $\mathbf{R}_s = \mathbf{R}(\boldsymbol{\Psi}_s)$ on orjasolmun 's' kiertymisoperaattori ja $\mathbf{R}_m = \mathbf{R}(\boldsymbol{\Psi}_m)$ on isäntäsolmun 'm' kiertymisoperaattori ja $\mathbf{R}_j = \mathbf{R}(\varphi \mathbf{e}_j)$ on kiertymisnivelen kiertymisoperaattori, missä φ on nivelen kiertymiskulma (positiivinen tai negatiivinen ja minkä kokoinen tahansa) ja $\mathbf{e}_j$ on kiertymisnivelen kiertymisakseli alkutilassa.

Varioimalla yhteys (28) saadaan kinemaattinen relaatio isäntä ja orjakiertymien välille

$$\delta\boldsymbol{\Theta}_s = \mathbf{R}_j^T \delta\boldsymbol{\Theta}_m + \mathbf{e}_j \delta\varphi, \tag{29}$$

missä $\delta\boldsymbol{\Theta}_m$ and $\delta\boldsymbol{\Theta}_s$ ovat aineellisia kiertymälisäysvektoreita isäntä ja orjasolmuissa. Kiertymisoperaattorin variaatiolle aineellisessa esitysmuodossa pätee yhteys $\delta\mathbf{R} = \mathbf{R}\delta\tilde{\boldsymbol{\Theta}}$, missä virtuaalinen aineellinen kiertymälisäysvektorille $\delta\boldsymbol{\Theta}$ ja virtuaaliselle kokonaiskiertymävektorille $\delta\boldsymbol{\Psi}$ on

voimassa relaatio

$$\begin{aligned}
&\delta\Theta = \mathbf{T}\cdot\delta\Psi,\\
&\mathbf{T} := \frac{\sin\psi}{\psi}\mathbf{I} - \frac{1-\cos\psi}{\psi^2}\tilde{\Psi} + \frac{\psi-\sin\psi}{\psi^3}\Psi\otimes\Psi,\\
&\psi := \|\Psi\|, \quad \mathbf{R} = \exp(\Psi), \quad \lim_{\Psi\to\mathbf{0}}\mathbf{T}(\Psi) = \mathbf{I},
\end{aligned} \tag{30}$$

missä tangentiaalinen muunnos $\mathbf{T}$ on singulaarinen kiertymäkulman arvolla 2π. Sijoittamalla yhteys $\delta\Theta_s = \mathbf{T}_s\delta\Psi_s$, missä $\mathbf{T}_s = \mathbf{T}(\Psi_s)$, kaavaan (29) saadaan orja- ja isäntäkiertymien välille kinemaattinen yhteys

$$\begin{aligned}
\delta\Psi_s &= \mathbf{B}_s\begin{pmatrix}\delta\Psi_m\\ \delta\varphi\end{pmatrix},\\
\mathbf{B}_s &= \begin{pmatrix}\mathbf{T}_s^{-1}\mathbf{R}_j^T\mathbf{T}_m & \mathbf{T}_s^{-1}\mathbf{e}_j\end{pmatrix},
\end{aligned} \tag{31}$$

missä orjakuvauksen $\mathbf{q}_s = \phi(\mathbf{q}_{mr})$ kinemaattinen operaattori $\mathbf{B}_s \in \mathbb{E}^{3\times4}$ ja $\mathbf{T}_m = \mathbf{T}(\Psi_m)$.

Orjasiirtymävektori $\mathbf{q}_s$, isäntäsiirtymävektori $\mathbf{q}_{mr}$ ja upotusavaruuden $\mathbb{E}^{16}$ siirtymävektori $\mathbf{q}$ ovat tässä tapauksessa

$$\mathbf{q}_s = \Psi_s \in \mathbb{E}^3, \quad \mathbf{q}_{mr} = \begin{pmatrix}\mathbf{d}_f\\ \Psi_f\\ \mathbf{d}_m\\ \Psi_m\\ \varphi\end{pmatrix} \in \mathbb{E}^{13}, \quad \mathbf{q} = \begin{pmatrix}\mathbf{q}_{mr}\\ \mathbf{q}_s\end{pmatrix} \in \mathbb{E}^{16}. \tag{32}$$

missä 'f' edustaa elementin vapaata solmua. Nyt parametrisointikuvauksen kinemaattinen operaattori $\mathbf{B}$ ja sen aikaderivaatat $\dot{\mathbf{B}}$ ja $\ddot{\mathbf{B}}$ ovat merkintöjen (32) mukaisesti

$$\mathbf{B} = \begin{pmatrix}\mathbf{I}_{16\times13}\\ (\mathbf{O}_{3\times9} \quad \mathbf{B}_s)\end{pmatrix} \in \mathbb{E}^{19\times13}, \quad \dot{\mathbf{B}} = \begin{pmatrix}\mathbf{O}_{16\times13}\\ (\mathbf{O}_{3\times9} \quad \dot{\mathbf{B}}_s)\end{pmatrix}, \quad \ddot{\mathbf{B}} = \begin{pmatrix}\mathbf{O}_{16\times13}\\ (\mathbf{O}_{3\times9} \quad \ddot{\mathbf{B}}_s)\end{pmatrix}, \tag{33}$$

missä orjakuvauksen kinemaattisen operaattorin aikaderivaatat ovat

$$\begin{aligned}
\dot{\mathbf{B}}_s &= \begin{pmatrix}\dot{\mathbf{T}}_s^{-1}\mathbf{R}_j^T\mathbf{T}_m + \mathbf{T}_s^{-1}\dot{\mathbf{R}}_j^T\mathbf{T}_m + \mathbf{T}_s^{-1}\mathbf{R}_j^T\dot{\mathbf{T}}_m & \dot{\mathbf{T}}_s^{-1}\mathbf{e}_j\end{pmatrix},\\
\ddot{\mathbf{B}}_s &= \begin{pmatrix}\ddot{\mathbf{T}}_s^{-1}\mathbf{R}_j^T\mathbf{T}_m + \mathbf{T}_s^{-1}\ddot{\mathbf{R}}_j^T\mathbf{T}_m + \mathbf{T}_s^{-1}\mathbf{R}_j^T\ddot{\mathbf{T}}_m + 2\dot{\mathbf{T}}_s^{-1}\dot{\mathbf{R}}_j^T\mathbf{T}_m + 2\dot{\mathbf{T}}_s^{-1}\mathbf{R}_j^T\dot{\mathbf{T}}_m + 2\mathbf{T}_s^{-1}\dot{\mathbf{R}}_j^T\dot{\mathbf{T}}_m & \ddot{\mathbf{T}}_s^{-1}\mathbf{e}_j\end{pmatrix}.
\end{aligned} \tag{34}$$

Lopuksi kaavan (17) mukainen geometrinen jäykkyystensori $\mathbf{K}_{\sigma mr}$ on

$$\mathbf{K}_{\sigma mr} = \begin{pmatrix}
\mathbf{O} & \mathbf{O} & \mathbf{O} & \mathbf{O} & \mathbf{0}\\
 & \mathbf{O} & \mathbf{O} & \mathbf{O} & \mathbf{0}\\
 & & \mathbf{O} & \mathbf{O} & \mathbf{0}\\
 & & & \mathbf{K}_{\Psi_m\Psi_m} & \mathbf{k}_{\Psi_m\varphi}\\
\text{symm.} & & & & k_{\varphi\varphi}
\end{pmatrix} \in \mathbb{E}^{13\times13}, \tag{35}$$

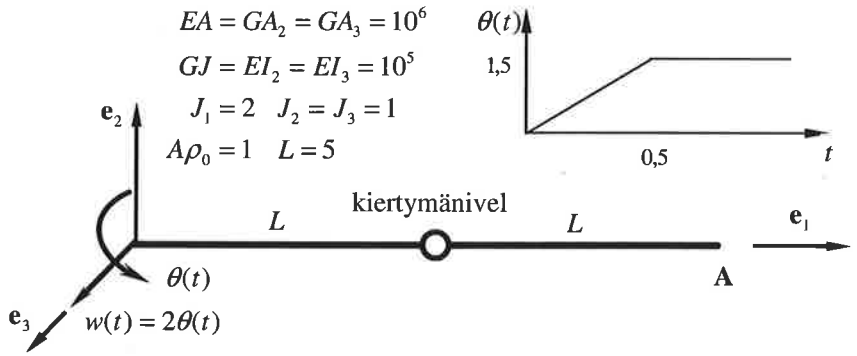
missä osatensorit voidaan esittää muodossa

$$\begin{aligned}
\mathbf{K}_{\Psi_m\Psi_m} &= \mathbf{C}_2\left(\mathbf{R}_j\mathbf{T}_s^{-T}\mathbf{f}_s,\Psi_m\right)+\mathbf{T}_m^T\mathbf{R}_j\mathbf{C}_6\left(\mathbf{f}_s,\Psi_s\right)\mathbf{T}_s^{-1}\mathbf{R}_j^T\mathbf{T}_m \quad &&\in\mathbb{E}^{3\times3},\\
\mathbf{k}_{\Psi_m\varphi} &= \mathbf{T}_m^T\mathbf{R}_j\mathbf{C}_6\left(\mathbf{f}_s,\Psi_s\right)\mathbf{T}_s^{-1}\mathbf{e}_j-\mathbf{T}_m^T\mathbf{R}_j\tilde{\mathbf{e}}_j^T\mathbf{T}_s^{-T}\mathbf{f}_s \quad &&\in\mathbb{E}^{3\times1},\\
k_{\varphi\varphi} &= \mathbf{e}_j\cdot\mathbf{C}_6\left(\mathbf{f}_s,\Psi_s\right)\mathbf{T}_s^{-1}\mathbf{e}_j \quad &&\in\mathbb{E}^{1\times1},
\end{aligned} \tag{36}$$

missä orjavoimavektori $\mathbf{f}_s\in\mathbb{E}^3$ vastaa orjakiertymävektorin Ψ_s vapausasteita. Tensorit $\mathbf{C}_2$ ja $\mathbf{C}_6$ sekä tangentiaalisen muunnoksen $\mathbf{T}$ aikaderivaatat ja käänteistensori $\mathbf{T}^{-1}$ sekä sen aikaderivaatat on esitetty lähteessä [1].

Voimavektori $\mathbf{f}_{mr0}$, tangenttitensorit $\mathbf{K}_{mr}$, $\mathbf{C}_{mr}$ ja massatensori $\mathbf{M}_{mr}$ parametriavaruudessa $\mathbb{E}^{13}$ saadaan kaavojen (16) avulla, kun upotusavaruuden $\mathbb{E}^{16}$ voimavektori $\mathbf{f}$, tangenttitensorit $\mathbf{K}_{load}, \mathbf{K}, \mathbf{K}_{cent}, \mathbf{C}_{gyro}$ ja massatensori $\mathbf{M}$ on laskettu. Nämä upotusavaruuden suureet ovat tunnettuja, sillä palkkielementin solmusiirtymävektori $(\mathbf{d}_f,\Psi_f,\mathbf{d}_m,\Psi_m)$ on osa upotusavaruuden siirtymävektoria $\mathbf{q}$.

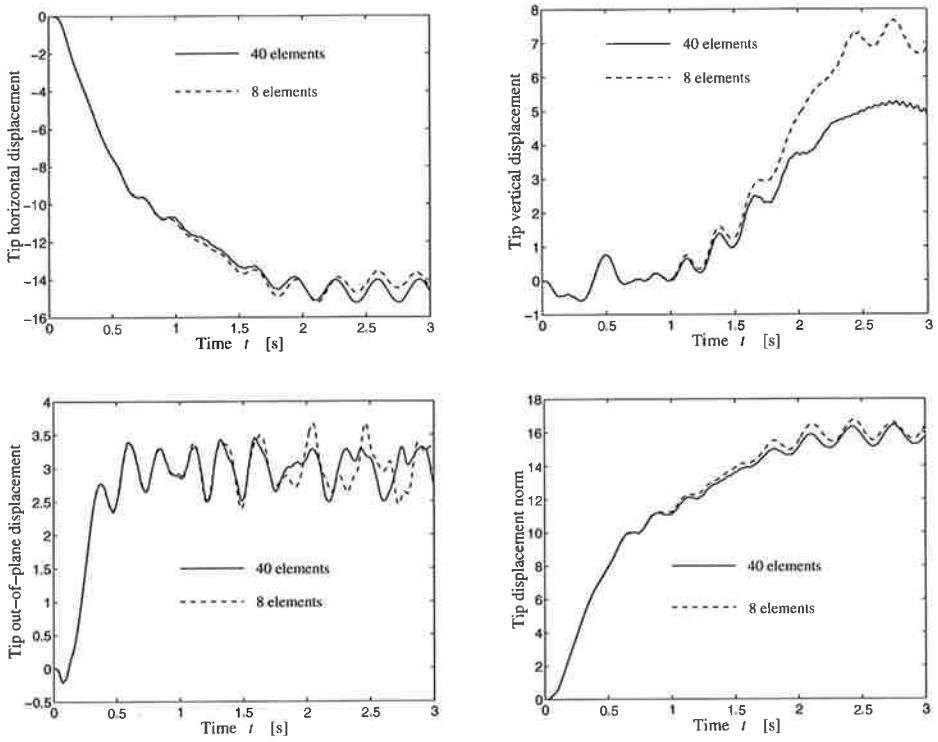
4 NUMEERINEN ESIMERKKI



Kuva 6 Kaksi palkki jotka on kytketty toisiinsa kiertymänivelellä

Numeerisena esimerkkiongelmana käytetään kuvassa 6 esitetty "kahden kappaleen ongelmaa", jossa kappaleet on kytketty toisiinsa kiertymä- eli sarananivelen avulla. Kiertymänivelen kiertymisakseli on alkutilassaan $\mathbf{e}_3$-suunnassa. Alkutilassaan origossa sijaitsevalle alkupäälle annetaan kuvan 6 mukainen ajasta riippuva pakkokiertymä $\theta(t)$ $\mathbf{e}_3$-suuntaa sekä samanaikainen pakkosiirtymä $w(t)=2\theta(t)$ myös $\mathbf{e}_3$-suuntaa. Transienttivaste lasketaan Newmarkin aikaintegroimismenetelmällä, jossa menetelmäparametreiksi valitaan $\beta=1/4$ ja $\gamma=1/2$, mikä vastaa vakiokiihtyvyyskaavaa. Aika-askeleena käytetään vakioaskelta $h=0{,}01$.

Ongelmasta tehdään kaksi laskentamallia, jossa toisessa kukin kappale jaetaan tasavälien neljään palkkielementtiin ja toisessa mallissa 20 palkkielementtiin. Tällöin toisessa laskentamallissa on kaikkiaan 8 palkkielementtiä ja toisessa 40 elementtiä. Kiertymänivel mallinnetaan kappaleessa 3.2 esitetyn kiertymänivelelementin avulla, lisäksi käytetään tarvittaessa kappaleessa 3.1 kuvattua komplementaarista palkkielementtiä. Esimerkkiongelman kärkipisteen A aikavasteet on esitetty kuvassa 7.



Kuva 7 Esimerkkiongelman siirtymävasteet, yläkuvissa kärkipisteen A siirtymä $\mathbf{e}_1$ -suuntaan (vas.) ja siirtymä $\mathbf{e}_2$ -suuntaan, sekä alakuvissa kärkipisteen siirtymä $\mathbf{e}_3$ -suuntaan (vas.) sekä kokonaissiirtymä

5 JOHTOPÄÄTÖKSET

Tässä esityksessä kuvattiin lyhyesti erästä monikappalemekaniikan mallinnustapaa, jossa holonomisten sidosehtojen muodostama sidosmonisto parametrisoidaan. Parametrisoimalla sidosmonisto päädytään liikeyhtälöihin, joissa sidosehtoja ei ole laisinkaan näkyvillä, vaan sidokset on upotettu sidosmoniston parametrisointikuvaukseen. Tätä sidosmoniston parametrisointimenetelmää kutsutaan elementtimenetelmässä isäntä-orjatekniikaksi. Lähteessä [2] on esitetty tasotapauksessa teleskooppipuomiston mallintaminen isäntä-orjatekniikkaa käyttäen.

Monikappalemekaniikan useimmat holonomiset sidokset, kuten erilaiset nivelet ja luistit, voidaan varsin yksinkertaisella tavalla parametrisoida. Tällä mallinnustavalla saavutetaan merkittäviä etuja: muuttujia liikeyhtälössä on minimimäärä sekä vältytään rajoiteyhtälöformulaatioden numeerisilta häiriöherkkyyksiltä, jolloin aikaintegroinnissa voidaan käyttää pidempää aika-askelta. Lisäksi sidosmoniston parametrisointi mahdollistaa konsistenttien tangenttitensoreiden laskemisen.

LÄHDEVIITTEET

[1] Mäkinen, J., (2004), "A Formulation for Flexible Multibody Mechanics – Lagrangian Geometrically Exact Beam Elements using Constraint Manifold Parametrization", *TTY, Teknillinen mekaniikka ja optimointi, tutkimusraportti 2004:3*, 89 s. URL: http://www.tut.fi/~jmamakin/vk.pdf

[2] Marjamäki H. & Mäkinen J., (2003), "Modelling Telescopic Boom – The Plane Case: Part I", *Computers & Structures*, **81**(16), pp. 1597-1609.

MICROCRACK CLOSURE EFFECT ON INDENTATION TESTING OF THERMALLY SPRAYED MATERIALS

Timo Manninen[1], Reijo Kouhia[1], Erja Turunen[2], Simo-Pekka Hannula[2,3]

[1]Helsinki University of Technology, Laboratory of Structural Mechanics
P.O. Box 2100, 02015 TKK, Finland

[2]VTT
P.O. Box 1000, FIN-02044 VTT, Finland

[3]Helsinki University of Technology, Laboratory of Materials Science
P.O. Box 6200, 02015 TKK, Finland

ABSTRACT

Depth-sensing nanoindentation is increasingly being used to study mechanical behaviour of materials. The method is also used for materials that exhibit cracks and pores. Microcracked materials, however, typically exhibit different behaviour in tension and compression due to the microcrack closure effect. The present work discusses the behaviour of microcracked heterogenous materials in indentation testing. As a representative example we consider indentation testing of thermally sprayed ceramic Al_2O_3-coatings.

1 INTRODUCTION

The mechanical properties of materials are in general a function of their microstructure. Therefore establishing cross-property correlations between microstructure and properties is a central theme of materials research.

Materials prepared by thermal spraying typically have much lower Young's moduli than the corresponding bulk materials. The complex structure of thermal spray (TS) materials consist of irregular shaped lamellae formed by rapid solidification of impacting molten droplets. The structure contains large number of cracks and spherical voids. Theoretical work [1, 2, 3] explains the decisive effect of cracks on the decrease of elastic moduli. In the literature cracks are assumed to be sufficiently opened so that their behavior is similar in tension and in compression. Such an approach, however, gives acceptable approximation only at very low stresses. High compressive stresses cause microcrack closure effect, and consequently, restoration of stiffness. Recently the effect of compressive stresses on Young's moduli of thermally sprayed materials has been recognized and studied by Kroupa and his coworkers [4, 5, 6]. Motivated by theoretical and experimental results the authors conclude in [5] that "the effect of pressure, especially that of sprayed ceramics, should be taken into account in theoretical studies and in interpreting experiments in cases with high compressive stresses".

Instrumented depth-sensing indentation is increasingly being used to study mechanical behavior of thin films. Thermally sprayed ceramic coatings are brittle and relatively thin

$(150 - 300\mu\text{m})$, and therefore it is convenient to use indentation tests for measuring their elastic properties. Standard methods used to characterize the elastic properties from indentation results are based on analytical solutions to the contact problem and assume linear elastic behavior. However, a very high compressive pressure is known to exist under the tip during indentation testing [7]. It is not clear how this compressive pressure influences the results; it might induce microcrack closure effects and an increase of elastic stiffness. Evidently, the effect of pressure should be considered and taken into account in interpreting the experiments.

In the present work, the influence of microcrack closure effect in indentation testing of thermally sprayed ceramic coatings is analyzed numerically using the FE-method. The coatings produced by high velocity oxygen fuel (HVOF) thermal spray method contain microcracks and pores in diverse shapes and orientations. The nonlinear material behaviour resulting from the microcrack closure effect is modeled using a three-dimensional approach based on continuum damage mechanics.

2 MODELLING THE MICROCRACK CLOSURE EFFECT (MCE)

The constitutive model used for modelling the microcrack closure effect (MCE) is derived using a thermodynamic approach where the material behaviour is completely described by defining the Helmholtz free energy ψ of the material. The Helmholtz free energy is a function strain ε_{ij} and internal state variables.

A number of quasibrittle damage models are founded on a second order tensorial damage variable

$$D_{ij} = \sum_k d^{(k)} n_i^{(k)} n_j^{(k)} \tag{1}$$

where $d^{(k)}$ represents the density of microcracks with normal $n_i^{(k)}$. In the discrete approach [15], the damage tensor is represented by independent couples of scalar crack density values $d^{(k)}$ and corresponding orientation tensors $N_{ij}^{(k)}$.

$$D_{ij} = \sum_k d^{(k)} N_{ij}^{(k)} \tag{2}$$

The orientation tensors $N_{ij}^{(k)}$ are constructed using a fixed set of directions in the physical space. An orthonormal base is defined in $\mathbb{R}^{3\times 3}$ as follows:

$$\begin{array}{ll} N^{(1)} = e_1 \otimes e_1 & N^{(4)} = \frac{1}{2}(e_1 + e_2) \otimes (e_1 + e_2) \\ N^{(2)} = e_2 \otimes e_2 & N^{(5)} = \frac{1}{2}(e_1 + e_3) \otimes (e_1 + e_3) \\ N^{(3)} = e_3 \otimes e_3 & N^{(6)} = \frac{1}{2}(e_2 + e_3) \otimes (e_2 + e_3) \\ & N^{(7)} = \frac{1}{2}(e_1 - e_2) \otimes (e_1 - e_2) \\ & N^{(8)} = \frac{1}{2}(e_1 - e_3) \otimes (e_1 - e_3) \\ & N^{(9)} = \frac{1}{2}(e_2 - e_3) \otimes (e_2 - e_3) \end{array} \tag{3}$$

Here (e_1, e_2, e_3) is a cartesian basis for $\mathbb{R}^3$. The orientation tensor base is associated with 9 crack density values $d^{(k)}$ regarded as internal state variables.

Presently it is postulated that the specific free energy can be decomposed in three parts

$$\psi = \psi_0(\varepsilon_{ij}) + \psi_1(\varepsilon_{ij}, D_{ij}) + \psi_2(\varepsilon_{ij}, D_{ij}) \tag{4}$$

The first term ψ_0 represents the free energy without damage. The damage effects intervene through the second term ψ_1. The third term ψ_2 contains the terms related to the microcrack

closure effect. The undamaged material is regarded as isotropic and linear elastic.

$$\rho\psi_0 = \frac{1}{2}\lambda\varepsilon_{kk}^2 + \mu\varepsilon_{ij}\varepsilon_{ij} \tag{5}$$

where λ and μ are the Lamé parameters of the undamaged material. According to the representation theorem of tensor functions, the most general form of an isotropic scalar function depending on two symmetric second-rank tensors ε_{ij} and D_{ij} can be expressed as the combination of 10 basic invariants of the tensors.

$$\begin{aligned}\rho\psi \;=\; & \rho\psi(\varepsilon_{ii}, \varepsilon_{ij}\varepsilon_{ji}, \varepsilon_{ij}\varepsilon_{jk}\varepsilon_{ki}, D_{ii}, D_{ij}D_{ji}, D_{ij}D_{jk}D_{ki}, \varepsilon_{ij}D_{ji}, \varepsilon_{ij}\varepsilon_{jk}D_{ki}, \\ & \varepsilon_{ij}D_{jk}D_{ki}, \varepsilon_{ij}\varepsilon_{jk}D_{kl}D_{li})\end{aligned} \tag{6}$$

The material behaviour is assumed linear elastic with constant damage, and therefore the Helmholtz free energy is quadratic in ε_{ij}. Furthermore, since the elastic energy decreases with progressing damage, the Helmholtz free energy is assumed linear in D_{ij}. Eventually, a simplified representation can be used. The following simple form is used to model the damage effects [15, 16]

$$\rho\psi_1 = \alpha\varepsilon_{ij}\varepsilon_{jk}D_{ki} = \alpha\sum_a d^{(a)}\varepsilon_{ij}\varepsilon_{jk}N_{ki}^{(a)} \tag{7}$$

where α is an unknown material parameter.

Continuity of stress-strain response and preservation of elastic energy in closed-opened sequences require , that ψ_2 should satisfy the conditions [14]

$$\psi_2 = 0 \quad \text{if } g = 0 \tag{8}$$

$$\frac{\partial\psi_2}{\partial\varepsilon_{pq}} = 0 \quad \text{if } g = 0 \tag{9}$$

$$\frac{\partial^2\psi_2}{\partial\varepsilon_{ab}\partial\varepsilon_{cd}} = s\frac{\partial g}{\partial\varepsilon_{ab}}\frac{\partial g}{\partial\varepsilon_{cd}} \tag{10}$$

where s is a continuous scalar function and g is the microcrack closure condition used.

Under uniform strain boundary conditions and dilute microcrack density, Pensee et al. [17] derived a microcrack closure condition for microcracks with orientation $N_{ij}^{(a)}$

$$g(\varepsilon_{ij}, N_{kl}^{(a)}) = M_{ij}^{(a)}\varepsilon_{ij} = 0, \tag{11}$$

where

$$M_{ij}^{(a)} = C_{ijkl}^0 N_{kl}^{(a)} = \left(\lambda\delta_{ij}\delta_{kl} + 2\mu\delta_{ik}\delta_{jl}\right)N_{kl}^{(a)} \tag{12}$$

The fourth order tensor C_{ijkl}^0 is the tensor of elasticity for the undamaged material. The microcrack closure condition for a particular discrete direction $N_{ij}^{(a)}$ depends only on strain and on the orientation tensor. Therefore each discrete microcrack direction can be considered separately and the terms $d^{(k)}N_{ij}^{(k)}$ can be decoupled in the third part of the Helmholtz free energy.

The continuity conditions and other requirements are satisfied if the third part of the Helmholtz free energy is given by

$$\rho\psi_2 = \beta\sum_a d^{(a)}H(-\varepsilon_{ij}M_{ij}^{(a)})(\varepsilon_{ij}M_{ij}^{(a)})^2, \tag{13}$$

where β is an unknown material parameter.

The theory can be extended to materials for which a finite compressive stress is needed for microcrack closure. The required modification concerns only the last term, which becomes in this case

$$\rho\psi_2 = \beta \sum_a d^{(a)} H(-\varepsilon_{ij} M_{ij}^{(a)} + \gamma)(\varepsilon_{ij} M_{ij}^{(a)} - \gamma)^2, \tag{14}$$

where γ is a material parameter describing the amount of compression needed for microcrack closure.

In addition to the Lamé parameters of the undamaged material, the model contains three additional material parameters α, β and γ. The parameter β is related to the stiffness recovery by crack closure. The stiffness recovery postulate [18] states that the stiffness in the direction normal to a closed microcrack is equal to its initial value. Imposing this recovery condition in a uniaxially microcracked state yields

$$\beta = \frac{-\alpha}{(\lambda + 2\mu)^2} \tag{15}$$

3 DEPTH-SENSING INSTRUMENTED INDENTATION

Hardness tests are perhaps the most commonly used means for testing material properties. The output of a traditional hardness test is a single numeric value that describes the penetration of the indenter tip into the sample tested. Recently many technologies have moved to smaller scales. Consequently characterization of mechanical properties of materials has become more difficult. One tool that is widely used for such measurements is depth-sensing instrumented indentation, often termed "nanoindentation". It is used to determine mechanical properties of materials which are available only in a small volumes, e.g. thin films or nanocrystals. In contrast to traditional indentation, the output of an instrumented indentation test is a timeseries describing the evolution of force P and displacement h continuously. The loading sequence can be specified in terms of the applied force or the indenter tip displacement and is feedback controlled by the equiplement.

Conventional analytical methods used to characterize the elastic properties from indentation load-depth curves are based on analytical solutions to the contact problem by Herz [9] and Sneddon [8]. These analytical solutions are based on following assumptions:

- The sample is isotropic, homogenous, flat, elastic half-space.
- The indenter tip is an isotropic, homogenous, elastic ball (Hertz) or a rigid revolved parabolus (Sneddon).
- Deformations are small.

The standard analysis method used the determine sample hardness H or effective elastic modulus E^* from measurement data is the Oliver-Pharr method.

3.1 THE OLIVER-PHARR METHOD

The Oliver-Pharr method is founded on Sneddon's analysis of elastic contact between a rigid axisymmetric parabolus and an elastic, isotropic, homogenous half-space. The analysis is done using the unloading part of the indentation load-displacement curve. The material behaviour is supposed to be completely elastic during the unloading phase. The analysis of hardness and elastic properties using Oliver-Pharr method [10, 11, 12] is given as Algorithm 1.

Algorithm 1 The Oliver-Pharr method.

1. Measure load $P(t)$ and displacement $h(t)$ during a loading-unloading sequence.

2. Subtract equipment frame deflection from the measured displacements.

$$h \rightarrow h - CP \tag{16}$$

where C is a compliance value determined using a reference sample.

3. Fit the powerlaw equation

$$P = c(h - h_f)^m \tag{17}$$

where h_f is the final displacement after full unloading, into the the upper 80% of the unloading part of $P(h)$. The exponent value $m = 1.5$ is used for spherical indentation.

4. Compute contact stiffness S

$$S := \frac{\partial P}{\partial h} = cm(h - h_f)^{m-1} \tag{18}$$

at maximum load P_{max}.

5. Compute contact depth h_c at maximum load using relation

$$h_c = h - \varepsilon \frac{P_{max}}{S} \tag{19}$$

For a spherical tip the constant ε equals to $\varepsilon = 0.75$.

6. Compute projected contact area $A_c = A(h_c)$ using the tip area function $A(h)$. The tip area function depends on tip geometry and is determined during equipment calibration using a reference sample.

7. Compute the elastic stifness of the sample $E_s/(1 - \nu_s^2)$ from equations

$$E^* = \sqrt{\frac{\pi}{4A_c}} S \quad \text{where} \quad \frac{1}{E^*} = \frac{1 - \nu_s^2}{E_s} + \frac{1 - \nu_i^2}{E_i} \tag{20}$$

The effective elastic modulus E^* is a function of the sample and tip elastic properties denoted by subscripts s and i, respoctively.

8. Compute hardness H.

$$H := \frac{P}{A_c} \tag{21}$$

The Oliver-Pharr method is based on several assumptions, the most important one being that Sneddon's solution for a rigid indenter can be used with the reduced modulus of elasticity E^* accounting for the elastic deformation of the tip [12]. Furthermore, the possible inelastic deformation is accounted for by subtracting the final depth h_f from the total displacement in eq. (17). However, if pile-up or sinking-in happens around the indenter tip, contact depth is not equal to that estimated by eq. (19). In such a case, the effective elastic modulus is not correctly estimated by the Oliver-Pharr analysis. The results reported by Zeng et al. [13] for 11 brittle glasses and ceramic materials show, that the Oliver-Pharr method underestimates the contact depth and overestimates the effective elastic modulus for these materials.

Accurate determination of machine compliance C and the tip area function $A(h)$ using a reference material sample is of great importance for the accurate characterization of the material properties. Reference samples made of synthetic amorphous silicon oxide (fused silica) are commonly used in calibration. It is worth noticing that the machine compliance value is determined by applying the Oliver-Pharr analysis to a measurement data obtained using a reference sample with known elastic properties. Therefore the compliance value also compensates errors caused by the approximations adopted in the Oliver-Pharr analysis method.

4 FE-SIMULATION OF MCE ON INDENTATION TESTING

Analytical solutions to Hertz contact problem are available only for isotropic, linear elastic materials. In the present work we examine the influence of the microcrack closure effect on indentation testing of materials containing large number of microcracks using numerical simulations. In order to isolate the influence of the microcrack closure effect, the Hertzian contact damage induced during indentation testing [19] is neglected. As an example materials we consider thermally sprayed ceramic Al_2O_3 coatings.

4.1 MATERIALS

The coating samples were produced by the HVOF (high velocity oxygen fuel) method on an AISI 316 stainless steel substrate. The coating process is described in detail elsewhere [21]. The thickness of the coating was on the average $t_c = 0.451$ mm and that of the substrate was $t_s = 2.0$ mm. The porosity of the coating was measured using image analysis method and it was approximately 5%. Figure 1 shows a micrograph of the coating cross-section.

The Young's modulus of the coating was measured using two methods: instrumented indentation technique and impulse excitation technique.

The indentation experiments were performed with Nanotest 550 nanoindentation equipment at VTT. The equipment assembly consists of a measuring unit with a pendulum structure, an optical microscope and a control unit. The calibration procedure before every experimental series included the load and depth calibration. Reference sample for the compliance determination and for depth and load calibration was fused silica (SiO_2). Measurements were carried out using a spherical WC-Co -tip with a radius of $R = 0.794$ mm under displacement control up to a maximum load of $P = 10$ N. The indentations were made on the coating surface in the through-thickness direction. The experimental data were analysed using the standard Oliver-Pharr method. According to the indentation experiments, the Young's modulus of the coating was $E = 93.7$ GPa.

The impulse excitation measurements were performed at the Laboratory of Strength of Materials in Helsinki University of Technology. In the test setup the sample is supported as a cantilever beam and its lowest natural frequency is measured before and after the coating

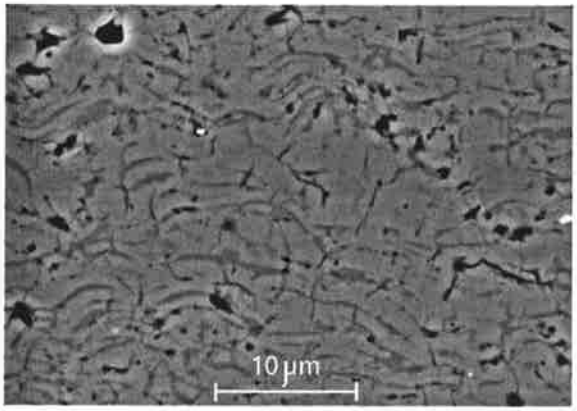


Figure 1: SEM microstructure of the coating.

process. Impulse hammer technique was used to excite small amplitude vibration in the first eigenmode. Based on the relative change of the lowest eigenfrequency, the Young's modulus of the coating is determined. The in-plane Youngs modulus was determined to be $E = (96.4 \pm 4.8)$ GPa.

4.2 DETERMINATION OF MATERIAL PARAMETERS

Due to rapid solidifaction and subsequent cooling of the molten droplets, cracks formed in the coating adopt a slightly convex oval shape. A finite compressive stress p_c is required to close the microcracks. The crack closing pressure dependens on the crack shape, but it is not very sensitive to crack form [4]. For typical elliptical or diamond-shaped cracks the pressure is approximately

$$\frac{p_c}{E} \approx \frac{1}{2}\frac{b}{a} \tag{22}$$

where a is the radius and b is the crack opening. For plasma sprayed alumina coatings the aspect ratio $\frac{b}{a}$ is typically of the order $10^{-2}...10^{-4}$ [5]. No experimental data is available at the moment for HVOF alumina coatings. The HVOF coatings are, however, considerably more dense than plasma sprayed ones [22]. Therefore different values in between $\frac{a}{b} \in (0.001, 0.003)$ and the upper and lower bounds $p_c = 0$ and $p_c = -\infty$ were used in the simulations.

Apart from microcracks, thermally sprayed ceramic coatings contain also globular pores. A dilute consentration of globular randomly distributed pores lowers the elastic stiffness of the coating in an isotropic manner. The reduction of elastic properties can be approximated with [20].

$$E = E_0 \left[1 + \frac{p}{1-p}\frac{3(1-\nu_0)(9+5\nu_0)}{2(7-5\nu_0)}\right]^{-1} \tag{23}$$

$$\nu = \nu_0 \frac{E}{E_0}\left[1 + \frac{p}{1-p}\frac{3(1-\nu_0)(1+5\nu_0)}{2(7-5\nu_0)}\right] \tag{24}$$

The powder used in the spray coating process consists of α–Al_2O_3. During the spraying metastable phases are formed and the HVOF sprayed alumina coating consists predominantly of γ-phase. The Young's modulus and Poisson ratio of this phase can be roughly estimated as $E_0 = 250$ GPa and $\nu_0 = 0.20$. The globular pores are not taken into account

in the continuum damage model. Instead, the properties of the base material are lowered accordingly. Given that the measured porosity was $p = 0.05$, the properties of the base material are $E = 225\,\mathrm{GPa}$ and $\nu = 0.185$.

The microstructure of HVOF sprayed coatings contains a variety of microcracks in different shapes and orientations. In order to express the damage in terms of microstructural parameters, the complexity of the microcracking distribution has to be reduced. Following [1] the microcrack distribution is identified as two families of strongly oblate spheroidal voids. The first family of cracks is approximately parallel to the subrate. The second family consists of random distribution of cracks perpendicular to the substrate. Consequently, the damage can be described using three crack density related state variables. In current case the through-thickness direction is chosen to be along the y-axis and the crack density values are related to the nine discrete orientations as follows:

$$d^{(2)} = d^t \tag{25}$$

$$d^{(1)} = d^{(3)} = d^{(5)} = d^{(8)} = d^p \tag{26}$$

$$d^{(4)} = d^{(6)} = d^{(7)} = d^{(9)} = d^d \tag{27}$$

The first state variable d^t corresponds to density of horizontal cracks, the second variable d^p descibes the density of vertical cracks and the third variable d^d describes the density of inclined cracks, i.e. the amount of orientational scatter in the horizontal and vertical crack families. In the present work, an isotropic damage orientation distribution was assumed.

$$d^t = d^p = d^d = \frac{1}{3}$$

The material parameter α related to the loss of elastic stiffness caused by microcracking was assigned the value

$$\alpha = 0.5739\frac{\lambda + 2\mu}{2} \tag{28}$$

This value was selected on the grounds that the reduction of elastic stiffness should correspond to the measured properties of the coating and the properties of the undamaged base material.

4.3 FINITE ELEMENT SIMULATION

An axisymmetric model was used for simulation of the indentation test The model consists of a sphrical indenter tip with a radius of $R = 0.794\mathrm{mm}$ and a cylindrical sample with a radius of$R = 1.0\mathrm{mm}$ and a heigth of $H = 1.8\mathrm{mm}$. The tip comprised of 943 quadratic triangular elements (CAX6M) and the sample of 2255 elements of same type. The finite element mesh is shown in fig. 2. The tip material was regarded isotropic and elastic with the following properties: Young's modulus $E = 614\mathrm{GPa}$ and Poisson's ratio $\nu = 0.22$. The Coulomb coefficient of friction was $\mu = 0.085$.

In the simulations a standard indentation test was performed up to a maximum load of $P = 10\mathrm{N}$. The load was applied to the upper edge of the tip, which was constrained to remain straight. The vertical displacement and the load values were recorded for one full loading-unloading cycle.

The load-displacement curves obtained are shown in fig. 3. The simulated data were analyzed using the Oliver-Pharr method. The compliance value used was obtained by simulation of indentation test on a virtual reference sample with the material properties given in [12] for fused silica glass. The results of the Oliver-Pharr analysis of the simulated $P(h)$ curves are summarized in table 1. The value $\nu = 0.185$ was used in estimating the

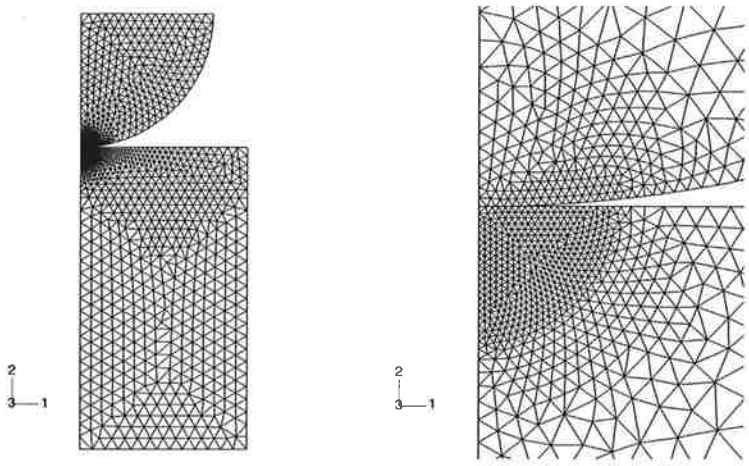


Figure 2: Finite element mesh used in numerical simulations. In the left: full model, on the right: detail.

Young's moduli from the indentation elastic stiffness values $E/(1-\nu^2)$. The given crack closure stress values were estimated based on material behavior in uniaxial compressive straining.

Table 1: The influence of material parameter γ and the corresponding crack closure stress on indentation Young's modulus.

γ (MPa)	0	200	400	600	∞
$\sim p_c$ (MPa)	0	125	250	375	∞
E (GPa)	123	99	91	87	72

The results show that the indentation Young's moduli increases due to the MCE. The size of the effect is dependent on the stress which is needed for microcrack closure. This on the other hand depends on the microcrack opening, i.e. the aspect ratio of the strongly oblate, spheroidal microcracks. For realistic aspect ratios of $\frac{a}{b} \in (0.001, 0.003)$, which correspond to $\gamma \in (200, 400)$MPa, the indentation Young's moduli equal to the experimentally measured value.

5 Conclusions and discussion

In the present work the influence of microcrack closure effect in indentation testing of thermally sprayed ceramic coatings was analyzed numerically using the FE-method. The nonlinear material behaviour resulting from the microcrack closure effect was modeled using a three-dimensional continuum damage mechanics -based model. The results obtained in a realistic example case show that the microcrack closure effect indeed can cause a significant increase in the indentation Young's modulus. Without the microcrack closure effect, the indentation Young's modulus was $E = 72$GPa. With the microcrack closure effect, however, the indentation Young's modulus values in the range of $E \in (72, 123)$GPA were obtained.

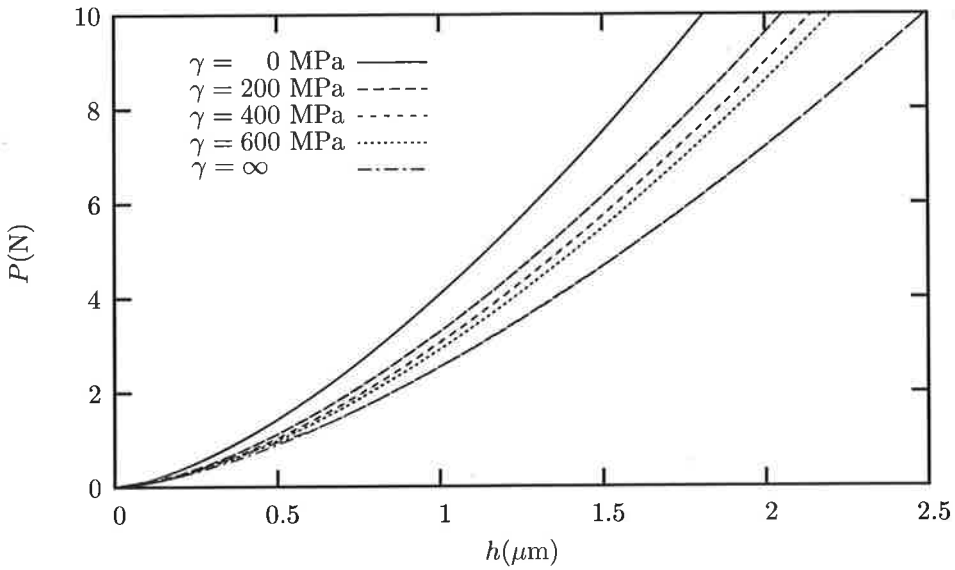


Figure 3: Simulated $P(h)$ curves for different values of parameter γ

ACKNOWLEDGEMENTS

This research has been supported by the Academy of Finland (decision number 210622) and by the Foundation of K. and A. Lippa.

REFERENCES

[1] Leigh, S.-H. and Berndt, C.C. Modelling of elastic constants of plasma spray deposits with ellipsoid-shaped voids. Acta Materialia. 1999. Vol. 47, pp. 1575-1586.

[2] Sevostianov, I. and Kachanov, M. Plasma-sprayed ceramic coatings: anisotropic elastic and conductive properties in relation to the microstructure; cross-prorty correlations. Mater. Sci. Eng. 2001. Vol. A 297, pp. 235-243.

[3] Sevostianov, I., Kachanov, M., Ruud, J., Lorraine, P. and Dubois, M. Quantitative characterization of microstructures of plasma-sprayed coatings and their conductive and elastic properties. Mater. Sci. Engr. 2004. Vol. A386, pp. 164-174.

[4] Kroupa, F. and Dubsky, J. Pressure Dependence of Young's moduli of thermal sprayed materials. Scripta Materialia. 1999. Vol. 40, pp. 1249-1254.

[5] Kroupa,F. and Plesek, J. Nonlinear elastic behavior in compression of thermally sprayed materials. Mater. Sci. Engr. 2002. Vol. A328, pp. 1-7.

[6] Landa, M., Kroupa, F., Neufuss, K. and Urbanek, P. Effect of Uniaxial pressure of ultrasound velocities and elastic moduli in plasma-sprayed ceramics. J. Thermal Spray Technology. 2003. Vol. 12, pp. 226-233.

[7] Giannakopoulos A. E. & Larsson P.-L. Analysis of pyramid indentation of pressure sensitive hard metals and ceramics. Mechanics of Materials. 1997. Vol. 25, pp. 1-35.

[8] Sneddon, I. N. The relationship between load and penetration in the axisymmetric Boussineque problem for a punch of arbitrary profile. Int. J. Engr. Sci. 1965. Vol. 3, pp. 47-57. ISSN 0020-7225.

[9] Johnson, K. L. Contact Mechanics. Cambridge, UK: Cambridge University Press, 1985. ISBN: 0-521-25576-7.

[10] Oliver, W. C., and Pharr, G. M. An Improved Technique for Determining Hardness and Elastic Modulus Using Load and Displacement Sensing Indentation Experiments. Journal of Materials Research. 1992. Vol. 7, pp. 1564-1583.

[11] Vanlandingham, M. R., Review of Instrumented Indentation. Journal of Research of the National Institute of Standards and Technology. 2003. Vol. 108, pp. 249-265. ISSN 1044-677X.

[12] Knapp, J.A., Follstaedt, D.M. Myers, S.M. and Barbour, J.C. Finite-element modeling of nanoindentation. J. Applied Physics. 1999. Vol. 85, pp. 1460-1474.

[13] Zeng, K., Söderlund, E., Giannakopoulos, A. E. and Rowcliffe, D. J. Controlled indentation: A general approach to determine mechanical properties of brittle materials. Acta Materialia. 1996. Vol. 44, pp. 1127-1141. ISSN 1359-6454.

[14] Curnier, A., He, Q. and Zysset, P. Conewise linear elastic materials. J. Elasticity. 1995. Vol. 37, pp.1-38.

[15] Bargellini, R., Halm D. and Dragon, A., Modelisation de l'endommagement anisotrope par mesofissuration: vers une approche discrete. CFM 2005, 29.8-2.9.2005, Troyes, France.

[16] Challamel, N., Lanos, C. and Casandjian, C. Strain-based anisotropic damage modelling and unilateral effects. International Journal of Mechanical Sciences. 2005. Vol. 47, pp. 459-473.

[17] Pensee, V. and Kondo, D. Micromechanics of anisotropic brittle damage: comparative analysis between a stress based and a strain based formulation. Mechanics of Materials. 2003. Vol. 35, pp. 747-761.

[18] Welemane, H. and Cormery, F. An alternative 3D model for damage induced anisotropy and unilateral effect in microcracked materials. J. Phys. IV. France. 2003. Vol. 105, pp. 329-336.

[19] Licht, V., Ernst, E. and Huber, N. Simulation of the Hertzian contact damage in ceramics. Modelling Simul. Mater. Sci. Engr. 2003. Vol. 11, pp. 477-486.

[20] Kachanov, M., Tsukrov, I. and Shafiro, B. Effective moduli of solids with cavities of various shapes. Applied Mechanics Reviews. 1994. Vol. 47, pp. 151-174.

[21] Turunen, E., Varis, T., Gustafsson, T.E., Keskinen, J., Fält, T. and Hannula, S.-P. Parameter optimization of HVOF sprayed nanostructured alumina and alumina-nickel composite coatings. Surface and Coatings Technology. 2006. Vol. 200, pp. 4987-4994.

[22] Kulkarni, A., Gutleber, J., Sampath ,S., Goland, A., Lindquist, W.B., Herman, H., Allen, A.J. and Dowd, B. Studies of the microstructure and properties of dense ceramic coatings produced by high velocity oxygen-fuel combustion spraying. Materials Science and Engineering. 2004. Vol. A369, pp. 124-137.

KIVEN SÄRKYMISEN NUMEERINEN MALLINNUS ISKUMAISESSA KUORMITUKSESSA

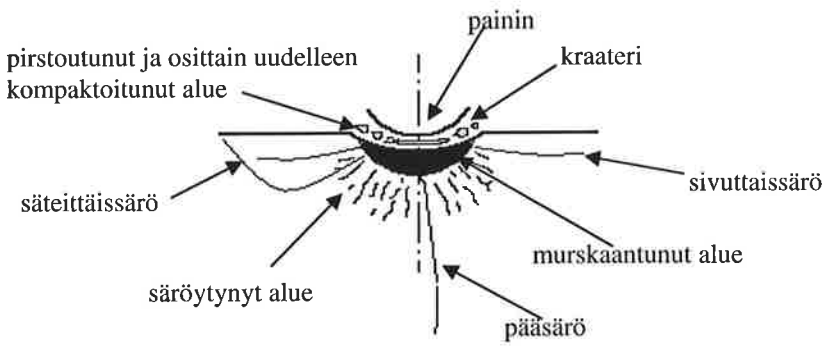
T. SAKSALA
Teknillinen mekaniikka ja optimointi
Tampereen teknillinen yliopisto
PL 589 FIN-33101, TAMPERE

TIIVISTELMÄ

Tässä työssä esitetään elementtimenetelmään perustuva numeerinen proseduuri kiven särkymisen simulointiin iskevän kuormituksen alaisena. Kiven säröily ja murskautuminen mallinnetaan vauriomekaniikan keinoin. Säröilyn alkamisen osoittamiseen käytetään Rankinen ja Mohr-Coulombin vauriokriteerejä veto- ja puristustyyppiselle vauriolle vastaavasti. Kiven materiaalinen heterogeenisuus mallinnetaan tilastollisesti. Diskretoidut liikeyhtälöt ratkaistaan eksplisiittisellä aikaintegraattorilla. Painin mallinnetaan deformoituvana kappaleena ja sen isku kiveen kontaktimekaniikkaa käyttäen. Kehitetyn menetelmän toimivuus testataan numeerisin esimerkein, joita tässä ovat painimen törmäyksen aiheuttaman vauriokuvion simulointi yhden ja kahden männän tapauksessa.

1. JOHDANTO

Kiven särkymisen numeerinen mallinnus on tärkeä ongelma maa- ja kalliomekaniikassa. Erityisesti kallionporauslaitteita valmistavat yritykset ovat kiinnostuneita porakruunun törmäyksen kiveen aiheuttaman vaurion numeerisesta simuloinnista. Tärkeimmäksi ongelmaksi muodostuu porakruunun yhden nastan painuman aiheuttaman murskautumisen ja säröilyn mallinnus. Alla olevassa kuvassa 1 on esitetty staattisessa painumakokeessa syntyvän vauriokuvion tyypilliset piirteet kovalle ja hauraalle kivilajille [1] (vastaavan laboratoriokokeen tulos on kuvassa 4).



Kuva 1. Yhden nastan kvasistaattisessa painumakokeessa syntyvä tyypillinen vauriokuvio

Tämä ongelma on monimutkaisuutensa vuoksi analyyttisten menetelmien ulottumattomissa. Sen ratkaisuun on staattisessa tapauksessa sovellettu mm. elementtimenetelmää, diskreettien elementtien menetelmää ja reunaelementtimenetelmää. Menetelmät ovat usein keskittyneet syntyvän jännitystilakentän ratkaisemiseen tai jonkin yksityiskohdan, kuten sivuttaissäröjen kasvun, mallintamiseen.

Kvasistaattisen painumaongelman vauriomekanismien kokonaisvaltaisemman numeerisen mallinnuksen on mahdollistanut Tangin (1997) [2] kiven murtumisen progressiiviseen simulointiin esittelemä koodi RFPA (rock failure process analysis). Tangin päähypoteesit ovat: (1) kiven globaalia epälineaarista käyttäytymistä voidaan mallintaa lineaarisella elementtimenetelmällä, kun kiven heterogeenisuus otetaan huomioon mallintaen materiaaliparametrit tilastollisesti Weibull-jakaumaa käyttäen; (2) säröjen aiheuttamia epäjatkuvuuksia voidaan mallintaa kontinuumimenetelmällä, jos vaurioituneiden elementtien jäykkyys- ja lujuusominaisuuksia asteittaisesti vähennetään eli särönkasvua mallinnetaan vauriomekaniikan (damage mechanics) hengessä. Käytetyssä vauriomallissa elementti voi vaurioitua joko veto- tai puristustilassa. Vauriokriteereinä käytettiin vetotyyppiselle vauriolle Rankinen kriteeriä ja puristustyyppiselle leikkausvauriolle Mohr-Coulombin kriteeriä.

Tässä työssä nämä ideat yhdistetään eksplisiittisen aikaintegroinnin kanssa. Ongelma siis ratkaistaan dynaamisena, koska se on oikeasti dynaaminen ja eksplisiittisen aikaintegroinnin edut ovat kiistattomat, kun lähestymistapa ongelmaan on "insinöörimäinen".

Kehitetyssä menetelmässä painin mallinnetaan deformoituvana kappaleena ja painimen ja kiven välinen törmäys solmu-solmuun -kontaktimallia käyttäen. Kontaktireunaehdot käsitellään eksplisiittisen aikaintegroinnin kanssa yhteensopivalla Lagrangen kertojien menetelmän modifikaatiolla. Äärellisen elementtimallin reunoilta tapahtuva jännitysaaltojen heijastuminen estetään asettamalla reunoille viskoosiin vaimennukseen perustuva heijastamaton reunaehto. Numeerisena esimerkkinä simuloidaan painimen iskun aiheuttamaa säröilyä yhden ja kahden painimen tapauksissa.

2. KIVEN HETEROGEENISUUDEN TILASTOLLINEN MALLINTAMINEN

Kovan ja hauraan kiven, kuten graniitin, mikrorakenne koostuu satunnaisesti suuntautuneista eri mineraalien muodostamista rakeista. Tästä syystä kivi ei ole homogeeninen, mutta mineraalien suuntien satunnaisuudesta johtuen sen voidaan olettaa olevan isotrooppista. Tässä työssä heterogeenisuutta mallinnetaan tilastollisesti Tangin [1] menetelmää seuraten.

Oletetaan, että kiven materiaaliparametrit, sisältäen kimmokertoimen E, veto- ja puristuslujuuden σ_t, σ_c, tiheyden ρ ja Poisson'n vakion ν, ovat Weibull-jakautuneet. Tämän jakauman tiheysfunktio on

$$f(u) = \frac{m}{u_0}\left(\frac{u}{u_0}\right)^{m-1} \exp\left(-\frac{u}{u_0}\right)^m \tag{1}$$

ja kertymäfunktio

$$Q(u) = 1 - \exp\left(-\frac{u}{u_0}\right)^m . \tag{2}$$

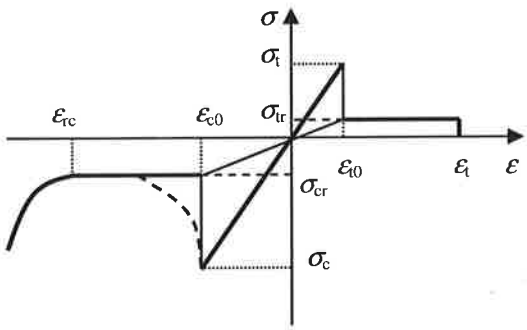
Kaavoissa (1) ja (2) parametri m vastaa mekaniikan mielessä tulkittuna homogeenisuusindeksiä siten, että mitä suurempi m, sitä homogeenisempaa on materiaali. Parametri u_0 on

skaalausparametri, joka lähestyy Weibull-jakauman odotusarvoa, kun m lähestyy ääretöntä. Siten sen voi tässä tulkita olevan materiaaliparametrin homogeeninen arvo.

Materiaaliparametrien liittäminen elementtiverkkoon tehdään siten, että välille [0,1] generoidaan tasaisesti jakautuneita satunnaislukuja (kertymäfunktion arvo) vastaten elementtien lukumäärää. Sitten ratkaistaan jokaiselle elementille materiaaliparametri u kertymäfunktiosta (2). Kiven kimmokertoimelle ja puristuslujuudelle käytetään omaa tasan jakautunutta satunnaisdataa, mutta samaa homogeenisuusindeksiä. Vetolujuudelle käytetään puristuslujuuden jakaumasta saatuja arvoja kerrottuna kertoimella 0.1. Poisson'n kertoimelle ja tiheydelle käytetään huomattavasti suurempaa homogeenisuusindeksiä kuin lujuuksille ja kimmokertoimelle. Menetelmän soveltaminen vaatii erittäin pienen elementtikoon.

3. KIVEN KONSTITUTIIVINEN LAKI JA VAURIOKRITEERIT

Kiven oletetaan olevan murtoon saakka (veto- ja puristuspuolella) lineaarisesti kimmoista. Konstitutiivinen laki on esitetty kuvassa 2 [4].



Kuva 2. Hauraasti murtuvan materiaalin konstitutiivinen malli

Vetopuolella murtuma on hauras eli materiaalin lujuus laskee jyrkästi vetolujuudesta σ_t jäännöslujuuteen σ_{tr}, jossa arvossa jännitys pysyy kunnes venymä saavuttaa arvon $\varepsilon_{tu} = \eta\varepsilon_{t0}$, missä η on skalaarikerroin ja $\varepsilon_{t0} = \sigma_t/E$. Tämän jälkeen elementti ei kykene kantamaan lainkaan kuormitusta. Puristuspuolella materiaali on myös lineaarisesti kimmoista murtojännitykseen σ_c saakka. Tämän jälkeen jännitys laskee jyrkästi (haurasmurtuma) tai pehmeämmin (sitkeämurtuma, ks. katkoviiva kuvassa 2) jäännösjännitykseen σ_{cr}. RFPA:n mallia seuraten oletetaan, että on voimassa $\sigma_t / \sigma_{tr} = \sigma_c / \sigma_{cr} = \lambda$. Kun venymä saavuttaa puristuspuolella arvon ε_{rc}, tapahtuu kivimateriaalin uudelleen tiivistymistä (recompaction), jolloin sen kimmomoduli kasvaa jonkin funktion mukaisesti.

Tässä tutkimuksessa käytetään RFPA:ssa käytettyjä Mohr-Coulombin (puristuspuoli) ja Rankinen (vetopuoli) kriteerejä osoittamaan ne jännitystilat, jotka johtavat vaurioon. Rankinen kriteeri (suurimman pääjännityksen kriteeri) olettaa, että materiaali murtuu, kun suurin pääjännitys ylittää vetolujuuden eli

$$\sigma_1 \le \sigma_t . \tag{3}$$

Mohr-Coulombin vauriokriteerin määrittelyssä oletetaan, että pääjännityksille pätee $\sigma_1 > \sigma_2 = \sigma_3$. Epäyhtälönä esitettynä kriteeri on

$$\sigma_3 - \frac{1+\sin(\varphi)}{1-\sin(\varphi)}\sigma_1 \geq \sigma_c, \tag{4}$$

missä φ on kiven sisäinen kitkakulma ja σ_c on kiven puristuslujuus. Mohr-Coulombin kriteeri ei tarkasti vastaa kokeiden antamia tuloksia ja sen mukaan materiaali kestää miten suuria jännityksiä tahansa, kunhan niiden suhde on sellainen, että epäyhtälö (4) ei toteudu. Yksinkertaisuuden vuoksi sitä kuitenkin käytetään tässä työssä.

4. ISOTROOPPINEN VAURIOMALLI

Isotrooppisen vauriomallin perusoletus on, että mikrosäröt ja muut viat ovat orientaatioltaan satunnaisia, jolloin niiden vaikutus kimmomodulin pienentymiseen on kaikissa suunnissa sama. Tällöin jännitysten ja venymien välinen yhteys on

$$\boldsymbol{\sigma} = (1-\omega)\mathbf{E}_e\boldsymbol{\varepsilon} \tag{5}$$

missä $\omega \in [0,1]$ on vaurioparametri, jonka arvo $\omega = 0$ tarkoittaa ehjää ja arvo $\omega = 1$ täysin vaurioitunutta materiaalia. Vetopuolella vaurionkehityslaki g on muotoa [4]

$$\omega = g(\varepsilon_{eqv}) = \begin{cases} 0, & \varepsilon_{eqv} < \varepsilon_{t0} \\ 1-\lambda\dfrac{\varepsilon_{t0}}{\varepsilon_{eqv}}, & \varepsilon_{t0} \leq \varepsilon_{eqv} < \varepsilon_{tu} \\ 1, & \varepsilon_{eqv} \geq \varepsilon_{tu} \end{cases}, \tag{6}$$

missä ε_{eqv} on ekvivalentti venymä, joka huomioi jännitystilan moniaksiaalisuuden. Materiaaleilla, joilla käyttäytyminen veto- ja puristustiloissa on hyvin erilaista, täytyy venymämitan kyetä huomioimaan tämä seikka: vain venymän positiiviset komponentit vaikuttavat vaurioon vetotilassa. Tässä käytetään ns. Mazars-tyyppistä alun perin betonille kehitettyä mittaa (myös RFPA käyttää tätä)

$$\varepsilon_{eqv} = \sqrt{<\varepsilon_1>^2 + <\varepsilon_2>^2 + <\varepsilon_3>^2}, \tag{7}$$

missä sulkeet $<x>$ tarkoittavat lauseketta $(|x|+x)/2$.

Puristustilassa vaurionkehityslaki g on haurasmurtumalle

$$\omega = \begin{cases} 0, & \varepsilon_3 > \varepsilon_{c0} \\ 1-\lambda\dfrac{\varepsilon_{c0}}{\varepsilon_3}, & \varepsilon_{rc} < \varepsilon_3 \leq \varepsilon_{c0} \\ 1-\lambda-(200(\varepsilon_{rc}-\varepsilon_3))^2, & \varepsilon_3 \leq \varepsilon_{rc} \end{cases}, \tag{8}$$

missä ε_3 on pienin (puristavin) päävenymä ja

$$\varepsilon_{c0} = \frac{1}{E_0}\left(-\sigma_c + \frac{1+\sin(\varphi)}{1-\sin(\varphi)}\sigma_1 - \nu(\sigma_2+\sigma_1)\right), \tag{9}$$

joka on saatu sijoittamalla yleistettyyn Hooken lakiin (venymälle ε_3) ε_{c0} ja σ_3 ratkaistuna Mohr-Coulombin kriteeristä (4). E_0 on ehjän materiaalin kimmomoduli. Sitkeämmälle murtumalle voidaan välillä $\varepsilon_3 \in [\varepsilon_{c0}, \varepsilon_{rc}]$ käyttää esim. kaavaa

$$\omega = \begin{cases} 1-\left(\dfrac{\varepsilon_{c0}}{\varepsilon_3}\right)^n, & \varepsilon_{c0}/\sqrt[n]{\lambda} < \varepsilon_3 \le \varepsilon_{c0} \\ 1-\lambda, & \varepsilon_{cr} < \varepsilon_3 \le \varepsilon_{c0}/\sqrt[n]{\lambda} \end{cases} \quad (10)$$

Edellisissä kaavoissa täytyy huomioida vaurion palautumaton luonne eli vaurioparametrin arvo voi kasvaa tai pysyä (esim. kuorman poistuessa) ennallaan. Siten kaavoissa (6), (8) ja (10) täytyy käyttää soveltuvaa historiamuuttujaa.

5. VAURION VAIKUTUKSEN DEAKTIVOINTI SÄRÖN SULKEUTUESSA

Vetotyyppisen vaurion yhteydessä vaurio on luonteeltaan unilateraalinen eli vauriolla on vaikutusta vain kun säröä kuormitetaan siten, että se aukeaa; särön sulkeutuessa vauriolla ei ole vaikutusta jännityksiin, jos oletetaan täydellinen sulkeutuminen, kuten on helppo ymmärtää tarkastelemalla 1D jännitystilaa. Yllä kuvattua isotrooppista vauriomallia (5) ei ole aivan yksinkertaista yleistää huomioimaan myös särön sulkeutumista, koska useampiaksiaalisessa jännitystilassa kuormituspolku vetopuolelta puristuspuolelle ei kulje origon kautta (vaan se on hypertaso).

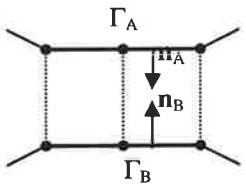
Tässä seurataan lähteessä [5] esitettyä tapaa, jossa lähdetään yleisestä Hooken laista ja erotetaan jännitystilasta (tässä venymätilasta) hydrostaattinen osa. Vaurion deaktivointi tehdään riippumattomasti päävenymille ja hydrostaattiselle venymälle seuraavasti.

$$\sigma_i = 2G(1-\omega H(\varepsilon_i))\varepsilon_i + K(1-\omega H(\varepsilon_V))\varepsilon_V, (i = 1,2,3) \quad (11)$$

missä G on liukumoduli, $K = E/((1+\nu)(1-2\nu))$, H on Heavisiden funktio ja $\varepsilon_V = \varepsilon_1 + \varepsilon_2 + \varepsilon_3$ on hydrostaattinen venymä. Tämä menetelmä säilyttää jännitysten ja venymien välisten kuvauksen jatkuvana.

6. PAINIMEN TÖRMÄYKSEN MALLINNUS

Jotta painimen törmäyksen synnyttämä jännitystilakenttä olisi mahdollisimman realistinen, mallinnetaan painin deformoituvana kappaleena ja painimen ja kiven välille asetetaan kontaktireunaehdot. Painimen ja kallion diskretointi voidaan tehdä siten, että kontaktireunalla (tai pinnalla 3D:ssä) elementtien solmujako on sama. Tällöin, koska kontaktiongelma on geometrisesti lineaarinen, voidaan käyttää yksinkertaisinta kontaktimallia, ns. solmu-solmuun –kontaktimallia (kuva 3). Lisäksi kontaktiin tulevat solmut tiedetään ennalta, joten kontaktinhakualgoritmia ei tarvita.



Kuva 3. Solmu-solmuun -kontaktimalli

Tällöin kinemaattiset kontaktireunaehdot (tunkemattomuusehdot) voidaan kirjoittaa muotoon

$$\mathbf{Gu} + \mathbf{b} \ge \mathbf{0} \quad \text{(reunalla } \Gamma_A \cup \Gamma_B) \quad (12)$$

missä **G** sisältää kontaktireunojen normaalien komponentit, **u** on solmusiirtymävektori ja **b** on kontaktipintojen alkuetäisyys.

7. DISKRETOIDUT LIIKEYHTÄLÖT JA AIKAINTEGROINTI

Liikeyhtälöt diskretoidaan käyttäen elementtimenetelmää ja eksplisiittistä aikaintegrointia. Elementtityyppinä käytetään bilineaarista elementtiä. Liikeyhtälöt ovat muotoa

$$\mathbf{M}\ddot{\mathbf{u}} + \mathbf{C}\dot{\mathbf{u}} + \mathbf{f}_{\text{int}} = \mathbf{f}_{\text{ext}}, \tag{13}$$

missä **M** on keskitetty massamatriisi, **C** on vaimennusmatriisi, joka sisältää kontribuution materiaalisesta vaimennuksesta ja heijastamattomista reunaehdoista, $\mathbf{f}_{\text{ext}}$ on ulkoisten voimien vektori ja

$$\mathbf{f}_{\text{int}} = \sum_{n,k=1}^{N_{GP}} t\mathbf{B}(g_n, g_k)^{\mathrm{T}} \boldsymbol{\sigma}(g_n, g_k, \omega) w_n w_k \det \mathbf{J}(g_n, g_k) \tag{14}$$

on sisäisten voimien vektori, joka on kirjoitettu tasotapaukselle. Kaavassa (14) t on alueen paksuus, **B** on kinemaattinen matriisi, $\boldsymbol{\sigma}$ on jännitysvektori, w_k, w_n ja g_k, g_n ovat Gaussin painokertoimia ja integrointipisteitä, vastaavasti, ja **J** on Jacobin matriisi.

Aikaintegrointiin valitaan eksplisiittinen modifioitu Eulerin menetelmä. Vaikka eksplisiittinen aikaintegrointi on ehdollisesti stabiili ja siten vaatii pienen aika-askeleen (varsinkin tämän menetelmän yhteydessä, kun elementtikoko on pieni), on sen edut selvät verrattuna implisiittiseen lähestymistapaan: Keskitetyn massamatriisin tapauksessa liikeyhtälöiden ratkaisu on triviaalia. Linearisointia ei tarvita, joten vauriomallien implementointi on yksinkertaista. Systeemin vaste tarvitaan vain siellä missä "tapahtuu" eli tässä ongelmassa vain niissä elementeissä, joihin painimen iskusta syntynyt jännitysaalto on ehtinyt saapua. Lisäksi menetelmällä saadaan insinöörimielessä kelpoja ratkaisuja ongelmille, joissa implisiittinen menetelmä ei toimi.

Eksplisiittisistä menetelmistä valitaan modifioitu Eulerin menetelmä [6], jolle vasteet lasketaan kaavoilla

$$\ddot{\mathbf{u}}^{t} = \mathbf{M}^{-1}\left(\mathbf{f}_{\text{ext}}{}^{t} - \mathbf{C}\dot{\mathbf{u}}^{t} - \mathbf{f}_{\text{int}}{}^{t}\right), \quad \dot{\mathbf{u}}^{t+\Delta t} = \dot{\mathbf{u}}^{t} + \Delta t\ddot{\mathbf{u}}^{t}, \quad \mathbf{u}^{t+\Delta t} = \mathbf{u}^{t} + \Delta t\dot{\mathbf{u}}^{t+\Delta t}. \tag{15}$$

Menetelmä on toista kertalukua tarkka, kuten keskeisdifferenssimenetelmä. Tämän menetelmän etu on, että nopeus saadaan laskettua ennen siirtymää. Tätä nopeutta tarvitaan heijastamattoman reunaehdon yhteydessä, jota käsitellään seuraavaksi.

8. HEIJASTAMATON REUNAEHTO

Äärellistä FEM-mallia käytettäessä mallin reunoilta heijastuva jännitysaalto muuttaa vaurioitumisprosessia. Koska todellisessa kallionporauksessa, jota halutaan simuloida, kallio on käytännössä ääretön, on käytettävä jotakin heijastamatonta reunaehtoa. Tässä käytetään viskoosiin vaimennukseen perustuvaa menetelmää, jossa mallin reunoille asetetaan viskoosit vaimentimet [7]. Kun jännitysaalto saapuu reunalle, syntyy partikkelinopeuteen verrannolliset normaalin ja tangentin suuntaiset traktiot

$$t_{\text{n}} = -\rho c_{\text{d}} v_{\text{n}}, \quad t_{\text{t}} = -\rho c_{\text{s}} v_{\text{t}}, \tag{16}$$

missä ρ on materiaalin tiheys, c_{d} ja c_{s} ovat dilataatio- ja leikkausaallon etenemisnopeudet kontinuumissa sekä v_{n} ja v_{t} ovat partikkelinopeuden normaalin ja tangentin suuntaiset komponentit, vastaavasti. Kun näihin sijoitetaan FEM-approksimaatiot $v_{\text{n}} = \mathbf{n}^{\mathrm{T}}\mathbf{N}\mathbf{v}$ ja $v_{\text{s}} = \mathbf{t}^{\mathrm{T}}\mathbf{N}\mathbf{v}$, saadaan ekvivalenttisiksi solmuvoimiksi dilataatio- ja leikkausaallolle, vastaavasti (tasotapaus)

$$\mathbf{f}_{qd} = -t\rho c_d \int_S \mathbf{N}^T \mathbf{n}\mathbf{n}^T \mathbf{N} dS\mathbf{v} = \mathbf{C}_{qd}\mathbf{v} \text{ ja } \mathbf{f}_{qs} = -t\rho c_s \int_S \mathbf{N}^T \mathbf{t}\mathbf{t}^T \mathbf{N} dS\mathbf{v} = \mathbf{C}_{qs}\mathbf{v}, \tag{17}$$

missä **n** ja **t** ovat reunan normaali- ja tangenttivektorit ja **v** on solmunopeusvektori. Tämä reunaehto voidaan siis käsitellä vaimennuksen tapaan.

9. MENETELMÄ KIVEN SÄRKYMISEN NUMEERISEEN SIMULOINTIIN

Modifioidun Lagrangen menetelmän mukaiset liike- ja rajoiteyhtälöt kontaktiongelmalle ovat [8]

$$\mathbf{M}\ddot{\mathbf{u}}^t + \mathbf{C}\dot{\mathbf{u}} + \mathbf{f}_{int} = \mathbf{f}_{ext}^t - \mathbf{G}^T\boldsymbol{\lambda}^t \quad \& \quad \mathbf{G}\mathbf{u}^{t+\Delta t} - \mathbf{b} = \mathbf{0}, \tag{18}$$

missä $\mathbf{C} = \mathbf{C}_m + \mathbf{C}_{qp} + \mathbf{C}_{qs}$ on yhdistetty vaimennusmatriisi ($\mathbf{C}_m$ on materiaalinen vaimennusmatriisi) ja $\boldsymbol{\lambda}$ on Lagrangen kertoimien vektori, jonka fysikaalinen tulkinta on kontaktivoimavektori. Kun nämä yhdistetään kaavojen (15) kanssa, saadaan

$$\begin{aligned} &\ddot{\mathbf{u}}^t = \tilde{\ddot{\mathbf{u}}}^t - \mathbf{M}^{-1}\mathbf{G}^T\boldsymbol{\lambda}^t && \tilde{\ddot{\mathbf{u}}}^t = \mathbf{M}^{-1}\left(\mathbf{f}_{ext}^t - \mathbf{C}\dot{\mathbf{u}}^t - \mathbf{f}_{int}^t\right) \\ &\dot{\mathbf{u}}^{t+\Delta t} = \dot{\mathbf{u}}^t + \Delta t\ddot{\mathbf{u}}^t && \text{, missä} \quad \tilde{\mathbf{u}}^{t+\Delta t} = \mathbf{u}^t + \Delta t\dot{\mathbf{u}}^t + \Delta t^2\tilde{\ddot{\mathbf{u}}}^t \\ &\mathbf{u}^{t+\Delta t} = \mathbf{u}^t + \Delta t\dot{\mathbf{u}}^t + \Delta t^2\ddot{\mathbf{u}}^t && \boldsymbol{\lambda}^t = \left(\Delta t^2\mathbf{G}\mathbf{M}^{-1}\mathbf{G}^T\right)^{-1}\left(\mathbf{G}\tilde{\mathbf{u}}^{t+\Delta t} - \mathbf{b}\right) \end{aligned} \tag{19}$$

Menetelmä (19) on eräänlainen ennustaja-korjaaja -menetelmä, jossa ensin oletetaan, että kontakteja ei ole (suureet, joiden symbolin päällä on aaltoviiva) ja sitten lasketaan kontaktivoimat saadun tunkeuman perusteella. Sitten kiihtyvyys korjataan vähentämällä kontaktivoimien vaikutus. Algoritmina esitettynä menetelmä on seuraavanlainen:

Laskut jokaisella aika-askeleella niille elementeille, joihin jännitysaalto on saapunut:

1. Lasketaan elementin keskipisteessä jännitykset $\boldsymbol{\sigma}^t$, pääjännitykset σ_1, σ_2, σ_3, päävenymät ε_1, ε_2, ε_3 ja tarkastetaan vauriokriteerit sekä päivitetään vaurioparametri $\omega^{t+\Delta t}$
2. Lasketaan voimat: $\mathbf{f}_{int}^t$, $\mathbf{f}_{ext}^t$, $\mathbf{f}_{damp}^t = (\mathbf{C}_m + \mathbf{C}_{qp} + \mathbf{C}_{qs})\dot{\mathbf{u}}^t$
3. Ennustetaan kiihtyvyys: $\tilde{\ddot{\mathbf{u}}}^t = \mathbf{M}^{-1}\left(\mathbf{f}_{ext}^t - \mathbf{f}_{damp}^t - \mathbf{f}_{int}^t\right)$
4. Ennustetaan siirtymä ilman kontaktivoimia: $\tilde{\mathbf{u}}^{t+\Delta t} = \mathbf{u}^t + \Delta t\dot{\mathbf{u}}^t + \Delta t^2\tilde{\ddot{\mathbf{u}}}^t$
5. Lasketaan kontaktivoimat: $\mathbf{f}_{cont}^t = \left(\Delta t^2\mathbf{G}\mathbf{M}^{-1}\mathbf{G}^T\right)^{-1}\left(\mathbf{G}\tilde{\mathbf{u}}^{t+\Delta t} - \mathbf{b}\right)$
6. Päivitetään kontaktivoimavektoria $\mathbf{f}_{cont}^t$ siten, että jos $(f_{cont}^t)_i > 0$, asetetaan $(f_{cont}^t)_i = 0$
7. Korjataan kiihtyvyys: $\ddot{\mathbf{u}}^{t+\Delta t} = \tilde{\ddot{\mathbf{u}}}^{t+\Delta t} - \mathbf{M}^{-1}\mathbf{G}^T\mathbf{f}_{cont}^t$
8. Lasketaan siirtymä ja nopeus: $\dot{\mathbf{u}}^{t+\Delta t} = \dot{\mathbf{u}}^t + \Delta t\ddot{\mathbf{u}}^t$, $\mathbf{u}^{t+\Delta t} = \mathbf{u}^t + \Delta t\dot{\mathbf{u}}^t + \Delta t^2\ddot{\mathbf{u}}^t$
9. Palataan kohtaan 1.

Vaste lasketaan vain niissä elementeissä, joihin dilataatioaalto on saapunut. Tämä tehdään laskemalla kivialueen elementtiverkossa dilataatioaallolle keskimääräinen nopeus ja kertomalla se ajalla t, jolloin saadaan sen alueen säde, johon aalto on edennyt. Sitten vaste lasketaan niissä elementeissä, jotka ovat alueen sisällä.

Menetelmä on laskennallisesti tehokas erityisesti keskitetyn massamatriisin ja solmu-solmuun -kontaktimallin yhteydessä, koska tällöin matriisi $\mathbf{G}\mathbf{M}^{-1}\mathbf{G}^T$ on diagonaalinen. Lisäksi, koska vapausasteet ovat kytkemättömiä, on menetelmän yhteydessä kontaktivoiman merkkiä seuraamalla

helppoa toteuttaa kineettinen kontaktireunaehto siten, että jos etumerkki on positiivinen (vetovoima), asetetaan vastaava komponentti nollaksi (kohta 6).

Elementtitasolla vauriokriteerit tarkastetaan elementin keskipisteessä, joka bilineaariselle elementille antaa keskiarvon Gaussin pisteissä saaduista arvoista. Vetomurtuman oletetaan RFPA-koodin ideaa seuraten olevan särön kasvun syy, joten sillä on prioriteetti molempien kriteerien täyttyessä. Kun elementti on täysin vaurioitunut (ω = 1), se jää elementtiverkkoon ns. ilmaelementtinä. Vauriokriteerien tarkistus ja vaurioparametrin arvon päivitys on esitetty algoritmina alla.

Laskut niille elementeille, joihin jännitysaalto on saapunut:

Jos $\omega^t < 1$, suorita:

1. Lasketaan lujuudet: $\sigma_{tr} = (1-\omega^t)\sigma_t$ ja $\sigma_{cr} = (1-\omega^t)\sigma_c$
2. Tarkistetaan vauriokriteerit: lasketaan $F_t = \sigma_1 - \sigma_{tr}$ ja $F_c = \sigma_3 - k\sigma_1 - \sigma_{cr}$;
   Jos $F_t > 0$, lasketaan ω_{koe} kaavalla (6). Jos $F_t < 0$ Ja $F_c > 0$, lasketaan ω_{koe} kaavalla (8) tai (10).
3. Päivitetään vaurioparametri: Jos $F_c > 0$ Ja $\varepsilon_3 \le \varepsilon_{rc}$ Ja $\omega_{koe} < \omega^t$, niin $\omega^{t+\Delta t} = \omega_{koe}$, Muuten; Jos $\omega_{koe} > \omega^t$, niin $\omega^{t+\Delta t} = \omega_{koe}$.

Kohdassa 3 huomioidaan uudelleentiivistymisen mahdollisuus puristustyyppisen vaurion yhteydessä. Mohr-Coulombin kriteerin kaavassa on huomioitu mekaniikan yleinen merkkisääntö ja k on kerroin kaavasta (4). Haurasmurtuman yhteydessä jäännöslujuudet ovat yksinkertaisesti $\sigma_{tr} = \lambda\sigma_t$ ja $\sigma_{cr} = \lambda\sigma_c$. Sisäisten voimien laskenta yhdelle bilineaariselle elementille on esitetty alla algoritmina tasovenymätilalle.

Silmukka Gaussin pisteille:

Jos $F_t < 0$ Ja $F_c > 0$, suorita (puristustyyppinen vaurio):

1. Lasketaan kimmomatriisi kaavalla $\mathbf{E} = (1-\omega)\mathbf{E}_e$.
2. Lasketaan kontribuutio Gaussin pisteessä: $\mathbf{f}_{int}^{GP} = \frac{1}{4} t \cdot a \cdot b \mathbf{B}^T \mathbf{E}(\omega)\mathbf{B}\mathbf{u}$
3. Summaus Gaussin pisteiden yli: $\mathbf{f}_{int}^{ele} = \mathbf{f}_{int}^{ele} + \mathbf{f}_{int}^{GP}$

Muuten lasketaan (vetotyyppinen vaurio):

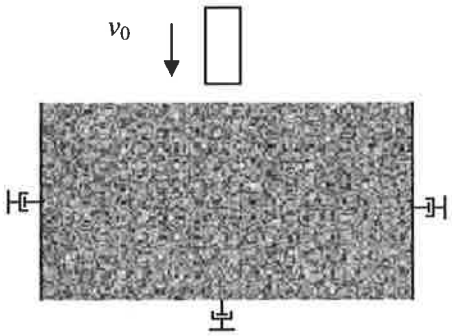
1. Lasketaan päävenymät ε_1, ε_2, Gaussin pisteissä
2. Lasketaan pääjännitykset σ_{prin} kaavoilla (11)
3. Muunnetaan jännitykset globaalikoordinaatistoon: $\boldsymbol{\sigma}_{xy} = \mathbf{T}\boldsymbol{\sigma}_{prin}$
4. Lasketaan kontribuutio Gaussin pisteessä: $\mathbf{f}_{int}^{GP} = \frac{1}{4} t \cdot a \cdot b \mathbf{B}^T \boldsymbol{\sigma}_{xy}$
5. Summaus Gaussin pisteiden yli: $\mathbf{f}_{int}^{ele} = \mathbf{f}_{int}^{ele} + \mathbf{f}_{int}^{GP}$

Yllä olevissa kaavoissa a ja b ovat elementin sivujen pituudet, t sen paksuus, $\mathbf{B}$ kinemaattinen matriisi ja $\mathbf{u}$ solmusiirtymävektori.

Kuten edellä olevista algoritmeista näkee, menetelmä on laskennallisesti huokea ja helppo implementoida. Seuraavaksi menetelmää testataan numeeristen esimerkkien avulla. Numeerinen implementointi suoritetaan Matlab-ohjelmistolla.

10. NUMEERISET ESIMERKIT

Ratkaistaan alla kuvattu ongelma kehitettyä menetelmää käyttäen. Elementtiverkko koostuu 140×80 = 11200 säännöllisestä bilineaarisesta elementistä (joiden koko 1mm×1mm). Kividomeenin reunoilla on heijastamaton reunaehto.



(a)

Painimen tiedot
$\rho = 7800$ kg/m^3
$\nu = 0.3$
$E = 200$ GPa
$h_p = 50$ mm,
$b_p = 20$ mm,
$t_p = 42$ mm

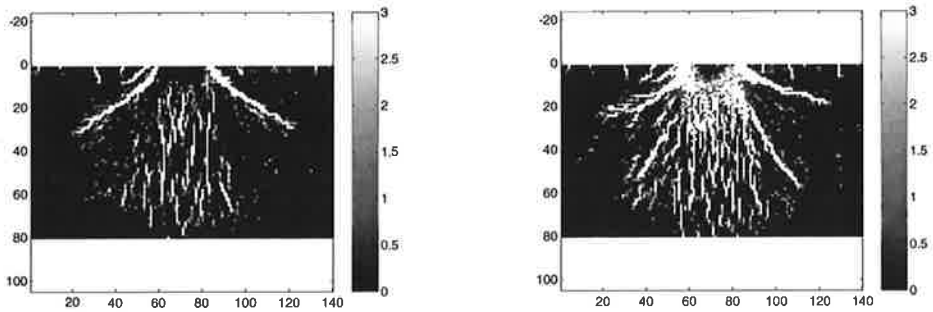


(b)

Kiven tiedot
$\rho_0 = 2600$ kg/m^3, $m_\rho = 100$
$\nu_0 = 0.16$, $m_\nu = 100$
$E_0 = 62.5$ GPa, $m_E = 6$
$\sigma_{c0} = 137$ MPa, $m_\sigma = 6$
$\sigma_t = 0.1\sigma_c$, $\varphi = 30°$,
$\lambda = 0.1$, $\eta = 5$, $\varepsilon_{rc} = 5\varepsilon_{c0}$
$t_k = 0.042$ m

Kuva 4. Ongelma ja materiaalitiedot (a) sekä laboratoriokokeen tulos [9] (b), h_p, b_p ovat painimen korkeus ja paksuus, vastaavasti

Alla olevissa kuvissa 5 on esitetty simuloinnin tulokset painimen nopeuksille $v_0 = 6$ m/s ja $v_0 = 8$ m/s.



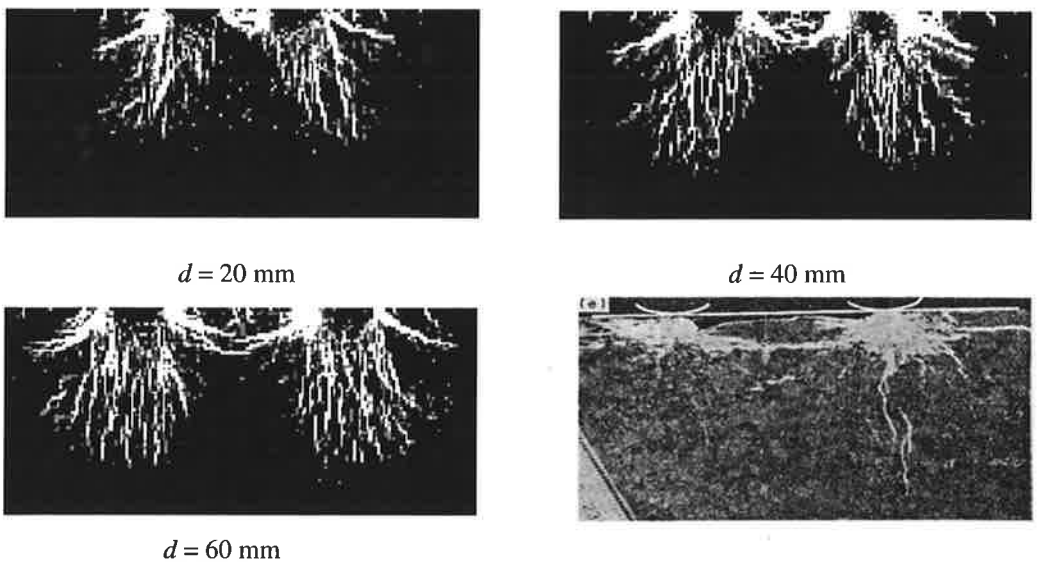
(a) (b)

Kuva 5. Simuloinnin tulokset painimen nopeuksille $v_0 = 6$ m/s (a) ja $v_0 = 8$ m/s (b)

Kuvista 5 voidaan selvästi havaita Hertsin kartiosärö, sivuttaissäröt ja useita pitkiä pystysuuntaisia pääsäröjä. Leikkausmurtumien määrä kasvaa huomattavasti, kun painimen nopeus kasvaa. Lisäksi

havaitaan, että painimen alla oleva puolipallon muotoinen alue (murskaantunut alue kuvassa 1), joka on puristusjännitystilassa, säilyy kohtalaisen ehjänä, koska pääjännitysten suhde on sellainen, että Mohr-Coulombin kriteeriä ei rikota. Jos tuloksia vertaa kvasistaattisessa laboratoriokokeessa saatuun vauriokuvioon (kuva 4 (b)), on niissä paljon yhtäläisyyksiä.

Seuraavassa mallinnetaan samaa ongelmaa kahden painimen tapauksessa ja tarkastellaan erityisesti painimien välisen etäisyyden d vaikutusta. Tulokset ja kvasistaattisen laboratoriokokeen tulos on esitetty kuvissa 6.



Kuva 6 Kahden painimen törmäyksen aiheuttaman vauriokuvion simulointi eri etäisyyden arvoilla ja vastaavan kvasistaattisen laboratoriokokeen tulos [9]

Kuvista 6 nähdään, että painimien etäisyyden kasvaessa niiden välistä irtoavan lastun paksuus kasvaa. Siten tämä etäisyys on tärkeä suunnitteluparametri. Liian suurella etäisyyden d arvolla sivuttaissäröt eivät välttämättä enää yhdy, jolloin lastu ei irtoa. Sivuttaissäröjen yhtyminen esiintyy myös kokeellisessa tuloksessa.

11. YHTEENVETO JA PÄÄTELMÄT

Tässä tutkimuksessa on kehitetty numeerinen menetelmä kiven vaurioitumisen dynaamiseen simulointiin. Eksplisiittiseen aikaintegrointiin ja lineaariseen elementtimenetelmään sekä vauriomekaniikkaan perustuvan menetelmän parhaat puolet ovat implementoinnin helppous ja laskennallinen huokeus keskitetyn massamatriisin tapauksessa, koska iterointia ei tarvita. Toinen etu on, että systeemin vasteen ratkaisu tarvitaan vain niissä elementeissä, joihin törmäyskohdasta syntynyt kiveen etenevä jännitysaalto on ehtinyt saapua. Kehitetyn menetelmän huono puoli on sen vaatima erittäin pieni elementtikoko.

Menetelmän toinen ongelma on eksplisiittisen aikaintegroinnin likimääräinen luonne: epälineaarista vastetta simuloitaessa ei missään vaiheessa iteroida ratkaisua tasapainoon, vaan pieniä aika-askelia käyttäen askelletaan eteenpäin korvaten tarkat liikeyhtälöiden derivaatat likimääräisillä differenssikaavoilla. Tällöin kyllä saadaan ”insinöörimäisiä” ratkaisuja ongelmiin,

joihin implisiittinen aikaintegrointi "kaatuu", mutta voidaan kysyä, ovatko ne fysikaalisesti järkeviä. Tässä tapauksessa, saatujen tulosten perusteella, kehitetyllä menetelmällä saadut tulokset vaikuttavat järkeviltä niin, että siitä on ainakin kvalitatiivista apua iskevien porauslaitteiden suunnittelussa ja tuotekehityksessä.

LÄHDELUETTELO

[1] S.Q. Kou et al. Rock Fragmentation Mechanisms induced by a Drill Bit. *Int. J. Rock Mech. Min. Sci.*, Vol. 41, Paper 2B11-SINOROCK2004 Symposium, 2004.

[2] C.A. Tang. Numerical Simulation of Progressive Rock Failure and Associated Seismicity. *Int. J. Rock Mech. Min. Sci.*, Vol. 34, 249-261, 1997.

[3] L.L. Mishnaevsky. Physical Mechanisms of Hard Rock Fragmentation under Mechanical Loading: A Review. *Int. J. Rock Mech. Min. Sci.*, Vol. 32, 763-766, 1995.

[4] W.C. Zhu and C.A. Tang. Micromechanical Model for Simulating the Fracture Process of Rock. *Rock Mechanics and Rock Engineering*, Vol. 37, 25-56, 2004.

[5] J. Lemaitre. *A Course on Damage Mechanics.* Springer-Verlag, 1992.

[6] G.D. Hahn. A Modified Euler Method for dynamical analyses. *International Journal for Numerical Methods in Engineering*. Vol. 32, 943 – 955, 1991.

[7] J. Lysmer and R. L. Kuhlemeyer. Finite dynamic model for infinite media. *Journal of Engineering Mechanics Division*, ASCE, Vol. 95, 377-392, 1969.

[8] N.J. Carpenter et al.. Lagrange Constraints for Transient Finite Element Surface Contact. *International Journal for Numerical Methods in Engineering*. Vol. 32. 103 – 128, 1991.

[9] H.Y. Liu. Numerical Modelling of the Rock Fragmentation Process by Mechanical Tools, Väitöskirja. Luleå University of Technology, 2004.

TREATMENT OF THE TANGENT MODULUS OF NONLINEAR CONTINUA

Sami Holopainen

Tampere University of Technology
Institute of Applied Mechanics and Optimization
P.O.Box 589 FI-33101, Tampere
E-mail: sami.holopainen@tut.fi

Abstract

Developing the nonlinear constitutive relations many problems concerned with the mathematical treatment of theory connected to the higher order tensors arise. As an important application for that is a tangent modulus which describes the relation between the stress and the corresponding conjugate strain. In this paper some special issues as differentiation of tensors, objectivity or spatial covariance, and the symmetry of tensors are discussed. Most generally, the given representations are valid for *anisotropic* materials with finite strains. As the possible applications can be considered e.g. certain plastic composites and biological soft tissues. Solving the mechanical systems made of such materials motivates to develop proper mathematical models and efficient numerical methods. As an illustration, the tangent modulus is developed for a certain anisotropic hyperelastic-plastic material with finite strains.

1 INTRODUCTION

When nonlinear equilibrium equations are linearized for solving the problem using Newton-type scheme, or the continuum based design sensitivity analysis w.r.t a certain design or perturbation parameter is done, the higher order tensors arises. Here, these tensors are connected to the constitutive relations leading to the fourth order tensor known as the tangent modulus. Despite of the active efforts, there is no unique definition for the derivative of second order tensor with respect to another symmetric one. Although this is required when a representation to the tangent modulus is obtained. I.e. the derivatives of a tensor function with respect to its arguments have to be determined. In many cases the tangent modulus is symmetric or it could be symmetrized. This is the situation e.g. when the tangent modulus is used associated to the double contraction with a symmetric tensor from both side to evaluate the strain energy. Symmetry is the essential property e.g. in solving the eigenvalue problems. Thus, the special treatment of symmetry is considered here. The results can be utilized both for a material but also a spatial tensor leading to the well known Lie-derivative, which ensures the objectivity of the results. The notation and the definitions for the tensor products and the corresponding contractions follow from the redefined differentiation rules of tensors based on the paper published by Itskov [8]. Consequently, the absolute notation can be used for tensor quantities leading to the correct invariance property of tensors with respect to any co-ordinate system. As an application, the differentiation of an isotropic tensor function with respect to its tensor arguments is obtained.

2 SOME TENSOR PRESENTATIONS OF LINEAR SPACES

Here, some important notations and definitions are expressed. More comprehensive representation is given in Refs. [5], [6], [8] and mathematical foundations in [3]. Tensors are universal representatives of linear maps. The representation of linear maps by tensors depends on the specific identification of linear spaces $\mathfrak{V}, \mathfrak{W}$, their dual spaces $\mathfrak{V}^*, \mathfrak{W}^*$, and tensor spaces. Let be two identifications of the linear map $Lin(\mathfrak{V}; \mathfrak{W})$ with the tensor spaces $\mathfrak{W} \otimes \mathfrak{V}^*$, and $\mathfrak{W} \otimes \mathfrak{V}$ [6]:

- $Lin(\mathfrak{V}; \mathfrak{W}) \cong \mathfrak{W} \otimes \mathfrak{V}^*$ for tensor algebra on manifolds and
- $Lin(\mathfrak{V}; \mathfrak{W}) \cong \mathfrak{W} \otimes \mathfrak{V}$ for classical tensor algebra.

In the case of the tensor algebra on manifolds the application of tensors on vectors is based on the dual pairing [6]. Let be $\mathbf{F} \in Lin(\mathfrak{V}; \mathfrak{W})$ be a linear map $\mathbf{F} : \mathfrak{V} \to \mathfrak{W}$ represented as $\mathbf{F} = \mathbf{u} \otimes \mathfrak{b} \in \mathfrak{W} \otimes \mathfrak{V}^*$. The linear mapping $\mathbf{Fa}, \mathbf{a} \in \mathfrak{V}$, is carried out by, $\mathbf{Fa} = (\mathbf{u} \otimes \mathfrak{b})\mathbf{a} = \langle \mathfrak{b}, \mathbf{a} \rangle_{\mathfrak{V}} \mathbf{u} \in \mathfrak{W}$. The classical tensor algebra is expressed in the inner product spaces (as Hilbert space) s.t. the linear map $\mathbf{F} \in Lin(\mathfrak{V}; \mathfrak{W})$ is simply the two-point tensor, $\mathbf{F} = \mathbf{u} \otimes \mathbf{b} \in \mathfrak{W} \otimes \mathfrak{V}$ with the operation $\mathbf{Fa}, \mathbf{a} \in \mathfrak{V}$ carried out by $\mathbf{Fa} = (\mathbf{u} \otimes \mathbf{b})\mathbf{a} = (\mathbf{b} \cdot \mathbf{a})\mathbf{u} \in \mathfrak{W}$. The tensor algebra on manifolds is developed without any structure of basis of coordinate system, i.e. the definition of base vectors with Cartesian coordinate functions of $\mathbb{R}$, $z^i, \mathbf{e}_i$ as $\mathbf{g}_\alpha = \partial z^i / \partial x^\alpha \mathbf{e}_i$ is not allowed. Without the Cartesian structures, a manifold as a basic notion of a body seems to offer essential clarifications and simplifications of the formulations in continuum mechanics [5]. This means first of all a clear distinction between vectors and covectors (defined below) and a explicit application of metrics (for Riemannian manifolds). A symmetric, positive-definite bilinear form $\zeta \in Sym_2^+(\mathfrak{V}, \mathfrak{V}; \mathbb{R})$ is called a *metric* on the vector space $\mathfrak{V}$. The metric assigns a real number $\zeta(\mathbf{a}, \mathbf{b})$ to any vectors $\mathbf{a}, \mathbf{b} \in \mathfrak{V}$. Let be the space of linear isomorphisms $Lis(\mathfrak{V}, \mathfrak{V}^*)$. ζ induces a linear bijection or just simply metric, $\mathbf{G} \in Lis(\mathfrak{V}, \mathfrak{V}^*)$, defined by $\langle \mathbf{Ga}, \mathbf{b} \rangle = \zeta(\mathbf{a}, \mathbf{b}) \, \forall \mathbf{a}, \mathbf{b} \in \mathfrak{V}$. Let be $\{\mathbf{G}_A\}$ and $\{\mathbf{g}_A\}$ the ordered bases of the vector spaces $\mathfrak{V}$ and $\mathfrak{W}$ respectively. W.r.t them the dual bases $\{\mathfrak{G}_A\}$ and $\{\mathfrak{g}_a\}$ on the dual spaces, $\mathfrak{V}^*, \mathfrak{W}^*$ respectively, are defined by

$$\langle \mathfrak{G}^A, \mathbf{G}_B \rangle_{\mathfrak{V}} = \delta_B^A, \quad \langle \mathfrak{g}^a, \mathbf{g}_b \rangle_{\mathfrak{W}} = \delta_b^a \tag{1}$$

where δ_B^A, δ_b^a are *Kronecker delta symbols*. On the vector spaces $(\mathfrak{V}, \mathbf{G})$ and $(\mathfrak{W}, \mathbf{g})$ equipped with a metric $\mathbf{G}$ or $\mathbf{g}$, the special, so called reciprocal bases to $\{\mathfrak{G}_A\}$ and $\{\mathfrak{g}_A\}$ respectively are defined by

$$\mathbf{G}_A \cdot \mathbf{G}^B = \delta_A^B, \quad \text{and} \quad \mathbf{g}_a \cdot \mathbf{g}^b = \delta_a^b \tag{2}$$

The relation between the dual and the reciprocal basis is generally $\mathfrak{G}^A = \mathbf{G}\mathbf{G}^A =: (\mathbf{G}^A)^\flat \in \mathfrak{V}^*$ or the covector associated to $\mathbf{G}^A$. I.e. the metric $\mathbf{G} = G_{AB}\mathfrak{G}^A \otimes \mathfrak{G}^B \in \mathfrak{V}^* \otimes \mathfrak{V}^*$ maps (base-)vector into dual space. For late usage, let us define the general smooth time-dependent embedding of the material body $\mathfrak{B}$ into the Euclidean space $\mathbb{E}$ as $\kappa_t : \mathfrak{B} \to \mathbb{E}$. Let $\mathcal{P}_0 := \kappa_{t=0}(\mathfrak{B}), \mathcal{P} = \mathcal{P}_\tau := \kappa_\tau(\mathfrak{B})$ denote the reference and the current placement of the material body $\mathfrak{B}$ with the position vectors $\mathbf{x} := \kappa(X, t) = \kappa_t(X) \in \mathcal{P}$, $\mathbf{X} := \kappa_{t=0}(X) := \kappa_0(X) \in \mathcal{P}_0$ respectively. In continuum mechanics, the linear tangent map known as the *deformation gradient* is defined locally by the composition map $\chi := \kappa_t \circ \kappa_0^{-1}$ as follows [6]

$$\mathbf{F} := T\chi_{|\mathbf{X}} : T_{\mathbf{X}}\mathcal{P}_0 \to T_{\mathbf{x}}\mathcal{P}, \quad \mathbf{X} \in \mathcal{P}_0, \mathbf{x} \in \mathcal{P}, \tag{3}$$

where $T_{\mathbf{X}}\mathcal{P}_0, T_{\mathbf{x}}\mathcal{P}$ are the tangent spaces of $\mathfrak{V}, \mathfrak{W}$ with the natural base vectors $\{\mathbf{G}^A\}, \{\mathbf{g}^a\}$ respectively. Similarly the corresponding dual bases on the cotangent spaces $T_{\mathbf{X}}^*\mathcal{P}_0, T_{\mathbf{x}}^*\mathcal{P}$ are $\{\mathfrak{G}^A\}, \{\mathfrak{g}^a\}$ respectively. Then the *deformation gradient* can be written as $\mathbf{F} = F_{.A}^a \mathbf{g}_a \otimes \mathfrak{G}^A$.

Its dual, inverse, dual-inverse, and transposed forms are as $\mathbf{F}^* = F^a_{.A}\mathfrak{G}^A \otimes \mathbf{g}_a, \mathbf{F}^{-1} = F^A_{a.}\mathbf{G}_A \otimes \mathfrak{g}^a, \mathbf{F}^{-*} = F^A_{a.}\mathfrak{g}^a \otimes \mathbf{G}_A, \mathbf{F}^T = F^b_{.B}G^{AB}g_{ab}\mathbf{G}_A \otimes \mathfrak{g}^a$ respectively, which are needed e.g. as a part of the pull-back or push-forward operations [5]. As one can see, the transposed form is not obtained simply interchanging the index of components. This result is given by [5] (**prop.** 3.4). In following, the Euclidean space is assumed, and the dual spaces $\mathfrak{V}^*, \mathfrak{W}^*$ are replaced by vector spaces $\mathfrak{V}, \mathfrak{W}$ and the dual vectors $\mathfrak{G}^A \in \mathfrak{V}^*, \mathfrak{g}^a \in \mathfrak{W}^*$ by resiprocal vectors $\mathbf{G}^A \in \mathfrak{V}, \mathbf{g}^A \in \mathfrak{W}$ respectively. I.e. $\mathbf{G} = \mathbf{I}, \mathbf{g} = \mathbf{i}$ is required. Thus the dual pairings are replaced by inner products with the correct metrics as follows $\langle \mathfrak{G}^A, \mathbf{G}_B \rangle_{\mathfrak{V}} = \mathbf{G}^A \cdot \mathbf{G}_B$ (G-metric) and $\langle \mathfrak{g}^a, \mathbf{g}_b \rangle_{\mathfrak{V}} = \mathbf{g}^a \cdot \mathbf{g}_b$ (g-metric). The dual map $\mathbf{F}^*$ is replaced by transposed map $\mathbf{F}^T$. Also it is assumed that $F^a_{.A} = \delta^a_{.A}$ or the *convective* Cartesian coordinate system. More comprehensive expressions considering e.g. the metrics and the dual, inverse, transposed or adjoint maps are given in [5] and [6]. Before closing this section a special remark is devoted to contraction of mixed variant second order tensor, called to *trace* [5].

Definition 2.1 Trace *denotes the contraction of a* mixed variant *second order tensor s.t* $trace(\mathbf{T}) = T^A_A$. *Further, the double contraction (inner product) between the contravariant and the covariant second order tensor* $\mathbf{T}, \mathbf{S}$ *is defined as* $(\mathbf{T} : \mathbf{S}) : Lin(T^*_{\mathbf{X}}\mathcal{P}; T_{\mathbf{X}}\mathcal{P}) \times Lin(T_{\mathbf{X}}\mathcal{P}; T^*_{\mathbf{X}}\mathcal{P}) \rightarrow \mathbb{R}$ *and* $(\mathbf{T} : \mathbf{S}^*) : Lin(T^*_{\mathbf{X}}\mathcal{P}; T_{\mathbf{X}}\mathcal{P}) \times Lin(T^*_{\mathbf{X}}\mathcal{P}; T_{\mathbf{X}}\mathcal{P}) \rightarrow \mathbb{R}$ *denotes the trace of* $\mathbf{T} \cdot \mathbf{S}$.

Thus, $trace(\mathbf{T} \cdot \mathbf{S}) = \mathbf{T} : \mathbf{S}^* = T^{AB}\mathbf{G}_A \otimes \mathbf{G}_B : S_{DC}\mathfrak{G}^C \otimes \mathfrak{G}^D = T^{AB}S_{DC}\delta^C_A\delta^D_B = T^{AB}S_{BA}$. One important special trace can be determined between the contravariant actual (spatial) stress tensor $\tau = \tau^{ab}\mathbf{g}_a \otimes \mathbf{g}_b \in Lin(T^*_{\mathbf{x}}\mathcal{P}; T_{\mathbf{x}}\mathcal{P})$ and the actual covariant metric tensor $\mathbf{g} = g_{cd}\mathfrak{g}^c \otimes \mathfrak{g}^d \in Lin(T_{\mathbf{x}}\mathcal{P}; T^*_{\mathbf{x}}\mathcal{P})$ as $trace(\tau \cdot \mathbf{g}) = \tau : (\mathbf{g})^* = \tau : \mathbf{g}$ or $\tau^{ab}g_{ba}$. Note, that by above trace-definition one could not pronounce as $trace(\tau \cdot \mathbf{i}) = trace(\tau)$ because $\mathbf{i}$ is a mixed variant tensor. Although, they are formally distinguishable on inner product spaces. The pull-backs of τ and $\mathbf{g}$ produces the trace between the contravariant reference stress $\mathbf{S}^\sharp = S^{AB}\mathbf{G}_A \otimes \mathbf{G}_B \in Lin(T^*_{\mathbf{X}}\mathcal{P}_0; T_{\mathbf{X}}\mathcal{P}_0)$ with the components as $S^{AB} = \tau^{ab}F^A_aF^B_b$ and the covariant right Cauchy-Green strain tensor $\mathbf{C}^\flat = C_{CD}\mathfrak{G}^C \otimes \mathfrak{G}^D \in Lin(T_{\mathbf{X}}\mathcal{P}_0; T^*_{\mathbf{X}}\mathcal{P}_0)$ with the components $C_{CD} = g_{cd}F^c_CF^d_D$ as follows $trace(\mathbf{S}^\sharp \cdot \mathbf{C}^\flat) = \mathbf{S}^\sharp : \mathbf{C}^\flat$ or $S^{AB}C_{BA}$. Similarly another trace for an actual covariant metric tensor with the contravariant one $\mathbf{g}^\sharp$ is as $\mathbf{g} : \mathbf{g}^\sharp = \delta^a_a$. The pull-backs of these tensors produce the trace of $\mathbf{C}^\flat \cdot (\mathbf{C}^{-1})^\sharp$ or $\mathbf{C}^\flat : (\mathbf{C}^{-1})^\sharp := \mathbf{C}^\flat : \mathbf{B}^\sharp$ or $C_{AB}B^{BA}$.

3 TENSOR ALGEBRA ON INNER PRODUCT SPACES

3.1 Basic notations and definitions

As mentioned above, the metric and the identity tensor $\mathbf{G}, \mathbf{I}$ or $\mathbf{g}, \mathbf{i}$, and also the inverse of the metric and the dual identity tensor $\mathbf{G}^{-1}, \mathbf{I}^*$ or $\mathbf{g}^{-1}, \mathbf{i}^*$ become indistinguishable and can be replaced by the identity tensor $\mathbf{I}$ or $\mathbf{i}$ both on the reference and the actual inner product vector spaces $T_{\mathbf{X}}\mathfrak{P}_0$ $(\mathbf{G} - metric)$ and $T_{\mathbf{x}}\mathfrak{P}$ $(\mathbf{g} - metric)$ respectively.

Remark 3.1 *It should be remembered that* $\mathbf{G}$ *and* $\mathbf{I}$ *or* $\mathbf{g}$ *and* $\mathbf{i}$ *are only formally identical but remains different objects also on the inner product spaces.*

Keeping in mind that remark, some partial derivatives of certain second order tensors will be determined in following.

Definition 3.2 *Let be* V *n-dimensional (real) vector-space and* $(\mathbf{g}_1, \mathbf{g}_2, ..., \mathbf{g}_n)$ *its basis. The covectors* $(\mathbf{g}^1, \mathbf{g}^2, ..., \mathbf{g}^n)$ *for which* $\mathbf{g}^j \cdot \mathbf{g}_i = \delta^j_i$ *(Kronecker's delta), form the basis of* V^*. *Specially* $dimV = dimV^*$. k-*covariant tensor in* V *is* k-*linear mapping,* l-*contravariant*

tensor in V is 1*-linear mapping and* k*-covariant,* 1*-contravariant tensor or* (k,l)*-tensor in* V *is* $(k+l)$*-linear mapping or*

$$V^k \to \mathbb{R}, \quad V^k = \underbrace{V \times ... \times V}_{k} \qquad V^{*l} \to \mathbb{R}, \quad V^{*l} = \underbrace{V^* \times ... \times V^*}_{l} \quad \text{and} \quad V^k \times V^{*l} \to \mathbb{R}.$$

respectively. Let denote $T^k(V) = k-$*covariant tensors set,* $T_l(V) = l-$*contravariant tensors set and* $T^k_l(V) = (k,l) -$ *tensors set.*

Additionally, let agree on that both the 0-covariant and 0-contravariant tensors are real numbers: $T^0(V) = T_0(V) = \mathbb{R}$. E.g. if V is a inner-product space, then the inner-product $\langle \cdot, \cdot \rangle : V \times V \to \mathbb{R}$ is 2-linear or bilinear mapping and thus 2-covariant tensor.

Definition 3.3 *Tensor product of tensor* $F \in T^k_l(V)$ *and* $G \in T^q_p(V)$ *in* V *is a tensor* $F \otimes G \in T^{k+p}_{l+q}(V)$,

$$F \otimes G(\mathbf{g}_1, ..., \mathbf{g}_{k+p}, \mathbf{g}^1, ..., \mathbf{g}^{l+q}) = F(\mathbf{g}_1, ..., \mathbf{g}_k, \mathbf{g}^1, ..., \mathbf{g}^l) G(\mathbf{g}_{k+1}, ..., \mathbf{g}_{k+p}, \mathbf{g}^{l+1}, ..., \mathbf{g}^{l+q})$$

Lemma 3.4 *Let be* V *n-dimensional (real) vector-space,* $(\mathbf{g}_1, \mathbf{g}_2, ..., \mathbf{g}_n)$ *its basis and the covectors* $(\mathbf{g}^1, \mathbf{g}^2, ..., \mathbf{g}^n)$ *for which* $\mathbf{g}^j \cdot \mathbf{g}_i = \delta^j_i$ *(Kronecker's delta) the dual-basis of* V^*. *Then tensors*

$$\mathbf{g}^{i_1} \otimes ... \mathbf{g}^{i_k} \otimes \mathbf{g}_{j_1} \otimes ... \mathbf{g}_{j_l}, \quad 1 \preceq j_p, i_q \preceq n,$$

form the basis of $T^k_l(V)$. *Specially* $dim T^k_l(V) = n^{k+l}$

That result follows easily from def. 3.3 noting $\mathbf{g}^j \cdot \mathbf{g}_i = \delta^j_i$. E.g. for a fourth order tensor $\mathcal{A} \in T^2_2(V)$ in 3-dimensional Euclidean vector space $(n = 3)$, $dim T^2_2(V) = 3^{2+2} = 81$. Much more comprehensive definitions for tensors are given in [3], [5]. Next certain type of tensors are expressed. A second order tensor (bold capital letter),

$$\begin{aligned} \mathbf{C} &= C_{ij}\mathbf{g}^i \otimes \mathbf{g}^j = C^{ij}\mathbf{g}_i \otimes \mathbf{g}_j = C^i_{.j}\mathbf{g}_i \otimes \mathbf{g}^j = C_{i.}{}^j \mathbf{g}^i \otimes \mathbf{g}_j \quad \text{s.t.} \\ & C_{ij}\mathbf{g}^i \otimes \mathbf{g}^j \in T^2(V), \quad C^{ij}\mathbf{g}_i \otimes \mathbf{g}_j \in T_2(V), \quad C^i_{.j}\mathbf{g}_i \otimes \mathbf{g}^j \in T^1_1(V) \end{aligned} \tag{4}$$

A fourth order tensor (Bold italic capital letter),

$$\mathcal{C} = \mathcal{C}_{ijkl}\mathbf{g}^i \otimes \mathbf{g}^j \otimes \mathbf{g}^k \otimes \mathbf{g}^l = \mathcal{C}^{ijkl}\mathbf{g}_i \otimes \mathbf{g}_j \otimes \mathbf{g}_k \otimes \mathbf{g}_l = \mathcal{C}^{i\ k}_{.j\ .l}\mathbf{g}_i \otimes \mathbf{g}^j \otimes \mathbf{g}_k \otimes \mathbf{g}^l = ... \tag{5}$$

where $\mathcal{C} = \mathcal{C}_{ijkl}\mathbf{g}^i \otimes \mathbf{g}^j \otimes \mathbf{g}^k \otimes \mathbf{g}^l \in T^4(V)$ etc. In following the set of linear mappings of V including all component variances is denoted by *Lin*. Tensor product of two second order tensors are defined as follows

$$\mathbf{A} \otimes \mathbf{B} := A^i_{.j}\mathbf{g}_i \otimes \mathbf{g}^j \otimes B^k_{.l}\mathbf{g}_k \otimes \mathbf{g}^l = A^i_{.j}B^k_{.l}\mathbf{g}_i \otimes \mathbf{g}^j \otimes \mathbf{g}_k \otimes \mathbf{g}^l \tag{6}$$

$$\mathbf{A} \times \mathbf{B} := A^i_{.j}\mathbf{g}_i \otimes \mathbf{g}^j \times B^k_{.l}\mathbf{g}_k \otimes \mathbf{g}^l = A^i_{.j}B^k_{.l}\mathbf{g}_i \otimes \mathbf{g}_k \otimes \mathbf{g}^l \otimes \mathbf{g}^j = A^i_{.l}B^k_{j.}\mathbf{g}_i \otimes \mathbf{g}^j \otimes \mathbf{g}_k \otimes \mathbf{g}^l \tag{7}$$

In the standard notation, $\mathbf{A} \times \mathbf{B}$ corresponds $\mathbf{A} \otimes \mathbf{B}$. Thus the transposition operator $(\mathbf{A} \times \mathbf{B})^R = \mathbf{A} \otimes \mathbf{B}$ can be defined [8]. Also the symbol as '$\odot$' is sometimes used in standard notation [2], and it corresponds to '$\otimes$' in that notation. Double contractions of a fourth order tensor with a second order one (4:2) and (2:4) are redefined to be consistent

with the differentiation rule will be introduced by Eqs. (17) and (27), s.t. the essential rate relation $\dot{\mathbf{A}}(\mathbf{B}) = \mathbf{A}_{,\mathbf{B}} : \dot{\mathbf{B}}$ is satisfied. Consequently,

$$\mathcal{C} : \mathbf{C} := \mathcal{C}^{i\ k}_{.j\ .l}\mathbf{g}_i \otimes \mathbf{g}^j \otimes \mathbf{g}_k \otimes \mathbf{g}^l : C^m_{.n}\mathbf{g}_m \otimes \mathbf{g}^n = \mathcal{C}^{i\ k}_{.j\ .l}C^j_{.k}\mathbf{g}_i \otimes \mathbf{g}^l \tag{8}$$

$$\mathbf{C} : \mathcal{C} := C^n_{m.}\mathbf{g}^m \otimes \mathbf{g}_n : \mathcal{C}^{i\ k}_{.j\ .l}\mathbf{g}_i \otimes \mathbf{g}^j \otimes \mathbf{g}_k \otimes \mathbf{g}^l := \mathcal{C}^{i\ k}_{.j\ .l}C^l_{i.}\mathbf{g}^j \otimes \mathbf{g}_k \tag{9}$$

The operations (2:4) and (4:2) both fulfills the associative and distributive rules [8].

Definition 3.5 *A k-covariant tensor T in V is symmetric if*

$$T(\mathbf{g}_1, ..., \mathbf{g}_i, \mathbf{g}_j, ..., \mathbf{g}_k) = T(\mathbf{g}_1, ..., \mathbf{g}_j, \mathbf{g}_i, ..., \mathbf{g}_k)$$

for all $1 \preceq i \prec j \preceq k$.
In the same way the symmetry can be defined for the l- contravariant and (k,l)-tensor in V. In following the set of symmetric linear mappings is denoted by $Sym \subset Lin$. Some special symmetry properties arise in continuum mechanics. E.g. transposition operations $(\bullet)^T$, $(\bullet)^t$ and ${}^t(\bullet)$ for fourth order tensors:

$$\mathcal{C}^T := \mathcal{C}^{i\ k}_{.j\ .l}\mathbf{g}^j \otimes \mathbf{g}_i \otimes \mathbf{g}^l \otimes \mathbf{g}_k = \mathcal{C}^{\ i\ \ k}_{j.\ l.}\mathbf{g}_i \otimes \mathbf{g}^j \otimes \mathbf{g}_k \otimes \mathbf{g}^l \tag{10}$$

$$\mathcal{C}^t := \mathcal{C}^{i\ k}_{.j\ .l}\mathbf{g}_i \otimes \mathbf{g}_k \otimes \mathbf{g}^j \otimes \mathbf{g}^l = \mathcal{C}^{ik}_{\ .jl}\mathbf{g}_i \otimes \mathbf{g}^j \otimes \mathbf{g}_k \otimes \mathbf{g}^l \tag{11}$$

$${}^t\mathcal{C} := \mathcal{C}^{i\ k}_{.j\ .l}\mathbf{g}^l \otimes \mathbf{g}^j \otimes \mathbf{g}_k \otimes \mathbf{g}_i = \mathcal{C}^{ki}_{lj.}\mathbf{g}_i \otimes \mathbf{g}^j \otimes \mathbf{g}_k \otimes \mathbf{g}^l \tag{12}$$

For a symmetric fourth order tensor is valid that $\mathcal{C} = \mathcal{C}^T$ and for a super-symmetric that $\mathcal{C} = \mathcal{C}^T$, $\mathcal{C} = \mathcal{C}^t$ and $\mathcal{C} = {}^t\mathcal{C}$. I.e. the first one means the major symmetry $\mathcal{C}^{ijkl} = \mathcal{C}^{jilk}$ and the two last the minor symmetries* $\mathcal{C}^{ijkl} = \mathcal{C}^{ikjl}$ and $\mathcal{C}^{ijkl} = \mathcal{C}^{ljki}$ respectively. Easily one can prove that the transposition operations are not commutative with each other or $[(\bullet)^t]^T \neq [(\bullet)^T]^t$ and $[{}^t(\bullet)]^T \neq {}^t[(\bullet)^T]$. But in a special case the commutativity is valid. E.g. for symmetric tensors $\mathbf{C}, \mathbf{D} \in Sym$ is valid that $\mathbf{C} : [(\mathbf{A} \times \mathbf{B})^T]^t : \mathbf{D} = \mathbf{C} : \mathbf{B} \times \mathbf{A}^T : \mathbf{D} = (\mathbf{C} : \mathbf{B})(\mathbf{A} : \mathbf{D})$ $\forall \mathbf{A}, \mathbf{B} \in Lin$. By Eqs (6) and (8) following results are also valid

$$\mathbf{A} \otimes \mathbf{B} : \mathbf{C} = \mathbf{A} \cdot \mathbf{C} \cdot \mathbf{B} \qquad \mathbf{C} : \mathbf{A} \otimes \mathbf{B} = \mathbf{A}^T \cdot \mathbf{C} \cdot \mathbf{B}^T \tag{13a}$$

$$\mathbf{A} \times \mathbf{B} : \mathbf{C} = (\mathbf{B} : \mathbf{C}) \cdot \mathbf{A} \qquad \mathbf{C} : \mathbf{A} \times \mathbf{B} = (\mathbf{C} : \mathbf{A}) \cdot \mathbf{B} \tag{13b}$$

$$\mathbf{A} \cdot (\mathcal{A} : \mathbf{C}) \cdot \mathbf{B} = (\mathbf{A} \cdot \mathcal{A} \cdot \mathbf{B}) : \mathbf{C} \qquad \mathbf{A} : \mathcal{A} : \mathbf{B} = (\mathcal{A}^T : \mathbf{A}) : \mathbf{B} \tag{13c}$$

The fourth order identity tensor is defined as

$$\mathcal{I} := \mathbf{I} \otimes \mathbf{I} = \mathbf{g}_i \otimes \mathbf{g}^i \otimes \mathbf{g}_j \otimes \mathbf{g}^j \tag{14}$$

It has following properties [8]: $\mathcal{I} : \mathbf{C} = \mathbf{C} : \mathcal{I} = \mathbf{C}$, $\mathbf{A} : \mathcal{I} : \mathbf{B} = A^j_{i.}B^i_{.j}$ and $\mathbf{A} \cdot \mathcal{I} \cdot \mathbf{B} = \mathbf{A} \otimes \mathbf{B}$, and for two vectors $\underline{\mathbf{a}} \cdot \mathcal{I} \cdot \underline{\mathbf{b}} = \underline{\mathbf{a}} \otimes \underline{\mathbf{b}}$.

Definition 3.6 *The symmetrization(-mapping) for a k-covariant tensor T in V, Sym: $T^k(V) \to T^k(V)$,*
$SymT = \frac{1}{k!}\sum_{\sigma \in S_k}({}^\sigma T)$,where S_k is the set $\{1, ..., k\}$ of permutations group and ${}^\sigma T$ is a k-covariant tensor,

$${}^\sigma T(\mathbf{g}_1, ..., \mathbf{g}_k) = T(\mathbf{g}_{\sigma(1)}, ..., \mathbf{g}_{\sigma(k)}).$$

$$\mathtt{Sym}T(\mathbf{g}_1, ..., \mathbf{g}_k) := \frac{1}{k!}\sum_{\sigma \in S_k} T(\mathbf{g}_{\sigma(1)}, ..., \mathbf{g}_{\sigma(k)})$$

*Determined in [1] for standard notation.

The quantity of S_k is $k!$ or $\mathtt{Sym}T$ is a "mean value" of ${}^{\sigma}T$ over all permutations $\sigma \in S_k$ [3]. The definition 3.6 is general producing fully symmetric tensor. E.g. the symmetrization of second order tensor is defined as, $\mathtt{sym}\mathbf{A} = \frac{1}{2}(\mathbf{A} + \mathbf{A}^T)$. But some partial symmetry-properties arise in continuum mechanics instead of fully symmetry. Considering a fourth order tensor, which is important when the tangent modulus including constitutive relations is determined. E.g. in the double-contraction $\mathbf{A} : \mathcal{C} : \mathbf{B} = \mathbf{B} : \mathcal{C}^T : \mathbf{A}$, where $\mathbf{A}$ and $\mathbf{B}$ are both symmetric second order tensors and often $\mathbf{A} \equiv \mathbf{B}$, for a fourth order tensor $\mathcal{C}$ can be set the following *partial symmetries* †

$$
\begin{aligned}
{}^{\sigma_q}T(\mathbf{g}_1, ..., \mathbf{g}_m) &= {}^{q}T(\mathbf{g}_1, ..., \mathbf{g}_{\sigma_q(i)}, ..., \mathbf{g}_{\sigma_q(j)}, ..., \mathbf{g}_{\sigma_q(m)}), ..., \\
{}^{\sigma_r}T(\mathbf{g}_1, ..., \mathbf{g}_m) &= {}^{r}T(\mathbf{g}_1, ..., \mathbf{g}_{\sigma_r(k)}, ..., \mathbf{g}_{\sigma_r(l)}, ..., \mathbf{g}_{\sigma_r(m)}). \\
\mathtt{Ssym}T(\mathbf{g}_1, ..., \mathbf{g}_m) &:= \frac{1}{c}\left[\frac{1}{a!}\sum_{\sigma_q \in S_q} {}^{q}T(\mathbf{g}_1, ..., \mathbf{g}_{\sigma_q(i)}, ..., \mathbf{g}_{\sigma_q(j)}, ..., \mathbf{g}_{\sigma_q(m)}) + ... \right. \\
&\qquad \left. \frac{1}{b!}\sum_{\sigma_r \in S_r} {}^{r}T(\mathbf{g}_1, ..., \mathbf{g}_{\sigma_r(k)}, ..., \mathbf{g}_{\sigma_r(l)}, ..., \mathbf{g}_{\sigma_r(m)})\right]
\end{aligned}
$$

where $\sigma_q \in S_q$ is the set $\{i, ..., j\}$ of permutations group, $..., \sigma_r \in S_r$ is the set $\{k, ..., l\}$ of permutations group, the quantities of $S_q, ..., S_r$ are $a!, ..., b!$ respectively, and c is the number of permutation groups. E.g. $S_1 = \{i, j, k, l\}$, $S_2 = \{i, k, j, l\}$, $S_3 = \{j, i, l, k\}$, $S_4 = \{j, l, i, k\}$, $S_5 = \{k, i, l, j\}$, $S_6 = \{l, j, k, i\}$, $S_7 = \{l, k, j, i\}$, and $S_8 = \{k, l, i, j\}$, i.e. $\sigma_1, ..., \sigma_8$ correspond to the transpositions in Eqs. $(10)_1$,...,$(10)_3$. Then this symmetrization is given as

$$
\mathtt{ssym}(\mathcal{A}) := \frac{1}{8}\Big(\mathcal{A} + \mathcal{A}^t + \mathcal{A}^T + (\mathcal{A}^T)^t + (\mathcal{A}^t)^T + {}^t\mathcal{A} + ({}^t\mathcal{A})^t + {}^t(\mathcal{A}^T)^t\Big) \tag{15}
$$

where it is noted that $({}^t\mathcal{A})^t = {}^t(\mathcal{A}^t) = {}^t\mathcal{A}^t$, ${}^t(\mathcal{A}^T) = (\mathcal{A}^t)^T$, $({}^t\mathcal{A})^T = (\mathcal{A}^T)^t$, $({}^t\mathcal{A}^t)^T = {}^t(\mathcal{A}^T)^t$, and $[({}^t\mathcal{A})^T]^t = {}^t[(\mathcal{A}^t)^T] = \mathcal{A}^T$. Above symmetrization produces a (fully) super-symmetric fourth order tensor. Often the super-symmetry denotes the symmetry obtained combining only the first five components in Eq. (15). This requirement corresponds to the double-contraction of fourth order tensor $\mathcal{C}$ from the right with a symmetric second-order tensor $\mathbf{B}$, or $\mathbf{A} = \mathcal{C} : \mathbf{B} = \mathcal{C}^t : \mathbf{B} = \mathbf{B} : \mathcal{C}^T$, $\mathbf{A}, \mathbf{B} \in Sym$. Further, the symmetric k-covariant tensor field (on topological manifold $\mathcal{M}$) is the k-covariant tensor field of which every value in every point $p \in \mathcal{M}$ is a symmetric tensor. Respectively one can determine the symmetric contravariant tensor field and tensor. The most important symmetric tensor field on $\mathcal{M}$ is the Riemannian metric of which every value in every point $p \in \mathcal{M}$ is a symmetric positive definite metric tensor $g \in T_p\mathcal{M} \times T_p\mathcal{M}$, where $T_p\mathcal{M}$ denotes the tangent space of $\mathcal{M}$ on p.

3.2 Differentiation of tensors

The differentiation of an arbitrary scalar valued tensor function $\alpha = \breve{\alpha}(\mathbf{C}) : Lin \to \mathbb{R}$ w.r.t a second order tensor $\mathbf{C} \in Lin$ is as

$$
\alpha(\mathbf{C})_{,\mathbf{C}} = \frac{\alpha}{C^i_{.j}}\mathbf{g}^i \otimes \mathbf{g}_j \tag{16}
$$

and $\alpha(\mathbf{C})_{,\mathbf{C}} \in Lin$. Obviously, the basis of $\mathbf{C}$ can be chosen arbitrary which means the invariance of $\alpha(\mathbf{C})_{,\mathbf{C}}$, because in the differentiation the basis and the corresponding metric

†E.g. when it is used independently as in FE-implementation

is required to be constant. α-function is said to be differentiable w.r.t $\mathbf{C}$ if the condition

$$\frac{d}{dt}\alpha(\mathbf{C}+t\mathbf{U})|_{t=0}, \quad \forall \mathbf{U} \in Lin$$

holds, which implies that the directional derivative (Gateux) exists in a neighbourhood of $\mathbf{C}$ and it is continuous at $\mathbf{C}$ [5], [9]. As the derivative of scalar valued function by Eq. (16), the material derivative of a second order tensor or tensor valued function $\mathbf{A} = \mathring{\mathbf{A}}(\mathbf{C}) \in Lin$ w.r.t its tensor argument $\mathbf{C} \in Lin$ is defined as the directional derivative [9]. Under this condition the derivative is as follows [9]

$$\frac{\partial \mathbf{A}}{\partial \mathbf{B}} = \mathbf{A}_{,\mathbf{B}} := \frac{\partial A^i_{.j}}{\partial B^k_{.l}} \mathbf{g}_i \otimes \mathbf{g}^k \otimes \mathbf{g}_l \otimes \mathbf{g}^j \tag{17}$$

I.e. the basis is required to remain as constant in the differentiation which means that basis $\mathbf{g}_i \otimes \mathbf{g}^j$ is independent of tensor components $B^k_{.l}$. Additionally, it is easy to proof [8] that the derivative is independent of the choice of co-ordinate system and the components variance. These are important properties because the *objectivity* or material *frame-indifference* of the tensor derivative is fulfilled and the absolute notation as $\mathbf{A}_{,\mathbf{B}}$ can be used. For a material tensor the differentiation is done as normal, but for a spatial tensor $\mathbf{t}$ the *pull-back* and *push-forward* operations [1], [5], [8] have to be used (see **example 1**). This derivative is known as the *Lie-derivative* of $\mathbf{t}$, which can be regarded as the material derivative of a spatial tensor to be formed by considering the deformed basis constant. It ensures the important objectivity or material frame-indifference property of its applications. Actually by covariance constitutive theory [5] the objectivity is embodied to the spatial covariance or the invariance under arbitrary spatial diffeomorphisms. Also symmetries of $\mathbf{t}$ are possessed by its Lie-derivative [5]. Consequently, by Eq. (17) $\mathbf{A}_{,\mathbf{A}} = \mathcal{I}$. The partial derivative of a second order tensor w.r.t its transverse counterpart is as [8]

$$\mathbf{C}_{,\mathbf{C}^T} = \mathbf{C}^T_{,\mathbf{C}} = \mathcal{I}^t := \mathcal{T} = \delta^i_k \delta^l_j \mathbf{g}^j \otimes \mathbf{g}^k \otimes \mathbf{g}_l \otimes \mathbf{g}_i = \mathbf{g}^j \otimes \mathbf{g}^i \otimes \mathbf{g}_j \otimes \mathbf{g}_i \tag{18}$$

where $\mathcal{T}$ is the transposition projection tensor for which is valid $\mathbf{B} : \mathcal{T} = \mathcal{T} : \mathbf{B} = \mathbf{B}^T$, $\mathbf{A} : \mathcal{T} : \mathbf{B} = A^j_{.i} B^i_{.j}$ and $\mathbf{A} \cdot \mathcal{T} \cdot \mathbf{B} = (\mathbf{A} \otimes \mathbf{B})^t$. Additionally, $(\mathbf{A} \otimes \mathbf{B})^t : \mathbf{C} = \mathbf{A} \cdot \mathbf{C}^T \cdot \mathbf{B}$ and $\mathbf{C} : (\mathbf{A} \otimes \mathbf{B})^t = \mathbf{B} \cdot \mathbf{C}^T \cdot \mathbf{A} = (\mathbf{A}^T \cdot \mathbf{C} \cdot \mathbf{B}^T)^T = \big(\mathbf{C} : (\mathbf{A} \otimes \mathbf{B})\big)^T$. For two vectors $\underline{\mathbf{a}} \cdot \mathcal{I}^t \cdot \underline{\mathbf{b}} = \underline{\mathbf{b}} \otimes \underline{\mathbf{a}}$. The definition in Eq. (18) is not unique for a symmetric tensor. In that case only six independent components are considered in differentiation and thus the derivative of arbitrary scalar and tensor valued function are defined as

$$\alpha_{,\mathbf{sym}\mathbf{C}} := \frac{1}{2} \sum_{i,j \leqslant i}^{3} \frac{\partial \alpha}{\partial C_{ij}} (\mathbf{g}_i \otimes \mathbf{g}_j + \mathbf{g}_j \otimes \mathbf{g}_i) = \frac{1}{2} \sum_{i,j \leqslant i}^{3} \frac{\partial \alpha}{\partial C^{ij}} (\mathbf{g}^i \otimes \mathbf{g}^j + \mathbf{g}^j \otimes \mathbf{g}^i) = \ldots \tag{19}$$

$$\mathbf{A}_{,\mathbf{sym}\mathbf{C}} := \frac{1}{2} \sum_{k,l \leqslant k}^{3} \frac{\partial \mathbf{A}^i_{.j}}{\partial C_{kl}} (\mathbf{g}_i \otimes (\mathbf{g}_k \otimes \mathbf{g}_l + \mathbf{g}_l \otimes \mathbf{g}_k) \otimes \mathbf{g}^j) = \ldots \tag{20}$$

where $\alpha = \mathring{\alpha}(\mathbf{C}) : Lin \to \mathbb{R}$. Consequently, the partial derivative of symmetric part $\mathbf{sym}\mathbf{C} := \frac{1}{2}(\mathbf{C} + \mathbf{C}^T)$ of a tensor $\mathbf{C}$ w.r.t symmetric part $\mathbf{sym}\mathbf{C}$ is as follows [8]

$$\begin{aligned} \mathbf{C}_{,\mathbf{sym}\mathbf{C}} &:= \frac{1}{2} \sum_{k,l \leqslant k}^{3} \frac{\partial \mathbf{C}^i_{.j}}{\partial C_{kl}} (\mathbf{g}_i \otimes (\mathbf{g}_k \otimes \mathbf{g}_l + \mathbf{g}_l \otimes \mathbf{g}_k) \otimes \mathbf{g}^j) = \frac{1}{2} \mathbf{g}_i \otimes (\mathbf{g}_j \otimes \mathbf{g}^i + \mathbf{g}^i \otimes \mathbf{g}_j) \otimes \mathbf{g}^j) \\ &= \frac{1}{2}(\mathcal{I} + \mathcal{T}) =: \mathcal{I}' = \mathbf{sym}\mathbf{C}_{,\mathbf{C}} = \mathbf{sym}\mathbf{C}_{,\mathbf{sym}\mathbf{C}} \end{aligned} \tag{21}$$

Similarly,

$$\alpha(\mathbf{C})_{,\mathtt{sym}\mathbf{C}} = \alpha_{,\mathbf{C}} : \mathbf{C}_{,\mathtt{sym}\mathbf{C}} = \alpha_{,\mathbf{C}} : \mathcal{I}' =: \mathtt{sym}(\alpha_{,\mathbf{C}}) \tag{22}$$

Let be α a smooth C^1 function of $\mathbf{C}$. Taking still the derivative of Eq. (22) w.r.t $\mathtt{sym}\mathbf{C}$ and taking into account that the arrangement of differentiation can be interchanged, one can obtain by means of Eq. (??)

$$(\alpha(\mathbf{C})_{,\mathtt{sym}\mathbf{C}})_{,\mathtt{sym}\mathbf{C}} = (\mathtt{sym}(\alpha_{,\mathbf{C}}))_{,\mathtt{sym}\mathbf{C}} = \mathtt{ssymm}\big((\alpha(\mathbf{C})_{,\mathbf{C}})_{,\mathbf{C}}\big) \tag{23}$$

Generalizing this result to the derivative of an arbitrary second order tensor delivers by chain rule

$$\begin{aligned} \mathbf{B}_{,\mathtt{sym}\mathbf{C}} = \mathbf{B}_{,\mathbf{C}} : \mathbf{C}_{,\mathtt{sym}\mathbf{C}} = \mathbf{B}_{,\mathbf{C}} : \mathcal{I}' = (\mathbf{B}_{,\mathbf{C}})', \quad \mathtt{sym}\mathbf{B}_{,\mathbf{C}} =' (\mathbf{B}_{,\mathbf{C}}), \\ \mathtt{sym}\mathbf{B}_{,\mathtt{sym}\mathbf{C}} = \mathtt{sym}\mathbf{B}_{,\mathbf{C}} : \mathbf{C}_{,\mathtt{sym}\mathbf{C}} =' (\mathbf{B}_{,\mathbf{C}})' \end{aligned} \tag{24}$$

where $(\cdot)' = \frac{1}{2}\big((\cdot) + (\cdot)^t\big), '(\cdot) = \frac{1}{2}\big((\cdot) + {}^t(\cdot)\big)$ and $'(\cdot)' = \frac{1}{4}\big((\cdot) + (\cdot)^t + {}^t(\cdot) + ({}^t(\cdot))^t\big)$. As mentioned above the commutativity property is valid for the transpositions as ${}^t((\cdot)^t) = ({}^t(\cdot))^t = {}^t(\cdot)^t$. From the properties of identity and transposition projection tensors, the transposition identity tensors (both from the left and right)[‡] have a following property $\mathbf{A}\cdot\mathcal{I}'\cdot\mathbf{B} = \mathbf{A}\cdot'\mathcal{I}\cdot\mathbf{B} = \frac{1}{2}(\mathbf{A}\otimes\mathbf{B} + (\mathbf{A}\otimes\mathbf{B})^t)$. For the product derivative of two second order tensor one can obtain [8], [9]

$$(\mathbf{A}\cdot\mathbf{B})_{,\mathbf{C}} = \mathbf{A}_{,\mathbf{C}}\cdot\mathbf{B} + \mathbf{A}\cdot\mathbf{B}_{,\mathbf{C}} \tag{25}$$

Consequently, $\mathbf{C}^2_{,\mathbf{C}} = \mathbf{I}\otimes\mathbf{C} + \mathbf{C}\otimes\mathbf{I}$ and the partial derivative of the inverse function $\mathbf{C}^{-1}_{,\mathbf{C}}$ is obtained by taking the derivative of product $(\mathbf{C}^{-1}\cdot\mathbf{C})_{,\mathbf{C}} = \mathbf{I}_{,\mathbf{C}} = \mathbf{0}$ which produces

$$\mathbf{C}^{-1}_{,\mathbf{C}} = -\mathbf{C}^{-1}\otimes\mathbf{C}^{-1} \quad \text{or} \quad (\mathbf{C}^{-1}_{,\mathbf{C}})^{i}_{.j}{}^{k}_{.l} = -(\mathbf{C}^{-1})^{i}_{.j}(\mathbf{C}^{-1})^{k}_{.l} \tag{26}$$

Other important differentiation rules can be formulated as follows [8]

$$(\alpha\mathbf{A})_{,\mathbf{B}} = \mathbf{A}\times\alpha_{,\mathbf{B}} + \alpha\mathbf{A}_{,\mathbf{B}} \quad (\mathbf{A}:\mathbf{B})_{,\mathbf{C}} = \mathbf{A}:\mathbf{B}_{,\mathbf{C}} + \mathbf{B}:\mathbf{A}_{,\mathbf{C}} \tag{27}$$

Next, the partial derivative of symmetric part of the inverse function, $(\mathtt{sym}\mathbf{C})^{-1}_{,\mathtt{sym}\mathbf{C}}$ is developed. Taking the partial derivative of product

$$(\mathtt{sym}\mathbf{C}\cdot(\mathtt{sym}\mathbf{C})^{-1})_{,\mathtt{sym}\mathbf{C}} = \mathbf{I}_{,\mathtt{sym}\mathbf{C}} = \mathbf{0}$$

leads to following result

$$\mathtt{sym}\mathbf{C}_{,\mathtt{sym}\mathbf{C}}\cdot(\mathtt{sym}\mathbf{C})^{-1} + \mathtt{sym}\mathbf{C}\cdot(\mathtt{sym}\mathbf{C})^{-1}_{,\mathtt{sym}\mathbf{C}} = \mathbf{0}$$

Noting Eq. (21) and multiplying by $(\mathtt{sym}\mathbf{C})^{-1}$ produces

$$(\mathtt{sym}\mathbf{C})^{-1}\cdot\mathcal{I}'\cdot(\mathtt{sym}\mathbf{C})^{-1} + (\mathtt{sym}\mathbf{C})^{-1}_{,\mathtt{sym}\mathbf{C}} = \mathbf{0} \quad \text{or} \quad (\mathtt{sym}\mathbf{C})^{-1}_{,\mathtt{sym}\mathbf{C}} = -(\mathtt{sym}\mathbf{C})^{-1}\cdot\mathcal{I}'\cdot(\mathtt{sym}\mathbf{C})^{-1}$$

where $(\mathtt{sym}\mathbf{C})^{-1}\cdot\mathcal{I}'\cdot(\mathtt{sym}\mathbf{C})^{-1} = \frac{1}{2}(\mathcal{C}^{-1} + \mathcal{C}^{-t})$ and $\mathcal{C}^{-1} := \frac{1}{2}(\mathbf{C}+\mathbf{C}^T)^{-1}\otimes\frac{1}{2}(\mathbf{C}+\mathbf{C}^T)^{-1}$. But if $(\mathtt{sym}\mathbf{C})^{-1} = \mathtt{sym}(\mathbf{C}^{-1}) = \mathbf{C}^{-1}$ $(\mathbf{C} = \mathbf{C}^T)$, then

$$(\mathtt{sym}\mathbf{C})^{-1}_{,\mathtt{sym}\mathbf{C}} = \mathbf{C}^{-1}_{,\mathtt{sym}\mathbf{C}} = -\mathbf{C}^{-1}\cdot\mathcal{I}'\cdot\mathbf{C}^{-1} = -\frac{1}{2}(\mathbf{C}^{-1}\otimes\mathbf{C}^{-1} + (\mathbf{C}^{-1}\otimes\mathbf{C}^{-1})^t) \tag{28}$$

which differs still from Eq. (26) [§]. Further, if $\mathbf{B} = \mathbf{B}^T$ and $(\mathtt{sym}\mathbf{C})^{-1} = \mathbf{C}^{-1}$, then $\mathtt{sym}\mathbf{C}^{-1}_{,\mathtt{sym}\mathbf{C}} : \mathbf{B} = \mathbf{C}^{-1}_{,\mathbf{C}} : \mathbf{B}$. Next, by means of above results some useful results will be obtained.

[‡]There is no identification symbol given in the literature for $'\mathcal{I}$

[§]That result equals to corresponding one given in [2]

4 DETERMINATION OF TANGENT MODULUS

4.1 Basic notations and definitions of deviatoric tensors

Here some important properties of the deviatoric tensors are given. This type of tensors arise e.g. in constitutive theory associated to the incompressible materials (as rubbers) or to the plasticity of metals and many plastic composites. Let be Sym the set of symmetric tensors, $Sym^+ \subset Sym$ the set of symmetric positive definite tensors and $\Omega \in \mathbb{R}^3$ a material body connected to the reference configuration, which is fixed in differentiation. In the constitutive theory, the (contravariant) material stress[¶] deviator $\mathbf{S}'$ of $\mathbf{S} \in Sym$ is determined as the differentiation of free energy $\hat{\Psi} = \Psi(\hat{\mathbf{C}}) : \Omega \times Sym^+ \to \mathbb{R}$ w.r.t its argument or the conjugate (covariant) strain $\mathbf{C} \in Sym^+$. Obviously the result fulfills the requirement of material frame indifference because $\Psi(\hat{\mathbf{C}}) = \Psi(\hat{\mathbf{C}}^*)$, $\mathbf{C}^* = \mathbf{C}$ in all rotations or proper orthogonal transformations $\mathbf{Q} \in SO(3)$. The expression of the (contravariant) material stress is obtained directly from the so-called *Doyle-Ericksen formula*[‖]. By that, chain rule, Eq. (21), and the symmetry $\mathtt{sym}\mathbf{C} = \mathbf{C}$, one can obtain

$$\begin{aligned}\mathbf{S}' &= 2\frac{\partial\hat{\Psi}}{\partial\hat{\mathbf{C}}} : \frac{\hat{\mathbf{C}}}{\mathbf{C}} = 2\mathtt{sym}(\frac{\partial\hat{\Psi}}{\partial\hat{\mathbf{C}}}) : J^{-\frac{2}{3}}(\mathcal{I}' - \frac{1}{3}\mathbf{C}\times\mathbf{C}^{-1}) = 2J^{-\frac{2}{3}}(\frac{\partial\hat{\Psi}}{\partial\hat{\mathbf{C}}} - \frac{1}{3}(\frac{\partial\hat{\Psi}}{\partial\hat{\mathbf{C}}} : \mathbf{C})\mathbf{C}^{-1}) \\ &=: 2J^{-\frac{2}{3}}DEV[\frac{\partial\hat{\Psi}}{\partial\hat{\mathbf{C}}}]\end{aligned} \tag{29}$$

where the distortional component of $\mathbf{C}$ is $\hat{\mathbf{C}} = J^{-2/3}\mathbf{C}$ and J is the determinant of the corresponding deformation gradient $\mathbf{F}$ defined as a map by (3) noting the comments below. I.e. $det(\hat{\mathbf{C}}) = 1$. Consequently, the deviatoric projection operator for the contravariant stress-like quantities can be defined as $DEV[\bullet] := [\bullet] - SPH[\bullet] = [\bullet] - 1/3([\bullet] : \mathbf{C})\mathbf{C}^{-1}$, where $SPH[\bullet]$ is the spherical part of the quantity determined by means of its trace by Def. 2.1 and the comments below. The push-forward produces the corresponding spatial operator as $dev[\cdot] = [\cdot] - 1/3([\cdot] : \mathbf{g})\mathbf{g}^{-1}$. Following results are valid for that deviatoric operator: $SPH[DEV[\bullet]] = \mathbf{0}$, $DEV[DEV[\mathbf{A}]DEV[\mathbf{B}]] \neq DEV[\mathbf{A}]DEV[\mathbf{B}] \neq DEV[\mathbf{A}\cdot\mathbf{B}]$ and consequently $SPH[DEV[\mathbf{A}]DEV[\mathbf{B}]]$ or $TR[DEV[\mathbf{A}]DEV[\mathbf{B}]] \neq 0$ generally. As an example, $DEV[\mathbf{A}^2] = \mathbf{A}^2 - 1/3\|\mathbf{A}\|^2\mathbf{C}^{-1}$, where $\mathbf{A}$ is a (contravariant) material tensor.
Taking still the derivative of a deviatoric material stress w.r.t its argument, symmetric conjugate (covariant) strain $\mathbf{C}$, produces the fourth order (contravarant) constitutive tensor known as the tangent modulus. I.e. taking twice the partial derivative of a strain energy function w.r.t its argument $\mathbf{C}$ produces

$$\begin{aligned}\mathcal{C}^{ea} &:= 4\frac{\partial^2\hat{\Psi}}{\partial\mathbf{C}\partial\mathbf{C}} = 4\hat{\Psi}_{,\mathbf{C},\mathbf{C}} = 4\frac{\partial}{\partial\mathbf{C}}\left(\frac{\partial\hat{\Psi}}{\partial\hat{\mathbf{C}}} : \frac{\partial\hat{\mathbf{C}}}{\partial\mathbf{C}}\right) = 4\frac{\partial}{\partial\mathbf{C}}\left(J^{-2/3}\frac{\partial\hat{\Psi}}{\partial\hat{\mathbf{C}}} : (\mathcal{I}' - \frac{1}{3}\mathbf{C}\times\mathbf{C}^{-1})\right) \\ &= 4\frac{\partial}{\partial\mathbf{C}}\left(J^{-2/3}\frac{\partial\hat{\Psi}}{\partial\hat{\mathbf{C}}} - J^{-2/3}\frac{1}{3}(\frac{\partial\hat{\Psi}}{\partial\hat{\mathbf{C}}} : \mathbf{C})\mathbf{C}^{-1}\right) = J^{-4/3}DEV[\hat{\mathcal{C}}^{ea}] + \\ &\quad J^{-2/3}\frac{2}{3}(\mathbf{S} : \mathbf{C})\left(\mathbf{C}^{-1}\otimes\mathbf{C}^{-1} - \frac{1}{3}\mathbf{C}^{-1}\times\mathbf{C}^{-1}\right) - \frac{2}{3}\left(\mathbf{S}'\times\mathbf{C}^{-1} + \mathbf{C}^{-1}\times\mathbf{S}'\right)\end{aligned} \tag{30}$$

where $\mathbf{S} := 2\hat{\Psi}_{,\hat{\mathbf{C}}}$, $\mathbf{S}' := J^{-2/3}DEV[\mathbf{S}]$, $\hat{\mathcal{C}}^{ea} := 4\hat{\Psi}_{,\hat{\mathbf{C}},\hat{\mathbf{C}}}$ and $DEV[\hat{\mathcal{C}}^{ea}]$ denotes a kind of fourth order deviatoric tensor obtained taking twice the partial derivative of a strain energy

[¶]Here $\mathbf{S}$ denotes a contravariant tensor $\mathbf{S}^\sharp$ (all component-indices raised) without the superscript "$\sharp$", and similarly $\mathbf{C}$ means a covariant tensor $\mathbf{C}^\flat$ (all component-indices lowered).

[‖]The expression for the second Piola-Kirchhoff stress in terms of free energy is given in [5], prop. 2.11

function w.r.t $\hat{\mathbf{C}}$ by means of the chain rule as,

$$DEV[\bullet] := (\bullet) - \frac{1}{3}((\bullet) : \mathbf{C}) \times \mathbf{C}^{-1} - \frac{1}{3}\mathbf{C}^{-1} \times (\mathbf{C} : (\bullet)) + \frac{1}{9}(\mathbf{C} : (\bullet) : \mathbf{C})\mathbf{C}^{-1} \times \mathbf{C}^{-1} \quad (31)$$

A direct consequence of that (contravariant) deviator is $\mathbf{C} : DEV[\bullet] = DEV[\bullet] : \mathbf{C} = \mathbf{0}$. The result in Eq. (30) is obviously symmetric because both $\mathbf{S}$ and $\mathbf{C}$ are symmetric tensors and due to the smoothness of potential (i.e. Ψ is C^1 function of $\mathbf{C}$), $\Psi_{,C_{ij}C_{kl}} = \Psi_{,C_{kl}C_{ij}}$ holds. Further, the result can be symmetrized to the super-symmetric form by Eqs. (15) and (23). Additionally the result is objective, because $\mathbf{C}^* = \mathbf{C}$ in all rotations or proper orthogonal transformations $\mathbf{Q} \in SO(3)$.

4.2 Some illustrations

Example 1 Let be a space of positive definite tensors (linear transformations) sym^+ and the material strain tensor $\mathbf{C} \in Sym^+$, strain energy function $\Psi = \breve{\Psi}(\mathbf{C})$ ** and the corresponding spatial one ψ. One can verify that the tangent modulus derived as above and by the well known representation,

$$\mathfrak{c} = (\mathbf{F} \otimes \mathbf{F}^T) : 4\frac{\partial^2 \Psi}{\partial \mathbf{C} \partial \mathbf{C}} : (\mathbf{F}^T \otimes \mathbf{F}), \quad \mathfrak{c} = 2\tau_{,\mathbf{g}} = 2\frac{\partial \tau}{\partial \mathbf{g}} = 4\frac{\partial^2 \psi}{\partial \mathbf{g} \partial \mathbf{g}} \quad (32)$$

are both symmetric ($\mathfrak{c} = \mathfrak{c}^T$) and coincide only if $\tau \in Sym$ is a spatial contravariant stress tensor with the basis which is independent of the components of corresponding covariant Riemannian metric tensor $\mathbf{g} \in Sym^+$ [8]. Using other variants would lead to the meaningless result. Consequently, the tangent modulus given by second representation cannot considered as the objective tensor (as the first presentation), because it depends not only on the components variance but also on the coordinate system to which these components are related! Instead, the first presentation is very generally valid, and it does not preclude anisotropic response subjected to the finite strains. The Lie-derivative of spatial stress tensor $\mathcal{L}_v \tau = \dot{\tau} - \mathbf{l}\tau - \tau \mathbf{l}^T = \mathfrak{c} : 1/2\mathcal{L}_v \mathbf{g} = \mathfrak{c} : \mathbf{d}$ ††, where $\mathbf{l}$ is known as the velocity gradient and $\mathbf{d} = \mathtt{sym}(\mathbf{l})$ is known as the rate of deformation tensor [1], [2].

Example 2 The uncoupled free energy function for a certain incompressible neo-Hookean material including plastic evolution with the finite strains is assumed to be a sum of isotropic and transversely isotropic parts as follows

$$\hat{\Psi}(\hat{\mathbf{C}}, \mathbf{C}^{a-1})_{iso} = \frac{1}{2}\mu[(\mathbf{C}^{a-1} : \hat{\mathbf{C}}) - 3], \quad (33)$$

$$\hat{\Psi}(\hat{\mathbf{C}}, \mathbf{C}^{a-1})_{trn} = [\alpha + \gamma(\hat{I}_4 - 1)](\hat{I}_4 - 1) - \frac{1}{2}\alpha(\hat{I}_5 - 1) \quad (34)$$

where $\hat{\mathbf{C}}, \mathbf{C}^a \in Sym^+$, i.e they are both symmetric, pos. definite strain tensors, called right Green-Lagrange and the plastic strain tensor respectively. α, γ, μ are material parameters. Obviously both parts fulfill the objectivity requirement [6]. Above expressions are obtained from the spatial counterparts (see e.g. [7]) or the counterparts associated to the intermediate configuration by pull-back operations [4]. The invariants are also the functions of the pull-backs of their spatial or intermediate counterparts as $\hat{I}_4 = \underline{\mathbf{A}} \cdot \hat{\mathbf{C}} \cdot \underline{\mathbf{A}}$, $\hat{I}_5 = \underline{\mathbf{A}} \cdot \hat{\mathbf{C}} \cdot \mathbf{C}^{a-1} \cdot \hat{\mathbf{C}} \cdot \underline{\mathbf{A}}$ and their derivatives are by Eq. (22) as follows

$$\frac{\partial \hat{I}_4}{\partial \hat{\mathbf{C}}} = \underline{\mathbf{A}} \otimes \underline{\mathbf{A}}, \qquad \frac{\partial \hat{I}_5}{\partial \hat{\mathbf{C}}} = 2\mathtt{sym}(\underline{\mathbf{A}} \otimes \mathbf{C}^{a-1} \cdot \hat{\mathbf{C}} \cdot \underline{\mathbf{A}})$$

**The objectivity requirements have to be fulfilled [1], [5], [6].

††$\mathtt{sym}(\mathbf{g})$ is now redundant because the symmetry of $\mathbf{g}$ is also possessed by $\mathcal{L}_v \mathbf{g}$.

Consequently, the differentiation of free energy function w.r.t $\hat{\mathbf{C}}$ is as,

$$\mathbf{S} := 2\frac{\partial \hat{\Psi}_{trn}}{\partial \hat{\mathbf{C}}} = \mu \mathbf{C}^{a-1} + 2\Big((\alpha + 2\gamma(\hat{I}_4 - 1))\underline{\mathbf{A}} \otimes \underline{\mathbf{A}} - \alpha \mathtt{sym}(\underline{\mathbf{A}} \otimes \mathbf{C}^{a-1} \cdot \hat{\mathbf{C}} \cdot \underline{\mathbf{A}}) \Big)$$

By virtue of Eqs (21), (23) and (25) the fourth order material tensor is defined as follows

$$\hat{\mathcal{C}}^{ea} := 4\frac{\partial^2 \hat{\Psi}}{\partial \hat{\mathbf{C}} \partial \hat{\mathbf{C}}} = 8\Big(\gamma(\underline{\mathbf{A}} \otimes \underline{\mathbf{A}}) \times (\underline{\mathbf{A}} \otimes \underline{\mathbf{A}}) - \alpha \mathtt{ssym}(\underline{\mathbf{A}} \otimes \mathbf{C}^{a-1} \otimes \underline{\mathbf{A}}) \Big) \tag{36}$$

The matrix form of the fourth order tensor is constructed from the mixed variant components (as in Eq. (17)) by equating the internal virtual work of a body or the product $\delta\mathbf{E} : \mathcal{C} : \mathbf{\Delta E}$ to the matrix product $\delta\mathbf{E}^T \mathbf{D} \mathbf{\Delta E}$ with the arrangement $\mathbf{E}^T = [E_{11}, E_{22}, E_{33}, E_{12}, E_{13}, E_{23}]$ to give, after some algebra,

$$\mathbf{D} = \frac{1}{2}\begin{bmatrix} 2\mathcal{C}^{1\,1}_{.1.1} & 2\mathcal{C}^{1\,2}_{.2.1} & 2\mathcal{C}^{1\,3}_{.3.1} & \mathcal{C}^{1\,1}_{.2.1} + \mathcal{C}^{1\,2}_{.1.1} & \mathcal{C}^{1\,1}_{.3.1} + \mathcal{C}^{1\,3}_{.1.1} & \mathcal{C}^{1\,2}_{.3.1} + \mathcal{C}^{1\,3}_{.2.1} \\ & 2\mathcal{C}^{2\,2}_{.2.2} & 2\mathcal{C}^{2\,3}_{.3.2} & \mathcal{C}^{2\,1}_{.2.2} + \mathcal{C}^{2\,2}_{.1.2} & \mathcal{C}^{2\,1}_{.3.2} + \mathcal{C}^{2\,3}_{.1.2} & \mathcal{C}^{2\,2}_{.3.2} + \mathcal{C}^{2\,3}_{.2.2} \\ symm. & & 2\mathcal{C}^{3\,3}_{.3.3} & \mathcal{C}^{3\,1}_{.2.3} + \mathcal{C}^{3\,2}_{.1.3} & \mathcal{C}^{3\,1}_{.3.3} + \mathcal{C}^{3\,3}_{.1.3} & \mathcal{C}^{3\,2}_{.3.3} + \mathcal{C}^{3\,3}_{.2.3} \\ & & & \mathcal{C}^{1\,1}_{.2.2} + \mathcal{C}^{1\,2}_{.1.2} & \mathcal{C}^{1\,1}_{.3.2} + \mathcal{C}^{1\,3}_{.1.2} & \mathcal{C}^{1\,2}_{.3.2} + \mathcal{C}^{1\,3}_{.2.2} \\ & & & & \mathcal{C}^{1\,1}_{.3.3} + \mathcal{C}^{1\,3}_{.1.3} & \mathcal{C}^{1\,2}_{.3.3} + \mathcal{C}^{1\,3}_{.2.3} \\ & & & & & \mathcal{C}^{2\,2}_{.3.3} + \mathcal{C}^{2\,3}_{.2.3} \end{bmatrix} \tag{37}$$

I.e. the result corresponds to the super-symmetric fourth order tensor with $6(6+1)/2 = 21$ independent components. That result is needed typically for the FE-implementation, where the symmetry of both $\delta\mathbf{E}$ and $\mathbf{\Delta E}$ has to be taken into account (only six components). Assuming the direction of anisotropy, $\underline{\mathbf{A}} = \mathbf{e}_1 = \mathbf{e}^1$, i.e. w.r.t the orthonormal basis $\mathbf{e}_i \otimes \mathbf{e}_j$. Then, as an example the symmetric material tensor $\hat{\mathcal{C}}^{ea}$ in Eq. (36) reduces to

$$\hat{\mathcal{C}}^{ea} = 8\Big(\gamma \mathbf{e}_1 \otimes \mathbf{e}_1 \otimes \mathbf{e}_1 \otimes \mathbf{e}_1 - \alpha (\mathbf{C}^{a-1})^{ij} \mathtt{ssym}(\mathbf{e}_1 \otimes \mathbf{e}_i \otimes \mathbf{e}_j \otimes \mathbf{e}_1) \Big) \quad i,j = 1,2,3$$

Taking the kind of deviatoric part of that result by Eq. (31) gives the first part of deviatoric tangent modulus as

$$\mathcal{C}^{ea,1} = J^{-4/3}\Big(\hat{\mathcal{C}}^{ea} - \frac{8}{3}\big((\gamma C_{11} \mathbf{e}_1 \otimes \mathbf{e}_1 - \alpha (\mathbf{C}^{a-1})^{ij} \mathbf{B}) \times \mathbf{C}^{-1} + \mathbf{C}^{-1} \times (\gamma C_{11} \mathbf{e}_1 \otimes \mathbf{e}_1 - \alpha (\mathbf{C}^{a-1})^{ij} \mathbf{B}) \big) + \frac{8}{9}\big(\gamma (C_{11})^2 - \frac{1}{2}\alpha (\mathbf{C}^{a-1})^{ij} (C_{11} C_{ij} + C_{1i} C_{1j}) \big) \mathbf{C}^{-1} \times \mathbf{C}^{-1} \Big)$$

where $\mathbf{B} := 1/4\mathtt{sym}(C_{11}\mathbf{e}_i \otimes \mathbf{e}_j + C_{1i}\mathbf{e}_1 \otimes \mathbf{e}_j + C_{1j}\mathbf{e}_i \otimes \mathbf{e}_1 + C_{ij}\mathbf{e}_1 \otimes \mathbf{e}_1)$. The components of corresponding matrix are as follows,

$$\hat{D}^{ea,1}_{11} = 8J^{-4/3}(\gamma - \alpha(\mathbf{C}^{a-1})^{11}) - (\mathcal{C}^{ea,1}_2)^{1111}, \quad \hat{D}^{ea,1}_{12} = -8J^{-4/3}\alpha(\mathbf{C}^{a-1})^{22} - (\mathcal{C}^{ea,1}_2)^{1221}, ...,$$
$$\hat{D}^{ea,1}_{22} = 0 - (\mathcal{C}^{ea,1}_2)^{2222}, ..., \hat{D}^{ea}_{66} = 0 - \frac{1}{2}\big((\mathcal{C}^{ea,1}_2)^{2323} + (\mathcal{C}^{ea,1}_2)^{2233} \big)$$

where $(\mathcal{C}^{ea,1}_2)^{ijkl}$ are the components of $\mathcal{C}^{ea,1}$ without $\hat{\mathcal{C}}^{ea}$. I.e.

$$(\mathcal{C}^{ea,1}_2)^{1111} = \frac{8}{3}J^{-4/3}\Big[\gamma C_{11}(\mathbf{C}^{-1})^{11}(2 + \frac{1}{3}C_{11}(\mathbf{C}^{-1})^{11}) - \alpha(\mathbf{C}^{a-1})^{ij}(\mathbf{C}^{-1})^{11}\big(2C_{11} - \frac{1}{6}(C_{11}C_{ij} + C_{1i}C_{1j})(\mathbf{C}^{-1})^{11}\big) \Big], \quad \text{etc.}$$

Similarly the matrix-components of the second part are as follows

$$\hat{D}_{11}^{ea,2} = \frac{2}{3}\Big(J^{-2/3}\frac{2}{3}S^{ij}C_{ij}\big((\mathbf{C}^{-1})^{11}\big)^2 - 2S'^{11}(\mathbf{C}^{-1})^{11}\Big),$$

$$\hat{D}_{12}^{ea,2} = \frac{2}{3}\Big(J^{-2/3}S^{ij}C_{ij}\big(\big((\mathbf{C}^{-1})^{12}\big)^2 - \frac{1}{3}(\mathbf{C}^{-1})^{11}(\mathbf{C}^{-1})^{22}\big) - S'^{11}(\mathbf{C}^{-1})^{22} - (\mathbf{C}^{-1})^{11}S'^{22}\Big), ...,$$

$$\hat{D}_{66}^{ea,2} = \frac{1}{3}\Big(J^{-2/3}S^{ij}C_{ij}\big(\frac{1}{3}\big((\mathbf{C}^{-1})^{23}\big)^2 + (\mathbf{C}^{-1})^{22}(\mathbf{C}^{-1})^{33}\big) - 4S'^{23}(\mathbf{C}^{-1})^{23}\Big).$$

5 CONCLUSIONS

There are still some problems concerned with the treatment of the differentiation of a tensor function with respect to a second order tensor. In applications e.g. the derivation of second order stress tensor with respect to second order strain tensor leads to the important fourth order tensor known as the tangent modulus. It is shown, that in many cases the correct differentiation leads to the symmetric tangent modulus or it could be symmetrized. Although, there is no unique definition for the derivative of (symmetric) second order tensor with respect to another, symmetric one. Here, some expressions concerned about the symmetry is determined. Also certain aspects connected to the objectivity are discussed. By means of the given results, a closed form expression for the tangent modulus can be obtained despite the complex constitutive relations including anisotropy and plastic evaluation of material with finite strains. At least for the hyper-elastic nature of the stress-response, also the closed-form consistent tangent modulus associated with the algorithm is possible to obtain, which is essential in preserving the asymptotic rate of quadratic convergence in Newton-type methods.

REFERENCES

[1] Belytschko T, Liu W.K, Moran B. *Nonlinear Finite Element for Continua and Structures* Wiley: Chichester, 2000.

[2] Holzapfel G.A. *Nonlinear Solid Mechanics.* Wiley: Chichester, 2001.

[3] Holopainen I. *Differential Geometry. Lectures 1999 and 2001* Manuscript, 2001. 77 p.

[4] Simo J.C, Hughes T.J.R. *Computational Inelasticity* Springer-Verlag: New York, 1999.

[5] Marsden J.E, Hughes T.J.R. *Mathematical Foundations of Elasticity* Dover: New York, 1993.

[6] Stumpf H, Hoppe U. The application of tensor algebra on manifolds to nonlinear continuum mechanics-invited survey artile, ZAMM (Z. Angew. Math. Mech). *Applied Mathematics and Mechanics* 1997; **77**(5):327–339.

[7] Bonet J, Burton A.J. A simple orthotropic, transversely isotropic hyperelastic constitutive equation for large strain computations. *Computer Methods in Applied Mechanics and Engineering* 1998; **162**(1-4):151–164.

[8] Itskov M. On the theory of fourth-order tensors and their applications in computational mechanics. *Computer Methods in Applied Mechanics and Engineering* 2000; **189**:419–438.

[9] Itskov M. The Derivative with respect to a Tensor: some Theoretical Aspects and Applications. *ZAMM Z. Angew. Math. Mech.* 2002; **82**:535–544.

DYNAMICAL TIME DOMAIN SIMULATION OF ROLL CONTACT

V.M. Järvenpää

Tampere University of Technology, Machine Design
Email: veli-matti.jarvenpaa@tut.fi

ABSTRACT

The softened rolling contact of two paper machine rolls is considered. The rolls are described by multibody substructuring modeling. The polymer cover layer between the rolls, which softens the contact, is modeled by contact spring reaction forces calculated according to its stiffness. The internal excitation due to viscolelastic material behavior of the polymer is introduced to the system by a time delay term. It is calculated from the penetration history of the cover layer. The solution of the system equations is obtained by numerical time integration by utilizing the method of steps. Some numerical results are illustrated.

1. INTRODUCTION

The rolling contact of two rolls in a paper calendering machine is studied. The calendering units of interests are used at the end phase of the paper manufacturing process to produce paper with constant thickness. In the unit the rolls are compressed together by hydraulic actuators to create optimal line loading. Then during calendering the paper web enters to this nip of rolls and undergoes deformations and surface polish to achieve equal thickness. It has been experienced that the dynamics of this system is sensitive to the operational and constructional parameter selections and this can create undesired vibrations during calendering with an unfavorable setup. The problem is that it is difficult to predict accurately enough the dynamics of the system by using current design methods. The aim in this paper is to determine some of the dynamical behavior of calendaring by creating a numerical time domain simulation model. The model is based on the test calendering unit in university's laboratory environment. This test unit is about half scale of the real size machine with 4 meter length cast iron rolls and it includes build-in wireless strain and acceleration measurement and data transfer system. However, the paper web has not been included in the test unit, but this still is very beneficial environment to verify the results of numerical models.

The simulation model is based on multibody dynamics. The equations of motions for each roll are expressed inside a rotating coordinate frame and by using modal coordinates with sets of lowest semi-definite eigenvectors. The rolls are modeled like simply supported beams but by using 3D continuum finite element meshes. The contact of the rolls is described by contact force coupling in the right hand side of the equations. One of the rolls is coated by soft polymer layer and another has hard surface without coating. The contact stiffness between the rolls is calculated according to the polymer layer stiffness. Because solid element meshes are used and the rolls are making rigid

body spin rotation, the contact line load needs to smoothly move on the surfaces within each element and across element boundaries. This has been modeled by describing equivalent element nodal forces to the surface elements as a function of the rigid body rotation angle. The solution of these system equations requires a non-linear time integration procedure and the time domain simulation is implemented in MATLAB environment. The numerical circumferential strain responses have been compared to the measured data.

The time delay effect of the cover deformations is included as follows. The method of steps is used. The deformation history of the cover is recorded as a penetration function and this is introduced to the system equations as a delayed feedback source. The time delay is non-constant depending on the roll rotation time. To obtain the correct deformation history at the right times according to the stepping of the time integration solution procedure, a time domain interpolation of the penetration history is used.

2. EQUATIONS OF MOTION

The following assumptions are used in the multibody modeling. Firstly, only one large global rotation about the longitudinal axis, the spin motion, is considered. The other two rotations remain small, because the roll bearings are mounted at roll ends and the rolls are driven in parallel rolling motion by their individual drives. The two other rotations as well as the reference translations are neglected due to this mounting. This simplifies the coordinate transformation significantly. Secondly, the lumped mass formulation is used and the finite element nodal masses are considered as point masses or mass particles. Linear continuum element meshes are used for determining the modal vectors of the rolls. Finally, the deformations of the bodies are described by sets of modal vectors. The modes with bearing boundary conditions are used. Figure 1 shows the system layout.

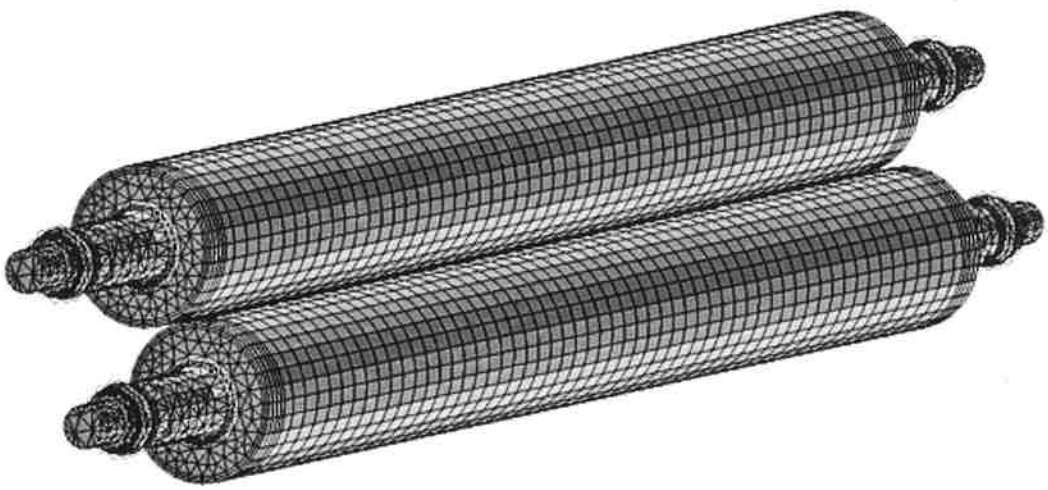


Figure 1. Layout of the roll system in the numerical simulations.

3. CONTACT MODELING

The key characteristic of the roll contact is that the polymer cover is much softer than the metallic rolls. This makes the contact spring force modeling most suitable for this type of a contact. The contact is described as a line contact by using non-uniform stiffness distribution function between the rolls. This function represents the stiffness of the polymer cover layer of the upper roll. This approach is similar as the elastic foundation model. However, the main difference is that nonlinear contact force of the foundation model depends on the contact width, which here is only considered in the pre-calculation of the stiffness distribution. It also turns out that the pre-calculated stiffness distribution is almost constant due to the proper design of the rolls. The contact line is rolling over element boundaries from element to element, according to the rotations of the rolls. The crowning of the rolls is introduced to the contact by the enforced displacement function, which also is pre-defined.

4. INTERNAL EXCITATION SOURCE

The contact spring force with the time delay term takes the form

$$N = k_n[\varepsilon(t) - \gamma\varepsilon(t-T)] + c_n\dot{\varepsilon}(t), \tag{1}$$

where k_n is the contact stiffness and c_n is the damping coefficient for a Kelvin-like polymer roll covering material. The contact penetration splits into three different components

$$\varepsilon(t) = x_1 - x_2 + z(t) \tag{2}$$

where the first two parts x_1 and x_2 represent the relative roll motion at the contact line and the third one $z(t)$ is the paper thickness variation, which is not considered here. γ is the decay factor. Depending on this factor, roll cover dynamics will be affected by the memory of past deformation so that when returning to the contact, the previous cover deformation is not completely vanished.

5. NUMERICAL RESULTS

5.1 Responses under normal running conditions

Some results of the metallic roll are shown next. Strains of one point on the inner surface at the center of the roll are observed. The constant rotation speeds were maintained during the simulation after the initial acceleration to their desired values. The rotation speed of the lower roll is illustrated in Figure 2 The roll contact is closed after 20 seconds. The contact line load response is shown in Figure 3. The circumferential strain result in Figure 4 illustrates similar behavior as obtained by the measurements. After the contact is closed the steady state amplitude looks very similar to the measured response with the major difference in the maximum peak value. Otherwise the general shapes of the two curves match each other quite well and the curves have similar width of the contact zone. The probable cause of the peak difference is the finite element mesh of the rolls, because the linear element type used makes the interpolation of a cylindrical surface difficult. The mesh refinement in the circumferential direction could improve the accuracy of the peaks. The axial strain result in Figure 5 gives much closer match to the measured amplitude. Obviously in this case the bending deformation is much less difficult to describe by the linear finite element mesh used. Also the axial strain amplitude before the contact is closed match well to a measured result not shown here

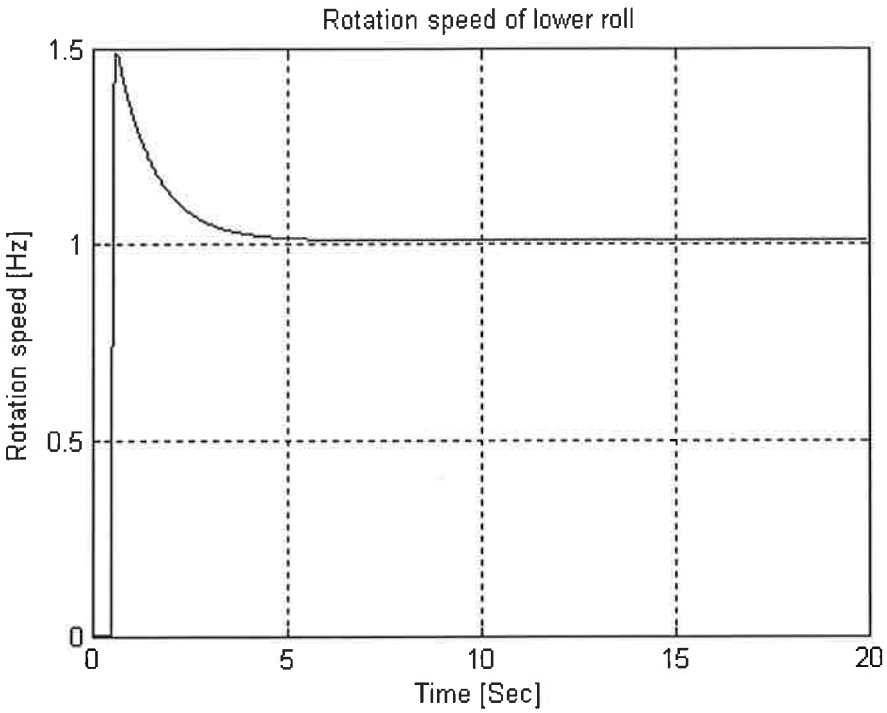


Figure 2. The initial acceleration to the desired running speed. 100 m/min. in this case.

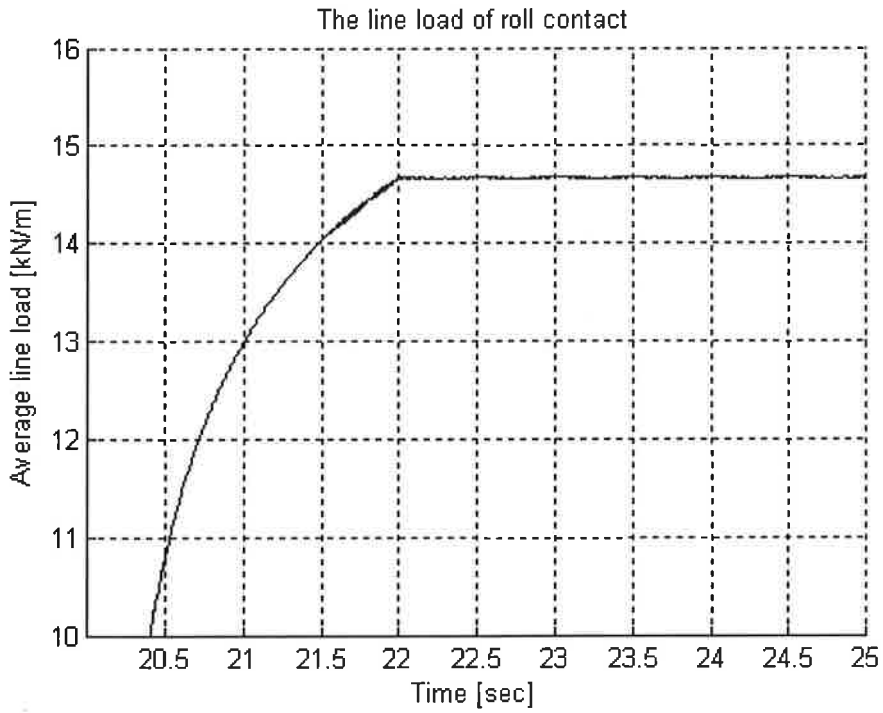


Figure 3. The line load history during the closing of the roll contact.

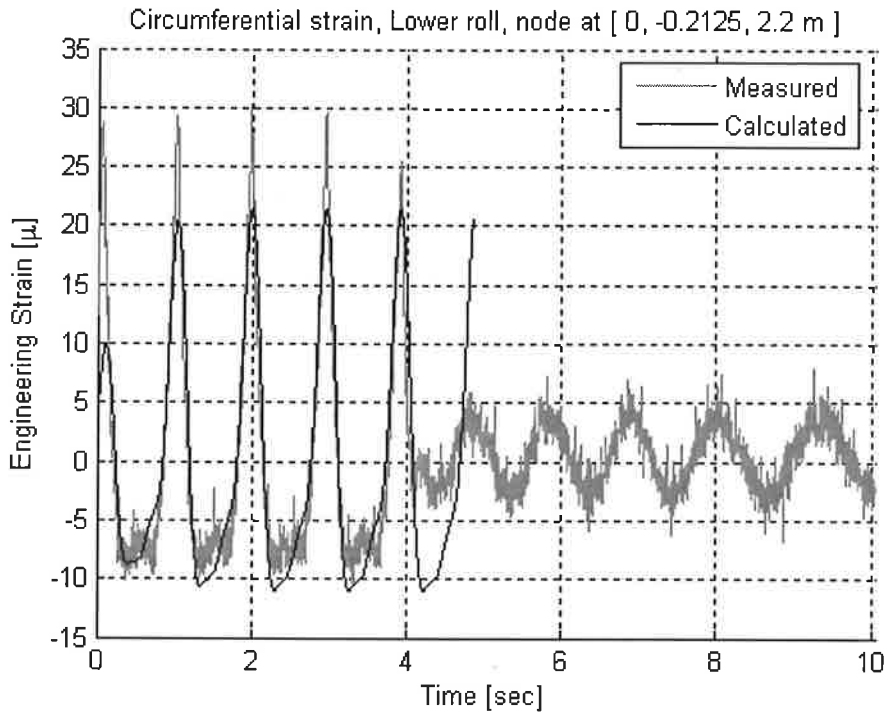


Figure 4. Circumferential strain response of the metallic roll.

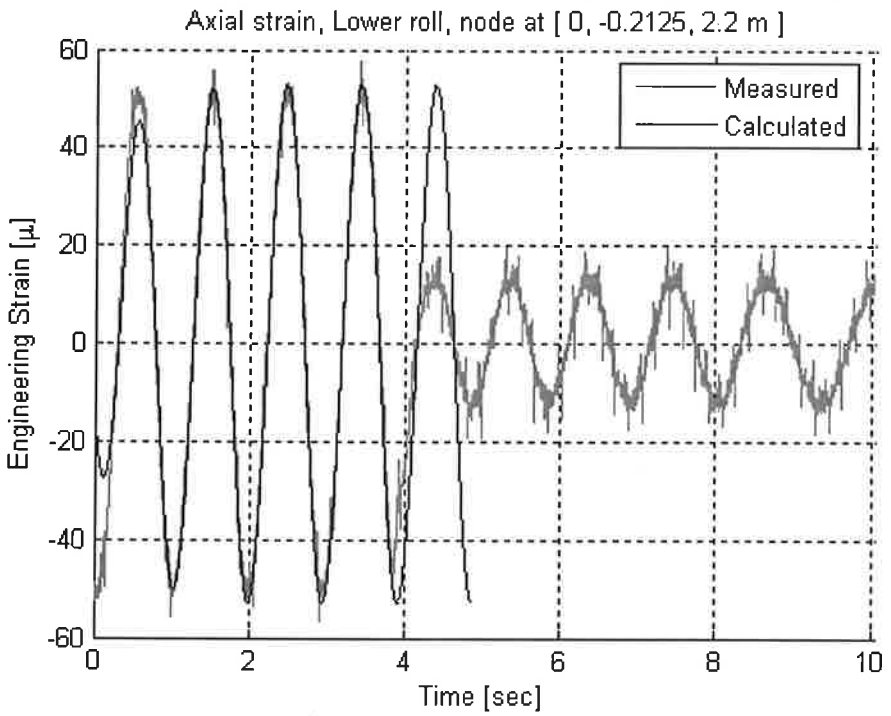


Figure 5. Axial strain response of the metallic roll.

5.2 Internal excitation

The key feature of the roll contact vibration is the excitation of the roll beating vibration mode. This mode means that the upper and lower rolls have bending vibrations with opposite phases and the rolls are beating each other. The natural frequency of this mode in the numerical model is about 109.5 Hz. Three different cases are considered with the different running speeds of 451 m/min, 442 m/min and 434 m/min. The first and third cases show relatively stable contact force responses in Figures 6 and 8 but the second case in Figure 7 is clearly unstable immediately. This result is expected because in the time delay systems in general have multiple stability boundaries in the frequency domain. The highest frequency component is the beating natural frequency. The responses also show some envelope patterning. The time period of an envelope in the curves is the delay time, which is another typical characteristic of a delay system. More explanation on the stability behavior can be obtained if the rotation frequencies are compared to the beating mode natural frequency. The division of the natural frequency by the rotation frequencies produces ratios of 25, 25.5 and 26, respectively. This means that one resonance and two anti-resonances are encountered. The consequence of this resonances is that the polymer cover layer will have equivalent number of circumferential out-of-roundness waves on its surface during the excitation.

6. CONCLUSIONS

The dynamic contact of two calendering rolls was simulated successfully. The multibody modeling, the contact force coupling and the use of non-linear time integration procedure provided a solution. The conclusion is that modeling seems to be robust enough to obtain the dynamics of the system. The accuracy could be improved by refining the finite element modeling of the rolls.

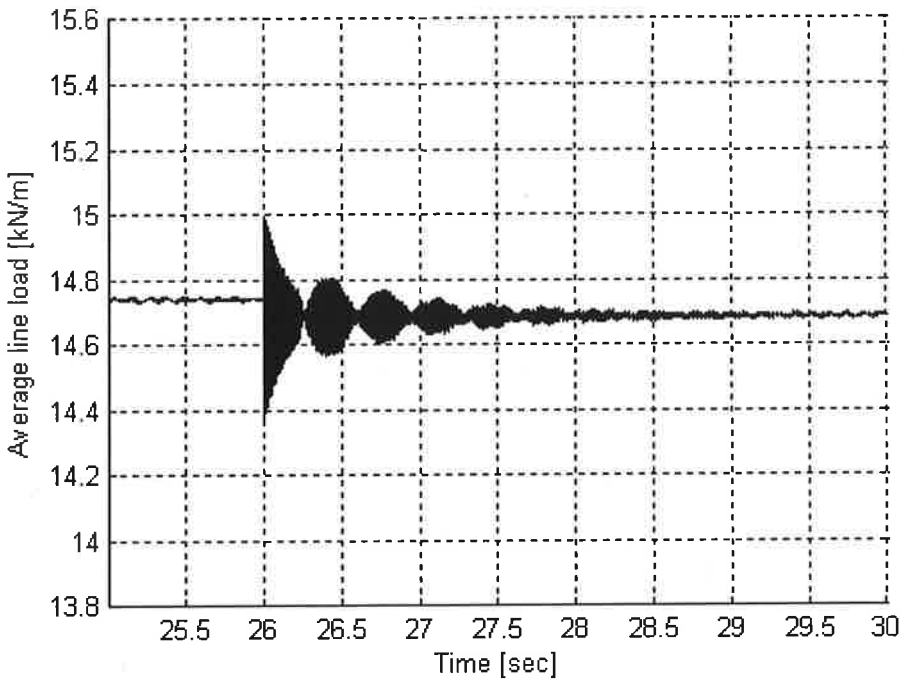


Figure 6. Line load history with time delay. Running speed of 451 m/min. Stable.

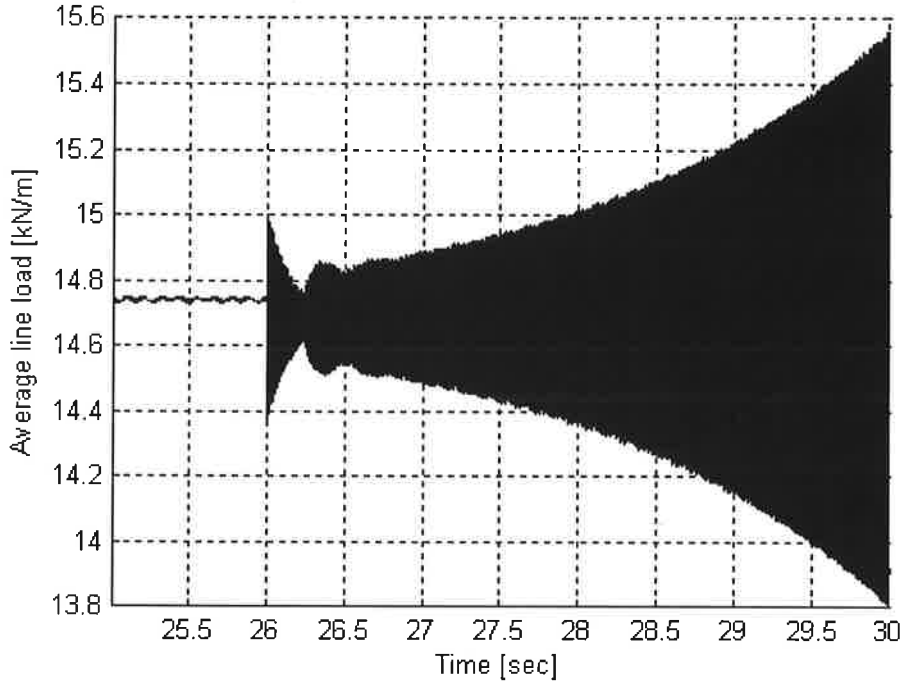


Figure 7. Line load history with time delay. Running speed of 442 m/min. Unstable.

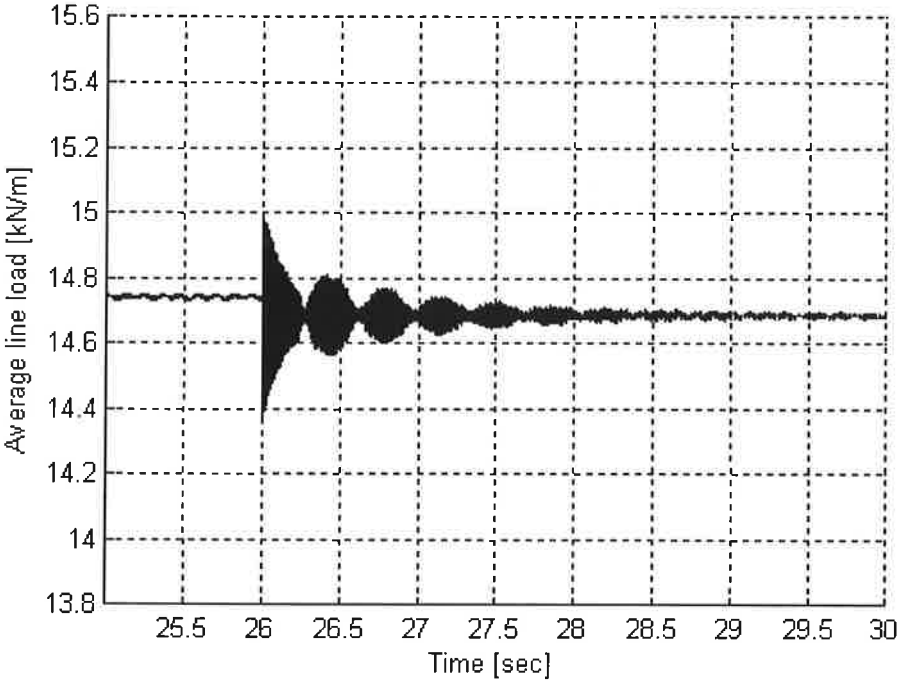


Figure 8. Line load history with time delay. Running speed of 434 m/min. Stable.

7. ACKNOWLEDGMENTS

The author would like to express gratitude to The Academy of Finland, which has provided funding for this project.

REFERENCES

Järvenpää V.M., Keskinen E., Dynamical modelling and simulation of calendering roll contact, Fifth Euromech Nonlinear Dynamics Conference, Enoc-2005, August 7-12, 2005, Eindhoven, Netherlands, 2005

Järvenpää V.M., Yuan. L., Numerical Modeling of Paper Machine Roll Contact with Regenerative Out-Of-Roundness Excitation, IUTAM 2006, Multiscale Problems in Multibody System Contacts, February 20 - 23, 2006, Stuttgart, Germany, 2005

Järvenpää V.M., Numerical Modeling of a Roll Mechanism for Multi-Objective Dynamical Analyses, Doctoral thesis, Tampere University of Technology, Publication 569, Tampere, 2005

MODAL MODEL APPROACH TO ELECTROMECHANICAL INTERACTION IN ROTORDYNAMICS OF ELECTRICAL MACHINES

A. Laiho[1], P. Klinge[2]

[1]VTT Industrial Systems
FIN-02044 VTT
Finland
e-mail: antti.laiho@vtt.fi

[2]VTT Industrial Systems
FIN-02044 VTT
Finland
e-mail: paul.klinge@vtt.fi

ABSTRACT

In this work the electromechanical interaction in electrical machines is studied. The eccentric rotor motion distorts the electromagnetical fields in the air-gap between the stator and rotor of the machine inducing a total force, the unbalanced magnetic pull, exerted on the rotor shaft. In order to study the phenomenon a parametric electromagnetic force model is coupled with finite element structural model of the machine. The main objective of the work is to study the effects of the electromechanical interaction on vibration characteristics of electrical machines.

1 INTRODUCTION

The electromagnetic field in the air gap of an electrical machine induces electromagnetic forces between the rotor and stator. An eccentric rotor position produces an unbalanced magnetic pull (UMP) appearing roughly over the shortest air gap. It is well known that one component of this eccentricity force induces additional static load, which influences bearing wear. In addition, the eccentricity force may couple the electromagnetic system with the mechanical one via the flexural vibration modes of the shaft. This interaction decreases the natural frequencies and the critical speeds related to these flexural modes. Moreover, the electromechanical interaction induces additional velocity-dependent forces, which may dampen the flexural rotor vibrations or produce a source for self-excited vibrations. In the worst case, the electromechanical interaction may induce rotordynamic instability leading to catastrophic failure due to stator-rotor contact during operation. Thus, to control the vibrations and rotordynamic behaviour of electrical machines, it is important to predict the effects of electromechanical interaction between the rotor and stator.

Freise & Jordan [1] presented the analytical equations for the UMP induced by the eccentric rotor motion. Further, they presented a simple formula to determine the first flexural critical speed starting from the negative spring coefficient induced by the electro-

magnetic fields. Früchtenicht, Jordan & Seinsch [2] derived the equations for the UMP when the rotor is in circular whirling motion with arbitrary whirling frequency. Using this model they determined the additional stiffness and damping coefficients induced by the electromagnetic field, and developed an electromechanical model to study the effects on the rotordynamic stability. Belmans, Vandenput & Geysen [3] extended the approach to the two-pole flexible-shaft machines including the effect of the unipolar flux.

Arkkio et al. [4] presented a simple parametric model for the electromagnetic force acting between the rotor and stator. They determined the model parameters of a 15 kW four-pole cage induction motor by numerical simulations including the non-linear saturation of magnetic materials. In addition, Arkkio et al. [4] validated the numerical results by extensive measurements. Holopainen et al. [5] derived a new parametric model for the unbalanced magnetic pull induced by an arbitrary rotor motion in transient operation. This new model included additional variables for the essential harmonic currents of the rotor cage. Holopainen et al. [6] derived an electromechanical rotor model by combining this electromagnetic force model with a simple rotor model. In addition, using this model they studied numerically the rotordynamic effects of electromechanical interaction in three induction motors.

The references given above, as well as most of the former studies, assume that the rotor and stator cores are rigid and their axes remain parallel during the eccentric rotor motions. This assumption is restrictive in actual electrical machines. Ha et al. [7], Ha & Hong [8], and Kim et al. [9] applied finite element method (FEM) to analyze the behavior of different electrical machines including the effects of electromechanical interaction.

The main purpose of this study is to derive a model for electromechanical interaction to be used with structural finite element (FE) analyses. This means that the electromechanical interaction model must be applied for general deformations of rotor and stator.

The present study was limited to the electrical machines without parallel paths in the stator windings. These parallel paths are assumed to induce additional electromagnetic forces by enabling circulatory currents in the stator winding resembling the effects of rotor cage currents.

2 METHODS

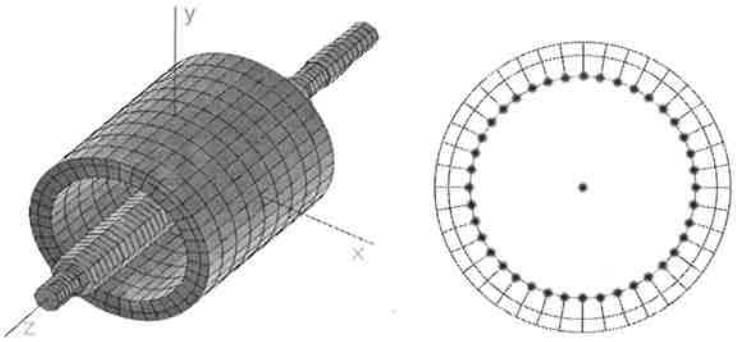
The electromechanical interaction is generated by the deformation of the narrow cylindrical air-gap between the stator and rotor of the machine. The interaction couples the mechanical system to the electromagnetic system.

We start from the electromagnetic force model introduced by Holopainen et. al. [5] in which the model was formulated by using variables deduced from the Fourier analysis of the rotor cage currents. In [6] an electromechanical interaction model was formulated by means of a single complex degree of freedom (DOF) for the stator-rotor displacement with two additional complex variables, referred to as the (rotor) cage current variables, modeling the currents in the rotor cage segments.

In the following analysis, we utilize the sliced structure of the rotor and stator FE models in the direction of the rotor shaft and apply the parametric model on each slice. However, the entire sliced structure involves only two cage current variables. That is, the separate slices in the slice model are coupled by the cage current formulation manifesting the continuity condition of the cage currents.

2.1 ELECTROMAGNETIC FORCE MODEL

Holopainen et al. [5] presented a simple parametric model for the electromagnetic force between the rotor and stator in electrical machine. This parametric model describes the total force in transversal plane. The following main assumptions are used in the derivation of the model: a) the rotor core is rigid cylinder, b) the axes of rotor core and stator bore remain parallel during the eccentric rotor motions, c) there are no parallel paths in the stator winding, and d) the unipolar flux, which may be associated with the eccentricity, particularly in two-pole machines [3], is neglected. In this paper we extend the model to handle general relative motion between the rotor and stator.



(a) Stator core and rotor FE models.

(b) Stator inner core nodes of a slice with rotor node in the middle.

Figure 1: Slicing the FE stator and rotor models. The stator deformation is implemented by averaging the stator inner core nodes by Eq. (1).

Let us align the z -axis along with the rotor shaft. The FE meshes of the stator core and rotor shaft are supposed to have a sliced structure consisting of N_c slices perpendicular to the rotor shaft. On each slice $\ell = 1, \ldots, N_c$ we have a single rotor node with N_ℓ stator inner core nodes $\{n_\sigma^\ell\}$, $\sigma = 1, \ldots, N_\ell$. The reduced transversal displacement degrees of freedom for slice ℓ are given by

$$\begin{aligned} \hat{u}_{x,s}^\ell &= \frac{1}{N_\ell} \sum_{\sigma=1}^{N_\ell} u_x(n_\sigma^\ell) \\ \hat{u}_{y,s}^\ell &= \frac{1}{N_\ell} \sum_{\sigma=1}^{N_\ell} u_y(n_\sigma^\ell) \end{aligned} \tag{1}$$

where $u_x(n_\sigma^\ell)$ and $u_y(n_\sigma^\ell)$ are the x- and y- displacement DOFs of the node n_σ^ℓ, respectively.

In the stator reference frame for the constant flux operation the electromagnetic force [5] exerted on the rotor in slice ℓ is given by

$$F_{em,r}^\ell = \frac{1}{N_c} \left[k_0(p_r^\ell - p_s^\ell) + c_- g_- + c_+ g_+ \right] \tag{2}$$

where $p_s^\ell = \hat{u}_{x,s}^\ell + j\hat{u}_{y,s}^\ell$ and $p_r^\ell = u_{x,r}^\ell + ju_{y,r}^\ell$ are the complex-valued reduced stator and rotor transversal displacements, respectively. Furthermore, in Eq. (2) the complex-valued variables $g_\pm$ are referred to as the cage current variables stemming from the fourier analysis of the rotor cage currents [5]. The subscripts $\pm$ refer to the dominating rotor cage harmonic currents $p \pm 1$ in which p is the number of pole pairs of the machine. The parameters k_0 and $c_\pm$ are given by a separate analysis [5]. The force exerted on the stator is given by $F_{em,s}^\ell = -F_{em,r}^\ell$.

The dynamic equations for the cage current variables $g_\pm$ introduced in Eq. (2) are given by

$$\dot{g}_\pm + a_\pm g_\pm + \frac{b_\pm}{N_c}\sum_{\ell=1}^{N_c}(\dot{p}_r^\ell - \dot{p}_s^\ell) + \frac{k_\pm}{N_c}\sum_{\ell=1}^{N_c}(p_r^\ell - p_s^\ell) = 0 \tag{3}$$

in which we have adopted the notions

$$\begin{aligned} a_\pm &= \tau_\pm^{-1} + j\omega_\pm \\ k_\pm &= jb_\pm\omega_\pm. \end{aligned}$$

Table 1: Electromagnetic force model parameters.

	description
p	number of pole pairs
$\tau_\pm$	cage current $p \pm 1$ time constants
$b_\pm$	cage current $p \pm 1$ eccentricity coefficients
$\omega_\pm$	relative operational angular frequency
ω_m,f_m	rotation frequency
ω_s,f_s	supply frequency
s	slip
k_0	eccentricity force geometric coefficient
$c_\pm$	eccentricity force cage-current coefficient
$R_\pm$	cage-current $p \pm 1$ rotor-cage resistances
$L_\pm$	cage-current $p \pm 1$ rotor-cage inductances

The relevant electromagnetic parameters are listed in Table (1). The time constants $\tau_\pm = L_\pm/R_\pm$ depend on resistances $R_\pm$ and inductances $L_\pm$ of the rotor cage current harmonic component. Furthermore, we have $\omega_\pm = \pm[\omega_s - \omega_m(p \pm 1)]$ where $\omega_s = 2\pi f_s$ and $\omega_m = 2\pi f_m$. The slip s between the fundamental magnetic flux and the rotor rotational speed is given by $(1-s)\omega_s = p\omega_m$.

In order to to couple the electromagnetic force model with the structural FE model of the machine we write Eqs. (2) and (3) in real matrix form as

$$F_{em} = K_0 u + Qg \tag{4}$$

and

$$\dot{g} + K_c u + B\dot{u} + Ag = 0 \tag{5}$$

where the matrices K_0, Q, K_c, B and A contain the electromagnetic parameters listed in Table (1).

2.2 STRUCTURAL ANALYSIS

Finite element (FE) structural analysis is carried out for an electrical motor, giving mechanical vibration characteristics of the machine. The modal analysis is performed by utilizing a commercial mechanical structural analysis program. As a result, the undamped natural modes and eigenfrequencies of the machine are obtained. The gyroscopic effect is taken into account by implementing three rigid disk elements on the rotor. Furthermore, modal damping is involved.

In our study we are interested in UMP induced by the relative motion between the stator and rotor. That is, we restrict to the low-frequency range where the rotor bending modes lie. The undamped normal modes of the machine are given by the equation

$$M\ddot{u} + Ku = 0 \tag{6}$$

with M denoting the mass and K the stiffness matrix of the machine, respectively. Equation (6) is solved for n lowest eigenfrequencies covering the frequency domain up to 2.5 times the highest relevant rotor bending mode [10]. The modal matrix $\Phi = (\phi_1, \ldots, \phi_n)$ is mass-normalized with

$$\begin{aligned} \Phi^T M \Phi &= I \\ \Phi^T K \Phi &= \Lambda \end{aligned} \tag{7}$$

in which I denotes the unit matrix and the diagonal matrix $\Lambda = \Omega_0^2$ is composed of the eigenfrequencies resulting from the structural FE modal analysis.

The gyroscopic effect is taken into account by attaching three rigid disks to the rotor shaft. The complete structural dynamic equations are thus given by

$$(M + M_G)\ddot{u} + (C + C_G)\dot{u} + Ku = F \tag{8}$$

in which the rigid disk gyroscopic matrix C_G and inertia matrix M_G are involved with C denoting the modal damping matrix and F external load on the system.

2.3 ELECTROMECHANICAL INTERACTION MODEL

By combining Eq. (4), Eq. (5) and Eq. (8) we obtain the electromechanical model of the machine given by

$$\begin{aligned} (M + M_G)\ddot{u} + (C + C_G)\dot{u} + (K - K_0)u - Qg &= F \\ \dot{g} + K_c u + B\dot{u} + Ag &= 0 \end{aligned} \tag{9}$$

By utilizing the transformation

$$u = \Phi\eta \tag{10}$$

and using Eq. (7) we write Eq. (9) in the state space form as

$$V\dot{\mu} + W\mu = f \tag{11}$$

in which

$$V = \begin{bmatrix} I + \Phi^T M_G \Phi & 0 & 0 \\ 0 & I & 0 \\ 0 & 0 & I \end{bmatrix}, W = \begin{bmatrix} C + \Phi^T C_G \Phi & \Lambda - \Phi_c^T K_0 \Phi_c & -\Phi_c^T Q \\ -I & 0 & 0 \\ B\Phi_c & K_c \Phi_c & A \end{bmatrix}, f = \begin{pmatrix} \Phi^T F \\ 0 \\ 0 \end{pmatrix} \tag{12}$$

where we have $\mu = (\dot{\eta}, \eta, g)^T$ and $\mathcal{C} = \Phi^T C \Phi$.

Let us consider the response of the electromechanical system given by Eq. (9) to the harmonic unbalanced mass excitation $F = F_0 e^{i\omega t}$. We substitute $f = f_0 e^{i\omega t}$ with $f_0 = (\Phi^T F_0, 0, 0)^T$ to Eq. (11). Response to the harmonic excitation given by $\mu = X(\omega) e^{i\omega t}$ yields $X(\omega) = (i\omega V + W)^{-1} f_0$. The displacements u are then obtained from Eq. (10).

3 RESULTS

In the following we apply the electromechanical interaction model for a 21 MVA generator. The generator was analyzed by using a FE model constructed with IDEAS 10 structural mechanics software. The system matrices given by Eq. (12) were constructed by means of the mechanical modal analysis data, FE model data and the electromagnetic parameters. The size of the system matrices and thus the computational time was dominated by the number of mechanical normal modes (30) included.

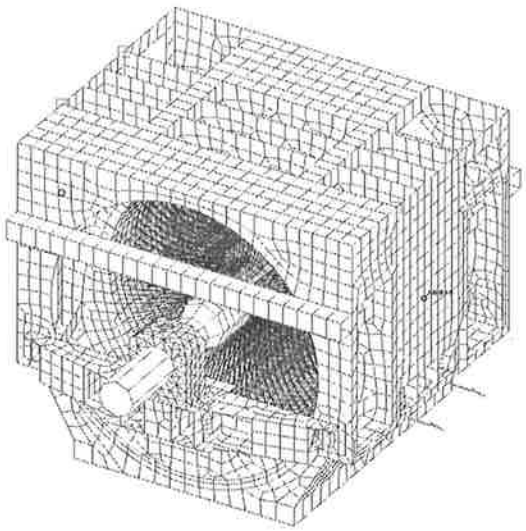


Figure 2: 21 MVA generator FE model.

The generator specifications are given in Table (2). The generator is standing on a flexible test rig.

Table 2: The main parameters of the 21 MVA generator.

parameter	value
rated power	21.3 MW
rated supply frequency	60 Hz
rated rotation speed	514 rpm
number of pole pairs	7
total mass	58000 kg
rotor mass	23600 kg

The FE model mesh of the generator is depicted in Fig. 2. The FE model includes 8905

elements and 9582 nodes with 3-6 DOFs each. The FE calculations show that the machine has two rotor bending modes at 20.8 Hz and 23.2 Hz. The electromechanical coupling was implemented by using 13 slices.

Table 3: Electromagnetic parameters of 21 MVA generator.

parameter	value
k_0	$3.79 \cdot 10^7$ N/m
c_-	10.0 N/A
c_+	20.0 N/A
a_-	$25.1 - i \cdot 55.8$ 1/s
a_+	$97.7 - i \cdot 51.3$ 1/s
b_-	$1.67 \cdot 10^6$ A/m
b_+	$1.16 \cdot 10^5$ A/m
k_-	$-i \cdot 9.32 \cdot 10^7$ A/ms
k_+	$-i \cdot 5.93 \cdot 10^6$ A/ms

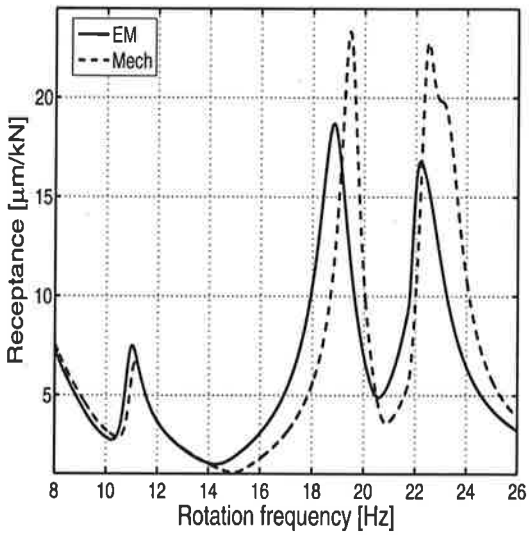


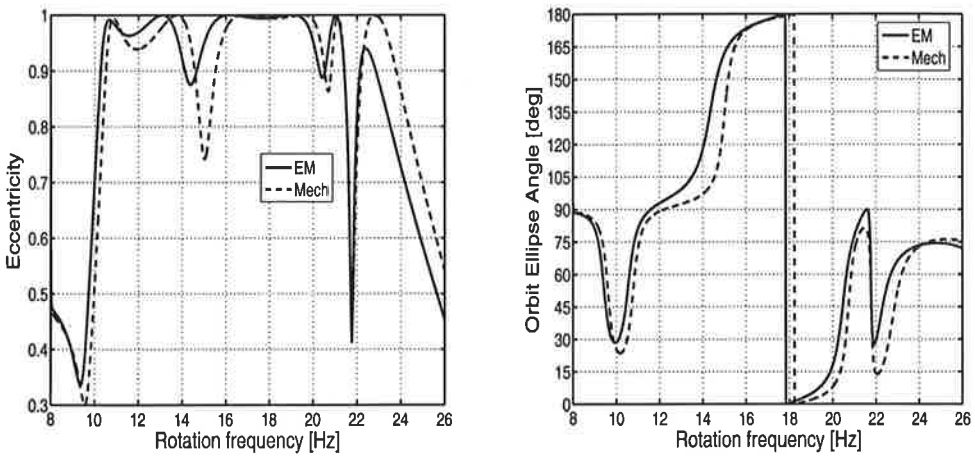
Figure 3: 21 MVA generator unbalanced mass frequency-receptance calculated by employing the electromechanical(EM) and mechanical(Mech) formulation.

Table 4: Receptance peak values (EM)

mode	frequency [Hz]	receptance [μm/kN]
rotor bending 1	18.8	18.7
rotor bending 2	22.1	17.0

Table 5: Receptance peak values (Mech)

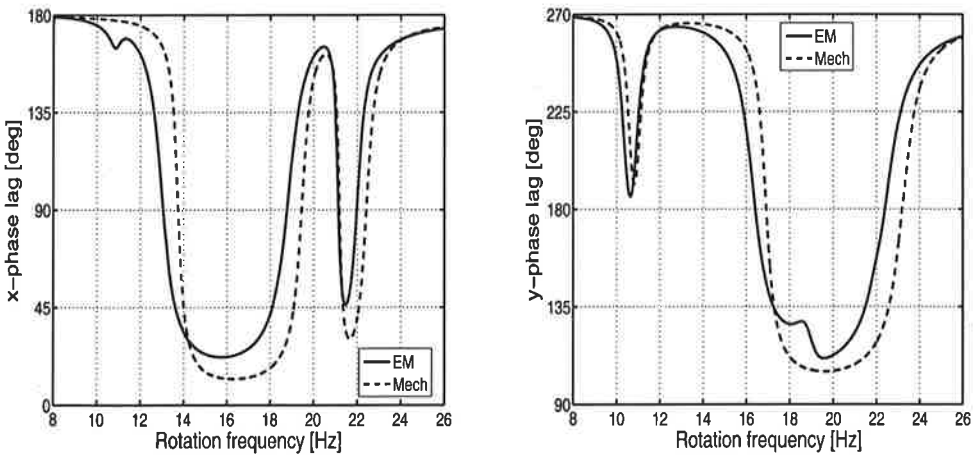
mode	frequency [Hz]	receptance [μm/kN]
rotor bending 1	19.4	23.3
rotor bending 2	22.5	22.8



(a) Eccentricity

(b) Semi-major axis angle

Figure 4: 21 MVA generator rotor center node elliptical orbit data in mechanical (Mech) and electromechanical (EM) system under unbalance mass excitation in rotor center node.



(a) x phase lag

(b) y phase lag

Figure 5: 21 MVA generator rotor center node phase lag between the unbalanced mass and displacement. Electromechanical(EM) and mechanical(Mech) formulations.

4 DISCUSSION AND CONCLUSIONS

A new simple model was presented to model the electromechanical interaction in rotordynamics of electrical machines. The model describes the main interaction forces between the rotor and stator. The interaction force is caused by the relative motion of the rotor and stator together with two harmonic components of the rotor cage currents. These cage-current components are described by two additional variables. A new feature of the presented approach was the method to model the axial variation of the interaction force. In addition, the approach determines the relative motion between the center lines of the rotor and the stator bore.

The interaction model was applied for a synchronous generator. A commercial FE-code was used to model the structural behavior. The modal approach was used to reduce the size of the problem. The method presented here is computationally efficient if a suitable number of mechanical modes covering the rotor bending frequency range are included.

The effect of the electromechanical interaction on the vibration of the generator was studied by comparing the calculated harmonic responses of the electromechanical system to the responses of the mechanical system alone. In Fig. 3 harmonic mass unbalance receptance is plotted against rotation frequency of the rotor. In Table (4) the receptance peak values are listed. The corresponding peak values of the mechanical system are given in Table (5). From the data we see that, due to the electromechanical interaction, the peak frequency of the first rotor bending mode has reduced by 3.2% and the receptance by 20.0%. The corresponding figures for the second rotor bending mode are 1.7% and 25.6%, respectively.

Furthermore, the effect of the electromechanical interaction on the elliptical whirling motion of the rotor can be seen in Fig. 4. In Fig. 5 the phase lag between the unbalance force and the response at the rotor center node is depicted.

In this study, the homopolar flux was ignored in the estimation of electromechanical force parameters. This homopolar flux may have remarkable effects on the vibrations of flexible-shaft two-pole motors [3]. Secondly, the presented model and results are limited to the electrical machines without parallel paths in the stator windings. The model was not validated by experiments. In order to carry out the experiments, the effects of the electromagnetic interaction should be recognized.

5 ACKNOWLEDGEMENTS

The authors are greatly indebted to Mr Pekka Koskinen, VTT Industrial Systems, for background arrangements providing the working conditions.

REFERENCES

[1] Freise, W. und Jordan, H., 1962. "Einseitige magnetische Zugkräfte in Drehstrommaschinen". *ETZ: elektrotechnische Zeitschrift, Ausgabe A.*, **83**, pp. 299-303.

[2] Früchtenicht, J., Jordan, H. und Seinsch, H. O., 1982. "Exzentrizitätsfelder als Ursache von Laufinstabilitäten bei Asynchronmaschinen, Teil 1 & 2". *Archiv fr Electrotechnik*, **65**, pp. 271-292.

[3] Belmans, R., Vandenput, A. and Geysen, W., 1987. "Influence of unbalanced magnetic pull on the radial stability of flexible-shaft induction machines". *IEE Proceedings*, **134**(2B), pp. 101-109.

[4] Arkkio, A., Antila, M., Pokki, K., Simon, A. and Lantto, E., 2000. "Electromagnetic force on a whirling cage rotor". *IEE Proceedings - Electric Power Applications*, **147**, pp. 353-360.

[5] Holopainen, T.P., Tenhunen, A., Lantto, E. and Arkkio, A, 2005. "Unbalanced magnetic pull induced by arbitrary eccentric motion of cage rotor in transient operation, Part 1 & 2". *Electrical Engineering*, **88**(1), pp. 13-34.

[6] Holopainen, T.P., Tenhunen, A. & Arkkio, A, 2005. "Electromechanical interaction in rotordynamics of cage induction motors". *Journal of Sound and Vibration*, **284**(3-5), pp. 733-755.

[7] Ha, K.-H., Hong, J.-P., Kim, G.-T., Chang, K.-C. and Lee, J., 2000. "Orbital analysis of rotor due to electromagnetic force for switched reluctance motor". *IEEE Transactions on Magnetics*, **36**(4), pp. 1407-1411.

[8] Ha, K.-H. and Hong, J.-P., 2001. "Dynamic rotor eccentricity analysis by coupling electromagnetic and structural time stepping FEM". *IEEE Transactions on Magnetics*, **37**(5), pp. 3452-3455.

[9] Kim, T.-J., Hwang, S.-M. and Park, N.-G., 2000. "Analysis of vibration for permanent magnet motors considering mechanical and magnetic coupling effects". *IEEE Transactions on Magnetics*, **36**(4), pp. 1346-1350.

[10] R. R. Craig Jr., R. R.,1987. "A review of time-domain and frequency-domain component mode synthesis method". *International Journal of Analytical and Experimental Modal Analysis*,**2**(2), pp. 59-72.

PUOMIN NOSTOLIIKKEEN MALLINNUKSESTA

H. MARJAMÄKI, J. MÄKINEN
Tampereen teknillinen yliopisto
PL 589, 33101 TAMPERE
s-posti: heikki.marjamaki@tut.fi
s-posti: jari.m.makinen@tut.fi

TIIVISTELMÄ

Koneenrakennuksessa käytetään runsaasti nostopuomeja, joiden nostoliike saadaan aikaan hydraulisylinterillä. Tässä työssä esitetään kolme vaihtoehtoista mallinnustapaa liikkeen aikaansaamiseksi. Mallinnustavat perustuvat epälineaarisen elementtimentelmän käyttöön. Ensimmäisessä tavassa puomin liike otetaan huomioon holonomista rajoiteyhtälöä käyttäen. Rajoiteyhtälössä on annettu hydraulisylinterin kiinnityssilmukoiden etäisyys ajan funktiona. Toisessa tavassa hydraulisylinterin liike on mallinnettu käyttäen pituuttaan muuttavaa sauvaelementtiä. Kolmannessa tavassa puomin liike aikaansaadaan mallintamalla hydraulisylinterin liike ensimmäisen kertaluvun differentiaaliyhtälönä, jolloin tilamuuttujina on mekaanisen järjestelmän siirtymien lisäksi hydraulisylinterin kammiopaineet. Syntyvä kytketty hydromekaaninen tehtävä ratkaistaan yhtenäisenä eli monoliittisena järjestelmänä, jolloin on otettu huomioon mekaanisen ja hydraulisen järjestelmän vuorovaikutukset.

Laskentamallin dynaaminen vaste lasketaan Newmarkin aikaintegrointina iteroimalla laskentamalli tasapainoon kullakin aika-askeleella ottaen huomioon kunkin edellä esitetyn mallinnustavan eroavaisuudet.

JOHDANTO

Koneenrakennuksessa käytetään runsaasti nostopuomeja, joiden nostoliike aikaansaadaan hydraulisylinterillä. Hydraulisylinterin liikkeen mallinnus käyttäen elementtimentelmää voidaan tehdä usealla eri tavalla [1,2]. Tässä työssä esitetään kolme vaihtoehtoista tapaa liikkeen aikaansaamiseksi. Mallinnustavat perustuvat epälineaarisen elementtimentelmän käyttöön, missä siirtymäsuureet on mitattu kiinteään koordinaatistoon nähden [3].

Ensimmäisessä tavassa puomin liike otetaan huomioon holonomista rajoiteyhtälöä käyttäen. Rajoiteyhtälössä on annettu hydraulisylinterin kiinnityssilmukoiden etäisyys ajan funktiona. Tällöin mallin ratkaisemissa on käytetty Lagrangen funktiota, jossa on energiayhtälöiden lisäksi rajoiteyhtälöstä aiheutuva termi ja lisätuntemattomana on Lagrangen kerroin.

Toisessa tavassa hydraulisylinterin liike on mallinnettu käyttäen pituuttaan muuttavaa sauvaelementtiä. Laskennan aikana sauvaelementin jännityksetön pituus L_c muuttuu vastaten sylinterin kiinnityssilmokoiden etäisyyttä. Koska laskentamallista syntyvä differentiaaliyhtälöryhmä ratkaistaan ilman algebrallisia sidosehtoja, niin ratkaisualgoritmista on saatu verrattain nopea. Lisäksi hydraulisylintereiden vaikutukset kokonaisjoustoon saadaan mallinnettua suoraan.

Kolmannessa tavassa puomin liike aikaansaadaan mallintamalla hydraulisylinteri ensimmäisen kertaluvun differentiaaliyhtälönä, jolloin tilamuuttujina on sylinterin kammiopaineet. Syntyvä kytketty hydromekaaninen tehtävä ratkaistaan yhtenäisenä eli monoliittisena järjestelmänä, jolloin on otettu huomioon mekaanisen ja hydraulisen järjestelmän vuorovaikutukset.

Laskentamallin dynaaminen vaste lasketaan Newmarkin aikaintegrointina iteroimalla laskentamalli tasapainoon kullakin aika-askeleella ottaen huomioon kunkin edellä esitetyn mallinnustavan eroavaisuudet.

LIIKEYHTÄLÖT

Mekaaninen järjestelmä ilman sidosehtoja

Mekaanisen järjestelmän, jossa vaikuttaa vain konservatiivisia voimia, Hamiltonin periaate voidaan kirjoittaa

$$\int_{t_1}^{t_2} \delta \mathcal{L}(\boldsymbol{q},\dot{\boldsymbol{q}})\,dt = \int_{t_1}^{t_2} [\delta \mathcal{T} - \delta \mathcal{V}]\,dt = 0 \tag{1}$$

missä $\mathcal{T}$ on systeemin liike-energia, $\mathcal{V}$ potentiaalienergia, joka koostuu ulkoisen voiman potentiaalista sekä kimmoenergiasta ja $\boldsymbol{q}$ on systeemin yleistetty asemavektori, saadaan mekaanisen järjestelmän liikeyhtälö muotoon

$$\boldsymbol{M}\ddot{\boldsymbol{q}} = \boldsymbol{g}(\boldsymbol{q},\dot{\boldsymbol{q}},t) \tag{2}$$

Missä $\boldsymbol{M}$ on massamatriisi

$$\boldsymbol{M} = \frac{\partial^2 \mathcal{T}}{\partial \dot{\boldsymbol{q}} \partial \dot{\boldsymbol{q}}} \tag{3}$$

Linearisoimalla liikeyhtälö saadaan

$$\boldsymbol{M}\Delta\ddot{\boldsymbol{q}} + \boldsymbol{C}_t \Delta\dot{\boldsymbol{q}} + \boldsymbol{K}_t \Delta\boldsymbol{q} = \boldsymbol{r}^* \tag{4}$$

missä $\boldsymbol{C}_t$ on tangentiaalinen vaimennusmatriisi

$$\boldsymbol{C}_t = -\frac{\partial \boldsymbol{g}}{\partial \dot{\boldsymbol{q}}} \tag{5}$$

ja $\boldsymbol{K}_t$ on tangentiaalinen jäykkyysmatriisi

$$\boldsymbol{K}_t = -\frac{\partial \boldsymbol{g}}{\partial \boldsymbol{q}} + \frac{\partial(\boldsymbol{M}\ddot{\boldsymbol{q}})}{\partial \boldsymbol{q}} \tag{6}$$

ja residuaalivektori

$$\boldsymbol{r}^* := \boldsymbol{g}(\boldsymbol{q},\dot{\boldsymbol{q}},t) - \boldsymbol{M}\ddot{\boldsymbol{q}} \tag{7}$$

Mekaaninen järjestelmä jossa on holonomisia sidosehtoja

Tarkastellaan taas konservatiivista mekaanista järjestelmää, jossa on holonomisia rajoitteita. Tällöin voidaan käyttää laajennettya Hamiltonin periaatetta

$$\int_{t_1}^{t_2} \delta\left[\mathcal{L}(\boldsymbol{q},\dot{\boldsymbol{q}}) - \boldsymbol{\lambda}^{\mathrm{T}}\boldsymbol{\Phi}(\boldsymbol{q},t)\right] dt = 0 \tag{8}$$

ja mekaanisen järjestelmän liikeyhtälö saadaan nyt muotoon

$$\boldsymbol{M}\ddot{\boldsymbol{q}} + \boldsymbol{B}^{\mathrm{T}}\boldsymbol{\lambda} = \boldsymbol{g}(\boldsymbol{q},\dot{\boldsymbol{q}},t) \tag{9}$$

missä holonomisten rajoite-ehtojen gradientti

$$\boldsymbol{B} = \frac{\partial \boldsymbol{\Phi}}{\partial \boldsymbol{q}} \tag{10}$$

Linearisoimalla liikeyhtälö saadaan

$$\begin{bmatrix} \boldsymbol{M} & \boldsymbol{0} \\ \boldsymbol{0} & \boldsymbol{0} \end{bmatrix}\begin{bmatrix} \Delta\ddot{\boldsymbol{q}} \\ \Delta\ddot{\lambda} \end{bmatrix} + \begin{bmatrix} \boldsymbol{C}_t & \boldsymbol{0} \\ \boldsymbol{0} & \boldsymbol{0} \end{bmatrix}\begin{bmatrix} \Delta\dot{\boldsymbol{q}} \\ \Delta\dot{\lambda} \end{bmatrix} + \begin{bmatrix} \boldsymbol{K}_t & \boldsymbol{B}^{\mathrm{T}} \\ \boldsymbol{B} & \boldsymbol{0} \end{bmatrix}\begin{bmatrix} \Delta\boldsymbol{q} \\ \Delta\lambda \end{bmatrix} = \begin{bmatrix} \boldsymbol{r}^* \\ -\boldsymbol{\Phi}^* \end{bmatrix} \tag{11}$$

missä $\boldsymbol{C}_t$ on tangentiaalinen vaimennusmatriisi

$$\boldsymbol{C}_t = -\frac{\partial \boldsymbol{g}}{\partial \dot{\boldsymbol{q}}} + \frac{\partial\left(\boldsymbol{B}^{\mathrm{T}}\boldsymbol{\lambda}\right)}{\partial \dot{\boldsymbol{q}}} \tag{12}$$

ja $\boldsymbol{K}_t$ on tangentiaalinen jäykkyysmatriisi

$$\boldsymbol{K}_t = -\frac{\partial \boldsymbol{g}}{\partial \boldsymbol{q}} + \frac{\partial\left(\boldsymbol{M}\ddot{\boldsymbol{q}}\right)}{\partial \boldsymbol{q}} + \frac{\partial\left(\boldsymbol{B}^{\mathrm{T}}\boldsymbol{\lambda}\right)}{\partial \boldsymbol{q}} \tag{13}$$

ja residuaalivektori

$$\boldsymbol{r}^* := \boldsymbol{g}(\boldsymbol{q},\dot{\boldsymbol{q}},t) - \boldsymbol{M}\ddot{\boldsymbol{q}} - \boldsymbol{B}^{\mathrm{T}}\boldsymbol{\lambda} \tag{14}$$

Kytketty hydro-mekaaninen järjestelmä

Lisätään mekaanisen järjestelmän liikeyhtälöön hydraulisylintereiden osuudet, jolloin saadaan

$$\begin{cases} \boldsymbol{M}\ddot{\boldsymbol{q}} = \boldsymbol{g}\left(\boldsymbol{q},\dot{\boldsymbol{q}},\boldsymbol{x}_{cyl},\dot{\boldsymbol{x}}_{cyl},t\right) \\ \dot{\boldsymbol{x}}_{cyl} = \boldsymbol{f}_{cyl}\left(\boldsymbol{x}_{cyl},\boldsymbol{q},\dot{\boldsymbol{q}}\right) \end{cases} \tag{15}$$

Linearisoimalla kytketty liikeyhtälö saadaan

$$\begin{bmatrix} \boldsymbol{M} & \boldsymbol{0} \\ \boldsymbol{0} & \boldsymbol{0} \end{bmatrix}\begin{bmatrix} \Delta\ddot{\boldsymbol{q}} \\ \Delta\ddot{\boldsymbol{x}}_{cyl} \end{bmatrix} + \begin{bmatrix} \boldsymbol{C}_t & -\dfrac{\partial \boldsymbol{g}}{\partial \dot{\boldsymbol{x}}_{cyl}} \\ \dfrac{\partial \boldsymbol{f}_{cyl}}{\partial \dot{\boldsymbol{q}}} & -\boldsymbol{I} \end{bmatrix}\begin{bmatrix} \Delta\dot{\boldsymbol{q}} \\ \Delta\dot{\boldsymbol{x}}_{cyl} \end{bmatrix} + \begin{bmatrix} \boldsymbol{K}_t & -\dfrac{\partial \boldsymbol{g}}{\partial \boldsymbol{x}_{cyl}} \\ \dfrac{\partial \boldsymbol{f}_{cyl}}{\partial \boldsymbol{q}} & \dfrac{\partial \boldsymbol{f}_{cyl}}{\partial \boldsymbol{x}_{cyl}} \end{bmatrix}\begin{bmatrix} \Delta\boldsymbol{q} \\ \Delta\boldsymbol{x}_{cyl} \end{bmatrix} = \begin{bmatrix} \boldsymbol{r}^* \\ \boldsymbol{s}^* \end{bmatrix} \tag{16}$$

missä residuaalivektorit

$$r^* := g\left(q, \dot{q}, x_{cyl}, \dot{x}_{cyl}, t\right) - M\ddot{q}$$
$$s^* := f_{cyl}\left(x_{cyl}, q, \dot{q}\right) - \dot{x}_{cyl} \tag{17}$$

RAKENNEOSIEN MALLINNUS

Nostopuomi on mallinnettu Reissnerin kinemaattiseen malliin perustuvilla palkkielementeillä [1] ja [3].

Sylinterin mallinnus holonomisella rajoiteyhtälöllä

Rajoiteyhtälö saadaan asettamalla kuvan 3 mukaisen sylinterin kiinnityssilmukoiden B ja D välinen etäisyys

$$\Phi(q) = \left(x_B - x_D\right)^{\mathrm{T}}\left(x_B - x_D\right) - l_{BD}(t) = 0 \tag{18}$$

missä t on laskenta-aika ja jäykäksi oletetun sylinterin pituus

$$l_{BD}(t) = \frac{\sqrt{5}}{2} + \left(\sqrt{\frac{5}{4} + \cos\left(\frac{5\pi}{6}\right)} - \frac{\sqrt{5}}{2}\right)\frac{t}{5} \tag{19}$$

Koska piste D oletetaan kiinteäksi, niin

$$\delta\Phi = 2\left(x_B - x_D\right)^{\mathrm{T}}\delta x_B = 2\left(x_B - x_D\right)^{\mathrm{T}} D\,\delta q = B\,\delta q \tag{20}$$

missä tasotapauksessa kytkentämatriisi

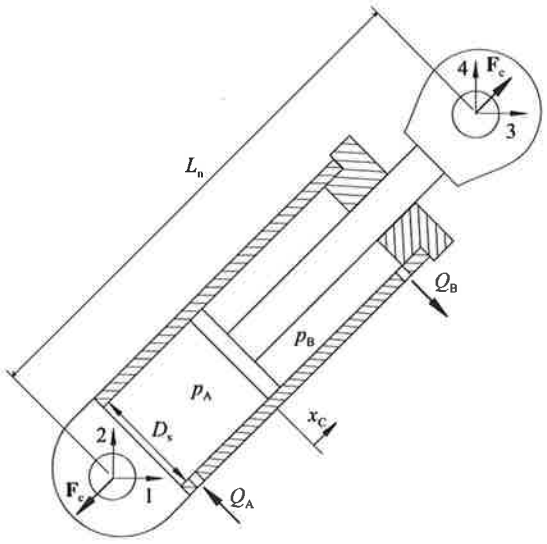
$$D = \begin{bmatrix} 0 & 1 & 0 & 0 & \dots & 0 \\ 0 & 0 & 1 & 0 & \dots & 0 \end{bmatrix}_{2*16} \tag{21}$$

Sylinterin mallinnus pituuttaan muuttavalla sauvalla

Tässä tapauksessa sylinterin liike mallinnetaan käyttäen massattomaksi oletettua pituuttaan muuttavaa sauvaelementtiä [1]. Laskennan aikana sauvaelementin jännityksetön pituus L_c muuttuu vastaten sylinterin kiinnityssilmukoiden etäisyyttä. Laskennassa sauvan jäykkyys on valittu siten, että se vastaa hydraulisylinterin nestepatsaiden jäykkyyttä alkutilassa.

Sylinterin mallinnus hydraulisylinterielementillä

Kuvassa 1 on esitetty kaksitoiminen hydraulisylinteri. Mitat, kuten siirtymät (1,2,3,4), jotka kytkevät sylinterin ja mekaanisen järjestelmän toisiinsa on esitetty kuvassa.



Kuva 1. Hydraulisylinteri ja sen laskennassa tarvittavia suureita

Sylinterin kiinnityssilmukoihin vaikuttava voimaresultantti saadaan

$$F_c = A_A p_A - A_B p_B \tag{22}$$

kammiopaineiden lausekkeet ovat

$$\begin{aligned} \dot{p}_A &= \frac{Q_A - \dot{x}_c A_A}{V_A + x_c A_A} B \\ \dot{p}_B &= \frac{-Q_B + \dot{x}_c A_B}{V_B - x_c A_B} B \end{aligned} \tag{23}$$

tai kompaktimmassa muodossa

$$\dot{\boldsymbol{x}}_{cyl} = \boldsymbol{f}_{cyl}(\boldsymbol{q}, \dot{\boldsymbol{q}}) \tag{24}$$

missä $x_c = L_n - L_0$, L_n on sylinterin pituus siirtyneessä tilassa, L_0 on sylinterin pituus alkutilassa, Q_A ja Q_B ovat sylinterin kammioihin tuleva ja lähtevä tilavuusvirta, V_A ja V_B ovat sylinterin kammioiden alkutilavuudet ja B on paineväliaineen kokoonpuristuvuus. Sylinterivoiman variaatio on

$$\delta F_c = A_A \delta p_A - A_B \delta p_B = \begin{bmatrix} A_A & -A_B \end{bmatrix} \delta \boldsymbol{x}_{cyl} = \boldsymbol{A}_A \delta \boldsymbol{x}_{cyl} \tag{25}$$

Sylinterivoimasta johtuva solmuvoimavektori saadaan

$$\boldsymbol{F}_{\text{int}} = F_c \begin{bmatrix} \boldsymbol{n}_c \\ -\boldsymbol{n}_c \end{bmatrix} = \frac{F_c}{L_n} \begin{bmatrix} \boldsymbol{C}\boldsymbol{x} \\ -\boldsymbol{C}\boldsymbol{x} \end{bmatrix} = -\frac{F_c}{L_n} \boldsymbol{A}\boldsymbol{x} \tag{26}$$

missä vektori $\boldsymbol{x} = (x_1, y_1, x_2, y_2)^{\mathrm{T}}$ sisältää sylinterin kiinnityspisteiden koordinaatit. Sylinterin suuntainen ykkösvektori

$$\boldsymbol{n}_c = \frac{\boldsymbol{x}_B - \boldsymbol{x}_D}{\|\boldsymbol{x}_B - \boldsymbol{x}_D\|} = \frac{\boldsymbol{x}_B - \boldsymbol{x}_D}{L_n} \tag{27}$$

Sylinterin kiinnityssilmukoiden välinen vektori saadaan

$$\boldsymbol{x}_B - \boldsymbol{x}_A = \begin{bmatrix} -1 & 0 & 1 & 0 \\ 0 & -1 & 0 & 1 \end{bmatrix} \boldsymbol{x} = \boldsymbol{C}\boldsymbol{x} \tag{28}$$

ja sylinterin pituus

$$L_n = \sqrt{(\boldsymbol{C}\boldsymbol{x})^{\mathrm{T}}\, \boldsymbol{C}\,\boldsymbol{x}} = \sqrt{\boldsymbol{x}^{\mathrm{T}}\boldsymbol{C}^{\mathrm{T}}\boldsymbol{C}\,\boldsymbol{x}} = \sqrt{\boldsymbol{x}^{\mathrm{T}}\boldsymbol{A}\,\boldsymbol{x}} \tag{29}$$

Sylinterin jäykkyysmatriisin lauseke saadaan varioimalla sylinterivoimasta johtuvan solmuvoimavektorin lauseketta

$$\delta \boldsymbol{F}_{\text{int}} = -\frac{1}{L_n}\boldsymbol{A}\boldsymbol{x}\,\boldsymbol{A}_A \delta \boldsymbol{x}_{cyl} - F_c \delta\left(\frac{1}{L_n}\right)\boldsymbol{A}\boldsymbol{x} - \frac{F_c}{L_n}\boldsymbol{A}\delta\boldsymbol{x} \tag{30}$$

koska

$$x_c = L_n - L_0 \qquad \Rightarrow \delta x_c = \delta L_n = \delta\sqrt{\mathbf{x}^{\mathrm{T}}\mathbf{A}\,\mathbf{x}} = \frac{1}{L_n}\mathbf{x}^{\mathrm{T}}\mathbf{A}\,\delta\mathbf{x} \tag{31}$$

Sylinterin pituuden käänteisarvon variaatio saadaan

$$\delta\left(\frac{1}{L_n}\right) = \left(\frac{-\delta L_n}{L_n^2}\right) = -\frac{1}{L_n^3}\boldsymbol{x}^{\mathrm{T}}\boldsymbol{A}\,\delta\boldsymbol{x} \tag{32}$$

ja jäykkyysmatriisi voidaan nyt koota

$$\delta \boldsymbol{F}_{\text{int}} = -\frac{1}{L_n}\boldsymbol{A}\boldsymbol{x}\,\boldsymbol{A}_A \delta \boldsymbol{x}_{cyl} + \frac{F_c}{L_n^3}\boldsymbol{A}\,\boldsymbol{x}\boldsymbol{x}^{\mathrm{T}}\boldsymbol{A}\,\delta\boldsymbol{x} - \frac{F_c}{L_n}\boldsymbol{A}\delta\boldsymbol{x} = \boldsymbol{k}_C \cdot \delta\boldsymbol{x}_{cyl} + \boldsymbol{k}_T \cdot \delta\boldsymbol{x} \tag{33}$$

AIKAINTEGROINTI

Nostoliikkeen eri mallinnustavat edellyttävät hieman erilaisia aikaintegrointi-implementaatioita. Tässä esityksessä on valittu aikaintegrointimentelmäksi implisiittinen Newmarkin aikaintegrointi [2], koska näin voidaan tilamuuttujat ja rajoiteyhtälö iteroida halutulla tarkkuudella ja integrointimenetelmä on hyvin tunnettu.

Seuraavaksi esitetään edellä mainittu aikaintegrointimentelmä sovitettuna eri nostoliikkeen mallinnustapoihin.

Mekaaninen järjestelmä ilman sidosehtoja

Valitaan kunkin aika-askeleen iteroinnin alkuarvaukseksi

$$\begin{aligned} \ddot{\boldsymbol{q}}_{n+1}^0 &= \boldsymbol{0} \\ \dot{\boldsymbol{q}}_{n+1}^0 &= \dot{\boldsymbol{q}}_n + (1-\gamma)h\ddot{\boldsymbol{q}}_n \\ \boldsymbol{q}_{n+1}^0 &= \boldsymbol{q}_n + h\dot{\boldsymbol{q}}_n + \left(\frac{1}{2} - \beta\right)h^2\ddot{\boldsymbol{q}}_n \end{aligned} \tag{34}$$

Korjataan alkuarvausta kullakin iterointikierroksella

$$\begin{aligned}\ddot{\boldsymbol{q}}_{n+1}^{k+1} &= \ddot{\boldsymbol{q}}_{n+1}^{k} + \frac{1}{\beta h^2}\Delta \boldsymbol{q} \\ \dot{\boldsymbol{q}}_{n+1}^{k+1} &= \dot{\boldsymbol{q}}_{n+1}^{k} + \frac{\gamma}{\beta h} + \Delta \boldsymbol{q} \\ \boldsymbol{q}_{n+1}^{k+1} &= \boldsymbol{q}_{n+1}^{k} + \Delta \boldsymbol{q}\end{aligned} \tag{35}$$

missä siirtymämuutos ratkaistaan

$$\begin{aligned}\boldsymbol{S}_T &= \boldsymbol{K}_T + \frac{\gamma}{\beta h}\boldsymbol{C}_T + \frac{1}{\beta h^2}\boldsymbol{M} \\ \boldsymbol{S}_T \Delta \boldsymbol{q} &= \boldsymbol{r}^*\end{aligned} \tag{36}$$

Aikaintegrointi etenee kuvan 2 vasemmanpuoleisen kaavion mukaisesti.

Mekaaninen järjestelmä jossa on holonomisia sidosehtoja

Kun laskentamalliin liittyy holonomisia sidosehtoja ja ne otetaan huomioon Lagrangen funktiota käyttäen tulee yhtälöryhmään lisätuntemattomana Lagrangen kertoimien vektori. Valitaan kunkin aika-askeleen iteroinnin alkuarvaukseksi

$$\begin{aligned}\ddot{\boldsymbol{q}}_{n+1}^{0} &= \boldsymbol{0} \\ \dot{\boldsymbol{q}}_{n+1}^{0} &= \dot{\boldsymbol{q}}_{n} + (1-\gamma)h\ddot{\boldsymbol{q}}_{n} \\ \boldsymbol{q}_{n+1}^{0} &= \boldsymbol{q}_{n} + h\dot{\boldsymbol{q}}_{n} + \left(\frac{1}{2} - \beta\right)h^2\ddot{\boldsymbol{q}}_{n} \\ \boldsymbol{\lambda}_{n+1}^{0} &= \boldsymbol{\lambda}_{n}\end{aligned} \tag{37}$$

Korjataan alkuarvausta kullakin iterointikierroksella

$$\begin{aligned}\ddot{\boldsymbol{q}}_{n+1}^{k+1} &= \ddot{\boldsymbol{q}}_{n+1}^{k} + \frac{1}{\beta h^2}\Delta \boldsymbol{q} \\ \dot{\boldsymbol{q}}_{n+1}^{k+1} &= \dot{\boldsymbol{q}}_{n+1}^{k} + \frac{\gamma}{\beta h}\Delta \boldsymbol{q} \\ \boldsymbol{q}_{n+1}^{k+1} &= \boldsymbol{q}_{n+1}^{k} + \Delta \boldsymbol{q} \\ \boldsymbol{\lambda}_{n+1}^{k+1} &= \boldsymbol{\lambda}_{n+1}^{k} + \Delta \boldsymbol{\lambda}\end{aligned} \tag{38}$$

missä siirtymän ja Lagrangen kerroinvektorin muutos ratkaistaan

$$\begin{aligned}\boldsymbol{S}_T &= \boldsymbol{K}_T + \frac{\gamma}{\beta h}\boldsymbol{C}_T + \frac{1}{\beta h^2}\boldsymbol{M} \\ \begin{bmatrix} \boldsymbol{S}_T & \boldsymbol{B}^{\mathrm{T}} \\ \boldsymbol{B} & \boldsymbol{0} \end{bmatrix} &\begin{bmatrix} \Delta \boldsymbol{q} \\ \Delta \boldsymbol{\lambda} \end{bmatrix} = \begin{bmatrix} \boldsymbol{r}^* \\ -\boldsymbol{\Phi}^* \end{bmatrix}\end{aligned} \tag{39}$$

Nyt aikaintegrointi etenee kuvan 2 keskimmäisen kaavion mukaisesti.

Kytketty hydro-mekaaninen järjestelmä

Hydro-mekaanisessa laskentamallissa on mekaanisen järjestelmän siirtymämuuttujien lisäksi on hydraulisylinterielementtien hydrauliset muuttujat eli tässä tapauksessa kammiopaineet. Valitaan taas kunkin aika-askeleen iteroinnin alkuarvaukseksi

$$
\begin{aligned}
\ddot{\boldsymbol{q}}_{n+1}^{0} &= \boldsymbol{0} \\
\dot{\boldsymbol{q}}_{n+1}^{0} &= \dot{\boldsymbol{q}}_{n} + (1-\gamma) h \ddot{\boldsymbol{q}}_{n} \\
\boldsymbol{q}_{n+1}^{0} &= \boldsymbol{q}_{n} + h \dot{\boldsymbol{q}}_{n} + \left(\frac{1}{2} - \beta\right) h^{2} \ddot{\boldsymbol{q}}_{n} \\
\left(\dot{\boldsymbol{x}}_{cyl}\right)_{n+1}^{0} &= \left(\dot{\boldsymbol{x}}_{cyl}\right)_{n} \\
\left(\boldsymbol{x}_{cyl}\right)_{n+1}^{0} &= \left(\boldsymbol{x}_{cyl}\right)_{n} + h\left(\dot{\boldsymbol{x}}_{cyl}\right)_{n}
\end{aligned}
\tag{40}
$$

Korjataan alkuarvausta kullakin iterointikierroksella

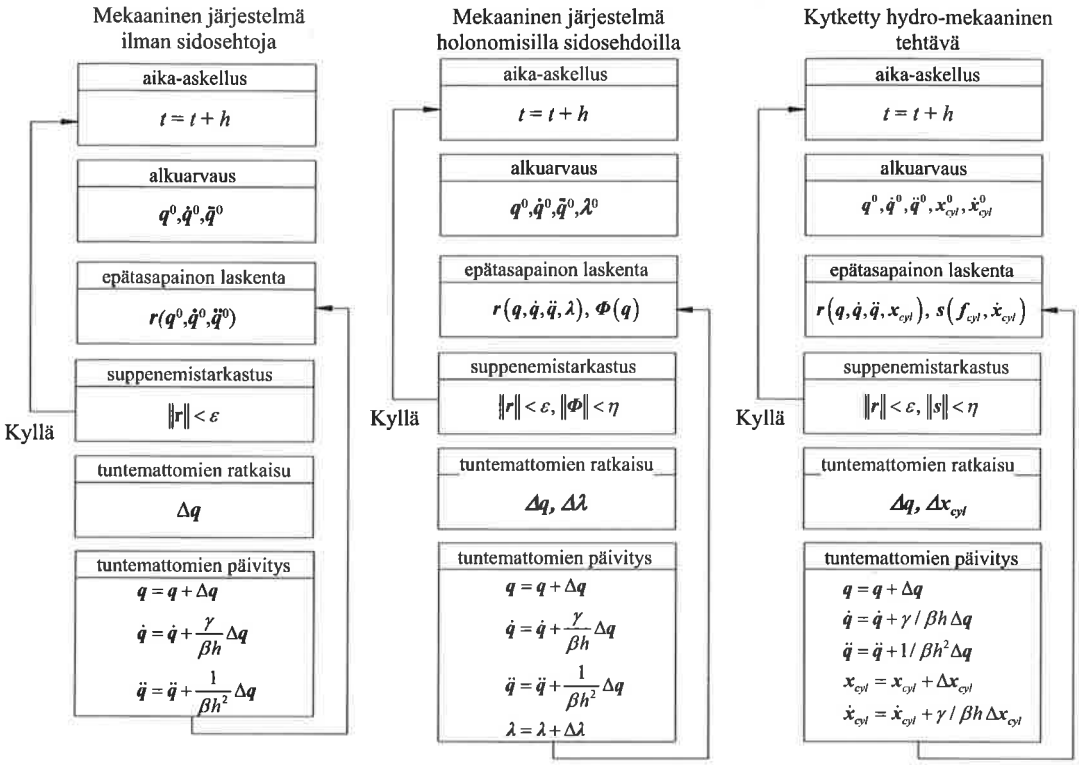
$$
\begin{aligned}
\ddot{\boldsymbol{q}}_{n+1}^{k+1} &= \ddot{\boldsymbol{q}}_{n+1}^{k} + \frac{1}{\beta h^{2}} \Delta \boldsymbol{q} \\
\dot{\boldsymbol{q}}_{n+1}^{k+1} &= \dot{\boldsymbol{q}}_{n+1}^{k} + \frac{\gamma}{\beta h} \Delta \boldsymbol{q} \\
\boldsymbol{q}_{n+1}^{k+1} &= \boldsymbol{q}_{n+1}^{k} + \Delta \boldsymbol{q} \\
\left(\dot{\boldsymbol{x}}_{cyl}\right)_{n+1}^{k+1} &= \left(\dot{\boldsymbol{x}}_{cyl}\right)_{n+1}^{k} + \frac{\gamma}{\beta h} \Delta \boldsymbol{x}_{cyl} \\
\left(\boldsymbol{x}_{cyl}\right)_{n+1}^{k+1} &= \left(\boldsymbol{x}_{cyl}\right)_{n+1}^{k} + \Delta \boldsymbol{x}_{cyl}
\end{aligned}
\tag{41}
$$

Hydraulisten muuttujien ja siirtymämuuttujien muutos ratkaistaan

$$
\begin{aligned}
\boldsymbol{S}_{T} &= \boldsymbol{K}_{T} + \frac{\gamma}{\beta h} \boldsymbol{C}_{T} + \frac{1}{\beta h^{2}} \boldsymbol{M} \\
\boldsymbol{U}_{T} &= \frac{\partial \boldsymbol{g}}{\partial \boldsymbol{x}_{cyl}} + \frac{\gamma}{\beta h} \frac{\partial \boldsymbol{g}}{\partial \dot{\boldsymbol{x}}_{cyl}} \\
\boldsymbol{L}_{T} &= \frac{\partial \boldsymbol{f}_{cyl}}{\partial \boldsymbol{q}} + \frac{\gamma}{\beta h} \frac{\partial \boldsymbol{f}_{cyl}}{\partial \dot{\boldsymbol{q}}} \\
\boldsymbol{H}_{T} &= \frac{\partial \boldsymbol{f}_{cyl}}{\partial \boldsymbol{x}_{cyl}} - \frac{\gamma}{\beta h} \boldsymbol{I} \\
\begin{bmatrix} \boldsymbol{S}_{T} & \boldsymbol{U}_{T} \\ \boldsymbol{L}_{T} & \boldsymbol{H}_{T} \end{bmatrix} \begin{bmatrix} \Delta \boldsymbol{q} \\ \Delta \boldsymbol{x}_{cyl} \end{bmatrix} &= \begin{bmatrix} \boldsymbol{r}^{*} \\ \boldsymbol{s}^{*} \end{bmatrix}
\end{aligned}
\tag{42}
$$

Nyt aikaintegrointi etenee kuvan 2 oikeanpuoleisen kaavion mukaisesti.

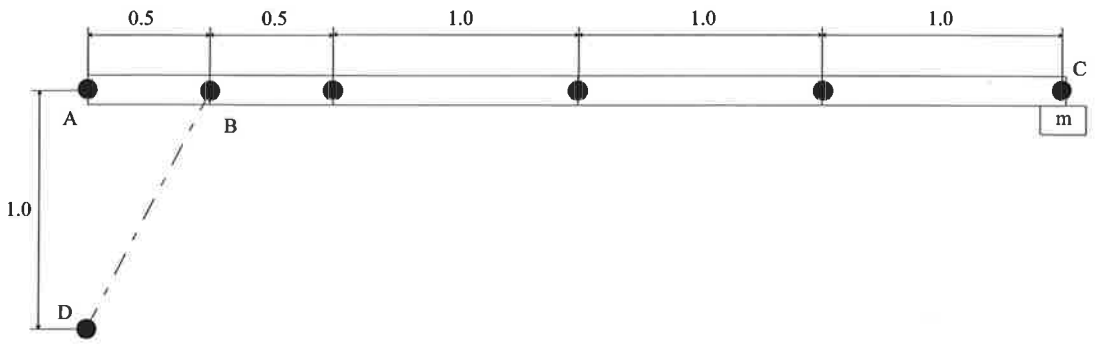
Kuvassa 2 on esitetty Newmarkin aikaintegrointi kaaviomaisesti eri nostoliikkeen mallinnustavoilla.



Kuva 2. Newmarkin aikaintegroinnin periaate eri mallinnustavoilla

LASKENTAMALLI

Tarkastellaan kuvan 3 mukaista puomia, jossa päämitat on esitetty metreinä. Puomin nostoliike tapahtuu pisteiden D ja B välissä olevan hydraulisylinterin avulla.



Kuva 3. Laskentamallin peraatekuva

Nostoliike on sovitettu siten, että puomi nousee 5 sekunnin aikana 60 asteen kulmaan, missä kulma on suoran AB ja vaakatason välillä. Puomin yleistetty asemavektori tasotapauksessa on

$$q = (\varphi_A, x_B, y_B, \varphi_B, x_3, y_3, \varphi_3, x_4, y_4, \varphi_4, x_5, y_5, \varphi_5, x_6, y_6, \varphi_6)^T \tag{43}$$

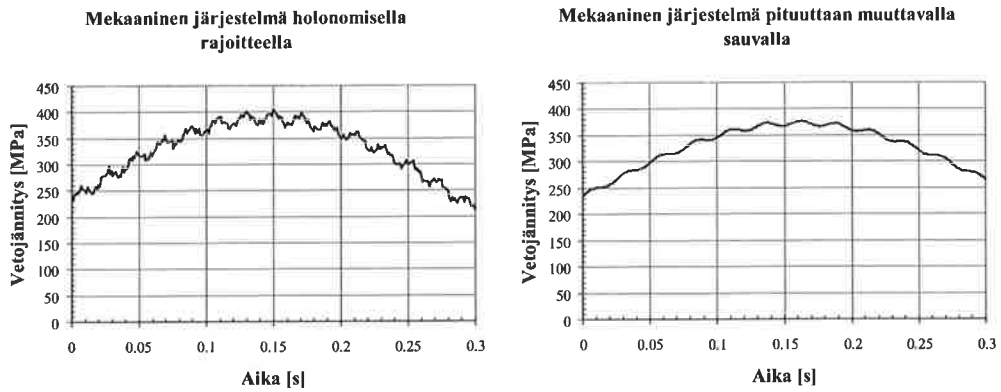
Nostopuomi A-C on mallinnettu käyttäen suorakaidepoikkileikkausta, jonka mitat ja muut lähtöarvot ovat taulukossa.

Taulukko 1. Laskentamallin lähtöarvot

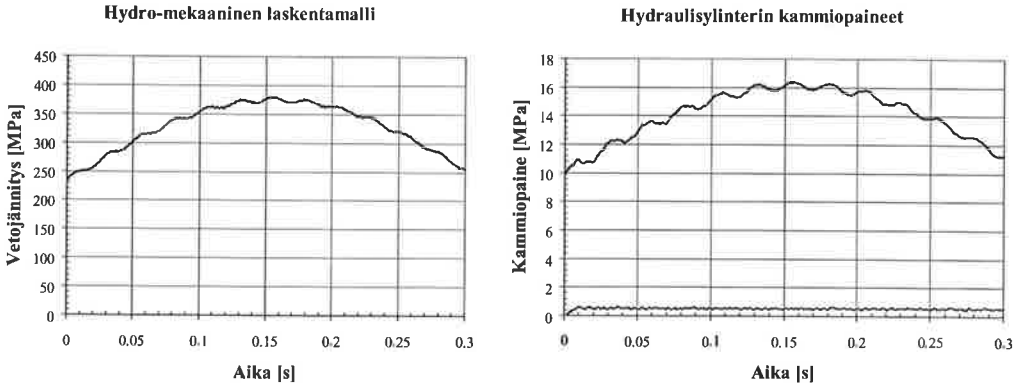
Suure	Arvo	Yks.
Kimmokerroin	210	Gpa
GA_s	EA	Pa
Palkkielementtien lukumäärä	5	kpl
Palkin korkeus	0.12	m
Palkin leveys	0.08	m
Seinämän paksuus	0.005	m
Poikkileikkauksen pinta-ala	0.0019	m^2
Neliömomentti	$3.756 \cdot 10^{-6}$	m^4
Pituustiheys	14.92	kg/m
Pistemassa puomin päässä	400	kg
Sauvan redusoitu kimmokerroin	11.9	GPa
Sauvan jännityksetön loppupituus	1.4755	m
Loppupituus $l_{BD}(5)$	1.4546	m
Tilavuusvirta Q_A	0.000261	m^3/s
Laskenta-aika t_{max}	0.3	s
Aika-askel	0.001	s
Sylinterin kammiopinta-ala A_A	0.003848	m^2
Sylinterin kammiopinta-ala A_B	0.002258	m^2

LASKENTATULOKSET

Laskentamallin painovoimasta johtuva alkutaipuma määritettiin kaikissa tapauksissa epälineaarisena statiikan tehtävänä ja saatu siirtymä ja hydromekaanisessa tehtävässä sylinterin kammion A paine asetettiin tilamuuttujien alkuarvoiksi. Laskentamallin vaste määritettiin Newmarkin aikaintegroinilla käyttäen vakio aika-askelelta, h = 0,001 s. Nostoliikkeen alkuvaiheen jännityshuipun selvittämiseksi kerättiin puomin poikkileikkauksen B yläpinnan vetojännitystä ajan funktiona. Kuvissa 4 ja 5 on esitetty edellä mainittu vetojännitys eri laskentatavoilla.



Kuva 4. Vetojännitys pisteessä B käyttäen rajoiteyhtälöä (vasen kuvaaja) ja pituuttaan muuttavaa sauvaelementtiä (oikea kuvaaja)



Kuva 5. Vetojännitys pisteessä B ja sylinterin kammiopaineet p_A ja p_B hydro-mekaanisella laskentamallilla

JOHTOPÄÄTÖKSET

Tässä esityksessä on kuvattu lyhyesti kolme erilaista tapaa mallintaa nostopuomin liike epälineaarista elementtimenetelmää käyttäen. Käytettäessä nostoliikkeen mallinnukseen rajoitetyhtälöä ja Lagrangen funktiota on nostoliikkeen aikana laskettu jännityshuippu suurempi kuin muilla menetelmillä saatu. Suuremmat jännitykset johtuvat laskentamallin liiallisesta jäykkyydestä. Mallinnustapa on myös numeerisesti häiriöalttiimpi. Rajoiteyhtälö voitaisiin huomioida myös muilla keinoin, kuten sakkomenetelmällä, jolloin valitsemalla sakkokerroin sopivasti, laskettu jännityshuippu pienenisi. Toisena menetelmänä nostoliike on mallinnettu käyttäen pituuttaan muuttavaa sauvaelementtiä, jolloin mekaanisen järjestelmän siirtymämuuttujien lisäksi ei tarvittu muita muuttujia, koska holonominen sidosehto on upotettu laskentamalliin isäntä-orjatekniikalla, kuten lähteessä [1] on tasotapauksessa esitetty. Tällöin saatu laskentamalli ei sisällä lainkaan sidosehtoja, jolloin vältytään numeerisiltä häiriöherkyysongelmilta. Laskettu jännityshuippu oli selvästi pienempi kuin rajoiteyhtälöä käyttäen. Viimeisenä on tarkasteltu liikkeen mallinnusta hydraulisylinterielementtiä käyttäen, jolloin laskentamalliin tuli siirtymämuuttujien lisäksi hydraulisylinterielementtien hydrauliset muuttujat eli tässä tapauksessa kammiopaineet. Laskentatulokset vastasivat jännityshuipun osalta edellisellä menetelmällä laskettua arvoa. Mallinnettaessa hydraulisylinterin aiheuttamaa liikettä mekaaniseen järjestelmään ovat pituuttaan muuttava sauva sekä hydromekaaninen malli suositeltavampia mallinnusvaihtoehtoja ja niillä myös pystytään mallintamaan realistisemmin hydraulisylinterin jousto, joka todellisuudessakin on merkittävä.

LÄHTEET

[1] Marjamäki, H., Mäkinen, J. Modelling telescopic boom - The plane case: part I, Computers & Structures 2003, 81(16), s.1597-1609.

[2] Geradin, M., Cardona, A., Flexible Multibody Dynamics: A Finite Element Approach, J. Wiley & Sons, Chichester, 2001, 327 s.

[3] Mäkinen, J. A Formulation for Flexible Multibody Mechanics - Lagrangian Geometrically Exact Beam Elements using Constraint Manifold Parametrization, Tampere University of Technology, Institute of Applied Mechanics and Optimization, Research Report 2004:3, 89 s. URL: http://www.tut.fi/~jmamakin/vk.pdf.

CRASH SAFE, ENERGY ABSORBING COMPOSITE LIGHTING COLUMN

J. KOVANEN, P. PYKÄLÄINEN, M. TANTTU AND M. KEMPPINEN
Mikkeli Polytechnic Research Centre YTI
P.O. Box 181, 50101 Mikkeli

A. NYLÉN
Mikkeli Polytechnic, Laboratory of Materials Technology
e-mail: aapo.nylen@mikkeliamk.fi

INTRODUCTION

National Governments at EU are committed to reduce the number and severity of accidents on the road caused by impact to roadside objects. The European Parliament proposed in 1998 that primary action should be taken to halve fatalities by the year 2010. Owing to that, standard EN 12767 [1] was established, in which safety categories are defined for support structures, direct rules for crash testing and also for interpretation of crash test results.

A procedure to reduce the number and severity of accidents is to use passive safety infrastructure: especially lighting columns with adequate energy absorbing properties are feasible to hazardous sites. In general, there are two different approaches to minimize the effect of collision when lighting columns are considered:

energy absorbing structures to slow the vehicle considerably, and thus the risk of secondary accidents with other structures, such as trees, pedestrians and other road users may be reduced, and

Non-energy absorbing structures that allow the vehicle to continue after the impact with a controlled reduction in speed.

Generally, the structure of the non-energy absorbing column, which may be detachable, is made of wood or rigid steel. During an impact, the column gets loose from a slip base or by other similar controlled mechanism.

Energy absorbing columns have impact properties to decelerate a vehicle and absorb energy during an impact. The desired behaviour can be achieved with a rigid lightweight structure that also have elements with suitable energy absorbing properties. During the impact, the energy absorbing structure flattens and rolls under a vehicle, thus absorbing anergy. Existing column products usually have rigid shell manufactured of steel, aluminium or composite that ruptures during a crash. Energy absorbing elements can be made of steel, composites, wood etc.

PROBLEM DEFINITION

Lighting columns at EU must fulfil the demands of updated Standards, long term influences of the environment (UV-radiation and corrosion) and the requirements of the production process.

Standard EN 40-3-3 (Lighting columns, Design and Verification, Verification by calculation) [2] defines the requirements for the verification of the design by calculation and can be applied for lighting columns with maximum height of 20 m (without brackets) and for height of 18 m if with brackets. The standard specifies the maximum deflection limits of the column and what the resistance of the structure against static and wind loadings should be.

Based on the standard EN 40-3-1 (Lighting columns, Design and Verification, Specification for characteristic loads) [3] design loads for lighting columns are determined. The definition of the characteristic wind pressure is based on regional wind speed (in Finland 23 m/s) and several factors, which take into account the shape coefficients of the column components, the dynamic factor of the column and the affect of the terrain category.

Standard EN 40-7 (Lighting columns, Requirements for fibre reinforced polymer composite lighting columns) [4] specifies the dynamic factor of the lighting column with composite structure. The definition is based on the specific frequency of the column. This standard also gives demands for the quality issues of the composite structure and for the quality control of the production.

Standard EN 12767 divides passive safety support structures into three different categories: HE – high energy absorbing, LE – low energy absorbing and NE – non-energy absorbing. The structure, in this case lighting column, should decelerate vehicle considerably to avoid collision with other structures and for example pedestrians. Furthermore, occupant safety level can be divided into four different categories. Classification of the occupant safety level into category 1, 2 or 3, two crash tests must be performed at selected speed class; crash test with low speed 35 km/h and with higher selected speed 50, 70 or 100 km/h. Class 4 includes unharmful products, when the product is approved with one crash test at selected speed class.

Standard EN 12767 obliges a manufacturer to specify the speed class at which the column is being tested. The speed class specifies also the speed class at which road regions the column can be used. The speed class should be selected to 100 km/h, to obtain broader sales- and marketing conditions. At selected speed class, the exit speed after impact determines the resulting energy absorption category according to the values shown in Table 1:

Table 1 Energy absorption categories

Impact speed km/h	50	70	100
Energy absorption category	Exit speed v_e after an impact km/h		
HE	$v_e = 0$	$0 < v_e < 5$	$0 < v_e < 50$
LE	$0 < v_e < 5$	$5 < v_e < 30$	$50 < v_e < 70$
NE	$5 < v_e < 50$	$30 < v_e < 70$	$70 < v_e < 100$

The occupant safety level is defined with ASI- and THIV –values. ASI (Accelerated Severity Index) is a computational value of accelerations, which the occupant undergoes during the impact process. THIV (Theoretical Head Impact Velocity) gives information concerning the deceleration of the occupant's head caused by the deceleration of the vehicle. Table 2 shows the classifications limits of different energy absorption classes based on ASI- and THIV –values. The aim of the design process was develop a column product which would be accepted to the HE 3 –energy absorption category with speed class of 100 km/h.

Table 2 Occupant safety

Energy absorption categories	Occupant safety level	Speeds			
		Mandatory low speed impact test 35 km/h		Speed class impact tests 50, 70 and 100 km/h	
		Maximum values		Maximum values	
		ASI	THIV km/h	ASI	THIV km/h
HE	1	1,0	27	1,4	44
HE	2	1,0	27	1,2	33
HE	3	1,0	27	1,0	27
LE	1	1,0	27	1,4	44
LE	2	1,0	27	1,2	33
LE	3	1,0	27	1,0	27
NE	1	1,0	27	1,2	33
NE	2	1,0	27	1,0	27
NE	3	1,0	11	0,6	11
NE	4	No requirement	No requirement	See standard EN 12767	See standard EN 12767

Other related standards concerning crash testing are specifying equipment of testing, data acquisition and method to calculate energy absorption properties of tested specimen: EN 1317-1 (Road restraint systems, Part 1, Terminology and general criteria for test methods) [5], EN 1317-2 (Road restraint systems, Part 2, Performance classes, impact test acceptance criteria and test methods for safety barriers) [6] and EN 1317-3 (Road restraint systems, Performance classes, impact test acceptance criteria and test methods for crash cushions) [7].

THE DESIGN OF A NEW CONCEPT

The design of the new column structure was based on Fibrocom Oy's channel composite product; rigid E-glass composite shell enforced with longitudinal extra reinforcements. Wind- and dead loads, deflection limits, resistance of the column structure were defined according to the above mentioned standards EN 40-3-1, EN 40-3-3 and EN 40-7.

Designing a product with excellent energy absorbing properties and with an adequate rigidity is challenging; the more resistance column has to bear the wind and dead loads, the higher ASI – values are presumed during an impact and vice versa. Also one hard-to-realize boundary condition was to remain the dimensions of the column similar to standard steel products. In addition, the less stiffness lighting column has, the dynamic factor defined by EN 40-7 increases, resulting in higher wind loads in static rigidity computations.

The resistance of the column to loads was calculated with FEM analysis (Finite Element Method) due to complex structure of the composite structure. The acceptance criteria for deflections are specified by EN 40-3-3 into three rigidity class, in which class 1 is the most rigid. The displacements and structural strains and stresses were calculated with linear FE-model. With the composite structure used in the project, the rigidity class is obligated to be low, class 3, to achieve decent results from impact tests.

THE STRUCTURE AND PRODUCTION PROCESS

The Fibrocom Oy's patented channel composite laminate is formed of 3D –glassfibre weave, which has parallel tubular channels along the walls of the conical column structure. The channels can be empty or filled with other materials. In this case, some columns have longitudinal stiffeners, which significantly improve the energy absorption properties. The resulting structure is a stiff and lightweight structure manufactured in a process vacuum infusion. Vacuum atmosphere improves driving of a resin into a laminate, gives a better fibre-to-resin ratio and also reduces the total process time.

PRELIMINARY TEST

Different composite and metal structures were pre-tested by YTI at railway yard at Pieksämäki, Finland. To make the tests simple and cheap, the tests were performed with a bogie vehicle (Figure 1), which was trailed by a car to achieve easy repeatability. The replaceable sheet metal bumper of the vehicle simulated a car nose. The mass of the vehicle was set the same as a crash car in the Standards, 950 kg. Target speeds for crash tests were 35, 50 and 70 km/h, which was hard to achieve in the relatively short railway yard. Preliminary deceleration values were measured with help of high speed video camera. Test results are shown in Table 3. Owing to promising pre-results, it was decided to continue towards official crash tests.

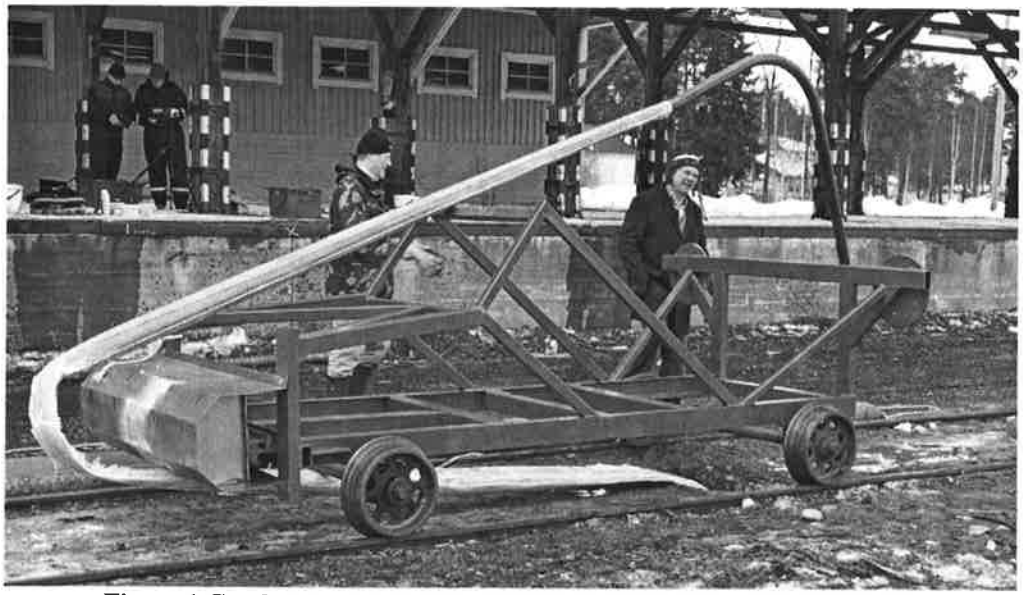


Figure 1 Crash test setup and result after impact with speed of 50 km/h

Table 3 Test results with different impact speeds.

Structure	Impact speed km/h	Exit speed km/h	ASI	THIV km/h
Winded E-glass	51	0	-	-
Winded E-glass with longitudal reinforcements	50	0	-	-
Channel composite with heavy longitudal reinforcements	49	0	0,53	27
Channel composite with light longitudal reinforcements	50	0	0,46	25
Channel composite with heavy longitudal reinforcements	35	0	0,53	24
Channel composite with heavy longitudal reinforcements	64	0	0,72	29
Channel composite heavy longitudal reinforcements	64	0	0,68	28

IMPACT TESTS BY HELSINKI UNIVERSITY OF TECHNOLOGY

Crash tests according to EN 12767 were performed by Helsinki University of Technology, Laboratory of Highway Engineering at the airport of Pori, Finland. The impact vehicle in each test was Peugeot 205 with identical mass to the bogie vehicle, 950kg. Decelerations for the computations of ASI –values were acquired with acceleration sensors, THIV –value was defined from high speed camera files.

Several tests with slightly varying structures for 10m high columns were performed during the summer 2005. All the ASI –results of 100 km/h test speed are shown in Figure 2. The results of selected test are summarized in Table 4.

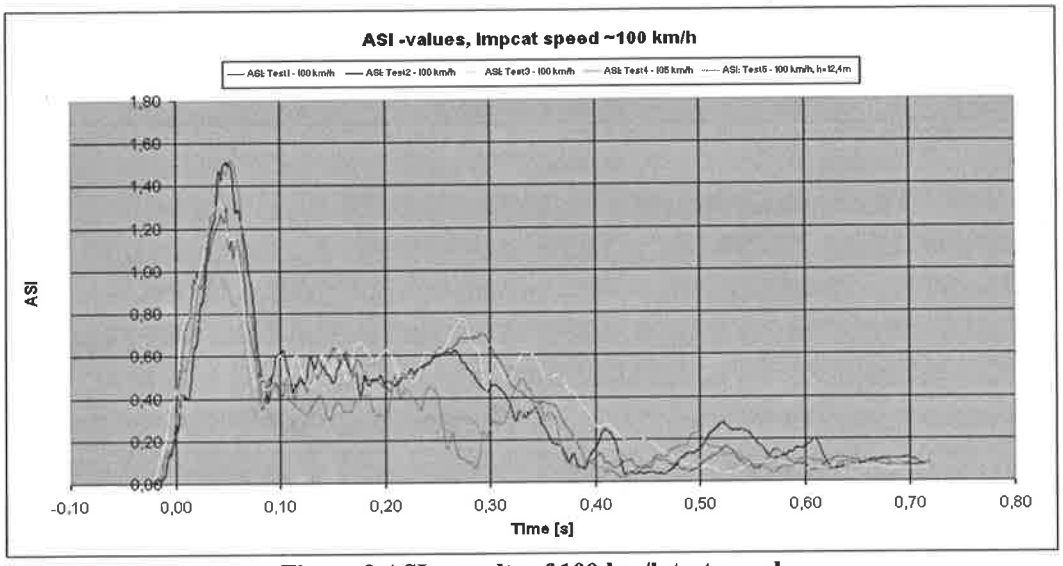


Figure 2 ASI –results of 100 km/h test speed.

Table 4 The results of selected test.

Height	Bracket projection	Lantern's weight	Column plinth	Target speed	Measured speed	ASI	THIV	Safety category
10,0 m	2,5 m	8 kg	RBJ-5SP	100 km/h	105 km/h	1,0	26 km/h	HE 3
10,0 m	2,5 m	8 kg	RBJ-5SP	35 km/h	33 km/h	0,5	22 km/h	HE 3
12,4 m	2,0 m	8 kg	RBJ-6SP	100 km/h	102 km/h	1,5	32 km/h	HE 1

Lighting column with height of 10 m obtained the best HE –energy absorption category with the highest occupant safety class 3. The column with height of 12,4 m reached only HE 1 –class due to overgrown vertical deceleration values. Figure 3 shows the deformed column (height 12,4 m) after crash test. Research and development to further improve the performance of the higher column is in progress.



Figure 3 Deformed column and vehicle after impact of 100 km/h. Impact tests performed by Helsinki University of Technology, Laboratory of Highway Engineering

FUTURE EXPECTATIONS

According to Tehomet Oy, the company for production of steel components, assembly, marketing, selling and distributing of the whole product, the demand for energy absorbing lighting columns is rapidly growing and international. Nowadays markets are even having a lack of proper column products, and this situation will now be getting better as Tehomet's product family is being released to the market.

The production of the first delivery batch is in progress and will be delivered to customer within a few weeks. Altogether, hundreds of columns should be delivered during the year 2006. There are still some challenges in production process to overcome, but ongoing process improvements will increase the capacity and make the prices even more competitive.

The product family won the Finnish reinforced plastics product award in November 2005 and JEC Innovation Awards 2006, in the Energy & Industry category.

A nice presentation of the product with exiting crash test videos can be downloaded from www.tehomet.fi , News.

REFERENCES

1. European Committee for Standardiazation: EN 12767 Passive safety of support structures for road equipment – Requirements and test methods. Draft proposal of revised EN 12767. 2005-06-02. 30 p.

2. European Committee for Standardization: SFS-EN- 40-3-3 Lighting columns - Part 3-3: Design and Verification - Verification by calculation. Helsinki: Finnish Standards Association, 2004. 73 p. ICS 93.080.40

3. European Committee for Standardization: SFS-EN 40-3-1 Lighting columns – Part 3-1: Design and Verification - Specification for characteristic loads. Helsinki: Edita Oyj, 2000. 32 p. ICS 91.160.20

4. European Committee for Standardization: SFS-EN 40-7 Lighting columns – Part 7: Requirements for fibre reinforced polymer composite lighting columns. Helsinki: Edita Oyj, 2003. 14 p. ICS 93.080.40

5. European Committee for Standardization: SFS-EN 1317-1 Road restraint systems, Part 1: Terminology and general criteria for test methods. Helsinki: Edita Oyj, 1998. 30 p. ICS 01.040.93; 13.200; 93.080.30

6. European Committee for Standardization: SFS-EN 1317-2 Road restraint systems, Part 2: Performance classes, impact test acceptance criteria and test methods for safety barriers. Helsinki: Edita Oyj, 1998. 15 p. ICS 13.200; 93.080.30

7. European Committee for Standardization: SFS-EN 1317-3 Road restraint systems, Part 3: Performance classes, impact test acceptance criteria and test methods for crash cushions. Helsinki: Edita Oyj, 2001. 19 p. ICS 13.200; 93.080.30

THE IMPACT SIMULATION OF CRASH SAFE COMPOSITE LIGHTING COLUMNS

A. BOROVKOV, O. KLYAVIN, A. MICHAILOV
St.Petersburg State Polytechnical University,
Computational Mechanics Laboratory (*CompMechLab*), Russia

M. KEMPPINEN, M. KAJATSALO
Mikkeli Polytechnic Research Centre YTI, Finland

ABSTRACT

Three Finnish associates, Tehomet Ltd, Fibrocom Ltd and Mikkeli Polytechnic Research Center YTI developed an internationally awarded energy absorbing lighting column product family in 2005. The design and dimensioning were completed with static FEM computations, preliminary impact tests and full-scale impact tests. For the structural optimization and further development YTI contacted the CompMechLab to perform impact simulations. CompMechLab generated LS-DYNA FEM models of different column type, featuring several nonlinearities: dynamic impact at different vehicle speed, plasticity in column and vehicle parts, contact interaction between simulated objects, progressive damage in column laminates. The LS-DYNA model of a real car was based on FHWA/NHTSA National Crash Analysis Center prototype. The car prototype and a lighting column model consisted of all together 216 materials.

The FE results had a good correlation with the measured, experimental deceleration data, maximum deviation being 14%. The simulated deceleration curves allowed calculating head injury criteria (HIC) estimate for all columns crush tests. All HIC values are below injury risk that shows a safe impact in all column types.

1. INTRODUCTION

National Governments at EU are committed to reduce the number and severity of accidents on the road caused by impact to roadside objects. The European Parliament proposed in 1998 that primary action should be taken to halve fatalities by the year 2010. Owing to that, standard EN 12767 [1−7] was established, in which safety categories are defined for support structures, direct rules for crash testing and also for interpretation of crash test results.

A procedure to reduce the number and severity of accidents is to use passive safety infrastructure: especially lighting columns with adequate energy absorbing properties are feasible to hazardous sites. In general, there are two different approaches to minimize the effect of collision when lighting columns are considered:

Energy absorbing structures to slow the vehicle considerably, and thus the risk of secondary accidents with other structures, such as trees, pedestrians and other road users may be reduced, and

Non-energy absorbing structures that allow the vehicle to continue after the impact with a controlled reduction in speed.

Generally, the structure of the non-energy absorbing column, which may be detachable, is made of wood or rigid steel. During an impact, the column gets loose from a slip base or by other similar controlled mechanism.

Energy absorbing columns have impact properties to decelerate a vehicle and absorb energy during an impact. The desired behaviour can be achieved with a rigid lightweight structure that also have elements with suitable energy absorbing properties. During the impact, the energy absorbing structure flattens and rolls under a vehicle, thus absorbing energy. Existing column products usually have rigid shell manufactured of steel, aluminium or composite that ruptures during a crash. Energy absorbing elements can be made of steel, composites, wood etc.

2. IMPACT TESTS BY HELSINKI UNIVERSITY OF TECHNOLOGY

Crash tests according to EN 12767 were performed by Helsinki University of Technology, Laboratory of Highway Engineering at the airport of Pori, Finland. The impact vehicle in each test was Peugeot 205 with identical mass to the bogie vehicle, 950kg. Decelerations for the computations of ASI–values were acquired with acceleration sensors, THIV –value was defined from high speed camera files.

The occupant safety level is defined with ASI- and THIV –values. ASI (Accelerated Severity Index) is a computational value of accelerations, which the occupant undergoes during the impact process. THIV (Theoretical Head Impact Velocity) gives information concerning the deceleration of the occupant's head caused by the deceleration of the vehicle.

Several tests with slightly varying structures for 10m high columns were performed during the summer 2005. All the ASI–results of 100 km/h test speed are shown in Fig. 1. The results of selected test are summarized in Table 1.

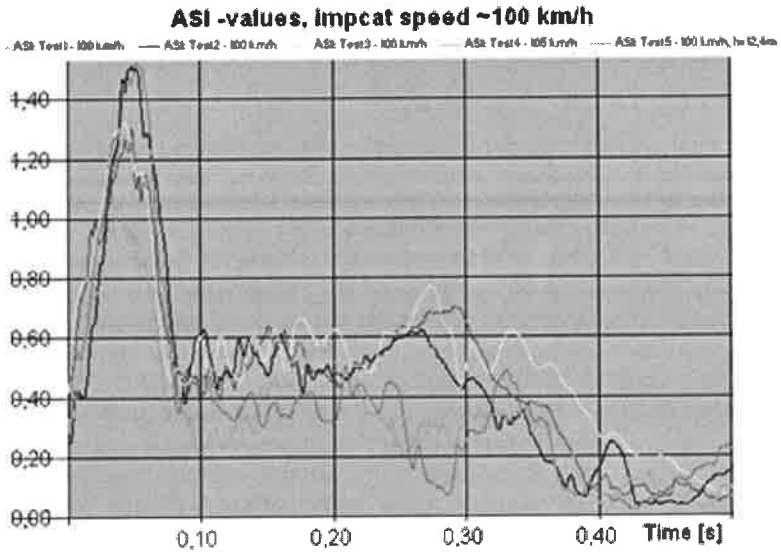


Fig. 1. ASI values

Table 1.

Height	Bracket projection	Lantern's weight	Column plinth	Target speed	Measured speed	ASI	THIV	Safety category
10,0 m	2,5 m	8 kg	RBJ-5SP	100 km/h	105 km/h	1,0	26 km/h	HE 3
10,0 m	2,5 m	8 kg	RBJ-5SP	35 km/h	33 km/h	0,5	22 km/h	HE 3
12,4 m	2,0 m	8 kg	RBJ-6SP	100 km/h	102 km/h	1,5	32 km/h	HE 1

Lighting column with height of 10 m obtained the best HE–energy absorption category with the highest occupant safety class 3. The column with height of 12,4 m reached only HE 1 –class due to overgrown vertical deceleration values. Fig. 2 shows the deformed column (height 12,4 m) after crash test. Research and development to further improve the performance of the higher column is in progress.



Fig. 2. Deformed column and vehicle after impact of 100 km/h. Impact tests performed by Helsinki University of Technology, Laboratory of Highway Engineering

3. LIGHTING COLUMNS CRASH TESTS FINITE ELEMENT SIMULATION

St.Petersburg State Polytechnical University, Computational Mechanics Laboratory (*CompMechLab*) performed crush tests simulations for several types of composite columns at different car speed. Finite Element (FE) system LS-DYNA [8] is used in this project to perform contact-impact non-linear dynamic analysis of the construction. LS-DYNA contains a lot of methods and algorithms to give solutions for various types of complicated mechanical problems. Contact-impact algorithms make it possible to simulate dynamic contact interaction of structure parts. Three-dimensional (3-D) FE model (Fig. 3) is achieved by the use of shell and solid elements. Developed fully 3-D CAD and FEM models of different types of columns (Fig. 4) allowed simulating next nonlinearities: impact at different vehicle impact speed, plasticity in column steel reinforcing parts and vehicle parts, contact interaction between simulated objects with large displacements/rotations/strains, progressive damage in column laminates.

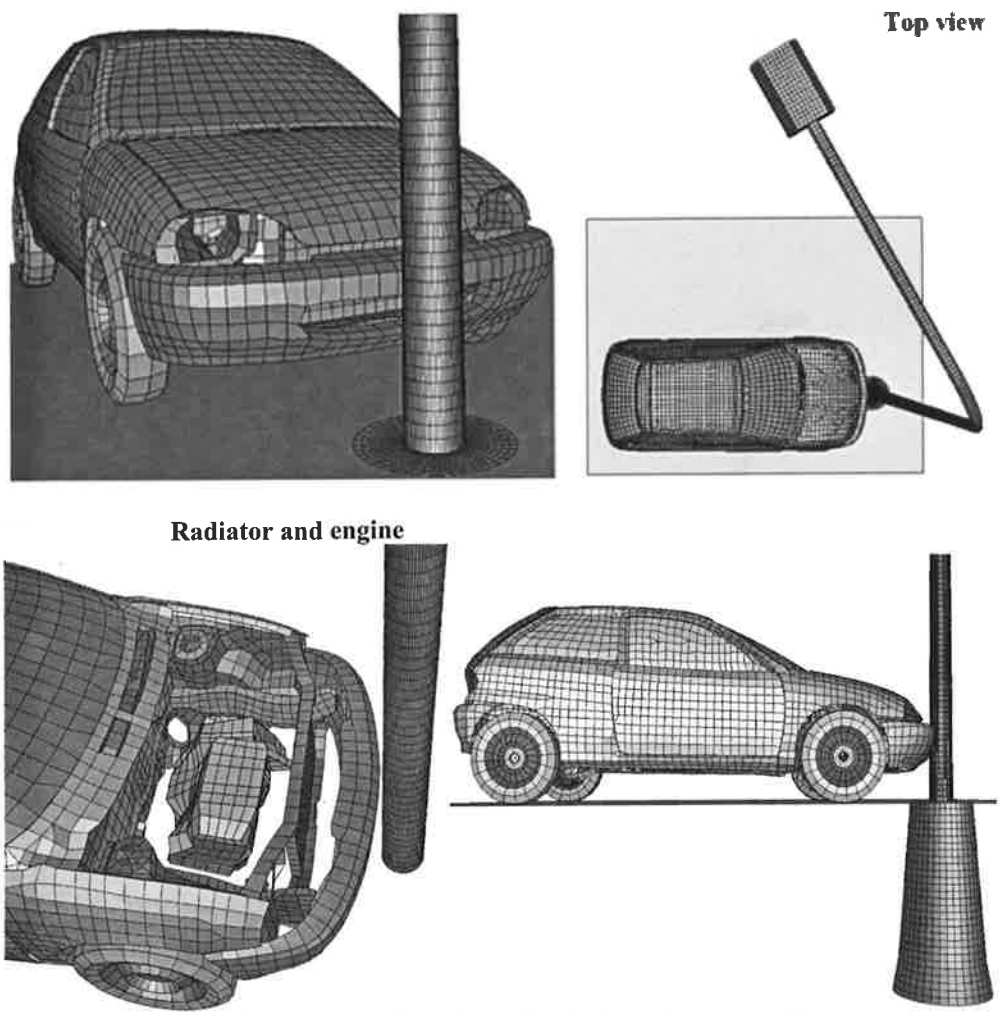


Fig. 3. Three-dimensional finite element model

3-D FE model of real car prototype based on FHWA/NHTSA National Crash Analysis Center (www.ncac.gwu.edu) prototype includes radiator, engine, front and rear suspensions, brake system and many other parts with ability of contact interaction and nonlinearities in material behavior. Prototype design debugged to make approximate similarity with car in experiment. Especially, radiator and engine positioned as at Peugeot 205, total mass of Geo Metro is equal to 1030 kg Peugeot mass.

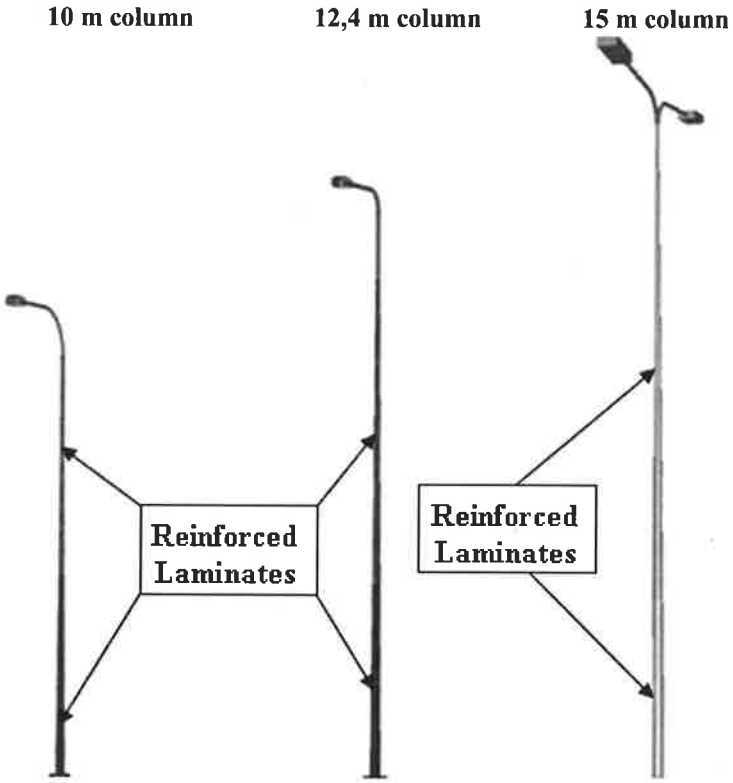


Fig. 4. Lighting columns 3-D models

Column 3-D FE model includes column stand, three different reinforced composite laminates, bracket with lanterns (single or double). Alltogether 216 different materials considered in car prototype with lighting column model. Experiment with computed deceleration curves comparison and deformed column view at the peak of deceleration are showed on Fig. 5.

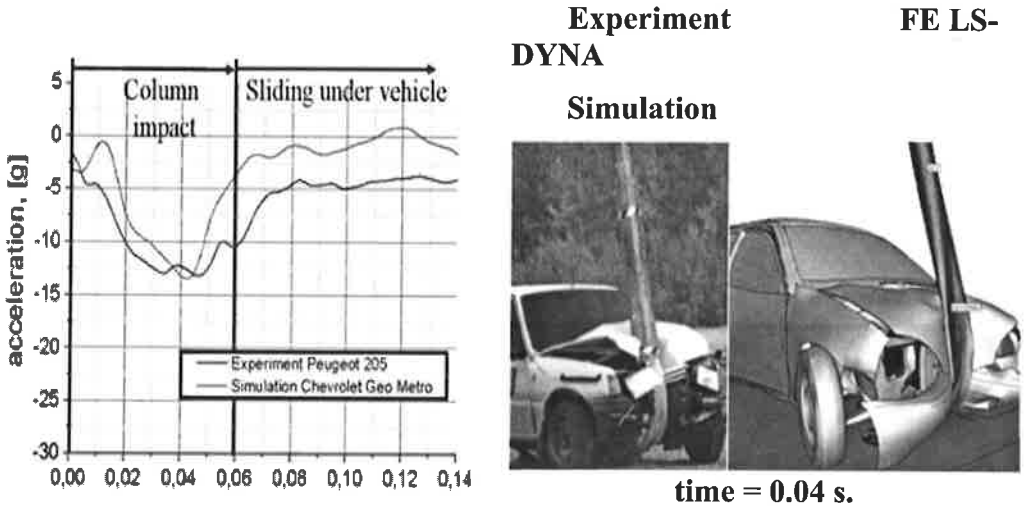
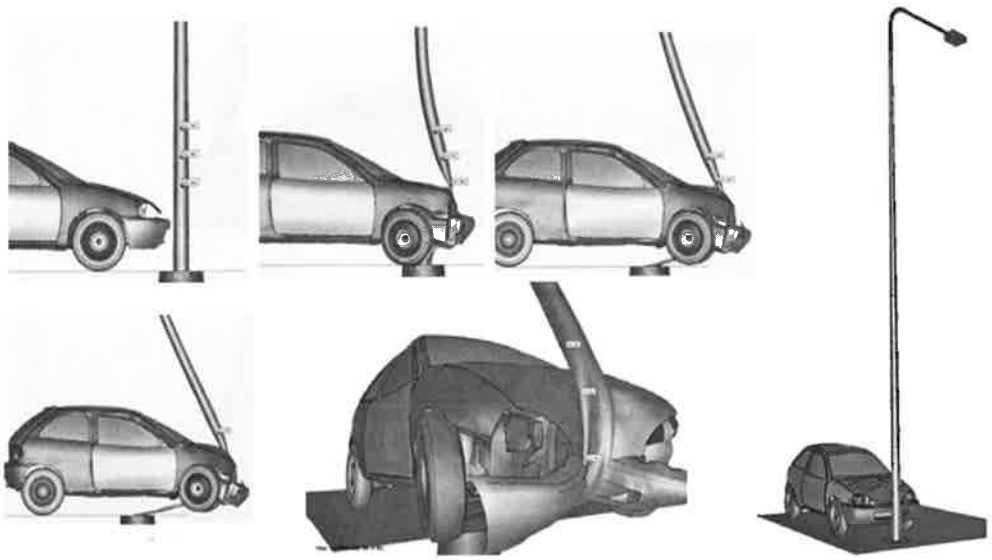


Fig. 5. Experiment with computed deceleration curves comparison

The process of vehicle deceleration from 100 to 0 km/h by column can be divided into two phases (Fig. 5) – first is impact and second – sliding of column pipe under vehicle. First phase characterize the maximum of deceleration peak. The duration of this phase for all columns is not above 0,06…0,1 sec. Main parameters influencing on maximal deceleration value is column cross section, outer diameter, number of reinforcing bars and bar diameter. The second phase is passing with low values of deceleration up to vehicle stop. That's why it is enough to analyze the first phase. Because of the maximal maximum peak of deceleration observes at duration of the first phase of impact.



Effective Plastic Strain distribution (ε_{eff})

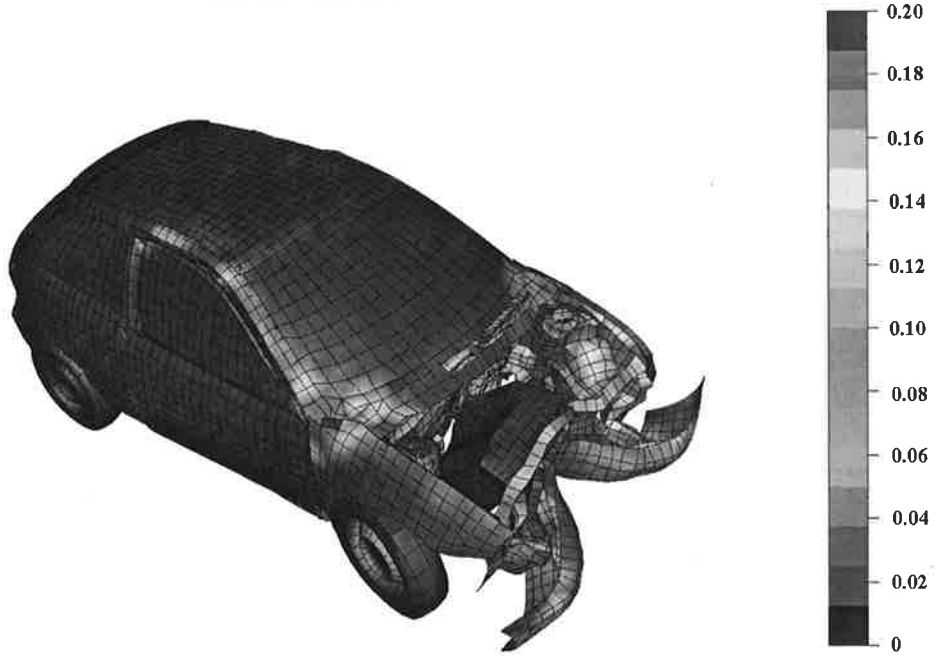


Fig. 6. Freeze frames of column sliding under vehicle and effective plastic strain in vehicle after stop

Fig. 7 illustrates freeze frames of impact at t=0.04 sec (this time point is a maximum for deceleration curve) for large 15 meter high lighting column (10 reinforcing bars in laminate structure) and deceleration curve at 100 km/h speed in comparison with 10 meter column and 15 meter column with decreased number of reinforcing steel bars in pipe laminate structure.

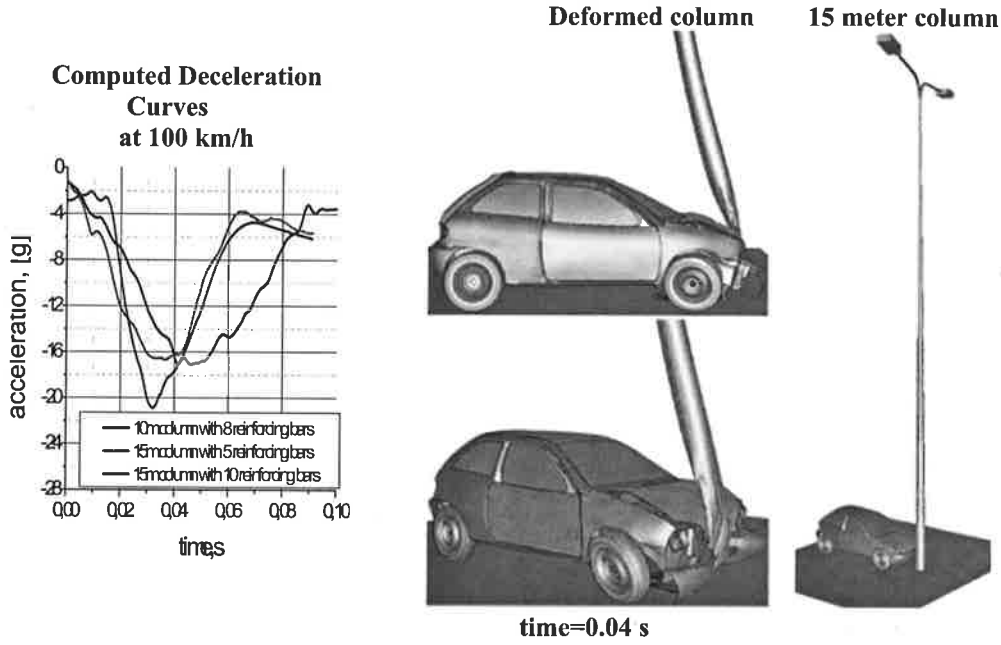


Fig. 7. Deceleration curve at 100 km/h speed in comparison with 10 m column and 15 m column

Values of maximal deceleration show a good correlation with experiment results. The obtained FE results, with these models, showed that correctness of FEM-computations approves with that experiment maximal deviation for maximal deceleration stand in 14% value, and good correlation between experiment and simulated deceleration curves.

The Head Injury Criteria (HIC) is currently used to assess head injury potential in automobile crash test dummies. It is based on the resultant translational acceleration rather than the frontal axis acceleration. The resultant simulated deceleration curves allowed calculating HIC – the unique among Federal Motor Vehicle Safety Standard (FMVSS) – and estimate safety reliability for all columns crush tests. Fig.8 illustrates comparison between real experiment by Helsinki University of Technology and LS-DYNA FE simulation results of first 0.15 sec of impact. Deformed vehicle and column after stop shown on Fig. 9. Some difference explains with differing hoods of Peugeot 205 and rebuilt Chevrolet Geo Metro FE model.

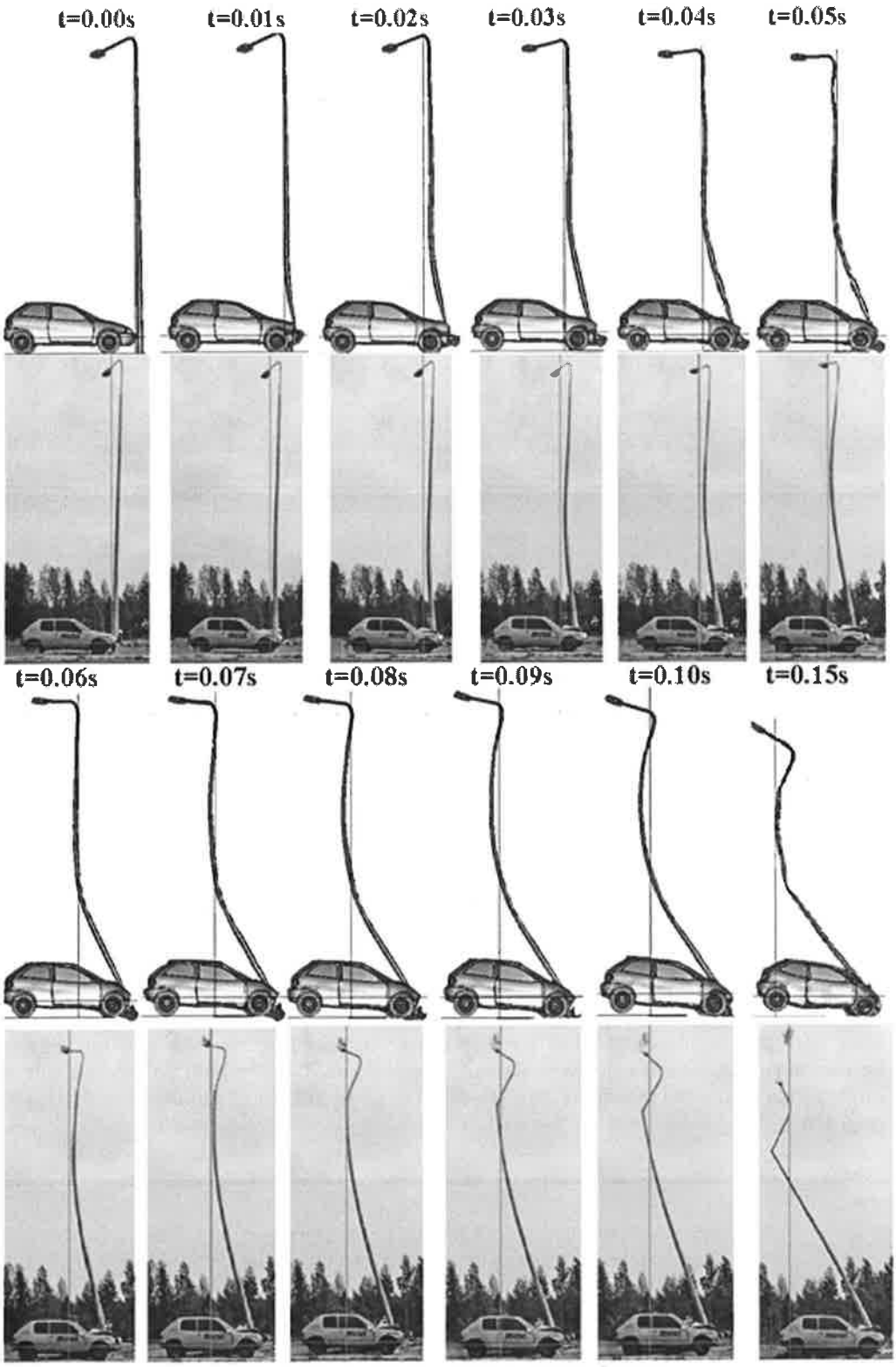


Fig. 8. Freeze frames of 12 m column impact

Bending of column at impact comparison between experiment and simulation shown on fig.8 start differ at time 0.07 sec, because of fracture at joint of column pipe and lantern bracket. But analysis of column without bracket showed that bracket influence insignificantly (table 2) on maximal value of deceleration. Column with bracket maximal deceleration stay at 16,42g and without bracket remain at 16,36g.

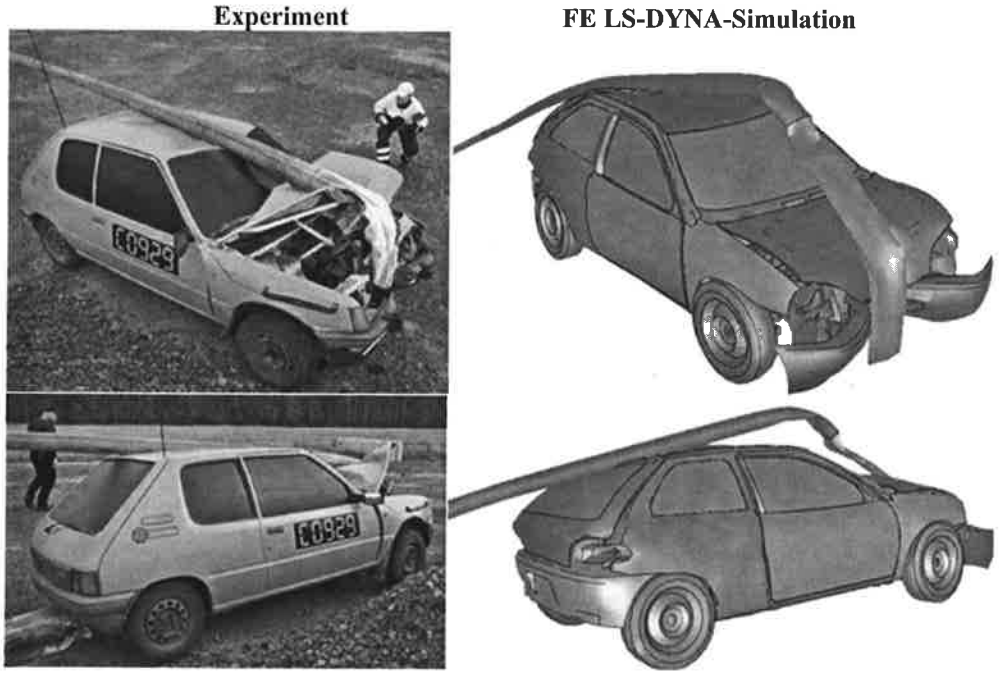
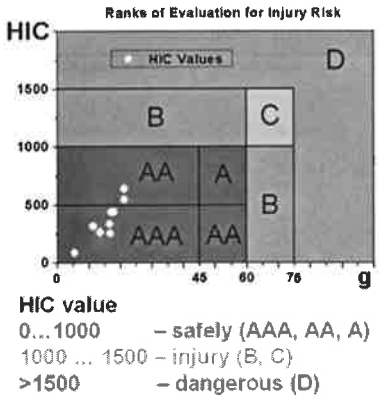


Fig. 9. Vehicle after stop

All HIC values are below injury risk (Table 2) that shows a safe impact in all column types (different height, pipe outer diameter – Dn and various number of reinforcing bars), and it is important to emphasize that all values are acceptable with safety standards for very young children and adults. Computed HIC values combined with maximal deceleration values provided validity of safety estimation. The 36 millisecond interval for HIC calculation is meant to encompass the maximum loading for impact waveforms which last longer than 36 ms. Relatively short duration waveforms tend to be associated with head contact whereas longer duration HIC intervals tend to be associated with head deceleration without impact. As of 2000, the NHTSA [9] final rule adopts limits which reduce the maximum time for calculating the HIC to 15 milliseconds (HIC_{15}) vs. the prior HIC_{36}.

Table 2. Computed HIC and maximal deceleration values

Column Type	**HIC_{15}**	**Deceleration, g**
10 meter 5 reinforcing bars 35 km/h	89,15	5,42
10 meter 5 reinforcing bars 105 km/h	320,70	11,32
10 meter 6 reinforcing bars 100 km/h	338,40	16,42
10 meter 8 reinforcing bars 100 km/h	444,00	17,12
12,4 meter 5 reinforcing bars 100 km/h	440,20	13,10
10 meter 6 reinforcing bars Dn=220mm (Dn=185mm) 100 km/h	266,90 (338,4)	13,45 (16,42)
10 meter 6 reinforcing bars column without bracket 100 km/h	256,72	16,36
15 meter 5 reinforcing bars 100 km/h	549,00	17,20
15 meter 10 reinforcing bars 100 km/h	643,00	21,30



REFERENCES

1. European Committee for Standardiazation: EN 12767 Passive safety of support structures for road equipment – Requirements and test methods. Draft proposal of revised EN 12767. 2005-06-02. 30 p.

2. European Committee for Standardization: SFS-EN- 40-3-3 Lighting columns – Part 3-3: Design and Verification – Verification by calculation. Helsinki: Finnish Standards Association, 2004. 73 p. ICS 93.080.40

3. European Committee for Standardization: SFS-EN 40-3-1 Lighting columns – Part 3-1: Design and Verification – Specification for characteristic loads. Helsinki: Edita Oyj, 2000. 32 p. ICS 91.160.20

4. European Committee for Standardization: SFS-EN 40-7 Lighting columns – Part 7: Requirements for fibre reinforced polymer composite lighting columns. Helsinki: Edita Oyj, 2003. 14 p. ICS 93.080.40

5. European Committee for Standardization: SFS-EN 1317-1 Road restraint systems, Part 1: Terminology and general criteria for test methods. Helsinki: Edita Oyj, 1998. 30 p. ICS 01.040.93; 13.200; 93.080.30

6. European Committee for Standardization: SFS-EN 1317-2 Road restraint systems, Part 2: Performance classes, impact test acceptance criteria and test methods for safety barriers. Helsinki: Edita Oyj, 1998. 15 p. ICS 13.200; 93.080.30

7. European Committee for Standardization: SFS-EN 1317-3 Road restraint systems, Part 3: Performance classes, impact test acceptance criteria and test methods for crash cushions. Helsinki: Edita Oyj, 2001. 19 p. ICS 13.200; 93.080.30

8. Hallquist J.O. LS-DYNA Theoretical Manual, Livermore Software Technology Corporation. 1998

9. Eppinger R., et al., Development of Improved Injury Criteria for the Assessment of Advanced Automotive Restraint Systems – II, NHTSA, Nov 1999

KEVYTRAKENTEISTEN ONTELOPALKKIEN LASKENTA JA TESTAUS

M. KAJATSALO, T. KARTTUNEN, J. KOVANEN, M. KEMPPINEN

Mikkelin ammattikorkeakoulu
YTI-tutkimuskeskus, materiaaliteknologian toimiala
PL 181, 50101 MIKKELI
e-mail: mikko.kajatsalo@mikkeliamk.fi

TIIVISTELMÄ

Ontelopalkit ovat kerroslevyrakenteisia palkkeja, joissa kahden pintalevyn välinen rakenne voidaan suunnitella monin eri tavoin haluttujen ominaisuuksien saavuttamiseksi. Komposiittien mahdollisuudet konepajateollisuudessa (KOMPA) projektissa on selvitetty erilaisten ontelopalkkirakenteiden suunnitteluun, valmistukseen ja käyttäytymiseen liittyviä kysymyksiä. Tarkoituksena on ollut selvittää voidaanko komposiitti-, vaahto- yms. materiaaleja käyttämällä saavuttaa palkille sellaisia ominaisuuksia, että se voi kilpailla perinteisen I-palkin kanssa tietyissä sovellutuksissa. Tutkittavina kohteina ovat olleet neljä teräksisiin pintalevyihin perustuvaa palkkia ja yksi puhtaasti lujitemuovista valmistettu palkki. Tutkimus jakautui kolmeen osioon seuraavasti: Ensimmäisessä vaiheessa palkit suunniteltiin ja simuloitiin YTI-tutkimuskeskuksessa Mikkelissä. Toisessa vaiheessa valmistettiin palkkien prototyypit. Kolmannessa vaiheessa palkeille suoritettiin dynaaminen testaus, taivutuskokeet, lämpökuormitus sekä yhdistetty lämpö- ja taivutuskuormitus. Dynaamiset mittaukset suoritettiin TKK:n lujuusopin laboratoriossa Espoossa ja staattiset sekä lämpökuormitukset YTI-tutkimuskeskuksessa Mikkelissä.

1. JOHDANTO

I-palkkeja on perinteisesti käytetty kohteissa, joissa vaaditaan suurta taivutusjäykkyyttä ja keveyttä. Teräksinen palkki on kuitenkin altis värähtelyille ja sen vaimennuskyky on hyvin alhainen. Lujitemuovikomposiiteilla on puolestaan hyvä värähtelynvaimennuskyky. Lisäksi lujitemuovien etuja teräkseen verrattuna ovat suuri ominaislujuus ja -jäykkyys, korroosionkestävyys, hyvä lämmöneristyskyky, korkea väsymislujuus ja keveys. Tutkimuksen tarkoituksena on ollut selvittää erilaisia rakenne- ja materiaalivaihtoehtoja perinteisen I-palkin korvaajaksi kohteissa joissa rakenteelta vaaditaan jäykkyyden lisäksi keveyttä ja hyvää värähtelynvaimennusominaisuutta.

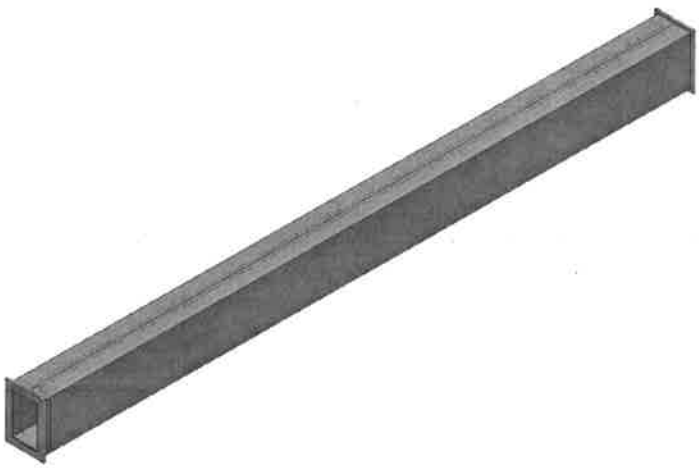
Tutkimus tehtiin yhteistyössä Metso Oyj:n kanssa. Tutkimus liittyy osana Komposiittien mahdollisuudet konepajateollisuudessa (KOMPA) projektiin, jossa tutkittiin uusia käyttökohteita komposiiteille perinteisessä konepajaympäristössä.

2. PALKKIEN SIMULOINNIT

2.1 LASKENTAMALLI

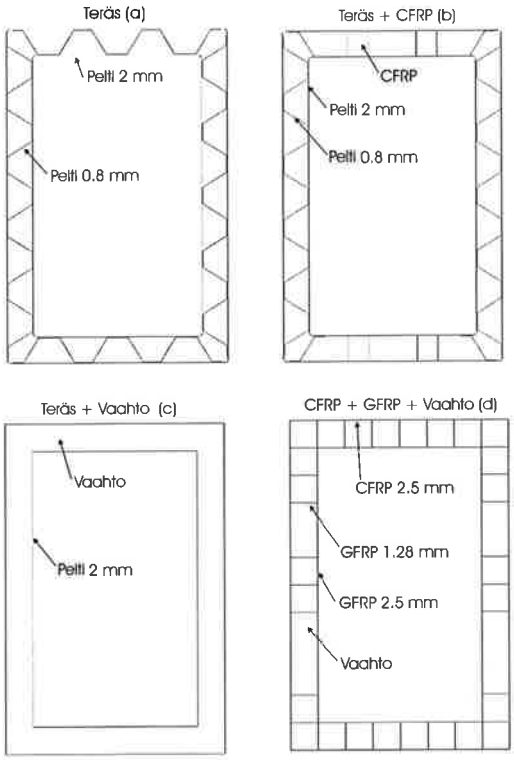
Simulointien avulla määritettiin palkkien staattisia, dynaamisia ja lämpöteknisiä ominaisuuksia. Jokaiselle palkille suoritettiin seuraavan kaavion mukaiset tarkastelut.

1. Staattiset laskennat
    a. Kuormituksena oma paino.
    b. Kuormituksena oma paino ja ulkoiset kuormat.
2. Dynaamiset laskennat
    a. Ominaistaajuudet
    b. Pakkoherätteen aiheuttama vaste, herätteenä 0.5 mm/s pakkoheräte taajuusalueella 0-30 Hz
3. Lämpölaskennat
    a. Vakiolämpötilan aiheuttamat jännitykset ja muodonmuutokset, kuormituksena 100 °C lämpötilaero



Kuva 1. Tutkittava palkki.

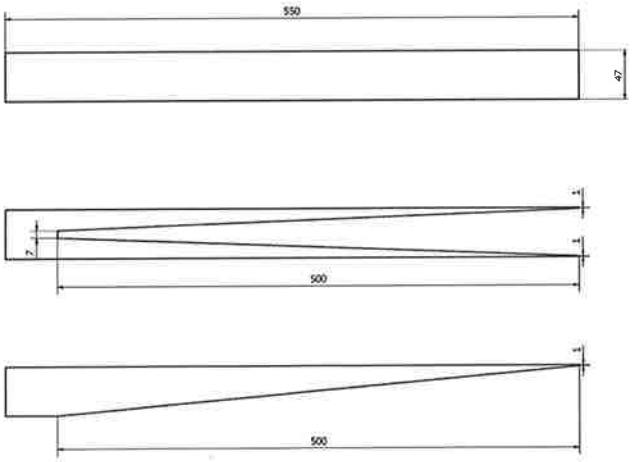
Mallinnus suoritettiin ABAQUS 6.4 -ohjelmistolla. Simuloitava rakenne on esitetty kuvassa 1. Simuloitavina kohteina oli yhteensä 4 erilaista poikkileikkausta, jotka on esitetty kuvassa 2. Kuvassa esiintyvät merkinnät CFRP ja GFRP viittaavat hiilikuitulujitettuun muoviin (Carbon Fibre Reinforced Plastic) ja lasikuitulujitettuun muoviin (Glass Fibre Reinforced Plastic). Vaahtona käytettiin ROHACELL 51 S polymetakryyli-imidi-solumuovia (PMI), johon päädyttiin sen hyvien palo-ominaisuuksien vuoksi (ei tuota myrkyllisiä palokaasuja). Jokaisessa palkissa oli kuvan 1 mukaiset rakenneteräksestä valmistetut päätylaput. Staattisissa ja lämpölaskuissa rakenteet mallinnettiin symmetriataso huomioiden kaksitukisina palkkeina. Elementteinä näissä analyyseissä käytettiin parabolisia kuori- ja solid elementtejä. Dynaamisissa analyyseissa elementteinä käytettiin lineaarisia kuori- ja solid elementtejä.



Kuva 2. Simuloitujen rakenteiden poikkileikkaukset.

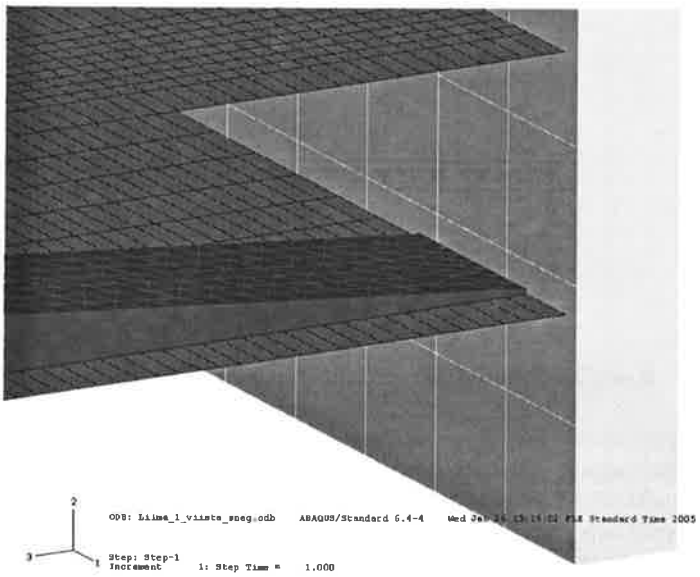
Staattisissa analyyseissä määritettiin palkkien siirtymät ja jännitykset kolmipistetaivutuksessa. Palkit olivat tuettu päätylappujen alareunoista ja niitä kuormitettiin tasaisesti jakautuneella viivakuormalla palkin reunalla sekä painekuormalla palkin keskellä.

Dynaamiset laskennat suoritettiin käyttämällä kolmea erilaista tuentaa. Ensimmäisessä mallissa (tuenta I) rakenne oli vapaana. Toisessa mallissa (tuenta II) rakenne on tuettu pystysuunnassa päätylappujen alapinnoilta. Kolmannessa mallissa (tuenta III) toisen päätylapun alapinta on edellisen lisäksi tuettu kaikissa translaatiovapausasteissa. Erilaisia tuentoja käyttämällä saatiin tietoa sekä itse rakenteen dynaamisista ominaisuuksista että tuennan vaikutuksesta sen dynaamiseen käyttäytymiseen.



Kuva 3. Lujitemuovin päädyn geometriat palkin sivulta katsottuna.

Lämpölaskennassa tutkittavana rakenteena oli hiilikuitulujitettu ontelopalkkirakenne (rakenne b). Analyysit tehtiin käyttämällä kolmea erilaista lujitemuovin reunan geometriaa kuvan 3 mukaisesti. Geometrioiden mitat on valittu siten, että ne lähteen /1/ mukaan minimoivat liimasauman leikkausjännityksen. Rakenteen teräsosat mallinnettiin lineaarisilla nelisolmuisilla kuorielementeillä, lujitemuovi lineaarisilla 8 solmuisilla kuutioelementeillä ja liima sekä lineaarisilla 8 solmuisilla kuutioelementeillä että lineaarisilla 4 solmuisilla tetraedrielementeillä. Liimasauma mallinnettiin yhdellä elementillä paksuuden yli. Vaadittavan tarkkuuden saavuttamiseksi elementtiverkkoa tihennettiin lujitemuovin reunan läheisyydessä, jossa elementtien pituutena käytettiin 4 mm:ä. Kuvassa 4 on esimerkki analysoinnissa käytetystä elementtiverkosta. Kuvassa teräs on vihreällä, lujitemuovi punaisella, teräksinen päätylappu keltaisella ja liimasauma sinisellä värillä. Rakenne on kuvassa leikattu pituussuunnassa siten, että lujitemuovi ja liimasauma näkyvät. Rakenteen kuormituksena analyyseissä on käytetty 100 °C:n lämpötilaeroa.



Kuva 4. Yksityiskohta liimasauman jännitysten laskennassa käytetystä FE -mallista.

2.2 TULOKSET

2.2.1 STAATTINEN LASKENTA

Taulukossa 1 on esitetty rakenteiden suurimmat siirtymät sekä oman painon että ulkoisen kuormituksen alaisena. Taulukossa on suluissa esitetty suureiden suhteellinen osuus verrattuna teräsrakenteeseen.

Taulukko 1. Rakenteiden siirtymät ja massat.

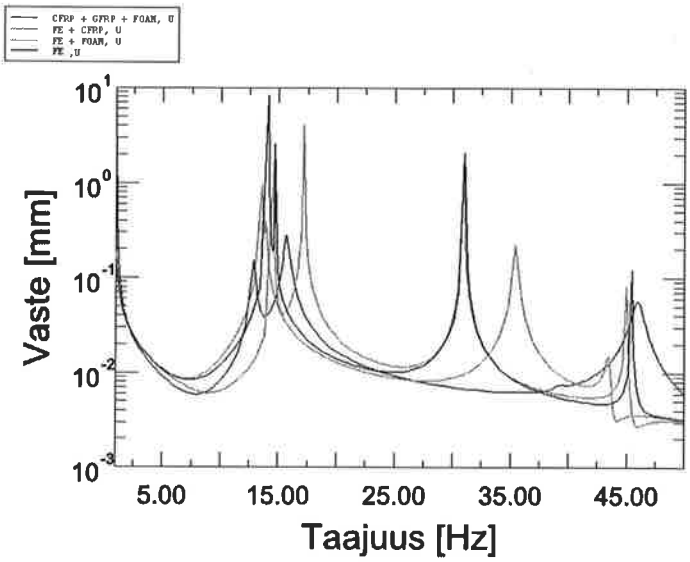
	Maksimi siirtymä [mm], oma paino	Maksimi siirtymä [mm], ulkoinen kuormitus	Massa [kg]	Massaan suhteutettu siirtymä
Teräsrakenne	1,50	6,49	920	1
Teräs + CFRP	1,08 (72 %)	4,43 (68 %)	994 (108 %)	1,36
Teräs + Vaahto	1,48 (99 %)	7,61 (117 %)	786 (85 %)	1,00
CFRP+GFRP+Vaahto	0,27 (18 %)	12,43 (192 %)	360 (39 %)	1,30

2.2.2 DYNAAMINEN LASKENTA

Taulukossa 2 on esitetty koottuna kutakin palkin perusmuotoa vastaavat ominaistaajuudet. Kuvassa 5 on esitetty esimerkki rakenteiden vasteista tuennalla III.

Taulukko 2. Neljää perusmuotoa vastaavat taajuudet eri tuennoilla.

Taajuudet (Hz)	1. puoliaalto	2. puoliaalto	1. täysi aalto	2. täysi aalto
Teräsrakenne				
tuenta I	19,1	26,4	51,4	70,6
tuenta II	19,1	14,3	51,4	54,0
tuenta III	14,7	14,1	45,4	54,6
Teräs + CFRP				
tuenta I	19,0	32,5	51,1	81,9
tuenta II	19,0	17,3	51,1	62,7
tuenta III	14,5	17,1	45,0	58,6
Teräs + Vaahto				
tuenta I	17,7	24,6	48,6	67,7
tuenta II	17,7	13,7	48,6	52,7
tuenta III	13,8	13,5	43,4	54,1
CFRP+GFRP+Vaahto				
tuenta I	14,9	23,9	41,6	64,2
tuenta II	14,9	15,8	41,6	55,5
tuenta III	12,8	15,7	39,2	58,6



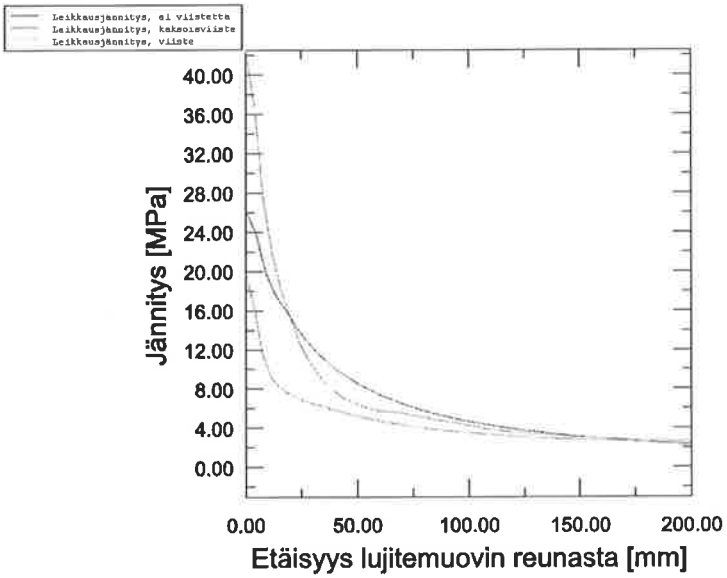
Kuva 5. Rakenteiden vasteet [mm], tuenta III.

2.2.3 LIIMALIITOKSET

Kuvassa 6 on esitetty liimasauman jännitykset lujitemuovin vapaan reunan läheisyydessä. Jännitykset on tulostettu kuvassa 4 näkyvän liimasauman keskeltä. Mallissa ulompi pintalevy oli kiinnitetty päätylappuun, joten suurimmat leikkausjännitykset tulevat ylempiin liimasaumoihin. Lisäksi symmetriasta johtuen kaikkien ulompien liimasaumojen jännitykset ovat itseisarvoltaan samansuuruiset. Kuvissa leikkausjännitys vastaa kuvan 4 23-suuntaa ja normaalijännitys 2-suuntaa. Taulukossa 3 on esitetty liimasaumojen leikkausjännityksen maksimiarvot.

Taulukko 3. Liimasaumojen suurimmat leikkausjännitykset.

Lujitemuovin päädyn geometria	τ [MPa]
Ilman viistettä	26,1
Yksi viiste	42,5
Kaksoisviiste	19,7



Kuva 6. Liimasaumojen leikkausjännitykset, 0-200 mm reunasta.

3. PALKKIEN VALMISTUS JA TESTAUS

Simulointien perusteella valittiin neljä palkkia, jotka valmistettiin ja testattiin. Palkkien valmistus suoritettiin yhteistyössä Janavalo Oy:n kanssa. Valmistuksessa yhdistyivät useat eri valmistusmenetelmät, kuten laserhitsaus, Tig-hitsaus sekä liimaus. Liimattavina materiaaleina olivat hiilikuitu ja PMI-vaahto. Valmistuksen haasteellisuuden johdosta päätettiin valmistaa vielä yksi palkki, jossa ei käytetty laserhitsausta lainkaan. Kyseinen palkki on alla olevassa luettelossa nimellä M ja sen vaipan sisällä on reunoilla PMI-vaahtoa ja ylä- sekä alapuolella hiilikuitua. Valmistetut palkit, niistä jatkossa käytetyt merkinnät sekä niiden vastaavuus simuloituihin palkkeihin ovat seuraavat.

- T-palkki vastaa teräsrakennepalkkia (a)
- HT-palkki vastaa teräs + CFRP-palkkia (b)
- V-palkki vastaa teräs + vaahto-palkkia (c)
- M-palkki vastaa YTI:n omavalmisteista teräs + CFRP + vaahto-palkkia
- H-palkki vastaa CFRP + GFRP + vaahto-palkkia (d)

3.1 TKK:N LUJUUSOPIN LABORATORIOSSA TEHDYT KOKEET

3.1.1 KOEJÄRJESTELY

Palkkia roikutettiin 4 mm paksun ja noin 1 m mittaisen terästangon varassa pystysuunnassa, millä simuloitiin vapaata reunaehtoa kuormitussuunnassa. Tanko oli kiinnitetty tiukasti palkkiin, jottei se aiheuttaisi lisävaimennusta systeemiin. Palkkia täristettiin sähkömagneettisella täristimellä alapäästään jäykempään (kiinnostavampaan) suuntaan ja tuotettu voima mitattiin. Vasteena mitattiin kiihtyvyyttä sekä täristyssuunnassa että tätä vastaan kohtisuorassa suunnassa. Herätesignaalina käytettiin valkoista kohinaa. Alun perin palkit oli tarkoitus herättää iskuvasaralla, mutta pienen vaimennuksen johdosta testejä ei voitu tehdä iskukokeina. Päämittaussuureena oli kiihtyvyyden ja voiman välinen taajuusvastefunktio. Taajuusvastefunktio estimoitiin sekä H1 että H2 estimaateilla. Tärkeimmät mittausparametrit olivat: 1024 keskiarvoa, 75% overlapping ja hanning-painotusikkuna. Taajuusalue oli 0 – 400 Hz ja taajuusresoluutio 0.5 Hz.

3.1.2 TULOKSET

Taulukossa 4 on esitetty moodianalyysin tuloksena saadut ominaistaajuudet f_n [Hz] ja suhteelliset viskoosivaimennuskertoimet ζ [%] kahdelle alimmalle taivutusmuodolle kumpaankin suuntaan. Tulokset perustuvat taajuusvastefunktion H2-estimaattiin.

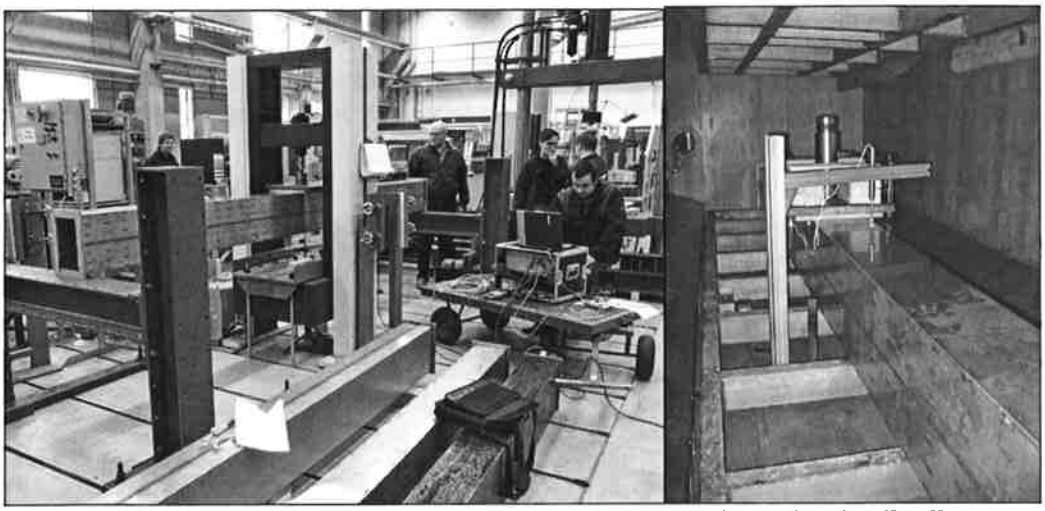
Taulukko 4. Moodianalyysin tulokset.

	JÄYKEMPI SUUNTA					JOUSTAVAMPI SUUNTA				
Palkki	V	H	HT	T	M	V	H	HT	T	M
f_1	99.8	99.66	129.4	106.1	126.3	69.50	70.15	77.95	75.51	63.5
ζ_{11}	0.07	0.22	0.12	0.02	0.22	0.18	0.30	0.07	0.08	0.81
f_2	240.4	219.7	303.5	268.2	241.0	171.1	159.0	192.6	189.8	
ζ_{12}	0.56	0.50	0.78	0.06	0.78	0.37	0.47	0.17	0.08	

3.2 MAMK:N LABORATORIOKOKEET

Ontelopalkeille tehtiin kaksi staattista kuormitustestiä, joiden välissä suoritettiin yksi uunitesti. Uunitestissä palkkia kuormitettiin korotetussa lämpötilassa. Kaikki palkkien kuormitukset tehtiin kolmipistetaivutuksena. Näiden jälkeen palkkien liimasaumoja yritettiin tutkia NDT-menetelmin ja lopuksi palkeille tehtiin kantokykytestit. Venymäliuskamittauksia tehtiin staattisissa testeissä sekä uunitesteissä. Staattiset testit ja kantokykytesti suoritettiin Mikkelin ammattikorkeakoulun (MAMK) materiaalitekniikan laboratoriossa Shimadzu-aineenkoetuslaitteella. Uunitestit tehtiin MAMK:n puulaboratorion lämpökäsittelyuunissa.

Uunitesteissä jännityksiä tarkasteltiin sekä lämpötilan suhteen että kuormituksen alaisena. Venymäliuskojen mittauspisteet sijaitsivat kaikissa palkeissa keskellä alapinnalla ja osassa palkeista myös yläpinnalla palkin päässä/päissä. Kuva 7 esittää staattisen testin ja uunitestin koejärjestelyjä. Uunitestien mittauksia haittasivat uunin karkea lämmitystekniikka ja palkkien epätasainen lämpeneminen sekä osaltaan lyhyt lämmitysaika. Hiilikuidun lämmönjohtavuuskerroin on hyvin alhainen ja siten palkin lämmitysaika olisi venynyt liian pitkäksi, jos olisi haluttu varmistaa myös hiilikuitujen tasainen lämpeneminen.



Kuva 7. Staattisten testien koejärjestely vasemmalla ja uunitestin oikealla.

3.2.1 STAATTISTEN KUORMITUSTESTIEN TULOKSET

Staattisissa testeissä tarkasteltiin palkkien siirtymiä ja jännityksiä. Palkkeja kuormitettiin useita kertoja siirtymäohjattuna 10kN, 20kN ja 30kN kuormiin asti. Ensimmäisen ja toisen staattisen kokeen voima-siirtymä–kuvaajasta (kuva 8) nähdään, että kaikkien palkkien siirtymät käyttäytyivät lineaarisesti kuormituksen suhteen. Kaikilla palkeilla esiintyi voiman ryömintää alaspäin 20kN ja 30kN kuormilla. Tämä johtui teräspalkilla hitsien ja liimatuilla palkeilla (V-, HT-, ja M-palkeilla) liiman myötäämisestä. Rakenteen myötääminen näkyi jäännösjännityksinä muissa paitsi H-palkissa.

Uunitestin jälkeisessä toisessa staattisessa testissä huomattiin, että HT-palkin jäykkyys on alentunut. Tämä johtuu todennäköisesti liimasaumojen osittaisesta pettämisestä. M-palkin jäykkyys on kuvan 8 mukaan saattanut hieman kasvaa. Ero on kuitenkin niin pieni, että se voi johtua kuormitusvoiman ryömimisestä kokeiden aikana. Liimasaumojen myötääminen kuormitusnopeuden ollessa epämääräinen aiheuttaa koetuloksiin lievää epätarkkuutta. Kuormitus hoidettiin kummassakin staattisessa testissä manuaalisesti siirtymäohjauksella, jolloin kuormitusnopeus ei ollut vakio.

3.2.2 UUNITESTIEN TULOKSET

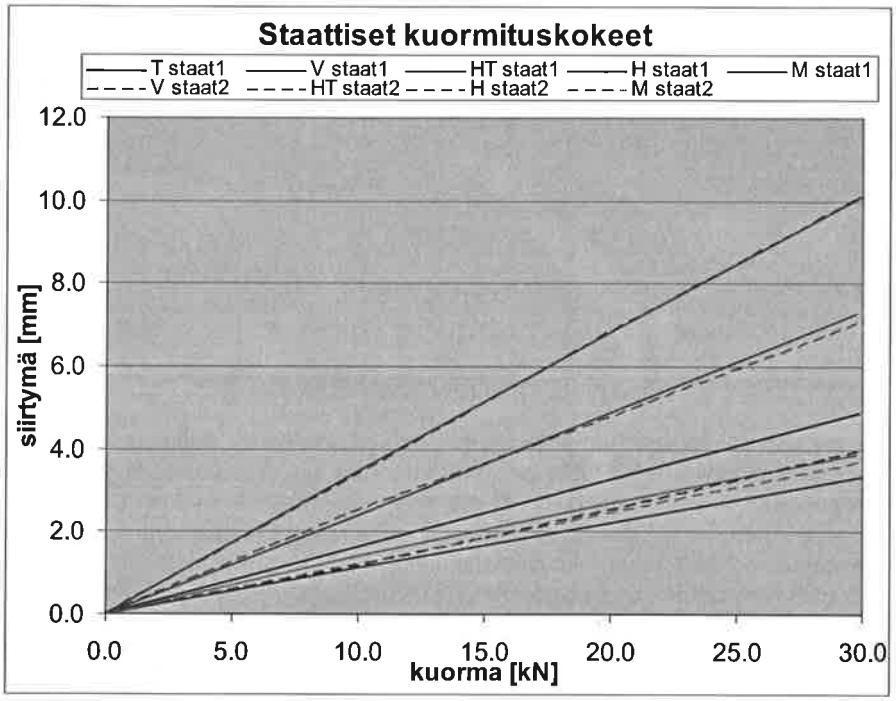
Uunitestissä palkkeja kuormitettiin noin 20kN:n voimalla suunnilleen 100 °C:n lämpötilassa. Aiottu liimasaumojen pettämisen seuranta lämmityksen aikana ei onnistunut uunin toimintaperiaatteen vuoksi. Uuni lämpeni voimakkaiden puhaltimien avulla, joiden suuntaa vaihdettiin lämmityksen aikana useaan otteeseen palkin tasaisemman lämmityksen vuoksi. Voimakkaiden ilmavirtojen vuoksi venymäliuskojen arvot muuttuivat lämmityksen aikana herkästi lämpötilan vaihteluiden mukana eikä liimasaumojen pettämistä voitu erottaa tuloksista.

Rakenteelliset jännitykset aiheutuvat materiaalien erisuurista lämpölaajenemiskertoimista. Suurimmat rakenteelliset lämpöjännitykset (40…70MPa) esiintyivät HT- ja M-palkkien keskikohdissa hiilikuitulattojen päällä. Palkin päiden mittauspisteissä esiintyi korkeintaan 26MPa:n jännityksiä.

Jäännösjännitysten perusteella kaikissa uunissa testatuissa palkeissa tapahtui pysyviä muodonmuutoksia kuormitettaessa niitä korotetussa lämpötilassa. Kuumana kuormitettaessa jäännösjännitykset olivat suuremmat kuin kylmänä kuormitettaessa. HT- ja M-palkeilla havaittiin myös jäykkyyden alenemista kuumana. HT-, H- ja M-palkeissa havaittiin jännitysten ryömintää eli kuormituksen muuttuessa jännitykset muuttuivat perässä, mutta hitaammin. V-palkin jännitykset käyttäytyivät lineaarisesti suhteessa voimaan ilman ryömintää ja muista palkeista eroten V-palkin jän-

nitykset stabiloituivat ensimmäisen kuormituksen jälkeen siten, että jäännösjännityksien osuus ei enää kasvanut.

Pysyvinä vaikutuksina uunitesti alensi HT-palkin jäykkyyttä ja korotti hieman M-palkin jäykkyyttä, kuten uunitestin jälkeisessä toisessa staattisessa testissä ilmeni. Muiden palkkien jäykkyyteen lämpötilalla ei ollut mainittavaa pysyvää vaikutusta.



Kuva 8. Ensimmäisen ja toisen staattisen kokeen voima-siirtymä-kuvaaja

3.2.3 NDT-TESTIT

Staattisten testien ja uunitestien jälkeen haluttiin saada selville ontelopalkkien liimaliitosten kunto. Vaihtoehtoina olivat liimasaumojen tutkiminen rikkomalla palkit liimasaumojen vierestä tai NDT-menetelmät. Palkkien rikkomisen katsottiin vaarantavan liimasaumat, joten se suljettiin pois vaihtoehdoista. NDT-menetelmistä päädyttiin röntgen-kuvaukseen ja UA-mittaukseen, joita käytetään yleisesti laadunvarmistuksessa komposiittien valmistuksen yhteydessä. Ko. menetelmien käyttökelpoisuutta liimasaumojen tutkimisessa selvitettiin koesauvoilla, jotka kuvasivat ontelopalkkien rakennetta. Kummallakaan NDT-menetelmällä ei kuitenkaan saatu tarpeeksi luotettavia tuloksia. Näin ollen palkkien liimasaumojen kuntoa ei saatu selvitettyä.

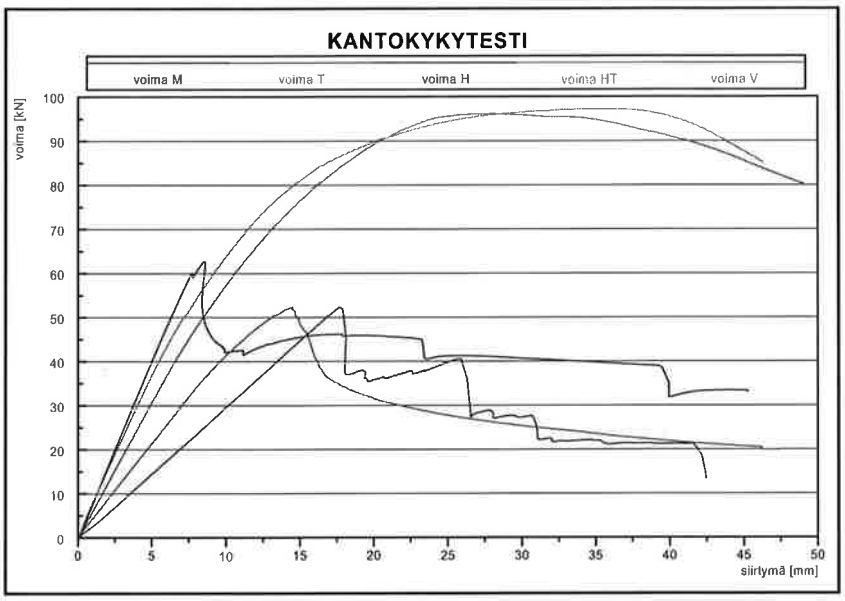
3.2.4 STAATTISET KANTOKYKYTESTIT

Viimeiseksi suoritettiin ontelopalkkien staattiset kantokykytestit. Tarkoituksena oli rasittaa palkkeja kolmipistetaivutuksena niiden murtumiseen asti ja todeta murtovoima. Testijärjestely oli samanlainen kuin aikaisemmissa staattisissa testeissä.

Ruostumattomilla teräspalkeilla vauriomekanismi näytti olevan pintalevyjen eriasteinen lommahtamien. Tähän tietysti liittyy myös muiden tukirakenteiden, kuten hiilikuitulattojen liimasaumojen pettäminen. T-palkissa näkyi myös lommahduskentät hitsien välillä ennen lopullista vaurioitumista. H-palkki petti rakenteen keskeltä ilman silmin havaittavien vauriomekanismeja syntymistä. M-palkista tuli kokeen aikana voimakas liiman haju, mikä kertoo siitä, että liima ei

ollut vielä täysin kovettunut. Siirtymä-voima -kuvaajasta (kuva 9) nähdään, että T- ja HT-palkit kestivät eniten, lähes 100kN (T-palkki 96kN, HT-palkki 97kN), M-palkki tuli seuraavaksi 63kN:n voimalla ja H- sekä V-palkit kestivät kumpikin 52 kN.

Testien jälkeen M-palkki (YTI:n hiilikuitulujitteinen palkki), HT-palkki (hiilikuitulujitteinen teräspalkki) ja V-palkki (vaahto) avattiin kulmahiomakoneella. Näin nähtiin liimauksien kunto kantokyvyn pettämisen jälkeen. M-palkissa painokohta oli mennyt pahasti mutkalle ja hiilikuitujen liimaukset olivat täysin irronneet. Hiilikuitulattojen liimaukset olivat yleisesti irronneet myös muualla. HT-palkin vauriot ovat melko samanlaiset M-palkin kanssa. Hiilikuitulattojen liimaukset olivat yleisesti irtoilleet. V-palkissa painokohdan ympäriltä vaahdot olivat irtoilleet ja rikkoontuneet. Vaahtokappaleiden liimasaumat olivat pettäneet myös muualta. Huomionarvoista oli myös, että V-palkin valmistuksen yhteydessä hitsaus ei ollut pahoin polttanut vaahtokappaleita.



Kuva 9. Palkkien siirtymä-voima –kuvaajat.

4. JOHTOPÄÄTÖKSET

Simuloidut ja valmistetut palkit erosivat ulkoisilta mitoiltaan toisistaan eikä projektissa ollut aikaa suorittaa simulointeja uudestaan testien jälkeen, joten testattujen ja simuloitujen tulosten vertailu ei ole mahdollista.

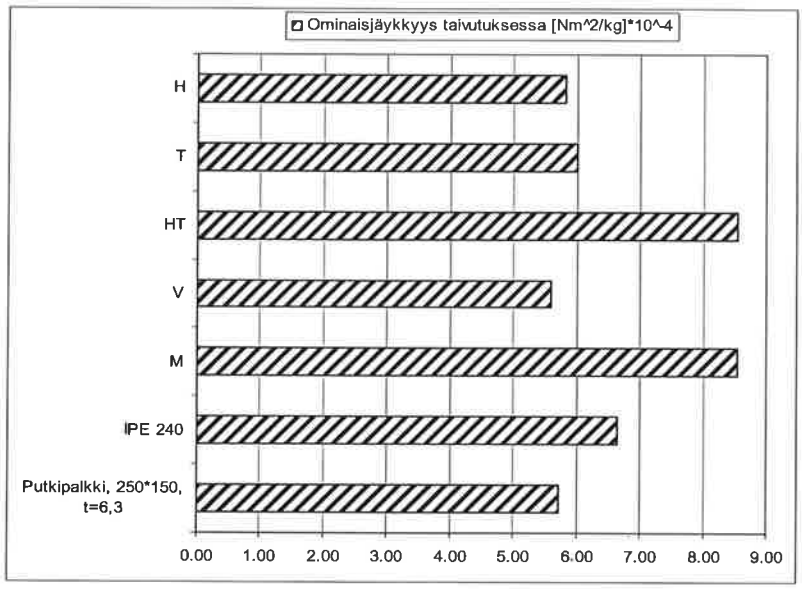
Staattisten simulointien perusteella hiilikuidun lisääminen teräkseen (rakenne b) lisäsi rakenteen staattista jäykkyyttä noin 30 %. Vaahdolla täytetyn rakenteen jäykkyys oli puolestaan n. 17 % ja hiilikuitua, lasikuitua ja vaahtoa sisältävän rakenteen 86 % pienempi. Kun jäykkyydet suhteutetaan palkkien massaan, saadaan vastaaviksi arvoiksi 36 %, 0 %, ja 30 %.

Dynaamisissa analyyseissä havaittiin rakenteiden ominaistaajuuksien olevan voimakkaasti riippuvaisia asetetuista reunaehdoista. Rakenteen tukeminen 2. puoliaaltoa vastaavasta suunnasta aiheutti vastaavan ominaistaajuuden putoamisen 46 %, 47 %, 44 % ja 34 % rakenteesta riippuen. Kaikkien translaatioiden kiinnittäminen toisen päätylapun alareunasta vaikutti ominaistaajuuksiin jopa niin paljon, että ensimmäistä ja toista ominaismuotoa vastaavat taajuudet kääntyivät toisin päin, eli 2. puoliaallon taajuus oli pienempi kuin 1. puoliaallon taajuus.

Analyysit osoittivat liimasaumojen päiden olevan hiilikuiduilla vahvistettujen palkkien heikoimmat kohdat. Liimojen plastisia ja lämpötilariippuvia ominaisuuksia ei ollut käytettävissä, joten liimasaumojen analyysit jouduttiin toteuttamaan lineaarisilla malleilla. Nämäkin mallit kuitenkin osoittavat, että teräksen ja hiilikuitulujitemuovin lämpölaajenemiskertoimien erisuuruisuus

aiheuttaa liimasaumojen päihin merkittäviä jännityskeskittymiä kun rakenteita kuormitetaan vakiolämpötilalla.

TKK:n suorittamien dynaamisten testien perusteella voidaan havaita H- (CFRP + GFRP + vaahto-palkkia) ja M-palkkien (YTI:n hiilikuitulujitteinen palkki) suhteellisten viskoosivaimennuskertoimien olevan koko joukon parhaat. M-palkin vaimennukseen vaikuttaa myös rakenteen valmistuksen epätarkkuus, jonka johdosta rakenteessa on suuret määrät vaimentavaa liimaa. Palkin suuri vaimennuskerroin joustavammassa suunnassa johtuneekin suurelta osin epätäydellisistä liimasaumoista. HT-palkin osalta havaitaan selvästi, että hiilikuidut vaimentavat rakennetta jäykemmässä suunnassa (hiilikuidut kaukana neutraaliakselilta), mutta eivät juurikaan juostavammassa suunnassa.



Kuva 10. Rakenteiden ominaisjäykkyydet.

Kuvassa 10 on esitetty mitattujen rakenteiden massaan suhteutetut jäykkyydet sekä jäykkyydeltään testattua teräsrakennepalkkia vastaavien perinteisen I-palkin ja putkipalkin vastaavat arvot. Kuvasta voidaan havaita hiilikuidulla jäykistämisen lisäävän rakenteen ominaisjäykkyyttä jäykemmässä suunnassa. H-palkin ominaisjäykkyys jäi syytä tai toisesta huomattavasti simuloitua arvoa alhaisemmaksi. Syynä voi olla hiilikuidun suuntauksen epäsuoruus, hartsin suuri suhteellinen osuus rakenteessa sekä hartsin jälkikovetuksen epäonnistuminen.

Uunitestien perusteella ei voitu varmasti todentaa liimasaumojen kestävyyttä. Lämmitysten jälkeen suoritetuissa staattisessa kokeessa havaittu HT-palkin suurempi joustavuus kuitenkin viittaa siihen, että liimasaumat ovat ainakin jossain määrin pettäneet lämmityksen johdosta. Uunissa liimasaumojen yläpuolelta palkin päistä mitatut venymät olivat simuloituja arvoja huomattavasti pienempiä, mikä voi kertoa liimasaumojen pehmenemisestä lämmityksen aikana. Tähän viittaa myös se, että HT- ja M-palkkien jäykkyys aleni korotetussa lämpötilassa.

LÄHTEET

1. Jung Deng, Marcus M.K. Lee, Stuart S.J. Moy. Stress analysis of steel beams reinforced with a bonded CFRP plate. Composite Structures, Volume 65, Issue 2, August 2004, Pages 205-215.

TERÄKSEN JA MUOVIKOMPOSIITTIEN VÄLISET LIIMALIITOKSET KONEPAJASOVELLUTUKSISSA

Timo Brander *, Kari Lumppio * ja Ola Muttilainen **

* Teknillinen korkeakoulu, Kevytrakennetekniikan laboratorio,
PL 4300, 02015 TKK
Timo.Brander@tkk.fi, Kari.Lumppio@tkk.fi
** Mikkelin ammattikorkeakoulu, YTI tutkimuskeskus,
PL 181, 50101 MIKKELI
ola.muttilainen@mikkeliamk.fi

TIIVISTELMÄ

Työssä tutkittiin kokeellisesti konepajateollisuuteen soveltuvien lujitemuovikomposiittien ja terästen keskinäistä liimattavuutta. Kokeet jaettiin esikokeisiin ja pitkäaikaiskokeisiin. Esikokeissa mitattiin liimaliitoksen staattinen lujuus kolmella lujitemuovilla, kolmella teräksellä, kuudella pintakäsittelyllä ja neljällä liimalla. Lujuuskokeina olivat limiliitoksen veto ja kiilakoe. Saatujen tulosten perusteella pitkäaikaiskokeisiin valittiin kaksi lujitemuovia, kaksi terästä, neljä pintakäsittelyä ja kolme liimaa. Pitkäaikaiskokeina olivat erilaiset ympäristöaltistukset, väsyminen ja viruminen. Kuormitusmuotoina olivat limiliitoksen veto ja kiilakoe. Kokeet paljastivat selviä eroja liimojen ja pintakäsittelyjen ympäristökestävyydessä. Tosin eri altistusten antamat tulokset olivat joissain tapauksissa ristiriitaisia. Väsytyskokeissa koekappalemäärät olivat vähäisiä ja hajonta suurta. Tuloksista selviää kuitenkin eri liimojen paremmuus. Virumiskokeissa liimasauman muodonmuutokset olivat niin vähäisiä, että käytetyn koejärjestelyn perusteella tulosten tulkinta oli erittäin vaikeaa.

1 JOHDANTO

Muovikomposiittien käytöllä on pitkät perinteet etenkin ilmailu-, vene- ja urheiluvälineteollisuudessa. Yleensä muovikomposiittien käytöllä voidaan keventää rakenteita, valmistaa integroituja kaksoiskaarevia rakenteita ja parantaa rakenteiden ympäristönkestävyyttä. Tavallisesti muovikomposiitti on korvannut puun tai alumiinin rakennemateriaalina. Yleisimmin käytetyllä lasikuitulujitteisella muovilla on suhteellisen alhainen jäykkyys, mutta hyvä lujuus. Tarvittaessa suurempaa muovikomposiitin jäykkyyttä, joudutaan käyttämään hiilikuidulla lujitettuja muovikomposiitteja. Yhdensuuntaisen hiilikuitulujitteisen lujitemuovin jäykkyys on samaa suuruusluokkaa teräksen kanssa, minkä johdosta teräksen ja hiilikuitulujitteisen lujitemuovin yhteiskäyttö rakenteellisissa sovellutuksissa on järkevää.

Lujitemuovien tehokkain liitostapa on liimaus. Siten myös teräs ja hiilikuitulujitettu muovikomposiitti kannattaa liittää toisiinsa liimaamalla. Toimiva liimaliitos edellyttää yhteensopivia materiaaleja ja liimattavien kappaleiden asianmukaista pintakäsittelyä. Kestävän

liimaliitoksen määrittelyssä avaintekijöitä ovat liiman valinta, asianmukainen pintakäsittely ja liitoksen geometrian määritys.

Projektissa "Komposiittien mahdollisuudet konepajateollisuudessa" tutkittiin terästen ja hiilikuitulujitteisten muovikomposiittien liimausta. Erityisesti haettiin liimoja ja liitettävien kappaleiden pintakäsittelyjä, jotka toimisivat tietyissä koneenrakennuksen sovellutuksissa. Työn toteuttivat Teknillisen korkeakoulun Kevytrakennetekniikan laboratorio (TKK/KRT) ja Mikkelin ammattikorkeakoulun YTI tutkimuskeskus. Osan kokeista teki Henkel Technologies Saksassa. Tässä esityksessä esitetään tehdyt kokeet ja niiden tulokset.

2 ESIKOKEET

Esikokeiden tavoitteena oli seuloa kiinnostavat materiaaliyhdistelmät pitkäaikaiskokeisiin. Kokeet tekivät YTI, TKK/KRT ja Henkel Technologies. Valtaosa kokeista oli limiliitoskappaleiden staattisia vetokokeita.

2.1 Materiaalit ja pintakäsittelyt

Koekappaleissa oli aina toisena liitettävänä materiaalina teräs ja toisena lujitemuovi. Tutkitut teräkset olivat: 1) ruostumaton teräs tyyppiä 1.4301 (RST), 2) pallovalurauta tyyppiä GRP 700 ja 3) rakenneteräs Fe52. Tutkitut lujitemuovit olivat: 1) suulakevedetty hiilikuitulujitteinen vinyyliesterilatta (CF-VE), 2) hiilikuitukudoslujitteinen epoksilaminaatti (CF-EP) ja 3) lasikuitukudoslujitteinen epoksilaminaatti (GF-EP). Ensin mainitun valmisti Exel Oyj ja kaksi viimeksi mainittua TKK/KRT.

Tutkittavina liimoina olivat kaksi epoksiliimaa, yksi akryyliliima ja yksi elastomeeri (MS-polymeeri). Liimat on esitetty taulukossa 1.

Taulukko 1 Käytetyt liimat

Tyyppi	Kauppanimi	Käytetty lyhenne
Epoksi	Hysol 9466	EP
Epoksi	Hysol 9492	EP2
Akryyli	Loctite 3342	PMMA
MS-polymeeri	Loctite 5069	MS

Kaikki liimat olivat huoneenlämpötilakovettuvia pastaliimoja. Epoksiliimoja käytetään tyypillisesti suurta kuormankantokykyä vaativissa rakenteellisissa liimaliitoksissa. Molemmat epoksiliimat ovat kaksikomponenttisia ja niiden oleellinen ero on lämmönkestossa, joka 9492:lla on parempi kuin 9466:lla. Akryyliliima on yksikomponenttinen sitkeä liima, jolla on myös varsin hyvä lämmönkesto. MS-polymeeri on ensisijaisesti tiiviste, jolla on myös hyvä tartunta useimpiin materiaaleihin. Sen lujuusominaisuudet ovat kuitenkin vaatimattomat.

Teräs- ja lujitemuovikappaleiden pintakäsittelyt erosivat merkittävästi toisistaan. Lujitemuovikappaleiden liimapinta käsiteltiin ennen liimausta seuraavasti:

1. karhennuskankaan poisto
2. pyyhintä liuottimella
3. kevyt puhallus alumiinioksidilla
4. pyyhintä liuottimella

Kyseinen pintakäsittely antoi kaikissa tapauksissa riittävän tartunnan.

Teräksille kokeiltiin useita eri pintakäsittelyitä. Tavoitteena oli, että pintakäsittely olisi mahdollisimman yksinkertainen ja mielellään mahdollista tehdä konepajaympäristössä ilman pintakäsittelylinjaa. Ennen varsinaista pintakäsittelyä koekappaleille tehtiin rasvanpoisto, joka oli pääsääntöisesti alkalinen pesu (Allaspesu 3). Rasvanpoistoa seurasi yleensä liimapinnan karhennus, joka tehtiin puhaltamalla alumiinioksidilla. Puhalluspölyn puhdistuksen jälkeen tehtiin varsinainen pintakäsittely. Taulukossa 2 on esitetty teräksisille koekappaleille käytetyt pintakäsittelyaineet.

Taulukko 2 Metallisten kappaleiden pintakäsittelyaineet

Lyhenne	Kuvaus
AP	Alkalinen pesu (Allaspesu 3)
EP	Pohjamaali Teroson 1K Etch Primer
S	Silaani Oxsilan MM-0705
BR	Kromaattipohjamaali BR-127
F	Fosfatointi Gardobond A4976
G	Silaani A-187 (OSi Specialities)

2.2 Koemenetelmät

Esikokeissa tutkittiin liimojen ja pintakäsittelyjen ominaisuuksia seuraavin kokein:

1. limiliitoksen vetokoe perustuen standardiin ASTM D 1002
2. lämpötilan vaihtelu (syklaus) ja sitä seuraava limiliitoksen vetokoe standardin DIN EN 1465 mukaisesti
3. kiilakoe perustuen standardiin ASTM D 3762

Limiliitoskoekappaleissa oli toisena liitettävänä materiaalina teräs ja toisena puolena lujitemuovilaminaatti. Koekappaleen leveys oli 25 mm, pituus 191 mm ja limityspituus 12,7 mm. Liitettävien kappaleiden paksuudet vaihtelivat välillä 5,0 ... 11,0 mm. Paksuudet määritettiin siten, että liitettävien kappaleiden taivutusjäykkyydet olivat yhtenevät. Koekappaleet kuormitettiin murtoon vedossa kuormitusnopeudella 1 mm/min. YTI valmisti kaikki limiliitoskoekappaleet. Limiliitosten vetokokeet teki YTI.

Osa limiliitoskoekappaleista lähetettiin Henkelille Saksaan, missä ne altistettiin lämpötilan vaihtelulle. Koekappaleet olivat kuuden syklin ajan ensin 2 tuntia +80 °C:ssa ja sitten 2 tuntia -20 °C:ssa. Altistusten jälkeen koekappaleet pidettiin 24 tunnin ajan +23 °C:n lämpötilassa ja 50 %:n suhteellisessa kosteudessa. Tämän jälkeen koekappaleet koestettiin standardin DIN EN 1465 mukaisesti kuormitusnopeudella 1 mm/min.

Tartunnan ja liiman lujuutta liimasaumaa aukirepivässä kuormituksessa tutkittiin kiilakokein. Myös kiilakoekappaleissa toinen puolisko oli terästä ja toinen lujitemuovia. Koekappaleet perustuivat standardiin ASTM D 3762. Koekappaleen leveys oli 25 mm ja pituus 152 mm. Liimattavien kappaleiden paksuudet poikkesivat standardin mukaisesta paksuudesta. Syynä tähän oli valurautakappaleiden valmistuksen ongelmat. Liitettävien kappaleiden paksuudet määritettiin siten, että liimasaumaa avaavaa kuormitusta kuvaava parametri G oli mahdollisimman sama kaikilla materiaaliyhdistelmillä.

Kokeen aloituksessa koekappaleen puoliskojen väliseen liimasaumaan painetaan määrämittainen kiila. Kiila aiheuttaa liimasaumaan avaavan voiman ja syntyneen särön avautumispituutta mitataan määrätyin välein. Välittömästi kiilan painamisen jälkeen mitattiin alkusärön pituus. Tämän jälkeen kiilakoekappaleet upotettiin +60 °C vesijohtoveteen. Särön etenemistä rekisteröitiin kahden viikon ajan. TKK/KRT valmisti koekappaleet ja teki kokeet.

2.3 Koeohjelma

Esikokeiden koeohjelma on esitetty taulukossa 3 ja pintakäsittelyjen käytetyt lyhenteet taulukossa 4. Muut käytetyt lyhenteet on esitetty aiemmin.

Taulukko 3 Esikokeiden koeohjelma

				Koekappaleiden lukumäärä per koe		
Teräs	**Lujitemuovi**	**Pintakäsittely**	**Liima**	**Limiliitoskoe**	**Syklaus**	**Kiilakoe**
RST/GRP 700	CF-VE	A	EP	6	3	5
RST/GRP 700/Fe52	CF-VE	B	EP	6	3	5
RST/GRP 700/Fe52	CF-VE	C	EP	6	3	5
RST/GRP 700/Fe52	CF-VE	D	EP	6	3	5
Fe52	CF-VE	E	EP	6	3	
RST/GRP 700	CF-VE	A	PMMA	6	3	
RST/GRP 700/Fe52	CF-VE	B	PMMA	6	3	
RST/GRP 700/Fe52	CF-VE	D	PMMA	6	3	
RST/GRP 700	CF-VE	A	MS	6	3	
RST/GRP 700/Fe52	CF-VE	D	MS	6	3	
RST/GRP 700	CF-EP	A	EP	6	3	
RST/GRP 700/Fe52	CF-EP	B	EP	6	3	
RST/GRP 700	CF-EP	C	EP	6	3	
RST/GRP 700	CF-EP	D	EP	6	3	
RST/GRP 700	CF-EP	A	PMMA	6	3	
RST/GRP 700	CF-EP	B	PMMA	6	3	
RST/GRP 700/Fe52	CF-EP	D	PMMA	6	3	
RST/GRP 700	CF-EP	A	MS	6	3	
RST/GRP 700/Fe52	CF-EP	D	MS	6	3	
RST/GRP 700/Fe52	GF-EP	D/D/D	EP	6	3	
RST/GRP 700/Fe52	GF-EP	D/A/D	PMMA	6	3	
RST/GRP 700/Fe52	GF-EP	D/D/D	MS	6	3	
RST	CF-VE	B	EP2	6		
RST	CF-VE	D	EP2	6	3	
Fe52	CF-VE	B	EP2	6		
Fe52	CF-VE	F	EP	6		

Taulukko 4 Esikokeiden pintakäsittelyt

Lyhenne	Kuvaus
A	alkalinen pesu + raepuhallus + BR 127
B	alkalinen pesu + raepuhallus + Terason 1K Etch Primer
C	alkalinen pesu + raepuhallus + silaani (MM-0705)
D	alkalinen pesu
E	rautafosfatointi (A 4932)
F	raepuhallus + paineilmahuuhtelu

2.4 Tulokset

Esikokeiden tulokset voidaan tiivistää seuraavasti:

1. Epoksiliimalla saavutettiin suurin liimaliitoksen lujuus.
2. Lasikuitulujitteisilla kappaleilla oli alhaisempi liitoslujuus kuin hiilikuitulujitteisilla kappaleilla.

3. Epoksiliimalla liitoslujuus valuraudan ja ruostumattoman teräksen liitoksissa vinyyliesterilaminaattiin oli yhtä suuri.
4. MS-elastomeerin lujuus on liian alhainen rakenteellisiin sovellutuksiin.
5. Akryyliliimalla saadaan suurempi liitoslujuus valuraudan ja vinyyliesterilaminaatin välille kuin ruostumattoman teräksen ja vinyyliesterilaminaatin välille.
6. Akryyliliima toimi hyvin kaikkien pintakäsittelyjen kanssa, murtumismuoto oli pääsääntöisesti liiman kohesiivinen pettäminen.
7. Tartuntapohjamaali Terason 1K Etch Primer (pintakäsittely B) tuotti hyvän tartunnan akryyliliiman kanssa, mutta erittäin huonon tartunnan epoksiliimojen kanssa. Pettämismuotona epoksiliimaliitoksissa oli pohjamaalin irtoaminen metallista (adhesiivinen pettäminen) tai itse pohjamaalin sisäisen lujuuden riittämättömyys (pohjamaalin kohesiivinen pettäminen). Akryyliliimalla esiintyi myös jonkin verran tartunnan pettämistä, mutta pääsääntöisesti murtumismuotona oli liiman kohesiivinen murtuma.
8. Kiilakokeissa pintakäsittelyt B ja D toimivat huonosti. Pintakäsittely D:n murtumismuoto oli joissakin ruostumattoman teräksen koekappaleissa tartunnan pettäminen metallista (adhesiivinen pettäminen).
9. Liimasauman jälkikovetus kannattaa aina: terminen syklaus paransi epoksi- ja akryyliliimaliitosten lujuutta 15 – 30 %. MS elastomeerilla parannus oli vähäinen.

2.5 Johtopäätökset

Esikokeiden perusteella pitkäaikaiskokeisiin valittiin liitettäviksi materiaaleiksi ruostumaton teräs, valurauta ja hiilikuituvinyyliesterilaminaatti. Liimoiksi valittiin kaksi epoksia ja akryyliliima. Pintakäsittelyiksi valittiin A, C ja E.

3 PITKÄAIKAISKOKEET

Pitkäaikaiskokeissa tutkittiin ympäristötekijöiden kuten lämmön, kosteuden ja öljyjen vaikutusta liimaliitoksen lujuuteen altistamalla koekappaleet kyseisiin ympäristöolosuhteisiin. Myös väsyttävän ja staattisen pitkäaikaiskuormituksen vaikutuksia tutkittiin pienellä koemäärällä.

3.1 Materiaalit ja pintakäsittelyt

Kohdassa 2.5 esitettyjen materiaalivalintojen lisäksi pitkäaikaiskokeisiin valittiin liitettäväksi materiaaliksi suulakevedetty hiilikuitulujitteinen epoksilatta sekä uudeksi pintakäsittelyksi silaanikäsittely silaanilla A-187. Kyseisessä pintakäsittelyssä rasvanpoistossa käytettiin liuottimena metyylietyyliketonia (MEK). Uusi pintakäsittely merkittiin koeohjelmassa tunnuksella G.

3.2 Koemenetelmät

Pitkäaikaiskokeet käsittivät seuraavat kokeet:

1. leikkauslujuus vanhennuksen jälkeen
2. kiilakoe
3. väsyminen
4. erityisympäristön vaikutus
5. viruminen
6. valuraudan öljyisyyden vaikutus

Vanhennuksessa limiliitoskoekappaleet pidettiin joko sääkaapissa 70 °C:n lämpötilassa ja 85 %:n suhteellisessa ilmankosteudessa tai upotettuna 60 °C vesijohtoveteen 24/72/168/840 tunnin ajan. Tänä aikana koekappaleisiin ei kohdistunut muuta kuin olosuhteista aiheutuva rasitus.

Koekappaleet koestettiin kolmen sarjoissa edellä mainittujen altistusaikojen jälkeen staattisesti vedossa ASTM D1002:n mukaisesti vetonopeudella 1 mm/min. Koekappaleiden lämmön annettiin tasaantua huoneenlämpöön ennen koestusta.

Kiilakokeet tehtiin kohdan 2.2 mukaisesti altistusajan ollessa 840 tuntia (35 vrk).

Väsytyskokeissa verrattiin ensisijaisesti liimojen ominaisuuksia, joten pintakäsittelyiksi valittiin kullekin liimalle parhaiten sopiva pintakäsittely. Koesarjoja oli kolme, joista yksi oli akryylilla liimattu valurauta/vinyyliesterihiilikuitu ja kaksi epokseilla liimattua ruostumaton teräs/vinyyliesterihiilikuitu-yhdistelmää (taulukko 5). Väsytyskokeet pyrittiin tekemään kullekin sarjalle kolmella kuormitustasolla, mutta käytännössä kuormitustasoja oli kolmesta viiteen. Tavoitteena oli valita kuormitustasot siten, että pettäminen tapahtuisi 25 000, 100 000 ja 1000 000 kuormituskerran jälkeen. Kuormituksena oli veto-veto-kuormitus. Minimi vetokuorma kaikissa kokeissa oli 0,5 kN.

Taulukko 5 Väsytyskokeiden koesarjat

Sarja	Materiaalit	Liima	Metallin pintakäsittely	Jälkikovetus	Murto-kuorma
GV3APMMA	Valurauta /vinyyliesterihiili	Akryyli Loctite 3342	Kromaattiprimer BR-127 (A)	2 t 80 °C	6,2 kN
RV3CEP	Ruostumaton teräs /vinyyliesterihiili	Epoksi Hysol 9466	Silaani MM-0705 (C)	Ei	10,0 kN
RV11CEP2	Ruostumaton teräs /vinyyliesterihiili	Epoksi Hysol 9492	Silaani MM-0705 (C)	2 t 80 °C	9,7 kN

Erityisympäristökokeissa limiliitoskoekappaleet upotettiin 70 °C mineraali- ja polyglykoliöljyyn enimmillään 840 tunnin ajaksi. Koeohjelmassa öljyt on merkitty öljy 1 ja öljy 2 vastaavassa järjestyksessä. Öljyt olivat vesihauteeseen upotetuissa säiliöissä, jotka suljettiin kansin altistuksen ajaksi veden kondensaation välttämiseksi. Öljyille suoritettiin vesipitoisuuden määritys Karl Fischer –titrauksella. Mineraaliöljy ei absorboinut lainkaan vettä altistuksen aikana, mutta polyglykoliöljyn vesipitoisuus muuttui 840 tunnin aikana 0,2 %:sta 1,82 %:iin. Mineraaliöljyupotuksen rasittavuutta kasvatettiin lisäämällä öljyn joukkoon aromaattisia hiilivetyjä. Ympäristöaltistettavat limiliitoskoekappaleet olivat kuormittamattomina altistusympäristössä aina koestukseen asti.

Koekappaleet koestettiin kolmen sarjoissa 24/72/168/840 tunnin pituisten altistusten jälkeen staattisesti vedossa ASTM D1002:n mukaisesti vetonopeudella 1 mm/min. Koekappaleiden lämmön annettiin tasaantua huoneenlämpöön ennen testausta.

Virumiskokeessa oli tarkoituksena verrata käytettyjen liimamateriaalien ominaisuuksia. Kullekin liimalle/metallimateriaalille oli valittu etukäteen yksi sille parhaimmaksi arvioitu pintakäsittelymenetelmä. Virumiskokeen tarkoituksena oli löytää kullekin liimalle virumisraja eli se voima, jolla liima alkaa virua huoneenlämpötilassa. Virumisrajan löydyttyä tehtiin virumiskokeita korotetussa lämpötilassa tavoitteena saada kuva virumisnopeudesta lämpötilan funktiona.

Virumiskokeet tehtiin Kevytrakennetekniikan laboratoriossa servohydraulisella aineenkoestuslaitteistolla. Koekappaleita kuormitettiin vakiokuormalla 2 tunnin ajan kerrallaan. Kuormituksen jälkeen koekappaleen annettiin palautua vuorokauden ajan ennen seuraavaa mittausta. Kappaleen virumista mitattiin koelaitteiston oman siirtymäanturin avulla.

Käytössä oleville valurautaisille koneenosille saattaa tulla korjaus- tai muutostarpeita. Tyypillisesti huokoiset valurautaosat ovat käytön aikana imeneet sisäänsä voiteluöljyä ym. liimausta haittaavia epäpuhtauksia. Tällaisten osien liimausmahdollisuuksien tutkimiseksi tehtiin liimauskokeita öljykyllästetyillä valurautakappaleilla.

Valurautaiset koekappaleet pidettiin upotettuina noin viikon ajan sekä mineraali- että polyglykoliöljyssä, jonka jälkeen niille tehtiin rasvanpoisto, pinnan raepuhallus ja pintakäsittely kuten muillekin testatuille limiliitoskappaleille. Myös liimaliitos valmistettiin samoin kuin muissakin kokeissa. Liitokset koestettiin vedossa huoneenlämmössä.

3.3 Koeohjelma

Pitkäaikaiskokeiden koeohjelma on esitetty taulukossa 6.

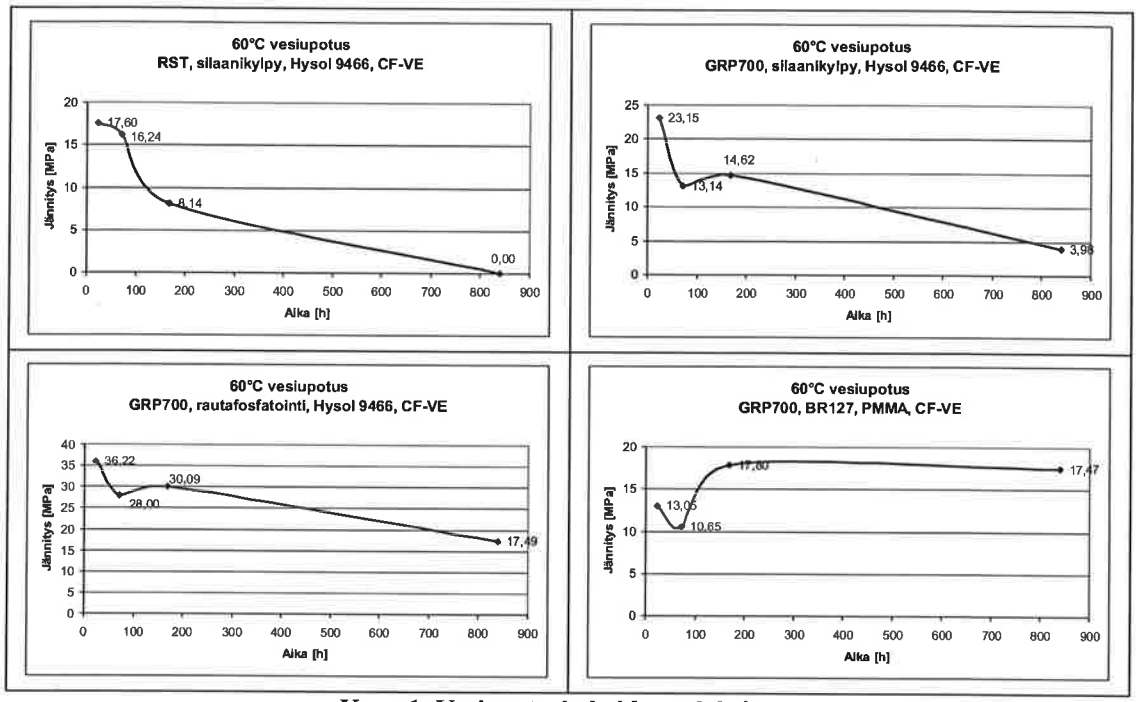
Taulukko 6 Pitkäaikaiskokeiden koeohjelma

				Koekappaleiden lukumäärä per koe							
Teräs	Komposiitti	Pinta-käsittely	Liima	Vanhennus Vesi 60°C 840 h	Vanhennus 70°C + 85%RH 840 h	Kiila-koe Vesi 60°C 840 h	Väsytys RT	Erityisympäristö Öljy 1 70°C 840 h	Erityisympäristö Öljy 2 70°C 840 h	Viruminen	Öljyinen valurauta
RST	CF-VE	C	EP	12	12	5	9	12	12	9	6
GRP700	CF-VE	A	PMMA	12	12	5	9	12	12	9	6
GRP700	CF-VE	C	EP	12		5					
RST	CF-VE	A	PMMA			5		12			
RST	CF-VE	G	EP			5					
RST	CF-EP	C	EP	12		5					
RST	CF-VE	C	EP2	12		5	9	12		9	
GRP700	CF-VE	E	EP	12		5					

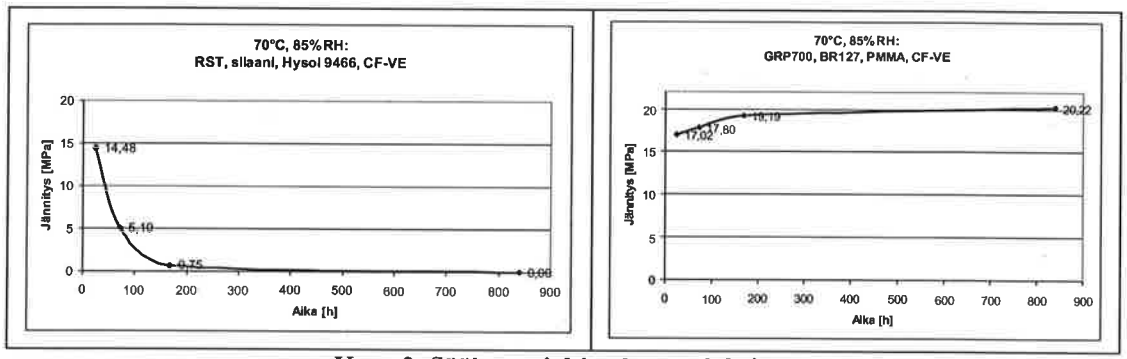
3.4 Tulokset

Kuvassa 1 on esitetty vesiupotuksessa vanhennettujen limiliitoskappaleiden vetokoetuloksia. Huomioitavaa on ruostumattoman teräs/silaani/epoksi/VE-hiilikuitu -yhdistelmän huono ympäristönkesto sekä valurauta/BR127/PMMA/VE-hiilikuitu -yhdistelmän erinomainen ympäristönkesto. Vastaava ilmiö on havaittavissa sääkaappialtistuksissa (kuva 2).

Epoksiliimojen tapauksessa koekappaleiden pääasiallinen murtumismuoto niin vesiupotuksessa kuin sääkaappialtistuksessakin oli tartunnan pettäminen metallipinnasta. Akryyliliimalla liimattujen koekappaleiden pääasiallinen murtumismuoto oli sen sijaan liiman kohesiivinen pettäminen.

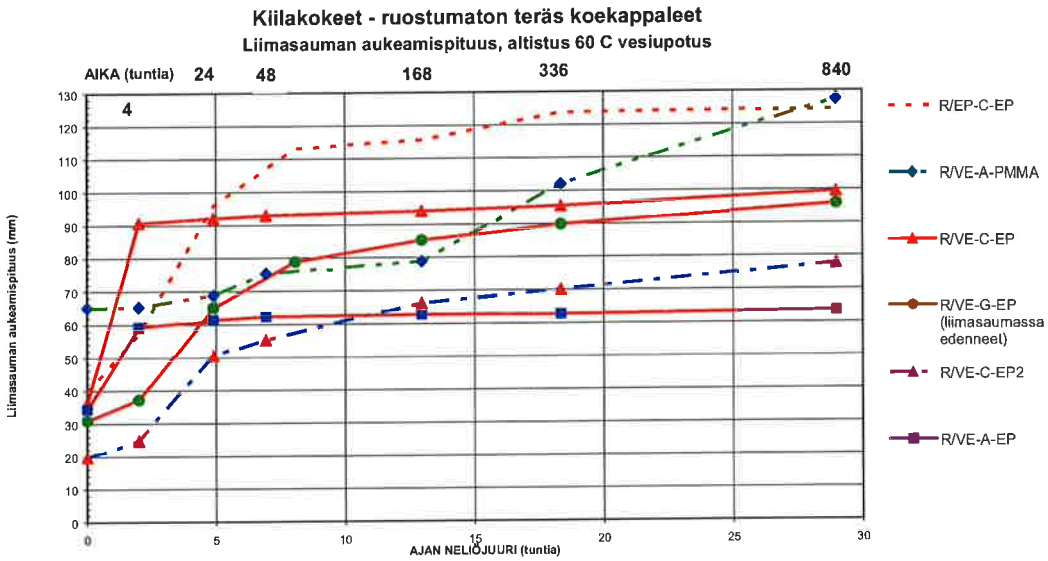


Kuva 1 Vesiupotuskokeiden tuloksia

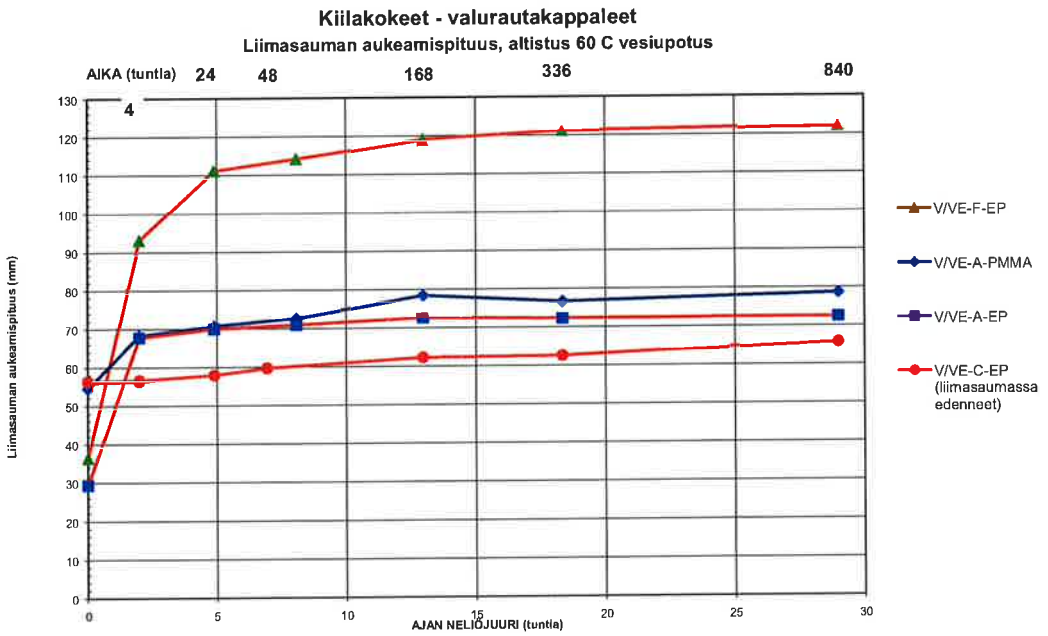


Kuva 2 Sääkaappialtistuksen tuloksia

Kiilakokeiden tulokset on esitetty kuvissa 3 ja 4. Yleisenä havaintona voidaan todeta, että kaikissa tapauksissa särö on kasvanut suhteellisen pitkäksi, mutta toimivilla materiaaliyhdistelmillä särönkasvu on lähes pysähtynyt. Särö kasvoi kaikissa tapauksissa liimasaumassa, joten käytetyt pintakäsittelyt toimivat hyvin koeympäristössä.



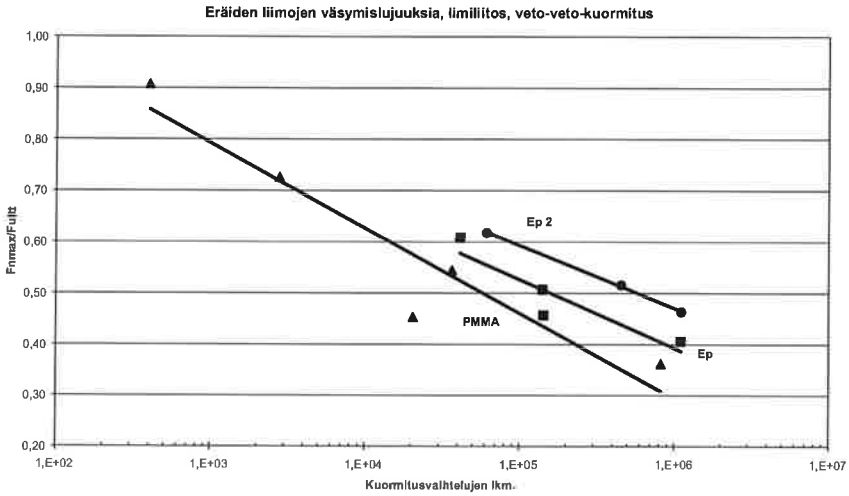
Kuva 3 Ruostumattoman teräksen kiilakoekappaleiden koetulokset



Kuva 4 Valuraudan kiilakoekappaleiden koetulokset

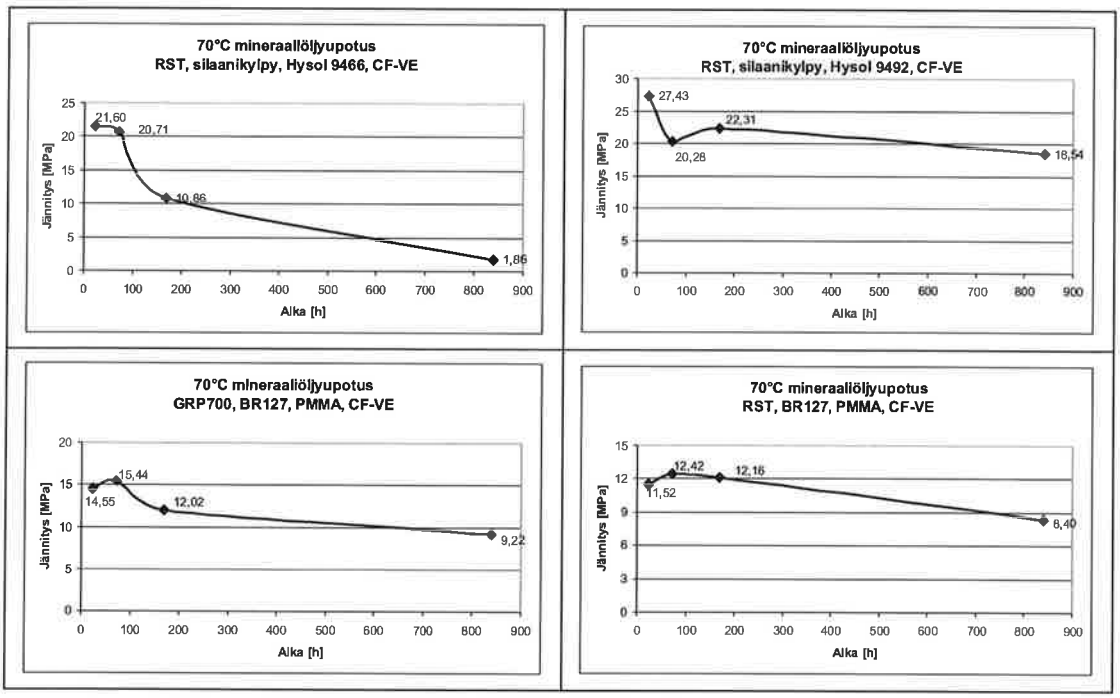
Väsytyskokeiden tulokset osoittavat selkeästi, että epoksiliimojen Hysol 9466 ja Hysol 9492 väsymislujuus on akryyliliimaa Loctite 3342 parempi sekä absoluuttisesti että staattiseen kuormankantokykyyn suhteutettuna (kuva 5). Toisaalta on huomattava, että tulokset perustuvat vain muutamiin väsytettyihin koekappaleisiin, joten tulosten tilastollinen luotettavuus on heikko. Yhdellä kuormitustasolla väsytettiin tyypillisesti kolme koekappaletta, joiden syklien keskiarvo on merkitty kuvaan. Näiden keskiarvojen perusteella on laadittu suuntaviiva (trendline). Murtoon

tarvittavien kuormitussyklien lukumäärä vaihteli suuresti samalla kuormitustasolla, mikä viittaa liimaliitosten epähomogeenisuuteen.

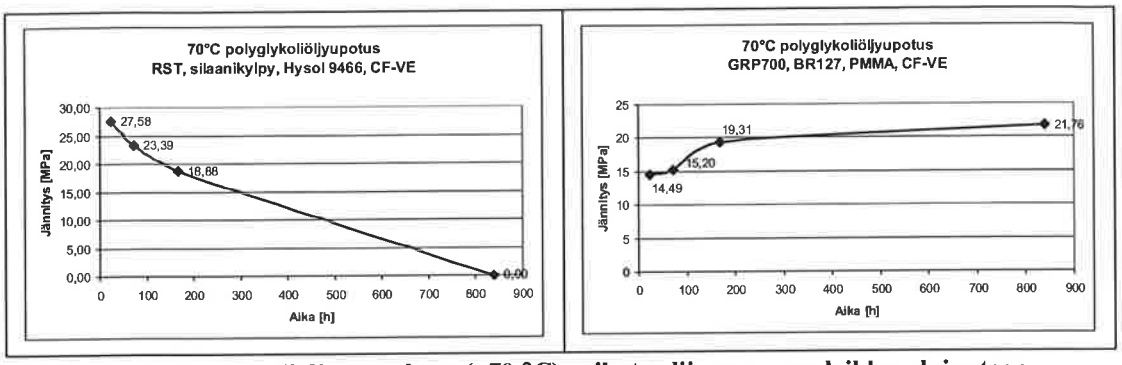


Kuva 5 Väsytyskokeiden tulokset

Kuvassa 6 on esitetty korotetun lämpötilan (+70 °C) mineraaliöljyupotuksen vaikutus liimaliitoksen lujuuteen. Kuvassa 7 on esitetty vastaavan polyglykoliöjyupotuksen tuloksia.



Kuva 6 Mineraaliöljyupotuksen (+70 °C) vaikutus liimasauman leikkauslujuuteen



Kuva 7 Polyglykoliöljyupotuksen (+70 °C) vaikutus liimasauman leikkauslujuuteen

Kuvista havaitaan, että epoksiliima 9466 toimii silaanipintakäsittelyn kanssa huonosti molemmissa öljyissä. Epoksiliima 9492 toimii sen sijaan hyvin mineraaliöljyssä. PMMA-liima toimii molemmissa öljyissä hyvin ja polyglygoliöljyssä jopa erinomaisesti.

Epoksiliimalla liimattujen koekappaleiden pääasiallinen murtumismuoto kummassakin öljyssä oli tartunnan pettäminen metallipinnasta. Akryyliliimalla pääasiallinen murtumismuoto kummassakin öljyssä oli liiman kohesiivinen pettäminen.

Virumiskokeissa mitattava liike oli niin pieni, että siirtymämittauksen tarkkuus ei ollut riittävä. Myös aineenkoestuskoneen rungon lämpötilan vaihteluista johtuvat liikkeet vääristivät mittaustuloksia. Luotettavia virumiskoetuloksia ei näin saatu.

Öljyisen valuraudan koetulokset erosivat selvästi vastaavista öljyaltistamattomien kappaleiden esikokeiden tuloksista. Valurauta/silaani/epoksi/VE-hiilikuitu-materiaaliyhdistelmän keskimääräinen leikkauslujuus oli 90,6 % esikokeissa mitatusta arvosta. Valurauta/strontiumkromaatti/akryyliliima/ VE-hiilikuitu–materiaaliyhdistelmän leikkauslujuus oli vain 70,7 % esikokeiden tuloksista. Liitoksen valmistuksen yhteydessä oli valuraudan pinnassa havaittavissa huokosista pintaan nousevaa öljyä jonkin ajan päästä raepuhalluksesta. Tulosten perusteella alkalisella pesuaineella tehdyllä rasvanpoistolla valuraudan huokosiin jää öljyjäämiä, mikä heikentää tartuntaa. Öljyisen valuraudan rasvanpoistoon tulisi kehittää tehokkaampi menetelmä. Mahdollisesti kyseeseen tulisivat orgaaniset liuottimet ja alipaineimun käyttö.

3.5 Johtopäätöksiä

Pitkäaikaiskokeiden tuloksista voidaan tehdä seuraavat huomiot:

1. Koekappaleet, joissa ruostumattomassa teräksessä oli silaanipintakäsittely (pintakäsittely C) ja liimana epoksi, toimivat huonosti vanhennuksen jälkeen. Toisaalta kiilakokeessa vastaavissa olosuhteissa kyseinen materiaaliyhdistelmä toimi hyvin. Erot johtunevat koekappaleiden erilaisesta kuormittumisesta. Myös liimaliitoksen valmistuksen toteutuksessa on saattanut olla eroavaisuuksia.
2. Koekappaleet, joissa valuraudassa oli pintakäsittely A ja liimana akryyliliima, toimivat erinomaisesti vesiupotuksen, sääkaappialtistuksen ja öljyupotuksen jälkeenkin.
3. Kiilakokeiden perusteella epoksiliima näyttäisi toimivan paremmin vesiupotuksessa (+60 °C) kuin akryyliliima.
4. Epoksihiilikuitulaminaatti toimi kiilakokeissa selvästi huonommin kuin vinyyliesterihiili-kuitulaminaatti.
5. Epoksiliimoilla on parempi väsymislujuus kuin akryyliliimalla. Sitkistetyllä epoksiliimalla on parempi väsymislujuus kuin sitkistämättömällä.

6. Väsytyskokeissa suuri tulosten hajonta vaikeutti tulosten tulkintaa.
7. Liimaliitoksen virumisen mittaaminen on vaikeaa johtuen hyvin pienistä mitattavista siirtymistä.
8. Tehtyjen kokeiden perusteella suositeltavin pintakäsittely tutkituille teräksille on kromaattipohjamaaliin perustuva pintakäsittely A.

4 YHTEENVETO

Tutkimuksen perusteella ei löydetty yhtä pintakäsittelyä, joka olisi toiminut hyvin kaikkien liimojen ja terästen kanssa. Liimaliitosten lujuuden muutokset eri ympäristöissä olivat merkittäviä. Samaten väsyttävässä kuormituksessa liimojen erot väsymislujuuden suhteen tulivat selvästi esiin. Hiilikuitulujitteisen muovikomposiitin matriisimateriaalilla oli myös merkittävä vaikutus liitoksen lujuuteen ainakin ruostumattoman teräksen liitoksissa. Huoneenlämpötilassa kovettuva liimaliitos kannattaa jälkikovettaa aina, kun se vain on mahdollista.

VIITTEET

1. ASTM D 1002 Test Method for Strength Properties of Adhesives in Shear by Tension Loading (Metal-to-Metal)

2. DIN EN 1465 Adhesives - Determination of tensile lap-shear strength of rigid-to-rigid bonded assemblies

3. ASTM D 3762 Test Method for Adhesive-Bonded Surface Durability of Aluminum (Wedge Test)

VERIFICATION OF A REYNOLDS-AVERAGED NAVIER-STOKES SOLVER FOR DIRECT NUMERICAL SIMULATION OF TURBULENT FLOW

J. SALORANTA, A. HELLSTEN

Helsinki University of Technology, Laboratory of Aerodynamics,
P.O.BOX 4400 FIN-02015 TKK,
e-mail: jsaloran@cc.hut.fi
e-mail: antti.hellsten@tkk.fi

ABSTRACT

In the present work we study the suitability of the finite-volume based FINFLO flow solver for direct numerical simulation (DNS) of turbulent flow. FINFLO is originally developed for the numerical solution of the Reynolds-averaged Navier-Stokes equations (RANS). DNS poses quite different requirements for the numerical methods applied than RANS, so formally higher-order schemes were implemented for both spatial and temporal discretization. The results indicated that FINFLO is capable of this kind of simulations and the obtained solution is converging towards the reference one, but the grid convergence rate is noticeable slower than with codes specially developed for DNS and large eddy simulations (LES). This seems to be the case even when formally fourth-order schemes are used for spatial discretization.

1 INTRODUCTION

There is a growing need to perform LES and DNS for turbulent flows in complex geometries. RANS simulations are known to predict poorly flows that are massively detached, for example a flow around an aeroplane at high angle of attack. Most of the versatile general in-house and commercial computational fluid-dynamics (CFD) codes are originally developed for RANS and yet they are increasingly used in LES and DNS. Both LES and DNS are known to be very sensitive to applied numerical methods and the accuracy of the results cannot be guarenteed when RANS solvers are used.

Most of the flows encountered in engineering practice are at least partially turbulent. Turbulent flows are three-dimensional, unsteady, randomly fluctuating and highly vortical and contain a wide range of scales both in time and space. In RANS-simulations the whole turbulence is modelled. In LES, as the name implies, only the large eddies are resolved and the smaller scales are modelled. In DNS the Navier-Stokes equations are solved without any averaging or modelling other than the necessary spatial and temporal discretization. From the conceptual point of view, it can be seen as the simplest approach to study turbulent flows. With the present computational resources, DNS is possible only at the low Reynolds numbers. This is due to the fact that the computational grid must be dense enough to describe even the smallest length scales of turbulence. However, DNS is a valid research tool and its use is essentially limited only by the available computational resources [1].

In the present work, we study the suitability of the finite-volume based FINFLO solver for direct numerical simulation (DNS) of turbulent flow. The FINFLO solver is developed in the Laboratory of Aerodynamics of Helsinki University of Technology and it has been used almost exclusively to RANS-simulations of turbulent flows [2]. In future, FINFLO is planned to be used for LES and RANS-LES hybrid simulations, and this work is a part of that process. The present version of FINFLO is a density based solver for compressible flow , while the codes developed for LES and DNS of turbulent flows are usually based on pressure correction method formulated for incompressible flow.

The test case in this study is a fully developed turbulent channel flow between two parallel walls at $Re_\tau = 180$ referred to friction velocity and channel half height. The Reynolds number referred to mean velocity and channel height is 5600. This case was chosen because high-quality reference data from spectral DNS is available [3] and this particular flow case has also been studied extensively at Laboratory of Aerodynamics and at Laboratory of Applied Thermodynamics using codes specially developed for LES and DNS [4,5].

2 NUMERICAL METHODS

2.1 Conservation law

For an arbitrary volume Ω, bounded by a surface S, one can write a conservation law

$$\frac{\partial}{\partial t}\int_\Omega \phi \, d\Omega + \int_S \vec{F} \cdot d\vec{S} = \int_\Omega Q \, d\Omega \tag{1}$$

where Q is a volume source, $\vec{F}$ is the flux of quantity ϕ and $d\vec{S}$ is the surface increment vector normal to surface S. Using Gauss's theorem for volume integrals ($\int_S \vec{F} \cdot d\vec{S} = \int_\Omega \nabla \cdot \vec{F} \, d\Omega$) Equation (1) can be written in the following form.

$$\frac{\partial}{\partial t}\int_\Omega \phi \, d\Omega + \int_\Omega \nabla \cdot \vec{F} \, d\Omega = \int_\Omega Q \, d\Omega \tag{2}$$

The above equations are the basis of the finite volume based solvers. The latter is used to derive the differential form and the first one to derive the integral form of the governing equations [6].

2.2 Governing equations in differential form

Because Equation (2) holds true to any volume Ω, the Navier-Stokes equations for compressible flow can be written in the following differential form

$$\frac{\partial U}{\partial t} + \frac{\partial (F_c - F_v)}{\partial x} + \frac{\partial (G_c - G_v)}{\partial y} + \frac{\partial (H_c - H_v)}{\partial z} = Q \tag{3}$$

where U is the vector of conservative variables and it can be written as $U = (\rho,\, \rho u,\, \rho v,\, \rho w,\, \rho E)^T$. Subscripts c and v refer to convective and viscous fluxes. The convective fluxes are

$$F_c = \begin{pmatrix} \rho u \\ \rho u^2 + p \\ \rho v u \\ \rho w u \\ (\rho E + p)u \end{pmatrix}, \; G_c = \begin{pmatrix} \rho v \\ \rho u v \\ \rho v^2 + p \\ \rho w v \\ (\rho E + p)v \end{pmatrix}, \; H_c = \begin{pmatrix} \rho w \\ \rho u w \\ \rho v w \\ \rho w^2 + p \\ (\rho E + p)w \end{pmatrix} \tag{4}$$

where ρ is density and the velocity vector is defined as $\vec{V} = u\vec{i} + v\vec{j} + w\vec{k}$. The total energy ρE is defined as

$$\rho E = \rho e + \rho \frac{u^2 + v^2 + w^2}{2} \tag{5}$$

where e is the specific internal energy. The pressure is calculated from equation of state $p = p(\rho, e)$ and for calorically perfect gas it is

$$p = \rho RT = (\gamma - 1)\rho e \tag{6}$$

where γ is the ratio between specific heats c_p and c_v. The viscous fluxes are respectively

$$F_v = \begin{pmatrix} 0 \\ \tau_{xx} \\ \tau_{yx} \\ \tau_{zx} \\ u\tau_{xx} + v\tau_{xy} + w\tau_{xz} + k\frac{\partial T}{\partial x} \end{pmatrix}, G_v = \begin{pmatrix} 0 \\ \tau_{xy} \\ \tau_{yy} \\ \tau_{zy} \\ u\tau_{yx} + v\tau_{yy} + w\tau_{yz} + k\frac{\partial T}{\partial y} \end{pmatrix},$$

$$H_v = \begin{pmatrix} 0 \\ \tau_{xz} \\ \tau_{yz} \\ \tau_{zz} \\ u\tau_{zx} + v\tau_{zy} + w\tau_{zz} + k\frac{\partial T}{\partial z} \end{pmatrix} \tag{7}$$

In viscous fluxes T stands for temperature and k is the heat conductivity coefficient. The terms of the viscous stress tensor τ_{ij} are defined as

$$\tau_{ij} = \mu \left[\frac{\partial u_j}{\partial x_i} + \frac{\partial u_i}{\partial x_j} - \frac{2}{3}\frac{\partial u_k}{\partial x_k}\delta_{ij} \right], \delta_{ij} = \begin{cases} 1 & \text{, when } i = j \\ 0 & \text{, when } i \neq j \end{cases} \tag{8}$$

where μ is the dynamic viscosity defined from Sutherland's formula. The vector Q includes the source terms and it has the following form

$$Q = \begin{pmatrix} 0 \\ \rho f_{ex} \\ \rho f_{ey} \\ \rho f_{ez} \\ \rho(u f_{ex} + v f_{ey} + w f_{ez}) + Q_H \end{pmatrix} \tag{9}$$

where f_{ex}, f_{ey} and f_{ez} are the components of the volume force vector and Q_H is a heat source.

2.3 Finite-volume method

In finite volume method (FVM) the computational domain is divided to control volumes. The control volume is usually called a cell in CFD. The finite volume form can be derived from the integral form of Equation (3) that can be written as

$$\frac{\partial}{\partial t}\int_\Omega U \, d\Omega + \int_S \vec{F} \cdot d\vec{S} = \int_\Omega Q \, d\Omega \tag{10}$$

In Figure 1 is presented the notations used in this work. The upper case letters refer to cells and the lower case letters refer to cell faces as shown in Figure 1. Using these notations the approximation for integral over surface S_e can be written as

$$\int_{S_e} \vec{F} \cdot d\vec{S} = \overline{F}_e S_e \approx F_e S_e \tag{11}$$

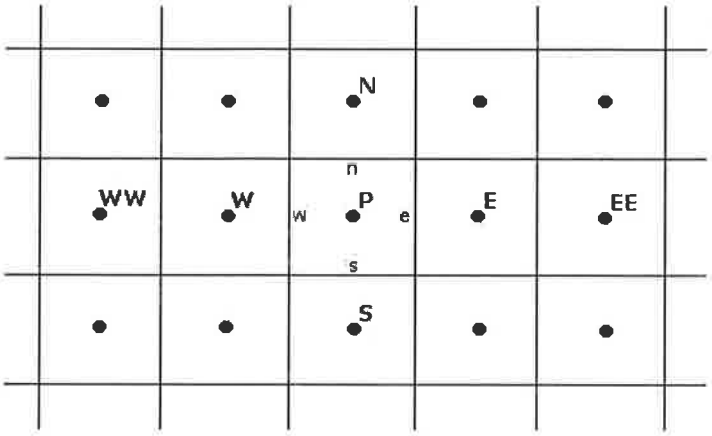


Figure 1: Cell notations used in this paper [7]

which is called a midpoint rule [7]. The overbar in above equation denotes the average over surface S_e and it is further approximated to be a function of the neighbouring cells.

So the Equation (10) can be written in the following form

$$\Omega_i \frac{dU_i}{dt} = -\sum_{\text{faces}} FS + \Omega_i Q_i \tag{12}$$

when applied to a cell i. Thus the problem is to define the fluxes F at the faces of cell i and it will be discussed in the next section. The Equation (12) is said to limit the spatial accuracy to second-order, but as shown in the next section, this is not necessarily the case. Higher-order approximations for surface integral are possible , for example Simpsons rule in two dimensional case [7], but their implementation to three dimensions is complex.

2.4 Spatial discretization

As mentioned, DNS is very sensitive to the choice of the numerical methods. Upwind-biased schemes used for convection terms in RANS contain numerical dissipation, which is not favourable in DNS of turbulent flows. Instead, central schemes are used, and they are not dissipative but dispersive by nature. Various combinations of formally 2nd- and 4th-order central schemes are used in the present work for convection plus pressure gradient and diffusion.

In this work, the finite difference method (FDM) is used to derive the equations for flux calculation at cell faces. On uniform orthogonal grid, FVM is equal to FDM in some simple linear cases. In the following examples the grid is assumed uniform and thus S and Ω are constants. Let us consider a one-dimensional continuous distribution of variable T at cell center in x-direction and a constant convection velocity u. This can be written as a simple convection equation

$$\frac{\partial T}{\partial t} + \frac{\partial uT}{\partial x} = \frac{\partial T}{\partial t} + u\frac{\partial T}{\partial x} = 0. \tag{13}$$

Second-order FDM approximation for the derivative of T at cell P is

$$\left(\frac{\partial T}{\partial x}\right)_P \approx \frac{T_E - T_W}{2\Delta x} \tag{14}$$

when notations shown in Figure 1 are used. Δx is the grid spacing in x-direction. When FVM is used, the flux is simply $F = uT$ and with constant u, only T needs to be approximated at cell faces. If the second-order approximation, which is simply an average, is used to calculate the cell face values T_e and T_w, the following is obtained from Equation (12)

$$\frac{\partial T}{\partial t} = \frac{S}{\Omega}\Big(-u\frac{T_P + T_E}{2} + u\frac{T_P + T_W}{2}\Big) = -u\frac{T_E - T_W}{2\Delta x} \tag{15}$$

which is identical to one obtained from (13) and (14). The flux in Equation (15) is assumed positive, when effecting in positive x-direction. The similarity between FDM and FVM schemes is used, when higher-order discretization schemes are derived for FVM.

As said earlier, Equation (12) is said to limit the spatial accuracy to second-order, even when higher-order schemes are used to calculate the fluxes. There is, however a way to trick the order of accuracy to be higher than two in linear cases. First, we choose a higher-order FDM scheme and then define the equation for cell face values in a way, that it gives us the chosen FDM scheme when used with Equation (12). A fourth-order difference approximation for the derivative of T by means of FDM is

$$\Big(\frac{\partial T}{\partial x}\Big)_P \approx \frac{-T_{EE} + 8T_E - 8T_W + T_{WW}}{12\Delta x}. \tag{16}$$

It is easy to prove that if we calculate the cell face values from the equation:

$$T_e \approx \frac{-T_{EE} + 7T_E + 7T_P - T_W}{12} \tag{17}$$

we end up in form identical to one obtained from Equations (13) and (16). So the formal order of spatial accuracy can be higher than two, despite the limitations related to Equation (12). The Equation (17) is in fact only second-order accurate for cell face values, but when combined with Equation (12) the result is fourth-order accurate. This is unfortunately true only, if the grid is uniform and we have a linear equation. For example, in FINFLO the cell face value for term ρuv is calculated as

$$(\rho uv)_e = \rho_e u_e v_e$$

so every variable is extrapolated individually to the cell face. This yields to the following derivative approximation on uniform grid spacing, when Equation (17) is used

$$\begin{aligned}\frac{\partial \rho uv}{\partial x} = {} & \frac{\rho_e \cdot u_e \cdot v_e - \rho_w \cdot u_w \cdot v_w}{\Delta x} \\ & - \frac{\Delta x^2}{12} \cdot \Big(\rho\frac{\partial}{\partial x}\Big[\frac{\partial u}{\partial x}\frac{\partial v}{\partial x}\Big] + v\frac{\partial \rho}{\partial x}\frac{\partial^2 u}{\partial x^2} + u\frac{\partial \rho}{\partial x}\frac{\partial^2 v}{\partial x^2} \\ & + 3\Big[\frac{\partial u}{\partial x}\frac{\partial v}{\partial x}\frac{\partial \rho}{\partial x}\Big] + \frac{\partial^2 \rho}{\partial x}\frac{\partial uv}{\partial x}\Big) + O(\Delta x^4)\end{aligned}$$

and we can see that it is no longer fourth-order accurate even for uniform grid spacing. One possibility would be, to calculate all the terms presented in Equations (4) and (7) at cell centers and after that extrapolate these terms to cell faces. However, it would mean more computational work and it would also increase the memory requirements so it was not used at present simulations. By means of error analysis methods, it can be shown that even though the order of accuracy is reduced to second with nonlinear terms, the use of higher-order schemes in defining the cell face values, does reduce the effective truncation error [8].

The diffusion terms are evaluated using a thin-layer approximation, which is equal to FDM in case of orthogonal grids. The fourth-order scheme for diffusion terms is obtained similarly as shown above for convection terms, by choosing a fourth-order FDM scheme for the second derivative and deriving the formula for cell face values from that.

2.5 Temporal discretization

The standard time accurate scheme in FINFLO is a second-order three-level fully implicit time integration method. However, in this work the time integration is performed using a 3rd-order 4-step compact Runge-Kutta scheme. This is an explicit scheme, so the time-step Δt is limited by the Courant-number (CFL) of the smallest cell. CFL is defined as $CFL = \Delta t \cdot (|u_i \pm c|)/\Delta x_i$, where subscript i refer to coordinate direction and c is the local speed of sound. Thus the CFL defines the number of times the acoustic waves moving at the characteristic velocity $u_i \pm c$ pass through a cell in x_i-direction during one timestep. This is one of the reasons for long computational times per one simulation. The CFL stability limit for this scheme is $\sqrt{8}$. For the present simulations the time integration scheme can be written as [9]

$$\begin{aligned} U^* &= U^n + \frac{8}{17}\frac{\Delta t}{\Omega}R(U^n) \\ U^{**} &= U^* + \frac{17}{60}\frac{\Delta t}{\Omega}R(U^*) - \frac{15}{68}\frac{\Delta t}{\Omega}R(U^n) \\ U^{***} &= U^{**} + \frac{5}{12}\frac{\Delta t}{\Omega}R(U^{**}) - \frac{17}{60}\frac{\Delta t}{\Omega}R(U^*) \\ U^{n+1} &= U^{***} + \frac{3}{4}\frac{\Delta t}{\Omega}R(U^{***}) - \frac{5}{12}\frac{\Delta t}{\Omega}R(U^{**}), \end{aligned} \tag{18}$$

where superscripts *, ** and *** refer to the solutions on intermediate time steps and the superscripts n and $n+1$ refer to the old and new time steps. R is called residual, and it is the right hand side of Equation (12). R is a function of the fluxes and source terms, and it is computed at every intermediate time step, so the governing equations are solved four times inside one physical time step. This means extra computational effort, but only one previous step result has to be stored in memory. The larger time step allowed by the Runge-Kutta scheme compensates some of the extra computational work and it has turned out to be quite effective at present simulations. For more complex flow cases the efficiency of Runge-Kutta drops and the implicit higher-order schemes are more suitable ones.

3 FULLY DEVELOPED TURBULENT CHANNEL FLOW

The DNS test case for FINFLO solver in the present work is a fully developed turbulent channel flow. It is widely used in studies of DNS and LES of turbulent flows e.g. [3, 4, 10]. The Reynolds number $Re_\tau = 180$ is based on friction velocity and channel half height. Friction velocity is defined as $\sqrt{\tau_w/\rho}$, where τ_w is the wall-shear stress.

The simulations were performed with various grid resolutions and domain sizes and different spatial discretization schemes were also tested. Most of the calculations were performed on *Scientific Computing Ltd.*'s (CSC) supercomputer *SEPELI*. DNS of turbulent flow is very time consuming and with the finest applied grid, one calculation took over a month running on 16 processors. The applied channel dimensions and grid resolutions are presented in Table 1, where MKM, TB and PM refer to [3–5] respectively.

The fact that FINFLO solves the Navier-Stokes equations for compressible flow limits the minimum possible Mach number to around 0.2. This is a common problem with density

Table 1: Domain dimensions and grid resolutions

	grid 1 / TB	grid 2	grid 3	MKM	PM
channel length/height	2.0	4.0	4.0	2π	3.2
channel width/height	1.6	2.0	2.0	$\frac{2}{3}\pi$	1.6
number of grid points:					
streamwise	80	96	128	128	64
wall normal	80	96	128	129	64
spanwise	64	128	128	128	64
resolution in wall unit:					
streamwise	9.0	15.0	11.25	17.7	18.0
wall normal (min)	0.63	0.74	0.55	0.11	1.0
wall normal (max)	6.96	7.12	5.39	8.74	16.8
spanwise	9.0	5.63	5.63	5.9	9.0

based solvers and the reason for this limit is the large ratio between acoustic and convective speeds at low Mach numbers. This leads to ill-conditioned flux Jacobian matrices. Lower Mach numbers are possible, when preconditioning is used, but it requires the use of implicit time integration [11]. In this work the Mach numbers 0.2 and 0.3 are used.

3.1 Boundary conditions

In streamwise and spanwise directions periodic boundary conditions are applied and no-slip condition is assumed on channel walls. The walls are also assumed to be adiabatic. The flow is driven by a uniform body-force effecting in streamwise direction and it is adjusted to give the desired Re_τ. The heat generated by viscous effects is removed using negative heat sources. When boundary conditions are defined in this way, the governing equations are numerically conservative apart from the streamwise momentum equation and the periodic boundary conditions can be used without problems.

3.2 Results

In this section, results from five different cases are discussed and the case definitions for them are presented in Table 2. The order of accuracy refers to formal order of accuracy for cell face values. Conclusions from cases other than shown here are discussed briefly at the end of this section.

Table 2: Case parameters

	case 1	case 2	case 3	case 4	case 5
grid	1	1	2	3	3
Mach number	0.2	0.3	0.3	0.3	0.3
formal order of accuracy:					
convection terms	2	4	4	4	4
diffusion terms	2	2	2	2	4

The obtained results are compared to reference data from [3–5] referred here to as MKM,

TB and PM respectively. MKM results are from spectral DNS and are widely used as a reference data. In TB the equations are solved using a pressure-correction based solver and a staggered grid. PM results are from a pressure correction based solver and a collocated grid is used. Thus the methods used at present work and the ones used in PM are most alike.

During the simulations, the instantaneous values of the conservative variables were stored in memory with a constant interval. When defined as follows, the interval in case 1 was $\Delta\tau \cdot U_{ref}/h = 0.05s \cdot 72.0\frac{1}{s} = 3.6$ and in cases 2–5 it was $\Delta\tau \cdot U_{ref}/h = 0.035s \cdot 105.0\frac{1}{s} = 3.7$, where U_{ref} is the mean value of streamwise velocity averaged in all coordinate directions and referred to channel height h and the $\Delta\tau$ is the physical interval in seconds. In all cases, the simulation was continued until at least two hundred of these were stored. With the finest grid applied this produced almost 40GB of raw data per one simulation. The Favre-averaging was then applied in streamwise and spanwise directions and in time. All velocities are decomposed to a mass-averaged part and to a fluctuating part denoted by superscript $''$, and they are scaled with the friction velocity u_τ. Coordinates are scaled with channel height h. The wall unit x_i^+ is defined as $x_i^+ = u_\tau x_i/\nu$, where subscript i refers to coordinate direction and ν is the kinematic viscosity defined as $\nu = \mu/\rho$.

One of the primary goals of this work was to study the benefits of the formally fourth-order central scheme compared to second-order one, for both convective and viscous terms. At first was studied the effect of fourth-order central scheme on discretization of the convection terms. In Figure 2 is presented the mean streamwise velocity U_{mean} and the Reynolds stress $\overline{\rho u'' v''}/\overline{\rho}$ for cases 1 and 2. The use of formally fourth-order central scheme improves

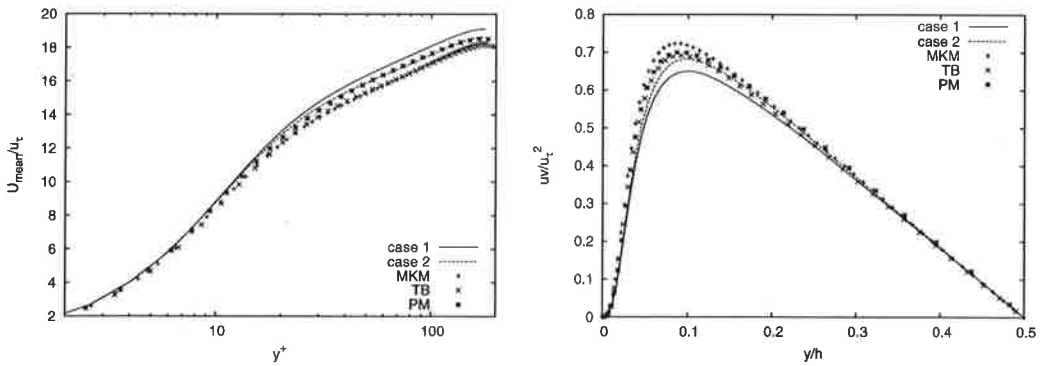


Figure 2: mean streamwise velocity U_{mean} and Reynolds stress $\overline{\rho u'' v''}/\overline{\rho}$ from case 1 and 2

both U_{mean} and $\overline{\rho u'' v''}/\overline{\rho}$ noticeably. But when compared with TB and PM against MKM, the results are still not as good, eventhough those are obtained with a second-order central scheme. In Figure 3 is shown the root mean square (RMS) values of the velocity fluctuation $u_{rms} = \sqrt{\overline{\rho u'' u''}/\overline{\rho}}$ in streamwise and $v_{rms} = \sqrt{\overline{\rho v'' v''}/\overline{\rho}}$ in wall-normal direction. The behaviour of RMS velocity fluctuation in spanwise direction is similar to the wall-normal velocity fluctuation and is not presented in this paper. The use of fourth-order central scheme on convective terms does not effect the u_{rms} much and it seems to be predicted most accurately out of the RMS of the velocity fluctuations. The change in v_{rms} does however clearly show the benefits of the fourth-order scheme compared to second-order one. The v_{rms} is throughoutly closer to reference values, but it is still underpredicted especially in the region of $y/h = 0.05 \ldots 0.25$.

The cases 1 and 2 showed that the results are qualitatively correct, but there is still a

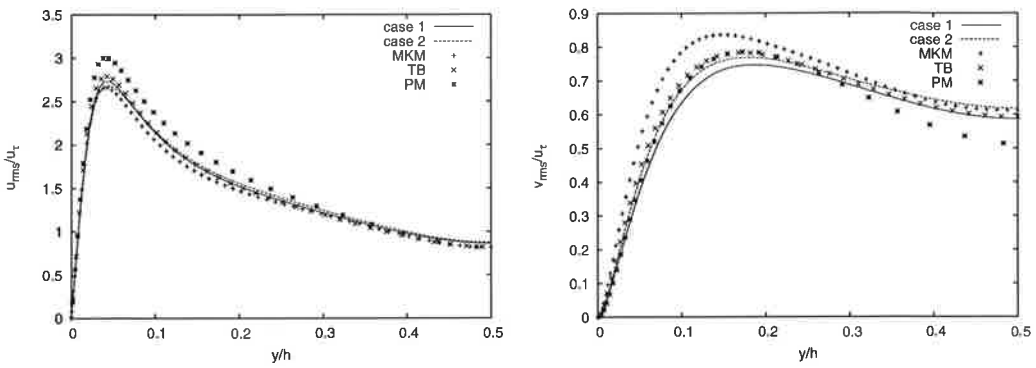


Figure 3: the RMS velocity components $\sqrt{\overline{\rho u'' u''}/\overline{\rho}}$ and $\sqrt{\overline{\rho v'' v''}/\overline{\rho}}$ of case 1 and 2

big difference to reference values. The next step was to find out the effect of domain size and grid resolution, thus a grid convergence study was performed. The grid convergence was studied with three different grids as presented in Table 1 and the case parameters are shown at Table 2. In Figure 4 is presented the mean streamwise velocity U_{mean} and the Reynolds stress $\overline{\rho u'' v''}/\overline{\rho}$ for cases 2, 3 and 4. The mean streamwise velocity is very similar

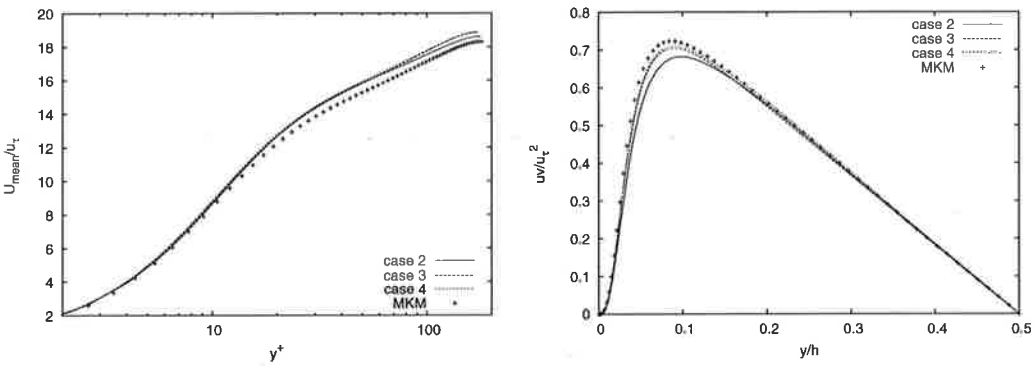


Figure 4: mean streamwise velocity U_{mean} and Reynolds stress $\overline{\rho u'' v''}/\overline{\rho}$ from cases 2, 3 and 4

in all of the three cases. The improvements in Reynolds stress $\overline{\rho u'' v''}/\overline{\rho}$ are noticeable, when the grid is refined. The step from case 3 to case 4 is minor, when we look at the Reynolds stress figure, but the curves of the RMS velocity components $\sqrt{\overline{\rho u'' u''}/\overline{\rho}}$ and $\sqrt{\overline{\rho v'' v''}/\overline{\rho}}$ in Figure 5 show that the improvement on individual fluctuating terms is larger. The u_{rms} is well predicted in cases 3 and 4, but the v_{rms} is still underpredicted in a large part of the channel. The grid convergence is obvious but slower than in TB and PM, even when formally fourth-order scheme is used for spatial discretization.

In all of the cases the mean streamwise velocity is overpredicted. This is caused by the underpredicted skin friction coefficient C_f. In Table 3 is presented the skin friction coefficient and the ratio between U_{ref} and u_τ for all five cases as well as the MKM values. The difference to MKM is caused mainly by the underpredicted u_τ, and the reason may be that the grid resolution in wall-normal direction near the wall is too coarse.

The terms of the transport equation for turbulent kinetic energy were also analysed, and

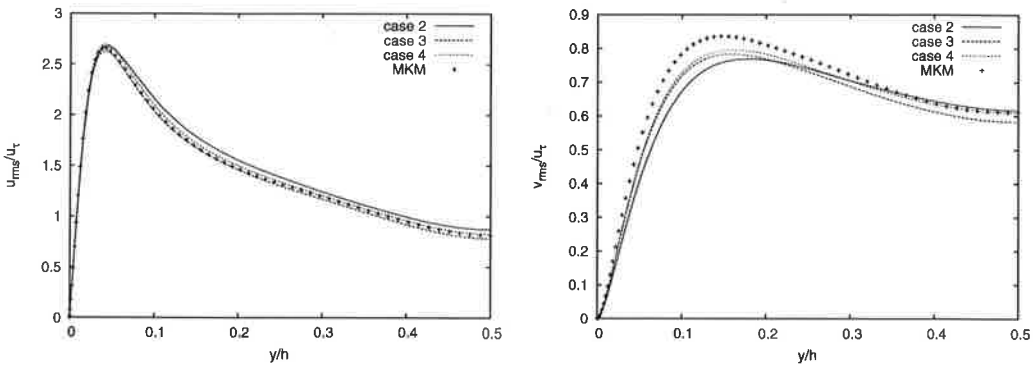


Figure 5: the RMS velocity components $\sqrt{\overline{\rho u'' u''}/\overline{\rho}}$ and $\sqrt{\overline{\rho v'' v''}/\overline{\rho}}$ of cases 2, 3 and 4

Table 3: The skin friction coefficient C_f and the ratio between U_{ref} and u_τ

	case 1	case 2	case 3	case 4	case 5	MKM
C_f	$7.32\text{x}10^{-3}$	$7.77\text{x}10^{-3}$	$7.68\text{x}10^{-3}$	$7.64\text{x}10^{-3}$	$7.61\text{x}10^{-3}$	$8.18\text{x}10^{-3}$
U_{ref}/u_τ	16.52	16.05	16.14	16.18	16.22	15.63

in compressible flow it has the following form

$$\overline{\rho}\frac{\partial k}{\partial t} + \overline{\rho}\widetilde{u}_j\frac{\partial k}{\partial x_j} = P - \varepsilon + \frac{\partial}{\partial x_j}\left[\overline{\tau_{ij}u_i''} - \overline{\rho u_j''\frac{1}{2}u_i''u_i''} - \overline{p'u_j''}\right] - \underbrace{\overline{u_i''}\frac{\partial p}{\partial x_i}}_{\text{PW}} + \underbrace{\overline{p'\frac{\partial u_i''}{\partial x_i}}}_{\text{PDila}} \tag{19}$$

The equation has two additional terms when compared to one for incompressible flow [12]. These terms vanish when density ρ is constant, as expected. On the left hand side in Figure 6 is presented the calculated terms of the k transport equation from case 4. All other terms fall into reference ones, except the dissipation ε, which is too small. We can see that the first additional term called pressure dilatation (PDila) is very small in this case. The second additional term, pressure work (PW), however plays an significant role. It can be interpret as an dissipative term and physically it can be seen as a process where kinetic energy is dissipated to heat due to compressibility of the flow. On the right hand side in Figure 6 is plotted the ratio between production P and dissipation ε form case 4. The ratio is shown for dissipation only and for a sum of dissipation and pressure work. The ratio for dissipation only is too large, but the sum curve is relatively close to MKM. This validates the dissipative nature of the pressure work term in this flow case. The balance of the transport equation for k should fall to zero. In cases 4 and 5 it is negative throughout the channel and it has slightly bigger variations than MKM. It is not clear what this means physically, but most likely it tells us from the error related to applied numerical methods.

The fourth-order central scheme for viscous terms was analysed in case 5. When results from case 5 were compared with case 4, they were almost identical. A slight improvement was found in spanwise and wall-normal RMS of velocity fluctuations. Thus it seems that the second-order central scheme is the most feasible choice for spatial discretization of viscous terms due to its easy use, when complex geometries are modelled.

The effect of Mach number on results was also tested. A simulation was performed on Mach numbers 0.2 and 0.3, while other parameters were kept exactly the same. The effect

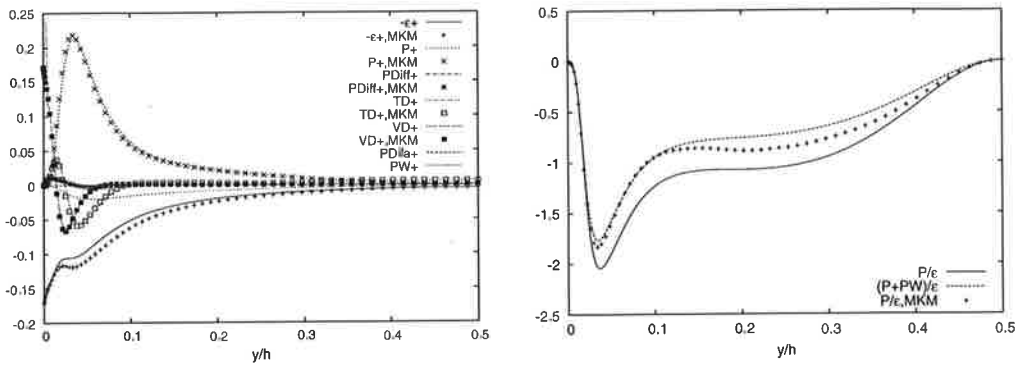


Figure 6: Terms of the transport equation for k and the ratio between production and dissipation from case 4

of Mach number was small, but 0.3 was a bit better and was chosen for the rest of the simulations. This particular flow case has been studied also in [13] at Mach number 0.3 and the results compare very well with MKM. This implies that the flow can be considered incompressible even at $Ma = 0.3$. It also means that the difference between present and MKM results comes most likely from the numerics rather than from the physics. The effect of computer round-off error was studied with a solver compiled to double precision. Practically it had no effect on the results, but the global conservation of mass and total energy became practically exact. When single precision is used, they both have a little variation during the simulation.

4 CONCLUSIONS

The obtained results indicate that FINFLO is indeed capable of DNS of turbulent flows. However, the poor grid convergence compared to codes specially developed for DNS and LES is evident. The difference between FINFLO and these codes is, that FINFLO solves Navier-Stokes equations for compressible flow while the special codes are usually formulated for incompressible flow. From this, one can conclude that the difference between FINFLO results and the reference data relates somehow to treatment of pressure. It seems that the difference in results is due to the numerics rather than the physics, as mentioned in the previous section. The density based solvers are known to behave poorly at low Mach numbers. Thus it is necessary to implement some method for incompressible flows to FINFLO, if it is going to be used for LES and DNS at low Mach numbers. The present and most realistic plan is to implement an artificial compressibility method proposed in [14]. The changes to present code structure are minor and the efforts of implementation and validation can be considered reasonable when limited resources are available.

5 ACKNOWLEDGEMENTS

Present work is a part of the TURBU-project funded mainly by the Finnish Technology Agency (Tekes) and most of the computational resources were offered by CSC. Authors would like to express gratitude to both instances.

REFERENCES

[1] Geurts B.J. *Elements of direct and large eddy simulation.* R.T. Edwards, Inc., R.T. Edwards, Inc., P.O. Box 27388, Philadelphia, PA 19118 USA, 2004. ISBN 1–930217–07–2.

[2] P. Kaurinkoski and A. Hellsten. FINFLO: the parallel multi-block flow solver. Report A-17, Helsinki University of Technology, Laboratory of Aerodynamics, Espoo, Finland, 1998. ISBN 951–22–3940–X.

[3] R. D. Moser, J. Kim, and N. N. Mansour. Direct numerical simulation of turbulent channel flow up to $\mathrm{Re}_\tau = 590$. *Physics of Fluids*, 11(4):943–945, April 1999.

[4] T. Brandt. *Studies on numerical errors in large eddy simulation.* Licentiate's thesis, Helsinki University of Technology, August 2004. ISBN 951-22-7192-3.

[5] P. Majander and T. Siikonen. Evaluation of Smagorinsky-based subgrid-scale models in a finite-volume computation. *International Journal for Numerical Methods in Fluids*, 40(6):735–774, 2002.

[6] Charles Hirsch. *Fundamentals of Numerical Discretization*, volume 1 of *Numerical Computation of Internal and External Flows.* John Wiley & Sons Ltd, Chichester, 1988. ISBN 0–471–91762–1.

[7] J.H. Ferziger and M. Perić. *Computational methods for fluid dynamics.* Springer-Verlag, Berlin, 1996. ISBN 3–540–59434–5.

[8] D. Tafti. Comparison of some upwind-biased high-order formulations with a second-order central-difference scheme for time integration of the incompressible navier-stokes equations. *Computers & Fluids*, 25(7):647–665, 1996.

[9] A. Lundbladh, S. Berlin, M. Skote, C. Hildings, J. Choi, J. Kim, and D. Henningson. An efficient spectral method for simulation of incompressible flow over a flat plate. Technical Report 11, Royal Institute of Technology, Department of Mechanics, Stockholm, Sweden, 1999.

[10] T. Kobayashi. Large eddy simulation for engineering applications. *Fluid Dynamics Research*, 38:84–107, 2006.

[11] E. Turkel and V.N. Vatsa. Local preconditioners for steady and unsteady flow applications. *Mathematical Modelling and Numerical Analysis*, 39(3):515–535, 2005.

[12] D.C. Wilcox. *Turbulence modeling for CFD.* DCW Industries Inc., La Cañada, California, second edition, 1998.

[13] H. Foysi, S. Sarkar, and R. Friedrich. Compressibility effects and turbulence scalings in supersonic channel flow. *Journal of Fluid Mechanics*, 509:207–216, 2004.

[14] M.M. Rahman and T. Siikonen. An artificial compressibility method for incompressible flows. *Numerical Heat Transfer, Part B*, 40:391–409, 2001.

CFD MODELING OF A SINGLE-BLADE PUMP

Mikko Auvinen, Juhaveikko Ala-Juusela, Timo Siikonen

Laboratory of Applied Thermodynamics
Helsinki University of Technology, TKK
P.O.Box 4400 FIN-02015 TKK
e-mail: firstname.lastname@tkk.fi

ABSTRACT

This report presents a numerical performance analysis of a single-blade pump. The computations were performed with the FINFLO Navier-Stokes solver, utilizing both quasi-steady and time-accurate solution methods. Two grid models were used to evaluate the effect of grid skewness, and physical error diagnostics were employed to investigate solution accuracy. The obtained results are compared to experimental measurements.

The study shows that rotating flow solutions are exceptionally sensitive to grid quality, rendering grid orthogonality a necessary condition for successful simulation. The analysis also reveals that in single-blade geometry any quasi-steady modeling fails, because the method produces non-physical flow structures and underestimates the pump performance. The predictions produced by time-accurate simulation, on the other hand, overestimate the pump efficiency and head, in accordance with expectations since external losses are not accounted for. Yet, the time-accurate flow field demonstrated strong fluctuations during a revolution, raising questions about proper boundary condition implementation and the role of evident discrepancies between the computational and physical models.

1 INTRODUCTION

Rotating flows in turbomachinery are among the challenges of CFD. In single-bladed pumps the geometry is difficult to handle and the resulting flow structure is complicated. Turbulence is affected by the rotating motion and its role is still not yet fully evaluated. The flow is unsteady, but traditionally quasi-steady simulations have been applied. In time-accurate simulations the impeller-volute interactions can be phenomenologically predicted, but the nature of the flow render RANS modeling questionable. In spite of the apparent difficulties, multi-blade pump flows have been successfully simulated with quasi-steady [1] and time-accurate RANS [2], as well as computationally intensive time-accurate LES [3] methods. According to the simulations made, it appears that the pump head can be relatively easy to predict, while the accuracy in efficiency predictions ends up less satisfactory. Nonetheless, comprehensive performance predictions are seldom provided.

In this work a single-blade pump is subject to a thorough computational performance analysis with the numerical Navier-Stokes solver FINFLO. The basic solver theory is described in [4] and [5], while the added pseudo-compressibility extension, which is utilized in this analysis, is covered in [6]. The study places particular emphasis on the role played by numerical analysis methodology and the utilization of physically meaningful error diagnostics. This work explores the utility of two contrasting methods that are based on the

principles of global energy balance and angular momentum balance. Two grid models of the same pump geometry are employed to investigate the effect that grid skewness has on numerical accuracy in such complex rotating flow systems. Both quasi-steady and time-accurate simulations were performed and subsequent results compared with experimental measurements provided by the pump manufacturer [7].

This paper is organized such that the next chapter entails the fundamental physical background of FINFLO solver, while the subsequent chapters are devoted to the derivation of the pump energy equation, a description of the computational models and applied methods as well as a brief discussion on the relevance and background of the applied physical error diagnostic methods. The results are analyzed and conclusions drawn at the end of the report.

2 GOVERNING EQUATIONS

The simulation of Newtonian fluid flow is based on the numerical solution of the complete Reynolds-Averaged Navier-Stokes equations coupled with an appropriate turbulence model. In a computational context it is most informative to present the equations in a following vector form

$$\frac{\partial U}{\partial t} + \frac{\partial (F_e - F_v)}{\partial x} + \frac{\partial (G_e - G_v)}{\partial y} + \frac{\partial (H_e - H_v)}{\partial z} = Q \tag{1}$$

where the vector U contains all the unknowns while F_e, G_e, H_e and F_v, G_v, H_v represent the inviscid and viscous cartesian flux vector terms. On the right hand side of the equation, Q, contains all the source terms through which additional physics can be accounted for. Since $k-\varepsilon$ turbulence model is utilized, the equations for turbulent kinetic energy k and its dissipation ε are presented as well. The vectors are written

$$U = \begin{pmatrix} \rho \\ \rho u \\ \rho v \\ \rho w \\ E \\ \rho k \\ \rho \varepsilon \end{pmatrix} \quad F_e = \begin{pmatrix} \rho u \\ \rho u^2 + p + \frac{2}{3}\rho k \\ \rho v u \\ \rho w u \\ (E + p + \frac{2}{3}\rho k)u \\ \rho u k \\ \rho u \varepsilon \end{pmatrix} \quad G_e = \begin{pmatrix} \rho v \\ \rho u v \\ \rho v^2 + p + \frac{2}{3}\rho k \\ \rho w v \\ (E + p + \frac{2}{3}\rho k)v \\ \rho v k \\ \rho v \varepsilon \end{pmatrix} \quad H_e = \begin{pmatrix} \rho w \\ \rho u w \\ \rho v w \\ \rho w^2 + p + \frac{2}{3}\rho k \\ (E + p + \frac{2}{3}\rho k)w \\ \rho w k \\ \rho w \varepsilon \end{pmatrix} \quad Q = \begin{pmatrix} 0 \\ 0 \\ \rho w \Omega \\ -\rho v \Omega \\ 0 \\ Q_k \\ Q_\varepsilon \end{pmatrix}$$

$$F_v = \begin{pmatrix} 0 \\ \tau_{xx} \\ \tau_{xy} \\ \tau_{xz} \\ u\tau_{xx} + v\tau_{xy} + w\tau_{xz} - q_x \\ \mu_k(\partial k/\partial x) \\ \mu_\varepsilon(\partial \varepsilon/\partial x) \end{pmatrix} \quad G_v = \begin{pmatrix} 0 \\ \tau_{xy} \\ \tau_{yy} \\ \tau_{yz} \\ u\tau_{xy} + v\tau_{yy} + w\tau_{yz} - q_y \\ \mu_k(\partial k/\partial y) \\ \mu_\varepsilon(\partial \varepsilon/\partial y) \end{pmatrix} \quad H_v = \begin{pmatrix} 0 \\ \tau_{xz} \\ \tau_{yz} \\ \tau_{zz} \\ u\tau_{xz} + v\tau_{yz} + w\tau_{zz} - q_z \\ \mu_k(\partial k/\partial z) \\ \mu_\varepsilon(\partial \varepsilon/\partial z) \end{pmatrix}$$

where u, v, w are the cartesian velocity components, ρ and p the fluid's density and pressure, respectively, and E the total energy of the fluid. The source vector Q contains contributions for both momentum and turbulence equations. The source terms for the y- and z-momentum equations arise from the rotational velocity Ω (in x-direction) of the control volume, while Q_k and Q_ε include terms for the turbulence equations described below. In the viscous flux vectors the stress tensor components, τ_{ij}, include both laminar and turbulent contributions

$$\tau_{ij} = \mu \left[\frac{\partial u_j}{\partial x_i} + \frac{\partial u_i}{\partial x_j} - \frac{2}{3}(\nabla \cdot \vec{V})\delta_{ij} \right] - \rho \overline{u_i'' u_j''} + \frac{2}{3}\rho k \delta_{ij} \tag{2}$$

where the Reynolds stresses are modelled according to Boussinesq's approximation

$$-\rho\overline{u_i'' u_j''} = \mu_T \left[\frac{\partial u_j}{\partial x_i} + \frac{\partial u_i}{\partial x_j} - \frac{2}{3}(\nabla \cdot \vec{V})\delta_{ij}\right] - \frac{2}{3}\rho k \delta_{ij} \tag{3}$$

in which δ_{ij} is the Kronecker's delta and μ_T signifies turbulent viscosity that is calculated from $\mu_T = c_\mu \rho k^2/\varepsilon$ where c_μ is an semi-empirical coefficient shown below.

A pseudo-compressibility method [6] is utilized in solving the incompressible flow system and the thermodynamic properties of water are determined from the following relations: $e = c_v T$, $\alpha = \mu c_p / Pr$, and

$$\frac{\partial \rho}{\partial p} = 5.0 \cdot 10^{-7} \frac{\mathrm{s}^2}{\mathrm{m}^2}, \quad \frac{\partial \rho}{\partial h} = -4.97 \cdot 10^{-5} \frac{\mathrm{s}^2}{\mathrm{m}^2}, \quad \mu = A \cdot 10^{[B/(T-C)]}$$

involving specific heat capacities at constant volume and pressure c_v and c_p, thermal conductivity α, Prandtl number Pr and empirical constants $A = 2.414 \cdot 10^{-5}$, $B = 247.8$ and $C = 140$.

The effect of turbulence is solved with Chien's $k-\varepsilon$ two equation model due to its robust behavior in internal flow analysis. The formulation of the k and ε equations are as shown in (1) - (2), yet, the source terms for the k and ε are explicitly written as

$$Q_k = P - \rho\varepsilon - 2\mu\frac{k}{y_n^2} \tag{4}$$

$$Q_\varepsilon = c_1 \frac{\varepsilon}{k} P - c_2 \frac{\rho\varepsilon^2}{k} - 2\mu\frac{\varepsilon}{y_n^2} e^{-y^+/2} \tag{5}$$

where P defines the production of turbulent kinetic energy, y_n the normal distance from the wall and y^+ the dimensionless normal distance, which depends, not only on the first cell height y_n, but also on the solution field,

$$y^+ = y_n \frac{\rho u_\tau}{\mu} = y_n \frac{\sqrt{\rho \tau_{wall}}}{\mu} = y_n \left[\frac{\rho |\nabla \times \vec{V}|}{\mu}\right]_{wall}^{1/2} \tag{6}$$

The production of turbulence P is modelled according to the Boussinesq approximation in equation (3):

$$P = -\rho\overline{u_i'' u_j''}\frac{\partial u_i}{\partial x_j} \Longrightarrow \left[\mu_T\left(\frac{\partial u_i}{\partial x_j} + \frac{\partial u_j}{\partial x_i} - \frac{2}{3}\delta_{ij}\frac{\partial u_k}{\partial x_k}\right) - \frac{2}{3}\delta_{ij}\rho k\right]\frac{\partial u_i}{\partial x_j} \tag{7}$$

This quantity is limited according to Menter such that $P = \min(P, 20\rho\varepsilon)$ to avoid excessive growth of μ_T. Finally, the calibration of the $k-\varepsilon$ model is achieved through five empirical coefficients embedded in the k and ε equations. They are defined as: $c_1 = 1.44$, $\sigma_k = 1.0$, $\sigma_\varepsilon = 1.3$, $c_2 = 1.92(1 - 0.22e^{-Re_T^2/36})$ and $c_\mu = 0.09(1 - e^{-0.0115y^+})$. In the expression for c_2, the Reynold's number is defined as $Re_T = \rho k^2/\mu\varepsilon$.

3 PUMP PERFORMANCE

Since the theoretical framework of the hydrodynamic system is fully contained in the Navier-Stokes equations, the solution, that is fixed by the appropriate initial and boundary conditions, embodies all the information concerning the hydrodynamic performance of the pump. Thus, the relevant information is attained by evaluating the individual terms in the energy balance of the system. The derivation of the desired form of the pump energy balance starts naturally from the first law of thermodynamics

$$dw + dq = d(\rho e_T) \tag{8}$$

which is written for an infinitesimal control volume, equating the change in applied work dw and heat dq with the change in total energy $d(\rho e_T)$. Transforming this into a rate equation and assigning the flow work to the right hand side yields

$$\frac{dw_s}{dt} + \frac{dq}{dt} = \frac{d(\rho h_T)}{dt} \tag{9}$$

where w_s represents the shaft work done per control volume and h_T is the total specific enthalpy given by $h_T = e_T + p/\rho = e + (\vec{V}\cdot\vec{V})/2 + k + p/\rho$. Integrating over the entire pump volume, utilizing Gauss's law on the right hand side and simplifying the notation results in

$$\int_V \frac{dw_s}{dt} dV + \int_V \frac{dq}{dt} dV = \int_V \frac{d(\rho h_T)}{dt}\, dV \tag{10}$$

$$\dot{W}_s + \dot{Q} = \int_A \rho u_n h_T dA. \tag{11}$$

where u_n is the velocity component normal to the surface element dA. Applying equation (11) to the pump with adiabatic walls ($\dot{Q} = 0$), it simplifies to

$$\dot{W}_s = \dot{m}\,(h_{T2} - h_{T1}) \tag{12}$$

as $\dot{m}$ is the mass flow rate through the system, while h_{T2} and h_{T1} stand for the specific total enthalpies at the outlet and inlet of the pump, respectively. Utilizing notation Δ to indicate differences between the values at outlet and inlet and the definition of total pressure in incompressible flow ($p_t = p + \rho\vec{V}\cdot\vec{V}/2$) the energy equation can be written

$$\dot{W}_s = \dot{m}\left(\Delta e + \Delta\frac{p_t}{\rho} + \Delta k\right) \tag{13}$$

Now, it is recognized that the only mechanism that adds to the fluid internal energy budget comes from losses due to fluid friction. This contribution is broken into two components: turbulent and viscous (i.e. laminar) dissipation, identified as ϕ_t and ϕ_v. Furthermore, given that T is the torque applied by the impeller to the fluid, the rate of shaft work done on the system becomes $\dot{W}_s = T\Omega$. Thus, with the definition of mechanical energy $E_M = \dot{m}(p_t/\rho)$, the energy equation of the pump reaches its final form

$$T\Omega = \Delta E_M + \phi_t + \phi_v + \dot{m}\Delta k \tag{14}$$

The analysis of the hydrodynamic performance of a pump primarily revolves around the evaluation of the individual components of this equation. It should be noted that the specification of a desired performance point requires the knowledge of only Ω and $\dot{m}$. The rest of the theoretical information follows from the numerical solution of the Navier-Stokes equations.

There are also two additional convenient measures that arise from (14) that are widely used in pump performance analysis: The total hydrodynamic head

$$H = \frac{\Delta p_t}{\rho g} = \frac{\Delta E_M}{\dot{m} g} \tag{15}$$

where g is the acceleration due to gravity, and the hydrodynamic efficiency of the pump

$$\eta = \frac{\Delta E_M}{T\Omega}. \tag{16}$$

It should be noted, however, that experimental measurements typically indicate the total (or shaft) efficiency of the system, which includes the associated bearing and shield losses.

4 CFD Analysis

4.1 Pump Geometry and Computational Models

As taught by experience, complicated geometries often lead to areas of poor grid quality that are typically characterized by skewed control volumes. It is recognized that skew elements contribute to discretization error, but, because the effects of grid skewness in rotational flows are not well documented, this aspect is also addressed in this study. Since the single-blade pump geometry contains features which render the structured grid generation difficult and the resulting grids sensitive to quality deficiencies, the numerical analysis was performed with two multi-block grids, shown in Figure 1, which embody two contrasting mesh qualities. The grid labelled *Skew* utilizes an unconventional block structure which gives rise to highly skewed control volumes in the impeller, while grid *Ortho* was generated as orthogonal as possible. Even though Grid *Ortho* has a much improved over-all grid quality, it still cannot be considered optimal.

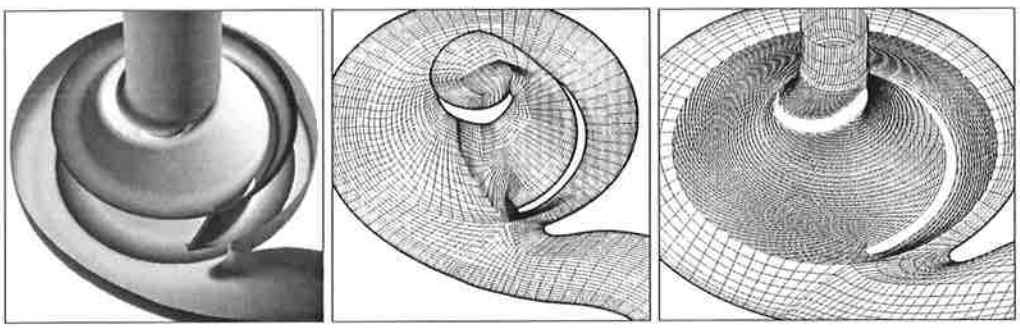


Figure 1: An overview of the pump geometry (left) and central bisecting grid planes from the *Ortho* (mid) and *Skew* (right) grids. 2^{nd} grid levels are displayed.

4.2 Quasi-Steady vs. Time-Accurate

The numerical performance analysis of the pump was carried out by completing four quasi-steady cases and a time-accurate simulation with both grid models. In a quasi-steady simulation the impeller walls are assigned the appropriate tangential velocity values, but the spatial domain of the model is kept fixed in time – meaning that the impeller blade's position remains fixed with respect to the volute, enabling a steady-state solution. The resulting system is clearly unphysical, but, depending on the involved flow physics, it may yield acceptable results. If the system is highly periodic, computation of a single case – one impeller-volute composition – may suffice, but, as the periodicity is reduced, the quasi-steady approximation becomes increasingly restrictive and a higher number of cases are required to produce potentially meaningful averages.

Although the considered single-blade pump, being 2π-periodic, is classified as a case that is, at face value, the least suitable for quasi-steady analysis, four cases – shown in Figure 2 – are included in the analysis because so little can be stated about the complex flow system a priori. Furthermore, due to the significant computational time savings gained compared to time-accurate simulation, it has become the primary method in industry and thereby obliges appropriate scrutiny.

In the time-accurate simulation a sliding plane interface is utilized between the rotating and stationary domains. Each time-step Δt the impeller's domain is rotated by an angle $\Delta\theta = \Omega\Delta t$ and a converged solution is sought within every time-step iteratively. The simulations were started from converged quasi-steady solutions and continued until the



Figure 2: Quasi-steady impeller-volute compositions. From left: $0°, 90°, 180°, 270°$.

flow field reached a periodic behavior.

4.3 Boundary Conditions and Computational Settings

One objective of this analysis was to replicate the conditions present at an experiment conducted by the manufacturer. The provided parameters are: rotational speed of the impeller Ω, constant mass-flow rate $\dot{m}_{in}/(\rho\Omega D^3) = 0.223$ (scaled) and the fluid's temperature $T_{in} = 293.15K$. With the given mass flow rate a developed pipe flow velocity profile was computed and imposed at the impeller's inlet. At the outlet of the domain, in turn, a constant total pressure and zero gradients are imposed. As all surfaces adhere to the no-slip condition, the velocity components on the rotating walls are assigned according to Ω. The ambient reference pressure was set at $p_\infty = 8\ atm$.

The convective variables are extrapolated to the cell faces with a third-order upwind biased discretization scheme (from $MUSCL$ formula), while the diffusion terms are evaluated with an ordinary second-order central difference scheme. For the quasi-steady computations multi-grid cycling was utilized to accelerate convergence. FINFLO employs a local pseudo time-step in advancing a solution – either in a steady-state mode or within a physical time-step – toward convergence. The size of this local time-step is determined by an assigned Courant number (CFL). In this study the specified Courant numbers fell within the range: $0.9 < CFL < 1.5$. The values used in time-accurate analysis were higher than in quasi-steady. The optimal Courant numbers were not determined.

5 SOLUTION ACCURACY

The impracticality of applying Richardson extrapolation method to industrial CFD applications has been reiterated in literature as multiple alternative error estimation schemes have been proposed. Optimization of the grid geometry often provides means to reduce numerical error, but, in the absence of mesh adaptation capabilities, the solution accuracy relies upon the quality of the original grid and the applied numerical methods. As always, it is important to gain knowledge of the error level associated with the performed numerical analysis and for such complicated cases the utilization of physically meaningful result diagnostics has proved highly convenient.

The basic idea of physical diagnostics is to test the validity of the obtained discretized solution with physical constraints which are not explicitly enforced by the numerical solution scheme. If the method is consistent and the discretization error small, the solution should satisfy these conditions. However, a single approach may not yield conclusive information about the result accuracy and, therefore, physical diagnostics are found most informative when different approaches are combined. In this study two contrasting methods were utilized to determine the level of discretization error in the solution: the angular momentum balance method and the global energy balance method.

5.1 Global Energy Balance

Equation (14) for the pump energy balance, derived in Section 3, is basically a rewritten global statement of the law of conservation of total energy. Therefore, according to the principle, the computational values should fulfill the following relation

$$T\Omega - (\Delta E_M + \phi_t + \phi_v + \dot{m}\Delta k) = 0 \tag{17}$$

However, due to the presence of discretization and possible modeling errors, the equality may not be reached. Therefore, evaluation of a numerical error term ϵ_E, given by

$$T\Omega - (\Delta E_M + \phi_t + \phi_v + \dot{m}\Delta k) = \epsilon_E \tag{18}$$

yields a global indicator for assessing the numerical accuracy of the solution. A small error in the global energy balance, however, does not guarantee the physical validity of the results because the solutions are subject to the applied boundary and initial conditions, including their associated approximations. Furthermore, it is possible that a small global error arises even in the presence of high local errors. This calls for a complementing method that allows a more local approach as well.

5.2 Angular Momentum Balance

In rotational flow systems, the principal conserved quantity is angular momentum. The conservation of angular momentum is not a distinct conservation principle, but a consequence of the conservation law of linear momentum that, in turn, is explicitly satisfied by most general-purpose CFD solvers. A solution based on conservation of linear momentum should therefore satisfy the conservation of angular momentum identically. But, it is recognized that the presence of discretization errors will lead to local and global imbalances in angular momentum. These imbalances will provide an indication of computational accuracy of the solution. The concept is introduced in [8], [9] and implementation is demonstrated in [10].

The discretized form of the angular momentum equation for a system with a non-deformable grid is simply obtained by cross-multiplying the linear momentum equation with the position vector $\vec{r}$. Utilizing the integral form of equation (1) with only the momentum terms and considering a steady-state solution where the time derivative is eliminated, the equation becomes

$$\int_S \vec{r} \times F n_x dS + \int_S \vec{r} \times G n_y dS + \int_S \vec{r} \times H n_z dS = \int_V \vec{r} \times Q \; dV \tag{19}$$

where simplified notation has been used for the combined flux vectors (F, G, H) and $n_{x,y,z}$ stand for the components of a unit surface normal vector. Bringing the source term to the left hand side, we form an expression which allows angular momentum imbalance ϵ_L to be evaluated for each control volume. In a discretized form the equation reads

$$\sum_j \vec{r}_j \times F_j n_x S_j + \sum_j \vec{r}_j \times G_j n_y S_j + \sum_j \vec{r}_j \times H_j n_z S_j - \vec{r}_i \times Q_i \; V_i = \epsilon_{Li} \tag{20}$$

as the summation is over all the faces of the cell. This expression is further simplified when applied to the pump because the work is transferred into the system through torque T which contributes only to the angular momentum balance along the axis of rotation. In this study the axis of rotation has been set to coincide with the x-axis and therefore the expression reduces to

$$\sum_j (-z_j G_j n_y S_j + y_j H_j n_z S_j) + (y_i \rho v_i \Omega + z_i \rho w_i \Omega) \, V_i = \epsilon_{Li} \tag{21}$$

Since ϵ_{Li} (or alternatively ϵ_{Li}/V_i) is evaluated for each computational cell, it can be visualized in the entire computational domain with a post-processing software. In general, plotting ϵ_{Li} tends to reveal areas of complex flow phenomena and insufficient grid density, while the plotting of ϵ_{Li}/V_i high-lights areas of poor grid quality. The visualization proves most informative because, in the absence of a universal scale, it demonstrates the level of local error variation and points out where the problems lie. The areas of high error arise from poor flow field resolution that may or may not coincide with areas of high residuals, which, in turn, result from poor convergence. Thus, to eliminate additional sources of error, proper convergence has to be achieved in order to exploit this method fully.

In order to gain a global indication about the level of angular momentum error in the system, an absolute sum of the individual error terms was computed ($\epsilon_L = \sum_i |\epsilon_{Li}|$).

6 RESULTS

The following graphs in Figure 3 display the evolution of $T\Omega$, η and H produced by the time-accurate simulations together with the quasi-steady results obtained at different blade positions. Plots of ϵ_E and ϵ_L, obtained from quasi-steady cases, are also included in Figure 3. The starting angle is set so that the tip of the impeller blade is lined up with the tongue of the volute. The mean values are summarized in Table 1. Together with the results visualizations in Figure 4, the information leads to the following deductions:

Table 1: Comparison of mean results.

	Shaft Power (Scaled) $(T\Omega/\rho\Omega^3 D^5)$	Efficiency (η)	Total Head (Scaled) $(H/\Omega^2 D^2)$
Experimental:	0.1628	71.1 %	0.0539
Ortho, Time-accurate :	0.1662	77.6 %	0.0587
Ortho, Quasi-Steady :	0.1489	67.9 %	0.0461
Skew, Time-accurate :	0.3026	43.6 %	0.0596
Skew, Quasi-Steady :	0.2203	46.1 %	0.0465

• **Grid Skewness:** Comparison of corresponding *Ortho* and *Skew* results reveals that grid skewness has a profoundly deteriorating effect on the solution accuracy. The assumption behind the *MUSCL*-type extrapolation scheme for convective variables implies that the cell face normal vector $\vec{n}$ points toward the node of the neighboring control volume. When this assumption is systematically violated – as in the impeller of the *Skew* grid model – the discretized system produces an erroneous flow field, which is made evident by the extremely poor convergence behavior demonstrated by the time-accurate evolution of η and H, and the dramatically higher ϵ_E-values in Figure 3. Furthermore, the relatively close agreement between total viscous losses shown in Figure 3 indicates that the grossly overestimated $T\Omega$-values of the *Skew* model stems from its spoiled pressure behavior. In accordance with experience, the time-accurate predictions for total hydrodynamic head H end up being optimistic regardless of the apparent numerical difficulties. It is therefore reiterated that total head values do not reflect overall solution accuracy.

For the *Skew* model the error in global energy balance ϵ_E provides an immediate signal about the inability of the discretized system to satisfy energy conservation. The numerical value of ϵ_E is easy to interpret because it is a quantity with a physical unit (W) and comparable to other evaluated entities in Equation (18). On the other hand, at first sight, the global measure of angular momentum balance ($\epsilon_L = \sum_i |\epsilon_{Li}|$) appears rather uninforma-

tive because the two grid models produce comparable error values. Yet, the significance of the angular momentum balance is revealed with a closer scrutiny: In Figure 4 the images depicting ϵ_{Li}-distribution illustrate how the error in *Skew* domain has primarily concentrated close to the pressure side of the blade – the area where critical momentum transfer occurs. This implies that the distortion of flow physics is most pronounced at the source of work input, $T\Omega$. Therefore, systematic propagation of error throughout the domain is anticipated. But, while the presence of local error in the *Skew* domain is obvious, perhaps surprisingly the *Ortho* case does not make an exception. Areas of escalated imbalances are clearly highlighted even though the associated ϵ_E value is small. This is, at least in part, explained by the nature of the quasi-steady analysis, which is discussed below.

It is recognized that the *Skew* model appears as an exaggeration in terms of grid skewness, but numerical tests with simplified geometries confirm that even moderate grid skewness (ca. 45°) in rotational flow applications can have a significant effect on the solution accuracy. Therefore, unless the code has a discretization scheme that accounts for the grid skewness, in such CFD analysis sufficient grid orthogonality deserves even greater priority than adequate grid density.

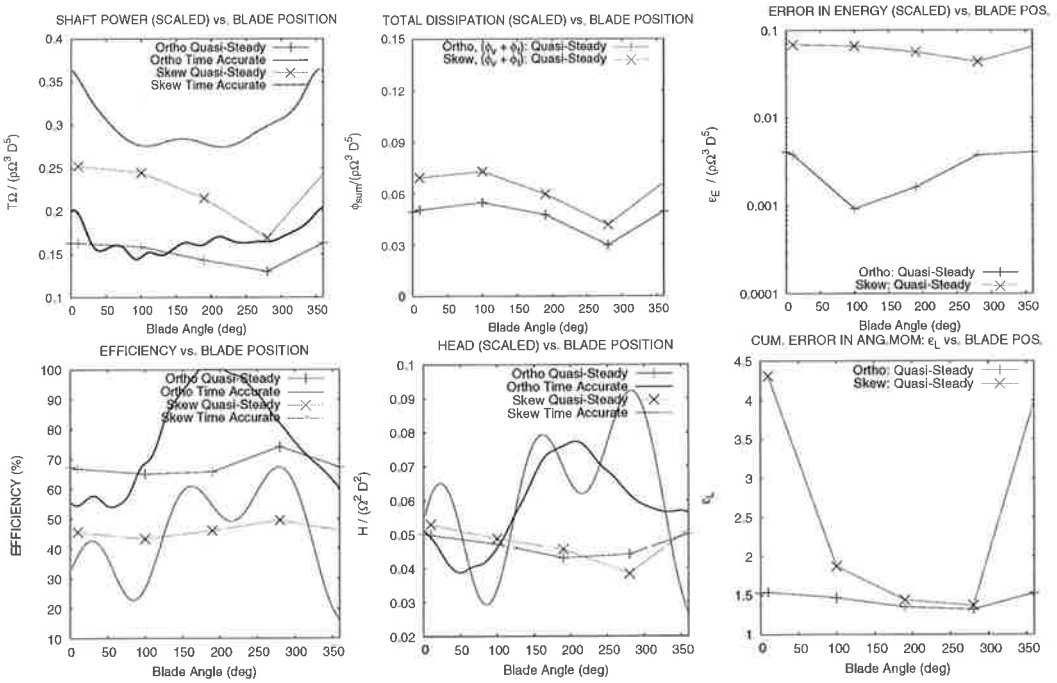


Figure 3: Result comparison, time-accurate vs. quasi-steady: $T\Omega$ (top left), $\phi_v + \phi_t$ (top mid), ϵ_E (top right) η (bottom left), H (bottom mid) and $\epsilon_L = \sum_i |\epsilon_{Li}|$ (bottom right)

• **Quasi-Steady vs. Time Accurate:** The quasi-steady analysis with the *Ortho* model succeeded in reaching a satisfactory global energy balance, but erred notably in performance predictions and demonstrated surprisingly high angular momentum imbalances. The source of these problems lies in the violations associated with the quasi-steady approximation.

As can be deduced from the results in Figure 3 and the velocity distributions shown in Figure 4, the quasi-steady analysis method fails to capture the 2π-periodic flow physics of the single-blade pump. It is therefore apparent that, in the considered single-blade system, the flow inertia plays a dominating role and does not allow the time-dependent

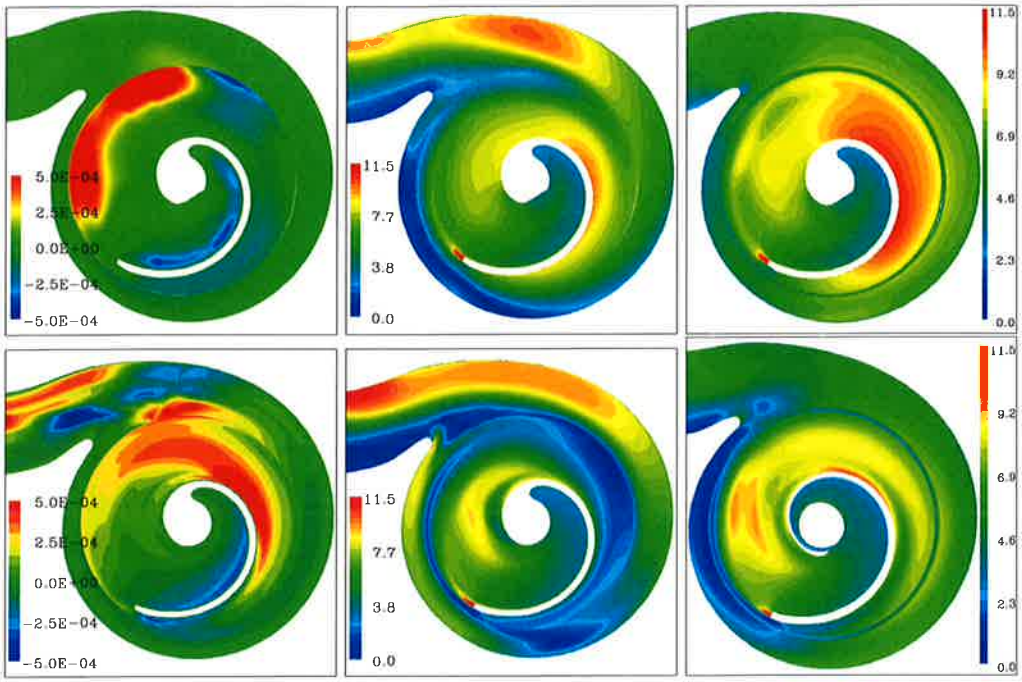


Figure 4: Visual comparison. *Ortho* (Top), *Skew* (Bottom): Angular momentum imbalance, ϵ_{Li} (left); Quasi-steady velocity distribution (mid); Time-accurate velocity distribution (right). Velocity scale units (m/s).

behavior to be neglected. The velocity distributions clearly demonstrate how the quasi-steady solution produces non-physical flow structures, which feature areas of reversed flow and high velocity gradients. It is most interesting to observe that, in the *Ortho* quasi-steady velocity distribution, the areas of unnaturally retarded flow within the rotating domain of the impeller are high-lighted with elevated angular momentum imbalances. This suggests that the angular momentum balance method in rotating applications can also provide an indication about the physical validity of local flow structures. Verification of this, however, requires further attention.

• **Time-Accurate Simulation:** According to the mean results, the time-accurate simulation with the *Ortho* model generated the most successful performance predictions. The time-dependent behavior of the flow field, however, demonstrates surprisingly strong fluctuations in the physical parameters. The mass flow rate was also observed to fluctuate $\pm 3\%$ at the outlet, which is in violation with the conservation of mass principle when the fluid is incompressible. Mass conservation was achieved, however, over a complete revolution, which indicated that the fluid attained some compressible attributes. It should be considered, though, that since the flow system, as the time-accurate simulation suggests, is strongly fluctuating especially in pressure, the validity of imposing constant mass flow rate at the inlet also becomes questionable. It is expected that the pressure fluctuations are carried readily upstream resulting in mass flow fluctuations in the incoming duct as well. Thus, a considerably longer incoming duct or a tank-like reservoir should be utilized with a constant mass flow inlet.

Furthermore, as the time-accurate shaft power $T\Omega$ curve illustrates, the power requirement is also strongly dependent on the blade position with respect to the volute. Yet,

regardless of the strong changes in the applied torque, the rotational speed of the impeller, Ω, does not fluctuate as it should in accordance with angular acceleration $\alpha = T/I$, where I is the rotational inertia of the impeller-motor combination. Due to the constant Ω, the magnitude of the arising fluctuations in, for example, H and η tend to be emphasized because the model impeller bulldozes through the fluid with an infinite inertia, completely oblivious to the prevailing conditions. This stands in conflict with the physical situation and its significance should be further investigated.

In analyzing the mean results listed in Table 1, it must be considered that the experimental measurements include the effects of bearing and pump shield losses, which are not present in the computational model. Therefore, the measured efficiency and total head ought to be lower than the CFD results, while the measured shaft power requirement should end up higher. This obviously complicates the comparison for the exact contributions of the bearing and shield losses are not available. Nonetheless, considering the discrepancies between the computational and physical systems, the time-accurate results do provide much cause for optimism. The obtained values for efficiency, η, and total head, H, possess anticipated margins with respect to the empirical measurement. This provides the expected indication that the sole hydrodynamic system always produces an improved efficiency compared to the physical entity. The numerical efficiencies should, however, be even higher because the shaft power, $T\Omega$, values suffer from the constant Ω boundary condition, as discussed earlier. Should the power peak not occur at the 0° blade angle, the time-averaged efficiency would further improve, while the computed shaft power requirement would fall below the measured value.

It is thereby recognized that a successful simulation of a complex flow system calls for an improved synthesis between the empirical and numerical regimes. The implementation of realistic boundary conditions, construction of accurate solution schemes and utilization of informative error diagnostics still pose challenges for CFD developers. The experimentalists, in turn, have to address the problem of how to extract the relevant hydrodynamic information from a system and single out the external effects.

7 CONCLUSIONS

A hydrodynamic performance analysis of a single-blade pump was completed with the three-dimensional Navier-Stokes solver FINFLO. The study yielded the following conclusions:

- The effect of grid skewness in rotating applications is particularly detrimental. The produced flow structures become distorted and their physical behavior erratic. The overall error was reflected by the global energy balance method, while the angular momentum balance method revealed strong local imbalances. The dramatic deviation from the experimental measurements verified the adverse influence of grid skewness.
- The quasi-steady analysis method fails to describe the 2π-periodic flow physics of a single-blade system. The obtained mean values grossly underestimate the shaft power requirement, efficiency and total hydrodynamic head. Visual comparison with the time-accurate solutions, and the presence of local angular momentum imbalances, provide further evidence about the unphysical nature of the quasi-steady flow system.
- The time-accurate simulation with an orthogonal grid yielded results that overestimated the efficiency and hydrodynamic head, in accordance with expectations since the CFD model does not take into account the pump bearing and shield losses. In the absence of information on the magnitude of such losses, conclusive judgements on the results' accuracy cannot be made. Still, the overall agreement with the empirical values is promising.

- The pronounced fluctuating behavior of the time-accurate simulation's flow field raises questions about the discrepancies between the physical and numerical models. For instance, the assumption that the impeller has an infinite rotational inertia – arising from the constant rotational velocity boundary condition – is likely to contribute to such strong oscillations in $T\Omega$. As a result, the predicted shaft power requirement ends up higher than the measured one, regardless of the exclusion of external losses.

REFERENCES

[1] Ojala, J., Rautaheimo, P., and Siikonen, T., "Numerical Simulation of a Centrifugal Pump Using a $k-\epsilon$ Model Including the Effects of Rotation," in *Proceedings of the Fourth ECCOMAS Conference*, (Athens), John Wiley & Sons, Ltd., Sept. 1998.

[2] Gonzalez, J., Fernadez, J., E., B., and Santolaria, C., "Numerical Simulation of the Dynamic Effect Due to Impeller-Volute Interaction in a Centrifugal Pump," *ASME Journal of Fluids Engineering*, Vol. 124, 2002, pp. 348–355.

[3] Byskov, R., Jacobsen, C., and Pedersen, N., "Flow in a Centrifugal Pump Impeller at Design and Off-Design Conditions – Part II: Large Eddy Simulations," *ASME Journal of Fluids Engineering*, Vol. 125, 2003, pp. 73–83.

[4] Siikonen, T., Hoffren, J., and Laine, S., "A Multigrid *LU* Factorization Scheme for the Thin-Layer Navier–Stokes Equations," in *Proceedings of the 17th ICAS Congress*, (Stockholm), pp. 2023–2034, Sept. 1990. ICAS Paper 90-6.10.3.

[5] Siikonen, T., "An Application of Roe's Flux-Difference Splitting for the $k-\epsilon$ Turbulence Model," *International Journal for Numerical Methods in Fluids*, Vol. 21, No. 11, 1995, pp. 1017–1039.

[6] Rahman, M., Rautaheimo, P., and Siikonen, T., "Numerical Study of Turbulent Heat Transfer from a Confined Impinging Jet Using a Pseudo-compressibility Method," in *Proceedings of the 2nd International Symposium on Turbulence, Heat and Mass Transfer*, (Delft), pp. 511–520, June 1997.

[7] Pedersen, N. and Sorensen, H., "Flow Investigation in a Single-Channel Pump Using laser doppler velocimetry," in *Conference on Modelling Fluid Flow (CMFF'03)*, (Budapest, Hungary), The 12^{th} International Conference on Fluid Flow Technologies, September 2003.

[8] Haworth, D., El Tahry, S., and Huebler, M., "A Global Approach to Error Estimation and Physical Diagnostics in Multidimensional Computational Fluid Dynamics," *International Journal for Numerical Methods in Fluids*, Vol. 17, 1993, pp. 75–97.

[9] Chang, S. and Haworth, D., "Adaptive Grid Refinement Using Cell-Level and Global Imbalances," *International Journal for Numerical Methods in Fluids*, Vol. 24, 1997, pp. 375–392.

[10] Nilsson, H. and Davidson, L., "Application of an Angular Momentum Balance Method for Investigating Numerical Accuracy in Swirling Flow," *Journal of Fluids Engineering*, Vol. 125, July 2003, pp. 723–730.

WEB DRYING SIMULATIONS BASED ON COMPUTATIONAL FLUID DYNAMICS

F. BERGSTRÖM*, J. ÅKERHOLM*, R. HANSSON**, R. MÖLLER**

*Process Flow Ltd Oy
Puolalanpuisto 1b A 21, 20100 Turku
e-mail: fredrik.bergstrom@processflow.fi

** Albany International, Research Center
Box 510, S-301 80 Halmstad Sweden

ABSTRACT

A coupling between a sophisticated fluid dynamics simulation of turbulent flow with a RANS method and a simple drying model for the paper web is demonstrated in this paper. The solution includes solving of the viscous region of the turbulent boundary layer. Sub models, which take into account the coupled mass and heat transfer between the web and the surrounding air, have been built into commercial software, Fluent. The model is aimed to be used for predicting the drying process in paper production environments. The results show, for example, local heat and mass transfer rates between paper and air along with temperature and moisture content distribution. All heat and mass transfer calculations are based the local variations in surrounding conditions.

1. INTRODUCTION

Computational fluid dynamics is an every day product development tool in the drying section of a paper machine. Accurate simulations including turbulent flow and moving porous media have been performed in order to study machine runnability. It is, among other, possible to study how dryer fabric structure influence the flow field in the dryer pocket and thus have effect on machine production capacity [1]. This modelling approach has been extended to include the heat transfer properties of fabrics as well, i.e. heat conduction and convection. The dryer fabrics influence the drying rate as they both secure an efficient heat transfer between cylinder and sheet [2] and provide a certain resistance for the mass transfer of the evaporated water.

Equally there are many paper web drying models available, in which the drying capacity of the dryer section or one individual dryer pocket can be analysed. The tools uses mass and heat transfer coefficients to model the heat and mass transfer from the paper web to the surrounding turbulent air flow. However usually [3, 4, 5] the heat transfer coefficients are based on measurements and taken as mean values of an area of considerable size and the moisture content of the surrounding air is taken as a mean value.

2. CFD SIMULATIONS

The CFD calculations are carried out with Fluent software with RANS models. The flow is turbulent and modelled with a k-e turbulence model. The wall treatment is however more sophisticated than for the standard wall function, which means far better boundary layer simulation compared to standard k-e turbulence modelling, at the cost of computational time and of course. The modelling is carried out in 2D which means that computation costs are still very moderate.

In Fluent's near-wall model, the viscosity-affected near-wall region is completely resolved all the way to the viscous sub layer [6]. In the approach, the whole domain is subdivided into a viscosity-affected region and a fully-turbulent region, thus called the two layer model. The demarcation of the two regions is determined by a wall-distance-based, turbulent Reynolds number, Re_y, defined as,

$$\mathrm{Re}_y = \frac{\rho y \sqrt{k}}{\mu} \tag{1}$$

where y is the normal distance from the wall at the cell centres. Other parameters are density, viscosity and the turbulent kinetic energy. In the viscosity-affected near-wall region ($Re_y < 200$), the one-equation model of Wolfstein [7] is employed. The enhanced turbulent law-of-the-wall for compressible flow with heat transfer and pressure gradients has been derived by combining the approaches of White and Cristoph [8] and Huang et al. [9]: The enhanced wall functions were developed by smoothly blending an enhanced turbulent wall law with the laminar wall law. By securing sufficiently high computation mesh resolution at the surface of the wall it is possible to compute the velocity profile starting from the laminar sub layer of the boundary, i.e.

$$\frac{du}{dy} = 1 + \alpha y, \quad \text{where } \alpha = \frac{\mu}{\rho^2 u^3}\frac{dp}{dx} \tag{2, 3}$$

y is the orthogonal distance from the wall and u is the velocity in the direction of the wall. The further away from the surface the computation cell is the large the effect of the enhanced turbulent wall law. The heat transfer and diffusion are modelled in a similar way starting from the laminar fluxes if mesh resolution is fine enough.

$$\dot{q} = \lambda \frac{dT}{dy} \tag{4}$$

$$j = D \frac{dc}{dy} \tag{5}$$

3. PAPER DRYING MODEL

The motivation for this work is to develop paper machine dryer fabrics. A model for paper drying has been developed in order to evaluate the influence from the dryer fabrics. The paper is of less interest than the fabric and therefore is paper modelled as one dimensional. This is an approximation while normally there are clear temperature and moisture gradients inside the paper. With this model the temperature and moisture content is the same at both sides. Still this model will show differences in paper properties (temperature, moisture content, drying intensity, etc.)

with different fabrics and other surrounding conditions. It's possible with relative ease to further develop the paper drying model.

3.1 Geometry

The paper is specified as a boundary wall with a shadow zone in Fluent. At a given temperature and moisture content the paper enters the model. The starting point of the paper must be inserted into the model. New temperatures and moisture contents will be calculated from that point forward.

All faces of the computational mesh in the calculation domain which lie on the paper boundary wall are sorted from the starting point to the end of the web. For every face in the paper there is incoming and outgoing moist paper. The water in the paper will evaporate to the neighbouring cells depending on the difference in mass fraction of water vapour Y_{h2o} at the paper surface and the neighbouring cell. The mass fraction can be defined from the moisture content $x_{air,s}$, which is a function of the saturation vapour pressure $p_{air,s}$. The vapour pressure is calculated from the paper temperature. Westerlund [10] suggests equations 7 and 8 as approximations for calculating the moisture content of water vapour at the surface and the saturation vapour pressure.

$$Y_{h2o} = \frac{x_{air,s}}{1 + x_{air,s}} \tag{6}$$

$$x_{air,s} = 0.622 \cdot \frac{p_{air,s}}{p_{tot} - p_{air,s}} \left(\frac{kg - H_2O}{kg - air(dry)} \right) \tag{7}$$

$$\left(\frac{p_{air,s}}{bar} \right) = \exp\left(11.78 \cdot \frac{\left(\frac{\vartheta_{paper}}{°C} \right) - 99.64}{\left(\frac{\vartheta_{paper}}{°C} \right) + 230} \right) \tag{8}$$

There is also energy transfer from the gas to the paper. The mass and heat transfer is calculated based on the local conditions in each face on the paper web and on the adjacent cells on both sides of the paper web. A cell size of 1 mm is typical in the machine direction, which means that heat and mass transfer characteristics will be calculated at 1 mm spacing. The paper drying model is schematically presented in figure 1, in which the index i is referring to the face index of the computational cell on the paper web.

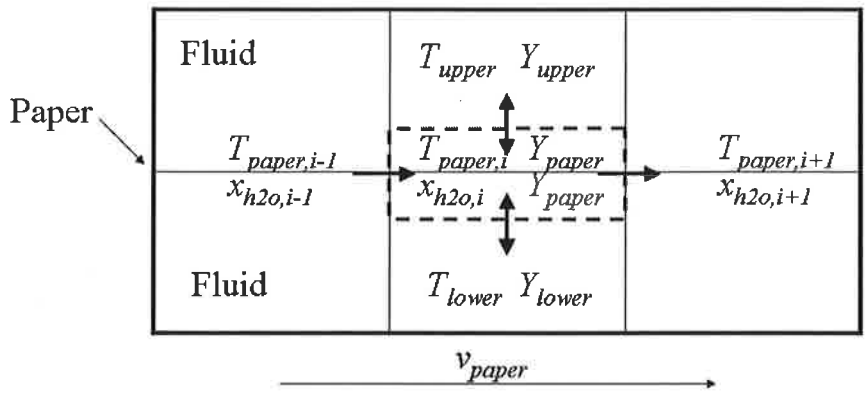


Figure 1. Paper model geometry.

3.2 Mass conservation (H_2O)

A mass balance for water is made over every face. There is water in the incoming and outgoing paper. At the paper surface the water vapour is transported to the fluid due to diffusion. The amount of evaporating water can be calculated from Fluent with equation 9. Evaporation occurs on both sides of the paper. The needed variables are read from the adjacent cells of the paper in the CFD calculation. The variables which are read are; the diffusion coefficient D_{h2o}, the difference in mass fraction of water between the surface and the neighbouring cell centre and the distance from the paper surface (face centre) to the cell centre Δs. The face area doesn't have to be equal throughout the domain and is thus dependent on the computational cell size.

$$j_{h2o} = \rho_{gas} \cdot D_{h2o} \frac{\Delta Y_{h2o}}{\Delta s} \tag{9}$$

$$\dot{m}_{vapor,i} = (j_{h2o,upper,i} + j_{h2o,lower,i}) \cdot A_{face,i} \tag{10}$$

The drying intensities (kg/s-m²), in this case the same as the diffusion fluxes, are stored so that they can be further post processed and analysed.

The moisture content of the incoming paper to each face is a function of the mass fraction of water per dry paper content in the previous face and paper mass flow.

$$\dot{m}_{h2o,i-1} = x_{h2o,i-1} \cdot \dot{m}_{paper} \tag{11}$$

The difference of the incoming water and evaporated water gives the amount of water going to the next face.

$$\dot{m}_{h2o,i} = \dot{m}_{h2o,i-1} - \dot{m}_{vapor,i} \tag{12}$$

The mass balance equations are solved simultaneously with the energy equations for the paper model.

3.3 Energy conservation

Both mass and energy must be conserved for the paper model. An energy balance over every face must be made additional to the mass balance. Due to convection there is heat flux to or from the paper. The heat flux for both sides of the paper can directly be accessed from the CFD solution.

$$\dot{q}_{conv} = \frac{\lambda \cdot \Delta \vartheta}{\Delta s} \tag{13}$$

The enthalpy change in the face can be calculated with the heat fluxes and the enthalpy for the evaporating water. The enthalpy change equals the difference between incoming and outgoing enthalpy for the moist paper.

$$\Delta\Phi_i = \dot{q}_{conv,upper,i} + \dot{q}_{conv,lower,i} - \dot{m}_{vapor,i} \cdot h_{vapor}(\vartheta_{paper,i})$$
$$\dot{H}_{paper,i} = \dot{H}_{paper,i-1} + \Delta\Phi_i \tag{14, 15}$$

The reference point for all the enthalpies are 0 °C. By adding the mass flows and specific heat capacity the new temperature is solved from the energy balance.

$$\vartheta_{paper,i} = \frac{(\dot{m}_{paper} \cdot c_{p,paper} + \dot{m}_{h2o,i-1} \cdot c_{p,h2o}) \cdot \vartheta_{paper,i-1} + \Delta\Phi_i}{\dot{m}_{paper} \cdot c_{p,paper} + \dot{m}_{h2o,i} \cdot c_{p,h2o}} \tag{16}$$

The new temperatures are calculated at a desired interval of the CFD iterations and the values of temperature and moisture are updated as boundary conditions in the CFD model. Some relaxation of the temperature can be needed for convergence. The paper drying model is hooked to the CFD software by using Fluent User Defined Functions.

4. SIMULATION RESULTS

The simulation model is validated with a simple test simulation. A wet paper web enters a simulation domain at 50°C with a velocity of 30 m/s. The calculation domain is 2m wide and the surrounding conditions are defined to be stationary air at 100°C and 1 % mass fraction of water vapour. The simulated boundary layers are described with figures 3-5. The velocity, temperature and moisture content boundary layers are plotted as functions of the orthogonal distance from the web at different distances from the starting point of the simulation domain. The velocity boundary layer and the locations of the plotted boundary layers in figures 3-5 are shown in figure 2.

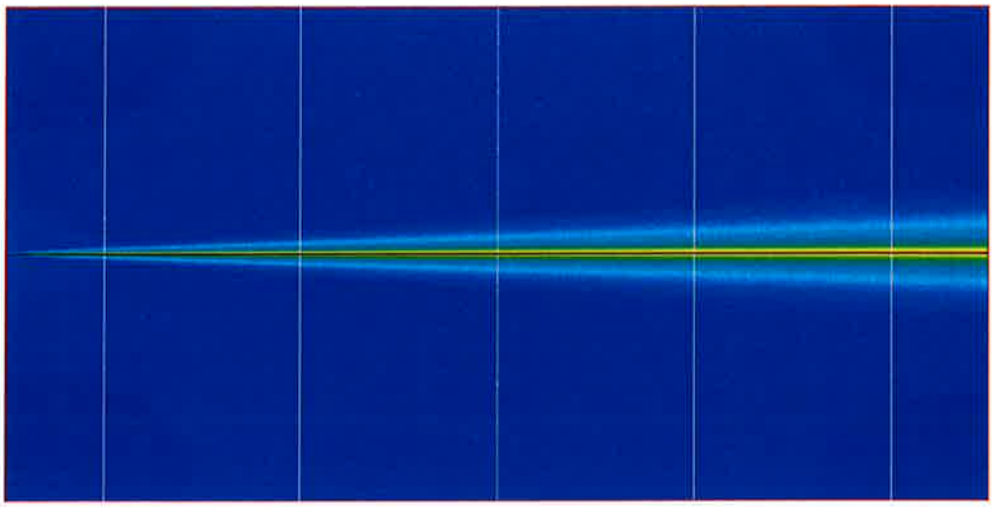


Figure 2. The figure shows the calculation domain. The vertical lines describe the locations where the boundary layers are plotted. The figure is coloured by air velocity.

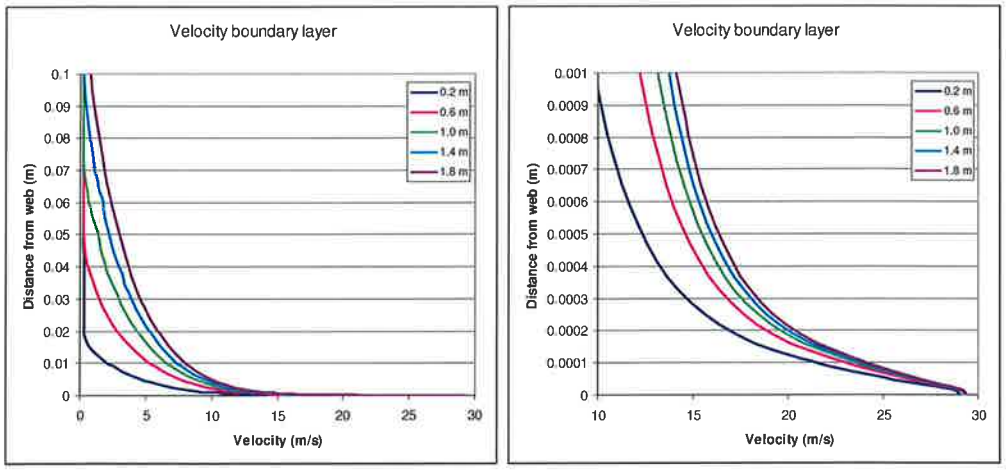


Figure 3. The figures show the velocity boundary layer on the top of the moving web. The graphs show that the boundary layer is growing throughout the model and that the growth speed is decreased in the latter part of the domain.

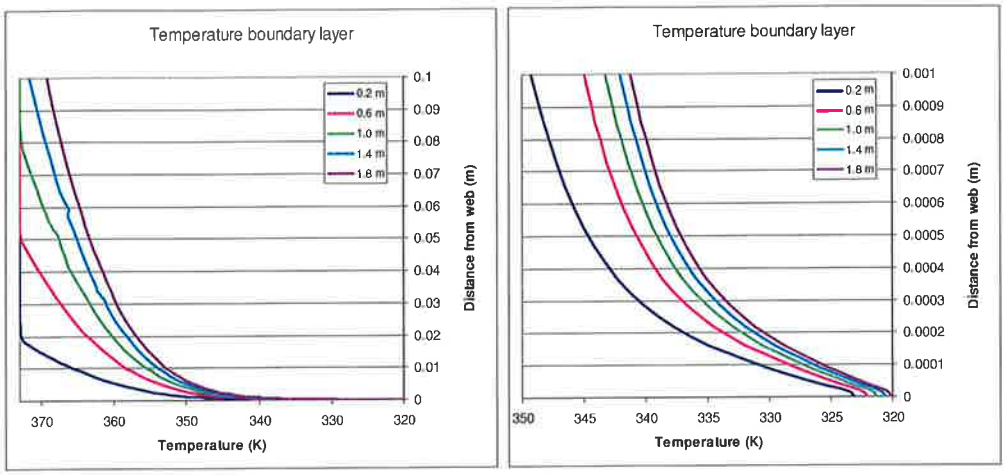


Figure 4. The figures show the temperature boundary layer on the top of the moving web. It can be seen that the air closest to the paper is cooler than the initial temperature of the paper (323 K). This influences the growth of the boundary layer.

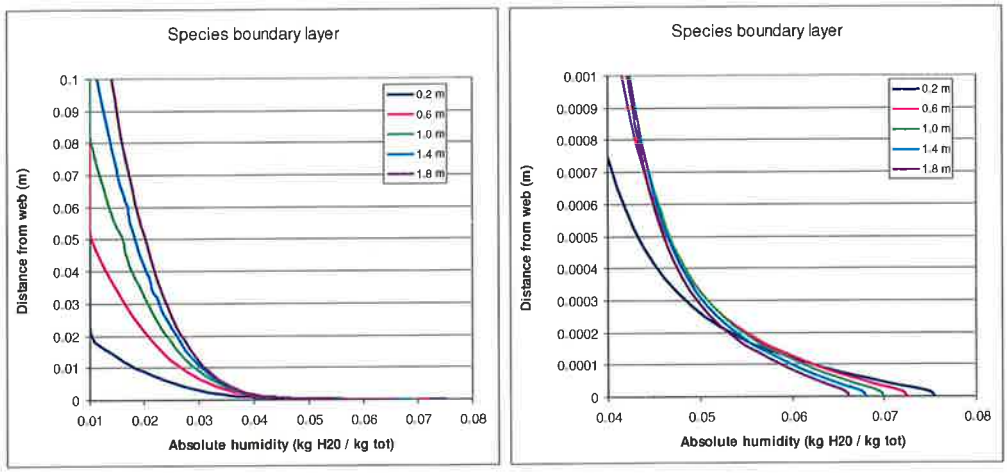


Figure 5. The figures show the moisture content boundary layer on the top of the moving web. The graph to the right shows that all curves are crossing each other at about 0.2 mm from the surface while the web and the air is cooled due to evaporation meaning that the saturation humidity is reached at a lower value.

The boundary layers show clear similarities with the experimental work carried out by Berg [11]. The temperature, moisture content and drying intensity of the paper is shown in figure 6. The properties are now plotted as function of web length. The graphs show high drying intensity in the beginning of the domain which means that the web is cooled although it enters a space with 50°C higher temperature than the web itself. This behaviour has large influence on the temperature and especially moisture content boundary layers.

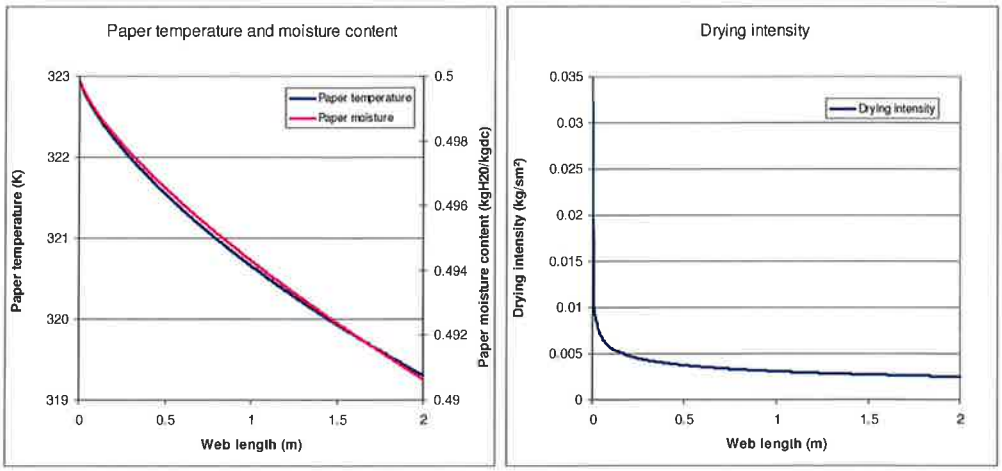


Figure 6. The graph to the right shows the paper temperature and moisture content as function of horizontal position in figure 2. The graph to the right shows the corresponding drying intensity.

The model is further validated as measurements and simulation results are compared in a full scale paper machine dryer pocket. The simulation includes a porous dryer fabric and a drilled roll for which additional models have been developed. The results of the simulations are shown in figure 7 and 8.

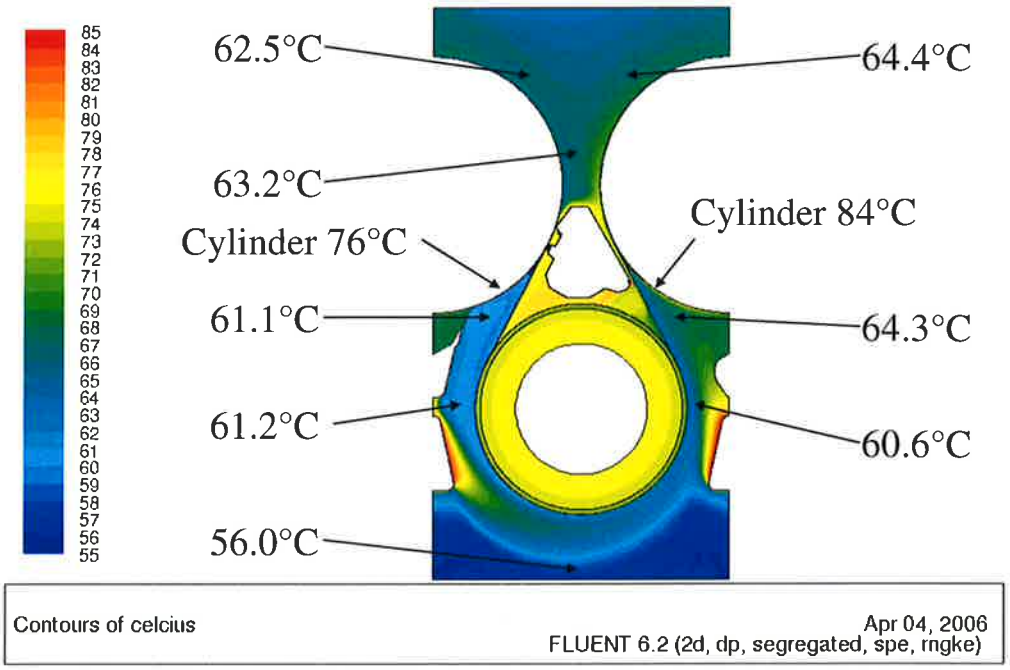


Figure 7. The figure shows the temperature distribution in a paper machine dryer pocket. The text and arrows show measured values.

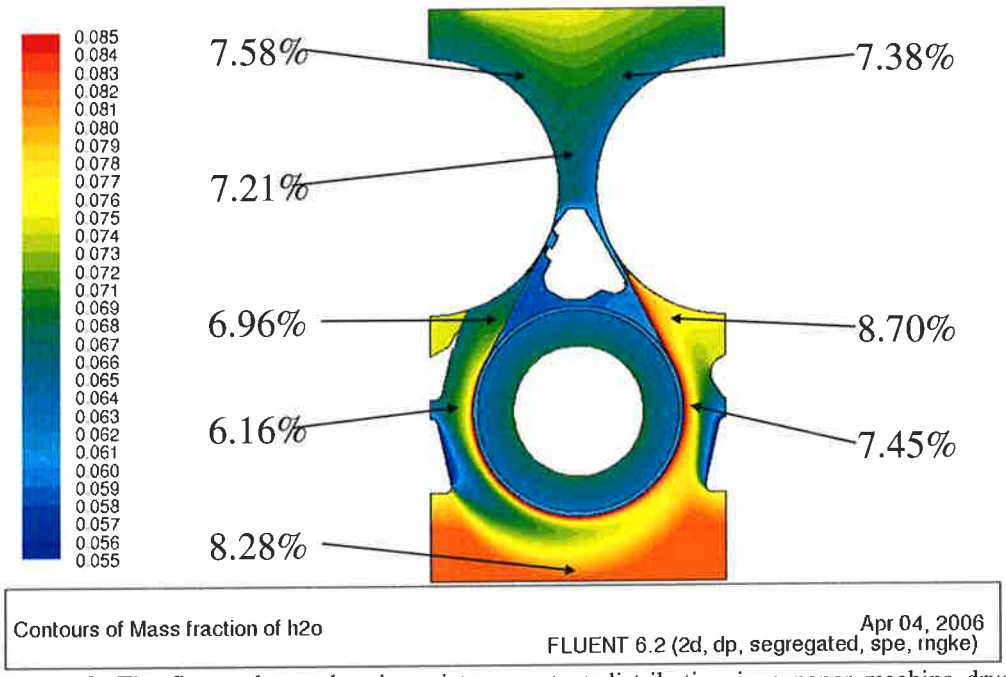


Figure 8. The figure shows the air moisture content distribution in a paper machine dryer pocket. The text and arrows show measured values.

5. CONCLUSIONS

A drying model for webs has been implemented into commercial CFD software (Fluent). This paper shows how boundary layer driven flow and mass and heat transfer can be coupled into an effective tool, which can be utilized to develop web drying unit processes. Dryer fabrics can for example be developed in order to maximise the drying efficiency in a paper machine with the help of the tool.

The simulation tool is validated with experiments and literature and it seems to provide very reasonable results.

CITED LITERATURE

1. K. Laakkonen, "Computational Flow-Field Modeling of Paper Machine Dryer Fabric", Tampere University of Technology, Publications 414, 2003
2. N. Milosavljevic, P. Heikkilä, M. Ojanen and J. Saari, "Influence of Fabric Structure on the Drying Rate and Cylinder-Paper contact heat transfer coefficient", 12th International Drying Symposium IDS2000
3. M. Karlsson, "Papermaking Part 2, Drying volume 9", Fapet Oy 2000
4. P. Heikkilä, "A Study on the Drying Process of Pigment Coated Paper Webs", Academic dissertation, Åbo Akademi University 1993
5. M. Soininen, "Modeling of Web Drying", report 94-133-A, Åbo Akademi University 1998
6. Fluent users manual

7. M. Wolfstein, "The Velocity and Temperature Distribution of One-Dimensional Flow with Turbulence Augmentation and Pressure Gradient", *Int. J. Heat Mass Transfer*, 12:301-318, 1969.
8. F. White and G. Christoph. "A Simple New Analysis of Compressible Turbulent Skin Friction Under Arbitrary Conditions", Technical Report AFFDL-TR-70-133, February 1971.
9. P. Huang, P. Bradshaw and T. Coakley. "Skin Friction and Velocity Profile Family for Compressible Turbulent Boundary Layers", *AIAA Journal*, 31(9):1600-1604, September 1993.
10. T. Westerlund, "Anläggnings och appratteknik", Åbo Akademi Univeristy 1998.
11. C-G. Berg, "Heat and Mass Transfer in Turbulent Moist Air Drying Processes" Åbo Akademi University Press, 1999

COMPARISON OF TURBULENCE MODELS IN A CASE OF SLANTED JETS IN CROSSFLOW

A. KARVINEN AND H. AHLSTEDT

Institute of Energy and Process Engineering
Tampere University of Technology
P.O. Box 589, FI-33101 TAMPERE
email: aku.karvinen@tut.fi

ABSTRACT

Slanted jets in a cross-flow are simulated numerically using the commercial CFD (computational fluid dynamics) code Fluent 6.2.16. A grid resolution study is performed to find a grid that yields a grid-independent solution. The k-ε model, the SST (Shear-Stress Transport) k-ω model, and one version of the Reynolds stress model (RSM) are compared. There are considerable differences between the results of the turbulence models. Of the turbulence models used, the SST k-ω model captures details of the complex flow field most accurately.

1 INTRODUCTION

The desire to increase the efficiency of jet engines and gas turbines has necessitated an increase in temperature in combustion chambers and in the turbine. This leads to an interest in efficient wall-protecting cooling methods. One efficient method for cooling a wall is effusion cooling, in which cooling air is led through the wall along perpendicular or slanted holes. In this method, there is a crossflow which deflects jets emerging on the cooled side of the wall, as shown in Fig. 1. Slanted jets provide better cooling because they do not travel so far from the plate as perpendicular jets, but deflect more rapidly. To provide adequate cooling, several jets in several rows are usually needed.

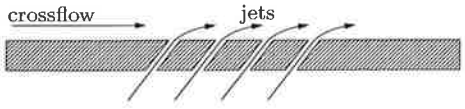


Figure 1: Slanted jets in crossflow.

Because the case of slanted jets in crossflow occurs in so many applications, it has been intensively studied for a long time. For instance, in articles [1, 2, 3, 4, 5, 6, 7, 8, 9] the case has been studied experimentally. Also numerical studies have been done, e.g. in articles [10, 11, 12, 13, 14, 15]. A more extensive review can be found in [16]. In article [17] there are both experimental and numerical results.

In many of the aforementioned articles, both velocity field and heat transfer are considered. In this study, a case introduced in [7] is investigated, and only the velocity field is considered.

2 GOVERNING EQUATIONS AND THEIR NUMERICAL SOLUTION

In this work incompressible, steady-state flow is assumed. In such a case, the Reynolds-averaged Navier-Stokes equations (RANS) are

$$\frac{\partial u_i}{\partial x_i} = 0, \tag{1}$$

$$u_j \frac{\partial u_i}{\partial x_j} = -\frac{1}{\rho}\frac{\partial p}{\partial x_i} + \nu \frac{\partial^2 u_i}{\partial x_j \partial x_j} + \frac{\partial}{\partial x_j}\left(-\overline{u_i' u_j'}\right), \tag{2}$$

where u_i is the mean velocity component in x_i direction, ρ is the density, p is the mean pressure, ν is the kinematic viscosity, and the overbar denotes time averaging.

2.1 Turbulence Models

In the k-ε models and the k-ω models, the Boussinesq hypothesis [18] is used. The Reynolds stresses, $-\overline{u_i' u_j'}$, are approximated with

$$-\overline{u_i' u_j'} = 2\nu_t S_{ij} - \frac{2}{3} k \delta_{ij}, \qquad S_{ij} = \frac{1}{2}\left(\frac{\partial u_i}{\partial x_j} + \frac{\partial u_j}{\partial x_i}\right), \tag{3}$$

where ν_t is the turbulent (or eddy) viscosity.

Standard k-ε Model In the standard k-ε model [19] the turbulence kinetic energy, k, and its dissipation rate, ε, are obtained from the modeled transport equations

$$u_j \frac{\partial k}{\partial x_j} = \frac{\partial}{\partial x_j}\left[\left(\nu + \frac{\nu_t}{\sigma_k}\right)\frac{\partial k}{\partial x_j}\right] + \nu_t S^2 - \varepsilon, \tag{4}$$

$$u_j \frac{\partial \varepsilon}{\partial x_j} = \frac{\partial}{\partial x_j}\left[\left(\nu + \frac{\nu_t}{\sigma_\varepsilon}\right)\frac{\partial \varepsilon}{\partial x_j}\right] + C_{1\varepsilon}\frac{\varepsilon}{k}\nu_t S^2 - C_{2\varepsilon}\frac{\varepsilon^2}{k}, \tag{5}$$

where $S \equiv \sqrt{2 S_{ij} S_{ij}}$. The turbulent viscosity is computed from $\nu_t = C_\mu k^2/\varepsilon$, where C_μ is a constant. The model constants have the following values [20]: $C_\mu = 0.09$, $C_{1\varepsilon} = 1.44$, $C_{2\varepsilon} = 1.92$, $\sigma_k = 1.0$, and $\sigma_\varepsilon = 1.3$.

Shear-Stress Transport (SST) k-ω Model The shear-stress transport (SST) k-ω model [21] has transport equations for the turbulence kinetic energy, k, and the specific dissipation rate, ω:

$$u_j \frac{\partial k}{\partial x_j} = \frac{\partial}{\partial x_j}\left[\left(\nu + \frac{\nu_t}{\sigma_k}\right)\frac{\partial k}{\partial x_j}\right] + \nu_t S^2 - \beta_\infty^* k\omega, \tag{6}$$

$$u_j \frac{\partial \omega}{\partial x_j} = \frac{\partial}{\partial x_j}\left[\left(\nu + \frac{\nu_t}{\sigma_\omega}\right)\frac{\partial \omega}{\partial x_j}\right] + S^2 - \beta_i \omega^2 + D_\omega, \tag{7}$$

where

$$\nu_t = \frac{k}{\omega}\frac{1}{\max\left[1, \frac{\Omega F_2}{a_1 \omega}\right]}, \qquad \Omega \equiv \sqrt{2\bar{\Omega}_{ij}\bar{\Omega}_{ij}},$$

$$\sigma_k = \frac{1}{F_1/\sigma_{k,1} + (1-F_1)/\sigma_{k,2}}, \qquad \sigma_\omega = \frac{1}{F_1/\sigma_{\omega,1} + (1-F_1)/\sigma_{\omega,2}},$$

$$F_1 = \tanh\left(\Phi_1^4\right), \qquad \Phi_1 = \min\left[\max\left(\frac{\sqrt{k}}{0.09\omega y}, \frac{500\nu}{y^2\omega}\right), \frac{4\rho k}{\sigma_{\omega,2} D_\omega^+ y^2}\right],$$

$$F_2 = \tanh\left(\Phi_2^2\right), \qquad \Phi_2 = \max\left[2\frac{\sqrt{k}}{0.09\omega y}, \frac{500\nu}{y^2\omega}\right],$$

$$D_\omega = 2\left(1 - F_1\right)\sigma_{\omega,2}\frac{1}{\omega}\frac{\partial k}{\partial x_j}\frac{\partial \omega}{\partial x_j}, \qquad D_\omega^+ = \max\left[2\rho\frac{1}{\sigma_{\omega,2}}\frac{1}{\omega}\frac{\partial k}{\partial x_j}\frac{\partial \omega}{\partial x_j}, 10^{-10}\right],$$

$\beta_i = F_1\beta_{i,1} + (1 - F_1)\beta_{i,2}$ and $\bar{\Omega}_{ij}$ is the mean rate-of-rotation tensor. The model constants are: $a_1 = 0.31$, $\beta_\infty^* = 0.09$, $\beta_{i,1} = 0.075$, $\beta_{i,2} = 0.0828$, $\sigma_{k,1} = 1.176$, $\sigma_{\omega,1} = 2.0$, $\sigma_{k,2} = 1.0$, and $\sigma_{\omega,2} = 1.168$.

Reynolds Stress Model In the Reynolds stress model (RSM) there are the exact transport equations for the transport of Reynolds stresses, $-\overline{u_i' u_j'}$ [22, 23]:

$$u_k\frac{\partial \overline{u_i' u_j'}}{\partial x_k} = \underbrace{-\frac{\partial}{\partial x_k}\left[\overline{u_i' u_j' u_k'} + \overline{\frac{p'}{\rho}\left(\delta_{kj}u_i' + \delta_{ik}u_j'\right)}\right]}_{D_{ij}^{\mathrm{t}}} - \left(\overline{u_i' u_k'}\frac{\partial u_j}{\partial x_k} + \overline{u_j' u_k'}\frac{\partial u_i}{\partial x_k}\right) +$$

$$\frac{\partial}{\partial x_k}\left[\nu\frac{\partial}{\partial x_k}\left(\overline{u_i' u_j'}\right)\right] + \underbrace{\overline{\frac{p'}{\rho}\left(\frac{\partial u_i'}{\partial x_j} + \frac{\partial u_j'}{\partial x_i}\right)}}_{\phi_{ij}} - \underbrace{2\nu\overline{\frac{\partial u_i'}{\partial x_k}\frac{\partial u_j'}{\partial x_k}}}_{\varepsilon_{ij}}, \quad (8)$$

where D_{ij}^{t} and ϕ_{ij} are modeled using the relations

$$D_{ij}^{\mathrm{t}} = \frac{\partial}{\partial x_k}\left(\frac{\nu_{\mathrm{t}}}{\sigma_k}\frac{\partial \overline{u_i' u_j'}}{\partial x_k}\right), \qquad \nu_{\mathrm{t}} = C_\mu\frac{k^2}{\varepsilon},$$

$$\phi_{ij} = \phi_{ij,1} + \phi_{ij,2} + \phi_{ij,\mathrm{w}}, \qquad \phi_{ij,1} \equiv -C_1\frac{\varepsilon}{k}\left[\overline{u_i' u_j'} - \frac{2}{3}\delta_{ij}k\right],$$

$$\phi_{ij,2} \equiv -C_2\left[\left(P_{ij} + F_{ij} - C_{ij}\right) - \frac{2}{3}\delta_{ij}\left(P - C\right)\right], \qquad P = \frac{1}{2}P_{kk}, \qquad C = \frac{1}{2}C_{kk},$$

and $\phi_{ij,\mathrm{w}}$ is a so-called wall-reflection term [24]. The dissipation tensor, ε_{ij}, is modeled as $\varepsilon_{ij} = 2\delta_{ij}\varepsilon/3$, where ε is obtained from (5) in which the second last term is replaced with $C_{1\varepsilon}P_{ii}\varepsilon/2k$. The turbulence kinetic energy is modeled as $k = \frac{1}{2}\overline{u_i' u_i'}$. The model constants are: $C_1 = 1.8$, $C_2 = 0.60$, $C_{1\varepsilon} = 1.44$, $C_{2\varepsilon} = 1.92$, $C_\mu = 0.9$, $\sigma_k = 1.0$, and $\sigma_\varepsilon = 1.3$.

2.2 Calculation of Near-Wall Area

When using the k-ε model or the RSM, the model should be modified in the vicinity of the no-slip walls. In this work, the method is used where the whole domain is subdivided into two regions, based on Re_y. In the fully turbulent region ($\mathrm{Re}_y > 200$), the k-ε model or the RSM is used. In the area where $\mathrm{Re}_y < 200$, basic model equations are retained, but [25, 26]

$$\nu_{\mathrm{t}} = C_\mu\sqrt{k}\ell_\mu, \qquad \ell_\mu = C_\ell y\left(1 - e^{-\mathrm{Re}_y/A_\mu}\right),$$

$$\varepsilon = \frac{k^{3/2}}{\ell_\varepsilon}, \qquad \ell_\varepsilon = C_\ell y \left(1 - e^{-\mathrm{Re}_y/A_\varepsilon}\right),$$

where $A_\mu = 70$ and $A_\varepsilon = 2C_\ell$ [26]. Between the inner ($\mathrm{Re}_y < 200$) and outer ($\mathrm{Re}_y > 200$) region, ν_t and ε are blended to ensure a smooth transition [24].

2.3 Calculation Procedure

All calculations were done using FLUENT 6.1.16 [24], a commercial software based on the finite volume method. All terms in all equations are discretized in space using second-order central differencing, apart from the convection term, which is discretized using a second-order upwind scheme. Pressure-velocity coupling was done using SIMPLE algorithm.

Default values of all constants are used. All options which are enabled by default are used. In addition, a low-Reynolds-number correction to the turbulent viscosity is enabled when using the SST k-ω model. All calculations are iterated until they approach the machine number, and therefore it can be assumed that iteration error is negligible. Relaxation parameters are reduced when needed.

3 COMPUTATIONAL DOMAIN AND MESH

The schematic of the computational domain and boundary conditions are shown in Figure 2. In the experiments there was a perforated plate with several rows of holes. Only a slice of the domain has been simulated and the periodic symmetry has been taken into account. Velocities in the inlets are chosen so that the freestream velocity of the crossflow ($u_0 = 17.5\,\mathrm{m/s}$) and the jet velocity in the center of the jet are close to the measured values when the k-ε model is used.

The computational grid consists of eight zones with non-matching interfaces: the plenum chamber, the six jets, and the main test section. Six different grid resolutions have been used such that the total number of control volumes used is 286,370, 615,714, 1,810,960,

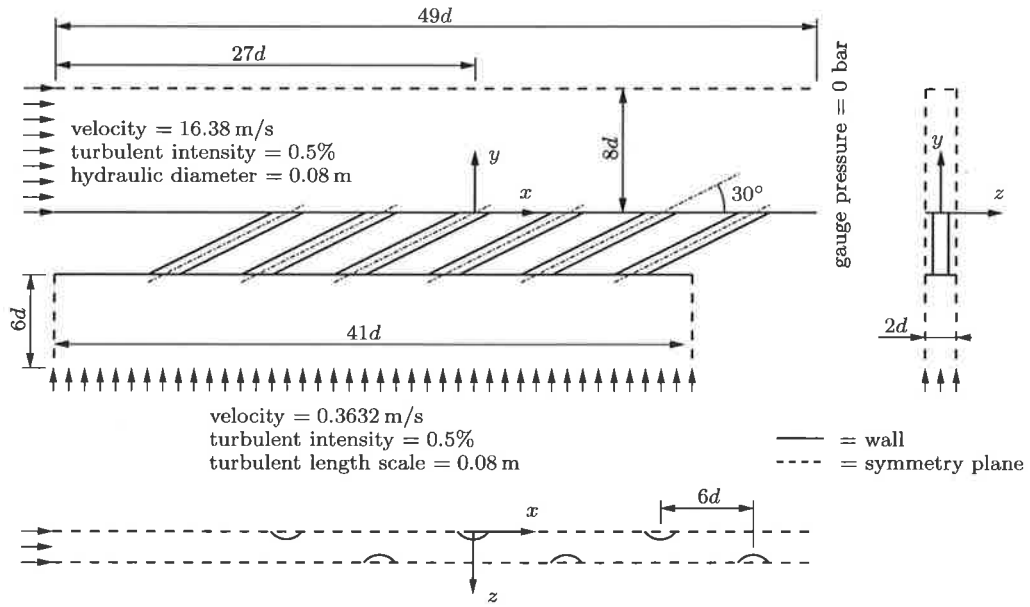


Figure 2: Computational domain and boundary conditions. Pipe diameter $d = 5\,\mathrm{mm}$.

1,848,200, 2,155,262, or 4,575,834. The three last-mentioned grids have been constructed by adapting the grid 1,810,960 in the region $-1 \leq x/d \leq 3$, $y/d \leq 1$, and $z/d \leq 0.75$ once, twice, and three times, respectively. All grids have been constructed so that the dimensionless wall unit, $y^+ = u_\tau y/\nu$, is close to unity at the wall-adjacent cells of all no-slip walls, except in the adapted region, where y^+ is less than unity. The grid 2,155,262 in the vicinity of one jet is shown in Figure 3.

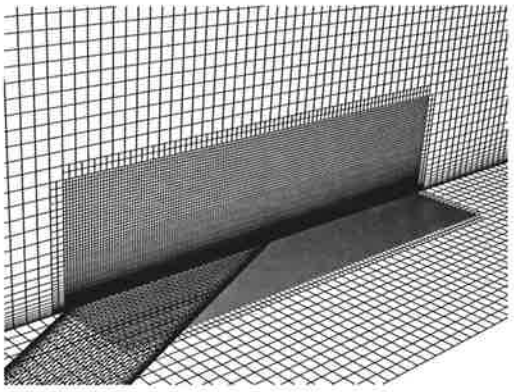


Figure 3: The grid 2,155,262 (used in turbulence model comparison) in the vicinity of one jet.

4 RESULTS

In this section, results of a grid resolution study and a turbulence model comparison are presented. According to [7], the velocity field in the vicinity of the jet is very complex, as shown in Fig. 4. It can be seen that a focus is present in the wake of the jet on each side of the symmetry plane. In addition, the off-wall nodal point (denoted by N) is situated in the downstream of the foci. All these details are difficult to capture by simulation. In the figure, S and S' denote saddle points.

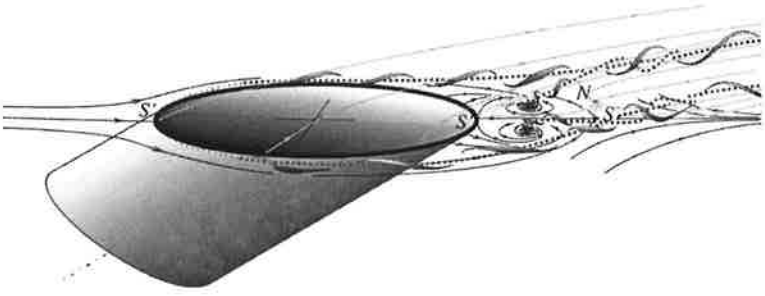
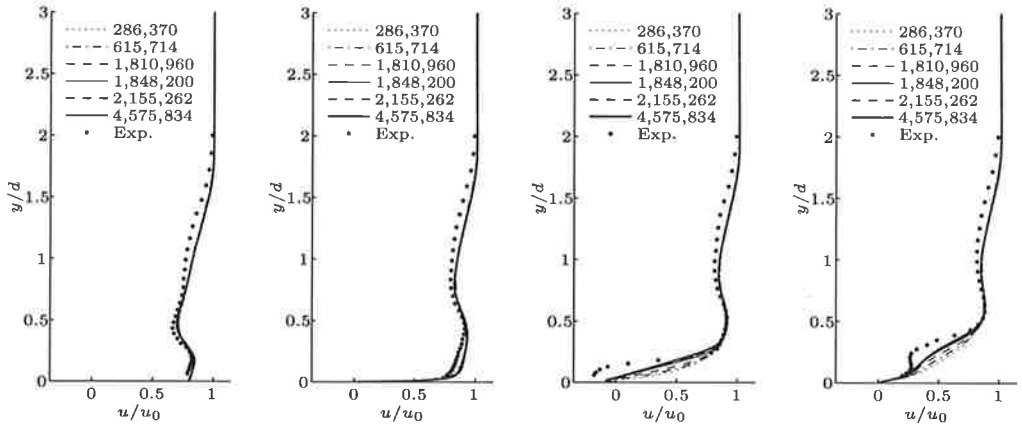


Figure 4: Interpretation of the measured velocity field and its topology according to [7].

4.1 Grid Resolution Study

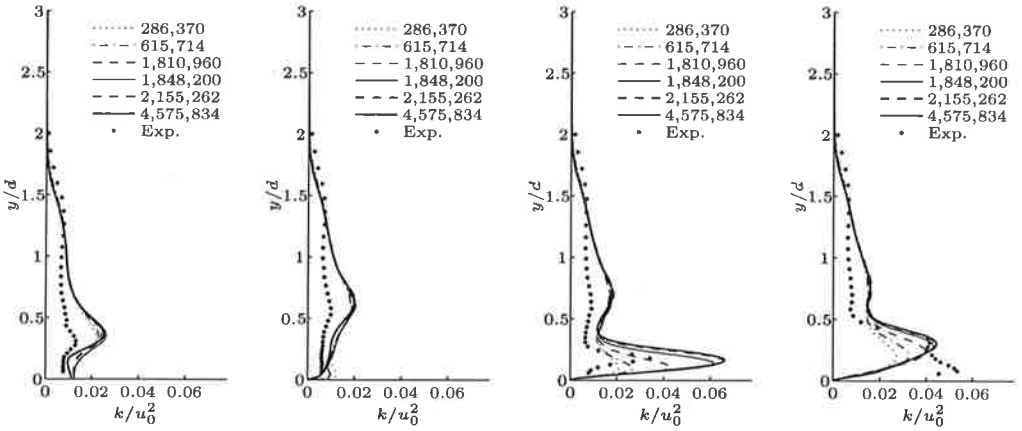
According to the results, a grid should be very fine to obtain a grid-independent solution (Figs. 5 and 6). Velocity profiles do not change significantly when the grid has been made

finer than one consisting of 615,714 control volumes. Significant changes in the turbulent kinetic energy (Fig. 6) can be seen, but changes are marginal when the grid consists of more than 2,155,262 control volumes. Therefore, a grid of 2,155,262 control volumes is used exclusively in the turbulence model comparison.



(a) $x/d = 0$ (b) $x/d = 1$ (c) $x/d = 1.48$ (d) $x/d = 2$

Figure 5: Grid resolution study. Horizontal velocity in selected locations in symmetry plane ($z/d = 0$). Measurements [7].



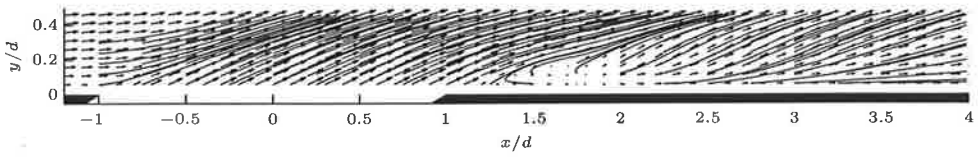
(a) $x/d = 0$ (b) $x/d = 1$ (c) $x/d = 1.48$ (d) $x/d = 2$

Figure 6: Grid resolution study. Turbulence kinetic energy in selected locations in symmetry plane ($z/d = 0$). Measurements [7].

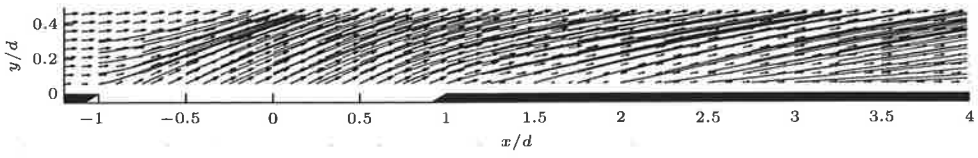
4.2 Turbulence Model Comparison

All calculations based on the k-ε model in the previous subsection converged quite easily. In contrast, the RSM calculations did not converge unless the k-ε model results were used as starting values. The SST k-ω model calculations did not converge even in this way when a single precision solver was used, and thus a double precision solver had to be employed.

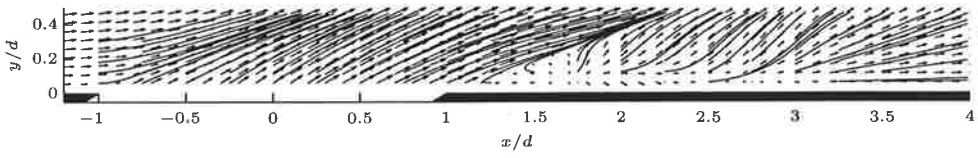
Fig. 7 presents the velocity field in the symmetry plane. Only the SST k-ω model captures the off-wall nodal point. The k-ε model does not find it at all, and results of RSM are quite peculiar. It can be seen from the velocity fields in the plane $y/d = 0.06$ (Fig. 8) that the k-ε model and the RSM do not capture the focus either. The RSM predicts negative horizontal velocity in the symmetry plane near the focus, but the backflow is too



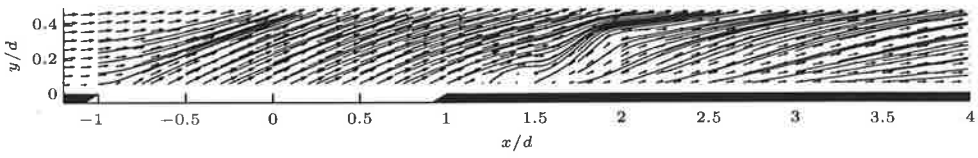
(a) Exp. [7]



(b) k-ε

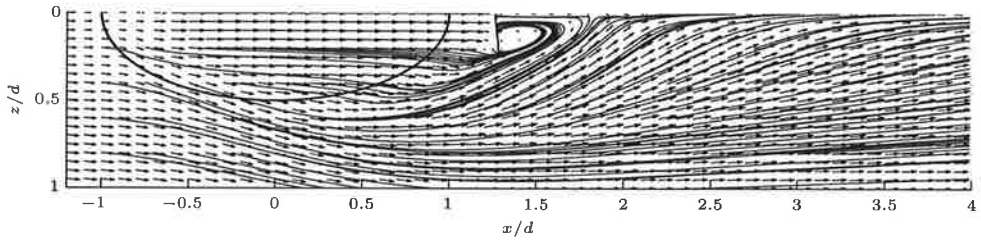


(c) SST k-ω

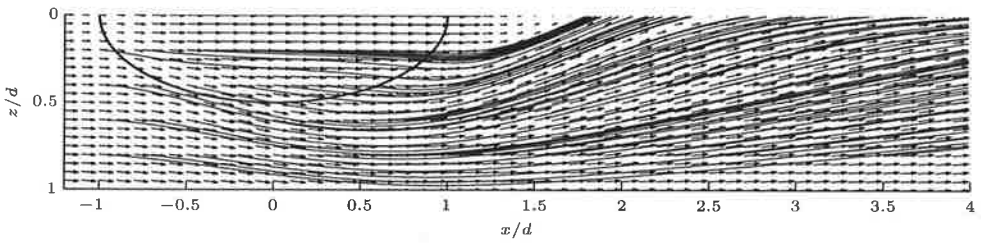


(d) RSM

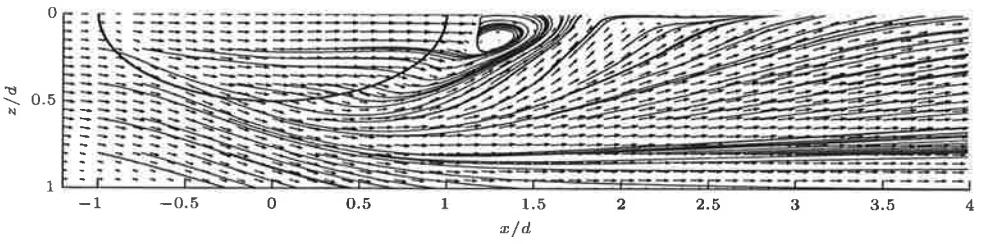
Figure 7: Turbulence model comparison. Sectional streamlines together with inplane (u,v) mean velocity vectors in symmetry plane ($z/d = 0$).



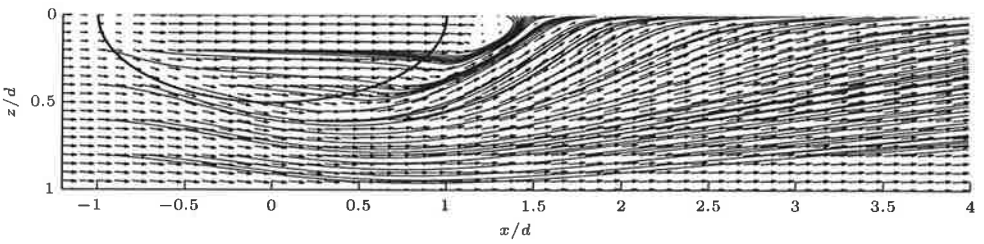
(a) Exp. [7]



(b) k-ε



(c) SST k-ω



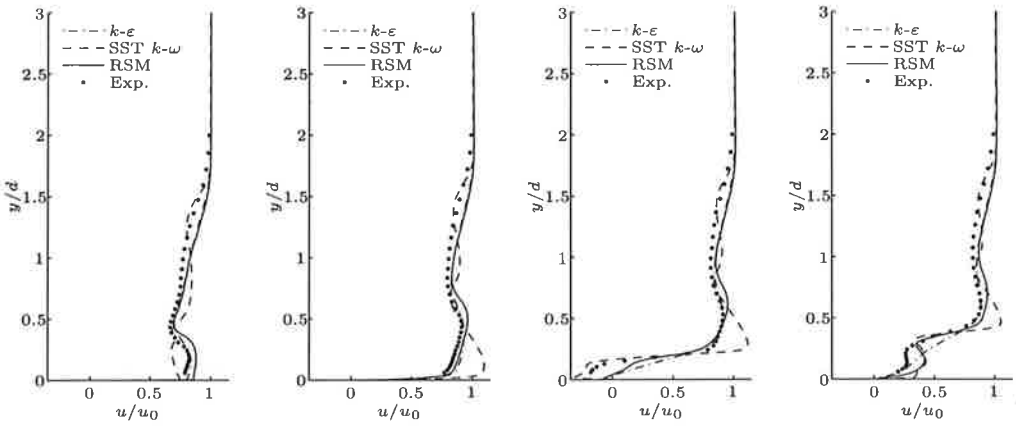
(d) RSM

Figure 8: Turbulence model comparison. Sectional streamlines together with inplane (u,w) mean velocity vectors in plane $y/d = 0.06$.

weak to produce the focus correctly. The focus of the SST k-ω model is quite correct in size and place. It should be noted that the streamlines in Fig. 8 go through the symmetry plane because normal velocities are zero only in computational accuracy.

In addition to the results presented in this study, the case has been calculated using the SST k-ω model and the grid 1,810,960. When this coarser grid was used, the SST k-ω model could not capture the focus either. This emphasizes the need for the grid-independent test.

In spite of the preceding observations, the horizontal and the vertical velocity profiles in the symmetry plane and the horizontal velocity profiles in the plane $z/d = 0.48$ of the k-ε model and the Reynolds Stress model are close to the measured values, but the results of the SST k-ω model are unrealistic (Figs. 9, 10, and 11). There are significant differences between the predicted turbulent kinetic energy profiles (Fig. 12). Profiles of the k-ε model are closest to the measured profiles.



(a) $x/d = 0$ (b) $x/d = 1$ (c) $x/d = 1.48$ (d) $x/d = 2$

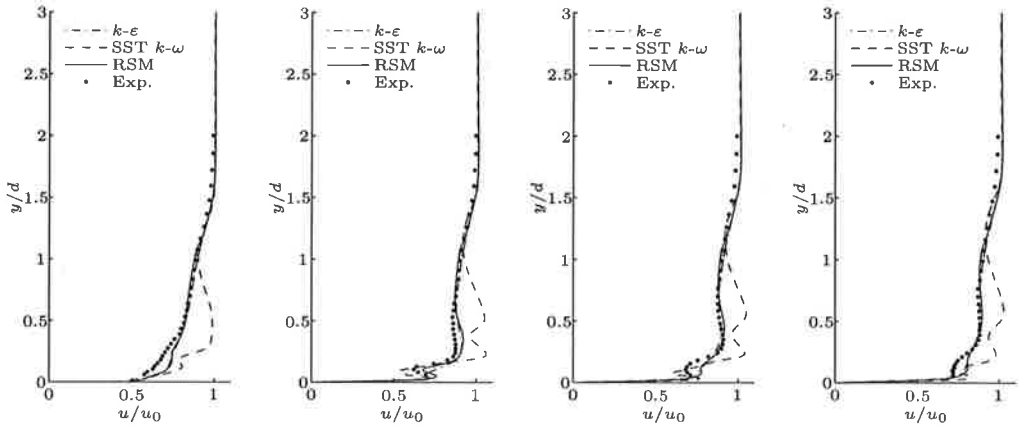
Figure 9: Turbulence model comparison. Horizontal velocity in selected locations in symmetry plane ($z/d = 0$). Measurements [7].

5 CONCLUSIONS

The grid resolution study illustrated that accurate calculation of the slanted jets in a crossflow requires a very fine grid. Even the structure of the flow field can be wrong if the grid used is not dense enough.

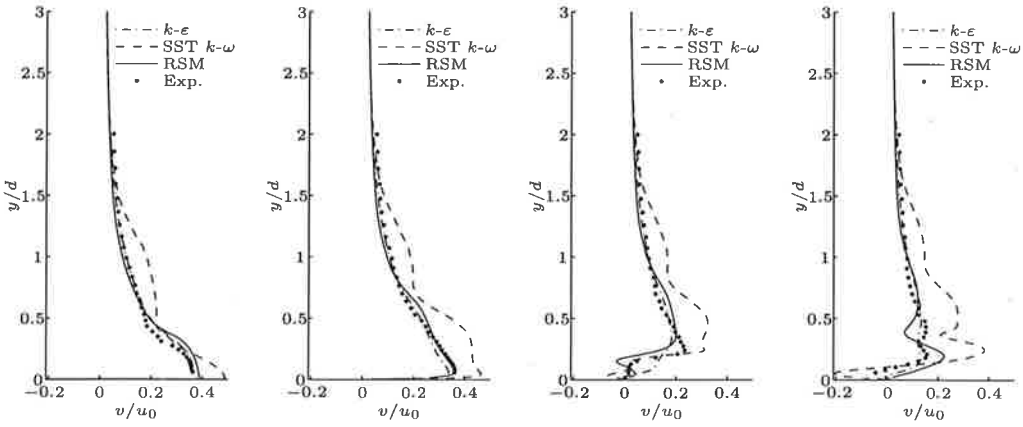
There are considerable differences between the results of the compared turbulence models. Only the SST k-ω model captures all details of the flow field, including the off-wall nodal point and the focus in the wake of the jet. The k-ε model does not find these details at all. It is possible to see marks of the nodal point and focus in the results of the RSM, but the backflow is too weak to produce a correct size focus.

Is spite of these observations, considered horizontal and vertical velocity profiles of the k-ε model and the Reynolds Stress model are quite close to the measured values. Velocity profiles of the SST k-ω model are unrealistic.



(a) $x/d = 0$ (b) $x/d = 1$ (c) $x/d = 1.48$ (d) $x/d = 2$

Figure 10: Turbulence model comparison. Horizontal velocity in selected locations in plane $z/d = 0.48$. Measurements [7].

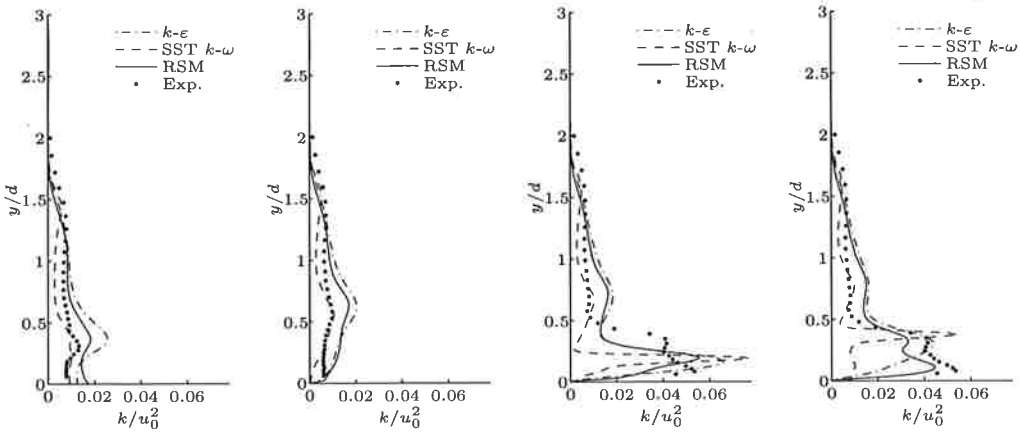


(a) $x/d = 0$ (b) $x/d = 1$ (c) $x/d = 1.48$ (d) $x/d = 2$

Figure 11: Turbulence model comparison. Vertical velocity in selected locations in symmetry plane ($z/d = 0$). Measurements [7].

ACKNOWLEDGMENT

The authors gratefully acknowledge the support from Tekes - The National Technology Agency of Finland, Andritz Oy, Enprima Oy, Fortum Nuclear Services Oy, Kværner Power Oy, Metso Paper Oy, Nokia Oy, Numerola Oy, Patria Aviation Oy, and Process Flow Ltd Oy.



(a) $x/d = 0$ (b) $x/d = 1$ (c) $x/d = 1.48$ (d) $x/d = 2$

Figure 12: Turbulence model comparison. Turbulence kinetic energy in selected locations in symmetry plane ($z/d = 0$). Measurements [7].

REFERENCES

[1] R. S. Colladay and L. M. Russell. *Streakline flow visualization of discrete hole film cooling for gas turbine applications*. Journal of Heat Transfer, **3**, 245-250 (1976).

[2] M. Sasaki, K. Takahara, T. Kumagai and M. Hamano. *Film cooling effectiveness for injection from multirow holes*. Journal of Engineering for Power, **101**, 101-108 (1979).

[3] N. W. Foster and D. Lampard. *The flow and film cooling effectiveness following injection through a row of holes*. Journal of Engineering for Power, **102**, 584-588 (1980).

[4] M. Salcudean, I. Gartshore, K. Zhang and I. McLean. *An experimental study of film cooling effectiveness near the leading edge of a turbine blade*. Journal of Turbomachinery, **116**, 71-79 (1994).

[5] S. Friedrichs, H. P. Hodson and W. N. Dawes. *Distribution of film-cooling effectiveness on a turbine endwall measured using the ammonia and diazo technique*. Journal of Turbomachinery, **118**, 613-621 (1996).

[6] S. W. Burd and T. W. Simon. *The influence of coolant supply geometry on film coolant exit flow and surface adiabatic effectiveness*. ASME Paper 97-GT-2597, presented at the 1997 Turbo Expo, Orlando, FL, 1997.

[7] K. M. B. Gustafsson. *Experimental Studies of Effusion Cooling*. Ph.D. thesis, Department of Thermo and Fluid Dynamics, Chalmers University of Technology, Gothenburg, Sweden, 2001.

[8] A. Kohli and D. G. Bogard. *Turbulent transport in film cooling*. Journal of Heat Transfer, **127**, 513-520 (2005).

[9] Y. Lin, B. Song, B. Lin and G. Liu. *Measured film cooling effectiveness of three multihole patterns*. Journal of Heat Transfer, **128**, 192-197 (2006).

[10] D. B. Bain, C. E. Smith and J. D. Holdeman. *CFD mixing analysis of jets injected from straight and slanted slots into confined crossflow in rectangular ducts.* Technical Report TM-105699, NASA, Cleveland, Ohio, 1992. PDF available from url: http://gltrs.grc.nasa.gov/reports/1992/TM-105699.pdf.

[11] D. B. Bain, C. E. Smith and J. D. Holdeman. *CFD assessment of orifice aspect ratio and mass flow ratio on jet mixing in rectangular ducts.* In *32nd Aerospace Sciences Meeting and Exhibit*, AIAA-1994-218. Reno, Nevada, 1994.

[12] S. Mendez, F. Nicoud and P. Miron. *Direct and large-eddy simulations of a turbulent flow with effusion.* In *ERCOFTAC Workshop on Direct and Large-Eddy Simulation-6, DLES-6*. Poitiers, France, 2005.

[13] A. Azzi and B. A. Jubran. *Numerical modelling of film cooling from converging slot-hole.* Heat and Mass Transfer. Published Online, 26 April, 2006.

[14] J.-M. Miao and H.-K. Ching. *Numerical simulation of film-cooling concave plate as coolant jet passes through two rows of holes with various orientations of coolant flow.* International Journal of Heat and Mass Transfer, **49**, 557-574 (2006).

[15] J.-M. Miao and C.-Y. Wu. *Numerical approach to hole shape effect on film cooling effectiveness over flat plate including internal impingement cooling chamber.* International Journal of Heat and Mass Transfer, **49**, 919-938 (2006).

[16] A. I. Leontiev. *Heat and mass transfer problems for film cooling.* Journal of Heat Transfer, **121**, 509-527 (1999).

[17] K. M. B. Gustafsson and T. G. Johansson. *Turbulence and velocity fields of slanted jets in crossflow – measurements and CFD simulations.* In *Turbulence, Heat and Mass Transfer 4*. Antalya, Turkey, 2003.

[18] J. O. Hinze. *Turbulence.* McGraw-Hill, New York, 1975.

[19] B. E. Launder and D. B. Spalding. *Lectures in Mathematical Models of Turbulence.* Academic Press, London, 1972.

[20] B. E. Launder and B. I. Sharma. *Application of the energy dissipation model of turbulence to the calculation of flow near a spinning disc.* Letters in Heat and Mass Transfer, **1**, 131-138 (1974).

[21] F. R. Menter. *Two-equation eddy-viscosity turbulence models for engineering applications.* AIAA Journal, **32**, 1598-1605 (1994).

[22] M. M. Gibson and B. E. Launder. *Ground effects on pressure fluctuations in the atmospheric boundary layer.* Journal of Fluid Mechanics, **86**, 491-511 (1978).

[23] B. E. Launder, G. J. Reece and W. Rodi. *Progress in the development of a Reynolds-stress turbulence closure.* Journal of Fluid Mechanics, **68**, 537-566 (1975).

[24] Fluent Inc. *FLUENT 6.2 user's guide.* Lebanon, 2005.

[25] M. Wolfshtein. *The velocity and temperature distribution of one-dimensional flow with turbulence augmentation and pressure gradient.* International Journal of Heat and Mass Transfer, **12**, 301-318 (1969).

[26] H. C. Chen and V. C. Patel. *Near-wall turbulence models for complex flows including separation.* AIAA Journal, **26**, 641-648 (1988).

RASKAAN KRANAATINHEITTIMEN LAUKAUSPAINEEN MITTAUSMENETELMIEN VERTAILU

S. MOILANEN & J. TERVOKOSKI

Patria Weapon Systems Oy
PL 18, Vammaksentie
38201 Vammala
e-mail: seppo.moilanen@patria.fi
janne.tervokoski@patria.fi

TIIVISTELMÄ

Sisäballistisen vaiheen painemittaus lienee tärkein mittaus asejärjestelmän laukausrasituksia määritettäessä. Painemittausmenetelmien perusteiden tuntemus ja mittaustuloksiin vaikuttavien virhelähteiden hallinta ovat uusien asejärjestelmien tuotekehityksen, testauksen ja tuote-erien hyväksymiskokeiden sekä vanhojen asejärjestelmien modernisointien onnistumisen perusedellytyksiä. 120 mm:n kranaatinheitinasejärjestelmien painevertailukoeammuntojen tulokset osoittivat, että mekaanisen crushermittauksen painearvo jäi (8…23) % sähköisesti mitattua kidepaineen maksimiarvoa alemmaksi. Suhteellinen paine-ero kasvoi painetason kohotessa. Aseen rekyyli- ja värähtelyliikkeen kiihtyvyydet vääristivät kidepainemittaustulosta yli 2 % rekylöivillä kranaatinheittimillä. Kidepainemittaus ja tuliputken ulkopinnan venymistä laskennallisesti määritetty paine olivat kohtuullisen yhtenevät. Putken taivutusmuodonmuutoksen kompensointi kahdella venymäliuskaparilla putken vastakkaisilla sivuilla ja putkiseinämän lämpötilagradientin aiheuttaman lämpövenymätilan kompensointi yksinkertaisella laskennallisella menettelyllä lisäsivät venymäliuskamittauksin määritetyn painetuloksen käyttökelpoisuutta. Venymäliuskamittauksen todettiin soveltuvan kranaatinheittimien tuliputkien vertailupainemittausmenetelmäksi sangen hyvin.

1. JOHDANTO

Aseiden ja ampumatarvikkeiden laukausrasitukset ovat seurausta sisäballistisen vaiheen aikana palavan ruudin palokaasujen paineesta. Lyhytkestoinen painepulssi kuormittaa aseen tuliputkea, sulkuosia sekä ammusta. Tulen kantaman ja tulinopeuden kasvattaminen sekä samanaikainen vaatimus tulen tarkkuuden parantamisesta (osumien pieni hajonta maalialueella) korostavat sisäballistisen vaiheen tapahtumien mittaustarkkuutta ja –luotettavuutta aseiden ja ampumatarvikkeiden tuotekehitys-, testausvaiheessa sekä tuote-erien hyväksymiskokeissa. Sisäballistisen vaiheen painemittaus lienee tärkein mittaus aseen ja ammuksen laukausrasitusten kannalta. Luotettavan painemittauksen edellytyksiä ovat mittausjärjestelmien tuntemus ja painemittaukseen liittyvien virhelähteiden hallinta.

Nykyisin käytössä olevien raskaiden asejärjestelmien tyypilliset maksimipaineet vaihtelevat perinteisten kranaatinheittimien ~100 MPa:sta panssarivaunukanuunoiden ~(500…800) MPa:iin ja ammuksen lähtönopeudet ovat vastaavasti ~200 m/s kranaatinheittimillä ja ~1800 m/s panssarivaunukanuunoilla. Epäsuoran tulen tykistöaseilla paineet ja lähtönopeudet asettuvat edellisten rajojen väliin. Paineen nousunopeus, maksimipaine saavutetaan muutamassa millisekunnissa ruudin syttymisestä, sekä pulssin lyhyt kestoaika rajoittavat mittausmenetelmien valintamahdollisuuksia.

Raskaiden aseiden ja ampumatarvikkeiden länsimaiset painemäärittelyt on esitetty standardissa Stanag 4110 [1]. Standardin mukaiset aseen ja ammuksen konstruktiiviset painerajat ovat perinteisestä suomalaisesta asepainejärjestelmästä poiketen puhtaasti lujuuslaskennallisia suureita, joita määritettäessä ei ole otettu kantaa painemittausmenetelmiin eikä mittausmenetelmistä mahdollisesti aiheutuvia, fysikaalisesta paineesta eroavia "mittaus-"painearvoja ole huomioitu. Periaatteena on, että asejärjestelmän alustavaan sisäballistiseen simulointiin perustuva suunnittelupaine on sopivan, kokemusperäisen varmuusmarginaalin verran asejärjestelmän toiminnan kannalta haitalliseen muodonmuutokseen tai muuhun vaurioon johtavaa painekuormaa alempi. Sallitut asejärjestelmän käyttöpainerajat ovat suunnittelupaineen alapuolella, mutta käyttöpainerajoissa huomioidaan olosuhdetietojen ohella myös asejärjestelmän osien (ase, ammus, panos, valmistuserä) painearvojen tilastolliset ominaisuudet. Ne määritetään painemittauksin koeammunnoissa, jolloin mittausmenetelmän mukaiset seikat on huomioitava. Ase- ja ammussuunnittelun nykysuuntauksena on varmuusmarginaalien pieneneminen laskennallisten menetelmien, mittausmenetelmien ja materiaalitutkimuksen kehityksen myötä [8, 9].

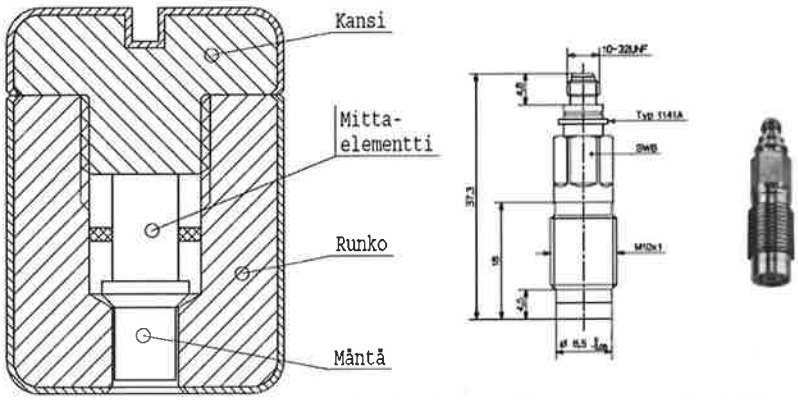
2. PAINEMITTAUSMENETELMÄT

Rutiiniluonteisina painemittausmenetelminä koeammunnoissa ovat mekaaninen crushermittaus ja sähköinen kidepainemittaus [2, 3]. Crushermittauksessa aseen panoskammioon sijoitetaan terässylinteri, jonka sisällä mittauselementtinä on kuparinen lieriö tai pallo, jota ruutikaasu puristaa männän välityksellä (Kuva 1). Kuparilieriön pituuden tai pallon halkaisijan muutos mitataan tarkkuusmikrometrillä laukauksen jälkeen ja mittamuutoksen perusteella määritetään paine crushervalmistajan toimittamaa vertailutaulukkoa tai muuta kalibrointitaulukkoa käyttäen. Crushermittauksella saadaan arvio laukauksen aikana aseessa esiintyneelle maksimipaineelle tai paremminkin arvio paineen jonkinmoiselle tehollisarvolle. Paineen aikariippuvuutta tai mahdollisia painevärähtelyjä ei kyetä crushermittauksella määrittämään. Crushermittauksen etuja ovat yksinkertaisuus, suhteellinen halpuus ja näennäinen mittauksen helppous sekä se, että painemittaus ei edellytä aseeseen mitään muutoksia, kuten läpivientejä seinämiin, jos crushermittari mahtuu aseen panoskammioon tai ammuksen hylsyyn ampumatarvikkeiden mukana. Haittoja ovat paineen aikariippuvuuden ja erityisesti terävän painepiikin katoaminen mittaustiedosta, vaikea tai paremminkin mahdoton varsinaisen mittaelementin kalibroitavuus sekä mittaustulosten sangen suuri hajonta. Painealueen mukaan on valittava "sopiva" crushermittari ja mitattavan maksimipaineen kohotessa kasvaa crushermittarin koko.

Sähköisillä mittausmenetelmillä voidaan painepulssi mitata ajan funktiona koko laukaussyklin kestoajalta. Asepaineiden mittauksissa käytetään pietsokideantureita, joiden toiminta perustuu pietsokiteen (pii-kiteen) varaustilan muuttumiseen muodonmuutoksen funktiona. Kun paine vs. aika käyrä $p(t)$ on mitattu sähköisesti, voidaan mittaustuloksesta laskea tai määrittää useita ampumatarvike- ja asesuunnittelun kannalta tärkeitä tunnusarvoja kuten: Paineen nousunopeus ja -aika, paineimpulssi, mahdollisten painevärähtelyjen taajuus (-det) ja amplitudi (-t) jne. Kidepainemittauksen etuja ovat luotettava mittaustulos, hyvä toistuvuus ja pieni hajonta, anturin kalibroitavuus ja erityisesti paineen aikariippuvuuden ja siihen liittyvien ilmiöiden mittausmahdollisuus. Varjopuolia ovat mittalaitteiden suhteellinen kalleus, antureiden, liittimien ja johtimien mekaaninen kestävyys aseen rekyyli- ja/tai värähtelyliikkeestä aiheutuvissa kuormituksissa, työlääs ja monimutkaiset mittausjärjestelyt verrattuna crusherpainemittaukseen, kohtuullisen kalliin dynaamisen painekalibrointilaitteiston tarve ja ylläpito sekä se, että paineanturin asennus vaatii mekaanisia muutoksia aseeseen.

Kolmantena painemittausmenetelmänä on edellisten yhdistelmä eli "sähköinen crushermittaus" tai "piezo-crusher". Siinä kidepaineanturi ja tarvittava mittauselektroniikka on sijoitettu metallisen suojakuoren sisään ja anturia käytetään koeammunnassa perinteisen crushermittarin tapaan. Laukauksen jälkeen painekäyrä $p(t)$ luetaan muistipiiriltä. Menetelmällä on molempien erillistapojen edut, mutta haittoina ovat normaalia crusheria suurempi koko, joka estää mittarin käytön ahtaissa panoskammioissa, mittaustuloksen aikakytkennän puute mahdollisiin muihin mittauksiin

sekä ainakin toistaiseksi anturin mekaaninen kestävyys ja hinta. Kranaatinheittimen laukauspainemittaukseen soveltuvaa sähköistä crushermittaria ei ole ollut käytettävissä kotimaisen puolustusteollisuuden koeammunnoissa.



Kuva 1. Mekaanisen crushermittarin rakennepiirros vasemmalla ja Kistler 6215 kidepaineanturin mittapiirros sekä kuva [5] oikealla. Kuvien mittakaava ei ole sama.

Viimeaikainen asepainemittaukseen liittyvä tutkimus [3, 4] on Suomessa keskittynyt tykistön asejärjestelmiin. Tutkimuksissa on pyritty ensisijaisesti parantamaan crushermittauksen luotettavuutta ja tulosten vertailukelpoisuutta kidepainemittaukseen nähden tykeissä esiintyvillä painetasoilla ja -pulsseilla. Päätelminä on todettu, että crushermittauksen painearvot lähenevät kidepainemittauksen tuloksia, jos crushermittauksessa kyetään huomioimaan mittaelementin materiaalin dynaamiset lujuusominaisuudet joko dynaamisella kalibroinnilla ja/tai mittaelementin materiaalin dynaamisilla aineenkoetuskokeilla määritettyjä materiaaliparametreja käyttämällä.

Kranaatinheittimien maksimipainetasot ovat tyypillisesti alle puolet tykkien tai panssarivaunukanuunoiden maksimipaineista, mutta paineen nousu ja lasku ovat nopeampia ja siten paine-aikakäyrä $p(t)$ on terävämpi kuin tykeillä. Modernit ajoneuvo- tai alusasenteiset kranaatinheitinasejärjestelmät kuten AMOS® (Kuva 2) lähenevät ominaisuuksiltaan tykkejä; painearvot ja ammuksen lähtönopeudet kasvavat, rekyylivaimennus, automaattinen lataus aseen perästä, koneellinen aseen koro- ja sivusuuntaus, ryöppyammunta, ammunta suorasuuntauksella jne. Niillä on kyettävä ampumaan myös perinteisiä kranaatinheittimien ampumatarvikkeita, jonka seurauksena rekylöivien kranaatinheittimien suhteellinen toimintapainealue on huomattavasti laajempi kuin tykeillä.

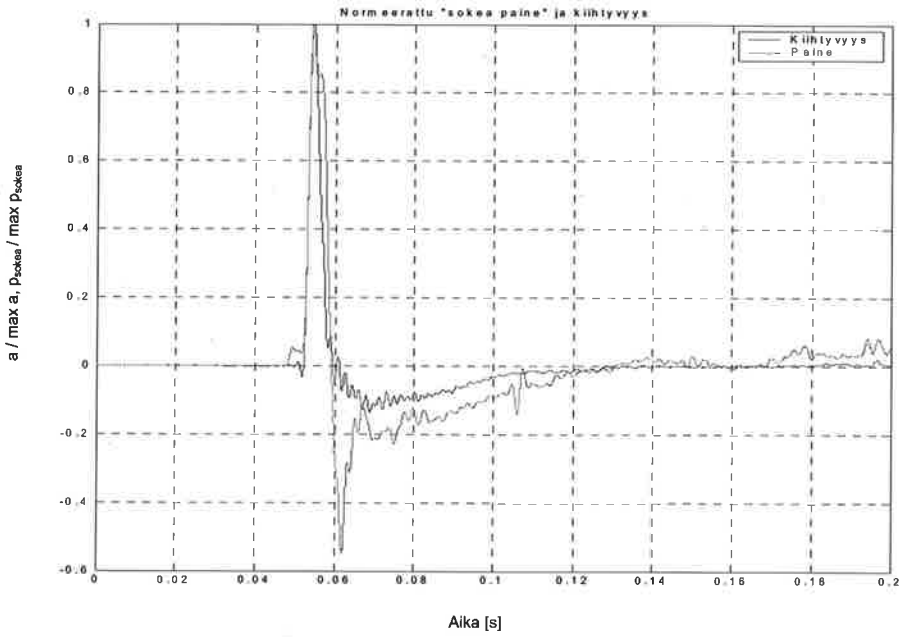


Kuva 2. Perinteinen 120 mm:n kranaatinheitin ja kaksiputkisella 120 mm:n kranaatinheitintornilla varustettu panssaroitu kranaatinheitinajoneuvo AMOS®-AMV Advanced MOrtar System-Armoured Modular Vehicle [12, 13].

3. KIIHTYVYYDEN VAIKUTUS KIDEPAINEMITTAUSTULOKSEEN

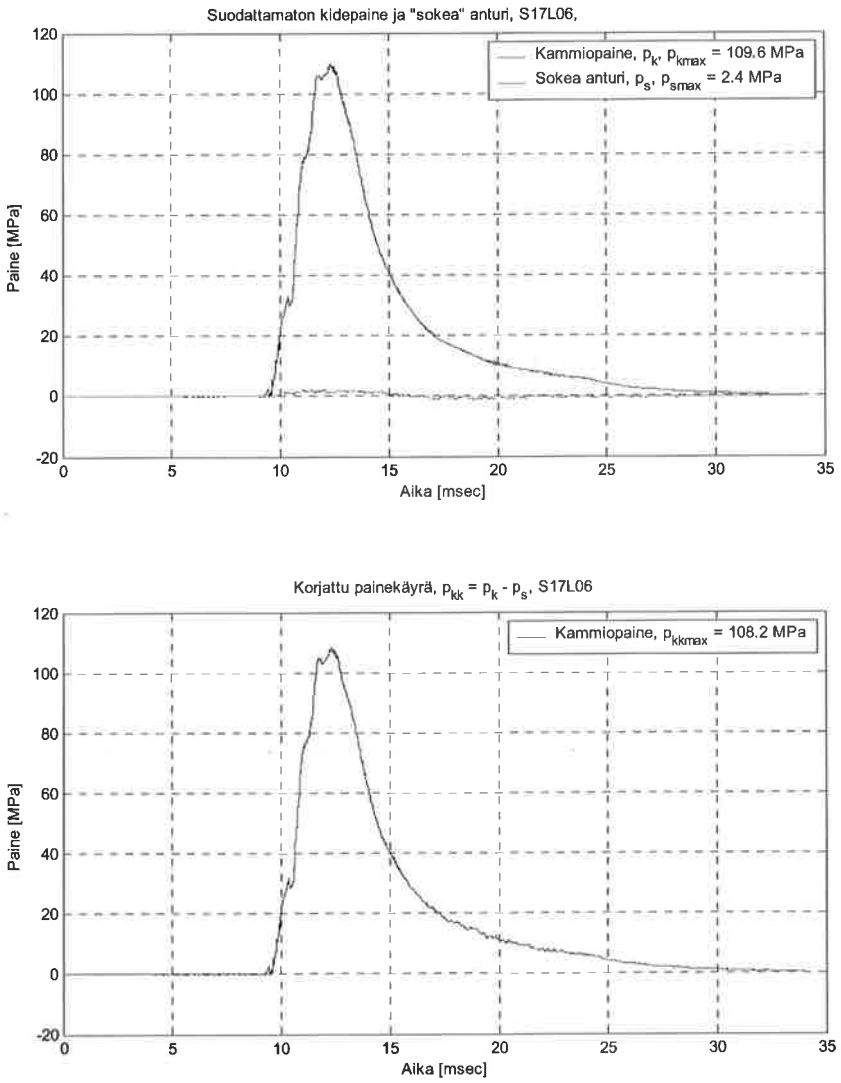
Rekylöivillä aseilla rekyyliliike aiheuttaa hitausvoimia myös mittalaitteisiin ja oletettavasti myös itse kidepaineanturin mittaelimeen syntyy muodonmuutoksia. Kidepaineantureita on saatavilla kiihtyvyyskompensoituina, mutta yleisimmät asepainemittauksiin käytetyt anturityypit eivät ainakaan toistaiseksi ole olleet kiihtyvyyskompensoituja lukuun ottamatta eräitä tutkimuksellisia erikoissovelluksia [7]. Rekylöivillä kranaatinheittimillä rekylöivät massat ovat ~1/10-osa ja rekyyliliikkeen pituus, paineen nousuaika sekä maksimipainekuormitus ovat n. puolet tykkien tai panssarivaunukanuunoiden vastaavista arvoista, joten kranaatinheittimillä sekä rekyyliliikkeen kiihtyvyys paineen nousuaikana että hidastuvuus syklin lopussa ovat selvästi suurempia ja rekyyliliike on rajumpi kuin tykeillä tai vaunukanuunoilla.

Kiihtyvyyden vaikutusta kidepaineanturin mittaustulokseen tutkittiin vertailumittauksella. Rekylöivään kranaatinheittimeen asennettiin panoskammiopainetta mittaava paineanturi normaalisti sekä sen vierelle "sokea anturi", jonka mittapäähän paine ei vaikuttanut. Kuvasta (Kuva 3), jossa on esitetty aseen rekyylikiihtyvyys (putken suuntainen kiihtyvyys) ja "sokea paine" normeerattuna, on selkeästi havaittavissa kidepaineanturin reagointi aseen rekyylikiihtyvyyteen sekä "sokean paineen" ja kiihtyvyyskäyrän samanmuotoisuus. Kidepaineanturi on "mitannut" aseen kiihtyvyyttä.



Kuva 3. Aseen normeerattu rekyylikiihtyvyys $a(t)$/max a ja normeerattu kidepaineanturin "sokea paine" $p_{sokea}(t)$/max p_{sokea} [11].

Mittauksin todettu kidepaineen suhteellinen kiihtyvyysvaikutuksen (max p_h-p_{sokea})/max p_h vaihteluväli oli (0,5…1,3) % maksimipaineen hetkellä ja se osoittautui yli kolminkertaiseksi anturivalmistajan ilmoittaman anturityypin poikittais- tai pitkittäiskiihtyvyysherkkyyden mukaan arvioituun vaikutukseen nähden. Koeammuntamittauksessa oli mukana koko mittausketju, jolloin tuloksiin saattoivat vaikuttaa myös johtimiin ja liittimin kohdistuvat mekaaniset kuormitukset. Niiden vaikutusta ei ole ehkä huomioitu tai se on voitu kompensoida anturivalmistajan laboratoriotesteissä.



Kuva 4. Kidepaine ja "sokea paine" yläkuvassa ja kiihtyvyyskorjattu paine alakuvassa ~100 MPa:n kammiopaineen tuottavalla laukauksella. Maksimipaineen suhteellinen virhe ~1,3 % ja absoluuttinen virhe Δp=1,4 MPa. Suurin laukauksen aikainen "kiihtyvyyspaine" p_{sokea}=2,4 MPa [11].

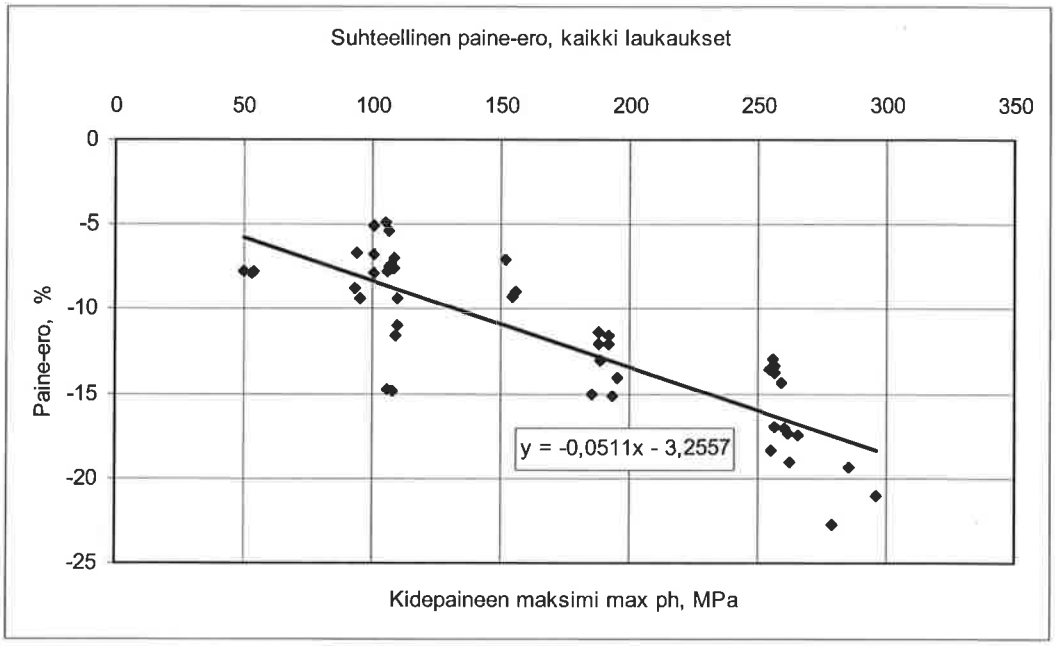
Koetulosten mukaan on perusteltua olettaa, että voimakkaasti rekylöivillä aseilla on huomioitava kiihtyvyysvaikutus kidepainemittauksien tuloksia arvioitaessa. Kiihtyvyyden vaikutuksen tutkimista kidepainearvoihin olisi syytä jatkaa eri anturityypeillä ja -asennuksilla sekä eri asejärjestelmillä, jotta kidepainemittaustulosten luotettavuudelle saataisiin arvio myös kiihtyvyyden osalta. Pitkäputkisilla aseilla kuten tykeillä ja vaunukanuunoilla ammuttaessa tuliputken sekä koko aseen poikittaisliikkeiden ja putken seinämän värähtelyliikkeen kiihtyvyydet saattavat aiheuttaa merkittävää virhettä kidepainemittaustuloksiin rekyylikiihtyvyyden lisäksi, etenkin tuliputken suulta painetta mitattaessa.

4. CRUSHER- JA KIDEPAINEMITTAUKSEN VERTAILU

Koska kotimainen asepainevertailututkimus on keskittynyt ensisijaisesti tykistön aseisiin [3, 4] ja uuden kranaatinheitinasejärjestelmän tuotekehitys, testaus ja hyväksyminen edellyttivät länsimaisten standardien [1] mukaisten koepainerajojen määrittämistä asejärjestelmän osille, AMOS®-asejärjestelmän tuotekehityksen loppuvaiheessa tehtiin kotimaisen aseteollisuuden mittakaavassa kohtuullisen laaja painevertailukoeammunta Patria Weapon Systems Oy:n ja Nammo Lapua Oy Vihtavuoren yhteistyönä. Eräänä tavoitteena oli määrittää crusher- ja kidepaineen maksimin välinen riippuvuus ja siihen vaikuttavia tekijöitä koeammuntaolosuhteissa eri aseilla ja ampumatarvikkeilla. Koeammunnassa vertailtiin Kistler 6215 kidepaineanturilla (Kuva 1) ja Handke 18-3 2*5 crushermittarilla, jossa mittaelementtinä on kuparilieriö ja jolle suositeltu painemittausalue on p_{cr} = (85...275) MPa, saatuja maksimipainetuloksia. Sähköisissä mittauksissa datan keruutaajuutena oli koko mittauksien ajan f_s=50 kHz.

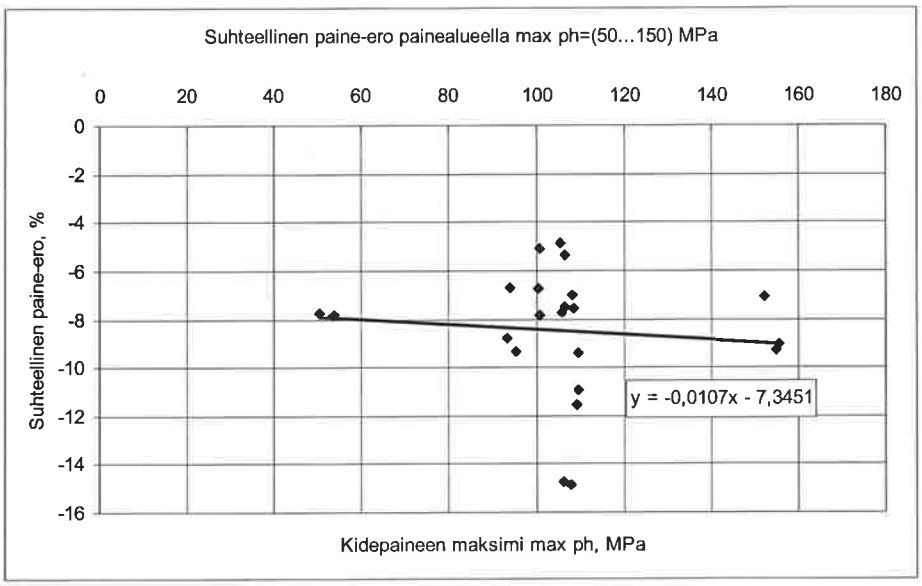
Suhteellinen paine-ero Δp(max p_h) crusherpaineen p_{cr} ja kidepainemaksimin max p_h välillä on esitetty kuvissa (Kuva 5,..., Kuva 7) ja se on laskettu kaavasta

$$\Delta p = \frac{p_{cr} - \max p_h}{\max p_h} \cdot 100\,\%.$$

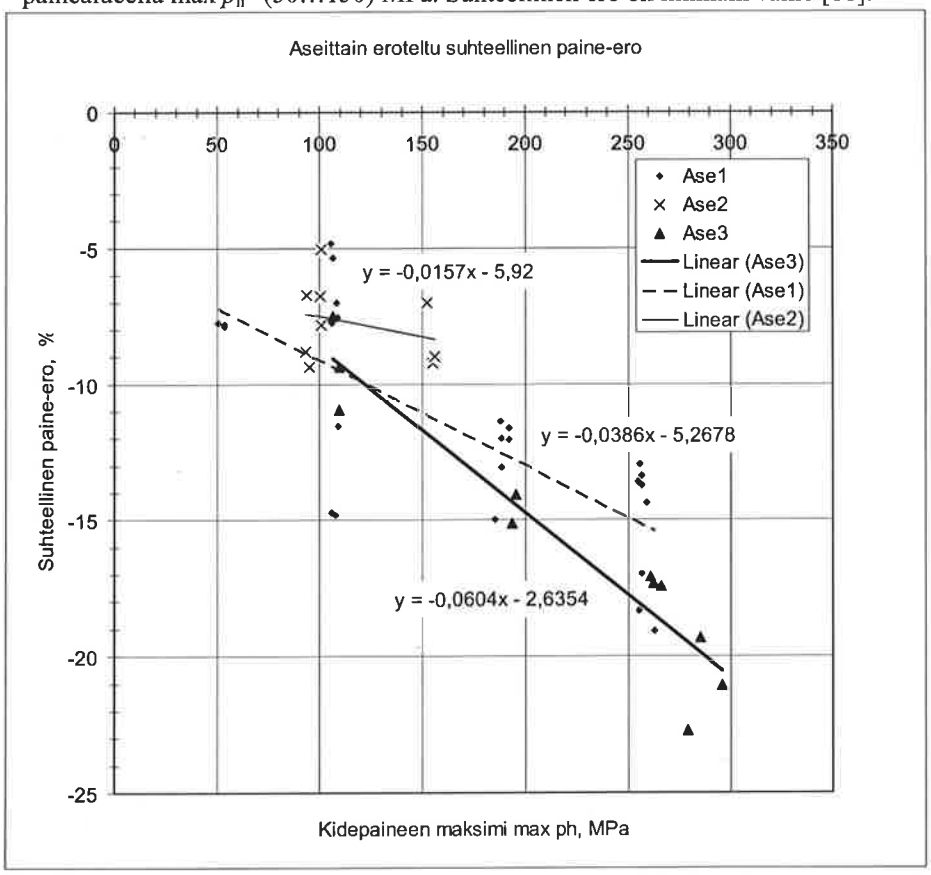


Kuva 5. Crusherpaineen ja kidepaineen maksimin suhteellinen ero vs. kidepaineen maksimi sekä pienimmän neliösumman suorasovitus koeammunnan kaikista laukauksista pl. kaksi selkeästi virheellistä painemittausta [11].

Koeammuntojen tulokset vahvistivat jo aiemmin tunnetun olettamuksen siitä, että paine-ero crusherpaineen ja kidepaineen maksimin välillä kasvaa painetason noustessa. Tähän lienevät syinä crusherelementin materiaalin dynaamiset lujuusominaisuudet, lujuus kasvaa muodonmuutosnopeuden kasvaessa paineen nousunopeuden mukana, ja korkeilla painetasoille tyypillinen painepulssin huipun terävyys. Suhteellinen paine-ero oli likimain vakio ~(8..9) % crushertyypin mittausalueen puoliväliin saakka (Kuva 6). Suhteellisen paine-eron todettiin olevan asekohtainen (Kuva 7). Yllättävän suuren asekohtaisen paine-eron syynä saattoi olla se, että aseella "Ase2" ammuttiin vain keskipainealueen laukauksia ja aseella "Ase3" ei ammuttu matalan painetason ampumatarvikkeita lainkaan.



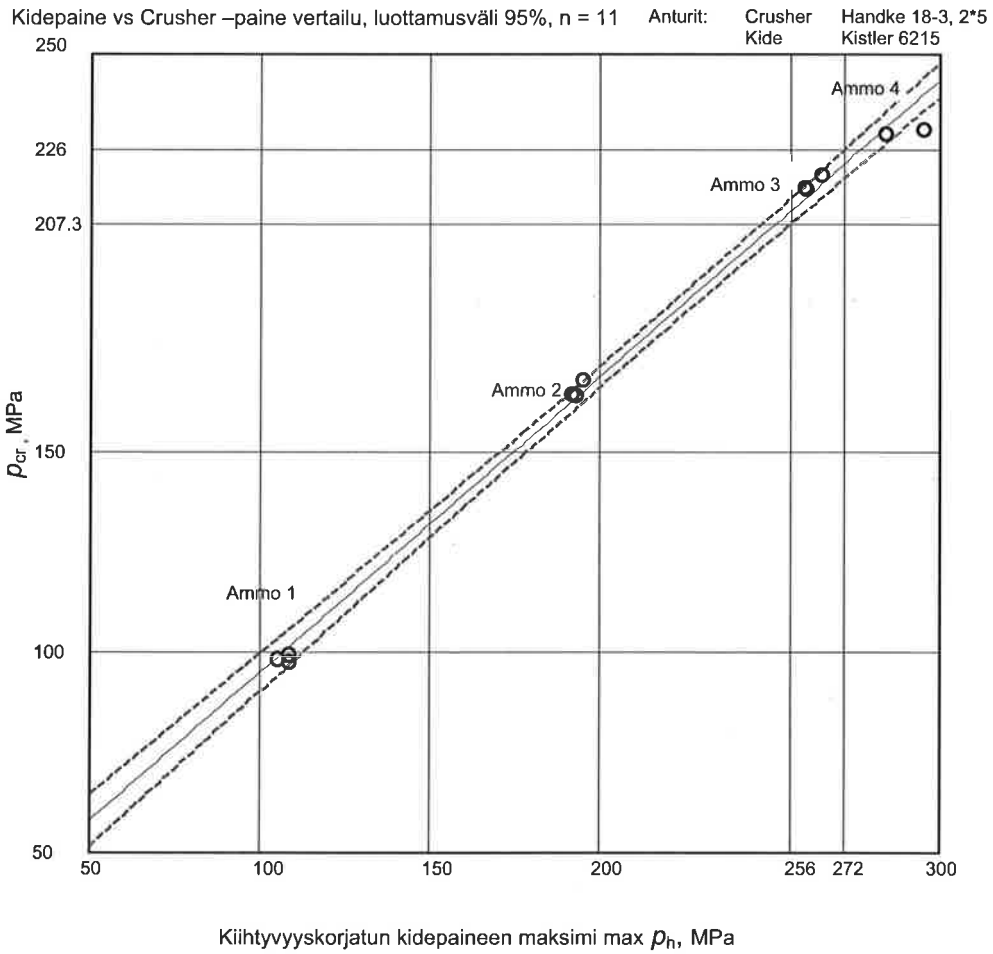
Kuva 6. Crusherpaineen ja kidepaineen maksimin suhteellinen ero ja suorasovitus painealueella max p_h~(50…150) MPa. Suhteellinen ero on likimain vakio [11].



Kuva 7. Aseittain eroteltu crusherpaineen ja kidepaineen maksimin suhteellinen ero sekä vastaavat suorasovitukset [11].

Koska kidepainemittaus on mahdollista vain painekoeaseilla tai painemittaukseen soveltuvia aseen erikoisosia käyttämällä, on palvelusaseiden vastaanotto- ja koeammunnoissa painemittausmenetelmänä käytettävä crushermittareita. Asejärjestelmän koepainerajat on määritettävä ja mittausmenetelmien mukaiset seikat on huomioitava, jotta asejärjestelmän käyttöturvallisuus ja riittävät turvamarginaalit toteutuvat myös äärikäyttöolosuhteissa. Perusolettamuksena on nykyisin pidetty sitä, että kidepainemittaus on "oikein" mittaustarkkuuden rajoissa ja crushermittauksen tulokset korjataan vastaamaan kidepainemittausta. Tosin "crusher-koulukuntakin" jatkaa sitkeästi olemassaoloaan, teknillisen mekaniikan katsannon kannalta sangen omituisin perustein.

Kuvassa (Kuva 8) esitetyn kaltaisilla tuloksilla voidaan tietyn crushermittarityypin painetulokset palauttaa kidepainemittauksiin ja niiden avulla voidaan määrittää tavoiteltava crusherpaine. Esitetyssä tapauksessa on huomioitu kiihtyvyyskorjaus kidepaineen maksimissa, joten menettelyä voidaan pitää jopa tavanomaista painekorjausta äveriäämpänä "fysikaalisen paineen" mielessä. Jos aseen, sen osan tai ampumatarvikkeen hyväksyminen tai muu testaus edellyttäisi koeammuntaa painevälillä max p_h= (256...272) MPa, niin vastaava paine Handke 18-3 2*5 crushermittarilla mitattuna tulisi olla välillä $p_{cr} \approx$ (210...223) MPa vastaavan luottamusvälin äärirajojen ollessa kuvaan merkityllä välillä $p_{cr} \sim$ (207...226) MPa.



Kuva 8. Rekylöivän kranaatinheittimen crusherpaine p_{cr} vs. kiihtyvyyskorjatun kidepaineen maksimin max p_h, suorasovitus ja 95 % luottamusväli painevälillä 100 MPa < max p_h < 300 MPa neljällä eri ampumatarvikkeella (Ammo i) määritettynä.

Kuvan (Kuva 8) tuloksia ei voida yleistää muihin aseisiin, ampumatarvikkeisiin eikä mitta-antureihin liittyviin testauksiin, mutta jonkinmoisia huomioita ja päätelmiä niistä sekä edeltävistä painevertailutuloksista voidaan esittää:

- Jos kiihtyvyyden vaikutusta kidepaineanturilla mitattuun paineeseen ei korjata, esimerkkitapauksessa tavoiteltua todellisen maksimipaineen sallittua vaihteluväliä Δp=16 MPa tulisi joko kasvattaa (tai siirtää kiihtyvyysvirheen verran, jos virhe on aina varmasti samaan suuntaan). Mittauksin todettu ~1,3 % suhteellinen painevirhe pienentäisi sallitun painemaksimin vaihteluvälin Δp =(16-2*0,013*250)MPa ≈ 9 MPa. Se on käytännön kokemuksien mukaan liian pieni kranaatinheittimen ampumatarvikkeille. Kiihtyvyyden vaikutus kidepaineeseen kaipaa jatkotutkimuksia, jotta sen vaikutuksen luonne ja merkittävyys varmistuvat
- Paine-erojen asekohtaisuus on huomioitava etenkin uuden tyyppisiä aseita käyttöönotettaessa. Vanhoilla aseilla vastaanotettujen ampumatarvikkeiden painerajojen vastaavuutta uusille aseille on syytä pohtia kriittisesti. On huomattava, että uusien aseiden rakenteelliset painerajat ovat vanhoja selkeästi korkeammalla, joten kriittisen pohdinnan kohde on (vanhojen) *ampumatarvikkeiden* painerajojen vastaavuus eri asejärjestelmissä muttei *aseen* kestävyys eikä *aseen* käyttökäyttöturvallisuus
- Aikaisemmissa kotimaisissa tutkimuksissa tykkiin liittyviä päätelmiä ei voitane sellaisenaan soveltaa kranaatinheittimien painemittaukseen, koska sekä kiihtyvyyden vaikutus että asekohtaiset paine-erot olivat yllättävän suuria tämän suppean koeaineiston mukaan
- Tilastollisen luotettavuuden varmistamiseksi mittaustuloksia olisi oltava enemmän.

5. VENYMÄLIUSKAMITTAUS LAUKAUSPAINEEN MITTAUSMENETELMÄNÄ

Koska tuliputket ovat kohtuullisella koneistustarkkuudella valmistettuja sylintereitä, voidaan niihin soveltaa sisäpuolisella paineella kuormitetun, päistään avoimen (normaalivoima N=0), vakio- ja paksuseinämäisen sylinteriputken kimmoisen muodonmuutoksen jännityksien lausekkeista johdettua sisäpuolisen paineen p ja venymien välistä yhteyttä [6]

$$p = \frac{\omega^2 - 1}{2} \cdot \frac{E}{1 - \nu^2} (\varepsilon_\Theta + \nu \varepsilon_x), \text{ jossa}$$

ω=D/d on putken ulko- ja sisähalkaisijan suhde, E kimmokerroin, ν Poisson kerroin sekä ε_Θ ja ε_x ovat putken ulkopinnan kehä-(tangentiaali-) ja aksiaalisuuntainen venymäkomponentti.

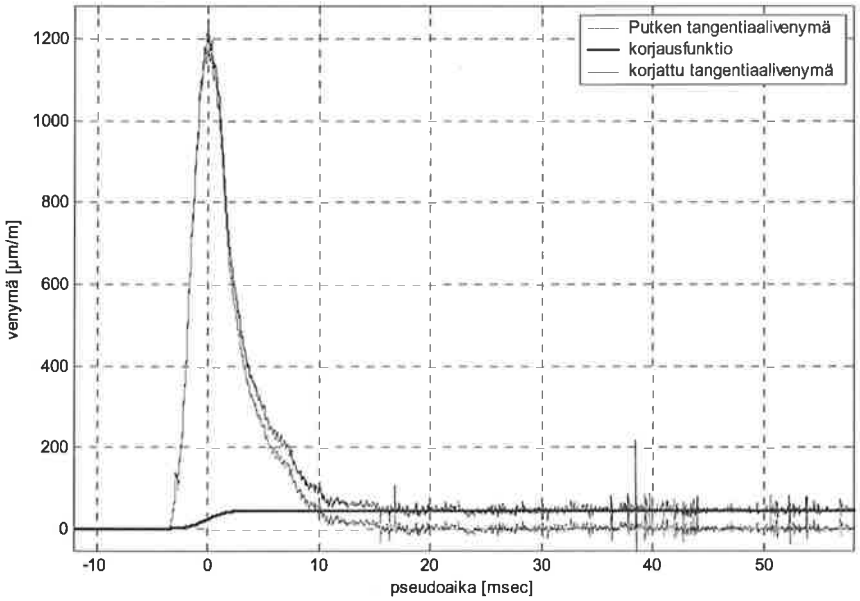
Koeammuntojen mittauksissa putken mahdollisen palkkitaivutuksen vaikutus kompensoitiin liimaamalla venymäliuskaparit putken vastakkaisille puolille ja "taivutuskorjattu paine" saatiin vastakkaisilta puolilta laskettujen paineiden p_i keskiarvona. Kuumat ruutikaasut lämmittävät tuliputken sisäpintaa voimakkaasti laukauksen aikana, jolloin putken seinämään syntyvä lämpötilagradientti aiheuttaa muodonmuutoksia (venymiä) myös ulkopinnalle. Lämpötilagradientin painevaikutus venymämittauksessa korjattiin "insinöörimäisesti runnoen" nk. logistista funktiota $k(t)$ käyttämällä

$$k(t) = \frac{b}{1 + e^{-st}},$$

missä t on aika, s funktion nousuajan määrittävä kerroin ja b on korjattavan termin jäännösarvo (venymän tai paineen) sisäballistisen vaiheen jälkeen. Jos korjaus tehdään paineelle, lämpötilakorjattu painekäyrä $p_k(t)$ saadaan vähennyslaskulla

$$p_k(t) = p(t) - k(t).$$

Funktion $k(t)$ nousuaika viritettiin siten, että se sai maksimiarvonsa noin 5 ms:n kuluttua mittauskohdan paineen huippuarvosta. Nousuaika vaihteli ampumatarvikkeittain, lähinnä panoksittain. Kuvassa (Kuva 9) on esitetty lämpötilankorjauksen vaikutus kehänsuuntaiseen venymädataan sovellettuna. Kuvan tapauksessa korjaus toimii hyvin. Putken pysyvä venymä palautui 0-tasolle laukauksen jälkeen, kuten painemittausmielessä tulee tapahtuakin painekuorman poistuttua.



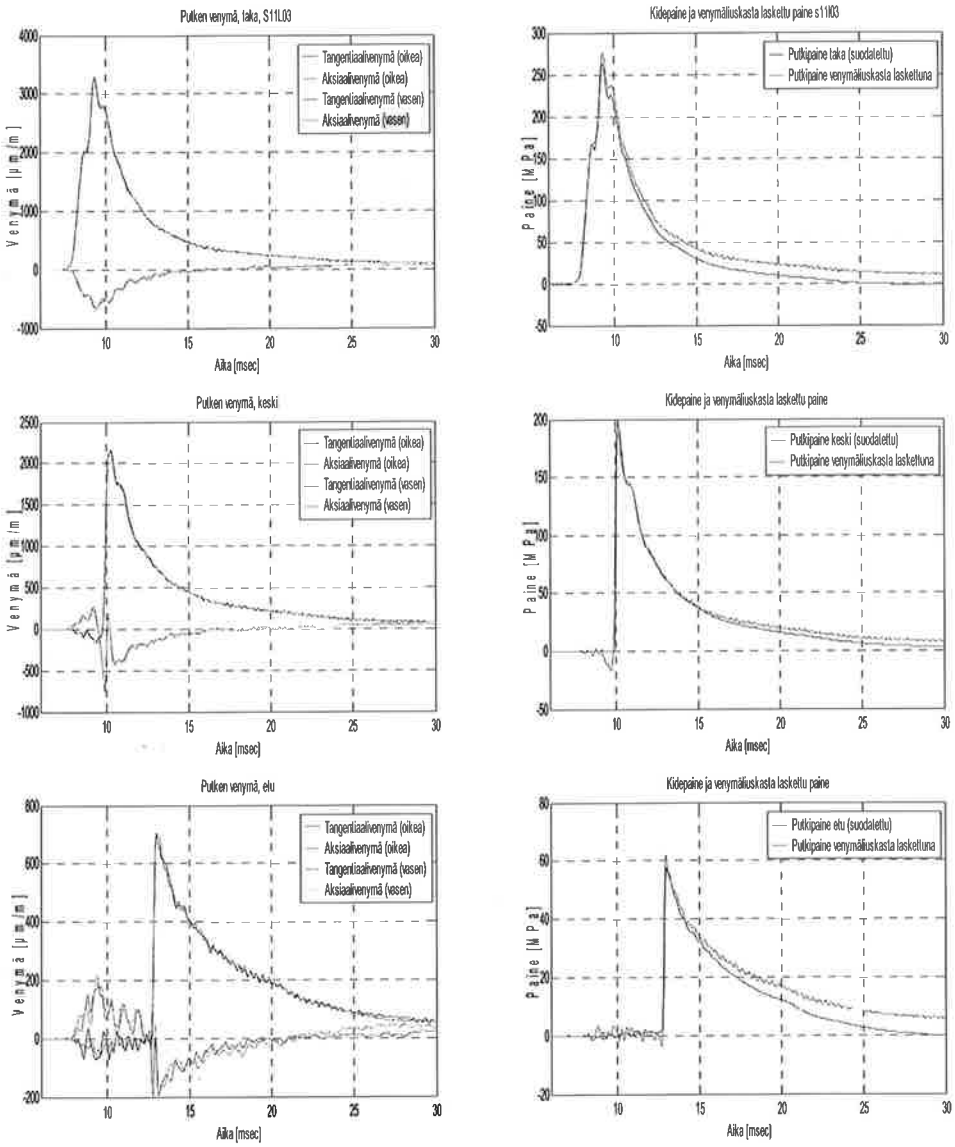
Kuva 9. Esimerkki logistisen funktion $k(t)$ lämpötilakorjauksesta tuliputken kehänsuuntaiseen venymään ε_Θ sovellettuna [11].

6. KIDEPAINEMITTAUKSEN JA VENYMÄLIUSKAMITTAUKSEN VERTAILU

Esimerkki koeammunnan venymämittaustuloksista sekä kidepaineen ja venymistä lasketun paineen vertailu on esitetty kuvassa (Kuva 10). Venymämittauksesta on nähtävissä, että putken palkkitaivutus on merkityksetön painekuormitukseen nähden ainakin kyseisellä aseella ja laukausyhdistelmällä, sillä vastakkaisilta puolilta mitatut venymät ovat likimain samat. Vain putken suulla (alin kuva) on kuvan mittakaavassa selkeämmin havaittavaa venymien poikkeavuutta. Painemittaus tuliputkesta voitaisiin tehdä yhdelläkin liuskaparilla/poikkileikkaus.

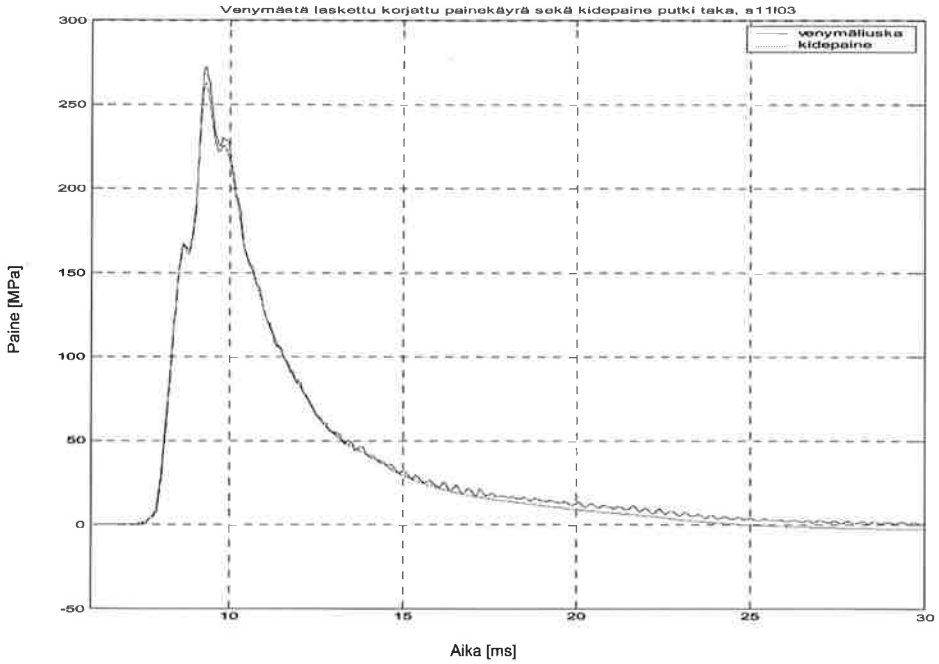
Toisena huomiona on, että putken seinämän kuoritaivutus (taivutus terävän, etenevän painerintaman reunalla) tulee selkeästi esiin niissä mittauspoikkileikkauksissa, jotka ammus ohittaa putkivaiheen aikana. Kuvan ylimmät käyrät ovat panoskammion alueelta, johon kohdistuu painekuorma ruudin palonopeuden mukaisesti eikä terävää, äkillistä painehuippua tai siitä johtuvaa muodonmuutosta niissä esiinny. Keskimmäiset käyrät ovat tuliputken keskivaiheilta ja alimmat käyrät putken suulta. Äkillinen painekuorman reunavaikutus on selkeästi havaittavissa ja venymistä lasketussa paineessa on seinämän taivutusmuodonmuutoksesta johtuva "negatiivinen paine"-indikaatio juuri ennen painerintamaa ja sen jälkeen seuraa huippupaineen "ylilyönti" painenousun lopuksi kidepaineeseen verrattuna.

Seinämän kuoritaivutuksen vaikutus korostunee tykistön aseilla ja ampumatarvikkeilla, joissa ammuksen ja tuliputken välinen tiivistys ja ammuksen rotaatioliike putkiaikana saadaan aikaan ammuksen johtorenkaan välityksellä. Johtorenkaan muovautuminen ja tiivistyspuristus putken rihloihin synnyttävät kapean ja terävän kontaktipainekuorman putken sisäpinnalle [10] ja sen vaikutus saattaa vaihdella ammusrakenteittain. Rihlatuilla putkilla ammuksen rotaatiokiihtyvyydestä aiheutuvan tuliputken vääntymän vaikutus venymämittaukseen lienee kompensoitavissa laskennallisesti tai liuskakytkennöin.



Kuva 10. Vasemmalla venymämittaustulokset ja oikealla putkipaine kidepaineanturilla mitattuna sekä venymistä laskettu paine kolmessa putken poikkileikkauksessa [11]. Ylin käyrästö on putken panoskammiosta, keskimmäinen putken keskivaiheilta ja alin putken suulta. Kuvan venymäkäyriä tai venymistä laskettuja painekäyriä ei ole lämpötilakorjattu!

Viimeisessä kuvassa (Kuva 11) on esitetty edellisen kuvan ylintä painekäyrästöä vastaava painetulos, jossa venymäliuskoista laskettu paine on lämpötilakorjattu. Kidepaineen ja venymistä lasketun, korjatun paineen yhteensopivuus on sangen hyvä. Venymäliuskat ja kidepaineanturi ovat mitanneet pienetkin painevaihtelut samaan tahtiin.



Kuva 11. Kidepaine ja venymistä laskettu, lämpötilakorjattu paine [11]. Vrt. Korjaamaton painekäyrä (Kuva 10, ylin kuva).

7. JOHTOPÄÄTÖKSET

Sisäballistisen vaiheen painemittaus lienee tärkein mittaus aseen ja ammuksen laukausrasitusten kannalta. Kolmen eri painemittausmenetelmän; mekaanisen crushermittauksen, sähköisen kidepainemittauksen ja tuliputken ulkopinnan venymistä lasketun paineen, mittaustulosten vertailu osoitti 120 mm:n kranaatinheitinasejärjestelmillä, että:

1. Crusherpaine saattaa jäädä suhteellisesti yli 20 % pienemmäksi kidepaineen maksimiin nähden. Suhteellinen paine-ero kasvaa painetason kohotessa vertailussa käytetyillä crushermittareilla ja aseilla. Perinteinen (10…15) % nyrkkisääntö aliarvioi paine-eroa korkeilla paineilla.
2. Aseen rekyyli- ja värähtelyliikkeen kiihtyvyydet vääristävät suhteellisesti yli 2 % (1,3 % maksimipaineella) kidepainemittaustulosta $p_h(t)$ rekylöivillä kranaatinheittimillä ja se on syytä huomioida kokeellisia painetuloksia tulkittaessa, jos sallitut painevaihtelut ovat tiukasti rajattuja. Kiihtyvyyden vaikutuksen arviointeja kidepainemittauksen tulokseen on syytä jatkaa.
3. Kidepainemittaus ja tuliputken venymistä laskennallisesti määritetty paine ovat yhtenevät ja venymämittausta voidaan käyttää aseen vertailupainemittausmenetelmänä. Sekä putken palkkitaivutuksen että seinämän lämpötilagradientin aiheuttamat venymätermit ovat kompensoitavissa kohtuullisen helposti kidepainemittauksen suhteellista virhettä pienemmälle tasolle.
4. Putken seinämän muodonmuutos korostaa laskennallista painemaksimia sellaisessa venymämittauskohdassa, jonka ammuksen tiivistekohta ohittaa, etenevän, terävän kuormitusportaan seurauksena.
5. Laukauspaineen määritys venymäliuskamittauksin tarjoaa luotettavan ja mittausteknisesti helpohkon vertailumittaustavan asejärjestelmien painearviointiin.
6. Asepaineiden kotimaista mittausteknistä tutkimusta on syytä jatkaa edelleen. Mittausteknisen, materiaaliteknisen ja sisäballistisen katsantokannan ohella mekaniikan ja lujuusopin näkemys saattaisi olla hyödyksi tutkimusta suunniteltaessa, toteutettaessa sekä tuloksia arvioitaessa.

Asejärjestelmien käyttöturvallisuuden kannalta päästäneen parhaimpaan lopputulokseen sekä loppukäyttäjän että järjestelmätoimittajan osalta, jos uusien asejärjestelmien painerajat ja niiden arvioinnit perustuvat alan kansainvälisiin standardeihin. Lisäksi on syytä ymmärtää se, milloin uusi asejärjestelmä poikkeaa teknisesti perinteisistä vastaavista aseista niin paljon, että vanhalle järjestelmälle laaditut ohjeet ja standardit eivät ehkä enää ole sovellettavissa sellaisenaan uuteen järjestelmään. Perästä ladattava, rekyylivaimennettu kranaatinheitin on aseteknisesti ja erityisesti painemittauksen kannalta lähempänä tykkiä kuin perinteistä suusta ladattavaa kranaatinheitintä. Painemittauksen haastavuutta lisäävät kranaatinheittimien ominaispiirteet, joita edellä on jonkun verran pyritty selvittämään asetekniikkaan sekä suppeaan mittauskoeaineistoon nojautuen.

Kirjoitelman laatijat esittävät kiitoksensa painevertailukoeammunnan tulosten julkaisuluvasta Patria Weapon Systems Oy:lle sekä erityisesti koeammuntaan osallistuneelle PWS:n ja Nammo Lapua Oy Vihtavuoren koetoimintahenkilöstölle. Ilman heidän työpanostaan vertailukoeammunta ei olisi toteutunut ja painemittaus, –rajojen määritys sekä niiden soveltaminen uusille kranaatinheitinasejärjestelmille perustuisivat edelleen kritiikittömästi "hyviin kansallisiin menetelmiin".

VIITTEET

1. Stanag 4110. *Definition of pressure terms and their interrelationship for use in the design and proof of cannons or mortars and ammunition.* North Atlantic Treaty Organization, Standardization Agreement, Stanag.
2. Järviniemi. A. *Asepainemittaus.* Ulko- ja sisäballistiikan koulutustilaisuus 1.10.2002. Valkeakoski. Julkaisematon luentomuistio. Puolustusvoimien Materiaalilaitoksen Esikunta. Tampere. 2002.
3. Järviniemi, A. *Asepainemittausjärjestelmien vertailtavuus.* Lisensiaatintutkimus. Tampereen teknillinen korkeakoulu. Automaatiotekniikan laitos. Tampere. 2000. 51 s.
4. Kuokkala, V.-T. & Rämö, J. & Järviniemi, A. *Korkeiden asepaineiden mittausmenetelmän tarkkuuden parantaminen.* Maanpuolustuksen Tieteellinen Neuvottelukunta MATINE hanke n:o 616. Loppuraportti. 2003. 29 s.
5. *Pressure Sensors for ultra-precise pressure measurement.* Kistler Instrumente AG, 900-650e-03.06 Mat2000. Winterthur. 2006. 121 p. (www.kistler.com).
6. Flynn, P.D. *Strain-gage Instrumentation for Ammunition Testing.* Experimental Mechanics. May 1975. pp. 192,...,200.
7. Moilanen, S. *Suurikaliiperisen ammuksen rasitusten mittaus sisäballistisen vaiheen aikana.* In: Aalto, J. & Salmi, T. Proceedings of the 6th Finnish Mechanics Days. Univ. of Oulu. Publication 56. Oulu. 1997. pp. 269,...,276.
8. Smith, D. & Coppola, E. *Safe Maximum Pressure Determination for the M829E3/M256 Cannon Qualification Program.* US Army ARDEC, Benet Laboratories. Technical Report ARCCB-TR-0213. Watervliet. 2002. 15 p.
9. Erkkilä, T. & Moilanen, S. *Muodonmuutosnopeuden vaikutus ase- ja ammusterästen myötölujuuteen.* Julkaisussa: Koski, J & Virtanen, S. VII Suomen mekaniikkapäivät. Nide 1. Tampereen teknillinen korkeakoulu, Teknillinen mekaniikka. 2000. Tampere. ss. 81,...,92.
10. Edwards, T.D. *Projectile driving band interactions with gun barrels.* In: Gun Tubes Conference 2005, 10-14 April, 2005. Keble College Oxford. RMCS Shrivenham. Presentation S7/P28. 7p.
11. Tervokoski, J. *Raportti painevertailuammunnan tuloksista.* Patria Weapon Systems Oy sisäinen, luottamuksellinen ja julkaisematon koeammuntaraportti. Vammala, 2005. 254 s.
12. Reunamäki, K. *AMOS (Advanced Mortar System).* In: Journal of Battlefield Technology. Argos Press Pty Ltd.Vol 5, No. 1. March 2002. pp. 9,...,13.
13. www.patria.fi.

MECHANICAL TESTING OF MATERIALS WITH THE HOPKINSON SPLIT BAR TECHNIQUE

M. HOKKA, V.-T. KUOKKALA, T. VUORISTO

Tampere University of Technology, Institute of Materials Science
P.O. BOX 589, FI-33100 Tampere Finland
Email: mikko.hokka@tut.fi

ABSTRACT

Mechanical behavior of materials at high strain rates differs considerably from that observed at quasi-static or intermediate strain rates. High strain rates occur in many processes and events of practical importance, such as in dynamic structural loadings, automotive collision protection systems, and even paper manufacturing. The design of structures for this kind of applications and utilization of the full capacity of the used materials is greatly facilitated by a thorough understanding of the high strain rate material behavior. This paper presents an overview of the Hopkinson Split Bar (HSB) technique, which is specially designed for studying material behavior at high strain rates.

1 INTRODUCTION

Materials research, including both development of new materials and enhancement of the properties of existing materials, is motivated by tightening environmental requirements, changing operating conditions, and new material forming methods. Typical mechanical properties required from today's materials are high strength and high ductility, and more often materials must also be suitable for applications where high rate deformations might occur. Typical examples of such applications are structural parts of cars, high-speed material forming methods, stone crushers, and paper machine rolls. For optimal materials selection and modeling of such high rate processes, the material properties must be known also as a function of strain rate. In fact, the automotive industry already demands reliable high strain rate data of steels from the steel manufacturers. This data can be used to better estimate strength and energy absorption of car structures in case of collisions.

Mechanical behavior of materials at high strain rates differs considerably from that observed at quasi-static or intermediate strain rates. In quasi-static deformation, the material is, at all times, in a state of static equilibrium, which means that, for example in a compression test, the forces acting on each face of the specimen are equal in magnitude but with opposite senses. However, when the deformation is imparted from the outside at a very high rate, one portion of the body is stressed while the other portion has not yet experienced this stress. In other words, stress has to travel through the body. Thus, dynamic deformation generally involves wave propagation, whereas quasi-static deformation can be considered as a sequence of states of equilibrium that can be treated by the well-known equations of mechanics of materials. In addition, at high strain rates the inertia forces caused by the kinetic energy of the material flowing radially or axially must be accounted for.

It is also known that most of the work of deformation is expended as heat; only 5 to 10 % of the work is actually stored in the defect (dislocation) structure of the deformed specimen. As the strain rate increases, there is insufficient time to transport this heat from the specimen, and the specimen temperature increases during the deformation. Therefore, the test conditions change from

the isothermal conditions at low strain rates towards adiabatic conditions at high strain rates. In fact, if the temperature dependence of flow stress is high enough, deformation may become highly localized at the center of the deformed part or specimen or, in the case of shear deformation, lead to the formation of so-called adiabatic shear bands.

In crystalline materials, the strain rate dependence of flow stress at low and intermediate strain rates (up to roughly 10^3 s^{-1}) is readily explained by thermally activated dislocation motion. At higher strain rates, a steep upturn in flow stress is frequently observed and explained in terms of viscous drag on dislocations. However, flow stresses at different strain rates are usually compared at equal strains, which may lead to incorrect interpretation of the test results since strain is not a proper state variable. This is because the microstructure, which is a true state variable, depends also on the rate of loading which brought the specimen to that strain. In other words, increased strain rate may not only raise the instantaneous flow stress because of the drag effects on moving dislocations but may also have a permanent effect on the work hardening behavior of the material [1-7]. Furthermore, when hardening is not based only on the increase of the dislocation density or the re-arrangement of the dislocation structure but also on phase transformations and/or twinning, hardening behavior may depend on the strain rate in a different way than normally observed in metals and alloys.

1.1 Strain rate dependence of metals

The strain rate dependence of metals can be illustrated either by plotting several stress strain curves at different strain rates in the same figure, or plotting the flow stress at a certain level of plastic strain as a function of strain rate on a semi logarithmic scale. Figure 1a shows compression stress strain curves of Form 220 and Figure 1b the curves showing flow stresses at 5 and 10% of plastic strain as a function of strain rate. Increase in strength of about 70% can clearly be seen in both figures as the strain rate is increased from 10^{-2} to$3*10^3$ s^{-1}. Increase of the maximum strain with increasing strain rate in Figure 1a is related to the test set up and does not reflect the true material behavior.

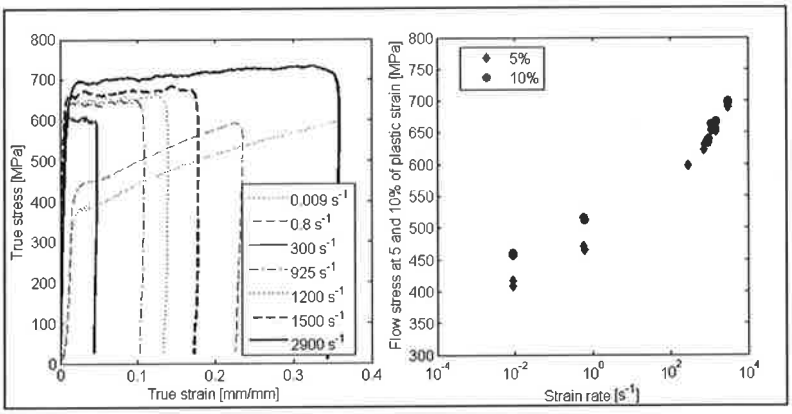


Figure 1. Deformation behavior of Form 220 C steel tube at different strain rates. a) stress-strain curves from quasi-static compression tests and high strain rate Hopkinson tests, b) flow stresses at 5 and 10% plastic strains as a function of strain rate.

At low and intermediate strain rates (<10^2 s^{-1}), the increase of strength as a function of strain rate can be explained by the thermally activated dislocation motion, where the driving force for the dislocation motion is a sum of external stresses and thermal lattice vibrations. The thermal vibration energy increases with temperature, as depicted in Figure 2a. The vibration amplitude is a

statistical variable, and therefore the magnitude of the available thermal energy also varies with time [8,9].

The obstacles cumbering the dislocation motion on a glide plane can be divided into thermal and athermal obstacles [8,9]. Thermal obstacles can be overcome by thermal energy. However, at increased strain rates or lowered temperatures, dislocations cannot wait for the thermal vibration energy to overcome the obstacle, and more external stress is needed to overcome also the thermal obstacles, as shown in Fig 2b. The external stress required to maintain plastic deformation can now be written as $\sigma = \sigma_0 + \sigma_G$, where the σ_0 and σ_G are the stresses required to overcome the thermal and athermal obstacles, respectively. As illustrated in Figure 2c, the thermal component of external stress becomes zero at a certain temperature depending on the strain rate. The athermal component, however, does not depend on the temperature due to the nature of the obstacles which extend over a wide area and cannot therefore be overcome by the thermal energy at any temperature.

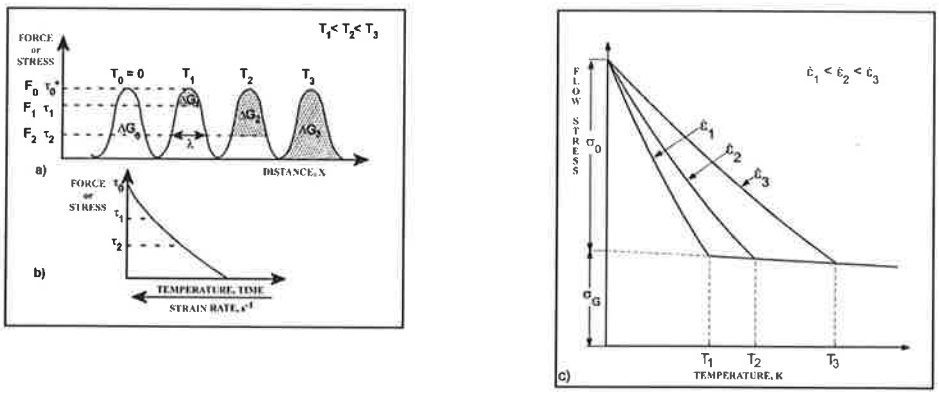


Figure 2. a-b) stress required for the dislocation to overcome a short-range barrier at different temperatures, c) flow stress at different temperatures and strain rates [after 8].

For most metals the flow stress increases steadily up to the strain rate of about 10^3 s^{-1}. At higher strain rates a steep upturn in the flow stress is observed, as Figure 1b shows. This behavior is usually explained by viscous drag on dislocations. In fact, the drag consists of several mechanisms that all consume energy and therefore cumber the dislocation motion [10-13]. Therefore, shear stress on the glide planes must be increased to maintain the desired strain rate, which is seen as increased strength of the material.

1.2 High strain rate test methods

Strain rates can be divided into different regimes, for example as shown in Figure 3. At quasi-static strain rates, which occur for example in conventional tensile testing, the specimen is at stress equilibrium at each moment, i.e., the deformation can be assumed to occur instantaneously or without delay in every section of the specimen. To be precise, this is not exactly true and the stress and strain travel with a constant speed that is unique for each material, which for example for steels is about 5000 m/s when the deformation is fully elastic. This means, for example, that when a steel rod of 1 meter in length is stressed at one end, the stress and strain will reach the other end only after about 200 μs. Normally this delay has no practical significance, but at higher strain rates where short stress pulses cause the deformation, it can hinder or even completely prevent reaching of the state of stress equilibrium. To achieve the stress equilibrium, the specimen must be very short compared to the length of the stress pulse. Two other significant differences between quasi-static and high rate loadings are that at higher strain rates the effect of radial and axial inertial forces must be accounted for and that at lower strain rates the deformation is practically isothermal

but becomes almost adiabatic at higher strain rates. Only about 5-10% of the total energy used for the plastic deformation is permanently stored in the defect structures of the material, and therefore the specimen temperature can increase even by several hundreds of degrees during the high rate adiabatic deformation.

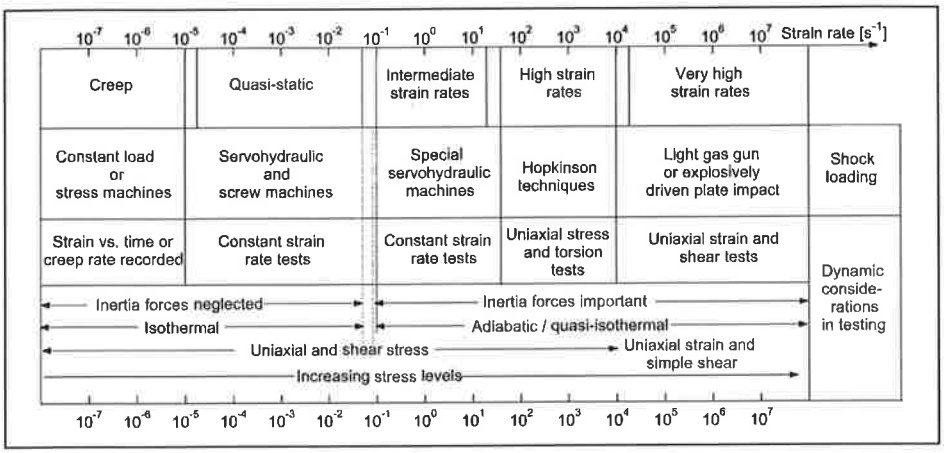


Figure 3. Strain rate regimes and the associated testing techniques [after 14].

At quasi-static strain rates, the material properties are usually determined using servohydraulic materials testing machines. Highest achievable strain rates with these machines are about 0.1 to 1 s^{-1}. With special high strain rate servohydraulic materials testing machines strain rates up to 500 s^{-1} can be achieved. However, these test set ups are usually troubled by extensive mechanical vibrations, which can be directly seen in the stress strain curves making the data analysis more difficult [15].

The most commonly used high strain rate testing method is the Hopkinson Split Bar (HSB) method, also known as the Split Hopkinson Pressure Bar or the Kolsky Bar.

2 HOPKINSON SPLIT BAR TECHNIQUE

Figure 4 shows schematically the construction of a HSB device. The device consists of two high strength steel or aluminum bars, with a typical length of 1-2 m and diameter of 10-25 mm, and a projectile usually made of the same material as the bars. The specimen is placed between the bars. When the projectile, or the striker bar, which is accelerated typically to a velocity of 2.5 to 40 m/s, hits the front end of the incident bar, a compressive stress wave is generated. The elastic stress wave propagates in the bar at the velocity of sound (~5000 m/s for steels) until it reaches the interface of the incident bar and the specimen, where part of the stress pulse is reflected back as a wave of tension, while the remaining part is transmitted through the specimen to the transmitted bar. The three stress pulses, the incident, reflected, and transmitted, are recorded by strain gages. Figure 4 shows an example of the stress pulses from a test where the steel striker bar length was 200 mm. Stress, strain, and strain rate in the specimen can be calculated from the measured strains in the pressure bars. The shape and the rise time of the pulse can be controlled by placing a pulse shaper between the incident bar and a striker bar. The pulse shaper is basically a thin disk of soft material such as annealed copper [16,17].

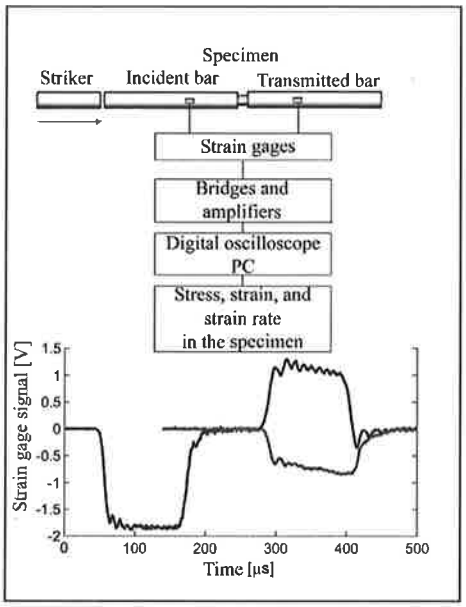


Figure 4. The Hopkinson Split Bar technique schematically.

Due to the very short rise time, the trapezoidal stress pulse created by the impact of the cylindrical striker bar consists of several frequency components, which usually cause oscillations in the measured pulses, as demonstrated in Figure 5. Because the velocity of the higher frequency components is lower than that of the lower frequency components, the amplitude and location of the oscillations change, the rise time of the pulse decreases, and the pulse width increases when the pulse travels in the bars. Therefore, the measured pulses do not correspond to those acting on the interface between the bars and the specimen. However, the phase differences can be corrected using a dispersion correction, in which all pulses are mathematically transferred to the specimen-bar interfaces [18-20]. The correction is done by using fast Fourier transforms (FFT). The phases of different frequency components are shifted in the frequency domain according to the Pochammer-Chree method either forward (incident pulse) or backward (reflected and transmitted pulses). After that, an inverse FFT is applied to return back to the time domain. An example of the dispersion correction is presented in Figure 5 for a test conducted without a specimen bars together. In this test, the distance between the strain gages and the bar interface was 1.4 m and 0.35 m in the incident and transmitted bars, respectively. Figure 5c shows the pulses at the bar interface without a dispersion correction, and Figure 5d after the correction. Also increasing the rise time of the stress pulse by using the pulse shaping techniques can decrease the oscillations in the stress pulses.

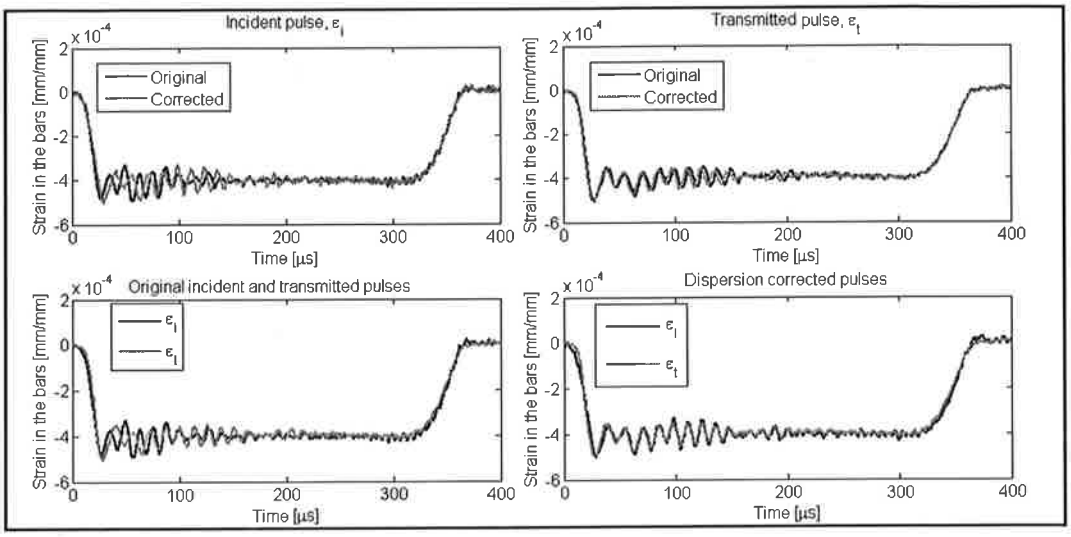


Figure 5. The effect of dispersion correction on the HSB signals. a) original and dispersion corrected incident bar signals, b) original and dispersion corrected transmitted bar signals, c) original incident and transmitted stress pulses aligned with respect to time, and d) dispersion corrected pulses transferred to the interface between the input and output bars. The test was made without a specimen, *i.e.*, the incident and transmitted bars were in direct contact with each other and no pulse shaper was used.

From the dispersion corrected pulses, stress, strain, and strain rate in the specimen are calculated according to equations 1-3. If stress equilibrium prevails in the specimen, i.e., the forces on the back and front faces of the specimen are equal, the calculations can also be made using simplified equations, where the stress is calculated from the transmitted pulse, and strain and strain rate from the reflected pulse only.

$$\varepsilon(t) = \frac{C_0}{L_s}\int_0^t (\varepsilon_t - \varepsilon_i + \varepsilon_r)\, dt \tag{1}$$

$$\dot{\varepsilon} = \frac{C_0\left[\varepsilon_t(t) - \varepsilon_i(t) + \varepsilon_r(t)\right]}{L_s} \tag{2}$$

$$\sigma(t) = \frac{A_b\, E\left[\varepsilon_i(t) + \varepsilon_r(t) + \varepsilon_t(t)\right]}{2A_s} \tag{3}$$

The HSB equipment can be modified also for high strain rate tensile testing [21,22]. Typically this is done by changing the test set up or specimen geometry. In the most common method, the striker bar is replaced by a striker tube, sliding on the incident bar. The striker tube is shot away from the specimen towards a flange at the free end of the incident bar. From the free end, the compression pulse is reflected as a wave of tension propagating towards the specimen. The biggest difference (and problem) compared to the compressive device is mounting of the specimen. In the compression system, the specimen is simply placed between the two bars without any special clamping mechanism, but in the tensile system the specimen must be firmly attached to the bars to allow the propagation of a tensile wave over the bar-specimen interface. The clamping, however, can cause disturbances in the elastic stress pulses, and typically the tensile test results are not as good in quality as the results from compression tests. Typically the specimen is mounted to the

bars with a thread which, however, is not a very convenient mounting method for sheet steels. For sheet steels the specimen can either be glued directly to the bars or to a special mounting head, which is then threaded to the bars. The data collection and analysis is done basically using the same routines as in the compression method.

In the HSB tests the amount of strain and strain rate are affected by the impact velocity, the length of the striker bar, and the initial length of the specimen. The stress, and therefore the elastic deformation in the bars, depends on the impact velocity according to equation 4. The duration of the stress pulse depends solely on the length of the striker bar according to equation 5. The length of the stress pulses is typically between 80 μs and 600 μs, while the forces vary between 5 and 200 kN. The amount of total plastic strain and strain rate can also be affected by changing the length of the specimen. This, however, usually also changes the diameter-length ratio of the specimen, which in compression tests should be kept between 0.2 and 1 to ensure stress equilibrium in the specimen. Free selection of strain and strain rates is limited by the fact that they both depend on the same test parameters, and for example to achieve high strain at low a strain rate can be quite difficult, as indicated by Figure 1.

$$\sigma = \frac{v_a \rho_a C_{0a}}{2} \tag{4}$$

$$T = \frac{2 L_a}{C_{0a}} \tag{5}$$

3 HIGH STRAIN RATE TESTING AT TAMPERE UNIVERSITY OF TECHNOLOGY

During 2000-2003, two compression HSB test systems were built at the Institute of Materials Science of Tampere University of Technology. With these devices, the compression behavior of materials can be studied in a strain rate range of $2*10^2$-10^4 s^{-1} [16, 20, 23-28]. In addition, a special tensile HSB test system for testing of sheet steels was designed and built in 2005. As special features, a sophisticated high/low temperature test system allows compression testing in the temperature range of –190°C to +1000 °C, and the specimen recovery (pulse reversal) system prevents the specimen from being loaded several times, thus preserving the microstructure of the sample. The recovery technique is essential when studying the microstructures of the deformed specimens for example with transmission electron microscopy [28,29].

Figure 6 shows a general view of the two compression HSB tests systems, which both are controlled by the same computer. The strain gage and other signals are recorded with two digital oscilloscopes, from which the data is read to the computer via a GPIB interface. The data is processed using MATLAB based calculation routines.

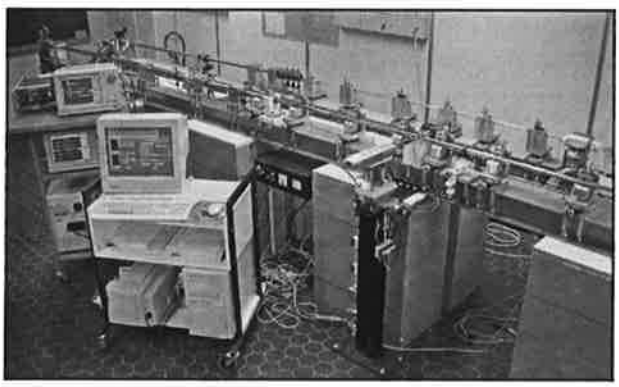


Figure 6. The compressive Hopkinson Split Bar devices at the Institute of Materials Science of TUT.

Figure 7 shows the high temperature and recovery systems in more details. Schematics of these systems are shown in Figure 8. The high (low) temperature test is carried out in the following way: the specimen is loaded in a special ceramic specimen holder, which is pushed into the furnace (or cooling chamber), located beside the bars, by a pneumatic arm. When the specimen has reached the desired temperature, the specimen is pulled to the centerline between the bars, the striker bar is shot, and just before the striker hits the incident bar, a special pneumatic manipulator pushes the bars and specimen together. This computer-controlled procedure ensures minimum contact time, less than 50 ms, between the bars and the specimen, thus preventing thermal gradients in the specimen. In the low temperature tests, the furnace is replaced by a cooling chamber, where the specimen is cooled by a nitrogen gas flow from a heat exchanger, which is immersed in liquid nitrogen. The temperature is controlled by changing the gas flow into the heat exchanger, using a PID- controlled piezo-electric proportional valve.

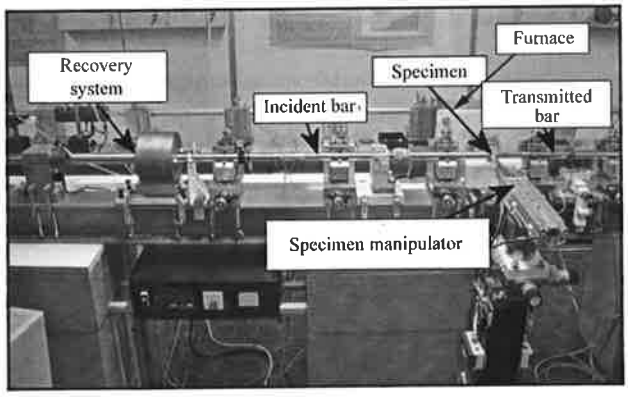
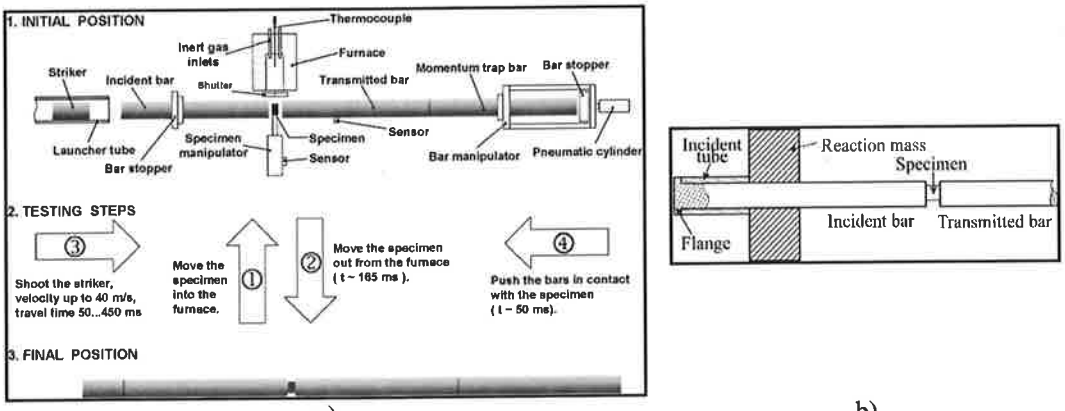


Figure 7. The high temperature system and the specimen recovery device in the HSB laboratory at TUT.



a) b)

Figure 8. a) High temperature HSB system and b) specimen recovery device schematically.

The schematics of the recovery system are shown in Figure 8b. The incident compression pulse is mechanically divided into two pulses with equal magnitude, of which one is propagating in the bar and one in the incident tube. As the pulse propagating in the incident tube reaches the end of the tube, it is reflected as a wave of compression due to the reaction mass resting against the end of the tube. The compression pulse in the incident tube is again reflected at the free end of the incident bar, and it now propagates in the bar as a wave of tension towards the specimen (the tension wave cannot cross the flange-tube interface). There are now two pulses propagating in the

incident bar, the original compression pulse followed by a tensile pulse with equal magnitude. After the compression pulse has deformed the specimen, the following tensile wave reverses the movement of the incident bar end, thus recovering the specimen. In practice, this means that only the first compression pulse deforms the specimen, because after that the incident bar will move away from the specimen. The recovery system can be used together with the high/low temperature systems, allowing structural studies of samples deformed at high strain rates at different temperatures [28].

3.1 Examples of the high strain rate testing of steels

The automotive industry uses different sheet steels in different sections of car bodies. Typical mechanical properties required from these steels are high strength and good deformability. These structures can be subjected to very high strain rates in a case of a sudden impact, in which case the dynamical material properties become relevant. Today the automotive industry requires knowledge on the dynamical material properties in the strain rate range of 250 s^{-1} to 1000 s^{-1} in addition to the quasi-static properties. In some critical components the strain rate in a car crash can reach values as high as 2000 s^{-1}.

Figure 9 shows quasi-static and HSB compression test stress strain curves for several dual phase (DP) steels at strain rates of 10^{-3} s^{-1} and 10^{3} s^{-1}, revealing that the strength of all these steels increases by about 20% with increasing strain rate.

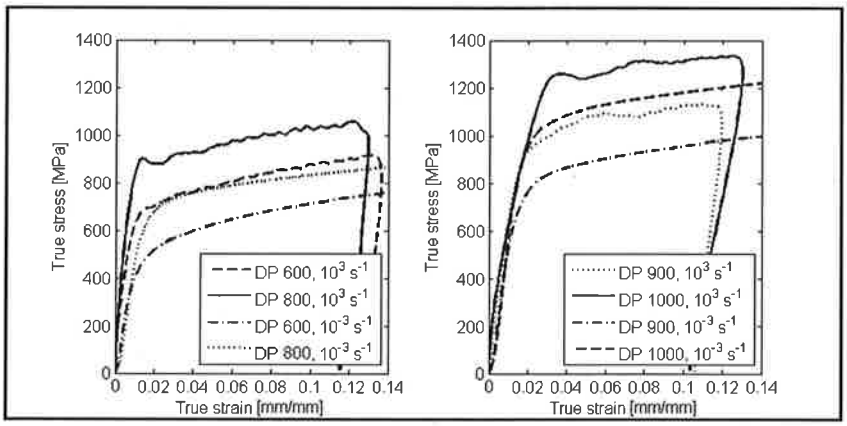


Figure 9. The behavior of dual phase steels DP600, DP800, DP900 and DP1000 at strain rates 10^{-3} s^{-1} and 10^{3} s^{-1}.

For some of the studied steels, also tensile test results are available from tests conducted with a high strain rate hydraulic materials testing machine. Figure 10 shows the yield strength values calculated from these tensile tests as well as from quasi-static compression tests and HSB compression tests. The yield strength of TRIP800, for example, is only slightly higher in compression than in tension, and the material has constant strain rate dependence in the studied region. In the HSB tests, however, at very small strains, the results may not be fully reliable, because the stress equilibrium may not yet have been achieved. For this reason, the Young's modulus cannot be normally determined from the HSB test results, and also the yield strength is typically determined by the so called backward extrapolation method. At strain rates over 500 s^{-1}, the yield strength of the dual phase steels is considerably higher in compression than in tension [30]. Partly this can be caused by the friction and inertia effects in the compression tests, but also the texture can have a significant effect, because the tensile tests were in this case done in the rolling direction (RD) and the compression tests in the through thickness (TT) direction.

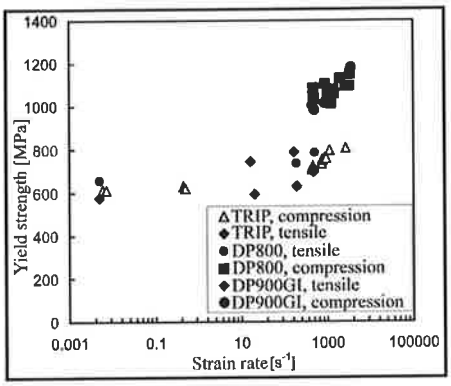
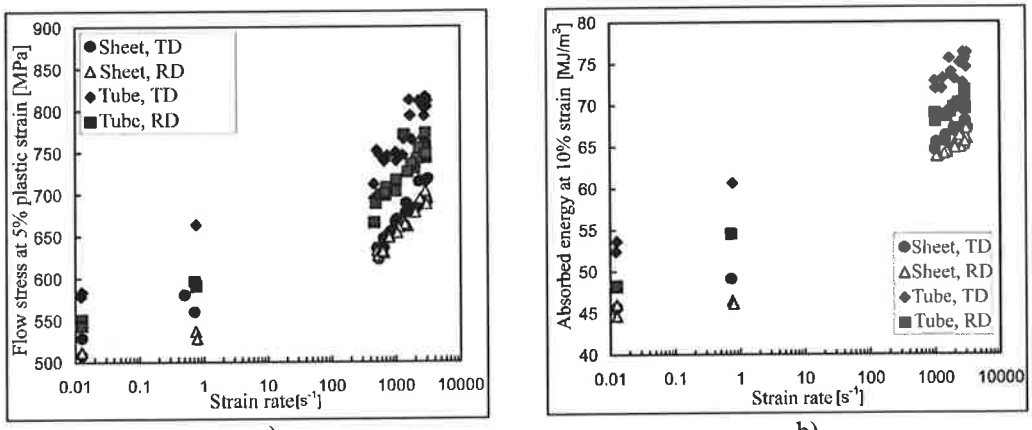


Figure 10. The behavior of dual phase steels DP800 and DP900 GI and a TRIP 800 steel at high strain rates in compression and in tension [30].

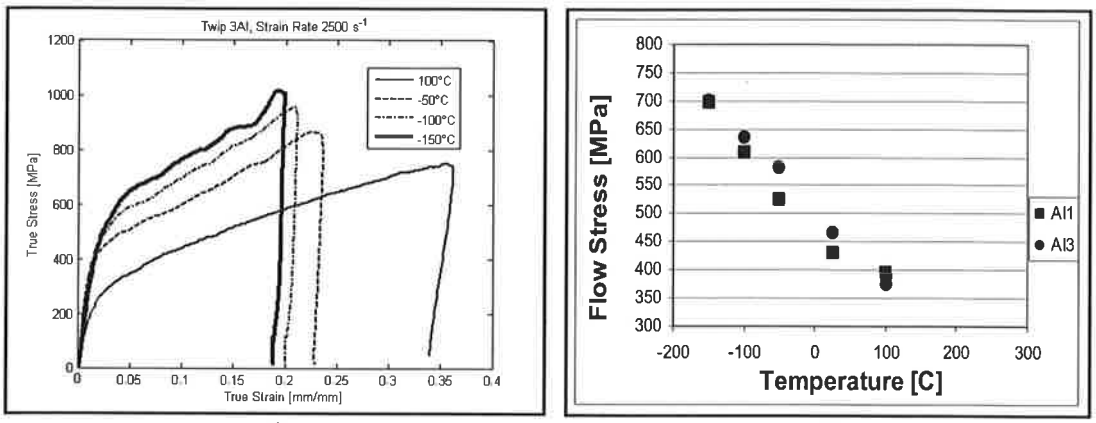
The behavior of both sheet steel and cold worked tubes of S355 structural steel was also studied in a wide range of strain rates. To reveal the influence of texture, tests were done in both rolling (RD) and transverse (TD) (perpendicular to the RD and TT directions) directions. Figure 11a shows the flow stress at 5% of plastic strain, and Figure 11b the absorbed energy at 10% of plastic strain. The energy absorption can only be calculated to a certain value of strain, because total energy absorption before necking or failure of the test piece cannot be calculated from the compression test results. However, the calculated energy absorption values can be used to compare the energy absorption capability of different materials for example in a car crash. According to Figure 11, both the loading direction and cold working in the manufacturing process of the tube affect the material behavior significantly.



a) b)

Figure 11. The behavior of S355 structural steel as a function of strain rate, a) flow stress at 5 % plastic strain, and b) absorbed energy at 10 % plastic strain for tube and strip in the transverse and longitudinal directions.

The effects of both temperature and strain rate have also been studied for advanced high strength steels. As explained in chapter 1.1, the flow stress increases with increasing strain rate and decreases with increasing temperature. The simultaneous effect of both temperature and strain rate can be very interesting. The stress strain curves at a strain rate of 2500 s^{-1} for two types of TWIP steels are shown in Figure 12a, and flow stress at 5% of plastic strain in Figure 12b.



a) b)

Figure 12. a) stress strain curves of TWIP 3Al steel at a strain rate of 2500 s^{-1}, and b) flow stress at 5% of plastic strain for TWIP steels 1Al and 3Al at different temperatures.

4 CONCLUSIONS

Material behavior at high strain rates differs significantly from that observed at low or quasi-static strain rates. For this reason, especially the automotive industry requires reliable data on the behavior of materials also at higher strain rates when modeling and designing the strength and energy absorption of materials and structures. The most used and most reliable high strain rate testing method is the Hopkinson Split Bar technique, which is based on the propagation of elastic stress waves in high strength steel or aluminum bars. The HSB technique enables characterization of the dynamic material properties in the strain rate range of $2*10^2$ to 10^4 s^{-1}. High strain rate deformation of steels and other metals, polymers, and different composites, are being intensively studied at the Institute of Materials Science of Tampere University of Technology using the Hopkinson Split Bar technique. At the moment there are several ongoing high strain rate research projects at TUT, which are funded by the Academy of Finland, TEKES, Graduate Schools, the Ministry of Education, TUT, and industry.

References

1. Follansbee P. S., Kocks U. F., A constitutive description of the deformation of copper based on the use of the mechanical threshold stress as an internal state variable. Acta Metallurgica 36 (1988) 81-93.
2. Follansbee P. S., High-strain-rate deformation of FCC metals and alloys, in Metallurgical Applications of shock-wave and high-strain-rate phenomena, Editors Murr L. E., Staudhammer K.P., Meyers M. A., Marcel Dekker, New York, 1986.
3. Lee W.-S., Lin C.-F., Impact properties and microstructure evolution of 304L stainless steel. Materials Science and Engineering A 308 (2001) 124-135.
4. Lee W.-S., Lam H.-F., The deformation behaviour and microstructure evolution of high-strength alloy steel at high rate of strain. Journal of Materials Processing Technology 57 (1996) 233-240.
5. Chiem C. Y., Duffy J., Strain rate history effects and observations of dislocation substructure in aluminum single crystals following dynamic deformation. Materials Science and Engineering 57 (1983) 233-247.
6. Klepazcko J. R., Thermally activated flow and strain rate history effects for some polycrystalline FCC metals. Materials Science and Engineering 18 (1975) 121-135.
7. Yasunaga K., Iseki M., Kiritani M., Dislocation structures introduced by high-speed deformation in BCC metals. Materials Science and Engineering A 350 (2003) 76-80.
8. Meyers M. A., Dynamic Behavior of Materials, John Wiley & Sons, Inc., New York, 1994.

9. Kettunen, P.O., Kuokkala, V.-T., Plastic Deformation and Strain Hardening, Materials Science Foundations Vol.16-18, Trans Tech Publications Ltd, Uetikon-Zuerich, 2003.
10. Kumar A., Hauser F. E., Dorn J. E., Viscous drag on dislocations in aluminum at high strain rates, Acta Metallurgica, 16 (1968) 1189-1196.
11. Mason W. P., Drag on dislocations due to thermal losses of the phonon-phonon interaction type. Journal of Applied Physics 35 (1964) 2779-2781.
12. Ferguson W. G., Kumar A., Dorn J. E., Dislocation damping in aluminum at high strain rates. Journal of Applied Physics 38 (1967) 1863-1869.
13. Kumar A., Kumble R. G., Viscous drag on dislocations at high strain rates in copper. Journal of Applied Physics 40 (1969) 3475-3480.
14. Nemat-Nasser S., Introduction to high strain rate testing, In ASM Handbook Vol. 8: Mechanical Testing and Evaluation. 2001, Materials Park, Ohio, p. 427-512.
15. Bleck W., Larour P., Measurement of the mechanical properties of car body sheet steels at high strain rates and non ambient temperatures. Journal de Physique 110 (2003) 489-494.
16. Vuoristo, T.: Effect of Strain Rate on the Deformation Behavior of Dual Phase Steels and Particle Reinforced Polymer Composites, väitöskirja. Tampereen teknillinen yliopisto, julkaisu 488, 2004.
17. Frew D. J., Forrestal M. J., Chen W., Pulse Shaping Techniques for Testing Brittle Materials with a Split Hopkinson Pressure Bar. Experimental Mechanics 42 (2002) 93-106.
18. Gorham D.A., A numerical method for the correction of dispersion in pressure bar signals, Journal of Physics E: Scientific Instruments 16 (1983) 477-479.
19. Gong J. C., Malvern L. E., Jenkins D. A., Dispersion investigation in the split Hopkinson pressure bar. Journal of Engineering Materials and Technology 112 (1990) 309-314
20. Vuoristo, T., Kuokkala, V.-T. and Keskinen, E.: Modeling of the deformation behavior of polymer composites at high strain rates and at elevated temperatures, Key Engineering Materials 221-222 (2002), p. 221-232.
21. Lindholm U. S., Yeakley L. M., High strain-rate testing: Tension and compression. Experimental Mechanics 8 (1968) 1-9.
22. Verleysen P., Degrieck J., Experimental investigation of the deformation of Hopkinson bar specimens. International Journal of Impact Engineering 30 (2004) 239-253.
23. Vuoristo, T., Kuokkala, V.-T. & Keskinen, E., Dynamic Compression Testing of Particle Reinforced Polymer Roll Cover Material. Composites: Part A 31 (2000), p. 815-822.
24. Vuoristo, T. and Kuokkala, V.-T.: Creep and recovery of soft roll cover materials, Mechanics of Materials 34 (2002), p.493-504.
25. Vuoristo, T., Apostol, M., Kuokkala, V.-T. and Peura, P.: Behavior of hot dip galvanized dual phase sheet steels at high rates of deformation, Journal de Physique IV 110 (2003) p. 213-218
26. Apostol, M., Vuoristo, T. and Kuokkala, V.-T.: High temperature high strain rate testing with a compressive SHPB, Journal de Physique IV 110 (2003) p. 459-464.
27. Vuoristo, T. and Kuokkala, V.-T.: Effect of strain rate, moisture and temperature on the deformation behavior of polymer roll covers. Experimental Mechanics 44 (2004) p. 313-319.
28. Apostol M., Kuokkala V-T., and Vuoristo T.: High temperature high strain rate behavior of OFHC copper with a compressive high temperature recovery Split Hopkinson Pressure Bar. ICEM12- 12th International Conference on Experimental Mechanics, Politecnico di Bari, Italy, 29 August - 2 September, 2004.
29. Nemat-Nasser, S., Isaacs, J.B., Starret, J.E., Hopkinson techniques for dynamic recovery experiments. Proceedings of the Royal Society of London A. 435 (1991) 371–391.
30. Vuoristo T., Kuokkala V-T., Apostol M., Peura P., Tulonen J. and Pirttijoki J.: Deformation and Work Hardening of Cold-Formed High Strength Steels at High Rates of Strain. Materials Science & Technology 2004 MS&T'04 September 26-29, 2004, New Orleans, Louisiana.
31. Cady C. M., Chen S. R., Gray G. T., Korzekwa D. A., Dynamic materials testing, texture, and yield-surface calculation of an automotive sheet steel. Metallurgical and Materials Transactions A 31 (2000) 2439-2449.

PALOSUOJALISÄAINEEN VAIKUTUS POLYESTERIHARTSIN MATERIAALIOMINAISUUKSIIN

A.-J. Vuotikka*, S.-G. Sjölind

Konetekniikan osasto
Box 4200, FIN-90014 Oulun yliopisto
*email: Antti-Jussi.Vuotikka@oulu.fi

TIIVISTELMÄ

Tässä työssä on tutkittu polyesterihartsin materiaalio minaisuuksien käyttäytymistä, kun hartsin sekaan lisätään palosuoja-ainetta. Varsinaisen mielenkiinnon kohteena oli materiaalin pitkäaikaiskäyttäytyminen, jonka lisäksi tehtiin testattavan materiaalin homogeenisuuden varmistamiseksi kimmokerrointestit.

Teoriaosassa käydään läpi lyhyesti teoreettiset perusteet materiaalitesteille. Kimmokertoimen testaaminen tehtiin ultraääni- ja värähtelymenetelmällä. Pitkäaikaiskäyttäytymistä tutkittaessa tehtiin aika–lämpötila- ja aika–jännityssuperpositiomenetelmien mukaiset virumistestit.

1 JOHDANTO

Polymeerimatriisikomposiittimateriaalin käyttömahdollisuudet ovat monipuoliset. Käyttökohteina voivat olla esimerkiksi kuljetuskalusto rautateillä ja liikenteessä. Tällaisissa kuljetuslaitteissa komposiitin lujuus–paino-suhde on eduksi, kun kalustoa voidaan keventää ja hyötykuormaa suurentaa.

Polymeerimatriisikomposiitin käyttö tuo keveytensä ja lujuutensa lisäksi myös ongelmia, jotka pääasiassa johtuvat polymeerimatriisista. Se ei käyttäydy ajasta riippumattomasti niin kuin metalliset rakenteet, vaan sen ominaisuudet voivat muuttua huomattavastikin ajan kuluessa. Tämän takia on tärkeää kehittää menetelmiä, joilla voitaisiin tehdä pitkän tähtäimen ennusteita polymeerin käyttäytymisestä. Materiaalin testausmenetelmien pitäisi olla kuitenkin suhteellisen lyhytkestoisia, jotta erilaisista polymeerimateriaaleista voidaan seuloa esiin sopiva polymeeri kohtuullisessa ajassa.

Tämän tutkimuksen tarkoituksena on tutkia polyesterihartsin aika–lämpötila- ja aika–jännityssuperponoituvuutta, kun hartsiin lisätään palosuoja-ainetta. Teoriaosassa käydään läpi lyhyesti termoreologisesti yksinkertaisen ja kompleksisen materiaalin teoriaa sekä niiden soveltamista aika–lämpötila- ja aika–jännityssuperpositiomenetelmään. Edellisessä tutkimuksessa [1] on käsitelty myös aika–vanhenemisaikasuperpositiota.

Työhön sisältyi materiaalitestien tekeminen polyesterihartsista valmistetuille koekappaleille. Koekappaleissa muuttujana toimii palosuoja-aineen määrä. Palosuoja-aineeksi valittiin ATH (alumiinitrihydroksidi), joka lisätään polymeerin sekaan valmistusvaiheessa. Vastaavasti on testattu myös lasikuitumatolla vahvistettuja polyesterihartsista valmistettuja koekappaleita, mutta niitä ei käsitellä tässä artikkelissa.

Testit aloitettiin materiaalin kimmokerrointesteillä, joilla varmistettiin koekappaleiden homogeenisuus. Ultraäänilaitteistolla mitattiin koekappaleiden akustinen impedanssi, jonka avulla voidaan laskea kimmokertoimet. Värähtelymenetelmällä selvitettiin kaikkien koekappaleiden kimmokertoimet, jotka saadaan koekappaleen alimman ominaistaajuuden avulla.

Kimmokertoimen testauksen jälkeen tehtiin noin kolme vuorokautta kestäneet virumistestit jokaiselle koekappaleelle ja niiden tuloksia analysoitiin teoriaosan pohjalta. Materiaaleille tehtyjen virumiskokeiden tulosten avulla muodostettiin aika–lämpötila- ja aika–jännityssuperposition kuvaamiseen tarvittavat siirtokertoimet ja siirtokerroinfunktiot sekä johtokäyrät. Polyesterikoekappaleiden tuloksia analysoidaan sekä pohditaan palosuojaaineen vaikutusta testatuissa koekappaleissa.

2 KIMMOKERTOIMEN LASKEMINEN

Ultraäänimenetelmällä voidaan selvittää materiaalin kimmokertoimen arvo. Menetelmän etu normaaliin vetokokeella tehtävään testiin on se, että tässä menetelmässä materiaalin viskoosisuus ei vaikuta mittaustuloksiin. Kiinteässä materiaalissa voidaan äänen nopeudelle johtaa erilaisia kaavoja materiaalin kimmo-ominaisuuksien, tiheyden ja materiaalin muodon perusteella. Pitkittäistasoaallon nopeus äärettömässä 3D-solidissa voidaan esittää seuraavan kaavan avulla:

$$c = \sqrt{\frac{E(1-\nu)}{\rho(1-2\nu)(1+\nu)}}, \tag{1}$$

missä materiaalin kimmokerrointa, Poissonin vakiota ja tiheyttä on merkitty E:llä, ν:lla ja ρ:lla. Solidi oletetaan tässä tapauksessa isotrooppiseksi ja homogeeniseksi. Äänen nopeudella c ja ultraäänellä mitattavalla akustisella impedanssilla Z on yhteys $Z = \rho c$. Näiden avulla kimmokertoimen yhtälöksi saadaan [2]

$$E = \frac{Z^2}{\rho}\frac{(1+\nu)(1-2\nu)}{1-\nu} \tag{2}$$

Ultraäänimenetelmän tuloksia haluttiin verifioida, mikä tehtiin mittaamalla kimmokertoimet värähtelymenetelmällä. Menetelmän ideana on kimmokertoimen selvittäminen toisesta päästä jäykästi tuetun palkin vapaasta värähtelystä. Oletetaan, että värähtely tapahtuu palkin pääjäyhyystasossa, palkki noudattaa Bernoullin otaksumaa ja materiaali noudattaa Hooken lakia. Palkin vapaan poikittaisvärähtelyn liikeyhtälö on $EIv'''' + \rho A\ddot{v} = 0$. Ratkaisemalla liikeyhtälö ja selvittämällä palkin poikittaisvärähtelyn alimman ominaistaajuuden f analyyttinen kaava voidaan kimmokertoimelle muodostaa seuraava yhtälö. [3]

$$E = \left(\frac{2\pi f l^2}{3.516}\right)^2 \frac{\rho A}{I}, \tag{3}$$

missä l on palkin vapaa pituus ja A sekä I ovat palkin poikkipinnan suureita.

3 VIRUMISTESTIEN TEORIAA

3.1 Termoreologinen yksinkertaisuus ja kompleksisuus

Useimmilla polymeerimateriaaleilla esiintyy erityinen materiaaliominaisuuksien lämpötilariippuvuus, jolle voidaan esittää analyyttinen kuvaus. Tätä ominaisuutta kutsutaan materiaalin termoreologiseksi yksinkertaisuudeksi. Esitetään virumisfunktio $J(t)$, missä t on aika, mielivaltaisesti valitussa peruslämpötilassa $T = T_0$. Annetaan lämpötilakentän muuttua tasaisesti uuteen vakiolämpötilaan ja esitellään vastaava virumisfunktio $\hat{J}(t, T)$, missä T

on uusi lämpötila. Asetetaan virumisfunktiot ekvivalenteiksi peruslämpötilassa ja tehdään samalla muuttujan vaihto virumisfunktiolle $J(t)$.

$$\hat{J}(t, T_0) = J(t) = L(\log t) \tag{4}$$

Seuraavalla kaavalla määritellään termoreologisesti yksinkertaisen materiaalin peruspostulaatti

$$\hat{J}(t, T) = L[\log t + \phi(T)] = L[\log t + \log \chi(T)], \tag{5}$$

missä $\phi(T)$ on siirtofunktio, jolle tehdään muuttujan vaihto siirtofunktioksi $\chi(T)$. $\phi(T)$ toteuttaa ehdot $\phi(T_0) = 0$ ja $\mathrm{d}\phi(T)/\mathrm{d}T > 0$ ja muuttujan vaihdon jälkeen siirtofunktio toteuttaa ehdot $\chi(T_0) = 1$ ja $\mathrm{d}\chi(T)/\mathrm{d}T > 0$. Yhtälön 5 merkitys voidaan selittää fysikaalisesti siten, että muutokset virumislämpötilassa aiheuttavat virumisfunktion siirtymisen oikeaan tai vasempaan suuntaan logaritmisella aika-asteikolla. Nyt kaava 5 saadaan kaavan 4 avulla seuraavaan muotoon

$$\hat{J}(t, T) = L[\log t\chi(T)] = J(\xi), \tag{6}$$

missä

$$\xi = t\chi(T) = t/a(T) \tag{7}$$

ja sitä kutsutaan redusoiduksi ajaksi. Siten virumisfunktio $\hat{J}(t, T)$ missä tahansa vakiolämpötilassa saadaan suoraan peruslämpötilan T_0 virumisfunktiosta $J(t)$ korvaamalla aika t redusoidulla ajalla ξ. Siirtofunktio $a_T = a(T)$ on materiaalin perusominaisuus ja se pitää selvittää materiaalitestejä tekemällä. Termoreologisen yksinkertaisuuden postulaattia kutsutaan myös aika–lämpötilasuperpositioperiaatteeksi. [4]

Superpositioperiaate perustuu oletukseen, että viskoelastisen spektrin muoto ja siten virumis- tai relaksaatiomodulit eivät vaihtele minkään parametrin kuten vanhenemisajan tai lämpötilan suhteen. Kaava 6 esittää aika–lämpötilasuperposition ilman vertikaalisiirtoa. Kuitenkin on havaittu, että vertikaalisiirtoja voidaan tarvita, kun eri lämpötilojen virumiskäyrät eivät asetu pelkän horisontaalisiirron avulla jouhevasti päällekäin. [5]

Termoreologinen kompleksisuus soveltuu kaikille niille tapauksille, joissa johtokäyrän muodostaminen pelkillä virumiskäyrien sivuttaissiirtymillä ei ole mahdollista. Polymeerimateriaalilla voi olla useita erilaisia relaksoitumismekanismeja, ja jokaisella niistä on oma lämpötilariippuvuus. Toisaalta materiaalin kokiessa erilaisia vanhenemisilmiöitä, kuten fysikaalista tai kemiallista vanhenemista, hapettumista, valon aiheuttamaa polymeeriketjujen ristiinlinkittymistä tai faasimuutoksia, sen käyttäytymistä ei voida myöskään kuvata termoreologisella yksinkertaisuudella. Termoreologisesti kompleksisia materiaaleja varten voidaan horisontaalisen siirtokertoimen lisäksi ottaa käyttöön vertikaalinen siirtokerroin.

$$\hat{J}(t, T) = b(T)J(\xi), \tag{8}$$

missä lämpötilasta riippuva kerroin $b(T)$ on vertikaalinen siirtokerroin. [6], [7]

3.2 Siirtokerroinfunktiot

Eri lämpötilojen virumisfunktiot on saatu yhteneviksi vertailulämpötilan virumisfunktion kanssa redusoidun ajan käsitteen avulla kaavojen 6 ja 8 mukaisesti. Todellisen ja redusoidun ajan välinen suhde pitää selvittää kokeellisesti materiaalin virumis- tai relaksaatiotesteillä. Toinen vaihtoehto on käyttää puoliempiirisiä siirtokerroinfunktioita, kuten WLF-yhtälöä tai Arrheniuksen funktiota. 1950-luvulta lähtien on ehdotettu kymmenittäin erilaisia kaavoja, joilla siirtokertoimien lämpötilariippuvuus kuvataan. [6]

Määritellään siirtokerroinfunktio viskositeetin pohjalta. Viskositeetin ja relaksaatiomodulin välille on muodostettu relaatio

$$\eta(T) = \int_0^\infty E(T,t)\mathrm{d}t. \tag{9}$$

$\eta(T)$ on polymeerin vetoviskositeetti lämpötilassa T. Termoreologisen yksinkertaisuuden perusteella kahdella relaksaatiokäyrällä, joista toinen on referenssilämpötilassa T_0 ja toinen mielivaltaisessa lämpötilassa, on yhteys

$$E(T_0, t_0) = E(T, t). \tag{10}$$

Yhtälön 7 pohjalta saadaan differentioimalla ajan suhteen

$$\mathrm{d}t = a_T \mathrm{d}t_0. \tag{11}$$

Sijoittamalla edellinen ja yhtälö 10 yhtälöön 9 saadaan

$$\eta(T) = \int_0^\infty E(T,t)\mathrm{d}t = \int_0^\infty E(T_0,t_0)a_T\mathrm{d}t_0. \tag{12}$$

a_T voidaan tuoda integraalin ulkopuolelle ja esittää viskositeettien avulla muodossa. Vastaavasti siirtokerroinfunktio voidaan esittää myös relaksaatioaikojen avulla. [8]

$$a_T = \frac{\eta(T)}{\eta(T_0)} = \frac{\tau(T)}{\tau(T_0)}. \tag{13}$$

Viskositeetille on esitetty useita erilaisia yhtälöitä, joista yleisimmin käytettyjä on Doolittlen yhtälö. Sen ideana on se, että vapaan tilavuuden muutos vaikuttaa polymeerin liikkeisiin. Mitä suurempi vapaa tilavuus on, sen helpommin polymeeriketjut reagoivat ulkoiseen kuormitukseen. Sen avulla voidaan johtaa WLF-yhtälö, jota käytetään lasipistelämpötilojen yläpuolella materiaalin kumimaisessa olotilassa. Kun siirrytään polymeerin lasialueelle, jossa tapahtuu kahden tai useamman tyyppisiä polymeeriketjun liikkeitä eri lämpötilariippuvuuksilla, WLF-yhtälö ja redusoidun ajan menetelmä eivät toimi. Jos tehdään oletus, että kaikilla relaksoitumisajoilla koskien tietyn tyyppistä molekyylin liikettä on sama lämpötilariippuvuus, niin redusoidun muuttujan menetelmää voidaan hyödyntää. Yleensä siirtokertoimen lämpötilariippuvuus lasialueella seuraa Arrheniuksen funktiota, jossa aktivoitumisenergia F_c on lämpötilasta riippumaton. Arrheniuksen siirtokerroinfunktion johtaminen lähtee siitä, että yhteys relaksaatioajan ja lämpötilan välillä on muotoa

$$\tau = \tau_0 e^{\frac{AF_c}{k_b T}}, \tag{14}$$

missä A on materiaalivakio ja k_b on Bolzmannin vakio. Yhtälöiden 13 ja 14 avulla voidaan siten muodostaa aika–lämpötilasiirtokertoimeksi Arrheniuksen funktio

$$\log a_T = \frac{AF_c}{k_b}\left(\frac{1}{T} - \frac{1}{T_0}\right). \tag{15}$$

Edellä on esitetty ajasta riippuva materiaalin käyttäytyminen, joka perustuu lämpötilan aiheuttamaan molekyylien liikkeisiin. Vastaavasti jännityksen kasvattaminen aiheuttaa polymeerissä lämpötilan vaikutukseen verrattavaa molekyylien liikkeen nopeutumista. Oletetaan, että viskositeetti riippuu lämpötilasta ja jännityksestä lineaarisesti. Oletetaan myös,

että on olemassa yhdistetty lämpötila-jännityssiirtokerroin $a_{T\sigma}$, jolloin yhtälö 13 voidaan esittää muodossa

$$a_{T\sigma} = \frac{\eta(T,\sigma)}{\eta(T_0,\sigma_0)}. \tag{16}$$

Määritellään jännityksen siirtokerroinfunktio vakio lämpötilassa a_σ^T ja lämpötilan siirtokerroinfunktio vakio jännityksessä a_T^σ seuraavalla tavalla

$$\eta(T,\sigma) = \eta(T,\sigma_0)a_\sigma^T = \eta(T_0,\sigma_0)a_T^{\sigma_0}a_\sigma^T = \eta(T_0,\sigma)a_T^\sigma = \eta(T_0,\sigma_0)a_\sigma^{T_0}a_T^\sigma, \tag{17}$$

jolloin saadaan

$$a_{T\sigma} = a_T^{\sigma_0}a_\sigma^T = a_\sigma^{T_0}a_T^\sigma. \tag{18}$$

Tämän yhtälön perusteella aikariippuvat viskoelastisen materiaalin mekaaniset ominaisuudet eri lämpötiloissa ja jännitystasoilla voidaan siirtää aika-akselilla muodostettaessa johtokäyrää annetussa lämpötilassa T_0 ja jännitystasossa σ_0. Siirtäminen tehdään joko yhdessä vaiheessa käyttämällä yhdistettyä lämpötila-jännityssiirtokerrointa tai kahdessa vaiheessa käyttämällä lämpötilasiirtokerrointa ja jännityssiirtokerrointa. Tässä tutkimuksessa on käytetty Arrheniuksen funktiota myös jännityssiirtokertoimena. [5], [8], [9], [10], [11]

Vertikaalisiirtokerroin ilmaisee lämpötilan tai jännityksen aiheuttaman materiaalin mekaanisten ominaisuuksien muutoksen. Lämpötilasta riippuvien vertikaalisten siirtokertoimien huomioiminen on paljon tärkeämpää lasipisteen alapuolella kuin yläpuolella, koska aikariippuvuus lasialueella on melko pieni [8]. Kirjallisuudessa on esitetty suhteellisen vähän siirtokerroinfunktioita vertikaalisiirrolle. Tässä tutkimuksessa käytetään lineaarista polynomifunktiota kuvaamaan vertikaalisiirtoa molemmissa tapauksissa.

$$b_T = aT + b, \qquad b_\sigma = a\sigma + b, \tag{19}$$

missä a ja b ovat parametrejä, T on lämpötila ja σ on jännitys.

3.3 Redusoidun ajan hyödyntäminen

Virumisvenymälle voidaan esittää seuraavanlainen kaava redusoidun ajan ja peruslämpötilassa olevan virumisjoustavuusmodulin J avulla. [12]

$$\varepsilon(t) = \int_0^t bJ(\xi - \xi')\frac{\mathrm{d}\sigma}{\mathrm{d}\tau}\mathrm{d}\tau, \tag{20}$$

missä b on vertikaalinen siirtokerroin ja τ on aika.

Materiaalin virumisjoustavuutta voidaan kuvata monilla erilaisilla matemaattisilla funktioilla. Tässä tutkimuksessa pitkäkestoisen virumisen mallintamiseen on käytetty yleistettyä Voigtin mallia eli Prony-sarjaa.

$$J(t) = J_0 + \sum_{k=1}^{K-1} J_k\left[1 - \exp\left(-\frac{t}{\tau}\right)\right], \tag{21}$$

missä K on termien määrä ja J_k:t ovat Prony-sarjan kertoimia [13].

4 KOEJÄRJESTELYT

4.1 Koekappaleet

Tutkimuksessa käytetty materiaali on esikiihdytetty keskireaktiivinen *ortophthalic*-hartsi. Se on laajasti käytetty, koska sillä on suhteellisen korkea lämmönkestävyys $HDT = 90\,^\circ\mathrm{C}$ ja hyvät mekaaniset ominaisuudet. Hartsin lasipistelämpötilaksi T_g on ilmoitettu $110\,^\circ\mathrm{C}$.

Palosuoja-aineena on käytetty alumiinitrihydroksidia ($Al(OH)_3$) eli ATH:ta, jota on sekoitettu täyteaineeksi polyesterihartsiin kahdella eri pitoisuudella. ATH:n etuja on se, että se toimii hartsin täyteaineena. Täyteaineet vähentävät orgaanisen materiaalin määrää, mitä tarvitaan palotapahtumassa ja samalla ne toimivat lämpönieluna. ATH hajoaa endotermisesti korkeissa lämpötiloissa absorboiden lämpöä samalla, kun se vapauttaa palon kehittymistä rajoittavaa vesihöyryä.

Koekappaleiden aihiot valettiin levyiksi, joissa muuttujana oli palosuoja-aineen määrä. Suorakaiteen muotoiset koekappaleet sahattiin irti levyaihiosta. Sauvojen leveys on 15 mm:ä ja paksuus on 5 mm:ä. Koesauvojen kumpaankin päähän porattiin 5 mm:n reikä virumistestauslaitteistoon kiinnittämistä varten. Tämän jälkeen sauvojen reunat hiottiin. Ensimmäiset hartsiaihiot eli palosuoja-ainettomat aihiot nimettiin kirjaimilla a ja b. Hartsiaihiot, joissa on palonsuoja-ainetta 25 %:a ja 50 %:a, nimettiin kirjaimilla d ja e.

4.2 Kimmokertoimen mittauslaitteisto

Ultraäänimenetelmällä testattiin osaa a- ja b-materiaalin koekappaleita. Ultraäänilaitteistona oli Sonoscan C-sam laitteisto, jossa käytettiin 15 MHz:n anturia akustisen impedanssin selvittämisessä. Koekappaleet upotettiin laitteiston vesialtaaseen ja sen jälkeen akustinen impedanssi mitattiin sauvan pinnalta kolmesta eri kohdasta. Mittausten jälkeen sauva kuivattiin huolellisesti.

Kaikkien hartsisauvojen kimmokertoimet selvitettiin värähtelymenetelmällä. Värähtelymenetelmällä kimmokertoimia etsittäessä tarvittava laitteisto sisälsi Laser-anturin, joka mittasi värähtelevän koekappaleen liikkeen, ruuvipuristimen, johon koekappaleet kiinnitettiin sekä tietokoneen, joka laski värähtelyn alimman ominaistaajuuden FFT-muunnoksella. Värähtely herätettiin kolmella eri sauvan vapaalla pituudella vasaraa käyttämällä.

4.3 Virumistestauslaitteisto

Testattavan koemateriaalin virumistestaus tehtiin lämpökäsittelyuunissa. Testilämpötiloiksi valittiin 40 °C, 60 °C ja 75 °C astetta. Koekappaleet kuormitettiin uunin katossa olevan reiän kautta vipumekanismin ja punnusten avulla. Testeissä käytettiin kolmea eri kuormaa, mikä aiheutti koekappaleisiin 3.3 MPa, 5.0 MPa tai 6.4 MPa jännityksen. Koekappaleiden viruminen mitattiin koesauvan kylkeen kiinnitettävällä siirtymäanturilla. Koekappaleeseen kohdistunut voima voidaan laskea käytettyjen punnusten ja vipuvarsien suhteen avulla. Mittausdatasta poimitaan joka kuuden sekunnin välein yksi mittapiste, ja testausaika uunissa on vähintään noin 3 vuorokautta. Koekappaleiden kimmokertoimien testaaminen aloitettiin noin kuukausi materiaalin valmistuksen jälkeen, ja testit valmistuivat parissa päivässä jokaisen materiaalierän kohdalla. Virumistestaus aloitettiin heti kimmokerrointestien jälkeen, ja testauskapasiteetin pienuuden takia mittaukset kestivät useita kuukausia.

Testausohjelma virumistestien osalta jakaantuu kahteen osaan: osalle sauvoista tehtiin aika–lämpötilasuperposition mukaisia testejä ja osalle aika–jännityssuperposition mukaisia testejä. Aika–jännitystesteissä testilämpötila pidettiin vakiona 40 °C asteessa ja aika–lämpötilatesteissä pidettiin 3.3 MPa:n vakiojännitys. Testausmenetelmän yhteinen referenssitila on siis 40 °C:een lämpötila ja 3.3 MPa:n jännitys. Lämpötilojen ja kuormitusten sekä testattujen koekappaleiden määrien eri yhdistelmät ovat taulukossa 1.

5 KIMMOKERROINTESTIT

Akustisesta impedanssista laskettiin perusaineen kimmokertoimen arvo teoriaosassa esitetyn kaavan avulla, kuva 1. Tulokseksi saatujen kimmokertoimien arvot olivat hieman suurempia kuin yleisesti kirjallisuudesta löytyvät arvot kyseisen materiaalin kimmokertoimille.

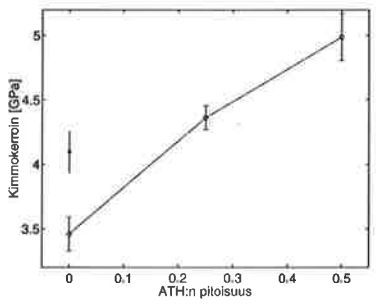
	3.3 MPa	5.0 MPa	6.4 MPa
40 °C	4	4	4
60 °C	4	-	-
75 °C	4	-	-

Taulukko 1: Koekappaleiden määrän jakautuminen eri testilämpötilojen ja -kuormitusten mukaan. b-materiaalisarjalle ei tehty 40 °C:ssa testejä suuremmilla kuormituksilla.

Ultraäänilaitteistolla yritettiin selvittää kimmokerroin myös toisella tavalla. Laitteistolla yritettiin selvittää koekappaleen paksuus. Jos koekappaleen paksuus olisi saatu selvitettyä, niin siitä olisi saatu signaalien heijastumisen välinen aikaero, ja tämän jälkeen olisi mahdollista laskea äänennopeus materiaalissa. Koekappaleen pohjakaikua ei löydetty luotettavasti. Koska materiaalin paksuus oli tiedossa, pohjakaikua yritettiin etsiä 5.5 millimetrin paikkeilta, mutta laite löysi sen kuitenkin vasta lähempää 7.0 millimetriä, joten tätä menettelyä ei voitu hyödyntää.

Värähtelymittauksissa mitatuista taajuuksista laskettiin materiaalin kimmokertoimet käyttämällä teoriaosassa esitettyä kaavaa. Koska kiinnityksen vaikutus pienentää kimmokertoimen todellista arvoa, korkein kimmokertoimen arvo on otettu edustamaan jokaista mitattua sauvaa. Eri vapailta pituuksilta saatujen kimmokertoimen arvojen vaihteluväli on alle 3 %:a jokaisella materiaalierällä. Sauvojen kimmokertoimien maksimiarvoista on otettu keskiarvo ja hajonta, jotka on esitetty kuvassa 1. Kuvassa perusaineen kimmokertoimen arvoksi on esitetty a- ja b-materiaalien yhdistetty kimmokertoimen arvo ja hajonta. Kimmokertoimien suhteellinen hajonta kaikilla hartsierillä on alle 5 %:a.

Kun tutkitaan kimmokertoimien arvoja virumistesteissä käytetyn jaottelun mukaan (taulukko 1), havaittiin testiryhmien välillä olevan vain vähän eroja. Perusmateriaaleilla eli a- ja b-materiaaleilla testiryhmän kimmokertoimen vaihtelu oli koko materiaalierän kimmokertoimen hajonnan sisällä kummassakin tapauksessa. Kun materiaaliin on lisätty ATH:a, kimmokertoimen vaihtelu testiryhmien välillä oli hieman suurempaa.



Kuva 1: Polyesterin kimmokertoimen vaihtelu ATH-pitoisuuden vaihdellessa 0 – 50 %:n välillä värähtelymenetelmällä mitattuna. Ultraäänimenetelmällä saatu perusmateriaalin kimmokerroin on myös esitetty kuvassa (yksittäinen piste).

Kimmokertoimien arvoa pohdittaessa voidaan todeta, että perusaineen mitatut kimmokertoimen arvot ovat samanlaiset kuin kirjallisuudessa polyesterille esitetyt arvot. a- ja b-materiaalierien kohdalla oli kimmokertoimien arvoissa pientä eroavaisuutta, joka todennäköisesti johtuu valmistuksesta. a-materiaalierään oli jäänyt huomattavasti enemmän ilmakuplia, millä voi myös olla merkitystä. Lisättäessä polyesterihartsiin ATH:a voidaan

sen metallioksidina olettaa nostavan materiaalin kimmokerrointa, mikä on myös nähtävissä kuvassa 1. Kimmokerroin näyttää nousevan lähes lineaarisesti.

6 VIRUMISTESTIT

Virumistesteistä saatujen virumiskäyrien analysointi on tehty Matlab R12 -ohjelmistolla. Mittauksissa on veymä tallennettu tiedostoon kuuden sekunnin välein. Analysointi tapahtuu logaritmisella asteikolla, joten mittausdatasta poimitaan logaritmisesti tasavälein olevat mittauspisteet analysoitavaksi. Samalla virumiskäyrät on muutettu virumisjoustokäyriksi. Kuvassa 3 on esitetty d-materiaalierän virumisjoustokäyrät.

Aika–lämpötilatesteissä selvisi, että viruminen on yksittäistapauksia lukuun ottamatta tapahtunut odotetusti. Lämpimimmässä lämpötilassa koestetut sauvat ovat viruneet eniten ja kylmimmässä lämpötilassa vähiten. Aika–jännitystuloksia tutkittaessa huomattiin, että kuormituksen kasvattaminen ei aiheuttanut vastaavaa virumisjoustavuuden kasvamista.

6.1 TRS ja TRC

Referenssitilan virumisjoustokäyrille tehtiin 7 termin Prony-sarjan sovitus Matlab-ympäristössä toimivalla Mfit-ohjelmalla. Sovittaminen tehtiin siten, että ohjelmalla haettiin g_i:lle arvot, kun τ_i:lle määriteltiin arvot 10^i välein. Alkuhetken virumisjoustokerrointa merkitään g:lla. Mikäli g_i:n arvo oli negatiivinen, se korvattiin 0:lla ja loput g_i:t sovitettiin uudelleen. Materiaalierän referenssikäyräksi valittiin se, johon saatiin mahdollisimman monen termin sovitus ja paras korrelaatiokerroin R^2. Taulukossa 2 on esitetty d-materiaalin referenssikäyrän parametrit. Sovittaminen onnistui kaikkien materiaalierien kohdalla hyvin, sillä korrelaatiokerroin jokaiselle referenssikäyrälle on lähellä yhtä.

i		0	1	2	3	4	5	6
g_i	2.66e-1	0	3.40e-2	4.23e-3	1.53e-2	7.40e-2	1.16e-1	0
τ_i		10^0	10^1	10^2	10^3	10^4	10^5	10^6

Taulukko 2: Taulukossa on esitetty d-materiaalierän referenssikäyrän parametrit, jonka R^2 on 0.989. g_i:n ensimmäinen termi kuvaa alkuhetken virumisjoustavuutta.

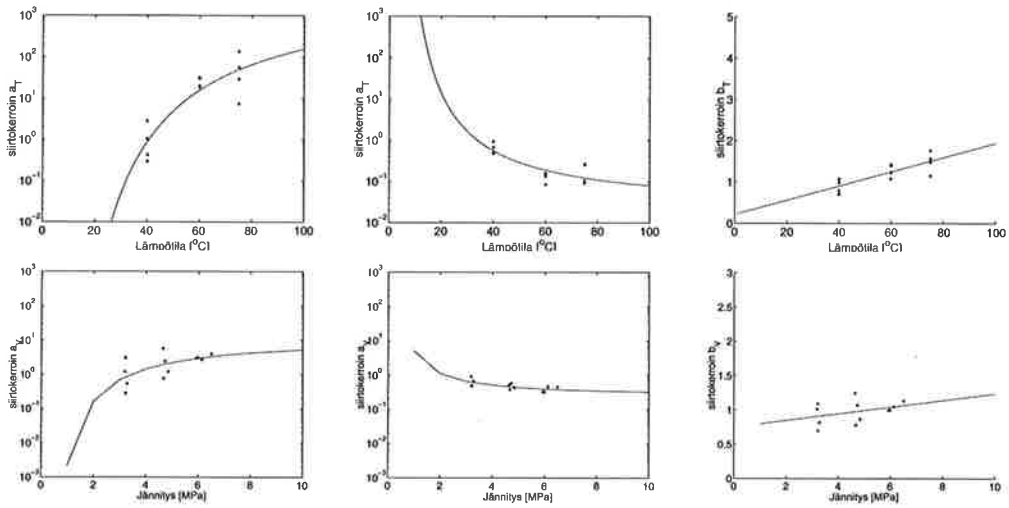
Muut käyrät siirrettiin referenssikäyrän suhteen TRS- ja TRC-tapauksissa. Siirrettäessä käyriä saadaan siirtokertoimet ja muodostetaan johtokäyrän sovittamista varten pisteistö. Siirretyt käyrät on esitetty kuvassa 4, jossa ylärivillä on aika–lämpötilatestien käyrät ja niiden alla aika–jännitystestien käyrät. Vertikaalisiirtojen huomioiminen pienensi kaikissa tapauksissa huomattavasti sovittamisesta syntyvää virhettä.

6.2 Siirtokertoimet

Siirtokerroinfunktiot on sovitettu saatuihin siirtokertoimiin pienimmän neliösumman approksimaation avulla ja ne on esitetty kuvassa 2. Siirtokerroinfunktiota sovitettaessa voidaan referenssiparametri valita testiohjelman perusteella, mutta tässä se on saatu sovituksen mukana. Sovituksen onnistumista seurattiin sovituksessa lasketun RMS-virheen avulla.

Aika–lämpötilasiirtokertoimien parametrien arvot TRS-tapauksessa ovat $T_0 = 40.6$ °C ja $\frac{AF_c}{k_b} = -344$ °C. Sovituksen RMS-virheeksi saatiin 173. TRC-tapauksessa horisontaalisen siirtokerroinfunktion parametrien arvot ovat $T_0 = 33.8$ °C ja $\frac{AF_c}{k_b} = 129$ °C, ja vastaavasti vertikaalisessa tapauksessa $a = 1.73e^{-2}\,°C^{-1}$ ja $b = 0.213$. Sovitusten RMS-virheen arvot ovat 197 ja 16. Kummankin tapauksen siirtokerroinfunktiot on piirretty kuvan 2 yläriville.

Aika–jännityssiirtokertoimien parametrien arvot TRS-tapauksessa ovat $\sigma_0 = 3.4\,\mathrm{MPa}$ ja $\frac{AF_c}{k_b} = -8.7\,\mathrm{MPa}$. Sovituksen RMS-virheeksi saatiin 154. TRC-tapauksessa horisontaalisen siirtokerroinfunktion parametrien arvot ovat $\sigma_0 = 2.1\,\mathrm{MPa}$ ja $\frac{AF_c}{k_b} = 3.1\,\mathrm{MPa}$, ja vastaavasti vertikaalisessa tapauksessa $a = 4.86^{-2}\,\mathrm{MPa}^{-1}$ ja $b = 0.750$. Sovitusten RMS-virheen arvot ovat 101 ja 16. Kummankin tapauksen siirtokerroinfunktiot on piirretty kuvan 2 alariville.



Kuva 2: Ylhäällä on aika–lämpötilasiirtokertoimet ja alhaalla aika–jännityssiirtokertoimet. Vasemmalla on esitetty TRS-tapauksen siirtokerroinfunktio. Keskellä sekä oikealla on esitetty TRC-tapauksen horisontaali- ja vertikaalisiirtokerroinfunktiot.

Siirtokerroinfunktion käyttäytymiseltä TRS-tapauksessa vaaditaan monotonista kasvua. Aika–lämpötilasuperpositiossa kaikkien materiaalien siirtokerroinfunktiot olivat monotonisesti kasvavia. Aika–jännitystapauksessa kaikissa tapauksissa tämä vaatimus ei täyttynyt. TRC-tapauksessa ei ole löytynyt vaatimuksia siirtokerroinfunktion käyttäytymiselle. Kummassakin testissä horisontaaliset siirtokerroinfunktiot olivat monotonisesti väheneviä. Vertikaaliset siirtokerroinfunktiot olivat kasvavia aika–lämpötilatapauksessa, mutta aika–jännityspuolella oli taas vaihtelua. RMS-virheitä tarkastelemalla huomataan, että sovitus on onnistunut kummassakin tapauksessa yhtä hyvin.

6.3 Johtokäyrät

Johtopisteistöön sovitettiin 9:n termin Prony-sarjakäyrät käyttämällä Mfit-ohjelmaa vastaavalla tavalla kuin referenssikäyrän sovituksessa. Laadun toteamiseksi jokaisen sovituksen korrelaatiokerroin R^2 laskettiin ja ne on esitetty taulukoissa 3. Johtokäyrät TRC-tapauksessa aika–lämpötila- ja aika–jännitystesteistä on esitetty kuvassa 5 a-, d- ja e-materiaaleille.

Prony-sarjan sovittaminen johtopisteistöön on onnistunut vaihtelevalla menestyksellä. Pääsääntöisesti pelkkien horisontaalisiirtojen avulla muodostettuun johtopisteistöön sovitettu käyrä ei saa niin hyvää korrelaatiokerrointa kuin vertikaalisiirtojen käytön yhteydessä.

Aika–lämpötilajohtokäyrien ja aika–jännitysjohtokäyrien kuvia tutkittaessa huomataan, että kummassakin tapauksessa virumisjoustavuus kasvaa palosuoja-ainepitoisuuden kasvaessa. Käyrien järjestys vaihtuu vasta käyrien loppupäässä. Tämän ilmiön aiheuttaa toden-

	Aika–lämpötilajohtokäyrät					Aika–jännitysjohtokäyrät			
TRS	a	b	d	e	TRS	a	b	d	e
R^2	0.17	0.12	0.14	0.65	R^2	0.30	-	0.57	0.001
TRC	a	b	d	e	TRC	a	b	d	e
R^2	0.59	0.36	0.53	0.56	R^2	0.45	-	0.48	0.66

Taulukko 3: Taulukossa on esitetty jokaisen materiaalierän johtokäyrän sovittamisen korrelaatiokertoimet TRS- ja TRC-menetelmillä kummassakin testitapauksessa.

näköisesti se, että testattavia koekappaleita oli tilastollisesti liian vähän. Tällöin yksittäinen referenssikäyrän suhteen siirretty käyrä voi vaikuttaa huomattavasti johtokäyrän muotoon, mikä on voimakkaimmillaan juuri johtokäyrän alku- ja loppupäässä.

7 YHTEENVETO

Kimmokertoimien mittaaminen värähtelymenetelmällä onnistui hyvin. Testattujen koekappaleiden lukumäärä oli riittävän suuri, jotta saatiin tilastollisesti pätevät tulokset. Mitatuissa kimmokertoimissa ei ollut suuria heittoja, joten ne olivat suhteellisen homogeenisia. Kimmokertoimien arvoa pohdittaessa voidaan todeta, että ilman palosuoja-ainetta mitatut kimmokertoimen arvot vastaavat kirjallisuudessa esitettyjä arvoja. Palosuoja-aineen lisääminen polyesterihartsiin kasvatti materiaalin kimmokerrointa, mikä on odotusten mukaista, koska ATH on metallioksidia.

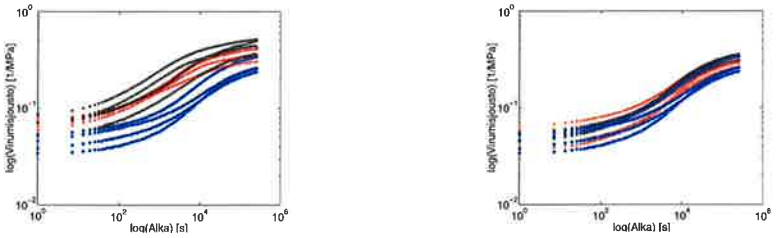
Ultraäänimmittausta käytettäessä ongelmana oli se, että orgaaninen materiaali absorboi ultraäänisignaalia. Kirjallisuudessa neuvottiin käyttämään matalataajuisempia antureita mittausten tekemiseen, jolloin absorboitumisongelma olisi ehkä vältetty. Testeissä käytettiin matalataajuisinta saatavilla ollutta anturia eli 15MHz:n anturia. Tämän ongelman takia ultraäänitestit tehtiin vain osalle koekappaleista.

Aika–lämpötilavirumistestit onnistuivat hyvin, mutta aika–jännitystesteissä oli hieman ongelmia. Todennäköisesti suurin ongelmien aiheuttaja virumistesteissä oli se, että materiaalien testaus sujui hitaasti uunin kapasiteettiongelmien takia. Koska koemateriaali toimitettiin testattavaksi kahdessa erässä ja aika–jännitystestit tehtiin myöhemmin, kapasiteettiongelmien takia aika–jännitystesteissä käytetyt koekappaleet ehtivät altistua eri vanhenemisilmiöille pitempään. Tästä ongelmasta pääsisi eroon, jos testauslaitteisto olisi mahdollistanut useamman kuin kahden sauvan testaamisen kerrallaan ja testattavaa materiaalia olisi valmistettu useammassa erässä. Jälkimmäisessä tapauksessa tulee kuitenkin mukaan valmistuserien välinen vaihtelu.

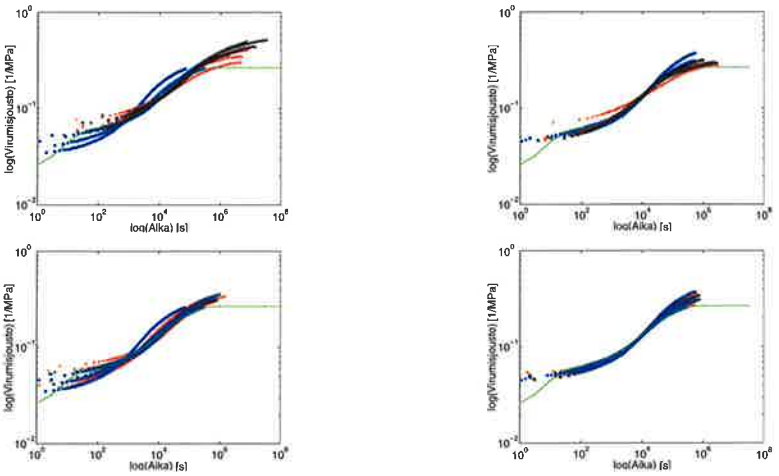
Toisena ongelmana aika–jännitystesteissä oli testeissä käytettyjen jännitysten pienet erot. Koemateriaalin käyttäytyminen olisi ehkä paremmin selvinnyt, jos olisi käytetty suurempia kuormia testeissä. Ongelmaksi tässä tuli kuitenkin koekappaleiden kiinnitys, joka ei kestänyt kuorman kovin suurta kasvattamista. Aika–lämpötila- ja aika–jännitystapausta verrattaessa aika–lämpötilatapaus näyttäisi toimivan paremmin.

Tutkimuksen aikana testattiin myös lasikuidulla lujitettuja koekappaleita, joissa käytettiin samoja polymeeriseoksia kuin tässä artikkelissa esitetyissä testeissä. Näiden testien tulokset esitetään lähteessä [14].

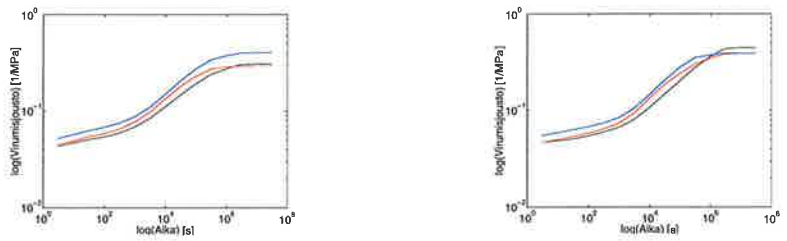
Tutkimuksen tuloksia voidaan hyödyntää suunnittelussa ainakin ABAQUS- ja Ansys-ohjelmistoja käyttämällä. Kumpaankin ohjelmaan voidaan antaa virumiskäyrät mittausdatana, joihin ohjelmistot sovittavat Prony-sarjan. Ohjelmistot mahdollistavat myös siirtokerroinfunktioiden käytön. Ohjelmistoissa on valmiina joitain siirtokerroinfunktioita ja tarvittaessa haluttu funktio voidaan ohjelmoida.



Kuva 3: Vasemmalla on esitetty aika–lämpötilavirumistestien ja oikealla aika–jännitystestien virumisjoustokäyrät d-materiaalille. Ensimmäisessä tapauksessa käytetty lämpötila on merkitty seuraavasti: musta = 75 °C, punainen = 60 °C ja sininen = 40 °C. Toisessa tapauksessa käytetty jännitys on merkitty seuraavasti: musta = 6.4 MPa, punainen = 5.0 MPa ja sininen = 3.3 MPa.



Kuva 4: Ylärivillä on aika–lämpötilasuperposition mukaiset virumisjoustokäyrien siirrot TRS- ja TRC-tapauksissa d-materiaalille. Alhaalla on vastaavasti siirretyt aika–jännityskäyrät. Vihreä käyrä kuvaa valittua referenssikäyrää.



Kuva 5: Vasemmalla on esitetty aika–lämpötilajohtokäyrät TRC-tapauksessa a-, d- ja e-materiaalierille (musta, punainen ja sininen käyrä). Oikealla on vastaavasti aika–jännitystapauksen johtokäyrät.

8 KIITOKSET

Kirjoittaja haluaa lausua kiitokset tutkimuksen rahoituksesta Tekniikan edistämissäätiölle, joka myönsi kokovuosiapurahan tutkimuksen tekemiseen sekä Oulun yliopistolle ja Tauno Tönning -säätiölle, jotka tukivat tutkimusta pienemmillä apurahoilla. Lisäksi lausutaan kiitokset Fibrocom Oy:lle, joka avusti tutkimuksen teossa valmistamalla käytetyt koekappaleet.

VIITTEET

[1] A.-J. Vuotikka. *Diplomityö*, Oulun yliopisto, 2003.

[2] H. Kolsky. *Stress Waves in Solids*, Oxford, Clarendon Press, 1953.

[3] A. Pramila. *Värähtelymekaniikka*, kirjassa: M. Airila et al. *Koneenosien suunnittelu 4: Erityisalueet*, Porvoo, WSOY, 1985.

[4] R. M. Christensen. *Theory of viscoelasticity: An Introduction*, New York, Academic Press, 1971.

[5] P. A. O'Connell and G. B. McKenna *Arrhenius-like temperature dependence of the segmental relaxation below Tg*, Journal of Chemical Physics, 110, (1999), 11054-11060.

[6] B. F. Oliveira and G. J. Creus. *An analytical-numerical framework for the study of ageing in fibre reinforced polymer composites*, Composite Structures, 65, (2004), 443-457.

[7] N. Heymans. *Constitutive equation for polymer viscoelasticity derived from hierarchical models in cases of failure of time-temperature superposition*, Signal Procecessing, 83, (2003), 2345-2357.

[8] Aklonis and MacKnight and Shen. *Introduction to Polymer Viscoelasticity*, New York, Wiley-Interscience, 1972.

[9] M. L. Williams and R. F. Landel and J. D. Ferry *The Temperature Dependence of Relaxation Mechanisms in Amorphous Polymers and Other Glass-forming Liquids*, Journal of the American Chemical Society, 77, (1955), 3701-3707.

[10] S. Jazouli and W. Luo and F. Bremand, T. Vu-Khanh. *Application of Time-Stress Equivalence to Nonlinear Creep of Polycarbonate*, Polymer Testing, 24, (2005), 463-467.

[11] W. Luo and T.-Q. Yang and Q. An. *Time-Temperature-Stress Equivalence and its Application to Nonlinear Viscoelastic Materials*, Acta Mechanica Solida Sinica, 14, (2001), 195-199.

[12] R. D. Bradshaw and L. C. Brinson. *Recovering Nonisothermal Physical Aging Shift Factors Via Continuous Test Data: Theory and Experimental Results*, Journal of Engineering Materials and Technology, 119, (1997), 233-241.

[13] R. D. Bradshaw and L. C. Brinson. *A Continuous Test Data Method to Determine a Reference Curve and Shift Rate for Isothermal Physical Aging*, Polymer Engineering and Science, 39, (1999), 211-235.

[14] A.-J. Vuotikka. *Lisensiaattityön käsikirjoitus*, Oulun yliopisto, 2006.

TAVARAVAUNUJONON PYSÄYTTÄMINEN KITKAN AVULLA

J.AALTO*, P.HASSINEN*, M.REIVINEN* & J.VALTONEN**
*Teknillinen korkeakoulu, Rakenteiden mekaniikan laboratorio
**Teknillinen korkeakoulu, Tietekniikan laboratorio
PL 2100, 02015 TKK

TIIVISTELMÄ

Artikkeli kuvaa kehitystyötä, jossa rakennetaan kitkaan perustuvaa pysäytinlaitetta poikkeustilanteessa liikkeeseen päässeen rautateillä liikkuvan vaunujonon pysäyttämiseksi hallitulla tavalla. Pysäytinlaitteen vertikaalinen puristava voima raidetta vasten syntyy vaunun massasta, josta pysäytinlaitteen aiheuttaman kitkailmiön avulla synnytetään vaunujonon liikettä jarruttava voima. Vertikaaliseen puristavaan voimaan verrattuna suuri kitkavoima saadaan aikaan kumiseoksella, jonka kitkakertoimelle on ominaista kertoimen pieneneminen puristavan voiman kasvaessa. Pysäytinlaite on mallinnettu kimmoisella alustalla olevana rakenteena. Kimmoinen alusta muodostuu kumikerroksesta, joka voi osittain myös irrota alustastaan. Kitkakertoimen riippuvuudelle kosketuspaineesta käytetään suoritettuihin kitkakokeisiin perustuvaa analyyttista lauseketta. Haasteena tehtävässä on myös laitteeseen kohdistuvien jarrutusvoimien määrittäminen, vaunun tai vaunujonon aiheuttamien dynaamisten herätteiden vuoksi.

1. KEHITYSTYÖN TAUSTA JA TAVOITTEET

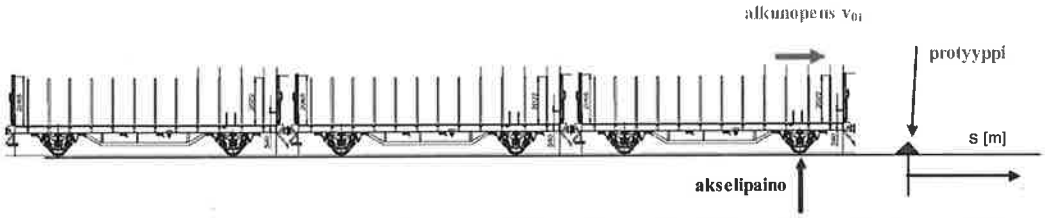
Liikennepaikan raiteelle pysäköity kalusto tai toisen junan kohtaamista odottava juna saattaa lähteä liikkeelle radassa olevan kaltevuuden, tuulen puuskan tai sysäyksen vaikutuksesta. Koska vaunujen pyörien vierimiskitka on vähäinen, kaltevalla radalla vaunujonon nopeus kasvaa. Tietyn nopeuden jälkeen vaunujonon liike-energia on niin suuri, että jonon pysäyttäminen on vaikeaa. Hallitsemattomasti liikkeelle lähtenyt kalusto saattaa ajautua muun liikenteen raiteelle aiheuttaen onnettomuusriskin. Ainoaksi vaihtoehdoksi saattaa jäädä vaunujonon suistaminen radalta, suurempien vahinkojen välttämiseksi. Myös suistuva kalusto voi ajautua väärälle raiteelle.

Ratahallintokeskuksen, VR-konsernin, Teknikum Oy:n ja Teknillisen korkeakoulun yhteistyönä on tutkittu pysäyttämislaitetta, jolla vaunujono saataisiin pysäytetyksi lyhyehköllä matkalla vähäisin kustannuksin ja vaurioin. Laite perustuu kiskon ympärille puristuvan kumiseoksen aiheuttamaan suureen kitkavoimaan. Pysäyttävä kitkavoima saadaan aikaan vaunujonon ensimmäisen akselin massan ja laitteen kumipinnan kitkakertoimen avulla. Käytännössä laitteen on suunniteltu toimivan siten, että vaunujonon siirryttyä sivuraiteelle pysäytinlaitteet nousevat kiskoille vaunujonon molemmin puolin automaattisesti.

Kehitystyön keskeisinä tavoitteina on

- varmistaa riittävän pysäytysvoiman syntyminen, jopa 3000 tonnia painavan vaunujonon pysäyttämiseksi kohtuullisella muutaman kymmenen metrin matkalla,
- varmistaa vaunujonon hallittu pysähtyminen myös siinä tilanteessa, jossa laitteeseen törmäävä vaunu on tyhjä ja kitkavoimaa aiheuttava akselipaino siten vähäinen,
- optimoida pysäytinlaitteen rakenne siten, että pysäyttäminen tapahtuu hallitulla ja turvallisella tavalla ja
- suunnitella pysäytinlaite mahdollisimman kevyeksi nostolaitteen toimintavarmuuden kannalta.

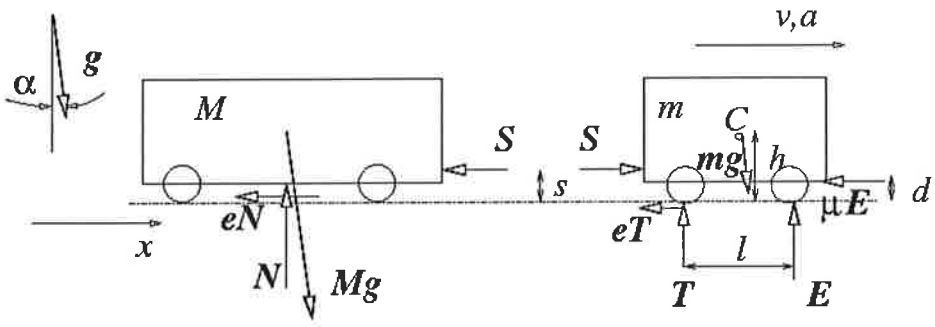
Kehitystyössä on tehty staattisiin ja dynaamisiin malleihin perustuvia laskelmia, pienoismallikokeita, kitkan mittauskokeita, pysäytinlaitteen rakenneanalyyseja ja täyden mittakaavan törmäyskokeita. Työ perustuu makroskooppisen tason insinöörimalleihin. Kehitystyö jatkuu edelleen. Laskennallisten analyysien ja koetulosten perusteella syntyneestä prototyypistä on tarkoitus kehittää sarjatuotantoon sopiva toimiva tuote. Artikkelissa esitetään laitteen teknisen toiminnan kannalta keskeisiä laskennallisia ja kokeellisia tuloksia.



Kuva 1. Vaunujonon eteen asennetulla pysäytinlaitteella pysäytetään poikkeustilanteessa liikkeelle lähtenyt vaunujono hallitulla tavalla.

2. PYSÄYTTÄMINEN KITKAN AVULLA

Vaunujonoa voidaan yksinkertaistaen kuvata kahdella vaunulla, joista ensimmäisen vaunu törmää pysäytinlaitteeseen ja sen ensimmäisen akselin paino tuottaa jarruttavan kitkavoiman. Toinen vaunu kuvaa muun vaunujonon massaa ja liike-energiaa. Näille kahdelle vaunulle piirretystä vapaakappalekuviosta (kuva 2) voidaan kirjoittaa seuraavat liikeyhtälöt.



Kuva 2. Jarruttavan vaunun ja sen takana olevan vaunujonon vapaakappalekuvio.

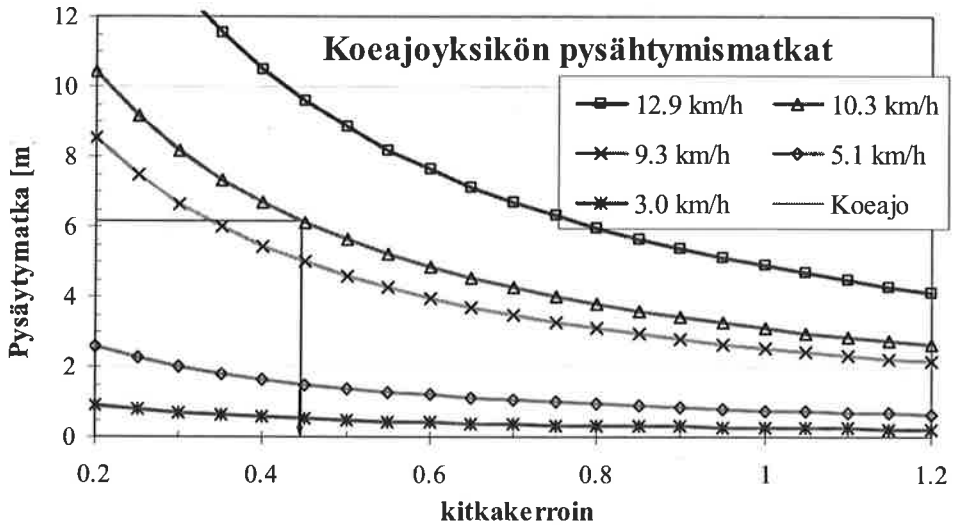
$$\begin{cases} -eN + Mg\alpha - S = Ma \\ S - eT - \mu E + mg\alpha = ma \\ (h-s)S - h(eT) - \frac{l}{2}T + \frac{l}{2}E - (h-d)\mu E = 0 \\ N - Mg = 0 \\ T + E - mg = 0 \end{cases} \qquad (1a,b,c,d,e)$$

Lausekkeessa μ pysäytinlaitteen kitkakerroin, α radan kaltevuus ja e pyörien vierintävastus. Kaltevuuden α oletetaan olevan pieni. Näistä yhtälöistä saadaan helposti lausekkeet jarruttavan vaunun akselikuormille T ja E, muiden vaunujen akselikuormalle N, jarruttavaan vaunuun kohdistuvalle vaakavoimalle S ja jarruttavan vaunun hidastuvuudelle a (kuva 2).

Jarrutusmatka arvioidaan vakiohidastuvuuteen perustuen törmäysnopeuden v perusteella.

$$v^2 + 2ax = 0 \qquad (2)$$

Yksinkertaisten staattiseen tasapainotilaan perustuvien lausekkeiden (1) ja (2) avulla voidaan laskea jarrutusmatka lähtönopeuden perusteella, kun pysäyttävän vaunun ja muun vaunujonon mittoja ja massoja koskevat tiedot ovat olemassa (kuva 3). Yksikertaisella mallilla saadaan käsitys tarvittavan pysäytysmatkan suuruusluokasta käytettävissä olevan kitkavoiman funktiona. Laskentamallia voidaan kehittää edelleen ottamalla huomioon vaunun puskinten ja pyörien jousto ja siitä aiheutuvat dynaamiset herätteet.



Kuva 3. Laskennallisesti määritetty vaunujonon jarrutusmatka alkunopeuden ja kitkakertoimen funktiona. Lähtötietoina on käytetty täyden mittakaavan kokeissa käytetyn, kahden veturin ja yhden kuormatun vaunun muodostaman yksikön mittoja ja massoja. Kuvaan on piirretty täyden mittakaavan kokeessa mitatun pysäytysmatkan perusteella määritetty kitkakerroin.

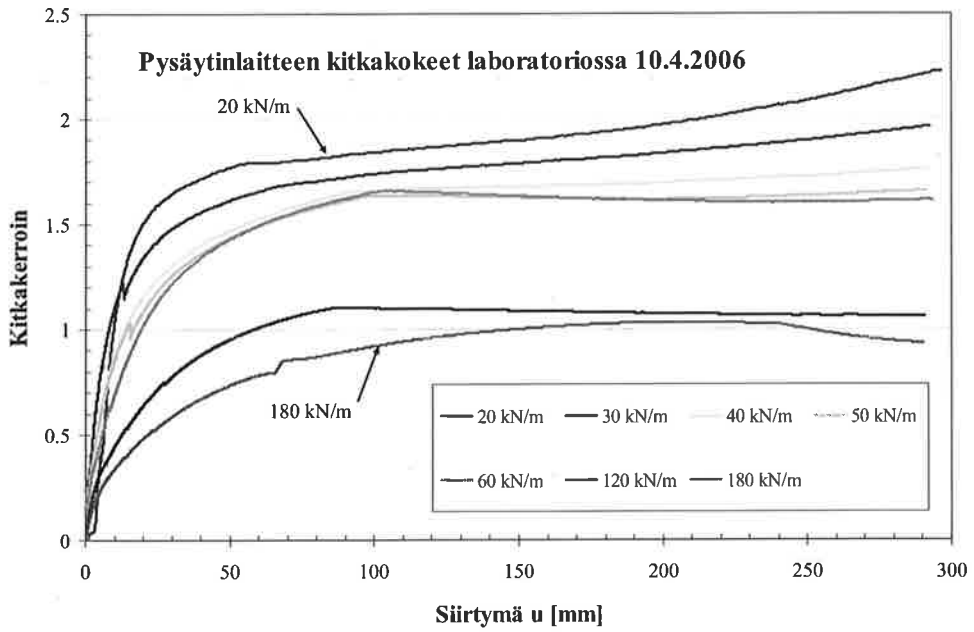
Täyden mittakaavan kokeissa mitatun törmäysnopeuden ja jarrutusmatkan avulla voidaan määritellä kokeessa vallinneen resultoivan kitkavoiman ja edelleen keskimääräisen kitkakertoimen

suuruus (kuva 3). Tärkein muuttuja tehtävässä on vaunujonon törmäysnopeus pysäytinlaitteeseen. Käytännössä samalla nopeudella jarrutusmatka ja siten kitkavoima ja kitkakerroin vaihtelevat mm. kiskon pinnan lämpötilan, kunnon, jatkosten ja puhtauden mukaan.

3. KOETULOKSIA

Olennainen parametri pysäytinlaitteen suunnittelussa on kiskon ja laitteen välinen kitka. Vulkanoidun kumikerroksen pysäytinlaitteeseen tuomaa kitkavoimaa on tutkittu kokeellisesti laboratorio-olosuhteissa. Kokeissa pysäytinlaitteen kitkaelementtejä on puristettu kiskon pintaa vasten erisuuruisilla vertikaalisen kuorman arvoilla F_2 ja kuormitettu kiskon suuntaisella kuormalla F_1. Kitkakerroin saadaan liukumismatkan funktiona siirtymän aikaansaamiseen tarvittavan kiskon suuntaisen voiman ja vertikaalisen voiman suhteen avulla $\mu = F_1 / F_2$ (kuva 4). Kokeet ovat osoittaneet kitkakertoimen pienenevän vertikaalisen kuorman kasvaessa. Kumikerroksen kitkakertoimen riippuvuus puristavasta kuormasta on niin voimakas, että se on otettava huomioon pysäytinlaitteen rakenneanalyysissa. Koetulosten perusteella on rakenneanalyysiä kirjoitettu lausekkeen (3) mukainen riippuvuus kitkakertoimen ja puristavan kuorman p välille. Vakioiden A ja B arvot määritetään pienimmän neliösumman avulla koetuloksista.

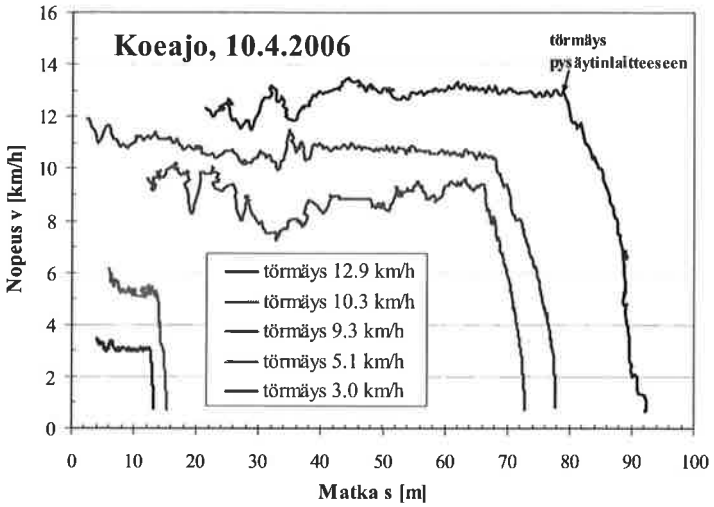
$$\mu(p) = \frac{1}{A + B\,p} \tag{3}$$



Kuva 4. Laboratoriossa mitattuja pysäytinlaitteen erään kitkaelementtisarjan kitkakertoimia vertikaalisen kuorman funktiona. Vertikaalinen kuorma kuvaa 500 mm pituisen koekappaleen ja kiskon välistä puristuskuormaa.

Koetuloskuvaajien nouseva alkuosa kuvaa kumikerroksen kimmoista muodonmuutosta. Liukumisvaiheen alkaminen näkyy kulmanmuutoksena, jonka jälkeen siirtymä kasvaa suunnilleen

vakiovoimalla (kuva 4). Pysäytinlaitteen kannalta liukumisvaiheessa vallitseva kitkakerroin on tärkeä. Laboratoriokokeissa siirtymänopeus oli koeteknisistä syistä alhainen. Todellisessa pysäytystilanteessa siirtymänopeus on 100 - 500-kertainen, mikä on eräs selittävä tekijä lämpötilan ohella täyden mittakaavan kokeissa ja laboratorio-olosuhteissa määritettyjen kitkakertoimien eroihin. Laboratoriokokeissa myös siirtymämatka oli pieni todelliseen tilanteeseen verrattuna (kuva 5).



Kuva 5. Kahden veturin ja yhden tavaravaunun törmäys pysäytinlaitetta vasten täyden mittakaavan kokeessa. Nopeuden muuttuminen matkan funktiona yksikön pysäytyksen aikana.

Vertaamalla laskennallisia ja kokeellisia tuloksia keskenään havaitaan, että täyden mittakaavan kokeen koetuloksen perusteella määritetty keskimääräinen kitkakerroin (kuva 3) on pienempi kuin laboratorio-oloissa määritetty kitkakerroin (kuva 4). Syinä tulokseen ovat mm. edellä mainittu siirtymänopeus ja lämpötila sekä maastossa kiskon pinnalla olevat kitkaa pienentävät kerrokset.

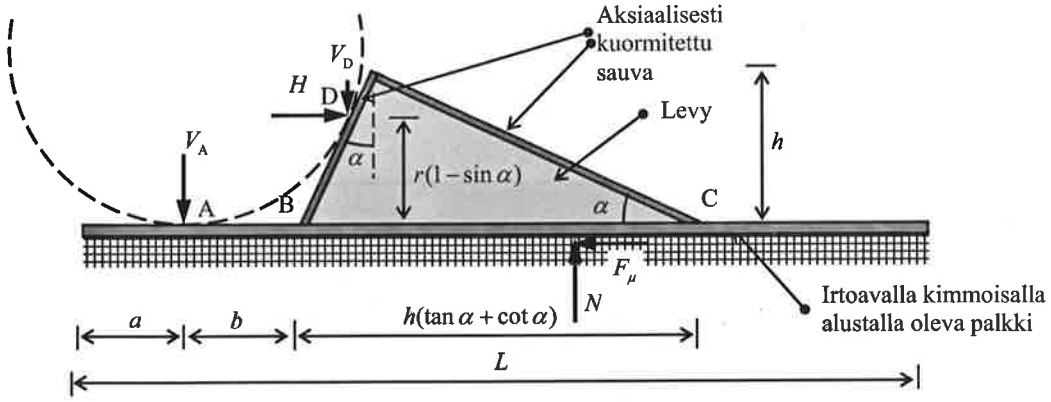
4. PYSÄYTINLAITTEEN RAKENNEANALYYSI

Pysäytinlaitteen kehitystyössä rajoitteina ovat olleet laitteen kestävyys suurimmalle siihen kohdistuvalle törmäyskuormalle, laitteen stabiilius törmäyksen ja pysäytyksen aikana, mahdollisimman lyhyt pysäytysmatka ja vaunun pyörän ylirullausriskin estäminen. Laitteen mitoitusta ja sen toiminnan arviointia varten on tunnettava laitteen kitkaelementtien ja kiskon välinen paine, joka vaihtelee laitteen pituuden matkalla siihen kohdistuvan paineen funktiona.

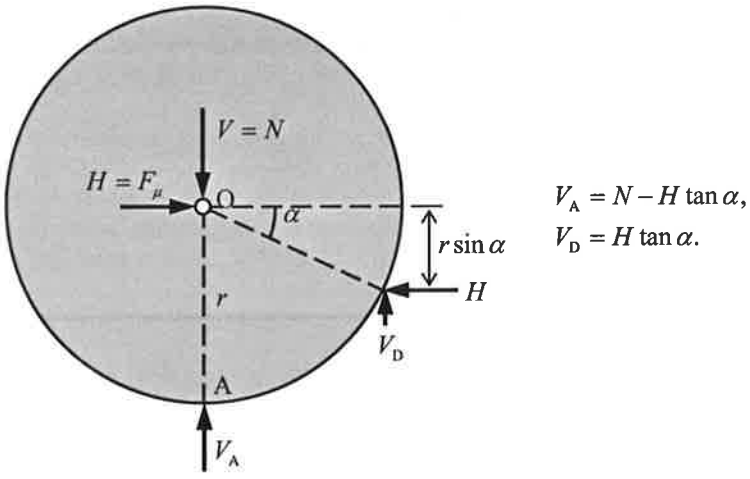
Pysäytyslaitteen rakenneanalyysin tavoitteena oli toisaalta arvioida laitteen eri osiin kohdistuvat rasitukset ja toisaalta määrittää laitteen keskimääräinen kitkakerroin, kun kitkakertoimen lausekkeen (3) mukainen riippuvuus kosketuspaineesta tunnetaan. Laitteen rakennemallina käytettiin kuvan 6 mukaista, irtoavalla kimmoisalla alustalla olevasta palkista, levystä ja kahdesta aksiaalisesti kuormitetusta sauvasta muodostuvaa rakennetta.

Alapalkin taivutusjäykkyys *EI* määritettiin palkin alkuosassa, kolmio-osan alueella ja palkin loppuosassa poikkileikkausmittoja vastaavasti erisuureksi. Alustaluku arvioitiin lähteeseen [2] perustuvalla likimenettelyllä.

Pysäytyslaite ja pyörä jarrukappaleineen otaksuttiin painottomiksi, jolloin pysty- ja vaakasuuntaisista tasapainoehdoista saadaan kiskosta laitteen alapintaan kohdistuvalle normaalivoimalle N ja vastaavalle kitkavoimalle F_μ tulokset $N = V$ ja $F_\mu = H$, missä V on puolet vaunun akselipainosta ja H on vaunusta pyörään kohdistuva vaakavoima. Pyörästä pysäytyslaitteeseen kohdistuva kuormitus muodostuu pyörän ja alapalkin kosketusvoimasta V_A sekä pyörän ja kolmio-osan kosketusvoimasta, jonka pystykomponentti on V_D ja vaakakomponentti on H. Näiden voimien suuruus voidaan arvioida pyörän ja jarruosan vapaakappalekuviosta kuvan 7 mukaisesti. Koska rakennemalli on otaksuttu painottomaksi, ei liikeyhtälöihin tule hitaustermejä ja analyysi voidaan suorittaa staattisena.



Kuva 6. Pysäytyslaitteen rakennemalli



Kuva 7. Pyörän ja jarrukappaleen vapaakappalekuvio

Koska laitteen keskimääräistä kitkakerrointa μ_{kesk} ei tunneta etukäteen, ei rakenteeseen kohdistuvaa vaakavoimaa $H = F_\mu = \mu_{kesk} N$ voida määrittää. Tämän vuoksi probleema joudutaan ratkaisemaan iteratiivisesti siten, että keskimääräiselle kitkakertoimelle otaksutaan sopiva alkuarvo μ^0_{kesk}, jolloin vaakavoima on $H^0 = \mu^0_{kesk} N$ ja rakenteen kuormitus on tunnettu. Ratkaistaan rakenne ensimmäinen kerran ja tuloksena saadaan kosketuspaineen jakauma $p^1(x)$. Tätä vastaava kitkakertoimen jakauma $\mu^1(x)$ saadaan nyt kaavalla (3). Ensimmäinen arvo kitkavoimalle saadaan näiden avulla kaavalla

$$F^1_\mu = \int_0^L \mu^1(x) p^1(x) dx, \tag{4}$$

Vaakavoiman uusi arvo on nyt $H^1 = F^1_\mu$ ja uusi iterointikierros voi alkaa. Iterointia jatketaan, kunnes kitkavoiman arvo ei enää muutu ja tasapainoehto $H = F_\mu$ on riittävällä tarkkuudella voimassa. Pysäytyslaitteen keskimääräisen kitkakertoimen arvo saadaan lopulta kaavalla $\mu_{kesk} = F_\mu / N$.



Kuva 6. Pysäytinlaitteen prototyyppi

5. YHTEENVETO

Poikkeustilanteessa liikkeeseen päässyt rautatiellä liikkuva kalusto on tarkoitus pysäyttää kohtuullisen lyhyellä matkalla pysäytinlaitteella, jonka toiminta perustuu laitteeseen ensimmäisenä törmäävän akselin massan aiheuttamaan vertikaaliseen kuormaan ja laitteen ja kiskon väliin puristuvan kumikerroksen suureen kitkakertoimeen. Kumin kitkakerroin pienenee puristavan voiman kasvaessa, mikä tasaa laitteeseen kohdistuvaa kitkavoimaa. Kitkakertoimen riippuvuudelle kosketuspaineesta käytetään suoritettujen kitkakokeiden tuloksiin sovitettua analyyttista lauseketta. Osa pysäytinlaitteen kosketuspinnasta saattaa jarrutustilanteessa irrota kiskosta. Tämä on otettu huomioon kuvaamalla kiskon ja laitteen välistä pintaa vetoakestämättömällä kerroksella. Käytetyt laskentamallit ovat tasapainoehtoihin ja kinemaattisiin ehtoihin perustuvia insinöörimalleja. Kumikerroksen vaikeasti kuvattavat monimutkaiset muodonmuutokset ja kumikerroksen ja kiskon välisen kontaktin kuvaaminen on toistaiseksi jätetty työn ulkopuolelle.

Rakennetun prototyypin toimintaa tutkitaan täyden mittakaavan kokeilla tavoitteena kehittää sarjatuotantoon sopiva pysäytinlaite. Suoritetuissa kokeissa pysäytinlaitteen prototyyppi on toiminut odotuksia vastaavalla tavalla ja laitteen kumikerros on kestänyt hyvin siihen pysäytystilanteessa kohdistuvat rasitukset. Kehitystyön kannalta tärkeä asia tällä hetkellä on käytännössä suurimpien tarvittavien pysäytysmatkojen selvittäminen. Jos matkat kasvavat liian suuriksi, ei laitteen hyödyntäminen ole käytännössä enää kannattavaa. Laitteen mekaaniseen toimintaan ja todelliseen pysäytysmatkaan liittyviä kysymyksiä selvitetään uusissa täyden mittakaavan kokeissa.

KIITOKSET

Teknillisen korkeakoulun Rakenteiden mekaniikan ja Tietekniikan laboratoriot osoittavat kiitokset Ratahallintokeskukselle, VR-konsernille ja Teknikum Oy:lle mielenkiintoisesta tutkimus- ja kehitystehtävästä ja mahdollisuudesta työn tulosten julkaisemiseen Suomen Mekaniikkapäivillä. Kiitokset rakentavista kommenteista Laura Järviselle, Matti Maijalalle, Taisto Tontille ja Antti Niemelle.

KIRJALLISUUSVIITTEET

1. Hofstetter, K., Eberhardsteiner, J. & Mang, H.A. 2006, Efficient treatment of rubber friction problems in industrial applications. Structural Engineering and Mehanics, 22(5), pp. 517-539.
2. P.-E. Austrell, M. Bellander, B. Stenberg, U. Carlsson, L. Kari and S. Persson 1998, Survey of the design methods and material characteristics in rubber engineering, Lund University, Division of Structural Mechanics, Sweden, REPORT TVSM-3036.

KONTINUUMIMEKANIIKKA OSANA GEOFYSIIKAN KENTTÄTEORIAN OPETUSTA

E. ELORANTA

Säteilyturvakeskus
PL 14, FI-00881 Helsinki
e-mail: esko.eloranta@stuk.fi

Teknillinen korkeakoulu, Rakennus- ja ympäristötekniikan osasto, Geoympäristötekniikka, laskennallinen geofysiikka
Helsingin yliopisto, Fysikaalisten tieteiden laitos, Geofysiikan osasto, matemaattinen geofysiikka

TIIVISTELMÄ

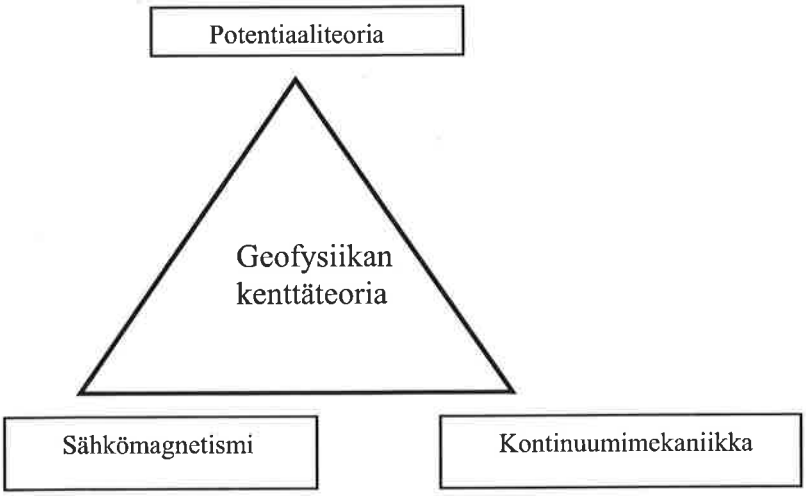
Kontinuumimekaniikka muodostaa yhden kolmesta keskeisestä geofysiikan kenttäteorian osa-alueesta. Kaksi muuta osa-aluetta ovat sähkömagnetismi ja potentiaaliteoria. Kontinuumimekaniikka jaetaan perinteisesti kiinteän aineen mekaniikkaan ja nesteiden mekaniikkaan. Kiinteän aineen mekaniikan osalta geofysiikan kontinuumimekaniikassa tarkastellaan seismisiä kimmoaaltoja ja kalliomekaniikkaa, joiden teoria pohjautuu pienten siirtymien teoriaan. Nestemekaniikkaan kuuluvana asiana käsitellään pohjaveden virtausdynamiikkaa. Myös lämmönsiirtyminen ja aineiden diffuusiokulkeutuminen kuuluvat geofysiikan kenttäteorian kontinuumimekaniikkaan. Kenttäteorian oppirakennelmassa yksi keskeinen periaate on erilaisten fysikaalisten kenttien välisten analogioiden hyödyntäminen. Yhtenä esimerkkinä tällaisesta tarkastellaan sähköistä virtausstaattista probleemia ja sen kanssa analogista kokoonpuristumattoman nesteen laminaarista virtausta sähköä ja vettä johtamattoman pallon tapauksessa. Kirjoituksessa tarkastellaan geofysiikan kenttäteorian sisältöön ja opetukseen liittyviä näkökohtia.

1. JOHDANTO

Geofysiikka on perusteiltaan matemaattinen luonnontiede, jonka pohjana ovat fysiikan ja mekaniikan kenttäteoriat. Kenttäteorioiden keskeinen sisältö muodostuu säilymisperiaatteista, joita ovat massan, varauksen, liikemäärän, energian ja liikemäärämomentin taselait. Nämä klassillisen fysiikan kulmakivet ilmenevät monin tavoin geofysiikassa, jossa niiden muodostamaa tieteenalaa ja sen soveltamista voidaan kutsua "geofysiikan kenttäteoriaksi". Geofysiikan kenttäteorian muodostavat kolme klassillisen fysiikan aihepiiriä, jotka ovat (1) jatkuvan aineen *sähkömagnetismi*, (2) *kontinuumimekaniikka* ja näihin monin tavoin liittyvä (3) *potentiaaliteoria* (kuva 1).

Tämän kirjoituksen tavoitteena on luoda katsaus geofysiikan kenttäteoriaan ja sen opettamiseen yliopistollisena oppiaineena. Geofysiikka on nimensä mukaisesti Maan ja lähiavaruuden fysiikkaa globaalissa eli maapallon laajuisessa ja lokaalissa eli paikallisessa mittakaavassa tutkiva tiede. Mainittujen mittakaavojen välissä on vielä ns. regionaalinen eli alueellinen mittakaava, kuten johonkin maantieteelliseen alueeseen tai sen osaan liittyvä mittakaava. Geofysiikka on paitsi puhdas luonnontiede, myös soveltava tiede, jonka tärkeimmät

sovelluskohteet ovat luonnonvarojen etsintä ja inventointi sekä maa- ja kallioperän eli ns. maankamaran rakennetutkimus.



Kuva 1. Geofysiikan kenttäteorian pääsisältö

Sovellettu geofysiikka tarkoitti terminä aiemmin - aina tieteenalan syntyhetkistä viime vuosisadan alkupuolelta jotakuinkin 1980-luvulle - lähinnä samaa kuin etsintägeofysiikka eli malminetsintään, pohjavedenetsintään ja öljynetsintään sovellettu geofysiikka. Sen jälkeen geofysiikan sovelluskohteiden kirjo on huomattavasti laajentunut. Mukaan ovat tulleet ympäristötutkimus sekä vaativat kalliotekniset rakennushankkeet. Ympäristötutkimukseen kuuluvat mm. ympäristön tilan monitorointi ja tämän myötä pohjaveteen ja sen liikkumiseen liittyvät erilaiset muutkin kuin etsintätekniset probleemit. Kallioteknisten sovellusten kannalta yksi viime vuosikymmenten huomattava ongelma-alue omassa maassamme liittyy käytetyn ydinpolttoaineen geologiseen loppusijoittamiseen. Tämän ns. ydinjätegeofysiikan tärkeiksi kysymyksiksi ovat muodostuneet mm. suunnittelun loppusijoitustilan pitkäaikaiskäyttäytyminen sekä ylipäätään loppusijoituksen pitkäaikaisturvallisuus. Ydinjätteen loppusijoituksessa tarkastellaan kymmenien ja jopa satojen tuhansien vuosien ajanjaksoja.

Nämä edellä mainitut uudet tutkimusalat ovat tuoneet sovelletun geofysiikan piiriin *jatkuvan aineen mekaniikan* eli *kontinuumimekaniikan* probleemit. Näitä ovat mm. kalliopohjaveden dynamiikka, lämmön- ja aineenkulkeutuminen huokoisessa ja rakoilleessa väliaineessa sekä kallioperän yleinen ns. kytketty termo-hydro-mekaniikka erilaisten kuormitusskenaarioiden valossa.

2. GEOFYSIIKAN KENTTÄTEORIA

Geofysiikan kenttäteoria tieteenalana ja yliopistollisena oppiaineena on ollut olemassa Suomessa 1960-luvun lopulta alkaen. Teknillisessä korkeakoulussa geofyysikkojen koulutus aloitettiin 1960-luvun alkupuolella. Jotta geofysiikan tutkimus ja opetus saivat vankat luonnontieteelliset perusteet, päätti Teknillinen korkeakoulu liittää geofyysikoiksi kouluttautuvien opetusohjelmaan pakollisen kenttäteorian kurssin. Kurssin painopiste oli alun alkaen ennen kaikkea sähkömagnetismissa ja potentiaaliteoriassa. Sittemmin, kuten jo johdannossa on kerrottu, aihepiiri on vaatinut myös kontinuumimekaniikan mukaanoton opetukseen. Tämä tapahtui 1990-luvun alkupuolella.

Huomionarvoista on, että kenttäteorian kurssi on räätälöity juuri geofyysikoille sopivaksi tarkoituksenmukaisin sisältöpainotuksin. On nimittäin osoittautunut, että yliopistojen opetusohjelmissa olevat kenttäteorian kurssit ovat aina jotakin sovellusaluetta painottavia tai sitten ne on suunnattu teoreettisen fysiikan opiskelijoille. Näin ollen kurssit sisältävät useimmiten paljon geofysiikan kannalta epätarkoituksenmukaista asiaa tai niistä puuttuu geofysiikan kannalta keskeisiä aihepiirejä. Siksi on ollut tarpeen luoda nimenomaan geofysiikan lähtökohtia ja tarpeita varten oma kenttäteorian opetus. Nämä opetuksen perinteet on luotu juuri Teknillisessä korkeakoulussa osana vuoriteollisuuden alan geofyysikkojen koulutusta. Opetusta annetaan myös Oulun yliopistossa ja nyttemmin vakiintuneena myös Helsingin yliopistossa.

Geofysiikan kenttäteoriasta on ilmestynyt julkaisu nimeltään "Geofysiikan kenttäteoria" (Eloranta, 2003). Se pohjautuu tämän kirjoituksen tekijän Teknillisessä korkeakoulussa vuodesta 1989 alkaen pitämiin kenttäteorian dosenttiluentoihin. Kirja on erityisesti teoriakirja. Sen oheiskirjaksi on parhaillaan työn alla esimerkkeihin ja sovelluksiin keskittyvä kirja.

"Geofysiikan kenttäteoria" -kirjan sisältö jakautuu kymmeneen lukuun. Ensimmäisessä luodaan yleiskatsaus kenttäteoriaan ja pyritään motivoimaan lukijaa tarttumaan haasteeseen. Luvussa hahmotellaan kenttäteorian yleinen struktuuri, johon kuuluvat säilymis- ja taseperiaatteisiin pohjautuvat *kenttäyhtälöt* ja väliaineeseen liittyvät *konstitutiiviset yhtälöt*.

Toisessa luvussa kerrataan kenttäteoriassa tarpeelliset matemaattiset apuneuvot ja työkalut. Näistä keskeisin on vektorianalyysi täydennettynä dyadi- ja tensorilaskennalla. Vektorianalyysin merkintätavoissa on noudatettu prof. Kalle Väisälän oppikirjaa (Väisälä, 1968). Matemaattisissa apuneuvoissa esitetään myös Diracin δ-funktio ja sen käyttö mm. pistemäisten singulariteettien hallitsemiseksi. Diracin δ-funktiota ei ole käytetty esim. Väisälän kirjassa, mutta moderneissa, erityisesti fysiikan sovelluksia painottavissa vektorianalyysin oppikirjoissa, se on jo vakioasiaa. Matemaattisissa apuneuvoissa esitetään lisäksi jonkin verran sarjaoppia ja erikoisfunktioita. Kaiken kaikkiaan luvun 2 on tarkoitus olla itseriittoinen esitys kirjan merkintätapojen ja käytetyn matematiikan selventämiseksi.

Kolmannessa luvussa aloitetaan varsinaisen kenttäteorian läpikäynti sähköstatiikasta. Approksimatiivisesta luonteestaan huolimatta sähköstatiikka muodostaa tärkeän "prototyypin" myös muiden ilmiöiden kenttäteorioille. Kirjassa noudatetaan ns. "varovaisen etenemisen periaatetta", jossa opiskelija asteittain perehtyy kenttäteoriaan ja sen käsitemaailmaan ilman, että tarvitsee vedota asioihin tai yhtälöihin, jotka eivät ole "läpinäkyvästi" perusteltavissa. Niinpä sähköstatiikan esityskin lähtee sähköstatiikan perusvuorovaikutuslaista eli Coulombin laista. Useissa edistyneille opiskelijoille ja tutkijoille tarkoitetuissa sähkömagnetismin kirjoissa (esim. Stratton, 1941) sähköstatiikan esitys aloitetaan ottamalla lähtökohdaksi sähkömagneettisia ilmiöitä yleisesti kuvaavat Maxwellin yhtälöt ja merkitsemällä niissä olevat aikaderivaattatermit nolliksi. Tällöin Maxwellin yhtälöt otetaan ikään kuin aksiomaattisena oppirakennelmana käyttöön. Koska useimmille opiskelijoille Maxwellin yhtälöt ovat vieraita eikä niiden taustalla olevaa fysiikkaa pysty suoraan näkemään niistä, valittu lähestymistapa on perusteiden ymmärtämisen tärkeyttä korostavassa opetuksessa mielekäs.

Sähköstatiikan jälkeen luvussa 4 esitetään sähköinen virtausstatiikka eli stationaaristen sähkövirtojen teoria kolmiulotteisessa avaruudessa pitäen lähtökohtana varauksen säilymislakia. Esityksessä johdetaan matemaattinen muoto varauksen säilymislaille yleisessä aikariippuvassa tilanteessa. Virtausstatiikkaan päästään merkitsemällä varauksen säilymislaissa aikaderivaattatermi nollaksi. Virtausstatiikassa voidaan tämän jälkeen hyödyntää lähes sellaisenaan sähköstatiikan esitystä, sillä mainittujen ilmiöiden kenttäyhtälöt ovat muodoltaan samat. Konstitutiivisena mallina on virrantiheyden ja sähkökentän voimakkuuden toisiinsa sitova Ohmin laki sekä isotrooppisen että anisotrooppisen sähkönjohtavuuden tapauksessa.

Luvussa 5 esitetään magnetostatiikan perusteet. Lähtökohtana on sähkövirtojen synnyttämän magneettikentän määrittäminen magneettisen voimavaikutuksen pohjalta käyttäen lähtökohtana Lorentzin voiman lauseketta. Umpinaisten virtasilmukoiden välisen ns. Ampèren voimalain avulla formuloidaan edelleen Biotin ja Savartin laki, jonka avulla voidaan määrittää tunnetun virtajakauman synnyttämä magneettivuon tiheyskenttä. Erikseen tarkastellaan magnetoituneen

aineen synnyttämää magneettikenttää, mikä on hyvin keskeinen aihepiiri geofysiikan anomalioitten laskennassa. Myös magnetostatiikan esityksessä päästään vahvaan analogiaan sähköstatiikan kanssa.

Luku 6 on suppea esitys yleisestä sähködynamiikasta. Sen tärkeimmät asiat ovat sähkömagneettinen induktio, siirrosvirta sekä sähkömagneettiset aallot ja niiden heijastuminen ja taittuminen. Luvussa esitetään lopulta yleiset Maxwellin yhtälöt perustellen ne. Maxwellin yhtälöt esitetään myös aikaharmonisessa muodossa.

Luku 7 esittää painovoiman teorian yhtenä potentiaaliteorian sovelluksena (Kellogg, 1954). Potentiaaliteoriaan on perehdytty jo sähköstatiikasta alkaen. Niinpä painovoiman kenttäteoria voidaan pohjata paljolti analogiaan sähköstatiikan kanssa.

Luvusta 8 alkaen siirrytään kontinuumimekaniikkaan. Luku 8 on johdatusta yleiseen kontinuumimekaniikkaan, jossa tärkeällä sijalla on kontinuumin kinematiikan kuvaaminen Lagrangen ja Eulerin esitystavoilla (Mase, 1970; Salonen, 1987). Lisäksi esitetään kontinuumimekaniikan aksioomat ja niiden pohjalle rakentuvat yleiset kenttäyhtälöt. Lämmönsiirtymisilmiöt kuuluvat oleellisena osana kontinuumimekaniikkaan. Kirjassa noudatetaan kontinuumimekaniikan jakoa kiinteän aineen mekaniikkaan ja nesteiden mekaniikkaan. Kontinuumimekaniikan yleinen aksiomatiikka nojautuu paljolti Malvernin (1969) esitykseen.

Luvussa 9 tarkastellaan kiinteän aineen mekaniikkaa pienten muodonmuutosten teoriaan nojautuen. Keskeisiä geofysikaalisia teorioita ovat seismisten kimmoaaltojen teoria sekä kalliomekaniikan kenttäteoria. Luvussa on vaikutteita Foxin (1967) mekaniikan oppikirjasta. Seismisten kimmoaaltojen teoriaa verrataan sähkömagneettisten aaltojen teoriaan. Kalliomekaniikan perinteinen teoria pohjautuu statiikkaan (Jaeger and Cook, 1976). Kalliomekaniikan moderneja epästationaarisia probleemeja, kuten raon kasvua ja kallion murtumismekaniikkaa, ei käsitellä tarkemmin.

Luku 10 keskittyy nesteiden mekaniikkaan. Sen tärkeät geofysikaaliset sovelluskohteet kiinteän maan geofysiikassa ovat pohjaveden virtaus ja aineiden kulkeutuminen huokoisessa väliaineessa (Bear, 1988). Luvussa esitetään myös newtonilaisen nesteen Navier-Stokesin yhtälöt. Näiden sovelluksena johdetaan geohydrologiassa paljon siteerattu ns. rakovirtauksen kuutiolaki. Rakovirtauksessa tarkastellaan kahden yhdensuuntaisen, sileän tasopinnan välissä tapahtuvaa kokoonpuristumattoman nesteen (veden) laminaarista ja stationaarista virtausta (Landau and Lifshitz, 1989).

Advektiivinen lämmönsiirtyminen esitetään luontevimmin nesteiden mekaniikan yhteydessä. Viimeisenä aiheena tarkastellaan diffuusiota, joka on tärkeä alue mm. saasteiden leviämistarkasteluissa sekä ydinjätteen loppusijoitustilan toiminta-analyyseissä.

Geofysiikan kenttäteoriassa yhtenä kantavana periaatteena ovat erilaisten kenttien väliset analogiat eli duaalisuus.

3. GEOFYSIIKAN KENTTÄTEORIAN OPETUKSEN HAASTEISTA

Kuten jo aiemmin esitettiin, Teknillisessä korkeakoulussa on annettu geofysiikan kenttäteorian opetusta jo lähes neljän vuosikymmenen ajan. Sittemmin opetusta ruvettiin antamaan myös Oulun yliopistossa siellä käynnistyneen sovelletun geofysiikan opetuksen myötä 1970-luvulla. Helsingin yliopistossa geofysiikan kenttäteoria on kuulunut erillisenä oppiaineena kiinteän maan geofysiikan opetusohjelmaan vasta vuodesta 2004 alkaen. Sitä ennen tarjolla olivat ainoastaan teoreettisille fyysikoille suunnatut kenttäteorian kurssit. Tämän kirjoituksen tekijä vastaa tällä hetkellä sekä Teknillisen korkeakoulun että Helsingin yliopiston tarjoamasta geofysiikan kenttäteorian opetuksesta.

Kenttäteoria on opiskelijalle vaativa oppiaine. Se edellyttää sitoutumista ja useimmiten huomattavan paljon enemmän työtä kuin moni muu geofysiikan oppiaine. Yhtenä syynä on tietenkin aiheen matemaattinen luonne, jota saatetaan vierastaa. Opiskelija saattaa helposti kadottaa mielenkiinnon aiheeseen, jos sitä ei jatkuvasti sidota geofysiikan menetelmiin ja niiden teoriaan.

Sähköstatiikka muodostaa monella tapaa "prototyypin" kaikelle muulle kenttäteorialle. Siksi sitä käsitellään perusteellisemmin kuin muita vähintäänkin yhtä tärkeitä kenttäteorioita. Näiden osalta vedotaan paljolti kenttien väliseen analogiaan. Esimerkiksi painovoimakentän teoriassa saavutetaan lähes täydellinen analogia sähköstatiikan kanssa, vaikka niiden kuvaamat fysikaaliset ilmiömaailmat ovatkin erilaiset. Myös kontinuumimekaniikan ilmiömaailman ja sähköstatiikan välillä on hyödynnettävissä olevaa analogiaa, kuten seuraavassa luvussa käsiteltävä esimerkki valaisee.

Geofysiikan kenttäteorian opetukselle yhden haasteen muodostaa myös opiskelijoiden tuleminen eri pääaineiden piiristä. On selvää, että fysiikan ja teoreettisen fysiikan parista tulevat opiskelijat eivät koe geofysiikan kenttäteoriaa mitenkään vieraaksi. Heiltä saatu palaute on useimmiten sen suuntaista, että kurssi selvensi yleisen kenttäteorian ilmenemistä ja soveltamista geofysiikassa, mikä on ollutkin kurssin tarkoitus.

Geologisten tieteiden, siis muiden kuin fysikaalisten tieteiden, parista tulevat opiskelijat sen sijaan saattavat pitää kenttäteoriaa ainakin aluksi liian teoreettisena ja ylitsepääsemättömän vaikeana oppiaineena. Se saattaa olla heidän kohdallaan ensimmäinen kurssi, jossa pitäisi osata hyödyntää matematiikan peruskurssien moniulotteista differentiaali- ja integraalilaskentaa. Myöskään fysiikan yleiset perusperiaatteet eivät kaikille opiskelijoille ole mitenkään selviä. Koska opetuksen tavoitteena on tarjota nimenomaan geologisten tieteiden opiskelijoita hyödyttävää kenttäteorian tietämystä, tulee heidän kannustamiseensa kiinnittää erityistä huomiota. On tärkeää, että opettaja jatkuvasti korreloi opetettavaa asiaa heidän mahdollisesti jo tuntemiinsa asiayhteyksiin.

Geofysiikan kenttäteoria ei ole elämälle vierasta. Opiskelijoille tulee tuottaa myös oppimiselämyksiä. Useinhan on niin, että matemaattisesti haastaviin kysymyksiin liittyy hyvin voimakkaita oppimiselämyksiä, jotka puolestaan saattavat ohjata tulevaa opiskelua ja jopa myöhempiä tutkimusintressejä. Tällaisten oppimiselämysten tuottaminen voi siten olla hyvin tärkeää – ja niin, ettei opettajalla ole ennakkoasenteita opiskelijoiden taidoista ja kyvyistä. Toki on niin, että monilla ei riitä motivaatiota selvitä ensimmäisten ongelmien yli ja ote oppiaineeseen pääsee siten herpaantumaan. Tällaisia opiskelijoita, jotka tietoisen valinnan kautta luopuvat kurssista, on valitettavasti aina joukossa. Jos opiskelija ei vain yksinkertaisesti saa otetta opiskelusta, hänen kannaltaan on useimmiten viisainta luopua kurssin suorittamisesta, varsinkin, jos kurssi ei kuulu hänen pakolliseen ohjelmaansa.

On myös tärkeää, että kurssilla on alusta alkaen selkeät tavoitteet ja vaatimukset. Tällöin opiskelija tietää, mihin on sitoutumassa ja mitä kurssin suorittaminen vaatii ja mitä valmiuksia se tuottaa. Kurssin suorittamistavat ovat aina yksi keskeinen kysymys kurssin alussa. Viime vuosina on Teknillisessä korkeakoulussa panostettu opetuksen laadulliseen kehittämiseen. Yhtenä osana tätä on kurssin erilaisten suoritustapojen ja –vaihtoehtojen käyttö. Perinteisen tentin tilalle tulisi tarjota myös muita suoritustapoja. Niinpä geofysiikan kenttäteorian kurssin suorittaminen Teknillisessä korkeakoulussa on ollut mahdollista ensimmäistä kertaa keväällä 2006 myös ns. oppimispäiväkirjatyöskentelyn avulla.

Oppimispäiväkirjassa opiskelija kirjoittaa kultakin luennolta 1-2-sivuisen esseetyyppisen selvityksen luennon aiheesta erityisesti oman oppimisensa kannalta. Opiskelijaa kehotetaankin esittämään oppimispäiväkirjassa, mitkä asiat tuottivat vaikeuksia ja mitkä olivat helppoja omaksua. Oppimispäiväkirja annetaan opettajalle aina seuraavan luentokerran alussa. Tällöin opettaja voi jo pikasilmäyksellä saada käsityksen edellisen kerran vaikeaksi koetuista asioista, jotka on kenties syytä kerrata. Kertaus kun tunnetusti on opintojen äiti. Oppimispäiväkirjan lisäksi opiskelijan tulee laskea myös ennalta sovitut laskutehtävät. Laskutehtävien joukossa on aina muutama perustehtävä sekä jokin hieman vaativampi, mutta kuitenkin kurssimateriaalin pohjalta ratkaistavissa oleva tehtävä. Ratkaisujen ei välttämättä tarvitse olla virheettömästi suoritettuja. Tärkeää on jo rehellinen yrittäminen.

Opettajan kannalta kurssin suorittaminen oppimispäiväkirjatyöskentelyllä on työläämpää kuin tentillä. Tentissä annetaan ratkaistavaksi 5-6 tehtävää, joiden arvosteluun pohjautuu kurssista saatava arvosana. Sen sijaan oppimispäiväkirjatyöskentelyssä opettajan tulee perehtyä ja arvioida

kunkin luentokerran oppimispäiväkirjamerkinnät ja laskutehtävät. Tämä on huomattavan paljon aikaa vaativaa noin kymmenen opiskelijan kurssilla.

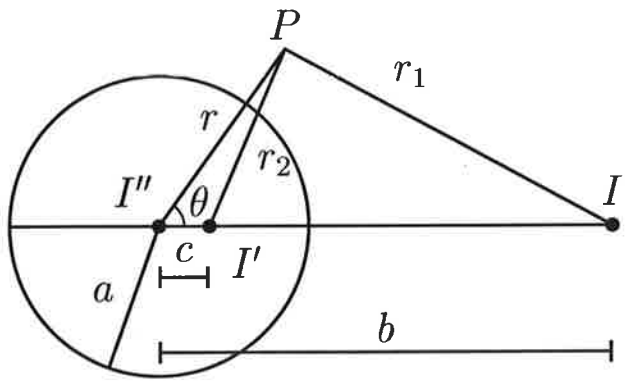
Oppimispäiväkirjamenetelmä soveltuu huonosti tai ei lainkaan massaopetukseen. Sen sijaan syventävässä laudatur-tasoisessa opetuksessa muutaman opiskelijan kurssissa se muodostaa varteenotettavan vaihtoehdon tentille. Kaikki opiskelijat eivät syystä tai toisesta halua käyttää oppimispäiväkirjamenetelmää kurssin suorittamiseen, vaan haluavat perinteistä tenttiä. Myös tähän tarjotaan mahdollisuus. Oppimispäiväkirjatyöskentelyn valinneet opiskelijat ovat kuitenkin varsin hyvin sitoutuneet siihen ja monen mielestä se on tenttiä "inhimillisempi" tapa kurssin suorittamiseksi. Oppimispäiväkirja on ennen kaikkea arvioinnin väline. Omat ensikokemukseni sen käytöstä ovat positiiviset.

4. ESIMERKKI ANALOGIAN KÄYTÖSTÄ KENTTÄTEORIAN OPETUKSESSA

Seuraavan esimerkin avulla pyrin valottamaan eri fysiikan alojen kenttäteorioiden samankaltaisuutta. Kysymyksessä on varsin klassinen, analyyttisesti ratkaistavissa oleva ongelma, jota käytetään paljon opetuksessa. Tehtävällä on myös käytännön relevanssia. Probleemi liittyy sähköiseen virtausstatiikkaan. Sen ratkaisussa tukeudutaan kuitenkin erääseen kontinuumimekaaniseen, tarkemmin sanottuna kokoonpuristumattoman nesteen laminaariseen, virtausprobleemiin. Analogioiden hyödyntäminen geofysiikan kenttäteorian opetuksessa on keskeistä jo senkin takia, että oppiaineelle on ominaista usean fysikaalisen osa-alueen ilmiön tarkastelu.

Geofysiikan ns. galvaanisten menetelmien avulla pyritään selvittämään maankamaran sähkönjohtavuusrakennetta syöttämällä maahan tasavirtaa ja mittaamalla virran aikaansaamia potentiaalieroja. Maankamara saatetaan galvaanisissa menetelmissä osaksi suljettua virtapiiriä. Yleinen käytäntö on mallintaa maankamarassa olevia epähomogeenisuuksia säännöllisen muotoisilla ja aineominaisuuksiltaan homogeenisilla kappaleilla. Pallomainen epähomogeenisuus on usein tarkoituksenmukainen varsinkin opetustarkoituksia, mutta myös monia käytännön ongelmia varten ns. ensimmäisenä approksimaationa. Pallosymmetristen probleemien suurena etuna on, että niille voidaan useimmiten esittää tarkka analyyttinen ratkaisu. Ratkaisun avulla on puolestaan varsin helppo oppia ymmärtämään kenttiin ja niiden lähteisiin liittyviä erityispiirteitä.

Monissa sähkömagnetiikan perusoppikirjoissa (esim. Reitz et al., 1993; Vanderlinde, 1993) esitetään ratkaisu tyhjiössä olevalle äärettömän hyvin johtavalle ja maadoitetulle pallolle (säde a [m]) pistevarauksen kentässä. Äärettömän hyvin johtavan pallon tapaus voidaan samastaa täysin vastaavan galvaanisen probleemin kanssa, kun varauksen tilalle asetetaan virtalähde ja tyhjiön permittiivisyys korvataan palloa ympäröivän aineen sähkönjohtavuudella σ [S/m]. Pallon ulkopuolella, etäisyydellä b [m] pallon keskipisteestä, on yksi erillinen "isoloitu" virtalähde, jonka voimakkuus (antoisuus) on I [A] (kuva 2).



Kuva 2. Sähköisesti äärettömän hyvin johtava pallo pistemäisen virtalähteen, I, kentässä.

Probleemin ratkaisu voidaan esittää sopivien kuvalähteiden avulla korvaamalla pallopinta tietyllä kuvalähteellä (I'), jonka sijainti ja voimakkuus määräytyvät probleemin geometrisista parametreista a ja b sekä ulkopuolisen virran voimakkuudesta. Kuvalähteen sijainti on etäisyydellä c pallon keskipisteestä:

$$c = \frac{a^2}{b}. \tag{1}$$

Kuvavirtalähteen voimakkuus on

$$I' = -\frac{a}{b} I. \tag{2}$$

Pallon keskipisteeseen voidaan asettaa lisälähde (I''), jolla voidaan säädellä pallon potentiaalin arvoa. Tämän ansiosta pallon ei tarvitse olla enää maadoitettu. Äärettömän hyvin johtava pallo muodostaa tasapotentiaalialueen. Pallon potentiaalin arvon ϕ_0 voi määrittää resiprookkisuusperiaatteesta saatavilla yhtälöillä

$$\phi_0 = \frac{I''}{4\pi\sigma}\frac{1}{a}; \quad I'' = \frac{a}{b} I. \tag{3}$$

Potentiaali pallon ulkopuolella mielivaltaisessa laskentapisteessä P voidaan laskea superpositioperiaatteen avulla saatavasta lausekkeesta

$$\begin{aligned} \phi(\mathbf{r}) = \phi(r,\theta,\varphi) &= \frac{1}{4\pi\sigma}\left[\frac{I}{r_1} + \frac{I'}{r_2} + \frac{I''}{r}\right] \\ &= \frac{1}{4\pi\sigma}\left[\frac{I}{\sqrt{r^2 + b^2 - 2rb\cos\theta}} + \frac{I'}{\sqrt{r^2 + c^2 - 2rc\cos\theta}} + \frac{I''}{r}\right]. \end{aligned} \tag{4}$$

Lauseke on esitetty pallokoordinaatiston muuttujien avulla, kun pallon keskipiste sijoitetaan koordinaatiston origoon. Useampien ulkoisten virtalähteiden vaikutukset voidaan määrittää myös superpositioperiaatteella.

Esitetty ratkaisu tunnetaan ns. Kelvinin inversiona, koska William Thomson (myöhemmin tunnettu lordi Kelvininä (1824-1907)) esitti tämän ratkaisun vuonna 1845 (Lindell and Hänninen, 2000). Nimitys inversio tulee yhtälön (1) mukaisesta "käänteisestä" relaatiosta $(c/a) = (b/a)^{-1}$. Ratkaisua on paljon käytetty ja hyödynnetty geofysiikassa ja sen opetuksessa jo vuosikymmenien ajan, joten mitään tieteellisesti uutta siihen ei sisälly. Ratkaisussa on kuitenkin mukana aimo annos klassisen fysiikan esteettisiä piirteitä.

Tämän probleemin varsin helposti mieleen tuleva jatkoprobleemi koskee äärettömän resistiivistä palloa pistemäisen virtalähteen kentässä. Tällaisen probleemin tarkasteluun liittyy samalla monia mielenkiintoisia tieteenhistoriallisia aspekteja. Itse asiassa lordi Kelvin yritti ratkaista myös tällaista probleemia kuvalähteiden avulla siinä kuitenkaan onnistumatta.

Tarkastelemme seuraavaksi siis sähkönjohtavuudeltaan äärettömän resistiivistä palloa, joka sijaitsee muutoin homogeenisessa kokoavaruudessa, jonka sähkönjohtavuus on σ [S/m]. Ongelmana on määrittää jälleen virran aiheuttama sähköinen potentiaali ϕ [V] pallon ulkopuolella.

Potentiaali noudattaa tunnetusti kyseisessä tilanteessa Laplacen yhtälöä. Pallon pinnalla ($r=a$) täytyy olla voimassa homogeeninen Neumannin ehto

$$\frac{\partial \phi}{\partial r} = 0. \tag{5}$$

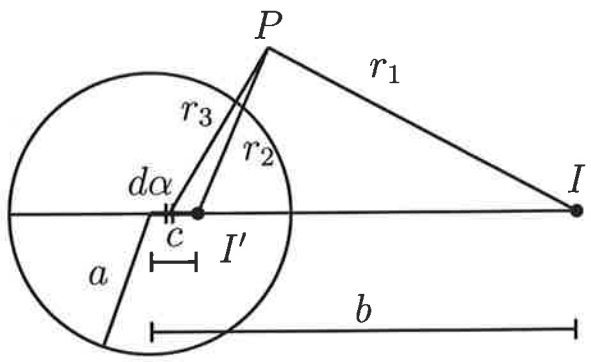
Tämä ehto takaa, että sähkövirtaa ei tunkeudu palloon, koska pallo on äärettömän resistiivinen. Lisäksi potentiaalin on vaimennuttava äärettömyyttä lähestyttäessä kuten $1/r$. Tuntemalla potentiaali saadaan sähkökentän voimakkuus siitä negatiivisen gradientin avulla. Ohmin lailla määritetään edelleen virrantiheyskenttä. Useampien virtalähteiden vaikutus voidaan saada sitten superpositioperiaatteella, kuten edellä äärettömän hyvin johtavan pallon tapauksessa.

Tämän probleemin ratkaiseminen onnistuu myös kuvalähdeperiaatteella, vaikka kuvalähteen löytäminen ei kuitenkaan ole mitenkään helppo tehtävä. Tässä yhteydessä astuu kuvaan mukaan tiede- ja oppiainerajat ylittävä tutkimus. Kirjallisuudesta löytyy nimittäin n. sata vuotta sitten esitetty ratkaisu analogiselle hydrodynaamiselle probleemille. Siinä vettäjohtamaton pallo on kokoonpuristumattoman nesteen laminaarisessa virtauskentässä. Nesteen lähde on pistemäinen ja se sijaitsee tietyllä etäisyydellä pallon keskipisteestä pallon ulkopuolella. Toisin sanoen pallo ei ole alun perinkään homogeenisessa virtauskentässä. Tehtävänä on määrittää virtauskenttä pallon lähialueella nopeuspotentiaalin avulla. Tiettyjä matemaattisia muunnoskaavoja käyttäen on onnistuttu osittain vahvan intuition ajamana päättelemään, että pallon sisälle tarvittava kuvalähde muodostuu kahdesta osasta. Toinen on yksinkertainen pistelähde, joka sijaitsee samalla etäisyydellä c (yhtälö (1)) pallon keskipisteestä kuin edellä äärettömän hyvin johtavan pallon tapauksessa. Sen voimakkuus on

$$I' = +\frac{a}{b} I. \tag{6}$$

Toinen kuvalähde on homogeenisesti jakautunut viivalähde (Sneddon, 1957, s. 166-167) pallon keskipisteen ja c-janan toisen päätepisteen välillä (kuva 3)

$$i'' = -\frac{I}{a}. \tag{7}$$



Kuva 3. Äärettömän resistiivinen pallo pistemäisen virtalähteen kentässä.

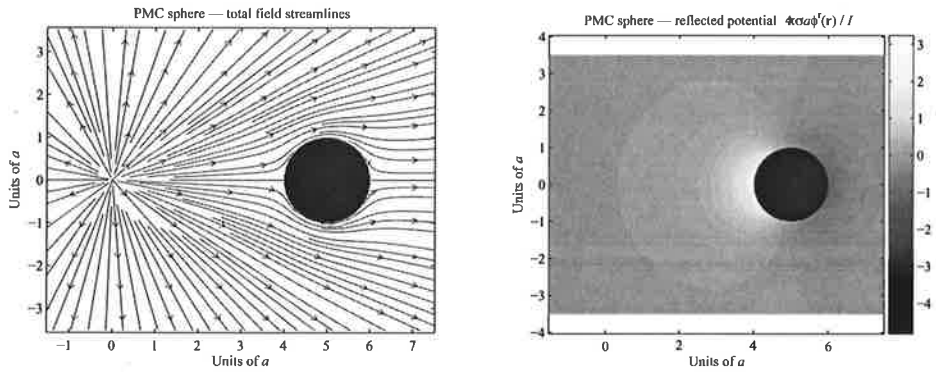
Näillä kuvalähteillä saadaan toteutumaan homogeeninen Neumannin ehto (5), kuten mekaanisella laskulla on tarkastettavissa. Potentiaali pallon ulkopuolella on näiden kaikkien lähteiden summa

$$\phi(\mathbf{r}) = \phi(r,\theta,\varphi) = \frac{1}{4\pi\sigma}\left[\frac{I}{r_1} + \frac{I'}{r_2} - \int_0^{a^2/b} \frac{I}{a}\frac{1}{r_3} d\alpha\right], \tag{8}$$

missä α on integrointimuuttuja ja

$$r_3 = \sqrt{r^2 + \alpha^2 - 2r\alpha\cos\theta}. \tag{9}$$

Tässä tapauksessa analogian käyttö osoittautui voimalliseksi keinoksi. Tämäkään ratkaisu ei tietenkään ole tieteellisesti uusi, mutta sen soveltaminen geofysiikassa on sitä. Siksi ratkaisuun tunnetaan edelleen myös käytännön mielenkiintoa. Kuva 4 näyttää virtaviivat ja sekundaaripotentiaalin eristepallon ympäristössä, kun virtalähde on viiden pallosäteen etäisyydellä pallon vasemmalla puolella. Tämän kuvan avulla voidaan selventää mm. pallon pinnalla olevien sekundaarilähteiden luonnetta. Sekundaaripotentiaali saadaan vähentämällä kokonaispotentiaalista ulkoisen virtalähteen, I, potentiaali eli ns. primaaripotentiaali.



Kuva 4. Eristepallo pistelähteen kentässä. Vasemmalla ovat virtaviivat, oikealla sekundaarinen potentiaalikenttä. Pistelähde sijaitsee viiden pallosäteen päässä pallon keskipisteestä pallon vasemmalla puolella.

Kuvasta näemme mm., että eristepallon tapauksessa virtalähteen puoleiselle pallon sivustalle muodostuu positiivinen sekundaarilähdejakauma. Vastakkaiselle puolelle tulee negatiivinen sekundaarilähdejakauma. Näiden ansiosta virtaviivat väistävät pallon. Kentän käyttäytyminen pallon ympäristössä tulee siten fysikaalisesti ymmärrettäväksi lähteittensä kautta.

Käsitelty esimerkki on yksi monista, jossa eri fysikaalisten kenttien välistä analogiaa hyödynnetään. Tällaiset analyyttisesti ratkaistavat perustapaukset ovat tärkeitä kenttien käyttäytymistä tutkittaessa.

5. JOHTOPÄÄTÖKSIÄ JA POHDINTAA

Geofysiikan kenttäteorian sisältö kattaa myös kontinuumimekaniikan keskeisten periaatteiden esittelyn. Kontinuumimekaniikka esiintyy kiinteän maan geofysiikan sovelluksissa ennen kaikkea

seismisissä menetelmissä sekä kallion mekaanisen käyttäytymisen tutkimisessa. Myös kalliopohjaveden dynamiikka muodostaa yhden keskeisen geofysiikan kontinuumimekaanisen probleemin. Rakoilleen kallion kytketyt termiset, mekaaniset ja hydrauliset prosessit ovat tärkeällä sijalla, kun pyritään ymmärtämään esimerkiksi lämpöä tuottavan käytetyn ydinpolttoaineen kallioperään sijoittamisen vaikutuksia. Näillä tiedoilla on tärkeä sija pyrittäessä ennustamaan ja ymmärtämään loppusijoitustilan pitkäaikaiskäyttäytymistä.

Geofysiikan kenttäteorian opetuksessa korostuvat eri fysiikan alojen yhteiset, analogiset piirteet. Kaiken perustana on itse asiassa vankka matemaattisten menetelmien, eritoten vektorianalyysin, hallinta. Erilaiset klassisten probleemien ratkaisut ovat edelleen käyttökelpoisia ja tärkeitä ainakin opetusmielessä. Vaikka numeeriset menetelmät ovat monilta osin syrjäyttäneet analyyttisiin ratkaisuihin perustuvat tarkastelut, analyyttisillä ratkaisuilla on edelleen merkitystä ennen kaikkea ymmärryksen lisääjinä. Opiskelijan on syytä ymmärtää, mihin ratkaistavat yhtälöt ja matemaattiset mallit perustuvat. Tässä kenttäteorioilla on edelleen keskeinen asema.

Nykysuuntaus varsinkin teknillisillä aloilla näyttää olevan matematiikan opetuksen vähentäminen. Pakollisten kurssien osuutta on vähennetty. Tästä seuraa, että vähänkin vaativamman analyysin soveltaminen on monille ylivoimaista. Ilmeisesti moderni tietotekniikka on jotenkin hämärtänyt asioitten todellista luonnetta. Kaiken täytyisi olla helppoa ja napin painalluksen päässä. Lukiomatematiikan opetusta sivusta seuranneena oletan, että syy asiantilaan löytyy ainakin osittain lukiovaiheesta. Lukiomatematiikan kursseihin on sisällytetty valtaisia määrä erilaisia asiakokonaisuuksia, jotka useimmiten käydään läpi vain "pintaraapaisuna". Eikö sittenkin olisi parempi keskittyä pariin keskeiseen aihepiiriin ja saada niistä hyvä pohja korkeakoulu- ja yliopisto-opintoja varten? Yksi välttämätön aihepiiri on ilman muuta differentiaali- ja integraalilaskenta, joka on myös insinöörimatematiikan keskeinen tukipilari.

KIITOKSET

"Geofysiikan kenttäteoria" -oppikirjan kirjoittamista on taloudellisesti tukenut Jenny ja Antti Wihurin rahasto. Teknillinen korkeakoulu myönsi kirjalle vuoden 2004 oppikirjapalkinnon. Säteilyturvakeskus hyväksyi kirjan käsikirjoituksen julkaistavaksi raporttisarjassaan.

Esitän kiitokset myös kollegoilleni, oppilailleni ja opettajilleni monista tässäkin artikkelissa esitetyistä näkökohdista, jotka ovat nousseet esiin vuoropuheluissamme. Esitän erityiset kiitokset monista antoisista keskusteluista Teknillisen korkeakoulun emeritus professoreille Eero-Matti Saloselle ja Martti Mikkolalle sekä prof. Rolf Stenbergille.

Tekn. toht. Jari J. Hänninen Teknillisen korkeakoulun sähkömagnetiikan laboratoriosta on ollut mukana tekemässä Kelvinin inversioon liittyvää tarkastelua. Esitän kiitokset hänelle mutkattomasta ja hyvästä yhteistyöstä.

KIRJALLISUUSVIITTEET

Bear, J., 1988. Dynamics of Fluids in Porous Media. Dover Publications, Inc., New York, 764 p.

Eloranta, E., 2003. Geofysiikan kenttäteoria. Säteilyturvakeskus, tutkimusraportti STUK-A198, Helsinki, 424 s. Sähköinen versio osoitteessa: http://www.stuk.fi/julkaisut/stuk-a/stuk-a198.pdf

Fox, E.A., 1967. Mechanics. Harper & Row, New York, 431 p.

Jaeger, J.C. and Cook, N.G.W., 1976. Fundamentals of Rock Mechanics, 2nd ed. Chapman and Hall, London, 585 p.

Kellogg, O.D., 1954. Foundations of Potential Theory. Dover Publications, Inc., New York, 384 p.

Landau, L.D. and Lifshitz, E.M., 1989. Fluid Mechanics, 2nd ed. Pergamon Press, Oxford, 539 p.

Lindell, I.V. and Hänninen, J.J., 2000. Static image principle for the sphere in isotropic or bi-anisotropic space. Radio Science, 35(3), 653-660.

Malvern, L.E., 1969. Introduction to the Mechanics of a Continuous Medium. Prentice-Hall, Inc., New Jersey, 713 p.

Mase, G.E., 1970. Theory and Problems of Continuum Mechanics. Schaum's Outline Series. McGraw-Hill Book Company, New York, 221 p.

Reitz, J.R., Milford, F.J., and Christy, R.W., 1993. Foundations of Electromagnetic Theory. 4th Ed. Addison-Wesley Publishing Company, Inc., 630 p.

Salonen, E.-M., 1987. Mekaniikan käsitteitä ja kaavoja. Opetusmoniste 6, Helsingin Teknillinen korkeakoulu, Tietotekniikan osasto, Mekaniikan laboratorio, Espoo.

Sneddon, I.N., 1957. Elements of Partial Differential Equations. McGraw-Hill Book Company, Inc., 327 p.

Stratton, J.A., 1941. Electromagnetic Theory. McGraw-Hill Book Company, New York, 615 p.

Vanderlinde, J., 1993. Classical Electromagnetic Theory. John Wiley & Sons, Inc., New York, 384 p.

Väisälä, K., 1968. Vektorianalyysi. WSOY, Porvoo-Helsinki, 6. painos, 159 s.

LARGE DEFORMATION ANALYSIS OF WOUND ROLL STRESSES

K. ÄRÖLÄ[1], R. VON HERTZEN[2]

[1]VTT –Technical Research Centre of Finland
Smart Machines, Structural Dynamics
P.O.Box 1000, FI-02044 VTT, Finland
e-mail: kilwa.arola@vtt.fi

[2]Lappeenranta University of Technology
Laboratory of Fatigue and Strength
P.O.Box 20, FIN-53851 Lappeenranta, Finland
e-mail: raimo.von.hertzen@lut.fi

ABSTRACT

A two-dimensional axisymmetric winding model for wound rolls made of thin web is developed. The model accounts for the changes of stress and strain in the radial and axial directions of the roll. While one–dimensional winding models only treat radial displacements and radial and circumferential stresses, the present model accounts for radial and axial displacements and radial, circumferential, transverse and shear stresses. The roll build–up is modeled as an incremental accretion process, where successive pretensioned hoops are shrunk–fit onto the underlying roll. The material behaviour of the roll is considered as hyperelastic, orthotropic and radially nonlinear. Large strains are incorporated into the model by employing the total Lagrangian formulation. The numerical solution is developed using the finite element method. The calculated examples deal with paper rolls in which the centrifugal forces may significantly affect the resulting stress distributions. Also, the effect of a nonuniform distribution of the incoming winding tension on the finished roll is considered. A remarkable stress leveling phenomenon is found where the effect of a non–constant incoming web tension is evened out in the roll axial direction.

1 INTRODUCTION

Thin sheet media such as paper, magnetic tape, polymer, and metal are generally wound into compact rolls for the subsequent handling and transportation. The roll form is by far the most economical and practical form of material storage. During the production process, the tensioned thin sheet or web is wrapped on a solid central core. At this stage, the stresses and strains in the roll are built up in an incremental manner. It should be noted that the resulting stresses determine to a large extent the quality of the roll and provide the most important piece of information for the evaluation of the future durability and functionality of the finished roll. Also, as the trend in winding technology is towards thinner media and faster winding speeds [1], the mechanical stability of the rolls becomes more and more critical. Although, in laboratory conditions, experimental data through the sandwiched pull

strip method and some other methods can be obtained, practical non-destructive techniques to measure the internal state of stress of a roll on a production line are still lacking. This applies to finished rolls as well as to rolls still in a wind up. Thus, to evaluate the quality of the winding, there is an obvious need for a physical model of the winding process.

In this work, a two–dimensional winding model for predicting the stress and strain fields within a wound roll of web material, in which the radial, circumferential, transverse, and shear stresses, and the radial and axial strains can vary in both the roll's radial and axial (cross–web) directions, is presented. The material behaviour of the roll is considered as orthotropically anisotropic, linearly elastic in the circumferential and axial directions and nonlinearly elastic in the radial direction. It should be noted that the elastic properties of the bulk roll may be quite different from those of a single isolated layer, and are strongly affected by air entrainment in the roll, asperity compliance at the individual web surfaces, ambient air temperature and humidity, and other factors. The roll is built up in an incremental manner and total equilibrium in the roll is required after adding of each single hoop. Here the tensioned hoop is allowed to shrink on the surface of the underlying roll so that the wound-in tension loss [2] is automatically accounted for. The effect of centrifugal forces is also taken into account. The numerical solution is developed using the finite element method. In particular, finite strains are incorporated in the model using the total Lagrangian formulation. Also the core is modeled by the finite element method so that cores with nonlinear material behaviour can be treated. The model is applied for the analysis of paper rolls. The effect of the finite width of the roll on the stress field near the roll's free ends is studied. Also, the effect of nonuniform distribution of winding tension is discussed.

The paper proceeds as follows. In §2 and §3 the governing equations of the roll model and the finite element equations utilizing the total Lagrangian formulation for finite strains are developed. In §4 the linearization and solution of the nonlinear set of equations is demonstrated. The outline of the simulated winding procedure and the reference configuration are discussed in §5. In §6 numerical results for several winding examples are presented. Finally, the conclusions are drawn in §7.

2 AXISYMMETRICAL KINEMATICS

In this work the kinematics of the roll is described by using the reference description, in which the independent variable is the position $\mathbf{X}$ of a particle or material point in a reference configuration. Let $\mathbf{e}_R$, $\mathbf{e}_\Theta$ and $\mathbf{e}_Z$ be the unit base vectors in the cylindrical coordinate system of Fig. 1. The position of a material point in the undeformed reference configuration is expressed as

$$\mathbf{X} = R\,\mathbf{e}_R + Z\,\mathbf{e}_Z\,, \tag{1}$$

where R and Z are the cylindrical coordinates of the material point. The displacement of a particle in terms of the cylindrical unit base vectors may be written as (see Fig. 1)

$$\mathbf{u} = u\,\mathbf{e}_R + v\,\mathbf{e}_\Theta + w\,\mathbf{e}_Z\,, \tag{2}$$

where $u = u(R, Z)$, $w = w(R, Z)$ due to the axisymmetry of the deformed roll. The position of a point in the current (deformed) configuration is

$$\mathbf{x} = \mathbf{X} + \mathbf{u}\,. \tag{3}$$

The deformation gradient $\mathbf{F}$

$$\mathbf{F} = \frac{\partial \mathbf{x}}{\partial \mathbf{X}}\,, \tag{4}$$

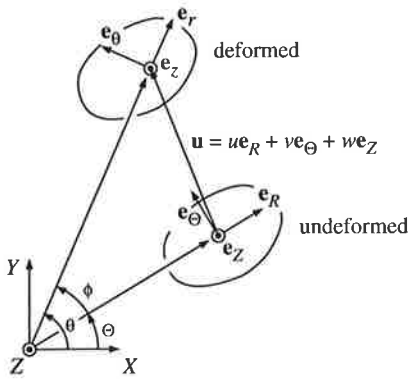


Figure 1: Base vectors $\mathbf{e}$ and displacement $\mathbf{u}$ in cylindrical coordinates. The view is projected on a plane of constant Z.

expressed in cylindrical coordinates in the case of axisymmetric deformation ($v = 0$, $\partial(\cdot)/\partial\Theta = 0$) can be written in matrix form as

$$[\mathbf{F}] = \begin{bmatrix} 1 + \partial u/\partial R & \partial u/\partial Z & 0 \\ \partial w/\partial R & 1 + \partial w/\partial Z & 0 \\ 0 & 0 & 1 + u/R \end{bmatrix} . \tag{5}$$

Using the deformation gradient, the Green (Green–Lagrange) strain tensor is written as

$$\mathbf{E} = \frac{1}{2}(\mathbf{F}^T\mathbf{F} - \mathbf{I}) \tag{6}$$

However, due to limited numerical accuracy of digital computers, in the solution process the Green strain can be calculated more accurately using the displacement gradient $\mathbf{H} = \mathbf{F} - \mathbf{I}$. The Green strain in terms of the displacement gradient becomes

$$\mathbf{E} = \frac{1}{2}(\mathbf{H} + \mathbf{H}^T + \mathbf{H}^T\mathbf{H}) . \tag{7}$$

3 DISCRETIZED EQUILIBRIUM EQUATIONS

In this work the problem solution is developed in terms of the total Lagrangian formulation in which Lagrangian measures of stress and strain are used and derivatives and integrals are taken with respect to material coordinates. The starting point for the derivation of the discretized equilibrium equations is the principle of virtual power which in the total Lagrangian formulation takes the form

$$\delta P = \int_{\Omega_0} \mathbf{S} : \delta\dot{\mathbf{E}}\, \mathrm{d}\Omega_0 - \int_{\Omega_0} \rho_0 \mathbf{b} \cdot \delta\mathbf{v}\, \mathrm{d}\Omega_0 - \int_{\Gamma_0} \mathbf{t} \cdot \delta\mathbf{v}\, \mathrm{d}\Gamma_0 = 0 , \tag{8}$$

where $\mathbf{S}$ is the second Piola–Kirchhoff stress, $\mathbf{b}$ the body force per unit mass, $\mathbf{t}$ the surface traction, $\delta\dot{\mathbf{E}}$ the virtual rate of Green strain and $\delta\mathbf{v}$ the virtual velocity. Note that the virtual power equation can be written in several forms using different conjugate pairs of stress and strain. Here, the use of the rate of Green strain and the second Piola–Kirchhoff stress is motivated by the choice of the constitutive equation. In the present work, the

consitutive model has to take into account the high anisotropy of paper. Hyperelastic materials, in which the stress is found by differentiating a stored energy function

$$\mathbf{S} = \frac{\partial \psi(\mathbf{E})}{\partial \mathbf{E}}\,, \tag{9}$$

provide a natural framework for the frame–invariant formulation of an anisotropic material response by simply embodying the anisotropy in the potential ψ.

Proceeding in the standard manner and expressing the virtual velocity field in terms of the element shape functions and nodal velocites, and taking into account the arbitrariness of the virtual velocities, the discretized equation of equilibrium for node I, written using Voigt notation, emerges as

$$\mathbf{f}_I^{int} - \mathbf{f}_I^{ext} = \mathbf{0}\,, \tag{10}$$

where the internal and external forces are

$$\mathbf{f}_I^{int} = \int_{\Omega_0} \mathbf{B}_I^T \{\mathbf{S}\}\, \mathrm{d}\Omega_0 \qquad \text{and} \qquad \mathbf{f}_I^{ext} = \int_{\Omega_0} N_I \rho_0 \mathbf{b}\, \mathrm{d}\Omega_0 + \int_{\Gamma_0} N_I \mathbf{t}\, \mathrm{d}\Gamma_0\,, \tag{11}$$

respectively. The matrix $\mathbf{B}_I$ in the expression of the internal forces relates the rate of Green strain to the nodal velocities. In the axisymmetric case this relation is written as

$$\{\dot{\mathbf{E}}\} = \sum_{I=1}^{n} \mathbf{B}_I \mathbf{v}_I \quad \Leftrightarrow \quad \left\{ \begin{array}{c} \dot{E}_{11} \\ \dot{E}_{22} \\ \dot{E}_{33} \\ 2\dot{E}_{12} \end{array} \right\} = \sum_{I=1}^{n} \left[\begin{array}{cc} B_{11}^I & B_{12}^I \\ B_{21}^I & B_{22}^I \\ B_{31}^I & B_{32}^I \\ B_{41}^I & B_{42}^I \end{array} \right] \left\{ \begin{array}{c} \dot{u}^I \\ \dot{w}^I \end{array} \right\}, \tag{12}$$

where n is the number of nodes in the element.

Any quantity $\phi(t)$ within an element is interpolated using the nodal values $\phi^I(t)$ and the element shape functions $N^I(\boldsymbol{\xi})$ as

$$\phi(t, \boldsymbol{\xi}) = \sum_{I=1}^{n} N^I(\boldsymbol{\xi})\, \phi^I(t) = N^I(\boldsymbol{\xi})\, \phi^I(t) \tag{13}$$

where t is time, $\boldsymbol{\xi}$ contains the parent element coordinates and n is the number of nodes in the element. We have adopted the conventions that capital indices, I, J, refer to node numbers, lower case indices, i, j, k, refer to tensor or matrix components and repeated indices mean summation. The derivatives of the shape functions with respect to the undeformed coordinates $\mathbf{X}$ are needed in the development of the finite element equations. These are obtained from

$$\frac{\partial N_I(\boldsymbol{\xi})}{\partial \mathbf{X}} = \Big(\frac{\partial \mathbf{X}}{\partial \boldsymbol{\xi}}\Big)^{-T} \frac{\partial N_I}{\partial \boldsymbol{\xi}}; \qquad \frac{\partial \mathbf{X}}{\partial \boldsymbol{\xi}} = \sum_{I=1}^{n} \mathbf{X}_I \otimes \frac{\partial N_I}{\partial \boldsymbol{\xi}}\,. \tag{14}$$

To get expressions for the components of the matrix $\mathbf{B}$ in Eq. (12), the rate of Green stain is first obtained by differentiating Eq. (6) with respect to time. This gives

$$\dot{\mathbf{E}} = \frac{1}{2}(\dot{\mathbf{F}}^T\mathbf{F} + \mathbf{F}^T\dot{\mathbf{F}})\,, \qquad \dot{E}_{ij} = \frac{1}{2}(\dot{F}_{ki}F_{kj} + F_{ki}\dot{F}_{kj})\,. \tag{15}$$

In the axisymmetric case the nonzero components of the rate of Green strain are $\dot{E}_{11}$, $\dot{E}_{22}$, $\dot{E}_{33}$ and $\dot{E}_{12}$ $(= \dot{E}_{21})$. The directions 1, 2 and 3 refer to the radial, axial and circumferential direction, respectively. Using the nodal displacements and shape functions, the time

derivative of the deformation gradient within an element becomes

$$\dot{\mathbf{F}} = \begin{bmatrix} N^I_{,R}\,\dot{u}^I & N^I_{,Z}\,\dot{u}^I & 0 \\ N^I_{,R}\,\dot{w}^I & N^I_{,Z}\,\dot{w}^I & 0 \\ 0 & 0 & N^I\dot{u}^I/R \end{bmatrix}, \tag{16}$$

where the notations $\partial(\cdot)/\partial R = (\cdot)_{,R}$ and $\partial(\cdot)/\partial Z = (\cdot)_{,Z}$ have been used. By inserting this interpolated rate of deformation gradient into Eq.(15) the matrix $\mathbf{B}^I$ corresponding to node I is found to be

$$\mathbf{B}^I = \begin{bmatrix} F_{11}N^I_{,R} & F_{21}N^I_{,R} \\ F_{12}N^I_{,Z} & F_{22}N^I_{,Z} \\ F_{33}N^I/R & 0 \\ F_{12}N^I_{,R} + F_{11}N^I_{,Z} & F_{22}N^I_{,R} + F_{21}N^I_{,Z} \end{bmatrix}. \tag{17}$$

By joining the contributions of all nodes $I = 1, \ldots, n$ in the form $\mathbf{B} = [\mathbf{B}^1, \ldots, \mathbf{B}^n]$ and $\dot{\mathbf{u}} = \{\dot{u}^1, \dot{w}^1, \ldots, \dot{u}^n, \dot{w}^n\}^T$, Eq. (12) can also be written in the form $\{\dot{\mathbf{E}}\} = \mathbf{B}\,\dot{\mathbf{u}}$.

4 LINEARIZATION AND SOLUTION

The discretized equilibrium equation, Eq. (10), written for all degrees of freedom in the model is

$$\mathbf{f}^{int} - \mathbf{f}^{ext} = 0\,. \tag{18}$$

Since this equation is nonlinear in the displacements, an iterative procedure is required to obtain a solution. This is done using Newtons method. Before the exact solution is found, the internal and external forces are not in balance. Thus, we write

$$\mathbf{f}^{int} - \mathbf{f}^{ext} = \mathbf{r}\,, \tag{19}$$

where $\mathbf{r}$ is the imbalance force, the residual. Linearizing the residual and equating the result to zero gives

$$\mathbf{r}(\mathbf{u}^k) + \frac{\partial \mathbf{r}(\mathbf{u}^k)}{\partial \mathbf{u}}\Delta\mathbf{u} = \mathbf{0}, \tag{20}$$

where k refers to the iteration number. Solving for $\Delta\mathbf{u}$ gives the increment in displacement

$$\Delta\mathbf{u} = -\Big(\frac{\partial \mathbf{r}(\mathbf{u}^k)}{\partial \mathbf{u}}\Big)^{-1}\mathbf{r}(\mathbf{u}^k)\,. \tag{21}$$

The next estimate for the solution is then obtained from $\mathbf{u}^{k+1} = \mathbf{u}^k + \Delta\mathbf{u}$. This procedure is repeated until the solution is found at a prescribed accuracy. In the linearization process we need to relate differentials of the internal and external forces to differentials of the nodal displacements, *i.e.*

$$\dot{\mathbf{f}}^{int} = \mathbf{K}^{int}\dot{\mathbf{u}} \qquad \text{and} \qquad \dot{\mathbf{f}}^{ext} = \mathbf{K}^{ext}\dot{\mathbf{u}}\,. \tag{22}$$

4.1 Linearization of the internal forces

We begin by linearizing the internal forces. The element internal nodal forces corresponding to node I are computed according to

$$\mathbf{f}^{int}_I = \int_{\Omega_0} \mathbf{B}^T_I\{\mathbf{S}\}\mathrm{d}\Omega_0\,. \tag{23}$$

Differentiating this gives

$$\dot{\mathbf{f}}_I^{int} = \int_{\Omega_0} \dot{\mathbf{B}}_I^T \{\mathbf{S}\} \mathrm{d}\Omega_0 + \int_{\Omega_0} \mathbf{B}_I^T \{\dot{\mathbf{S}}\} \mathrm{d}\Omega_0 \,. \tag{24}$$

Since the integral is always taken in the undeformed reference configuration, the volume Ω_0 remains constant throughout the deformation. The derivative of $\mathbf{B}^I$ is found by differentiating Eq.(17). Then using the interpolated rate of deformation gradient (Eq. (16)) and the nodal velocities, and after some algebra taking the vector of nodal velocities outside the integral, allows the first term on the right hand side of Eq. (24) to be written as

$$\int_{\Omega_0} \dot{\mathbf{B}}^T \{\mathbf{S}\} \mathrm{d}\Omega_0 = \mathbf{K}_{geo}\, \dot{\mathbf{u}} \,, \tag{25}$$

where the geometric stiffness matrix $\mathbf{K}^{geo}$ is

$$\mathbf{K}^{geo} = \int_{\Omega_0} \begin{bmatrix} \mathbf{K}^{11} & \dots & \mathbf{K}^{1n} \\ \vdots & \ddots & \\ \mathbf{K}^{n1} & \dots & \mathbf{K}^{nn} \end{bmatrix} \mathrm{d}\Omega_0, \quad \text{with } \mathbf{K}^{IJ} = \begin{bmatrix} K_{11}^{IJ} & 0 \\ 0 & K_{22}^{IJ} \end{bmatrix} . \tag{26}$$

Here, the diagonal elements of the submatrices $\mathbf{K}^{IJ}$ are

$$K_{11}^{IJ} = N_{,R}^I N_{,R}^J S_{11} + N_{,Z}^I N_{,Z}^J S_{22} + N^I N^J / R^2 S_{33} + (N_{,R}^I N_{,Z}^J + N_{,Z}^I N_{,R}^J) S_{12} \,, \tag{27}$$

$$K_{22}^{IJ} = N_{,R}^I N_{,R}^J S_{11} + N_{,Z}^I N_{,Z}^J S_{22} + (N_{,R}^I N_{,Z}^J + N_{,Z}^I N_{,R}^J) S_{12} \,. \tag{28}$$

The second term on the right hand side of Eq. (24) can be formed by using the constitutive equation. Differentation of the hyperelastic constitutive equation, Eq. (9), gives for the time derivative of $\mathbf{S}$ the expression

$$\dot{\mathbf{S}} = \frac{\partial^2 \psi}{\partial \mathbf{E} \partial \mathbf{E}} \dot{\mathbf{E}} = \mathbf{C}^{SE} : \dot{\mathbf{E}} \,. \tag{29}$$

Writing this in matrix form using Voigt notation and utilizing the expression $\{\dot{\mathbf{E}}\} = \mathbf{B}\,\dot{\mathbf{u}}$ for the rate of Green strain gives the material stiffness matrix

$$\mathbf{K}^{mat} = \int_{\Omega_0} \mathbf{B}^T [\mathbf{C}^{SE}]\, \mathbf{B}\, \mathrm{d}\Omega_0 \,. \tag{30}$$

4.2 Linearization of the external forces

The centrifugal force caused by the rotation of the roll is taken into account as a body force. The element nodal force for node I due to a general body force $\mathbf{b}$ is

$$\mathbf{f}_I^{ext} = \int_{\Omega_0} N^I \rho_0 \mathbf{b}\, \mathrm{d}\Omega_0 \,, \tag{31}$$

where ρ_0 is the density of the material in the reference state. A constant angular velocity ω introduces the force $\mathbf{b} = \omega^2 r\, \mathbf{e}_r$ per unit mass, where r is the current radius. Since the body force depends on the current radius r, and is thus a function of the displacement, it has to be linearized for the equilibrium iteration process. By differentiating the expression for the external forces the load stiffness $\mathbf{K}^{ext}$ due to the centrifugal force is found to be

$$\mathbf{K}^{ext} = \int_{\Omega_0} \mathbf{N}^T \begin{bmatrix} \omega^2 & 0 \\ 0 & 0 \end{bmatrix} \mathbf{N}\, \mathrm{d}\Omega_0, \quad \text{where } \mathbf{N} = \begin{bmatrix} N^1 & 0 & \dots & N^n & 0 \\ 0 & N^1 & \dots & 0 & N^n \end{bmatrix} . \tag{32}$$

However, since the cumulative process of building the roll requires a large number of steps in which elements are added to the roll, the displacements during one load step are small. Considering this, and the magnitudes of the roll angular velocities found in practice, the linearization of the centrifugal force is not mandatory. In many cases it is, in fact, computationally more efficient to discard the linearization of the centrifugal force from the Jacobian of the residual.

5 REFERENCE CONFIGURATION

The characterisation of deformation requires an initial or reference configuration, to which the current configuration is compared. In the present case, the most convenient choice is to consider the state of the incoming web before it is attached to the roll as the reference state. The refence state and the steps in the process of adding a new layer to the roll are depicted in Fig. 2. Since each added layer has its own initial displacement and strain state at the time when it becomes part of the growing roll, the strain field of the roll is, in general, discontinuous. After the attachment of a new layer, the roll and the new layer form a continuous medium and the increments of strain from here on are continuous.

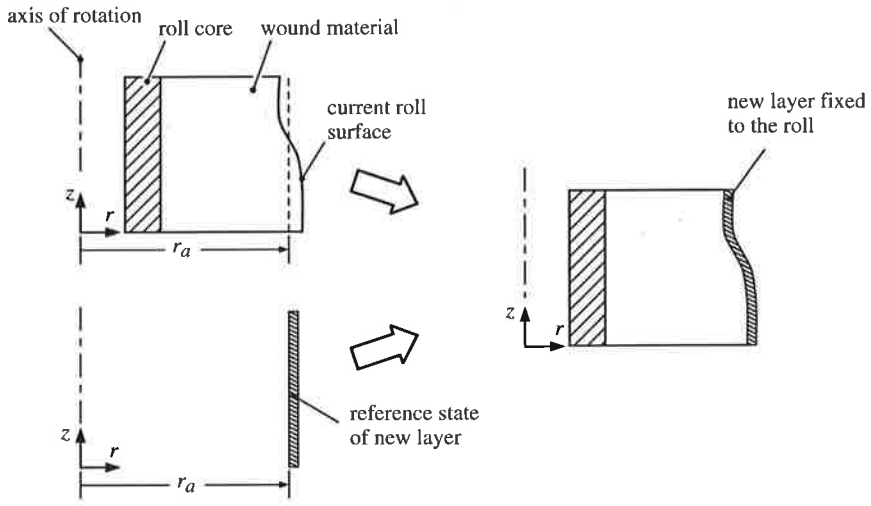


Figure 2: Process of adding a new layer to the roll. The average radius of the deformed roll surface is r_a

In the present model, the process of adding a new layer on the roll can be divided into three steps.

- First, the reference state of the new layer is a cylindrical shell with a circumferential strain equal to the strain of the incoming web and with an inner radius r_a and shell thickness h. The dimension r_a is the average radius of the current roll outer surface as shown in Fig 2.
- Second, displacements of the inner surface of the new layer are prescribed so that they bring this surface in contact with the current roll outer surface. The surfaces are fixed together so that from here on their displacements are equal.

- Third, the new layer is allowed to tighten around the current roll and the corresponding FE–equations are solved to find the new equilibrium state of stress and deformation for the new roll (including the new layer).

6 NUMERICAL EXAMPLES

In this section calculated examples are given. First, the effect of the centrifugal force due to the rotation of the wound roll during winding is demonstrated in a plane strain case. Second, examples of the effect of the finite axial length of the roll is presented. Cases where the tension of the incoming web is either constant or linearly varying in the web width direction are considered. The values for the material parameters used in the calculations are given in Appendix I. The tangent modulus in the radial direction of the paper roll is assumed to be a linear function of the radial stress $E_r = \partial S_{11}/\partial E_{11} = C_0 - C_1 S_{11}$, where S_{11} is the radial stress and C_0 and C_1 are positive constants. The stress measure used in the following examples is the Cauchy stress (true stress), which is obtained from the second Piola–Kirchhoff stress by the formula $\boldsymbol{\sigma} = J^{-1}\mathbf{F}\cdot\mathbf{S}\cdot\mathbf{F}^T$, where $J = \det\mathbf{F}$.

6.1 EFFECT OF CENTRIFUGAL FORCES

Modern high speed winders can be run at web speeds of 50 m/s. With a radius of 300 mm, for example, this corresponds to an angular velocity of almost 170 rad/s. Since the centrifugal body force acting on the rotating paper roll is proportional to the square of the angular velocity, high forces are bound to be generated. The centrifugal force tends to decrease the compressive radial pressure in the roll, since part of the incoming web tension is used up in opposing the centrifugal force. For a trouble free unwinding it would be beneficial if the pressure and web tension distributions in the roll were as constant as possible in the radial direction. Since the centrifugal force tends to decrease the radial pressure in the finished roll, it is evident that increasing the wound-in tension could at least partially compensate for the loosening effect of the centrifugal force. A first approximation for the required compensative winding force can be developed by noting that the radial pressure under the topmost layer of the paper roll is

$$p = \frac{T_{in}}{R} - \rho\omega^2 hR \tag{33}$$

where T_{in} is the incoming web tension, R the current radius of the roll, ρ the paper density and h the web thickness. In the case $\omega = 0$ and $T_{in} = T_0$ this reduces to $p = T_0/R$. It can be seen that by using a compensated incoming web tension

$$T_{in} = T_0 + \rho h\omega^2 R^2, \tag{34}$$

the radial pressure under the topmost layer of the rotating case equals that of the nonrotating and noncompensated case. To see how well the compensation works, a test case was calculated. In the test case the web speed during winding was first accelerated from zero to 50 m/s using an acceleration 1.0 m/s^2. After this the web speed remained constant at 50 m/s. Finally, the roll angular velocity was restored back to zero during the last 1500 roll revolutions by decreasing the angular velocity linearly as a function of roll rotations. The finished roll had 6000 paper layers and an outer diameter of approximately 1050 mm.

The radial pressure distributions for three different winding conditions are shown in Fig. 3 (left). The solid line is calculated using a constant incoming web tension of 600 N/m and zero (or very low) winding speed. The typical plateau in the radial pressure familiar already from the Hakiel model [3] can be seen. The dashed line is calculated using the same

constant incoming web tension 600 N/m and the winding velocity profile described above. The decrease of the plateau value due to the centrifugal force is clearly visible. Finally, the dotted line is calculated using the compensated incoming web tension proposed by Eq. (34). It can be seen from the figure that adding the compensation term effectively evens out the effect of the centrifugal force and a final radial pressure distribution almost equal to that of the nonrotating (or slowly rotating) case is obtained.

The tangential stresses in the roll for the aforementioned calculation cases are shown in Fig. 3 (right). Again the stress distributions in the zero winding speed (solid line) and the tension compensated (dotted line) cases are practically identical. The effect of the centrifugal force on the tangential stress is clearly displayed by the dashed line. It can be seen from Fig. 3 that the outer radius of the finished roll is larger in the case of the dashed line. This is as expected since, due to the centrifugal force, the pressure in the roll becomes smaller and, therefore, the paper layers are less compressed in the radial direction.

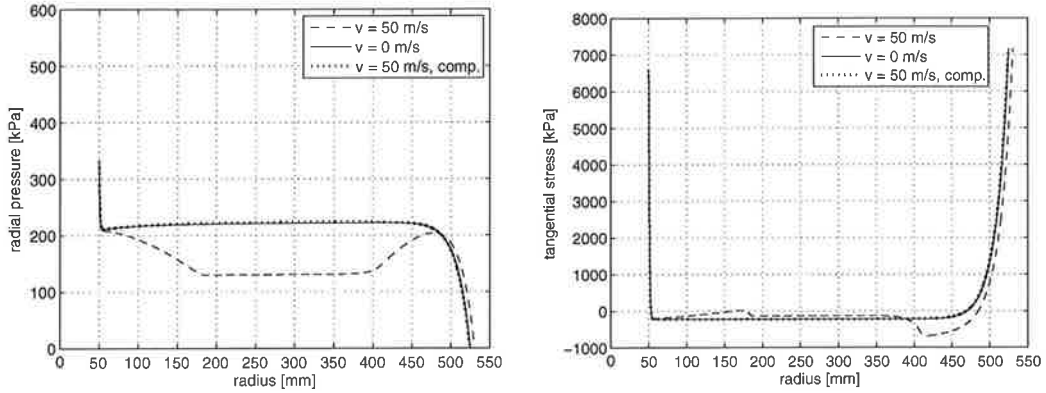


Figure 3: Radial pressure p (left) and tangential stress σ_θ (right) in the wound roll.

6.2 Uniform incoming web tension

Let us consider next the stress variations of the paper roll in the axial direction of the roll. First, a simple case with a constant incoming web tension in the web width direction is studied. The width of the web is 300mm, the roll has 3000 paper layers of initially 83 μm thick and the final outer radius of the roll is 290 mm. Plots of the stress distributions in the finished roll are shown in Figs. 4 and 5. The radial pressure shows only small variations in the roll axial direction. Although not apparent from the figure, it was found that along a cut of constant radius, the pressure is slightly lower at the edges of the roll (width = 0 and 300 mm) than inside the roll. At the core (radius = 50 mm) high pressure values are found at the edges of the rolls (the red spikes). It is well known that at a point where three dissimilar materials join (in this case paper, core and ambient air), a stress singularity is actually encountered [4, 5]. The same phenomenon was also noticed by Lee and Wickert in their two–dimensional roll model [6]. In reality, the stresses are limited by the yield strength of the materials and in the case of a paper roll, in particular, by the slippage between the paper layers. When moving further from the singular points the stress levels are rapidly smoothened and usable results are obtained. In the tangential stress the variation of the stress in the axial direction of the roll is more significant. As can be seen from Fig. 4, the compressive tangential stresses are clearly higher at the free sides of the roll. The shear and

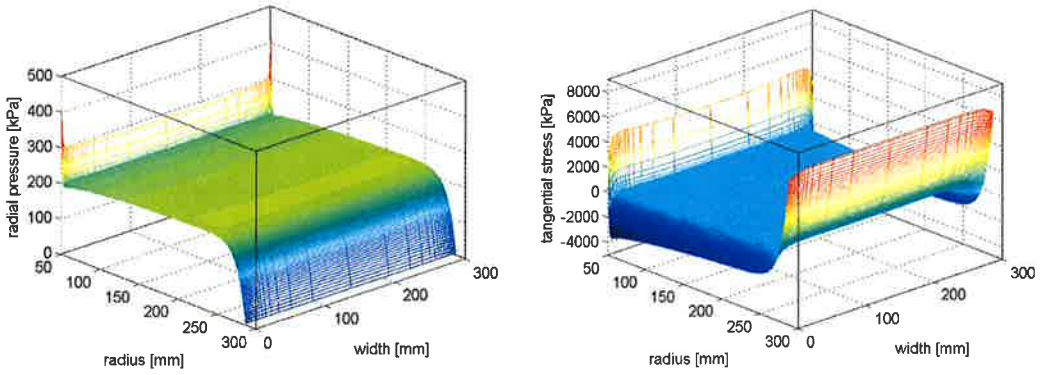


Figure 4: Radial pressure p (left) and tangential stress σ_θ (right) in the wound roll when the incoming web tension is constant across the web width.

axial stresses in the roll are shown in Fig. 5. The distribution of the axial stress shows some variation in the axial direction. At the free sides of the roll (width = 0 and 300), the axial stress rapidly goes to zero within a narrow zone. Due to the symmetry of the structure and loading, the shear stress is antisymmetric with respect to the radial line at the center of the roll (width = 150 mm). High shear stresses are found near the roll core, and particularly near the free sides of the roll, due to the difference of the material properties of the core and paper web. High shear stress gradients are found near the edges of the roll as the shear stress drops to zero at the free edges.

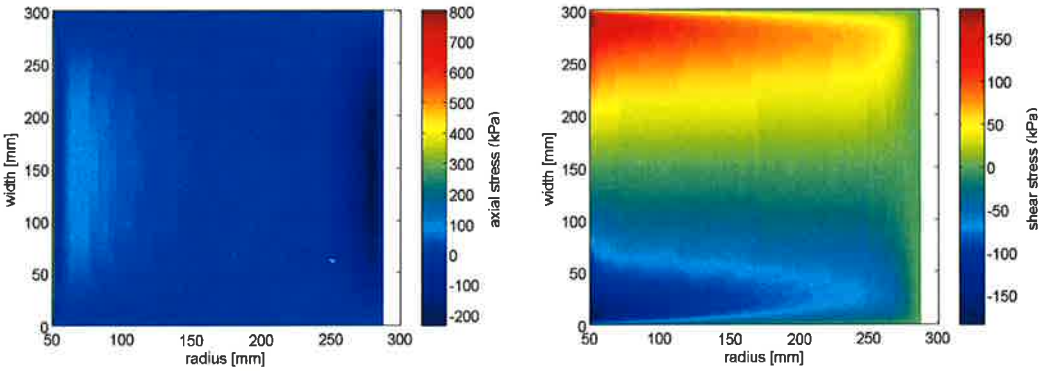


Figure 5: Axial stress σ_z (left) and shear stress τ_{rz} (right) in the wound roll when the incoming web tension is constant across the web width.

6.3 Nonuniform web tension

In practice, the tension of the incoming web is not necessarily constant throughout the width of the web. Misalignment of the rollers, variations in the material properties and moisture content of the web, and a varying web thickness profile, for example, can all contribute to the tension distribution of the incoming paper web. To study the effect of

a non-uniform incoming web tension on the stress distribution of the finished paper roll, a case with a linearly varying tension distribution across the web width was studied. The tension ranged from 400 N/m at $z = 0\,\text{mm}$ to 800 N/m at $z = 300\,\text{mm}$. With the web thickness of 83.3 μm these values correspond to the tensional stresses 4.8 MPa and 9.6 MPa of the incoming web, respectively. All other parameters used in this calculation are the same as those used in the previous case of uniform web tension.

The distributions of the radial pressure p and circumferential stress σ_θ are shown in Fig. 6. The effect of the linearly increasing incoming stress distribution is clearly seen near the roll core, where an almost linear distribution of radial pressure and circumferential stress is clearly visible in Fig. 6. However, as more layers are wound on the roll, the stress changes

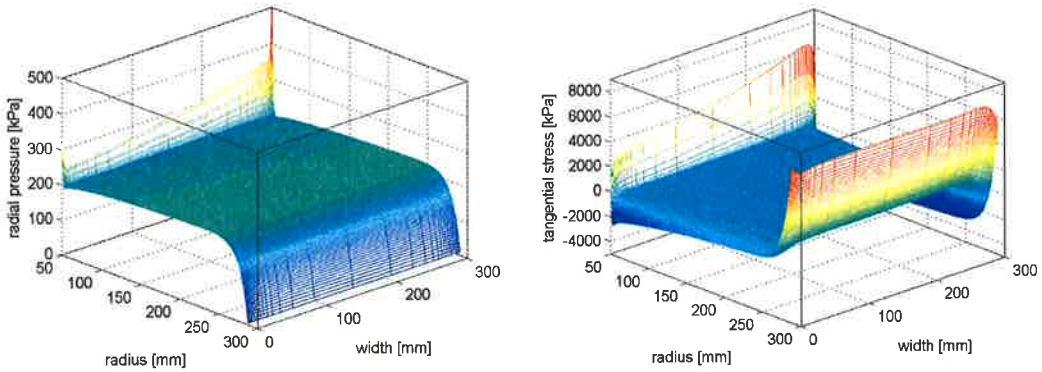


Figure 6: Radial pressure p (left) and tangential stress σ_θ (right) in the wound roll when the incoming web tension is linearly distributed across the web width.

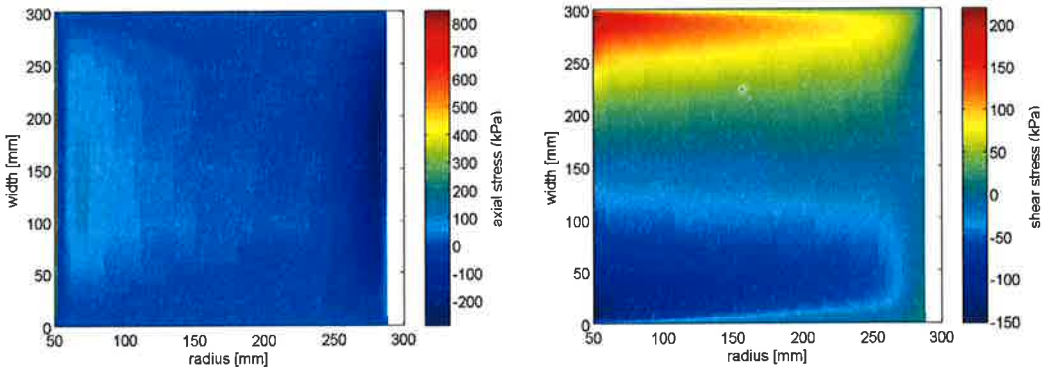


Figure 7: Axial stress σ_z (left) and shear stress τ_{rz} (right) in the wound roll when the incoming web tension is linearly distributed across the web width.

are, remarkably, evened out in the roll axial direction. As can be seen from Fig. 6, already at a few millimeters away from the roll core the radial pressure and circumferential stress in the roll are practically constant in the roll axial direction. Some drop in the circumferential stress occurs at the roll edges.

The axial stress σ_z and shear stress τ_{rz} in the roll are shown in Fig. 7. The distribution of axial stress is almost symmetric with respect to the radial center line and differing from zero only near the roll core and outer surface of the roll. As in the case of constant web tension, at the free sides of the roll (width = 0 and 300) the axial stress rapidly goes to zero within a small zone. In contrast to the axial stress, a nonzero shear stress is penetrated throughout the roll. This shows that the cross–coupling of the stresses in the axial direction occurs mainly via the shear stress τ_{rz}. It can also be seen that the shear stress is almost antisymmetric with respect to the roll's central cross section.

7 CONCLUSIONS

In this work a two-dimensional axially symmetric winding model accounting for large deformations and centrifugal forces was developed. A nonlinear orthotropic constitutive law for the wound material was used. Large strains were modelled using the total Lagrangian formulation and the equations were solved using the finite element method. The model was applied to the winding of paper rolls. In the calculated examples, radial strains of the order of 10% were found in the roll emphasizing the importance of a large deformation analysis in paper winding. The associated decrease of the roll radius and the length of the added layers should be also taken into account when calculating the roll mass as a function of the number of layers in the roll and the eigenfrequencies of a two-drum winder, for example. The model was used to study the effect of roll rotation during winding on the finished roll. Due to the high winding speeds of modern winders, the centrifugal forces had a significant effect on the radial and tangential stresses in the roll. By applying an additional, properly selected, compensatory incoming tension to the web, the changes in the roll stresses due to rotation could be effectively eliminated. A remarkable stress leveling phenomenon was discovered. Namely, for a linearly distributed incoming web tension in the roll width direction, almost width-independent radial and tangential stress distributions were found. This leveling off could be attributed to the Poisson's ratios between the radial and axial directions of the web material. In this way a clear role to the Poisson's ratios in the winding process could be addressed. The results of several earlier one–dimensional studies have consistently shown that in plane stress or plane strain cases the Poisson's ratios have hardly had any effect on the roll stresses and, therefore, have been set to zero in most calculations. Also, large stress gradients near the roll core and roll edges were found. It is evident that by properly selecting the elastic moduli of the core, the high stresses near the core could be at least partly eliminated. In future work, the effect of the width-wise variation of the elastic moduli and caliper of the web on the finished roll should be studied, since these variations frequently occur in real paper webs.

APPENDIX I

The values of the material parameters and dimensions used in the calculations.

Roll					
Radial modulus coefficient	C_0	3.518 MPa	Poisson's ratios	$\nu_{\theta z}$	0.3
Radial modulus coefficient	C_1	12.815		$\nu_{\theta r}$	-1.71
Elastic moduli	E_θ	5100 MPa		ν_{zr}	-0.39
	E_z	2600 MPa	Shear modulus	G_{rz}	26 MPa
Core					
Inner radius	r_i	44 mm	Poisson's ratios	$\nu_{z\theta}$	0.3
Outer radius	r_o	50 mm		ν_{zr}	3.0
Elastic moduli	E_r	130 MPa		$\nu_{\theta r}$	2.4
	E_θ	6500 MPa	Shear modulus	G_{rz}	234 MPa
	E_z	4000 MPa			

REFERENCES

[1] D. Roisum. *Pushing web handling to the limit*, Converting Magazine, **17**, 72–76 (1999).

[2] J.K. Good, J.D. Pfeiffer and R.M. Giachetto. *Losses in wound-on tension in the centerwinding of wound rolls*, Web Handling, ASME AMD-149, ASME, New York, 1–12 (1992).

[3] Z. Hakiel. *Nonlinear model for wound roll stresses*, Journal of the Technical Association of the Paper and Pulp Industry, **70**, 113–117 (1987).

[4] D. B. Bogy. *On the problem of edge–bonded elastic quarter–planes loaded at the boundary*, International Journal of Solids and Structures, **6**, 1287–1313 (1970).

[5] E. S. Folias. *On the stress singularities at the intersection of a cylindrical inclusion with the free surface of a plate*, International Journal of Fracture, **39**, 25–34 (1989).

[6] Y. M. Lee and J. A. Wickert. *Stress field in finite width axisymmetric wound rolls*, ASME Journal of Applied Mechanics, **69**, 130–138 (2002).

ON THE EFFECT OF GEOMETRIC IMPERFECTION ON THE NUMERICAL PREDICTION OF CYLINDRICAL COMPOSITE SHELL POST-BUCKLING BEHAVIOUR

P. KERE[1,3], M. LYLY[2]

[1]Tampere University of Technology, Institute of Applied Mechanics and Optimization
P.O. Box 589, FI-33101 Tampere
e-mail: Petri.Kere@tut.fi

[2]CSC – Scientific Computing Ltd.
Box 405, FI-02101 Espoo
e-mail: Mikko.Lyly@csc.fi

ABSTRACT

The present study deals with the geometrically nonlinear post-buckling response of carbon fibre reinforced plastic cylindrical shells under axial compression. Reissner-Mindlin-Von Kármán type facet model implemented in the Elmer computational tool for multi-physics problems is used in the computations. The effect of geometric imperfection shape and amplitude on the shell post-buckling response is discussed. Numerical-experimental correlation is performed using the results of experimental buckling tests found in the literature.

1 INTRODUCTION

Carbon fiber reinforced plastic (CFRP) composite shells are important structural elements found in many areas of modern lightweight construction. Due to their unique strength and stiness properties, CFRP composites are usually thin laminated shell structures that are prone to buckling with long geometrically nonlinear post-buckling behaviour. Designing with high performance materials may enable weight reduction without loss of structural life by permitting post-buckling under ultimate load. To achieve that aim, improved, fast, and reliable computational methods for analysis and design optimization of composite shell structures in the post-buckling field are required.

In this study, post-buckling numerical analysis and experimental correlation of cylindrical CFRP shells is considered. A computational model is based on specimens that were used in experimental tests [2]. The specimens were characterised by an internal diameter and an overall length including two tabs provided at the top and bottom surfaces for attaching them to the loading equipment. The specimens were fabricated from CFRP unidirectional and fabric tape materials, for which the nominal ply properties are given in Table 1. Detailed description of the test specimens, equipment, and procedure is given by Bisagni and Cordisco [2].

The effects of small imperfections in the computational model have been found to reproduce accurately the observed behaviour [1, 15]. The effect of axisymmetric and diamond shape geometric imperfections on the numerical prediction of cylindrical composite shell post-buckling behavior

[3]Employed by National Board of Patents and Registration, P.O. Box 1106, FI-00101 Helsinki

is investigated using Reissner-Mindlin-Von Kármán type facet model. Geometric imperfections measured on the real specimens [1] are accounted for the finite element model.

	Unidirectional CFRP	Fabric CFRP
E_1 [GPa]	113.0	52.0
E_2 [GPa]	9.0	52.0
G_{12} [GPa]	3.82	2.35
ν_{12}	0.73	0.302
t_{ply} [mm]	0.15	0.33

Table 1: Mechanical properties of the CFRP plies used in the experimental tests and in the computational model.

Modeling the structure is based on a facet approximation of the undeformed mid-surface for a laminated shell. The potential energy functional where the linearized strain tensor has been replaced by the nonlinear functions, i.e., the Von Kármán model for large deformation is formulated [8]. The kinematical unknowns are determined from the condition that they minimize the potential energy of the shell. In the computations we solve these nonlinear equations iteratively by Riks' method with Crisfield's constraint for arc-length. The linearized equations are then discretized by the finite element method. In the FE implementation we use bilinear stabilized MITC elements [3, 13].

The facet model was implemented in the Elmer open-source computational tool for multiphysics problems [4]. Our aim is to find geometric imperfection shape and amplitude suitable for use in structural optimization purposes such that the computational time remains reasonable still offering accuracy for post-processing results like local failure prediction of composite [9, 10].

2 REISSNER-MINDLIN-VON KÁRMÁN TYPE FACET MODEL

The plate bending problem is formulated for a thin or moderately thick laminated composite plate which in its undeformed configuration occupies the region $\Omega \times (-t/2, t/2)$, where $\Omega \subset \mathbb{R}^2$ is the midsurface and $t > 0$ is the laminate thickness. The kinematical unknowns in the model are transverse deflection w, in-plane displacement $u = (u_1, u_2)$, rotation of the middle surface $\beta = (\beta_1, \beta_2)$, and drilling rotation ω. The plate is subjected to the in-plane load $f = (f_1, f_2)$ and the transverse pressure g.

We use standard dyadic notation of tensor calculus. The functions u, w, β, and ω are determined from the condition that they minimize the potential energy of the plate. The energy is defined as

$$
\begin{aligned}
\Pi(u, w, \beta, \omega) = & \frac{1}{2} \int_\Omega \varepsilon(u) : A : \varepsilon(u) \, d\Omega + \int_\Omega \varepsilon(u) : B : \varepsilon(\beta) \, d\Omega \\
& + \frac{1}{2} \int_\Omega \varepsilon(\beta) : D : \varepsilon(\beta) \, d\Omega + \frac{1}{2} \int_\Omega \gamma(w, \beta) \cdot A^\star \cdot \gamma(w, \beta) \, d\Omega \\
& + C \int_\Omega [\omega - rot(u)]^2 \, d\Omega + \frac{1}{2} \int_\Omega \varphi(u, w) : A : \varphi(u, w) \, d\Omega \\
& + \int_\Omega \varepsilon(u) : A : \varphi(u, w) \, d\Omega + \int_\Omega \varepsilon(\beta) : B : \varphi(u, w) \, d\Omega \\
& - \int_\Omega f \cdot u \, d\Omega - \int_\Omega g w \, d\Omega
\end{aligned} \tag{1}
$$

where ε is the linear strain tensor

$$\varepsilon(u) = \frac{1}{2}(\nabla u + \nabla u^T) \tag{2}$$

φ is the nonlinear membrane strain tensor

$$\varphi(u, w) = \frac{1}{2}(\nabla u_1 \otimes \nabla u_1 + \nabla u_2 \otimes \nabla u_2 + \nabla w \otimes \nabla w) \tag{3}$$

γ the transverse shear strain vector

$$\gamma(w, \beta) = \nabla w - \beta \tag{4}$$

and $C > 0$ is a penalty parameter for imposing the condition $\omega = rot(u)$, see [5].

The tensors A, B, D, and $A^\star$, are defined according to the Classical Lamination Theory [6] as

$$A = \sum_k \int_{z_{k-1}}^{z_k} \bar{Q}\, dz = \sum_k (z_k - z_{k-1})\bar{Q}^{(k)} \tag{5}$$

$$B = \sum_k \int_{z_{k-1}}^{z_k} \bar{Q} z\, dz = \frac{1}{2}\sum_k (z_k^2 - z_{k-1}^2)\bar{Q}^{(k)} \tag{6}$$

$$D = \sum_k \int_{z_{k-1}}^{z_k} \bar{Q} z^2\, dz = \frac{1}{3}\sum_k (z_k^3 - z_{k-1}^3)\bar{Q}^{(k)} \tag{7}$$

$$A^\star_{ij} = \sum_k \int_{z_{k-1}}^{z_k} \bar{Q}_{3i3j}\, dz = \sum_k (z_k - z_{k-1})\bar{Q}^{(k)}_{3i3j} \tag{8}$$

where $\bar{Q}^{(k)}$ defines the constitutive relation for linear orthotropic materials in plane stress state for layer k in the laminate coordinate system. Detailed expression for computing $\bar{Q}^{(k)}$ as well as deriving the model is considered more thoroughfully in [7], for instance.

In the FE-implementation we use bilinear stabilized MITC plate elements [3, 13]. The shear energy term is modified as

$$\frac{1}{2}\,\frac{t^2}{t^2 + \alpha_h h^2}\int_\Omega \gamma_h(w, \beta) \cdot A^\star \cdot \gamma_h(w, \beta)\, d\Omega \tag{9}$$

where $\alpha_h > 0$ is a numerical stabilization parameter, h is the mesh parameter (largest side length), and γ_h is the reduced shear strain [3, 13]. For the bilinear quadrilateral element used in the numerical example, the reduced shear is defined locally such that

$$\gamma_h(w, \beta)_{|K} = \begin{bmatrix} a_K + c_K y \\ b_K + d_K x \end{bmatrix} \tag{10}$$

for every element K. The parameters a_K, b_K, c_K, and d_K are determined from the condition

$$\int_e [\gamma(w, \beta) - \gamma_h(w, \beta)] \cdot \tau\, ds = 0 \tag{11}$$

for every edge e of K. Here τ is the tangent to the edge.

3 GEOMETRICALLY NONLINEAR STRUCTURAL ANALYSIS

To obtain the load-displacement curve and to sudy the stability behaviour, the non-linear equations are solved iteratively by Riks' method with Crisfield's elliptical constraint for arc length [11, 12, 14, 16, 17]. The linearized equations are then discretized by the finite element method. In the post-buckling region the algorithm follows the principal equilibrium path with the minimal stiffness.

Let the equilibrium equation be defined as

$$F(q,\lambda) \equiv \lambda P(q) - R(q) = 0 \tag{12}$$

where the unbalanced or residual force is denoted by F, P and R are the external and internal loads, respectively, $q = (u_1, u_2, w, \beta_1, \beta_2, \omega)$ are the nodal displacements of the FE solution and λ is the load scaling factor serving as a control parameter of the system. In this work, the reference load P is assumed to be independent of q.

Using the arc-length methods for solving the nonlinear equilibrium equations, the load-displacement constraint G is added to the system

$$H(q,\lambda) = \begin{cases} F(q,\lambda) = 0 \\ G(q,\lambda) = 0 \end{cases} \tag{13}$$

Solution of the nonlinear system is obtained by an incremental approach with the elliptical constraint and the algorithm as follows:

1. Given a solution (q_e, λ_e) to Eq. 14, define $G(q,\lambda) = (q-q_e)^T W(q-q_e) + \alpha^2(\lambda-\lambda_e)^2 - s^2$, where W is a positive weighting matrix for the displacements, α is a load scaling parameter, and s is the arc length.

2. Linearize in the intermediate state (q_i, λ_i) as

$$H(q,\lambda) \approx \begin{cases} F(q_i,\lambda_i) + \frac{\partial F}{\partial q}(q_i,\lambda_i)(q-q_i) + \frac{\partial F}{\partial \lambda}(q_i,\lambda_i)(\lambda-\lambda_i) = 0 \\ G(q_i,\lambda_i) + \frac{\partial G}{\partial q}(q_i,\lambda_i)(q-q_i) + \frac{\partial G}{\partial \lambda}(q_i,\lambda_i)(\lambda-\lambda_i) = 0 \end{cases} \tag{14}$$

   or

$$\begin{cases} F(q_i,\lambda_i) + K(q-q_i) + P(\lambda-\lambda_i) = 0 \\ G(q_i,\lambda_i) + 2(q_i-q_e)^T W(q-q_i) + 2\alpha^2(\lambda_i-\lambda_e)(\lambda-\lambda_i) = 0 \end{cases}$$

   where $K = \frac{\partial F}{\partial q}(q_i,\lambda_i)$ is the tangential stiffness.

3. Solve (q,λ) from Eq. 11. If $|H(q,\lambda)| \leq \delta$ goto Step 4 else set $(q_i,\lambda_i) = (q,\lambda)$ and goto Step 2.

4. Set $(q_e,\lambda_e) = (q,\lambda)$ and goto Step 1.

4 THE CFRP CYLINDRICAL SHELL

The model considers a complete cylinder with ply properties represented in Table 1 and geometric dimensions same of those of the real specimens used. The FE-model length is assumed to be 540 mm, equal to the length of the specimen central part excluding the tabs at the top and bottom surfaces [2]. The top and bottom surfaces of the FE-model are constrained to remain plane and circular and to maintain the initial radius while the axial compression is transferred to nodal forces.

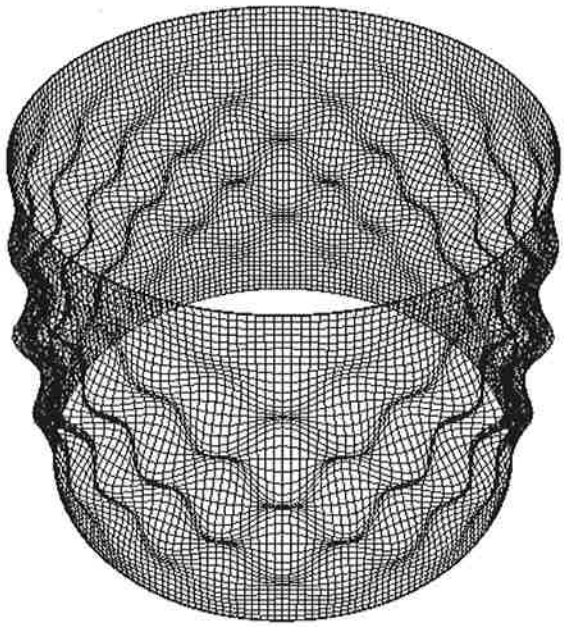


Figure 1: Elmer numerical buckling shape for the cylinder with the fabric $[0/+45/-45/0]$ lay-up.

The mesh sensitivity on the buckling load prediction by linear eigenvalue analysis was studied by Bisagni [1]. According to the study, the accuracy of the buckling load prediction depends highly on the FE-mesh resolution. Good convergence for critical loads was achieved with 220×52 quadrilateral elements, i.e., 220 elements in the circumferential direction and 52 elements in the axial direction, when compared to the analytical solutions. Hence, the FE-mesh with 11440 quadrilateral elements as shown in Figure 1 was employed in this investigation as well.

The midsurface of the cylinder is considered as the reference surface where the initial imperfections are given. A cylindrical coordinate system is employed and the nodal coordinate in the radial direction is taken as $r = R + w^{\circ}$, where $R = 350$ mm is the nominal radius of the cylinder and w° is the amplitude of the imperfection shape.

The buckling shapes for the CFRP shells depend on the stacking sequences. Two stacking sequences representing different buckling shapes were included in the study. The cylinder with the unidirectional $[(+45/-45)2]_{\mathrm{SE}}$ laminate structure exhibits an axisymmetric buckling shape while the fabric $[0/+45/-45/0]$ lay-up exhibits a diamond one.

Our aim is to find geometric imperfection shape and amplitude suitable for use in structural optimization with various laminate lay-ups. Hence, we consider axisymmetric and diamond shape imperfections on the shell geometry [1]. The analytical expression used to define the axisymmetric imperfection shape is

$$w^{\circ}(z, \vartheta) = a \sin(m\pi z/L) \tag{15}$$

where m is the number of axial semi-waves, z is the axial coordinate, ϑ the circumferential coordinate, and L the cylinder length. The analytical expression used to define the diamond imperfection shape is

$$w^{\circ}(z, \vartheta) = a \sin(m\pi z/L) \cos(n\vartheta) \tag{16}$$

where m is the number of axial semi-waves and n the number of circumferential waves. The

analysis is performed using different values for the non-dimensional imperfection amplitude defined as $\varepsilon = a/t$, where t is the shell thickness and $\varepsilon \in [0, 1]$.

5 RESULTS

Results of a preliminary study on the effect of the imperfection shape and amplitude on the post-buckling behaviour of the cylindrical shells are presented. The cylindrical shells are composed of the unidirectional $[(+45/-45)2]_{\mathrm{SE}}$ and the fabric $[0/+45/-45/0]$ lay-ups with thicknesses 1.20 mm and 1.32 mm, respectively. The corresponding radius-to thickness ratios for the shells are 292 and 265, respectively. The axisymmetric shape imperfection is made up of 5 axial semi-waves. The diamond shape imperfection is made up of 13 circumferential and 5 axial semi-waves. The non-dimensional imperfection amplitude values $\varepsilon = 0.05 - 0.25 - 0.50 - 1.00$ are modeled.

The critical load (CL) is determined by increasing gradually the applied load to search for the maximum of the load-displacement curve. The maximum displacement $\max |d(u_1, u_2, w)|$ is registered to compare the post-buckling displacements of the shells. Elmer numerical load-displacement curves are illustrated in Figure 2. The experimental load-displacement diagrams are given by Bisagni and Cordisco [2]. Comparison among critical loads and post-buckling displacements using Crisfield's arc-length method with the arc length scale factor $\alpha = 0.8$, $W = 0.1$, and $\alpha_h = 0.2$ for the shells with the unidirectional $[(+45/-45)2]_{\mathrm{SE}}$ and the fabric $[0/+45/-45/0]$ laminates with the diamond shape imperfection on the shell geometry are represented in tables 2 and 3, respectively. Results also from the Elmer [4] linear eigenvalue analysis are presented.

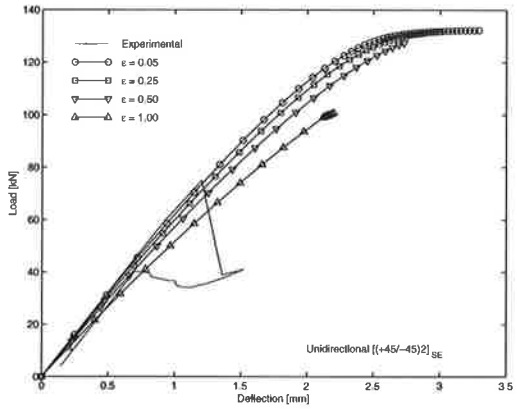
	CL [kN]	d [mm]
Experimental [2]	74.93	1.52
Elmer nonlinear, ε=0.50	76.68	1.39
Elmer nonlinear, ε=0.25	115.33	2.13
Elmer nonlinear, ε=0.05	124.63	2.35
Elmer nonlinear, ε=0.0	130.75	2.70
Elmer linear buckling, ε=0.0	132.46	

Table 2: Comparison among critical loads and post-buckling deflections for the unidirectional $[(+45/-45)2]_{\mathrm{SE}}$ cylindrical shell with the initial diamond shape imperfection, $m = 5, n = 13$.

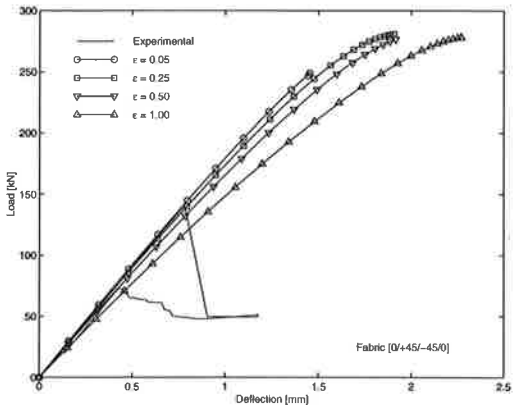
Results show that in all cases there is a significant discrepancy between numerically predicted critical loads and the ones observed in experiments when perfect shell geometry is employed in the model. The high sensitivity of the cylindrical shell critical load to the geometric imperfections can be oserved in all cases.

Using a dimond shape imperfection for the cylinder composed of the $[(+45/-45)2]_{\mathrm{SE}}$ laminate that exhibits an axisymmetric numerical buckling shape gives only a slightly higher critical load compared to the measured buckling load. Increasing the imperfection amplitude improves the critical load prediction, giving the most accurate result with the greatest used imperfection amplitude $\varepsilon = 0.50$ with variation 2.3 %.

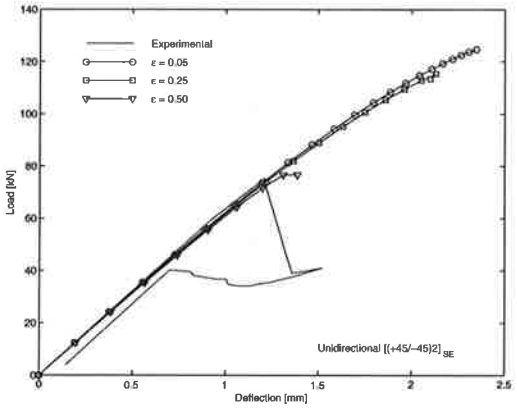
For the cylinder composed of the fabric $[0/+45/-45/0]$ laminate that exhibits a diamond numerical buckling shape, smaller imperfection amplitude $\varepsilon = 0.25$ gives the most accurate critical load with variation 3.0 %. Increasing the imperfection amplitude causes too critical prediction for the post-buckling behaviour.



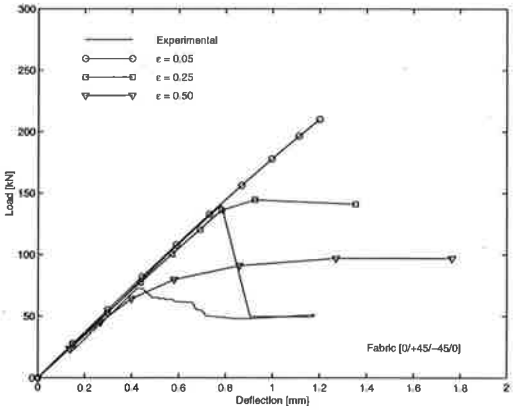
(a) Unidirectional shell, $m = 5$.



(b) Fabric shell, $m = 5$.



(c) Unidirectional shell, $m = 5, n = 13$.



(d) Fabric shell, $m = 5, n = 13$.

Figure 2: Elmer numerical-experimental correlation for the cylindrical CFRP shells with the unidirectional $[(+45/-45)2]_{\mathrm{SE}}$ and the fabric $[0/+45/-45/0]$ lay-up configurations and with the initial axisymmetric and diamond shape imperfections on the shell geometry.

	CL [kN]	d [mm]
Experimental [2]	140.20	1.18
Elmer nonlinear, ε=0.50	97.05	1.76
Elmer nonlinear, ε=0.25	144.46	1.35
Elmer nonlinear, ε=0.05	210.03	1.20
Elmer nonlinear, ε=0.0	270.36	1.63
Elmer linear buckling, ε=0.0	246.27	

Table 3: Comparison among critical loads and post-buckling deflections for the cylindrical shell with the fabric $[0/+45/-45/0]$ lay-up and the initial diamond shape imperfection, $m = 5, n = 13$.

Table 4 reports the knock-down factor Λ, i.e., the ratio between the buckling loads obtained for the cylinders with diamond imperfections and those of the cylinders without imperfections for the two considered lay-ups. The knock-down factor reflects the sensitivity of the buckling load with respect to the considered geometric imperfections. It can be seen that the diamond shape imperfection seems to be more critical for the cylinder with the fabric $[0/+45/-45/0]$ laminate structure than for the unidirectional $[(+45/-45)2]_{\mathrm{SE}}$ lay-up.

ε	Λ $[(+45/-45)2]_{\mathrm{SE}}$	Λ $[0/+45/-45/0]$
0.00	1.000	1.000
0.05	0.953	0.777
0.25	0.882	0.534
0.50	0.586	0.359

Table 4: Knock-down factors Λ for a diamond shape imperfections.

6 CONCLUSIONS

In this paper geometrically nonlinear post-buckling response of CFRP cylindrical shells under axial compression using Reissner-Mindlin-Von Kármán type facet model is considered. The study demonstrates that reasonable accuracy can be achieved with the numerical analysis compared to the experimental results by taking the geometric imperfection into account in the finite element model. Results show that bringing the diamond shape geometric imperfection in the model significantly improves the correlation in simulating cylindrical shell post-buckling response. The cylinder with the unidirectional $[(+45/-45)2]_{\mathrm{SE}}$ laminate structure appears less sensitive to the geometric imperfections than the cylinder with the fabric $[0/+45/-45/0]$ lay-up. The model was implemented in the Elmer open-source computational tool for multi-physics problems. The model is realiable in accuracy and computationally efficient to be used in engineering design and optimization of composite shells in the post-buckling field.

7 ACKNOWLEDGEMENT

The work of the first author was funded by the Academy of Finland postdoctoral researcher appropriation, Grant 202283, Project 204061.

REFERENCES

[1] C. Bisagni, Numerical Analysis and Experimental Correlation of Composite Shell Buckling and Postbuckling. *Composites: Part B*, **31**, 655–667, 2000.

[2] C. Bisagni and P. Cordisco, An Experimental Investigation into the Buckling and Postbuckling of CFRP shells under combined axial and torsion loading. *Composite Structures*, **60**, 391–402, 2003.

[3] F. Brezzi, M. Fortin, and R. Stenberg, Error analysis of mixed-interpolated elements for Reissner-Mindlin plates. *Math. Models Methods Appl. Sci.*, **1**, 125–151, 1991.

[4] *ElmerSolver Manual: Numerical Solution of Partial Differential Equations*. Espoo: CSC – Scientific Computing Ltd., 2004. Elmer web site at www.csc.fi/elmer.

[5] T. J. R. Hughes and F. Brezzi, On drilling degrees of freedom. *Computer Methods in Applied Mechanics and Engineering*, **72**, 105–121, 1989.

[6] R. M. Jones, *Mechanics of Composite Materials*, New York: Hemisphere Publishing Corporation, 1975.

[7] P. Kere and M. Lyly, Nonlinear Analysis and Design of Laminated Composites using Reissner-Mindlin-Von Kármán Type Plate Model. *Proc. 4th European Congress on Computational Methods in Applied Sciences and Engineering, ECCOMAS 2004*, Jyväskylä, Finland, 24–28 July, 2004. Vol. II, Minisymp. Multiobjective Optimization and Its Applications I.

[8] P. Kere and M. Lyly, Reissner-Mindlin-Von Kármán type plate model for nonlinear analysis of laminated composite structures. *Composite Structures*, **71**, 289–292, 2005.

[9] P. Kere and M. Lyly, "On Post-Buckling Analysis and Experimental Correlation of Cylindrical Composite Shells with Reissner-Mindlin-Von Kármán Type Facet Model", To appear in *Proc. III European Conference on Computational Mechanics, ECCM-2006*, Lisbon, Portugal, 5–9 June, 2006.

[10] P. Kere, J. Lento, M. Lyly, and A. Teräs, "A Structural Design Optimization System Exploiting Distributed Grid Resources", To appear in *Proc. 47th AIAA/ASME/ASCE/AHS/ASC Structures, Structural Dynamics and Materials Conference*, Newport, NY, USA, 1-4 May, 2006

[11] R. Kouhia, On the Solution of Non-linear Finite Element Equations, *Computers and Structures*, **44**, 243–254, 1992.

[12] R. Kouhia and M. Mikkola, Some Aspects on Efficient Path Following. *Computers and Structures*, **72**, 509–524, 1999.

[13] M. Lyly, On the connection between some linear triangular Reissner-Mindlin plate bending elements. *Numer. Math.*, **85**, 77–107, 2000.

[14] E. Ramm, Strategies for Tracing the Nonlinear Response Near Limit Points. *Nonlinear Finite Element Analysis in structural Mechanics*, Bochum, Germany, Springer Verlag, 63–89, 1981.

[15] R. Reitinger and E. Ramm, Buckling and Imperfection Sensitivity in the Optimization of Shell structures. *Thin-Walled Structures*, **23**, 159–177, 1995.

[16] W. C. Rheinboldt, *Numerical Analysis of Parametrized Nonlinear Equations*, Wiley, 1986.

[17] E. Riks, The Application of Newton's Method to The Problem of Elastic Stability, *Journal of Applied Mechanics*, **39**, 1060–1065, 1972.

ANALYSIS OF STRONGLY COUPLED FLUID-STRUCTURE INTERACTION PROBLEM USING OPTIMIZATION PRINCIPLE

Matti Kurki
Metso Paper
P.O.B. 587 Jyväskylä
matti.kurki@metso.com

Johan Åkerholm
Process Flow Ltd.
Puolalanpuisto 1b A21, 20100 Turku
johan@processflow.fi

ABSTRACT

Numerical analysis of both structural and fluid dynamics problems has reached inevitable position in modern engineering. In mechanical engineering, complicated shapes and nonlinear problems are forming an area where numerical analyses are most beneficial – and often the only way - in finding accurate results.
In this paper we present a strongly coupled engineering problem, where coupled analysis method of turbulent air flows and moving slender web is performed. Nonlinear, sensitively coupled web conveyance has been analysed together using proper fluid dynamics analysis program, Fluent. Nonlinear web behaviour is assumed in two dimensions including tension dependence according out-of-plane deformations.

1. INTRODUCTION

In papermaking the appropriate processing and careful handling of moving web is one of the most important factor supporting paper machine 's good efficiency.
The upcoming limitations appearing in high-speed papermaking are coming from physics; fluid flow along the moving web and inertial laws are creating environment where smooth, undisturbed (and boring) web conveyance becomes difficult. Especially, paper making processes accompanied with water are difficult. In those occasions, also the deterioration of material will further increase web handling challenge.

In this article, we present a method solving fluid-structure interaction (FSI) problem created by moving web and surrounding air. Due to the nature of air, which includes, low density accompanied with low viscosity, the nature of fluid flow is always turbulent. On the other hand,

the moving, relatively light paper web with large area connected with turbulent fluid flow creates a challenging environment both for real life web handling but also for reliable FSI computations.

2. DYNAMICS OF MOVING WEB

Dynamics of moving web is studied widely earlier and applied in industry in different applications [1; 2; 3; 4]. In the case of nonlinear, large displacement analysis of moving, tensioned medium, the variation between models is greater. For example, equation for transverse non-linear vibration derived using Hamilton's principle is following (for vertical displacement w) [1]:

$$\rho A \frac{\partial^2 w}{\partial t^2} + 2\rho A c \frac{\partial^2 w}{\partial x \partial t} + \left(\rho A c^2 - EA\right)\frac{\partial^2 w}{\partial x^2} + EI\frac{\partial^4 w}{\partial x^4} + \left(EA - F_0\right)\frac{\left(1+\frac{\partial u}{\partial x}\right)^2 \frac{\partial^2 w}{\partial x^2} - \left(1+\frac{\partial u}{\partial x}\right)\frac{\partial w}{\partial x}\frac{\partial^2 u}{\partial x^2}}{\left[\left(1+\frac{\partial u}{\partial x}\right)^2 + \left(\frac{\partial w}{\partial x}\right)^2\right]^{\frac{3}{2}}} = 0 \quad (1)$$

, where

A	=	Cross-sectional area of the web or string, m^2
c	=	Axial velocity, m/s
E	=	Modulus of elasticity, N/m^2
F	=	Axial force, N
u	=	Axial displacement, m
w	=	Vertical displacement, m
ρ	=	Web density, kg/m^3

In above approach also longitudinal strain component $\partial u/\partial x$ has been included in order to take account the nonlinear tensioning of the web with non-zero displacements [1]. This approach is suitable for closed loop web tensioning system but does not apply in the case of open, continuous web conveyance system. Another approach is to use arc-shaped differential element in derivation of the force balance equations. In the case oh mixed Euler-Lagrange formulation this leads to different non-linear approach, especially, higher order non-linearities are possible to include in the force balance equation [5]:

$$T = \Delta p R + m g R \cos\Theta + \frac{E h^3}{12}\frac{\partial^4 w}{\partial x^4} R + m R \cos\Theta\left[\frac{\partial^2 w}{\partial t^2} + 2\frac{du}{dt}\frac{\partial^2 w}{\partial x \partial t} + \left(\frac{du}{dt}\right)^2 \frac{\partial^2 w}{\partial x^2}\right] - \frac{1}{2} C_d \rho_a R\left[\left(\frac{dw}{dt}\right)^2 \cos^2\Theta - \left(\frac{du}{dt}\right)^2 \sin^2\Theta\right] \quad (2)$$

, where

C_d	=	Drag constant of the web
g	=	gravitational constant, 9.81 m^2/s
h	=	Thickness of the web, m
m	=	Basis weight, kg/m^2

Δp = External pressure load difference between surfaces of the web, N/m^2
R = R(x) = Local radius of the web, m
T = Web tension, N/m
ρ_a = Air density, kg/m^3
Θ = Local out-of-plane angle of the web, radian

Radius R = R(x) can be expressed also:

$$\frac{1}{R} = \frac{\frac{\partial^2 w}{\partial x^2}}{\left[1+\left(\frac{\partial w}{\partial x}\right)^2\right]^{\frac{3}{2}}} \tag{3}$$

Also, forces developing along the web length can be included in the model, but are omitted from above presentation for simplicity.

In the case of FSI system, we have two approaches to solve the problem, time-dependent transient analysis or steady-state moving web system. In the latter approach, the actual time dependency is not used, rather, the web is assumed to move with transfer speed $\dot{u}$ (or c in Eq. 1) in continuous, undisturbed manner. The transfer speed $\dot{u}$ is [5] :

$$\frac{du}{dt} = v\cos\Theta - \frac{\partial w}{\partial t}\sin\Theta\cos\Theta \tag{4}$$

where,

v = tangential velocity, m/s

If we substitute Eq. 3 to Eq. 2 and omit time-dependent term we will obtain following steady-state equation for moving web in unsupported, open draw environment:

$$T = \Delta p\, R + m\, g\, R\cos\Theta + \frac{E\, h^3}{12}\frac{\partial^4 w}{\partial x^4} R + mv^2 \quad , \text{or} \tag{5}$$

$$\frac{\partial^2 w}{\partial x^2}\left(T - mv^2\right) = \left[1+\left(\frac{\partial w}{\partial x}\right)^2\right]^{\frac{3}{2}}\left(\Delta p + m\, g\sqrt{1+\left(\frac{\partial w}{\partial x}\right)^2} + \frac{E\, h^3}{12}\frac{\partial^4 w}{\partial x^4}\right) \tag{6}$$

$$T = K\varepsilon = \frac{\Delta v}{v} \tag{7}$$

, where

K = Stiffness (elasticity) of the web, N/m
ε = Strain applied to web in the end of open draw, 1
h = Thickness of web, m

The nature of Eq. 5 becomes apparent with an example. Tension T in Eq. 5 defines the state of tension unambiguously, external loads or other force components do not affect the tension level, those only change the geometrical shape of the moving web path.

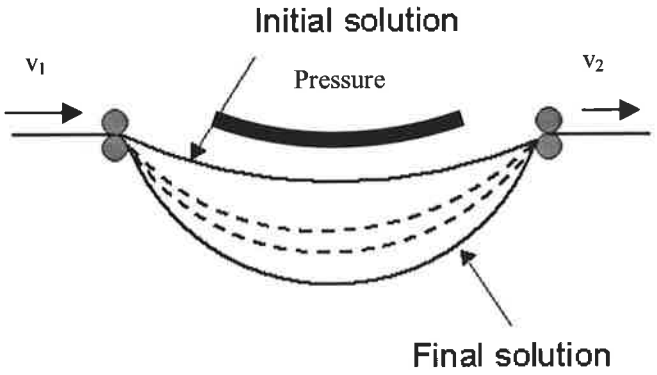


Figure 1. The geometrical shape change of web span as function of velocity, see Fig. 2. [5].

Same effect can be observed with the case of speed increase. Web velocity increases the tension distribution between components presented in Eq. 5. Schematic behavior can be seen in Fig. 2. With same, constant strain value also the tension remains same, and it is not depending on web velocity. This, however, leads to excessively small web radiuses, especially centripetal tension component, mv^2 increases, since it is not dependent on web curvature [5; 6; 7].

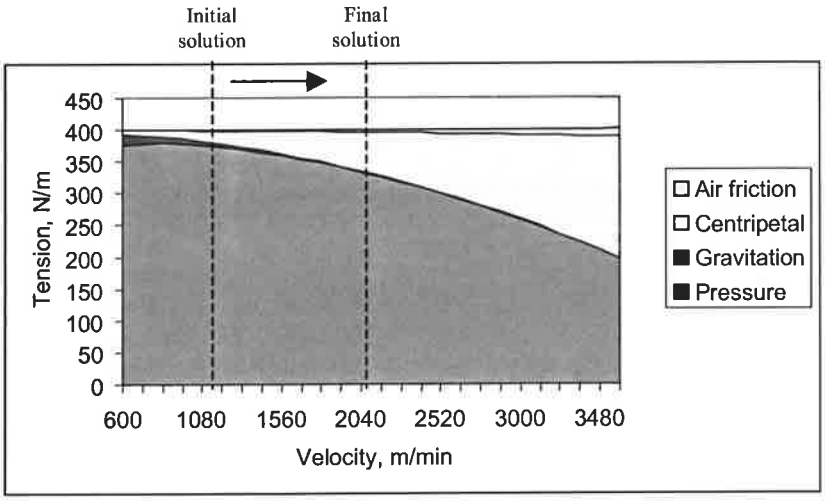


Figure 2. Exemplary tension behaviour & tension component distribution of moving web system under unchanged open draw strain level [5].

On the other hand in practical situations, too large geometric deformations are more susceptible to runnability deterioration and unstable web behavior. For this reason, web tension must be increased, if geometrical path of the web will be kept constant.

3. CFD OF THE AIR FLOWS IN PAPER MAKING ENVIRONMENT

A paper machine environment puts high demand on computational fluid dynamics. Most of the flows are boundary layer driven, which puts extra demand on the near wall treatment in modelling. Typical simulations include moving porous medias, such as fabrics, press felts and drilled, permeable rolls. A porous media usually transports much air and dominates easily the flow field, thus an accurate modelling of the moving web materials is essential. Models based on small scale to large scale flow field transformations have been develop in order to coupe with the difficult flow behaviour and the impact on turbulence in the calculation domain [8].

The CFD calculations are carried out with Fluent software with RANS model. The flow is turbulent and modelled with a k-e turbulence model. The wall treatment is however more sophisticated than for the standard wall function, which means far better boundary layer simulation, at the cost of computational time. The modelling is carried out in 2D, which means that computation time is still very moderate. Mass and momentum conservation are presented with Eqs. 8 and 9 [9].

$$\frac{\partial \rho_g}{\partial t} + \nabla(\rho_g v) = S_m \tag{8}$$

$$\frac{\partial v}{\partial t}\rho_g + \nabla(\rho_g vv) = -\nabla p + \nabla\tau + \rho_g g + F \tag{9}$$

where,

v	= Velocity vector, m/s
p	= Static pressure, Pa
ρ_g	= Density of the fluid (gas), kg/m^3
τ	= Stress tensor, N/m^2
F	= Body force, N/m^3

The body force F includes also source terms as from porous media. S is presenting mass Source terms. ρ_g refers now to the gas density, as these equations are only applied to the fluid .

The transport equation for the turbulent kinetic energy, k, can be written according to Eq. 10:

$$\frac{\partial k}{\partial t}\rho_g + \frac{\partial k}{\partial x_i}\rho_g v_i = \frac{\partial}{\partial x_j}\left(\alpha_k \mu_{eff}\frac{\partial k}{\partial x_j}\right) + G_k + G_b - \rho_g \varepsilon - Y_M + S_k \tag{10}$$

And the corresponding transport equation for the turbulent dissipation rate, ε_t, according to Eq. 11:

$$\frac{\partial \varepsilon_t}{\partial t}\rho_g + \frac{\partial \varepsilon_t}{\partial x_i}\rho_g v_i = \frac{\partial}{\partial x_j}\left(\alpha_k \mu_{eff}\frac{\partial \varepsilon_t}{\partial x_j}\right) + C_{1\varepsilon}\frac{\varepsilon_t}{k}(G_k + C_{3\varepsilon}G_b) - C_{2\varepsilon}\rho_g\frac{\varepsilon_t^2}{k} - R_\varepsilon + S_\varepsilon \tag{11}$$

In these equations, G_k represents the generation of turbulence kinetic energy due to the mean velocity gradients. G_b is the generation of turbulence kinetic energy due to buoyancy. Y_M represents the contribution of the fluctuating dilatation in compressible turbulence to the overall dissipation rate. The quantities α_k and α_e are the inverse effective Prandtl numbers for k and ε, respectively. S_k and S_e are user-defined source terms. All experimental coefficients are marked

with C_X. The effective fluid viscosity μ_{eff} in the RNG k-e model is calculated using nominal viscosity μ with Eq. 12.

$$\frac{d}{d\mu_{eff}/\mu}\left(\frac{\rho_g{}^2 k}{\sqrt{\varepsilon_1 \mu}}\right) = 1.72\frac{\mu_{eff}/\mu}{\sqrt{(\mu_{eff}/\mu)^3 - 1 + C}} \tag{12}$$

In Fluent's near-wall model, the viscosity-affected near-wall region is completely resolved all the way to the viscous sub layer. In the approach, the whole domain is subdivided into a viscosity-affected region and a fully-turbulent region, thus called the two layer model. The demarcation of the two regions is determined by a wall-distance-based, turbulent Reynolds number, Re_y, defined as

$$Re_y = \frac{\rho_g y\sqrt{k}}{\mu} \tag{13}$$

where y is the normal distance from the wall at the cell centres. In the viscosity-affected near-wall region (Re_y < 200), the one-equation model of Wolfstein [10] is employed. The enhanced turbulent law-of-the-wall for compressible flow with heat transfer and pressure gradients has been derived by combining the approaches of White and Cristoph [11] and Huang et al. [12]. Enhanced wall functions are developed for smoothly blend an enhanced turbulent wall law with the laminar wall law. By securing sufficiently high computation mesh resolution at the surface of the wall it is possible to compute the velocity profile starting from the laminar sub layer of the boundary, i.e.

$$\frac{du}{dy} = 1 + \alpha y, \qquad \text{where } \alpha = \frac{\mu}{\rho_g{}^2 u_w^3}\frac{dp}{dx} \tag{14, 15}$$

y is the orthogonal distance from the wall and u is the velocity in the direction of the wall. The further away from the surface the computation cell is the large the effect of the enhanced turbulent wall law and thus there are more approximations and modelling errors present.

4. FSI SOLUTION WITH OPTIMIZATION ALGORITHM

The paper web mechanics and fluid dynamics are coupled using a stand-alone program. The developed model couples the preprocessor and the CFD solver with the mechanical model, which is functioning as a master process. The program gives instructions to the preprocessor and complete re-meshing can be carried out if desired. The boundary conditions of the CFD solver are also set by the program, while a new mesh file is provided.

The web is discretized into small pieces, not necessarily as small as the computational grid for the CFD-analyses however. The shape of the web is optimized so that the values of C_{func} in Eq. 16, are as small as possible of each piece of the web. Eq. 16 is a direct rewriting of Eq. 5 and includes the pressure force and the bending stiffness of the web.

$$C_{func} = \left|\frac{1}{R} + \frac{\Delta p}{mv^2 - T} + \frac{Eh^3}{12\cdot(mv^2 - T)}\cdot\frac{3}{R^3}\right| \tag{16}$$

Three moving points, according to figure 1 points X-3, X-2 and X-1, define one web segment. The pressure difference over each piece is the difference between mean pressure above and below the web in the CFD grid cells, which are located between point x-3 and X-1. The radius R, or curvature 1/R, is assumed to have circumferential shape.

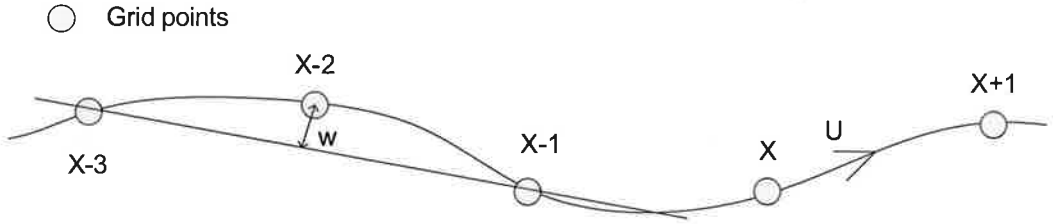


Figure 3. A schematic picture of the discretized web.

The coupling between pressure and place and shape of the web is anything but linear. Sometimes there is a very loose coupling, i.e. the web can be moved several millimeters, but the pressure remain at the same level. However, there is quite often tighter coupling between the pressure and the shape of the web. This makes the modeling much more difficult, while you cannot calculate a new place and shape of the web, directly from the pressure information you get from a CFD run, mainly because of the geometrical restrictions. This means that the movement of the web has to be carried out iteratively and that the web cannot be moved very much at each step. Eq. 11 gives a value on how much the current web shape is in conflict with the pressure difference over the web. This value is minimized by moving the optimization points, but the movement of the points has to be relaxed. The relaxation is dependent on the simulation case and the coupling characteristics.

5. COMPARISON WITH MEASUREMENTS

Developed model has been tested and results between measurements and simulations have been compared. The experimental setup is described in with Fig. 4. There are air jet nozzles on each side of the paper web. The air velocity in the nozzles, web tension, the basis weight of the web and web speed has been experimental parameters. The results shown in this paper are taken from a situation with web speed 2200 m/min, air velocity in nozzle 30 m/s, paper weight 50 g/m² with variable web tension.

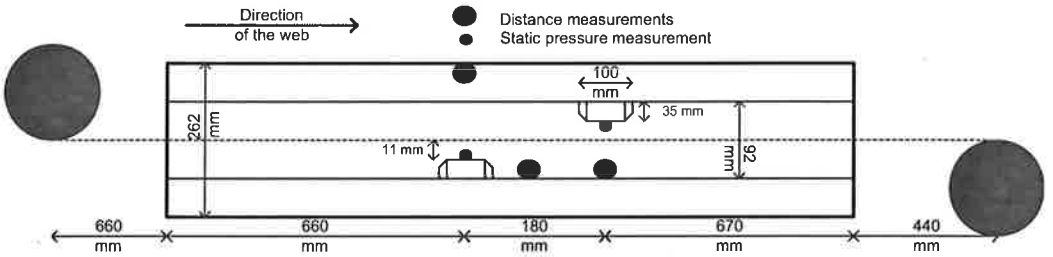


Figure 4. A schematic presentation of the experimental setup.

The general results from the simulation model are presented in Figs. 5-7. The simulation results of web coordinates and static pressure at the nozzles are compared with the experimental data in Figs. 8 and 9. The mechanical model predicts the shape of the web rather well, as can be seen from the results below. Both the trends and the absolute values of the measurements and the simulation fit with each other.

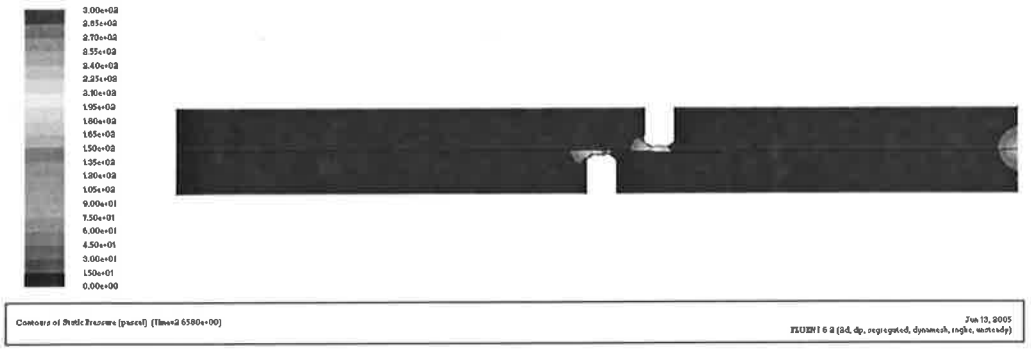


Figure 5. The figure shows the static pressure in the calculation domain. The pressure difference is mainly located in the nozzles.

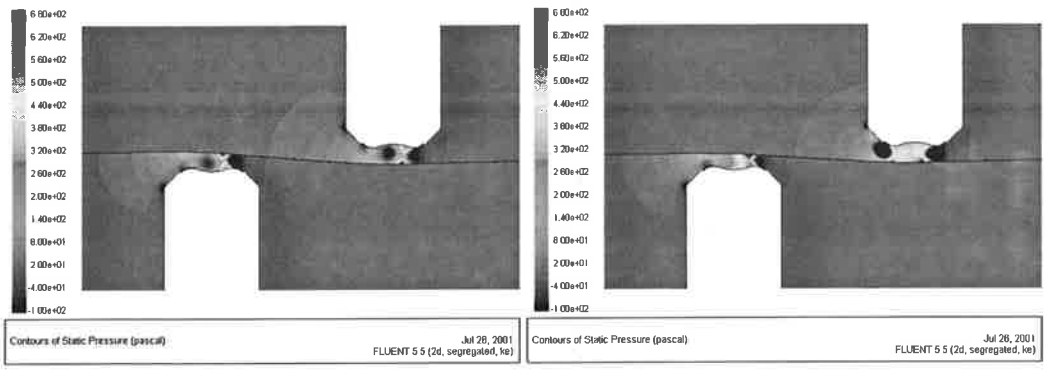


Figure 6. The picture on the left shows the pressure at the nozzles when the web has low web tension (100 N/m). Picture on the right shows the situation when all settings, except the web tension which is increased to 300 N/m, are kept constant.

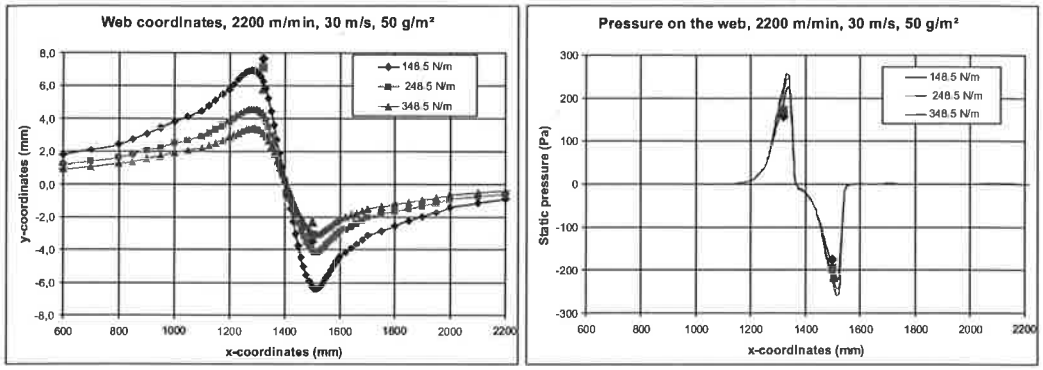


Figure 7. To the left the web coordinates for cases with three different levels of web tension are presented and to the right you see the corresponding static pressure difference over the web.

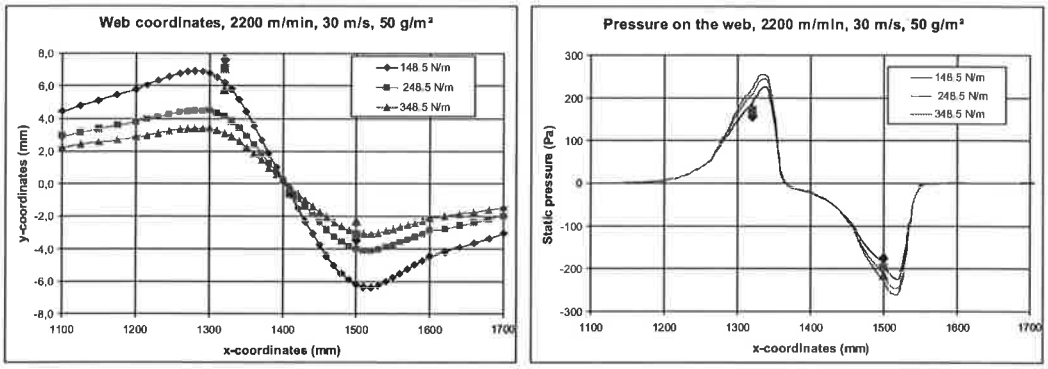


Figure 8. These figures show close-ups of the nozzle regions in the figures above.

6. DISCUSSION AND CONCLUSIONS

In fluid-structure interaction (FSI) problem area generally the flow of gaseous medium accompanied with the movement of contacting structure forms a special kind of combination. Viscosity & density properties of gases are generally very low and therefore from the viewpoint of FSI, fluid flow analysis is nearly always turbulent.

For these reasons, the functionality and selection appropriate turbulence model of used CFD analysis program is in essential position. As described earlier, only slight movements in the boundary of the structure can cause great changes in the nature of the flow.

Generally, in moving web-air flow analysis area problem can be 1) steady-state moving-web – surrounding pressure analysis or 2) time-dependent analysis. Time-dependent analysis can be further divided in two categories, where 2a) fluid flow presents time-dependent behaviour but movements of the web are so slow, that actual inertial time-dependent vibration or flutter does not exist. On fully time-dependent analysis 2b) both air and web movements are coupled creating often difficult, self-amplifying physical system. Obviously, numerical analysis of this kind of system is very challenging.

Each of these cases creates a situation, where the CFD problem solver has to chosen carefully. In the case of slow, time-dependent solving it is not always necessary to use time-dependent CFD model, (Larger Eddy Simulation / LES, Direct Numerical Solving / DNS) since their usage does not give any extra value to the accuracy of the results.
Web handling simulation tool presented here gives excellent possibilities to evaluate steady-state behaviour of moving web, especially in paper making environment. Most important stabilization criteria is the web tension, which also often determines the nature of web conveyance. When web tension lowers, potential to the instability of the web becomes higher and finally we are reaching situation where no stable solution could be found. Thus, one of the key items will be in the finding of the areas where stability of the web can be ensured.
In future, higher emphasis will be targeted to the solution speed and solution stability of presented web handling analysing tool. This will include the usage of FEM solution of the web dynamics in order to take account better the nonlinearities. Also, time-dependent analysis will become more important since paper machine production speeds are increasing and sufficient web handling must be performed also with higher web velocity levels [13].

ACKNOWLEDGEMENTS

Authors would like to thank Tekes, Kenneth Eriksson from Process Flow ltd. and Metso Paper for supporting the development and research work in realization of this model.

REFERENCES

1. Thurman, A., L. and Mote C., D. Jr., Free, Periodic, Nonlinear Oscillation of an Axially Moving Strip. J. App. Mech., (3), 83…91, 1969.

2. Ulsoy, A., G. and Mote, C., D. Jr., Vibration of Wide Band Saw Blades. ASME J. Eng. Ind., 104(1), 71…78, 1982.

3. Perkins, N., C. and Mote, C., D. Jr., Three Dimensional Vibration of Travelling Elastic Cables. J. Sound Vib, 114 (2), 325…340, 1987.

4. Pramila, A. Sheet Flutter and the Interaction Between Sheet and Air. TAPPI Journal, 69(7), 70…74, 1986.

5. Kurki, M. "Modeling of Kinematical and Rheological Web Line Behavior in a Papermaking Environment". Licentiate Thesis, University of Lappeenranta, 2005.

6. Pakarinen, P., Ryymin, R., Kurki, M. & Taskinen, P. On the Dynamics of Web Transfer in an Open Draw. Proceedings of the Second International Conference of Web Handling, 1993. Stillwater, Oklahoma: Web Handling Research Center, section 10, p. 1…18.

7. Kurki, M., Vestola J., Martikainen P. & Pakarinen P. The Effect of Web Rheology and Peeling on Web Transfer in Open Draw, Proceedings of the Fourth International Conference of Web Handling, 1997. Stillwater, Oklahoma: Web Handling Research Center. p. 443.

8. K. Laakkonen, "Computational Flow-Field Modeling of Paper Machine Dryer Fabric", Tampere University of Technology, Publications 414, 2003

9. Fluent Users Manual version 6.2.16, published 2005

10. M. Wolfstein, "The Velocity and Temperature Distribution of One-Dimensional Flow with Turbulence Augmentation and Pressure Gradient." *Int. J. Heat Mass Transfer*, 12:301- 318, 1969.

11. F. White and G. Christoph. "A Simple New Analysis of Compressible Turbulent Skin Friction Under Arbitrary Conditions."Technical Report AFFDL-TR-70-133, February 1971.

12. P. Huang, P. Bradshaw, and T. Coakley. "Skin Friction and Velocity Profile Family for Compressible Turbulent Boundary Layers." *AIAA Journal*, 31(9):1600-1604, September 1993.

13. Kurki, M., Kouko, J., Kekko, P., Saari, T., Laboratory scale measurement procedure of paper machine wet web runnability. Part 1, Paperi ja Puu, 86(4):2004, 256...262.

SURFACE TENSION PROBLEMS, VIRTUAL WORK AND FREE BOUNDARY

M. REIVINEN, E.-M. SALONEN
Department of Civil and Environmental Engineering
Helsinki University of Technology
P.O.Box 2100, FIN-02015 HUT
e-mail: mika.reivinen@tkk.fi

ABSTRACT

The problem considered consists of the determination of the shape of the interface between a liquid and vapor. The interface is attached to a solid surface. A part of the contact line between the interface and the solid may be free. In more detail, this means that the position of the contact line is initially unknown and only the contact angle, determined by the Young's equation, is known. The consideration in this initial study is restricted to two dimensions. The problem is expressed by using the principle of virtual work. Special emphasis is put on the proper representation of the virtual work terms emerging from the free boundary. A discrete formulation employing a line segment model is described and applied to a simple model problem.

1. INTRODUCTION

When, say, a fluid drop rests on a solid surface, the contact angle θ the fluid surface makes with the solid surface is usually assumed to obey the so-called Young's equation (e.g. [1] and [2])

$$\sigma \cos\theta = \sigma_{sv} - \sigma_{sl} . \tag{1}$$

The quantities σ, σ_{sv} and σ_{sl} are the surface energy densities or surface tensions of the liquid-vapor, solid-vapor and solid-liquid interfaces, respectively. These quantities are considered as given material parameters and determine the value of the contact angle. In a shape determination problem the position of the contact line where the Young's equation is valid is usually unknown and forms a part of the problem. The contact line may be called as a free boundary.

We consider in this article the shape determination in surface tension problems having a free boundary. The problem is expressed using the principle of virtual work. Special emphasis is put on the proper representation of the virtual work terms emerging from the free boundary. Some peculiarities concerning real and virtual displacements in surface tension problems compared with ordinary structural problems are discussed. A discrete formulation employing a line segment model is described and applied to a simple model problem.

2. NOTATIONS AND GOVERNING EQUATIONS

The contents of this article may be considered as an initial study to find the applicability of our discrete formulation with respect to the free boundary so the problem is simplified here to be two-dimensional. The basic setting, presented in Figure 1, consists of a liquid (l), surrounded by a vapor (v) and resting in equilibrium on a solid (s). The task is to determine the position of the interface C between the liquid and vapor. The shape $\hat{C}$ of the solid surface is considered as given.

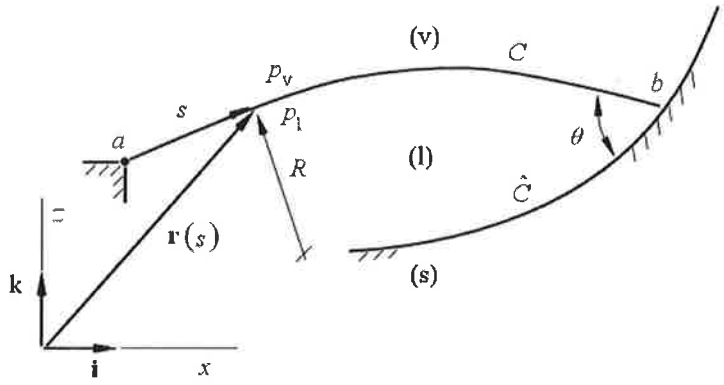


Figure 1 Some notations.

The arc length s along the interface is used as the curve parameter and the position vector to a generic point on the interface curve C is thus expressed by the function $\mathbf{r} = \mathbf{r}(s)$ to be determined. We assume according to Figure 1 that at point a the interface position is fixed and point b corresponds to the free boundary.

At the liquid-vapor interface the well-known Laplace equation (e.g. [1], [2]) is valid:

$$p_l - p_v = \frac{\sigma}{R}. \tag{2}$$

Here p_l and p_v are the pressures in the liquid and vapor, respectively, evaluated at the interface and $1/R$ is the curvature of the interface positive when the center of curvature is on the liquid side.

Shortly, the shape determination problem consists here mathematically of equations (2) and (1) with the shape of the solid surface given and at point a fixed. Additionally, something must be assumed about the pressure fields.

As we are here mainly interested in studying how the discrete formulation can cope with the free boundary, we neglect among other things gravity effects and assume in the application that a given constant pressure difference $p_l - p_v$ acts on the interface. Then the analytical exact solution is simply a segment of a circle.

Quite often, contrary to what is considered here, the volume (or here the cross-sectional area) of the liquid is given. Then the pressure level in the liquid is an unknown. By assuming here the pressure difference as given means physically that the liquid can be in contact with liquid environment through a "hole" in the solid surface.

3. VIRTUAL WORK

The virtual work equation associated with the liquid-vapor interface is

$$\delta' W \equiv \delta' W^{\text{int}} + \delta' W^{\text{ext}} + \delta' W^{\text{bound}} = 0. \tag{3}$$

The virtual work consists of the virtual work of internal forces, of external forces and of the contribution associated with the free boundary, We will consider these terms separately in the following. We will give the appropriate expressions for shortness of presentation without detailed derivations. The validity of the expressions comes finally by deducing the strong forms corresponding to (3).

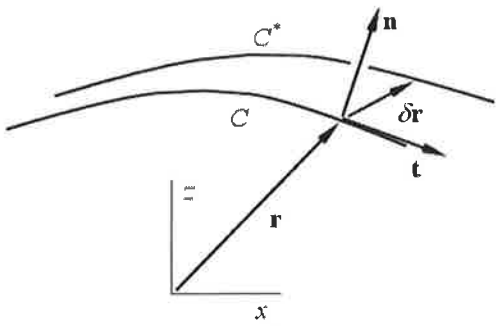


Figure 2 Position vector **r** and virtual movement $\delta\mathbf{r}$.

As mentioned above, let the position vector to a generic point on the interface curve C be denoted by $\mathbf{r}(s)$ and let the corresponding point on a varied comparison curve C^* be given by $\mathbf{r}(s)+\delta\mathbf{r}(s)$ (Figure 2). The principle of virtual work is normally applied to closed mechanical systems consisting of identifiable particles or continuum points whose positions and movements can at least in principle be followed. With a "soap bubble surface" we deal with a kind of mathematical surface and we no more can keep track of the positions of individual particles. For instance, if we imagine a comparison configuration defined by a "virtual displacement" $\delta\mathbf{r}$, contrary to normal mechanical systems, vector $\delta\mathbf{r}$ does not necessarily correspond to a displacement of a particle but it is just a directed line segment defining in a certain direction the distance to the neighboring surface. Further, we are not sure if our system is closed; maybe at a comparison configuration some material has arrived from the surroundings, say through the free boundary to the interface. Thus we may be somewhat unsure about applying the principle of virtual work just the way we are used to. To emphasize the present situation, we will employ instead of the term virtual displacement the term virtual movement for $\delta\mathbf{r}$. This terminology appears also in [2].

The virtual work of internal forces is

$$\delta' W^{\text{int}} = -\int_s \sigma\,\delta\varepsilon\,\mathrm{d}s \tag{4}$$

where the virtual relative change of length of an arc differential element

$$\delta\varepsilon = \mathbf{t}\cdot\frac{\mathrm{d}(\delta\mathbf{r})}{\mathrm{d}s}. \tag{5}$$

t is the unit tangent vector to the interface curve (Figure 2). As σ is here a constant, it can, if wanted, be taken outside the integral sign in (4).

The virtual work of external forces is (here we consider the general case where the pressure difference can vary arbitrarily along the interface)

$$\delta' W^{\text{ext}} = \int_s (p_{\text{l}} - p_{\text{v}})\,\delta n\,\mathrm{d}s \tag{6}$$

where the virtual movement component in the normal direction

$$\delta n = \mathbf{n}\cdot\delta\mathbf{r}. \tag{7}$$

n is the unit normal vector to the interface curve (Figure 2).

The virtual work from the free boundary is

$$\delta' W^{\text{bound}} = \sigma \delta e + (\sigma_{sv} - \sigma_{sl}) \delta \hat{e} \tag{8}$$

where

$$\delta e = -\frac{\hat{\mathbf{n}} \cdot \delta \mathbf{r}}{\sin \theta} \tag{9}$$

and

$$\delta \hat{e} = \frac{\mathbf{n} \cdot \delta \mathbf{r}}{\sin \theta}. \tag{10}$$

Of course, these terms must be evaluated at the free boundary. $\hat{\mathbf{n}}$ is the unit normal vector to the solid surface directed towards the liquid-vapor side.

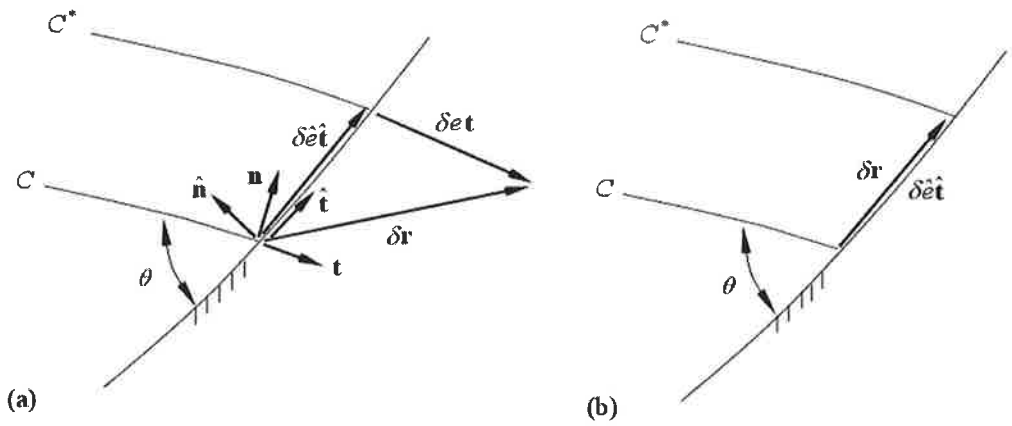


Figure 3 (a) Details around the free boundary. **(b)** Virtual movement along the solid surface.

Figure 3 (a) shows some details corresponding to formulas (8) to (10). In fact, quantities δe and $\delta \hat{e}$ appear in the representation

$$\delta \mathbf{r} = \delta e \mathbf{t} + \delta \hat{e} \hat{\mathbf{t}} \tag{11}$$

where $\hat{\mathbf{t}}$ is the unit tangent vector to the solid surface.

If the movement is taken along the solid surface (Figure 3 (b)), (8) simplifies as δe is zero. However, $\delta \mathbf{r}$ can be directed here anywhere at the free boundary. We may note the following. If Figure 3 (a) would refer to, say, a rod end on a roller support, conventional virtual displacement would have to be taken along the tangent to the surface. This because otherwise the originally unknown support reaction force would appear in the virtual work equation. Here, however, σ, σ_{sv} and σ_{sl} are given quantities in (8) and nothing special happens if the direction of $\delta \mathbf{r}$ deviates from $\hat{\mathbf{t}}$.

Collecting all the terms given above, the virtual work equation (3) obtains the form

$$-\int_s \sigma \mathbf{t}\cdot\frac{\mathrm{d}(\delta\mathbf{r})}{\mathrm{d}s}\mathrm{d}s+\int_s (p_\mathrm{l}-p_\mathrm{v})\mathbf{n}\cdot\delta\mathbf{r}\,\mathrm{d}s.$$
$$-\sigma\frac{\hat{\mathbf{n}}\cdot\delta\mathbf{r}}{\sin\theta}\Big|_{s=s_\mathrm{b}}+(\sigma_{\mathrm{sv}}-\sigma_{\mathrm{sl}})\frac{\mathbf{n}\cdot\delta\mathbf{r}}{\sin\theta}\Big|_{s=s_\mathrm{b}}=0. \tag{12}$$

Additionally, $\delta\mathbf{r}$ is restrained to vanish at the fixed boundary point *a*. To deduce the strong forms from the weak form (12), we have to integrate by parts the first term on the left-hand side:

$$-\int_s \sigma\mathbf{t}\cdot\frac{\mathrm{d}(\delta\mathbf{r})}{\mathrm{d}s}\mathrm{d}s=\int_s \sigma\frac{\mathrm{d}\mathbf{t}}{\mathrm{d}s}\cdot\delta\mathbf{r}\,\mathrm{d}s-\Big|_{s_\mathrm{a}}^{s_\mathrm{b}}\sigma\mathbf{t}\cdot\delta\mathbf{r}$$
$$=-\int_s\frac{\sigma}{R}\mathbf{n}\cdot\delta\mathbf{r}\,\mathrm{d}s-\sigma\mathbf{t}\cdot\delta\mathbf{r}\Big|_{s=s_\mathrm{b}} \tag{13}$$

Frenet formula $\mathrm{d}\mathbf{t}/\mathrm{d}s=-\mathbf{n}/R$ has been applied. Equation (12) becomes

$$\int_s\left[-\frac{\sigma}{R}+p_\mathrm{l}-p_\mathrm{v}\right]\mathbf{n}\cdot\delta\mathbf{r}\,\mathrm{d}s$$
$$+\left[-\sigma\left(\mathbf{t}+\frac{\hat{\mathbf{n}}}{\sin\theta}\right)+(\sigma_{\mathrm{sv}}-\sigma_{\mathrm{sl}})\frac{\mathbf{n}}{\sin\theta}\right]\cdot\delta\mathbf{r}\Big|_{s=s_\mathrm{b}}=0. \tag{14}$$

From the integral we get immediately the correct field equation

$$p_\mathrm{l}-p_\mathrm{v}=\frac{\sigma}{R},\quad s_\mathrm{a}<s<s_\mathrm{b}. \tag{15}$$

From the geometry of Figure 3 (a)

$$\hat{\mathbf{n}}=-\sin\theta\,\mathbf{t}+\cos\theta\,\mathbf{n}. \tag{16}$$

Thus,

$$\mathbf{t}+\frac{\hat{\mathbf{n}}}{\sin\theta}=\frac{\sin\theta\,\mathbf{t}+\hat{\mathbf{n}}}{\sin\theta}=\frac{\cos\theta\,\mathbf{n}}{\sin\theta}. \tag{17}$$

The free boundary term in (14) becomes

$$\frac{1}{\sin\theta}\left[-\sigma\cos\theta+\sigma_{\mathrm{sv}}-\sigma_{\mathrm{sl}}\right]\mathbf{n}\cdot\delta\mathbf{r}\Big|_{s=s_\mathrm{b}} \tag{18}$$

and the correct condition

$$\sigma\cos\theta=\sigma_{\mathrm{sv}}-\sigma_{\mathrm{sl}} \tag{19}$$

follows.

As the virtual work approach does not need, say, potential energy concepts etc. (as for example in [3]), it seems to be both the most general and the most straightforward basis for discrete methods in surface tension problems. Further, Young's equation is still obtained as a natural boundary condition.

4. DISCRETE FORMULATION; LINE SEGMENTS

The liquid-vapor interface is discretized by two-noded line segments or elements. Figure 4 shows the notations for a generic line segment. The position vector along the segment is given by

$$\mathbf{r} = (1-\xi)\mathbf{r}_1 + \xi\mathbf{r}_2 \tag{20}$$

where instead of the local arc length s the dimensionless coordinate $\xi = s/L$ is used. The length of the segment is given by

$$L = \sqrt{(x_2 - x_1)^2 + (z_2 - z_1)^2}. \tag{21}$$

The generalized coordinates are (normally) the nodal Cartesian coordinates x_1, z_1, x_2, z_2. More correctly, as discussed below, the generalized coordinates or movements are defined in principle always anew with respect to a preliminary geometry (guessed or updated). Let the coordinates of the segment in the preliminary position be denoted $\overline{x}_1$, $\overline{z}_1$, $\overline{x}_2$, $\overline{z}_2$. Then the generalized movements are in more detail $\Delta x_1 = x_1 - \overline{x}_1$, $\Delta z_1 = z_1 - \overline{z}_1$, $\Delta x_2 = x_2 - \overline{x}_2$, $\Delta z_2 = z_2 - \overline{z}_2$.

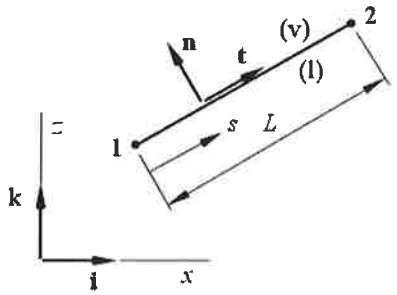


Figure 4 A generic line segment.

The virtual movements of the nodes are by variation ($\overline{x}_1$ etc. are fixed)

$$\begin{aligned} \delta\mathbf{r}_1 &= \delta(\Delta x_1)\mathbf{i} + \delta(\Delta z_1)\mathbf{k} = \delta x_1\mathbf{i} + \delta z_1\mathbf{k}, \\ \delta\mathbf{r}_2 &= \delta(\Delta x_2)\mathbf{i} + \delta(\Delta z_2)\mathbf{k} = \delta x_2\mathbf{i} + \delta z_2\mathbf{k}. \end{aligned} \tag{22}$$

From (20) by variation, the virtual movement along the segment is

$$\delta\mathbf{r} = (1-\xi)\delta\mathbf{r}_1 + \xi\delta\mathbf{r}_2 = \left[(1-\xi)\delta x_1 + \xi\delta x_2\right]\mathbf{i} + \left[(1-\xi)\delta z_1 + \xi\delta z_2\right]\mathbf{k}. \tag{23}$$

The virtual work contribution from a generic segment obtains finally the form

$$\delta' W = X_1\delta x_1 + Z_2\delta z_1 + X_2\delta x_2 + Z_2\delta z_2 \tag{24}$$

where X_1, $\cdots$ are the generalized forces corresponding to Δx_1, $\cdots$. The generalized forces consist similarly as the virtual work from terms corresponding to internal and external forces and to the free boundary.

From internal forces, the generalized forces are found to be

$$X_1^{\text{int}} = \frac{x_2 - x_1}{L}\sigma, \quad Z_1^{\text{int}} = \frac{z_2 - z_1}{L}\sigma,$$
$$X_2^{\text{int}} = -\frac{x_2 - x_1}{L}\sigma, \quad Z_2^{\text{int}} = -\frac{z_2 - z_1}{L}\sigma. \tag{25}$$

Due to the constant pressure difference, the generalized forces are

$$X_1^{\text{ext}} = -\frac{z_2 - z_1}{2}(p_l - p_v), \quad Z_1^{\text{ext}} = \frac{x_2 - x_1}{2}(p_l - p_v),$$
$$X_2^{\text{ext}} = -\frac{z_2 - z_1}{2}(p_l - p_v), \quad Z_2^{\text{ext}} = \frac{x_2 - x_1}{2}(p_l - p_v). \tag{26}$$

The free boundary contribution is treated here in some detail. Equating

$$\delta\mathbf{r} = \delta x\mathbf{i} + \delta z\mathbf{k} \tag{27}$$

with (11) (both at the free boundary) and some further manipulations give

$$\delta e = \frac{\mathbf{i}\cdot\hat{\mathbf{n}}}{\mathbf{t}\cdot\hat{\mathbf{n}}}\delta x + \frac{\mathbf{k}\cdot\hat{\mathbf{n}}}{\mathbf{t}\cdot\hat{\mathbf{n}}}\delta z = -\frac{\mathbf{i}\cdot\hat{\mathbf{n}}}{\sin\theta}\delta x - \frac{\mathbf{k}\cdot\hat{\mathbf{n}}}{\sin\theta}\delta z \tag{28}$$

and

$$\delta\hat{e} = \frac{\mathbf{i}\cdot\mathbf{n}}{\hat{\mathbf{t}}\cdot\mathbf{n}}\delta x + \frac{\mathbf{k}\cdot\mathbf{n}}{\hat{\mathbf{t}}\cdot\mathbf{n}}\delta z = \frac{\mathbf{i}\cdot\mathbf{n}}{\sin\theta}\delta x + \frac{\mathbf{k}\cdot\mathbf{n}}{\sin\theta}\delta z. \tag{29}$$

Let node 2 of the element be at the free boundary. The virtual work expression (8) becomes

$$\delta' W^{\text{bound}} = X_2^{\text{bound}}\delta x_2 + Z_2^{\text{bound}}\delta z_2 \tag{30}$$

where the corresponding generalized forces are

$$\begin{aligned} X_2^{\text{bound}} &= -\sigma\frac{\mathbf{i}\cdot\hat{\mathbf{n}}}{\sin\theta} + (\sigma_{sv} - \sigma_{sl})\frac{\mathbf{i}\cdot\mathbf{n}}{\sin\theta} \\ &= -\sigma\frac{\mathbf{i}\cdot\hat{\mathbf{n}}}{\sin\theta} + (\sigma_{sv} - \sigma_{sl})\left(\mathbf{i}\cdot\hat{\mathbf{t}} + \frac{\mathbf{i}\cdot\hat{\mathbf{n}}}{\tan\theta}\right), \\ Z_2^{\text{bound}} &= -\sigma\frac{\mathbf{k}\cdot\hat{\mathbf{n}}}{\sin\theta} + (\sigma_{sv} - \sigma_{sl})\frac{\mathbf{k}\cdot\mathbf{n}}{\sin\theta} \\ &= -\sigma\frac{\mathbf{k}\cdot\hat{\mathbf{n}}}{\sin\theta} + (\sigma_{sv} - \sigma_{sl})\left(\mathbf{k}\cdot\hat{\mathbf{t}} + \frac{\mathbf{k}\cdot\hat{\mathbf{n}}}{\tan\theta}\right). \end{aligned} \tag{31}$$

The last forms are obtained using the relation (see Figure 3 (a))

$$\mathbf{n} = \sin\theta\hat{\mathbf{t}} + \cos\theta\hat{\mathbf{n}}. \tag{32}$$

It is expected that in the discrete formulation it is better to have the local information about the solid boundary orientation to be included into the formulation and thus the latter expressions (31) seem more appropriate.

5. DISCRETE FORMULATION; SYSTEM EQUATIONS

The geometry of the discrete interface model is fixed by a list consisting of the nodal Cartesian coordinates, say **X**, and of the global node numbers of the segments in the model. The task is to determine that **X** for which the system equations (equilibrium equations) are satisfied. As the problem is strongly non-linear, the solution must be found iteratively.

The generalized coordinates or perhaps better said, the generalized movements (often here later just movements) q_i (quite often the generalized coordinates are called in the literature somewhat incorrectly also degrees of freedom) are in principle defined here in general always anew for the current system configuration. For example, we could have only one movement per node where the direction of the movement would be, say, roughly in the average normal direction to the current model interface (at the free boundary in the tangential direction to the solid surface). If the initial guess of **X** is reasonable, the iterative process described below should finally produce a correct approximate solution. This is in strong contrast with a similar structural problem. Let us consider the interface replaced by an elastic membrane. A discrete model of the membrane consisting of line segment elements might look at first sight quite the same as for the liquid-vapor interface. However, the essential difference is that the membrane is a material surface consisting of material points. In tracking the movement of the membrane we must follow the material particles and two coordinates are really needed for each node to fix the position of the material point in question. In contrast, the liquid-vapor interface is a kind of mathematical surface in the sense discussed earlier and an updated position of the discretized surface can be obtained just by moving each node a certain amount in a certain fixed direction. However, here we will employ in general two movements Δx_k and Δz_k for a generic node k. The drawback is that the number of unknowns doubles, but the treatment is found to become more robust; for example, an initially bad geometry guess does not lead to widely different element sizes.

The virtual work for the interface model (with respect to a current configuration) obtains the form

$$\delta' W = \sum_{i=1}^{N_{\mathrm{dof}}} Q_i \, \delta q_i \tag{33}$$

where Q_i is the i:th generalized force corresponding to the i:th movement q_i and N_{dof} the total number of movements. According to the principle of virtual work, the discrete system equations are thus

$$Q_i = 0, \quad i = 1, 2, \cdots N_{\mathrm{dof}} . \tag{34}$$

For a generic node k inside the mesh where the movements Δx_k and Δz_k are used, the corresponding two discrete system equations in (34) are in more detail

$$\begin{aligned} X_k &= 0, \\ Z_k &= 0. \end{aligned} \tag{35}$$

For a given **X** — initially guessed or updated — the left-hand sides in (34) are usually not zero. Let the value of the left-hand side in (34) for a given $\bar{\mathbf{X}}$ be $\bar{Q}_i$. The necessary movements q_j towards a hopefully better configuration are determined from the system

$$\bar{Q}_i + \sum_{j=1}^{N_{\text{dof}}} \frac{\partial Q_i}{\partial q_j} q_j = 0, \quad i = 1,2,\cdots N_{\text{dof}} . \tag{36}$$

The derivatives $\partial Q_i / \partial q_j$, — often called sensitivities — are evaluated at the current configuration, that is, at all q zero. The left-hand side in (36) is a first order Taylor expansion approximation for the generalized force in a new configuration with finite movements. A new updated $\bar{\mathbf{X}}$ is obtained through the values of q_j with respect to the old $\bar{\mathbf{X}}$. The iteration process consisting of solving (36) repeatedly is continued until the values of $\bar{Q}_i$ have hopefully become small enough. In detail, the sensitivities have been obtained here in an approximative way numerically as follows. Small finite changes $\bar{q}_j$ are taken, the generalized forces for the new geometry are determined, the changes in the values of the generalized forces are determined by subtraction and finally the approximate derivatives are found by division with $\bar{q}_j$. The value used for $\bar{q}_j$ ($\Delta\bar{x}_k$, $\Delta\bar{y}_k$) has been about 0.001 times the typical segment length.

When using the two degrees of freedom (Δx and Δz) per node formulation, it was found that the calculations did not proceed well without a modification. Additional elastic membrane forces proportional to the segment length changes were introduced in the sensitivity calculations. The need for this has an obvious explanation: If two neighboring segments are parallel, the movement of the middle node in the direction parallel to the segments is found to have no resistance from the pure surface tension; the corresponding sensitivity becomes zero. Obviously, when the segments are nearly parallel, some similar behavior (very small derivatives) is to be expected. It should be emphasized, however, that this trick of using elastic forces is applied just in the sensitivity calculations and has nothing to do with the final generalized force unbalances, where the terms from internal forces come only from the surface tension. A similar modification has been applied also at the free boundary node consisting in effect of an elastic horizontal spring during the sensitivity calculation.

The generalized forces and sensitivities are assembled from the element contributions in the standard way described in the finite element literature.

The node on the free boundary needs some comments. We can experiment with two possibilities. Firstly, we can employ the same movements Δx and Δz as for the rest of the nodes. The updated position of the node does not probably remain on the solid surface and a final correction must be performed by bringing the node in some manner back to the surface.

As a second alternative, we can employ only one degree of freedom at the free boundary node. The obvious movement q is then in the tangential direction to the surface given by the local unit vector $\hat{\mathbf{t}}$ (Figure 3). In general, if the movements differ from the Cartesian ones this can be taken into account by the well-known transformation rules for forces and stiffness matrices given in the finite element literature. We do not present the necessary formulas here. Finally, at least with a curved solid surface, the updated position of the free boundary node does not even in this version usually lie exactly on the solid surface and a correction must be performed.

Initial numerical experiments showed that the second alternative (one degree of freedom at the node on the free boundary) produced more accurate results and in the application example below only results with this formulation are reported.

6. APPLICATION

The geometry of a very simple model problem is described in Figure 5. We consider two cases: $\sigma_{\text{sv}} - \sigma_{\text{sl}} = 1/\sqrt{2} \cdot \sigma$ and $\sigma_{\text{sv}} - \sigma_{\text{sl}} = -1/\sqrt{2} \cdot \sigma$ so that Young's formula gives $\theta = 45°$

and $\theta = 135^\circ$, respectively. The constant pressure difference is expressed as $p_l - p_v = \sigma / l$ where l is a characteristic length. As the exact solution is a segment of a circle obeying equation (2), the radius R of the circle becomes l.

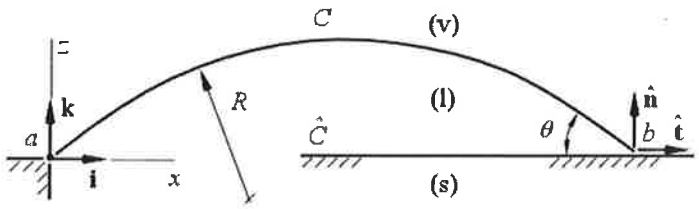


Figure 5 Example geometry.

The solid surface is horizontal and thus $\hat{\mathbf{t}} = \mathbf{i}$ and $\hat{\mathbf{n}} = \mathbf{k}$ and from (31),

$$X_2^{\text{bound}} = \sigma_{sv} - \sigma_{sl},$$
$$Z_2^{\text{bound}} = -\sigma \frac{1}{\sin\theta} + (\sigma_{sv} - \sigma_{sl}) \frac{1}{\tan\theta}. \tag{37}$$

The computational model consists of 11 nodal points and 10 line segments. In both cases the initial geometry has chosen to be more flat than the final geometry. The number of iterations needed to satisfy equations (34) properly and to obtain the final shape is found to be between ten and fifteen.

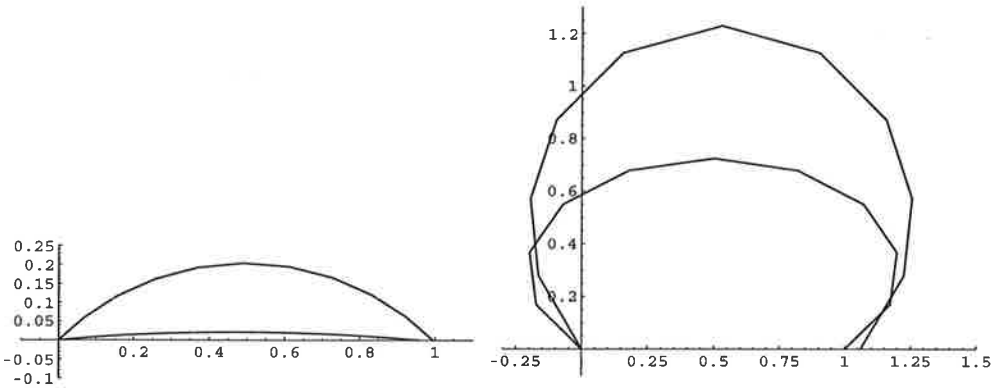


Figure 6 (a) Initial and final geometry; $\theta = 45^\circ$. **(b)** Initial and final geometry; $\theta = 135^\circ$.

7. CONCLUDING REMARKS

The results obtained in this initial study seem to show that the presented formulation based on virtual work is correct. Possible future extensions of the formulation are e.g.: proper form of the virtual work principle in three dimensions, a discrete formulation using facet elements, algorithms for returning the contact line on the solid surface, which is presented in some discrete manner and use of analytical expressions for the sensitivities.

REFERENCES

1 R. Finn. *Equilibrium capillary surfaces*. Springer-Verlag, 1986.

2 Tabor. *Gases, liquids and solids and other states of matter*. Cambridge University Press, 1991.

3 S. D. Iliev. Iterative method for the shape of static drops. *Comput. Methods Appl. Mech. Engrg.* 126 (1995) 251-265.

MONITAVOITTEISEN EPÄLINEAARISEN SEKALUKUOPTIMOINTITEHTÄVÄN PARETO-OPTIMIEN RATKAISUALGORITMI

Kristo Mela[1], Juhani Koski[2], Risto Silvennoinen[3]

[1]Tampereen teknillinen yliopisto – Teknillisen mekaniikan ja optimoinnin laitos
PL 589, 33101 Tampere
e-mail: kristo.mela@tut.fi

[2]Tampereen teknillinen yliopisto – Teknillisen mekaniikan ja optimoinnin laitos
PL 589, 33101 Tampere
e-mail: juhani.koski@tut.fi

[3] Tampereen teknillinen yliopisto – Matematiikan laitos
PL 551, 33101 Tampere
e-mail: risto.silvennoinen@tut.fi

TIIVISTELMÄ

Monitavoitteinen optimointi on vahva työkalu erilaisissa suunnittelu- ja päätöksentekotehtävissä. Ratkaisumenetelmiä on kehitetty runsaasti jatkuvan muuttujan tehtäville. Sen sijaan diskreettejä muuttujia sisältävät tehtävät ovat jääneet vähemmälle huomiolle.

Seuraavassa esitellään algoritmi monitavoitteisen sekalukuoptimointitehtävän ratkaisemiseksi. Perusideana on ratkaista vuorotellen yksitavoitteisia MINLP-tehtäviä ja monitavoitteisia jatkuvan muuttujan tehtäviä, kunnes kaikki Pareto-optimaaliset pisteet on löydetty. Samalla pyritään välttämään sellaisia diskreettien muuttujien arvoja, joilla ei saavuteta Pareto-optimeja. Algoritmia sovelletaan artikkelissa yksinkertaiseen ristikkoesimerkkiin.

1 JOHDANTO

Rakenteiden optimointi on yksi varhaisimmista monitavoitteisen optimoinnin sovellutusalueista [8]. Ensimmäisissä töissä käsiteltiin pääosin jatkuvan muuttujan tehtäviä, joille suurin osa ratkaisumenetelmistäkin on kehitetty. Nykyisin on yhä enenevässä määrin alettu kiinnittää huomiota myös monitavoitteisiin tehtäviin, joissa muuttujat ovat diskreettejä [2]. Esimerkiksi tuoreissa töissä [1] ja [6] käsitellään diskreettiä monitavoiteoptimointia komposiittirakenteiden suunnittelussa. Sen sijaan sekä jatkuvia, että diskreettejä muuttujia sisältäviä monitavoitteisia tehtäviä – monitavoitteisia sekalukuoptimointitehtäviä (*Multiobjective mixed-integer programming, MOMIP*) – on tutkittu vähän. Usein sekalukutehtävissä diskreettejä muuttujia ei kuitenkaan voida jättää pois tai käsitellä jatkuvina, sillä tällöin mallin oikeellisuus kärsii. Siksi on tärkeää, että myös diskreettejä muuttujia sisältäville monitavoitteisille optimointitehtäville kehitetään ratkaisumenetelmiä, joissa diskreettien muuttujien aiheuttamat erityispiireet huomioidaan.

Seuraavassa esitellään menetelmä monitavoitteisen epälineaarisen sekalukutehtävän ratkaisemiseksi. Menetelmä on luonteeltaan "tarkka", mikä tarkoittaa, että tehtävän ratkaisemiseen ei käytetä stokastisia keinoja (esim. geneettisiä algoritmeja), jotka ovat olleet tähän saakka eräitä käytetyimpiä työkaluja diskreettejä muuttujia sisältävien tehtävien ratkaisemisessa.

Artikkeli on jaoteltu siten, että osiossa 2 kerrataan monitavoiteoptimoinnin peruskäsitteet ja määritellään tarkasteltava tehtävä. Osiossa 3 esitellään kehitetyn algoritmin idea ja osiossa 4 algoritmi käydään läpi vaihe vaiheelta. Algoritmia sovelletaan osiossa 5 neljän sauvan ristikkoon. Lopuksi artikkelin ajatukset ja johtopäätökset kootaan yhteen osiossa 6.

2 MONITAVOITEOPTIMOINNIN PERUSKÄSITTEITÄ

Tässä artikkelissa käsiteltävä monitavoitteinen optimointitehtävä on muotoa

$$\min_{(x,y)\in\Omega} f(x,y) = [\, f_1(x,y),\, f_2(x,y), \ldots,\, f_k(x,y)\,]^\top \tag{1}$$

missä $x \in \mathbb{R}^{n_1}$ on jatkuvat muuttujat sisältävät vektori, $y \in \mathbb{Z}^{n_2}$ diskreetit muuttujat sisältävä vektori ja

$$\Omega = \{\, (x,y) \in \mathbb{R}^{n_1} \times \mathbb{Z}^{n_2} \mid g(x,y) \leq 0, h(x,y) = 0 \,\} \tag{2}$$

on tehtävän käypä joukko. Vektorifunktiota $f : \mathbb{R}^n \to \mathbb{R}^k$ kutsutaan kohdefunktioksi ja sen komponenttifunktioita $f_i : \mathbb{R}^n \to \mathbb{R}$ kriteereiksi. Avaruutta $\mathbb{R}^n$ kutsutaan suunnitteluavaruudeksi ja avaruutta $\mathbb{R}^k$ kriteeriavaruudeksi. Käyvän joukon kohdefunktion kuvajoukkoa, $f(\Omega)$, kutsutaan saavutettavien arvojen joukoksi (ks. [7]). Vektorifunktiot $g : \mathbb{R}^{n_1} \times \mathbb{Z}^{n_2} \to \mathbb{R}^p$ ja $h : \mathbb{R}^{n_1} \times \mathbb{Z}^{n_2} \to \mathbb{R}^q$ ovat tehtävän rajoitusfunktiot ja relaatiot $g(x,y) \leq 0$ ja $h(x,y) = 0$ rajoitusehdot. Merkinnät $a \leq b$ ja $a = b$ ymmärretään vektoreille a ja b komponenteittain. Esimerkiksi $g(x,y) \leq 0 \Leftrightarrow g_i(x,y) \leq 0 \forall\, i = 1, \ldots, p$. Merkitään kaikkien mahdollisten diskreettien muuttujien arvojen kombinaatioiden joukkoa $\mathcal{Y}(\mathbb{Z}^{n_2})$. Jatkossa oletetaan, että kriteerit ja rajoitusfunktiot ovat jatkuvasti derivoituvia, kun diskreettejä muuttujia pidetään jatkuvina. Lisäksi ainakin yhden kriteerin tai rajoitusfunktion oletetaan olevan epälineaarinen.

Määritellään joukko $\mathbb{R}^k_+ = \{z \in \mathbb{R}^k \mid z_i \geq 0\}$. Kahden joukon U ja V summalla tarkoitetaan joukkoa $U + V = \{w \mid w = u + v \text{ joillakin } u \in U, v \in V\}$.

Seuraavaksi kerrataan monitavoitteisen tehtävän myöhemmin tarvittavat käsitteet. Ensiksi on määriteltävä, mitä tehtävän (1) minimillä tarkoitetaan. Tätä varten määritellään

Määritelmä 1 (Pareto-optimaalisuus, [11], ks. [10]). Piste $x^* \in \Omega$ on *Pareto-optimaalinen*, jos ei ole toista pistettä $x \in \Omega$ siten, että $f_i(x) \leq f_i(x^*) \quad \forall i = 1, \ldots, k$ ja $f_j(x) < f_j(x^*)$ jollakin indeksillä j.

Pareto-optimaalisten pisteiden joukkoa merkitään $\mathcal{P}$ ja niiden kuvajoukkoa $\mathcal{Z}_N = f(\mathcal{P})$. Joukon $\mathcal{Z}_N$ alkioita kutsutaan *minimaalisiksi pisteiksi.*

Tehtävän (1) minimeillä tarkoitetaan minimaalisia pisteitä ja tehtävän ratkaisut ovat Pareto-optimaaliset pisteet.

Kriteeriavaruuden alkioiden paremmuutta voidaan vertailla dominoinnin käsitteellä.

Määritelmä 2 (Dominointi, ks. [12]). Olkoot z ja w kaksi kriteeriavaruuden $\mathbb{R}^k$ pistettä. Piste z *dominoi* pistettä w, jos $z_i \leq w_i \; \forall\, i = 1, \ldots, k.$ ja $z_j < w_j$ jollakin j.

Piste z on minimaalinen, jos yksikään toinen saavutettavien arvojen joukon piste ei dominoi sitä.

Tässäkin artikkelissa käytettyjä ratkaisumenetelmiä varten määritellään myös Pareto-optimaalisuuden heikompi muoto sekä tehtävän (1) ideaalinen piste.

Määritelmä 3 (Heikko Pareto-optimaalisuus, ks. [10]). Piste $x^* \in \Omega$ on *heikosti Pareto-optimaalinen*, jos ei ole toista pistettä $x \in \Omega$ siten, että

$$f_i(x) < f_i(x^*) \quad \forall i = 1, \ldots, k.$$

Määritelmä 4 (Ideaalinen piste, ks. [10]). Kriteeriavaruuden alkio $z^* = [z_1^*, \ldots, z_k^*]^\top \in \mathbb{R}^k$, jonka komponentit ovat

$$z_i^* := \min_{x \in \Omega} f_i(x) \tag{3}$$

on tehtävän (1) *ideaalinen piste.*

Yksitavoitteisen sekalukuoptimoinnin ratkaisumenetelmissä kiinnitetään usein osana ratkaisuprosessia kokonaislukumuuttujille jotkin tietyt arvot ja ratkaistaan näin saatu jatkuvan muuttujan tehtävä. Diskreettien muuttujien arvoja vaihtelemalla saadaan erilaisia jatkuvan muuttujan tehtäviä, joista saatua tietoa hyödynnetään ratkaisuprosessin edetessä. Menetelmät pyrkivät välttämään kaikkien diskreettien muuttujien arvojen kombinaatioiden täydellistä läpikäyntiä, sillä niiden lukumäärä kasvaa eksponentiaalisesti diskreettien muuttujien lukumäärän suhteen. [5, 4]

Diskreettien muuttujien arvojen kiinnittämien on houkuttelevaa myös monitavoitteisissa sekalukutehtävissä. Jos nimittäin kriteerit tai rajoitusfunktiot ovat epälineaarisia ja halutaan käyttää tavallisimpia monitavoitteisten tehtävien ratkaisumenetelmiä (esim. painokerroinmenetelmä, rajoitusmenetelmä [10]), on jokaista Pareto-optimaalista pistettä kohti ratkaistava epälineaarinen sekalukutehtävä (*mixed-integer nonlinear programming, MINLP*). Kun MINLP-tehtävien ratkaisemisen tiedetään olevan kompleksisuudeltaan NP-vaikeaa [5], tuntuu järkevältä pyrkiä ratkaisemaan näitä tehtäviä mahdollisimman vähän.

Toinen diskreettien muuttujien arvojen kiinnittämisen ja jatkuvan muuttujan monitavoitteisten tehtävien ratkaisemisen puolesta puhuva seikka on, että monitavoitteisten sekalukutehtävien saavutettavien arvojen joukon ominaisuuksista ei voida tehdä mitään yleisiä oletuksia tehtävän funktioiden perusteella [9]. Saavutettavien arvojen joukko voi olla esimerkiksi epäyhtenäinen tai siinä voi olla reikiä.

Edellisen perusteella myöhemmin esitellyssä algoritmissa ratkaistaan jatkuvan muuttujan tehtäviä diskreettien muuttujien ollessa kiinnitettyinä. Koska diskreettien muuttujien kombinaatioita on tavallisesti paljon, on laskentaresurssien ylikuormittamista vältettävä pyrkimällä kiinnittämään diskreeteille muuttujille ainoastaan sellaisia arvoja, joilla saadaan Pareto-optimeja.

Diskreettien muuttujien kiinnittämiseen liittyen tarvitaan seuraava merkintä.

Määritelmä 5 (Komponentti). Tehtävän (1) *$\hat{y}-$komponentiksi* (lyh. komponentiksi) kutsutaan kriteeriavaruuden osajoukkoa

$$K(\hat{y}) = \{z \in \mathbb{R}^k \mid \exists\, x \in \mathbb{R}^{n_1} :\ (x, \hat{y}) \in \Omega, z = f(x, \hat{y})\}. \tag{4}$$

Merkitään komponenttiin $K(\hat{y})$ kuvautuvia jatkuvia muuttujia

$$K^{-1}(\hat{y}) = \{x \in \mathbb{R}^{n_1} \mid (x, \hat{y}) \in \Omega\}. \tag{5}$$

Nyt $\mathcal{Z}$ voidaan kirjoittaa komponenttien avulla

$$\mathcal{Z} = \bigcup_{y \in \mathcal{Y}(\mathbb{Z}^{n_2})} K(y). \tag{6}$$

Määritelmä 6 (Pareto-optimaalisuus komponentissa). Piste $x^* \in K^{-1}(\hat{y})$ on *Pareto-optimaalinen komponentissa* $K^{-1}(\hat{y})$, jos se toteuttaa määritelmän 1 ehdot, missä $\Omega = K^{-1}(\hat{y})$. Tällöin piste $z = f(x^*, \hat{y})$ on *minimaalinen komponentissa* $K(\hat{y})$.

3 ALGORITMIN PERIAATE

Seuraavaksi esitellään algoritmin perusidea ja ne osatehtävät, joita ratkotaan ratkaisuprosessin edetessä. Tätä ennen perehdytään kuitenkin tehtävän (1) ominaisuuksiin, jotka ratkaisumenetelmän tulee huomioida:

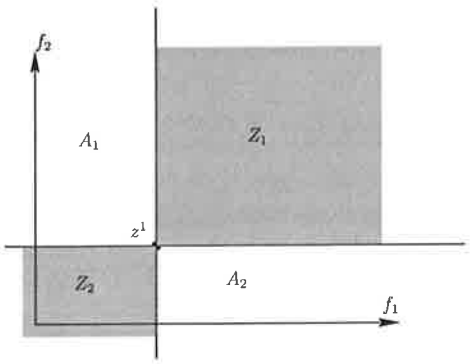
i) Komponenttien lukumäärä. Kuten osiossa 2 todettiin, tehtävällä (1) on diskreettien muuttujien lukumäärään nähden eksponentiaalisesti komponentteja. Tästä seuraa, että komponenttien täydellinen läpikäynti on käytännössä mahdotonta, jos diskreettejä muuttujia on paljon tai niiden arvojoukot ovat suuria. Näin ollen ratkaisumenetelmä ei voi perustua kaikkien komponenttien eksplisiittiseen tutkimiseen.

ii) Minimaalisten pisteiden joukko $\mathcal{Z}_N$ voi olla epäyhtenäinen. Vaikka tehtävän kaikki funktiot olisivat konvekseja, on joukon $\mathcal{Z}_N$ epäyhtenäisyyteen varauduttuva, sillä tavallisesti diskreetit muuttujat aiheuttavan sen, että käypä joukko ei ole yhtenäinen eikä näin ollen konveksi.

iii) Joukko $\mathcal{Z}_N + \mathbb{R}^k_+$ ei välttämättä ole konveksi, vaikka kriteerit ja rajoitusfunktiot olisivat konvekseja. Tämäkin seikka johtuu siitä, että diskreettien muuttujien vaikutuksesta käypä joukko ei ole konveksi. Tämä ominaisuus rajoittaa sellaisten menetelmien käyttöä, jotka vaativat tehtävän konveksisuutta, jotta niillä voitaisiin löytää kaikki optimaaliset pisteet (esim. painokerroinmenetelmä) [3].

Kehitetty algoritmi perustuu havaintoon, että jos löydetään yksi minimaalinen piste, z^1, kriteeriavaruus voidaan jakaa kolmeen osaan:

1. $Z_1 = \{z \in \mathbb{R}^k \mid z^1 \leq z\}$; (Dominoitu alue)
2. $Z_2 = \{z \in \mathbb{R}^k \mid z \leq z^1\}$; (Dominoiva alue)
3. $Z_3 = \{z \in \mathbb{R}^k \mid z \not\leq z^1 \ \& \ z^1 \not\leq z\}$. (Tutkittava alue)



Kuva 1: Kaksikriteerisen tehtävän dominoitu ja dominoiva alue (Z_1 ja Z_2) sekä etsintäalueet A_1 ja A_2. Tehtävän minimaaliset pisteet sijaitsevat alueella $Z_3 = A_1 \cup A_2$.

Selvästi Z_1 ei voi sisältää minimaalisia pisteitä. Jotta voitaisiin taata, että myöskään alueella Z_2 ei ole minimaalisia pisteitä, on pisteen z^1 löytämiseksi käytetty menetelmä valittava sopivasti. Esimerkiksi kun piste z^1 saadaan yleisesti tunnetun ns. *Tshebyshev-tehtävän*

$$\min_{(x,y)\in\Omega} \max_{i=1,\ldots,k} |f_i(x,y) - z_i^*| \tag{7}$$

ratkaisuna, voidaan olla varmoja siitä, että alueella Z_2 ei ole minimaalisia pisteitä [10]. Tehtävässä (7) z^* on tehtävän (1) ideaalinen piste tai jokin muu sopiva vertailupiste. Apumuuttujan avulla tehtävä (7) saadaan derivoituvaan muotoon

$$\begin{array}{rl} \min & \alpha \\ \text{siten, että} & f_i(x,y) - z_i^* \leq \alpha \quad \forall\, i = 1,\ldots,k, \\ & (x,y) \in \Omega \end{array} \tag{8}$$

missä $\alpha \geq 0$ on reaalinen muuttuja. Tässä muodossa Tshebyshev-tehtävä on MINLP-tehtävä, jonka kohdefunktio on lineaarinen. Tehtävä (8) voidaan ratkaista halutulla (esimerkiksi jollain artikkelissa [4] esitellyllä) menetelmällä.

Itse asiassa tehtävän (7) ratkaisu on yleisessä tapauksessa heikosti Pareto-optimaalinen [10]. Tästä ei ole kuitenkaan haittaa, sillä kriteeriavaruus voidaan jakaa myös heikkoa Pareto-optimia käyttäen.

Tehtävän (1) loput minimaaliset pisteet sijaitsevat alueella Z_3. Algoritmin ideana on jakaa tämä alue erillisiin osiin ja etsiä näistä osista loput minimaaliset pisteet.

Kun kriteereitä on kaksi, tutkittavia etsintäalueita on kaksi. Yleisesti etsintäalueita on $2^k - 2$ kappaletta. Kaksikriteerisessä tehtävässä etsintäalueet määräytyvät pisteen z^1 perusteella seuraavasti:

$$A_1 = \{z \in \mathbb{R}^k \mid z_1 \leq z_1^1\ ,\ z_2 \geq z_2^1\} \tag{9}$$

$$A_2 = \{z \in \mathbb{R}^k \mid z_1 \geq z_1^1\ ,\ z_2 \leq z_2^1\} \tag{10}$$

Tutkittava alue valitaan lisäämällä tehtävän (1) käypään joukkoon valitun etsintäalueen määrittävät rajoitusehdot.

Kun tutkittava etsintäalue on valittu, ratkaistaan Tshebyshev-tehtävä uudelleen. Olkoon saatu ratkaisu (x^2, y^2). Seuraavaksi kiinnitetään diskreeteille muuttujille arvot y^2 ja ratkaistaan komponentin $K(y^2)$ minimaaliset pisteet. Ratkaistavana oleva monitavoitteinen jatkuvan muuttujan tehtävä on muotoa

$$\min_{(x,\hat{y})\in\Omega} [f_1(x,\hat{y}),\ldots,f_k(x,\hat{y})]^\top, \tag{11}$$

missä $\hat{y}$ on kiinteä diskreettien muuttujien kombinaatio (esim. edellä käsitelty y^2).

Kun komponentti $K(y^2)$ on tutkittu, lisätään käypään joukkoon rajoitusehto, joka estää diskreettien muuttujien kombinaation y^2 tulemasta seuraavan Tshebyshev-tehtävän ratkaisuksi.

Etsintäalueen tutkimista jatketaan ratkomalla vuorotellen tehtäviä (8) ja (11), kunnes etsintäalueesta ei löydy uusia minimaalisia pisteitä sisältäviä komponentteja. Tämän jälkeen siirrytään seuraavaan

4 ALGORITMIN VAIHEET

Seuraavaksi käydään läpi yksityiskohtaisesti edellä kuvailtu algoritmi.

Algoritmin vaiheita 1–5 voidaan nimittää alustukseksi. Tässä vaiheessa ratkaistaan ensimmäinen (heikko) Pareto-optimaalinen piste, jonka kuvapiste jakaa kriteeriavaruuden 2^k-2 tutkittavaan alueeseen. Kun tätä pistettä vastaavan komponentin minimaaliset pisteet on etsitty, asetetaan ylimääräinen rajoitusehto, joka estää käytetyn diskreettien muuttujien kombinaation tulemasta myöhemmin Tshebyshev-tehtävän ratkaisuksi. Tämän jälkeen aloitetaan varsinainen iteraatio, joka koostuu kohdista 6–10.

Iteraatiovaihe sisältää kaksi sisäkkäistä silmukkaa. Ulommaisessa silmukassa (kohta 6) valitaan tutkittava etsintäalue ja sisemmässä (kohdat 7–10) valittu alue tutkitaan täydellisesti. Ulompaa iteraatiota jatketaan niin kauan kuin etsintäalueita on tutkimatta, ja sisempi

Algoritmi 1 `Monitavoitteisen MINLP-tehtävän ratkaisualgoritmi`

1. Etsi ideaalinen piste tai sen approksimaatio.
2. Ratkaise Tshebyshev-tehtävä (8). Saadaan heikosti Pareto-optimaalinen ratkaisu (x^1, y^1), $z^1 = f(x^1, y^1)$. Tutkittava komponentti on

$$K(y^1) = \{z \in \mathbb{R}^k \mid \exists\, x \in \mathbb{R}^{n_1} : \ (x, y^1) \in \Omega, z = f(x, y^1)\}.$$

   Aseta komponenttien laskuri $j = 1$.
3. Jaa kriteeriavaruus $2^k - 2$ etsintäalueeseen.
4. Ratkaise komponentin $K(y^1)$ minimaaliset pisteet tehtävästä (11).
5. Kiellä käytetty diskreettien muuttujien kombinaatio.
6. Jos tutkimattomia etsintäalueita on jäljellä, valitse yksi etsintäalue. Muuten LOPETA.
7. Ratkaise Tshebyshev-tehtävä (8). Jos tehtävälle ei löydy käypää optimiratkaisua, mene kohtaan 6. Muuten aseta $j = j + 1$. Tutkittava komponentti on nyt $K(y^j)$, missä y^j on tehtävän (8) ratkaisun kokonaislukumuuttujien kombinaatio.
8. Ratkaise komponentin $K(y^j)$ minimaaliset pisteet tehtävästä (11).
9. Poista lokaalit Pareto-optimit.
10. Kiellä käytetty diskreettien muuttujien kombinaatio ja mene kohtaan 7.

iteraatio päättyy epäkäypään Tshebyshev-tehtävään, mikä on merkki siitä, että etsintäalue on tutkittu kokonaan.

Perehdytään algoritmin vaiheisiin tarkemmin.

4.1 ALUSTUS

Algoritmin alustus koostuu vaiheista 1–5. Edellä on kuvattu lyhyesti alustuksen tavoitteet, ja nyt tutkitaan tarkemmin alustuksen toteuttamiseen liittyviä seikkoja.

Vaihe 1:

Määritelmän 4 mukaan ideaalisen pisteen selvittämiseksi on ratkaistava k kappaletta yksitavoitteisia optimointitehtäviä. Kun tehtävässä on mukana diskreettejä muuttujia ja funktiot ovat epälineaarisia, ovat nämä optimointitehtävät MINLP-tyyppisiä. Koska epälineaarinen sekalukuoptimointi on NP-vaikeaa, saatetaan ideaalisen pisteen selvittämiseksi tarvita melko paljon laskentaresursseja. Tästä syystä olisi ideaaliselle pisteelle hyvä löytää jokin helposti laskettava approksimaatio.

Vaihe 2:

Edellisessä kohdassa valitun referenssipisteen avulla ratkaistaan Tshebyshev-tehtävä (joka on siis MINLP-tyyppinen), jonka ratkaisun kuva jakaa kriteeriavaruuden etsintäalueisiin. Saatu ratkaisu $(x^\star, y^\star)$ on heikosti Pareto-optimaalinen. Tämä tarkoittaa, että samalla muuttujan α arvolla (ks. (8)) voidaan löytää myöhemmin piste, joka dominoi pistettä $(x^\star, y^\star)$. Vaikka $(x^\star, y^\star)$ ei olisikaan Pareto-optimaalinen, kriteeriavaruus voidaan kuitenkin jakaa sen avulla. Tällöin piste $(x^\star, y^\star)$ poistetaan myöhemmin, kun sitä dominoiva piste löydetään. Komponentti $K(y^\star)$ voi joka tapauksessa sisältää tehtävän (1) minimaalisia pisteitä, joten pisteen $(x^\star, y^\star)$ heikko Pareto-optimaalisuus ei ole kovin haitallista.

Vaihe 3:

Kun kriteeriavaruuden dimensio on k, se voidaan jakaa valitun pisteen suhteen 2^k alueeseen, joista kaksi eivät voi sisältää minimaalisia pisteitä (dominoitu ja dominoiva alue). Loput $2^k - 2$ aluetta tutkitaan yksi kerrallaan. Kaksikriteerisen tehtävän etsintäalueet on esitelty edellä (ks. (9) ja (10)).

Tutkittavien alueiden määrä kasvaa eksponentiaalisesti kriteerien lukumäärän suhteen. Tavallisesti k ei ole kuitenkaan kovin suuri, joten tämä etsintäalueiden lukumäärän ekspo-

nentiaalinen kasvu ei haittaa menetelmää ratkaisevasti.

Vaihe 4:

Kun Tshebyshev-tehtävä on ratkaistu, on löydetty yksi heikosti Pareto-optimaalinen piste. Seuraavaksi etsitään loput sellaiset optimaaliset pisteet, joiden diskreetit muuttujat saavat tämän pisteen diskreettien muuttujien arvot. Kokonaislukumuuttujia pidetään siis vakioina, jolloin jäljelle jää jatkuva monitavoitteinen tehtävä, joka voidaan ratkaista millä tahansa sopivalla menetelmällä.

Vaihe 5:

Kun komponentin $K(y^j)$ Pareto-optimaaliset pisteet on löydetty, kielletään käytetty kokonaislukukombinaatio $y^j = [y_1^j, ..., y_{n_2}^j]^\top$ lisäämällä rajoitusehtoihin sopiva ehto. Kun diskreetit muuttujat ovat binäärisiä, ehto on muotoa

$$d_j : \sum_{i \in B_1} y_i^j - \sum_{i \in B_0} y_i^j \leq |B_1| - 1 \tag{12}$$

missä $B_1 = \{i \mid y_i^j = 1\}$ ja $B_0 = \{i \mid y_i^j = 0\}$ sekä $|B_1|$ on B_1:n alkioiden lukumäärä [5].

4.2 ITERAATIO

Iteraatiovaiheessa kaikki alustuksessa muodostetut etsintäalueet tutkitaan yksi kerrallaan.

Vaihe 6:

Tutkimaton etsintäalue valitaan lisäämällä tehtävään valittavan alueen määrittävät rajoitusehdot. Koska rajoitusehdot määritellään suunnitteluavaruudessa, on lisäehdot kirjoitettava muuttujien x ja y avulla. Esimerkiksi kaksikriteerisessä tapauksessa etsintäalue A_1 (ks. (9)) valitaan lisäehdoilla

$$\begin{aligned} c_1 : &\quad f_1(x,y) \leq z_1^1 \\ c_2 : &\quad f_2(x,y) \geq z_2^1. \end{aligned}$$

Itse asiassa ehto c_2 on tarpeeton, sillä jokainen Pareto-optimaalinen piste, joka toteuttaa ehdon c_1, toteuttaa myös ehdon c_2 (jos ei toteuttaisi, ko. piste olisi ollut Tshebyshev-tehtävän ratkaisu ennen pistetä z^1). Kun etsintäalue määräytyy ehdosta c_1, saadaan tässä alueessa ratkaistavan Tshebyshev-tehtävän käyväksi joukoksi

$$\Omega' = \Omega \bigcap c_1 \bigcap_{j=1}^{M} d_j,$$

missä M on kiellettyjen diskreettien muuttujien kombinaatioiden lukumäärä. Jokainen ehto d_j vastaa yhden kombinaation kieltoa (vrt. (12)).

Kun kriteereitä on enemmän kuin kaksi, etsintäalueen valitsemiseksi on lisättävä useampia lisärajoituksia. Tällöin uusi käypä joukko on

$$\Omega' = \Omega \bigcap_{i=1}^{N} c_i \bigcap_{j=1}^{M} d_j, \tag{13}$$

missä $i = 1, \ldots, N$ ja N on etsintäalueen määrittämiseksi tarvittavien rajoitusten lukumäärä.

Seuraavalla iteraatiokierroksella Tshebyshev-tehtävän avulla löydetyn (heikosti) minimaalisen pisteen on siis sijaittava valitussa etsintäalueessa ja se ei saa kuulua edellisillä kierroksilla tutkittuihin komponentteihin.

Jokaisella kierroksella käypää joukkoa rajoitetaan lisäämällä yksi uusi rajoitusehto d_j. Nämä ehdot pysyvät mukana iteraation loppuun saakka. Ehdot c_i sen sijaan korvautuvat aina etsintäaluetta vaihdettaessa uuden etsintäalueen vastaavilla ehdoilla. Lisäksi ehtoja c_i voidaan päivittää iteraation edetessä.

Vaihe 7:
Kullakin iteraatiokierroksella ratkaistaan Tshebyshev-tehtävä, jolla etsitään minimaalisia pisteitä sisältäviä komponentteja. Iteraatiota jatketaan, kunnes tehtävälle (8) ei löydy käypää ratkaisua. Tällöin etsintäalue on tutkittu kokonaan, jolloin voidaan siirtyä seuraavalle alueelle. Käypä joukko (13) on tyhjä viimeistään silloin, kun kaikki etsintäalueen komponenttien diskreettien muuttujien arvojen kombinaatiot on kielletty.

Vaihe 8:
Ks. alustuksen kohta 4. Tässä vaiheessa on jätettävä etsintäalueen rajoitusehdot pois, sillä tutkittava komponentti voi olla jakautunut useammalle alueelle ja saattaa siten sisältää minimaalisia pisteitä monella etsintäalueella. Tässä kohdassa ratkaistavan tehtävän käypä joukko on siis

$$\Omega(y^j) = \{x \in \mathbb{R}^{n_1} \mid g(x, y^j) \leq 0,\ h(x, y^j) = 0\}.$$

Vaihe 9:
Edellisessä kohdassa löydetyt Pareto-optimaaliset pisteet ovat optimaalisia iteraatiokierroksen diskreettien muuttujien komponentissa, mutta vielä on tarkistettava, ovatko ne tehtävän (1) optimimaalisia pisteitä. Muut komponentithan jätettiin täysin huomiotta jatkuvaa tehtävää ratkaistaessa, joten on mahdollista, että jonkun aiemmin löydetyn komponentin osa dominoi jotain vastalöydettyä osaa ja päin vastoin.

Vaihe 10:
Ks. alustuksen kohta 5. Kuten edellä todettiin (kohta 6), kokonaislukukombinaatioita kieltävät ehdot kumuloituvat alkuperäiseen tehtävään ja ne pysyvät mukana myös etsintäalueesta toiseen siirryttäessä. Tshebyshev-tehtävän käypä joukko on siis (13):n mukainen. Ainoastaan ehdot c_i muuttuvat etsintäaluetta vaihdettaessa.

4.3 ETSINTÄALUEEN PÄIVITTÄMINEN

Tarkastellaan seuraavaksi tehtävää, jossa on kaksi kriteeriä. Tällöin tutkittavat etsintäalueet ovat muotoa (9) ja (10). Kun etsintäalueilla ratkaistaan Tshebyshev-tehtäviä, alueisiin liittyviä rajoja voidaan päivittää iteraation edetessä. Näin algoritmin suoritusta pyritään nopeuttamaan.

Oletetaan, että ensimmäinen Tshebyshev-tehtävä on ratkaistu ja referenssipiste z^1 on löydetty. Tätä pistettä vastaava muuttujan α arvo olkoon α_1. Tarkastellaan algoritmin etenemistä alueessa A_2 (ks. (10)). Tämän alueen määrittävä ehto on

$$f_2(x, y) \leq z_2^1. \tag{14}$$

Tässä alueessa ratkaistaan jälleen Tshebyshev-tehtävä, jonka käypään joukkoon on lisätty pistettä z^1 vastaavan kokonaislukumuuttujien kombinaation kieltävä ehto. Olkoon tämän tehtävän ratkaisun kuva z^2 ja vastaava minimaalinen muuttujan α arvo α_2 (ks. (8)).

Nyt jos $\alpha_2 > \alpha_1$, ehtoa (14) voidaan päivittää pistettä z^1 vastaavan komponentin avulla: uudeksi rajaksi valitaan $\hat{z}_2$, missä

$$\begin{aligned} \hat{z}_2 := \min \quad & f_2(x, y^1) \\ \text{ehdoin} \quad & f_1(x, y^1) \leq z_1^2 \\ & x \in K^{-1}(y^1), \end{aligned} \tag{15}$$

missä y^1 on pistettä z^1 vastaava kokonaislukukombinaatio.

Uutta rajaa selvitettäessä tutkitaan ne Ky:n pisteet, jotka dominoivat pistettä z^2. Näistä pisteistä valitaan se, jonka kriteerin 2 arvo on pienin.

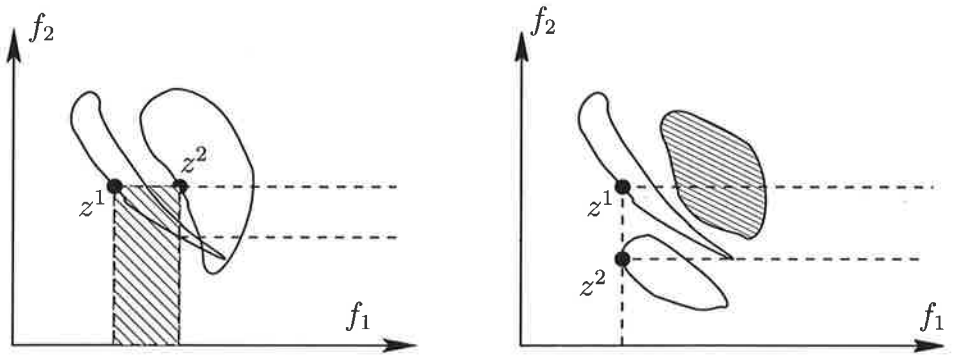
Jos tehtävän (15) ratkaisulle $\hat{z}_2$ pätee $\hat{z}_2 > z_2^2$, voidaan ehdon (14) uudeksi rajaksi valita yksinkertaisesti z_2^2. Tällöin päivitetyn etsintäalueen määrittelee ehto

$$f_2(x, y) \leq z_2^2. \tag{16}$$

Käytännössä tehtävää (15) ei tarvitse ratkaista optimointitehtävänä, vaan uusi etsintäalueen raja voidaan valita niiden minimaalisten pisteiden perusteella, jotka on saatu tehtävän (11) ratkaisuina.

Kuva 2a havainnollistaa tätä päivitysideaa. Kuvan tilanteessa uudeksi rajaksi saadaan alempaa poikittaista katkoviivaa vastaava z_2:n arvo, joka löydetään tutkimalla pistettä z^1 vastaavan komponentin minimaalisia pisteitä varjostetulla alueella.

Jos toisessa Tshebyshev-tehtävässä $\alpha_2 = \alpha_1$, piste z^2 on pisteen z^1 "alapuolella" (vrt. kuva 2b). Tällöin uudeksi rajaksi saadaan suoraan z_2^2. Kuva 2b havainnollistaa rajan päivityksen hyötyä: vain lokaalisti minimaalisia pisteitä sisältävä varjostettu alue jää löytymättä, kun etsintäaluetta on pienennetty. Jos rajaa ei olisi päivitetty, varjostetulta alueelta olisi löydetty Tshebyshev-tehtävälle ratkaisu, jolloin oltaisiin tehty ylimääräistä työtä, kun tätä aluetta oltaisiin tutkittu.

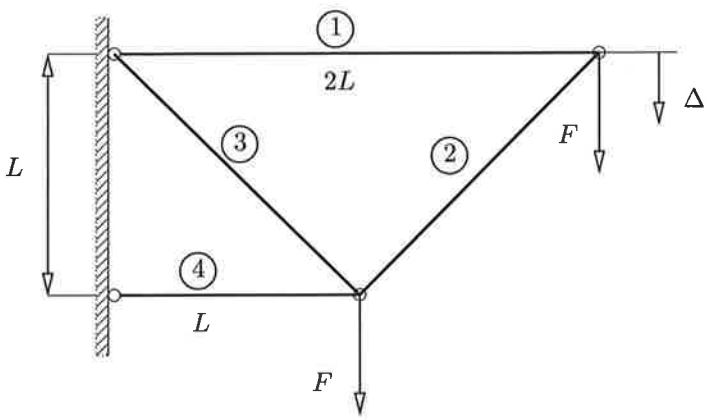


Kuva 2: Etsintäalueen päivitys. (a): Koska piste z^2 on Tshebyshev-tehtävän ratkaisu, tiedetään, että varjostetulla alueella ei voi olla muita minimaalisia pisteitä kuin pistettä z^1 vastaavan komponentin $K(y^1)$ minimaaliset pisteet. Tällöin etsintäaluetta voidaan rajoittaa komponentin $K(y^1)$ avulla. (b): nyt yksikään $K(y^1)$:n piste ei dominoi pistettä z^2, joten etsintäaluetta voidaan päivittää suoraan pisteen z^2 avulla.

5 NELJÄN SAUVAN RISTIKKOESIMERKKI

Seuraavassa tarkastellaan neljän sauvan ristikkoa, joka on kuvan 3 mukainen. Esimerkkiongelma on pieni, mutta se on sopiva havainnollistamaan sekalukutehtävän ominaisuuksia. Lisäksi kriteereille ja rajoitusfunktioille saadaan eksplisiittiset lausekkeet. Koska tehtävässä on vain kaksi jatkuvaa muuttujaa, voidaan kunkin komponentin, $K(y)$, Pareto-optimaaliset pisteet ratkaista analyyttisesti, jolloin algoritmin tuloksia päästään vertaamaan tarkkoihin ratkaisuihin.

Rakenteen kahta ulointa niveltä kuormitetaan kumpaakin pistevoimalla F. Tavoitteena on minimoida sauvojen materiaalitilavuutta V ja oikeanpuoleisen nivelen pystysiirtymää



Kuva 3: Neljän sauvan ristikkorakenne kuormituksineen

Δ, jotka ovat siis tehtävän kriteerit. Suunnittelumuuttujiksi valitaan sauvojen poikkipinta-alat A_i, missä $i = 1, \ldots, 4$. Indeksit vastaavat kuvaan 3 merkittyä sauvojen numerointia. Muuttujien alarajat määräytyvät jännitysrajoituksista, ja ylärajat on annettu.

Tehtävä voidaan kirjoittaa standardimuodossa

$$\begin{aligned}
\min \quad & \begin{bmatrix} V \\ \Delta \end{bmatrix} = \begin{bmatrix} (2A_1 + \sqrt{2}A_2 + \sqrt{2}A_3 + A_4)L \\ \left(\frac{2}{A_1} + \frac{2\sqrt{2}}{A_2} + \frac{4\sqrt{2}}{A_3} + \frac{6}{A_4}\right)\frac{FL}{E} \end{bmatrix} \\
\text{ehdoin} \quad & \frac{F}{\sigma_{\text{sall}}} \leq A_1 \leq 5\frac{F}{\sigma_{\text{sall}}} \\
& \sqrt{2}\frac{F}{\sigma_{\text{sall}}} \leq A_2 \leq 5\frac{F}{\sigma_{\text{sall}}} \\
& 2\sqrt{2}\frac{F}{\sigma_{\text{sall}}} \leq A_3 \leq 5\frac{F}{\sigma_{\text{sall}}} \\
& 3\frac{F}{\sigma_{\text{sall}}} \leq A_4 \leq 5\frac{F}{\sigma_{\text{sall}}}
\end{aligned} \tag{17}$$

missä L on kuvan 3 mukainen pituus, E on kimmomoduuli ja σ_{sall} on sallittu jännitys. Tehtävän parametreille valittiin arvot $F = 10\,kN$, $\sigma_{\text{sall}} = 10\,kN/cm^2$, $L = 200\,cm$ ja $E = 2 \cdot 10^4\,kN/cm^2$. Laskuissa käytetään yksikköjärjestelmää (kN, cm). Tällöin rajoitusehtojen termi $F/\sigma_{\text{sall}} = 1$.

Muuttujien A_1 ja A_4 oletetaan saavan ainoastaan kokonaislukuarvoja rajoitusehtojen määrämältä väliltä. Edellä mainituilla parametriarvoilla näiden muuttujien arvojoukoiksi saadaan

$$A_1 \in \{1, 2, 3, 4, 5\}$$
$$A_2 \in \{3, 4, 5\}.$$

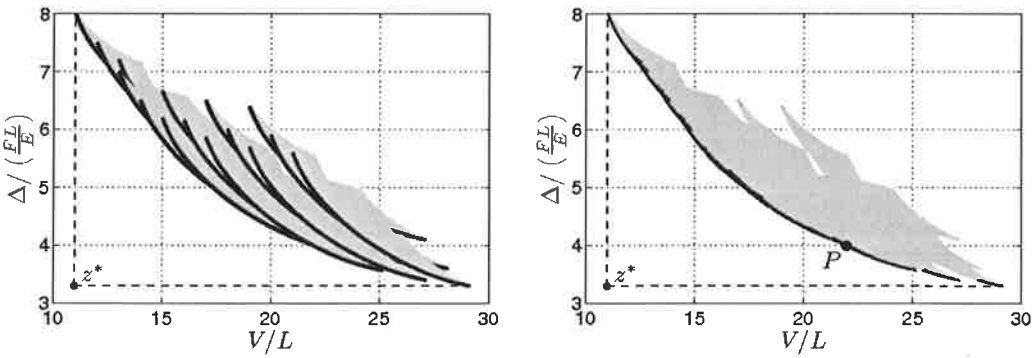
Diskreettien muuttujien kombinaatioita on yhteensä 15 kappaletta. Tehtävän (17) saavutettavien arvojen joukko on siis 15 komponentin yhdiste. Nämä komponentit ja niiden minimaaliset pisteet on piirretty kuvaan 4(a). Kuvassa on käytetty $(V/L, \Delta/(FL/E))$-koordinaatistoa, sillä vakiot L ja FL/E jätettiin pois tehtävää ratkaistessa. Kuvasta on syytä huomata, että komponenttien minimaalisten pisteiden joukot leikkaavat toisiaan. Näin tehtävän (17) minimaalisten pisteiden joukko koostuu useamman komponentin minimaalisten pisteiden osajoukoista. Leikkauskohdissa saadaan samat minimaaliset kriteerien arvot

kahdella *eri* Pareto-optimaalisella ristikolla. Näissä kohdissa minimaalisten pisteiden muodostama käyrä näyttäisi myös olevan epäsileä.

Tehtävällä (17) on 8 minimaalisia pisteitä sisältävää komponenttia. Kun tehtävä ratkaistiin algoritmilla 1, ratkaistiin 12 Tshebyshev-tehtävää. Algoritmin suorituksen aikana tutkittiin siis neljä komponenttia, jotka eivät sisältäneet minimaalisia pisteitä. Kuitenkin kolme minimaalisia pisteitä sisältämätöntä komponenttia jätettiin tutkimatta, joten diskreettien muuttujien täydelliseen läpikäyntiin nähden säästettiin 25% laskentaresursseja. Diplomityössä [9] tehdyt algoritmin testit osoittavat, että tämä säästö kasvaa selvästi, kun diskreettejä muuttujia on enemmän, jolloin tehtävän minimaalisia pisteitä sisältäviä komponentteja on komponenttien lukumäärään nähden suhteessa vähemmän kuin tehtävässä (17).

Kuvaan 4(b) on piirretty algoritmilla löydetyt minimaaliset pisteet. Huomattakoon, että minimaalisten pisteiden joukko on epäyhtenäinen. Tshebyshev-tehtävät ratkaistiin laajennetulla leikkaustasomenetelmällä [13] ja monitavoitteiset jatkuvan muuttujan tehtävät ratkaistiin diplomityössä [9] esitetyllä intervallilaskentaan perustuvalla algoritmilla. Minimaaliset pisteiden joukko koostuukin tämän algoritmin tuottamista pisteistä ja minimaalisia pisteitä sisältävistä intervallilaatikoista, jotka aiheuttavat kuvaan "rosoisuutta".

Esimerkkitilanteessa suunnittelija valitsee minimaalisen ratkaisun $P = [21.9896, 3.9882]$, jota vastaa Pareto-optimaalinen ristikko suunnittelumuuttujien arvoilla $A_1 = 3$, $A_2 = 3.2433$, $A_3 = 4.5276$, $A_4 = 5$ (cm^2). Tällöin kriteereille saadaan likimääräiset arvot $V \approx 4400\, cm^3$ ja $\Delta \approx 0,4\, cm$.



(a) (b)

Kuva 4: (*a*): Tehtävän (17) saavutettavien arvojen joukko on piirretty harmaalla. Kunkin komponentin minimaaliset pisteet on piirretty mustalla viivalla. Tällä korostetaan sitä seikkaa, että komponentit ovat kriteeriavaruudessa lomittain, ja tehtävän minimaaliset pisteet koostuvat useamman komponentin pisteistä. (*b*): Tehtävän (17) algoritmilla 1 löydetyt minimaaliset pisteet on piirretty mustalla. Lisäksi kuvaan on merkitty valittu minimaalinen piste P, jota vastaava ristikko Pareto-optimaalinen ristikko on esitetty tekstissä.

6 YHTEENVETO

Tässä artikkelissa esiteltiin algoritmi, jolla voidaan ratkaista monitavoitteisia epälineaarisia sekalukuoptimointitehtäviä. Lähtökohtana oli välttää kaikkien diskreettien muuttujien kombinaatioiden eksplisiittinen läpikäynti ja keskittyä tehtävän globaaleja Pareto-optimeja sisältäviin komponenetteihin. Esimerkin avulla todennettiin algoritmin toteuttavan tämän

vaatimuksen. Lisäksi menetelmällä selvitään mm. minimaalisten pisteiden joukon epäyhtenäisyydestä ja epäkonveksisuudesta. Esitetty menetelmä on havaittu toimivaksi, mutta etsintäalueiden tutkimista on tarpeen tehostaa. Nykymuodossa menetelmällä saatetaan nimittäin joutua ratkaisemaan paljon ylimääräisiä Tshebyshev-tehtäviä, joilla löydetään Pareto-optimeja sisältämättömiä komponentteja.

VIITTEET

[1] M. Aho, *Discrete Optimization of Large Scale Laminated Composite Structures*, Väitöskirja, Tampereen teknillinen yliopisto, 2003.

[2] M. Ehrgott, X. Gandibleux, *A survey and annotated bibliography of multiobjective combinatorial optimization* OR Spektrum, 22, 425–460, 2000.

[3] M. Ehrgott, *Multicriteria Optimization, 2nd Edition* Springer, 2005.

[4] I.E. Grossmann, *Review of Nonlinear Mixed-Integer and Disjunctive Programming Techniques*, Optimization and Engineering, 3, 227–252, 2002.

[5] J. Kallrath, *Gemischt-ganzzahlige Optimierung: Modellierung in der Praxis*, Vieweg Verlag, 2002.

[6] P. Kere, *Multi-Criteria Optimization of Composite Lamination for Maximum Failure Margins with an Interactive Descent Algorithm*, Väitöskirja, Tampereen teknillinen yliopisto, 2002.

[7] J. Koski, *Bicriterion Optimum Design Method for Elastic Trusses*, Väitöskirja, Tampereen teknillinen korkeakoulu, 1984.

[8] R.T. Marler, J.S. Arora, *Survey of multi-objective optimization methods for engineering*, Structural and Multidisciplinary Optimization, 26, 369–395, 2004.

[9] K. Mela, *Algoritmi monitavoitteisen epälineaarisen sekalukuoptimointitehtävän ratkaisemiseksi*, Diplomityö, Tampereen teknillinen yliopisto, 2006.

[10] K. Miettinen. *Nonlinear Multiobjective Optimization*, Kluwer Academic Publishers, 1999.

[11] V. Pareto, *Cours d'economie politique*, F. Rouge, 1896.

[12] G.R. Ruetsch, *An interval algorithm for multi-objective optimization*, Structural and Multidisciplinary Optimization, 30, 27–37, 2005.

[13] T. Westerlund, R. Pörn, *Solving Pseudo-Convex Mixed Integer Optimization Problems by Cutting Plane Techniques*, Optimization and Engineering, 3, 253–280, 2002.

KAUPALLISEN FEM-OHJELMAN KÄYTTÖ KANTAVIEN RAKENTEIDEN OPTIMOINNISSA

J. OJALA [1] & J. JALKANEN [2]

1) Abaqus Finland Oy
Hämeenkatu 23A, 33200 Tampere
jani.ojala@abaqus.fi

2) Tampereen teknillinen korkeakoulu, Teknillinen mekaniikka ja optimointi
PL 589, 33101 Tampere
jussi.jalkanen@tut.fi

TIIVISTELMÄ

Artikkeli käsittelee kaupallisen FEM-ohjelman ja optimointialgoritmin yhdistämistä rakenteiden mekaniikan optimointitehtävässä. Rakenteen FEM-analyysi tehdään Abaqus-ohjelmistolla ja optimointialgoritmiksi on valittu heuristinen parveilualgoritmi (particle swarm optimization, PSO). FEM-ohjelmiston käyttämistä kantavien rakenteiden optimoinnissa on havainnollistettu kahdella esimerkkitehtävällä, joista ensimmäinen käsittelee kannakkeen muodon optimointia ja jälkimmäinen dynaamisesti kuormitetun kotelon mitoitustehtävää. Kannake-esimerkissä suunnittelumuuttujat ovat jatkuvia ja rakenneanalyysi on lineaarinen statiikan tehtävä. Koteloesimerkissä on sekä jatkuvia että diskreettejä suunnittelumuuttujia ja rakenneanalyysi on epälineaarinen dynamiikan tehtävä.

JOHDANTO

Käytännön lujuusopillisissa suunnittelutehtävissä kappaleen geometria on usein monimutkainen ja erilaiset epälineaarisuudet tulisi pystyä ottamaan huomioon. Tällöin rakenteen siirtymien, venymien ja jännitysten ratkaiseminen analyyttisesti on mahdotonta ja täytyy turvautua numeerisiin analyyseihin. Elementtimenetelmä (Finite Element Method, FEM) on hyvin yleiskäyttöinen rakenteiden mekaniikan ongelmien numeerinen ratkaisukeino. Kaupalliset FEM-ohjelmistot tarjoavat kattavasti valmiita rutiineita erilaisten tehtävien ratkaisemiseen.

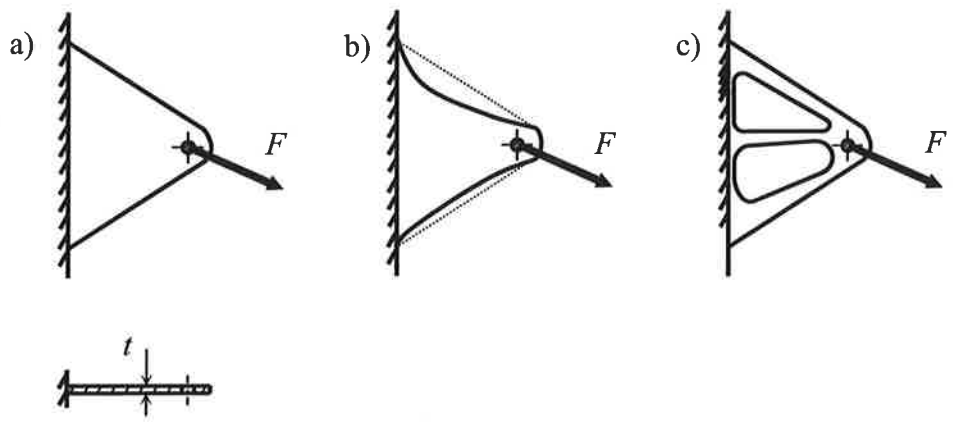
Tyypillisessä suunnittelutehtävässä on tarkasteltavalla rakenteella ennalta tunnettuja kuormituksia ja tuentoja sekä erilaisia toiminnallisuudesta tai valmistettavuudesta aiheutuvia rajoitusehtoja, kuten esimerkiksi rakenteen suurimmat sallitut siirtymät tai jännitykset. Tavallisesti suunnittelija tyytyy vertailemaan muutamaa kokemuksen ja intuition perusteella valittua ratkaisukandidaattia, jotka täyttävät annetut vaatimukset. Formuloimalla ja ratkaisemalla sopiva optimointiongelma olisi kuitenkin mahdollista löytää vielä parempia rakenteita, jotka ovat muuten vaikeasti etukäteen arvattavissa. Usein jonkin asian tai laitteen parantelua kuulee sanottavan optimoinniksi ja näin saatua lopputulosta väitettävän optimoiduksi. Tällaisessa prosessissa ei kuitenkaan ole kyse optimoinnista, vaan yleensä tavallisesta tuotekehityksestä.

Valmiin FEM-koodin käyttö optimoinnissa on tärkeää, koska kaupalliset ohjelmistot ovat tyypillisesti se työkalu, jota teollisuudessa käytetään rakenteiden mekaniikan tehtävien analysoinnissa. Kaupallisen FEM-koodin ja optimointialgoritmin kytkeminen mahdollistaa optimoinnin erittäin vaativissa ongelmissa, kuten esimerkiksi voimakkaasti epälineaarisissa tehtävissä. Suunnittelija voi periaatteessa hyödyntää rakenneanalyysissä kaikkia niitä ominaisuuksia, joita FEM-ohjelmistot tarjoavat. On kuitenkin muistettava, että optimointi saattaa vaatia satoja tai tuhansia FEM-analyysejä, joten yksittäisen analyysin tarvitsema laskenta-aika ei saa olla kovinkaan suuri. Monipuolisten analyysiominaisuuksien lisäksi kaupallisen ohjelmiston etuna on päivitys- ja kehitystyö, jota ohjelmistotalot jatkuvasti tekevät. Useimmiten kaupallinen ohjelmisto tarjoaa numeerisen ratkaisijan lisäksi myös monipuoliset esi- ja jälkikäsittelytyökalut.

Tässä artikkelissa optimointialgoritmiksi on valittu parveilualgoritmi (particle swarm optimization, PSO). PSO on perusidealtaan suhteellisen yksinkertainen ja melko tuore heuristinen optimointimenetelmä. Se sopii hyvin myös diskreettejä suunnittelumuuttujia sisältävien laskennallisesti työläiden optimointiongelmien likimääräiseen ratkaisemiseen. Vaikka parveilualgoritmi ei pystykään takaamaan globaalin optimin löytymistä, päädytään usein yhteen tai useampaan ratkaisuun, jotka ovat selvästi parempia kuin paras siihen asti tunnettu. Parveilualgoritmia käytettäessä ei tarvita kohde- ja rajoitusehtofunktioiden derivaattoja suunnittelumuuttujien suhteen ja riittää kun pystytään laskemaan kohde- ja rajoitusehtofunktioiden arvot annetussa suunnitteluavaruuden pisteessä.

KANTAVIEN RAKENTEIDEN OPTIMOINTI

Kantavien rakenteiden optimoinnilla (structural optimization) tarkoitetaan hyvien lujuusopillisten rakennevaihtoehtojen systemaattista hakua optimoinnin tarjoamia keinoja hyväksikäyttäen. Kantavien rakenteiden optimoinnissa voidaan erottaa kolme luonteeltaan toisistaan poikkeavaa tehtävätyyppiä: mitoituksen, muodon ja topologian optimointi. Mitoitustehtävässä ongelmana on valita rakenteen poikkileikkausmitoille sellaiset arvot, että rakenteesta tulisi optimaalinen. Rakenteen tyyppi ja geometria ovat jo lyöty lukkoon ja tehtävänä on vain mitoittaa osat parhaalla mahdollisella tavalla. Esimerkiksi levymäisellä rakenteella tämä tarkoittaa valmistamiseen käytetyn levyn paksuuden valitsemista sopivasti.



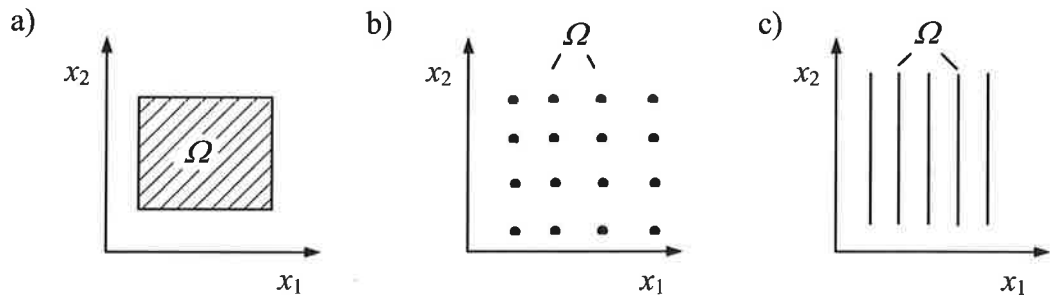
Kuva 1. Levymäisen korvakkeen optimointi, kun kyseessä on a) mitoitustehtävä, b) muodon optimointi ja c) topologian optimointi.

Muodon optimoinnissa on puolestaan ideana muutella optimoitavan rakenteen muotoa. Pyritään siis valitsemaan sellainen muoto tai reunaviiva, että esimerkiksi materiaalin kulutus minimoituu ja rakenne vielä kestää. Muodon optimointi yhdistetään usein mitoitustehtävän kanssa, jolloin levymäisellä kappaleella muuteltaisiin reunaviivan kanssa samanaikaisesti myös levyn paksuutta.

Topologian optimoinnissa on kyse astetta pidemmälle viedystä optimoitavan kappaleen geometrian muuttelemisesta kuin muodon optimoinnissa. Nyt tarkoituksena on löytää paras mahdollinen ratkaisu vaikuttamalla mukaan tulevien rakenneosien määrään, tyyppiin ja sijoitteluun. Ristikolla voidaan valita optimiratkaisuun mukaan vain osa alun perin mahdollisista sauvoista tai levymäiseen kappaleeseen voidaan tehdä sopiva määrä reikiä. Topologian optimointi yhdistetään usein muodon optimoinnin ja mitoitustehtävän kanssa.

Kantavien rakenteiden optimoinnissa on useita tyypillisiä vaihtoehtoja valita minimoitava tai maksimoitava kohdefunktio. Voidaan esimerkiksi ajatella, että kevein mahdollinen vaaditun kuormituksen kestävä rakenne on edullisin ja siten paras. Muita mahdollisia valintoja kohdefunktioksi ovat valmistuskustannukset, rakenteen jonkin pisteen siirtymä, luotettavuus tai vaikkapa alin ominaistaajuus. Kohdefunktioita voi olla myös kerrallaan useampia kuin yksi, jolloin puhutaan monitavoitteisesta optimointiongelmasta ja sen minimoitavista tai maksimoitavista kriteereistä. Kriteerit ovat keskenään ristiriitaisia eli monitavoitteisessa ongelmassa pyritään esimerkiksi yhtä aikaa mahdollisimman keveään ja jäykkään rakenteeseen.

Rajoitusehtojen tarkoituksena on huolehtia optimoidun rakenteen käyttökelpoisuudesta. Esimerkiksi massan minimointiongelmassa rakenteen keventyessä muodonmuutokset ja jännitykset kasvavat ja varmuus stabiilisuuden menettämisen suhteen pienenee. Jossakin vaiheessa saavutetaan tilanne, missä rakennetta ei voida enää keventää sen vaurioitumatta tai menettämättä toimivuuttaan tarkoitetulla tavalla. Siirtymä-, jännitys- ja stabiilisuusrajoitusten lisäksi kantavien rakenteiden optimoinnissa tavallisia rajoitusehtoja ovat ominaistaajuus-, luotettavuus-, tilavuus- ja symmetriarajoitukset.



Kuva 2. Käypä joukko Ω, kun kyseessä on a) jatkuvat suunnittelumuuttujat, b) diskreetit suunnittelumuuttujat ja c) sekalukutehtävä.

Optimointiongelmat voidaan jakaa suunnittelumuuttujien tyypin perusteella jatkuviin ja diskreetteihin ongelmiin sekä sekalukutehtäviin. Jatkuvassa optimointiongelmassa kukin suunnittelumuuttujista voi saada mitä tahansa arvoja joltakin sallitulta väliltä. Diskreetissä ongelmassa kaikki suunnittelumuuttujat voivat saada pelkästään joitakin tiettyjä arvoja, eivätkä mitään arvoa näiden välistä. Sekalukutehtävä on puolestaan näiden kahden edellisen yhdistelmä eli

se sisältää sekä jatkuvia että diskreettejä muuttujia. Suunnittelumuuttujiin perustuva optimointiongelmien jaottelu on oleellista, koska sekalukutehtävät ja diskreetit ongelmat ovat usein huomattavasti työläämpiä ratkaista kuin pelkkiä jatkuvia muuttujia sisältävät ongelmat. Esimerkkinä jatkuvasta tehtävästä voidaan mainita levystä hitsatun I-palkin uuman korkeuden ja laipan leveyden valitseminen optimaalisesti. Diskreettejä muuttujia tarvitaan puolestaan tehtävässä, missä optimoidaan vaikkapa muovikomposiitin kuitukerrosten lukumäärää.

PARVEILUALGORITMI

Parveilualgoritmi voidaan luokitella ns. populaatiopohjaisiin heuristisiin optimointimenetelmiin, kuten myös sitä paljon laajemmalti käytetty geneettinen algoritmikin (GA). Heuristiset menetelmät perustuvat usein johonkin luonnosta matkittuun päättelyyn, joka ei täytä ankaria loogisia vaatimuksia, mutta johtaa usein oikeaan tulokseen. On siis tavallaan kyse älykkäiden arvausten menetelmästä, joka optimoinnissa yleensä tuottaa hyvän lopputuloksen, muttei kuitenkaan välttämättä ongelman optimia. Heuristiset optimointimenetelmät ovat melko yksinkertaisia ja ne on helppo ohjelmoida tietokoneelle. Monet niistä ovat pienellä työllä muutettavissa eri sovellusalueiden ongelmien ratkaisuun sopiviksi. Heuristiset algoritmit ovat usein stokastisia, mutta eivät kuitenkaan välttämättä aina.

Ideana parveilualgoritmissa on matkia ruokaa tai pesäpaikkaa etsivän lintu-, hyönteis- tai kalaparven sosiaalista käyttäytymistä luonnossa. Parven jäsenet yrittävät sopeutua mahdollisimman hyvin ympäristöönsä käyttäen hyväksi omaa kokemustaan ja parven yhdessä keräämää tietoa ympäristöstä. Yksittäisen jäsenen, ja samalla myös koko parven, kannalta on hyödyllistä jakaa jäsenten tietoon tullut informaatio ympäristöstä kaikkien käyttöön parvessa. Parveilualgoritmin tutkimus on käynnistynyt 90-luvun puolivälissä [3] ja sitä on aikaisemmin sovellettu mekaniikan ongelmiin artikkeleissa [1] ja [4].

Parveilualgoritmissa jäsenen i uusi paikka iteraatiokierroksella k $\mathbf{x}_{k+1}^i$ riippuu sen nykyisestä paikasta $\mathbf{x}_k^i$ ja nopeudeksi nimitetystä termistä $\mathbf{v}_{k+1}^i$

$$\mathbf{x}_{k+1}^i = \mathbf{x}_k^i + \mathbf{v}_{k+1}^i \ . \tag{1}$$

Nopeus lasketaan kaavasta

$$\mathbf{v}_{k+1}^i = w\,\mathbf{v}_k^i + c_1 r_1\left(\mathbf{p}_k^i - \mathbf{x}_k^i\right) + c_2 r_2\left(\mathbf{p}_k^g - \mathbf{x}_k^i\right) \ , \tag{2}$$

missä $\mathbf{p}_k^i$ on jäsenen i ja $\mathbf{p}_k^g$ koko parven löytämä paras paikka iteraatiokierrokseen k mennessä. Tällöin siis ainakin yhden jäsenen paras paikka vastaa koko parven löytämää parasta paikkaa. Termiä w kutsutaan inertiaksi, r_1 ja r_2 ovat satunnaislukuja siten, että $r_1, r_2 \in [0,1]$, ja c_1 sekä c_2 ovat skaalausparametreja. Inertia w kontrolloi, kuinka laajasti hakuavaruutta tutkitaan optimointiprosessissa, ja tyypillinen valinta sen suuruudelle on $0{,}8 \le w \le 1{,}4$. Inertia voi olla tyypiltään dynaaminen, jolloin w:n arvo on aluksi suurempi ja pienenee optimoinnin kuluessa haun tarkentuessa kohti lupaavimpia alueita. Skaalausparametrit c_1 ja c_2 kontrolloivat, miten paljon parven jäsen i luottaa itseensä ja toisaalta parveen. Tyypillinen valinta niiden arvoiksi on $c_1 = c_2 = 2$.

Parveilualgoritmi on periaatteessa suunnittelumuuttujiltaan jatkuvien optimointitehtävien ratkaisumenetelmä. Diskreetit suunnittelumuuttujat voidaan huomioida yksinkertaisesti pyöristämällä muuttujien arvot aina lähimpään sallittuun arvoon. Rajoitusehdot käsitellään

parveilualgoritmissa sakottamalla epäkäypiä ratkaisuita verrannollisesti niiden epäkäypyyteen nähden. Standardimuotoinen epäyhtälörajoitettu optimointiongelma

$$\begin{aligned} &\min f(\mathbf{x}) \\ &g_i(\mathbf{x}) \le 0 \qquad i = 1,\ldots,n \end{aligned} \tag{3}$$

korvataan uudella vapaalla ongelmalla

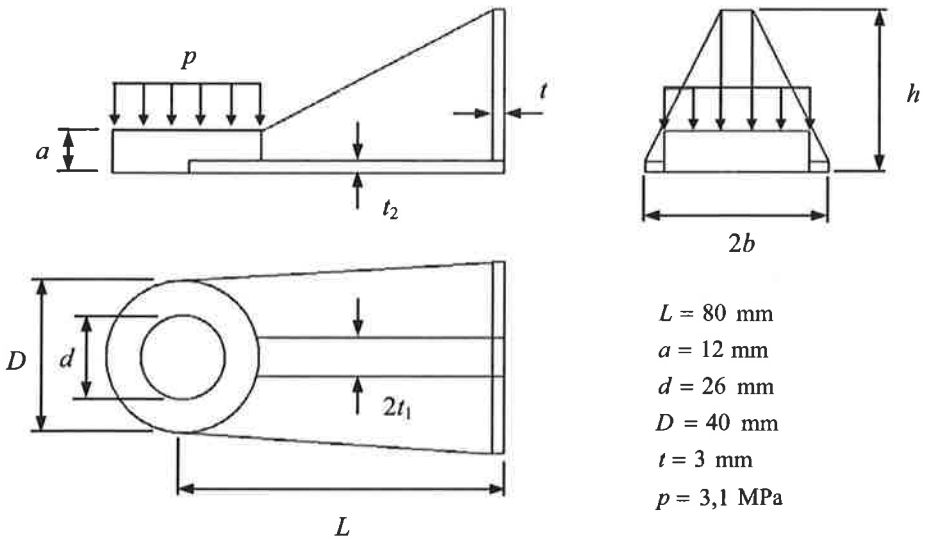
$$\min f(\mathbf{x})\left[1+\sum_{g_i(\mathbf{x})>0} R\, g_i(\mathbf{x})\right], \tag{4}$$

missä R on sakkokerroin. Sakotuksessa tulee pitää kirjaa parhaasta tiedetystä käyvästä ratkaisusta, koska muuten paras tiedetty ratkaisu $\mathbf{p}_k^g$ voi olla epäkäypä.

Lopetuskriteerinä voidaan käyttää tiettyä kiinteää iteraatiokierrosten lukumäärää $k^{\max}$ tai vaihtoehtoisesti tarkkailla parhaan tiedetyn kohdefunktion arvon $f(\mathbf{p}_k^g)$ kehitystä ja lopettaa optimointi ellei se ole enää parantunut $\bar{k}^{\max}$ kierroksen kuluessa (Lopeta, jos $f(\mathbf{p}_k^g) = f(\mathbf{p}_{k-\bar{k}^{\max}}^g)$ kierroksella k).

KANNAKKEEN MUODON OPTIMOINTI

Ensimmäinen esimerkki käsittelee kuvan 3 mukaista teräskannaketta, jota kuormitetaan tasaisella painekuormalla toisesta päästä vastakkaisen päädyn ollessa jäykästi tuettu. Tavoitteena on valita kappaleen muotoa sääteleville suunnittelumuuttujille sellaiset arvot, että sen massa minimoituu ja von Mises-vertailujännitys ei ylitä missään kohdin rakennetta suurinta sallittua arvoa $\sigma^{\max} = 237$ MPa. Suunnittelumuuttujat t_1, t_2, h ja b ovat tyypiltään jatkuvia ja niille kullekin on asetettu taulukon 1 mukaiset kiinteät ala- ja ylärajat.



Kuva 3. Massaltaan minimoitava kannake, jonka suunnittelumuuttujina ovat t_1, t_2, h ja b.

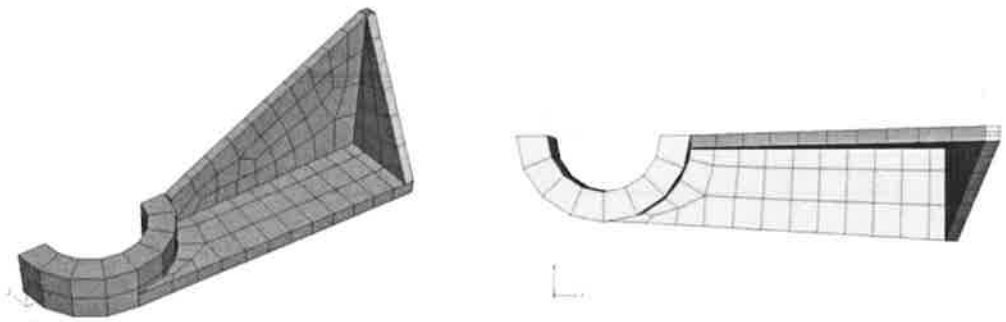
Taulukko 1. Kannakkeen optimointitehtävän suunnittelumuuttujien ala- ja ylärajat.

Suunnittelumuuttuja	alaraja [mm]	yläraja [mm]
t_1	1	9
t_2	1	15
h	40	100
b	25	80

Matemaattisesti esitettynä optimointiongelma on

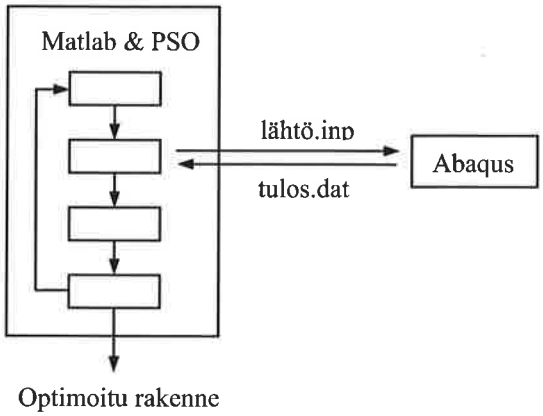
$$\begin{aligned} &\min \quad m(\mathbf{x}) \\ &\sigma_{\text{mises}}(\mathbf{x}) \le \sigma^{\max} \\ &t_1^{\min} \le t_1 \le t_1^{\max} \qquad t_2^{\min} \le t_2 \le t_2^{\max} \\ &h^{\min} \le h \le h^{\max} \qquad b^{\min} \le b \le b^{\max} \\ &\mathbf{x} = \left[t_1 \; t_2 \; h \; b \right]^{\mathrm{T}} \end{aligned} \tag{5}$$

Kannakkeen lineaarisen statiikan mukainen rakenneanalyysi tehdään Abaqus-ohjelmalla. Elementteinä mallissa on käytetty lineaarisella interpolaatiolla ja redusoiduilla integroimispisteillä varustettuja kuutioelementtejä. Kannakkeen elementtiverkko on esitetty kuvassa 4.



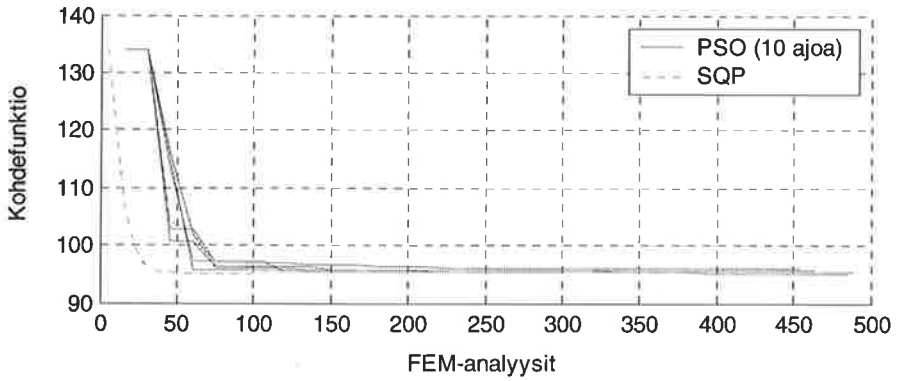
Kuva 4. Kannakkeen elementtiverkko. Tehtävässä on hyödynnetty symmetriaa mallintamalla rakenteesta vain puolet.

Optimoinnissa käytetty parveilualgoritmi on implementoitu Matlabiin, josta se aina tarvittaessa käynnistää Abaquksen tekemään FEM-analyysin halutunlaiselle rakenteelle. Tämä tapahtuu muuttamalla alkuperäistä tekstimuotoista lähtötiedostoa niin, että se vastaa uusien suunnittelumuuttujien arvoja. FEM-analyysin jälkeen luetaan Abaquksen tekstimuotoinen tulostiedosto ja lasketaan tarvittavat kohdefunktion ja rajoitusehtojen arvot. Kuva 5 esittää kaavakuvamaisesti optimoinnin toteutusta.



Kuva 5. Parveilualgoritmi on implementoitu Matlabiin, josta tarvittaessa käynnistetään Abaqus tekemään rakenneanalyysi.

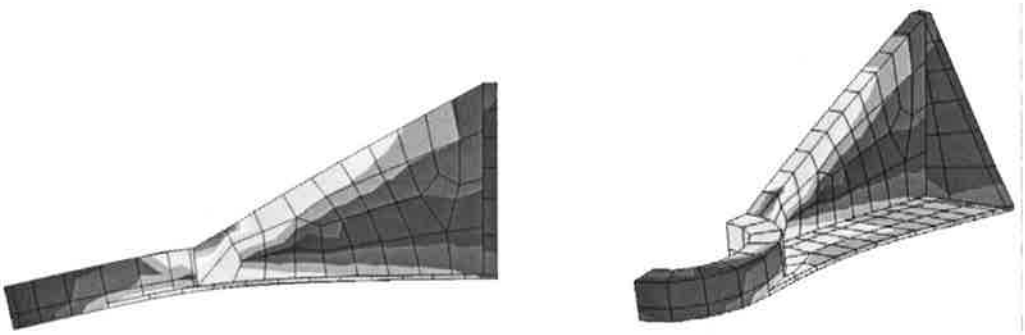
Stokastista optimointialgoritmia käytettäessä luotettavien tulosten saamiseksi tulee optimointi tehdä useampaan kertaan. Kannakkeen massan minimointiongelmaan on haettu ratkaisua 12 kertaa peräjälkeen parveilualgoritmilla käyttäen kussakin optimointiajossa 15 yksilön kokoista parvea ja 30 iteraatiokierrosta. Alkuparvi on arvottu, eikä se muutu eri optimointikerroilla. Vertailun vuoksi optimointi on tehty myös käyttäen SQP–algoritmia, missä menetelmän tarvitsemat kohdefunktion ja rajoitusehtofunktion derivaatat suunnittelumuuttujien suhteen lasketaan numeerisesti. SQP:n alkuarvauksena on PSO:n alkuparven paras yksilö. Eri optimointiajoilla saatu massan kehitys on esitetty kuvassa 6 ja kevein löydetty rakenne taulukossa 2. Kuvasta 7 selviää keveimmän löydetyn kannakkeen deformoitunut muoto ja von Mises–vertailujännitysjakauma.



Kuva 6. Massan kehitys kannakkeen muodon optimointiongelmassa 12 perättäisellä PSO:n ja yhdellä SQP:n ajolla laskentaan kuluneiden FEM-analyysien funktiona.

Taulukko 2. Kannakkeen optimointitehtävässä löydetyt keveimmät rakenteet.

	suunnittelumuuttujat					
	t_1	t_2	h	b	massa [g]	σ_{mises} [MPa]
PSO	3,963	1,000	40,000	25,000	95.141	236.954
SQP	3,962	1,000	40,000	25,001	95,131	236,962



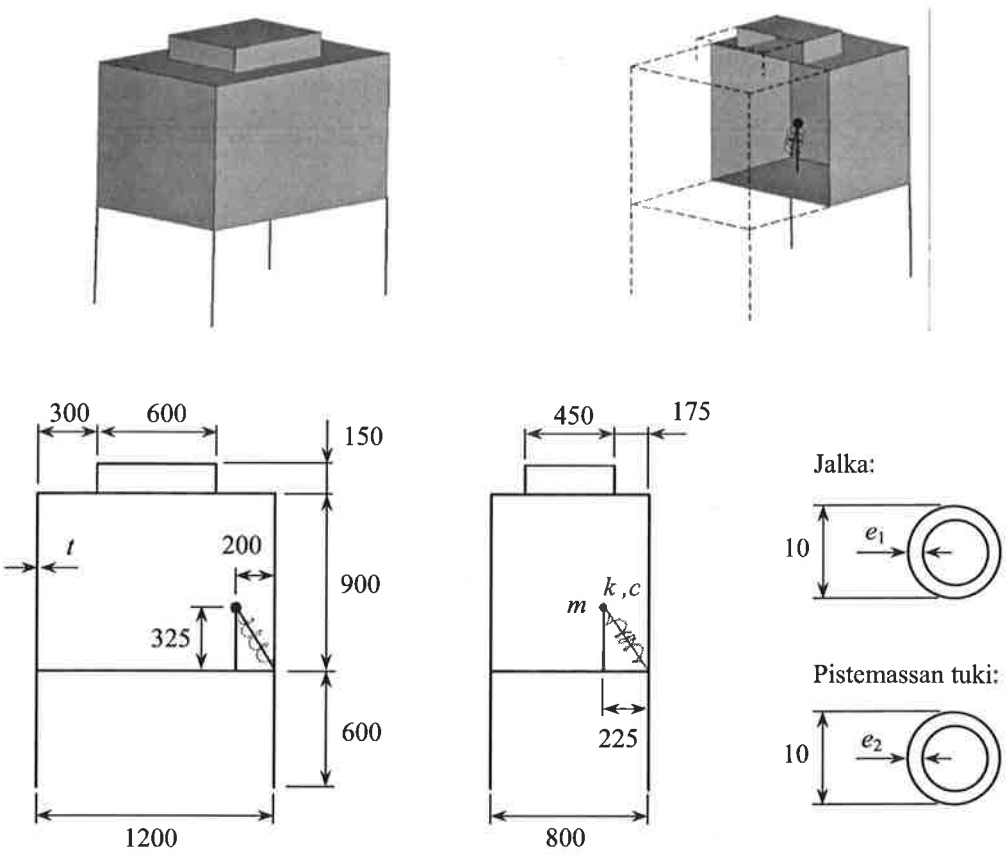
Kuva 7. Keveimmän löydetyn kannakkeen deformoitunut muoto ja von Mises-vertailujännitysjakauma.

Taulukon 2 perusteella nähdään, että PSO ja SQP päätyvät molemmat samaan rakenteeseen, missä pohjalevyn paksuus t_2 sekä päädyn korkeus h ja leveyden puolikas b ovat kukin alarajoillaan. SQP näyttäisi kuvan 6 mukaan toimivan selkeästi tehokkaammin kuin PSO. Kannakkeen optimointiongelmassa tehtävän koko on vielä niin pieni, että SQP:n tarvitsemien derivaattojen laskeminen numeerisesti ei käy kohtuuttoman työlääksi. Tilanne muuttuu kuitenkin hyvin nopeasti PSO:n eduksi suunnittelumuuttujien ja rajoitusehtojen lukumäärän kasvaessa.

DYNAAMISESTI KUORMITETUN KOTELON MITOITUSTEHTÄVÄ

Toisessa esimerkissä optimoinnin kohteena on kuvassa 8 esitetty kotelo, johon kohdistuu dynaaminen heräte. Rakenne muodostuu suorakulmaisen särmiön muotoisesta teräskotelosta, joka on tuettu maahan neljällä putkijalalla. Kotelon sisällä on putken päähän kiinnitetty pistemassa, joka on tuettu lisäksi yhteen nurkkaan jousi-vaimennin-systeemillä. Tavoitteena on löytää kevyt rakenne, missä pistemassan kokonaiskiihtyvyys olisi mahdollisimman pieni. Siten kohdefunktioksi on valittu rakenteen kokonaismassan ja analyysin aikaisen maksimikiihtyvyyden painotettu summa. Diskreettejä suunnittelumuuttujia ovat putkien seinämänvahvuudet e_1 ja e_2 sekä kotelon seinämän paksuus t ja jatkuvia suunnittelumuuttujia puolestaan jousivakio k, vaimennusvakio c sekä pistemassan suuruus m. Taulukossa 3 on esitetty suunnittelumuuttujien sallitut arvot. Von Mises-vertailujännityksen osalta vaaditaan, että se ei ylitä arvoa 355 MPa missään kohdin rakennetta. Kotelorakenteen jalkoihin kohdistuvan siirtymäherätteen muoto jäljittelee eräässä maanjäristyksessä tallennettua herätettä [1].

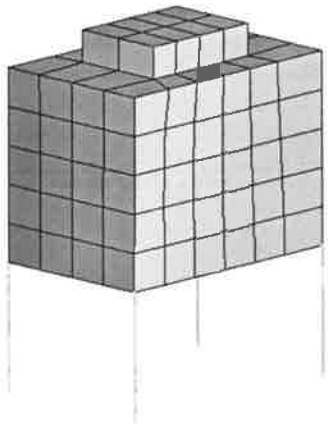
Rakenneanalyysi on tehty ensimmäisen esimerkin tapaan Abaqus-ohjelmistolla. Putket on mallinnettu lineaarisilla palkkielementeillä ja kotelorakenne lineaarisella kuorielementillä. Rakenteen FEM-diskretoinnissa on käytetty melko harvaa elementtiverkkoa, joka on esitetty kuvassa 9. Tällä on haluttu varmistaa, ettei yhden FEM-laskennan kesto ole liian pitkä. Dynaamisen FEM-analyysin ja implisiittisen ratkaisijan (Abaqus/Standard) luonteesta johtuen rakenteen tasapaino joudutaan iteroimaan analyysin aikana monta kertaa, vaikka tarkasteltu aika on vain 3 sekuntia. Esimerkin FEM-analyysissä on lisäksi käytetty suurten siirtymien teoriaa.



Kuva 8. Optimoitava dynaamisesti kuormitettu kotelorakenne, jonka suunnittelumuuttujina ovat e_1, e_2, t, k, c ja m. Mitat ovat millimetrejä.

Taulukko 3. Suunnittelumuuttujien sallitut arvot kotelorakenteen optimointitehtävässä.

Diskreetit suunnittelumuuttujat		
Suunnittelumuuttuja	Käypä joukko [mm]	
e_1	0.5 , 1 , 1.5 , 2 , 2.5 , 3 , 3.5 , 4 , 4.5 , 5	
e_2	0.5 , 1 , 1.5 , 2 , 2.5 , 3 , 3.5 , 4 , 4.5 , 5	
t	0.5 , 1 , 1.5 , 2 , 2.5 , 3 , 3.5 , 4 , 4.5 , 5	
Jatkuvat suunnittelumuuttujat		
Suunnittelumuuttuja	alaraja	yläraja
k	100000 N/m	500000 N/m
c	1000 N·s/m	7000 N·s/m
m	10 kg	200 kg



Kuva 9. Kotelorakenteen analysoinnissa käytetty elementtiverkko.

Dynaamisesti kuormitetun kotelorakenteen optimointitehtävä on matemaattisesti esitettynä

$$\min \quad \frac{1}{2}\left(\frac{m_{\text{tot}}(\mathbf{x})}{m_0}+\frac{a_{\max}(\mathbf{x})}{a_0}\right)$$

$$\sigma_{\text{mises}}(\mathbf{x}) \le \sigma^{\max}$$

$$e_1 \in \left\{e_1^1, e_1^2, \ldots, e_1^n\right\}$$
$$e_2 \in \left\{e_2^1, e_2^2, \ldots, e_2^n\right\}$$
$$t \in \left\{t^1, t^2, \ldots, t^n\right\} \qquad (6)$$

$$k^{\min} \le k \le k^{\max}$$

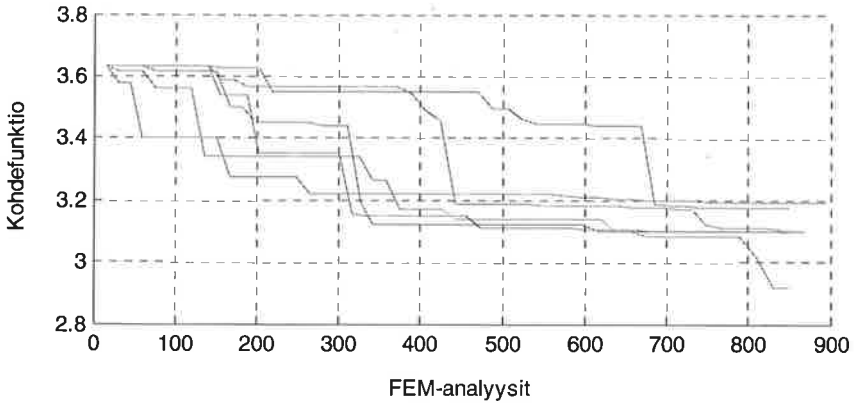
$$c^{\min} \le c \le c^{\max}$$

$$m^{\min} \le m \le m^{\max}$$

$$\mathbf{x} = \left[e_1 \quad e_2 \quad t \quad k \quad c \quad m\right]^{\mathrm{T}}$$

$m_{\text{tot}}(\mathbf{x})$ tarkoittaa rakenteen kokonaismassaa ja $a_{\max}(\mathbf{x})$ suurinta pistemassan kiihtyvyyden resultanttia analyysin aikana. Skaalausparametreina on käytetty arvoja $m_0 = 1000\,\text{kg}$ sekä $a_0 = 25\,\text{m/s}^2$.

Kuvassa 10 on esitetty PSO-algoritmilla saadut tulokset kuudesta eri optimointiajosta. Parven koko on ollut 15 yksilöä, iteraatiokierrosten lukumäärä 50 ja alkuparvi on arvottu kerran. Taulukossa 4 on vielä esitetty parhaan löydetyn rakenteen suunnittelumuuttujien arvot. Tällä kertaa vertailuratkaisun laskeminen SQP:llä ei onnistu, koska kyseessä on sekalukutehtävä.



Kuva 10. Dynaamisesti kuormitetun kotelorakenteen kohdefunktion arvon kehittyminen FEM-analyysien funktiona eri optimointiajoilla.

Taulukko 4. Parhaan löydetyn ratkaisun suunnittelumuuttujien arvot dynaamisesti kuormitetun kotelon mitoitustehtävässä.

Suunnittelumuuttuja	Suunnittelumuuttujan arvo
e_1	4,5 mm
e_2	5,0 mm
t	2,0 mm
k	482435,86 N/m
c	4069,90 N·m/s
m	60,85 kg

Optimoinnin tuloksena kohdefunktio parani noin 20%. Pistemassan kokema suurin kiihtyvyys laski arvosta 159,7 m/s^2 arvoon 123,1 m/s^2, mutta rakenteen massa nousi arvosta 880,6 kg arvoon 908,7 kg. FEM-analyysejä on kunkin optimointiajon aikana tehty yli 800. FEM-analyysien suuri määrä rajoittaa varsinkin esimerkin kaltaisessa epälineaarisissa dynamiikan ongelmassa laskentamallin kokoa.

YHTEENVETO

Optimointi on luonnollinen jatke kantavien rakenteiden tietokoneavusteiselle analysoinnille. Suunnittelijan ei kannata tyytyä muutaman vaihtoehdon keskinäiseen vertailuun FEM-laskelmien perusteella, vaan on paljon järkevämpää pistää tietokone hakemaan optimoinnin avulla uusia entistä parempia ratkaisuja. Kantavien rakenteiden optimoinnin merkitys tulee tulevaisuudessa kasvamaan, koska se tarjoaa selkeän keinon saavuttaa etua totuttuihin suunnittelumenetelmiin nähden. Tietokoneiden kasvava laskentakapasiteetti ja kehittyvät optimointialgoritmit mahdollistavat yhä suurempien ongelmien ratkaisemisen kohtuullisessa ajassa. Näillä näkymin ei ole mitään syytä uskoa, etteikö tähän asti voimakkaana jatkunut kehitys jatkuisi myös tulevaisuudessa.

Monissa käytännön sovelluksissa tarkastelun kohteena olevan rakenneosan monimutkaisesta geometriasta, suurista siirtymistä ja mahdollisesti vielä epälineaarisesta materiaalimallista tai kontaktista johtuen rakenneanalyysissä on käytettävä jotakin kaupallista FEM-ohjelmaa. Jotta näissä tapauksissa voitaisiin hyödyntää optimointia, tulee se pystyä kytkemään valmiin FEM-

ohjelman kanssa yhteen. Tämä onnistuu ulkopuolisella ohjelmalla, joka pyörittää optimointialgoritmia ja aina tarvittaessa käynnistää FEM-ohjelman tekemään rakenneanalyysin halutuilla suunnittelumuuttujien arvoille. Kommunikointi FEM-ohjelman kanssa hoidetaan kirjoittamalla sekä lukemalla tekstimuotoisia lähtö- ja tulostiedostoja. Koska valmisohjelmien lähdekoodia ei päästä muuttamaan kohde- ja rajoitusehtofunktioiden derivaattojen laskemiseksi, on optimoinnissa käytettävä algoritmeja, joille riittää kohdefunktion ja rajoitusehtojen arvojen laskeminen tietyissä suunnitteluavaruuden pisteissä.

Pitkälle kehittyneet laskentamenetelmät eivät poista sitä tosiasiaa, että optimoinnin soveltamisessa käytännön ongelmaan tarvitaan kulloisenkin sovellusalan ymmärrystä. Optimointimallin muodostaminen vaikuttaa pitkälle mahdollisuuksiin onnistua menestyksellisesti mallin ratkaisemisessa. Tällaisten päätösten tekemiseen tarvitaan hyvää peruslujuusopin ja elementtimenetelmän tuntemusta.

LÄHTEET

[1] Chopra, A. K., & Chakrabarti, P. 1973. The Koyna Earthquake and the Damage to Koyna Dam, *Bulletin of the Seismological Society of America*, vol. 63, no.2, pp. 381–397.

[2] Fourie P.C. & Groenwold A. A. 2002. The particle swarm optimization algorithm in size and shape optimization. *Structural and Multidisciplinary Optimization*, 23, 259-267.

[3] Kennedy J., Eberhart R. 1995. Particle Swarm Optimization. *Proceedings of the IEEE International Conference on Neural Networks*, Perth, Australia.

[4] Venter G., & Sobieszczanski-Sobieski J. 2003. Particle Swarm Optimization. *AIAA Journal*, Vol. 41, No 8, 1583-1589.

EFFICIENT MULTIPHYSICS SIMULATIONS AND OPTIMIZATIONS USING COMMERCIAL SIMULATION TOOLS

A. NIEMISTÖ, K. HILTUNEN, J. KORPIJÄRVI and H. TUOMOLA
Numerola Oy, Väinönkatu 7 C
P.O. Box 126
FI-40101 Jyväskylä , FINLAND
e-mail: Antti.Niemisto@numerola.fi

We study the case of solving multiphysics and optimization problems where at least part of the model is solved by using commercial simulation software. We develope a set of formulations for the main problem and present efficient computer realizations to solve the problem. We demonstrate the characteristics of the resulting methods by means of fluid-structure interaction problem and shape optimization problem.

COST OPTIMIZATION OF WELDED STEEL STRUCTURES

J. JALKANEN
Institute of Applied Mechanics and Optimization
Tampere University of Technology
P.O. 589
FIN-33101 Tampere, FINLAND

ABSTRACT

The topic of this paper is the cost minimization of welded steel structures. The sum of material and manufacturing costs is chosen to be the minimized object function and the displacements, strength and buckling constraints take care that the optimized structure remains feasible. Based on the literature the paper introduces different ways to form the cost function. Particle swarm optimization (PSO) method is chosen as an optimization algorithm and two practical example problems illustrate the cost optimization. In the first example the analysis of the structure is done by using commercial ABAQUS finite element method program.

INTRODUCTION

The analysis of steel structures has been under growing research interest during last decades. A lot of work has also been done to ensure the safety of the steel design codes which have very important role in applications. In structural and mechanical engineering the next natural step is to move from the analysis to the optimization of steel structures. In this paper discussed optimization means finding the best solution to the formulated problem by using means of mathematics. This is a different thing than the traditional product development by using designer's experience, intuition and the method of trial and error.

In structural optimization the ultimate target is usually the minimization of the cost of a structure. The cost of the welded steel structure consists of material, fabrication, transportation, erection and maintain costs. Since the cost of a steel structure can be approximated up to certain point based on the material consumption the mass of the structure is traditionally chosen as the minimized object function. In many mechanical engineering applications the low weigh is also natural benefit because for example it helps to reach the low fuel consumption in transport vehicles. The cost of the structure is not the only choice and other often chosen possibilities for the object function are for example stiffness (displacements), the lowest natural frequency and the maximum stress in fatigue. In some cases it is useful to consider several conflicting object functions at the same time and to use the methods of multicriteria optimization instead of traditional single criteria optimization.

The amount of material cost from the total cost varies depending on the type of the welded steel structure. If the structure is simple and requires only moderate welding the material cost is typically 60-70% from the total cost. On the other hand complex shape, several parts and difficult welds cause that the material cost is only about 20-30% of total cost. Sometimes the manufacturing cost is almost the same regardless of the mass of the structure and the mass minimization provides the lowest total cost. However in work intensive cases the mass minimization does not necessary lead to the minimum cost structure. It can be difficult to know in

advance whether the mass minimization is enough or should the manufacturing cost also be considered in optimization. In this study the sum of material and manufacturing costs is chosen as the minimized object function and transportation, erection and maintain costs are ignored. Earlier the cost optimization of welded steel structures has been considered in the articles of Jármai and Farkas ([1], [2], [4], [5] and [6]) and in the paper of Pavlovčič, Krajnc and Beg [8].

In most cases the structural optimization problem is a nonlinear and constraint optimization problem which includes often some discrete design variables. In addition several applications demand that the analysis of structure should be done by using some commercial finite element software program which works as a black box. Heuristic optimization algorithms like genetic algorithm (GA) and simulated annealing (SA) are suitable methods for solving such difficult optimization problems. In this paper a new population based heuristic method called particle swarm optimization PSO is used to improve the performance of the welded steel structures.

COST FUNCTION

This paper considers only the material and the manufacturing costs and all the other like transportation, erection and maintenance costs are ignored in the minimized cost function. Since steel has a certain price per kilogram, the material cost can be calculated simply multiplying the mass of the structure by the current material cost factor k_m. The calculation of the manufacturing cost is more complicated and there are several ways to do it. The common approach is to divide the manufacturing process into several production stages and to consider the cost of each stage. Typical production stages of welded steel structures are the cutting of plates and edge grinding, surface preparation, welding including preparation, assembly and tack welding and surface finishing.

The manufacturing cost depends on the technical level of machine workshop, the level of labor cost and the volume of production. By using highly automated production lines and serial production the manufacturing cost per product is lower than what it is in the hand welding of unique structures. The level of wages is substantially higher in highly developed countries than in developing countries. Different production conditions makes it difficult to obtain a single universal cost function and there will be always some case-specific factors in the cost function.

Cost function according to Jármai and Farkas

Jármai and Farkas have presented the following cost function for welded steel structures

$$K = K_m + K_f = k_m \rho V + k_f \sum_i T_i \qquad (1)$$

where K_m and K_f are the material and the manufacturing costs and k_m and k_f are the corresponding cost factors. ρV is the mass of the structure and T_i is the time [min] for production stage i. Instead of Eq. (1) the minimized cost function can be also expressed in the form

$$\frac{K}{k_m} = \rho V + \frac{k_f}{k_m}\left(T_1 + T_2 + T_3 + T_4 + T_5 + T_6\right) . \qquad (2)$$

According to Jármai and Farkas the ratio k_f/k_m varies between 0–2 kg/min and it is 2 kg/min in USA and Japan, 1-1,5 kg/min in Western Europe and 0,5 kg/min in developing countries. There is only one cost factor k_f for all production stages which helps application but it is also a clear simplification at the same time.

T_1 is the time for preparation, assembly and tack welding and it can be calculated using formula

$$T_1 = C_1 \Theta_d \sqrt{\kappa \rho V} \quad . \qquad (3)$$

C_1 is a constant, Θ_d is a difficulty factor ($\Theta_d = 1, \ldots, 4$) and κ is the number of structural elements to be assembled.

T_2 and T_3 are the times for welding and additional fabrication costs like chancing the electrode, deslagging and chipping. The formula for the sum of T_2 and T_3 is

$$T_2 + T_3 = 1{,}3 \cdot \sum_i C_{2i} a_{wi}^n L_{wi} \tag{4}$$

where a_{wi} is the size [mm] and L_{wi} the length [m] of weld i. Constant C_{2i} and exponent n depends on the welding technology, the type of the weld and welding position as presented in [4].

T_4 is the time for surface preparation which means the surface cleaning, sand-spraying, etc. The formula for T_4 is

$$T_4 = \Theta_{ds} a_{sp} A_s \ . \tag{5}$$

Θ_{ds} is a difficulty factor, $a_{sp} = 3 \cdot 10^{-6}$ min/mm^2 is a constant and A_s means the area of surface to be cleaned [mm^2].

T_5 means the painting time of ground and topcoat. It can be calculated using formula

$$T_5 = \Theta_{dp} \left(a_{gc} + a_{tc} \right) A_s \tag{6}$$

where Θ_{dp} is the difficulty factor for painting, $a_{gc} = 3 \cdot 10^{-6}$ min/mm^2 and $a_{tc} = 4{,}15 \cdot 10^{-6}$ min/mm^2 are constants and A_s is the area of surface [mm^2].

The time for cutting and edge grinding T_6 can be calculated using formula

$$T_6 = \sum_i C_{6i} t_i^n L_{ci} \ . \tag{7}$$

t_i is the thickness of plate and L_{ci} is the length of cut i. Constant C_{6i} and exponent n depends on the cutting technology as presented in [4].

In case of tubular structures (7) can be replaced by formula

$$T_6 = \Theta_{dc} \sum_i L_{ci} \left(4{,}54 + 0{,}4229\, t_i^2 \right) \ . \tag{8}$$

It is a slightly modified version from the formula for hand cutting and machine grinding of struts ends presented in [6]. Θ_{dc} is the difficulty factor, L_{ci} is the length of cut i and t_i is the corresponding wall thickness.

Cost function according to Pavlovčič, Krajnc and Beg

Pavlovčič, Krajnc and Beg have presented a more detailed cost function than Jármai and Farkas in the article [8]. It can expressed in the following form

$$\begin{aligned} K &= K_m + K_f + K_e \\ &= k_m \rho V + \sum_i k_{T_i} T_i + \sum_j k_{M_j} M_j + K_e \end{aligned} \tag{9}$$

where K_m, K_f and K_e are material, manufacturing and other costs. The material cost K_m is calculated exactly the same as in Eq. (1) but the manufacturing cost K_f is divided into actual production costs and material costs due to production. T_i is the time of production stage i and M_j is the material cost in production stage j. k_{T_i} and k_{M_j} are corresponding cost factors. K_e consists of transportation and erection costs which are not included to the object function in this paper.

The cost function (9) is rather elaborate and thereby it can be supposed to give results which correspond well the real world. Unfortunately given parameter values are connected to certain Slovenian highly automated machine workshop and welded I-profiles which reduces the usability of method. Parameter values connected to (9) are considered more detailed in the context of the first example problem.

Welding cost according to Vartiainen

Vartiainen represents an alternative method to calculate the welding cost based on empirical data collected from Finnish machine workshops in his dissertation [10]. The welding cost function is

$$K_w = T_w C_h + K_b \tag{10}$$

where T_w is the welding time, C_h the cost of working hour and K_b the filler wire cost. There are several formulas for the welding time in [10] and T_w can be calculated from suitable one depending on the current case. In these formulas T_w is the function of the volume of weld V_w [mm^3], the mass of the structure m [kg] and the number of welds N_w and the length of welds L_w [mm] or the number of parts N_{par}. For example the formula

$$T_w = 0{,}271\, N_w + 5{,}58 \cdot 10^{-6} V_w + 0.00149\, m \tag{11}$$

can be used in case that the mass of the structure $m \geq 1000$ kg.

PARTICLE SWARM OPTIMIZATION

Particle swarm optimization was developed by Kennedy and Eberhart in the mid 1990s [7]. The basic idea of stochastic PSO is to model the social behavior of a swarm (e.g. birds or fishes) in nature. A swarm of particles tries to adapt to its environment by using previous knowledge based on the experience of individual particles and the collective experience of the swarm. It is useful for a single member, and at the same time for the whole swarm, to share information among other members to gain some advantage. PSO belongs to the class of population based optimization methods, like genetic algorithm, because there is the group of solutions instead of a single solution. It can be seen that the group can offer some extra benefit compared to a single individual. In addition [7] references [3] and [11] concern the basics of PSO.

In PSO the new position $\mathbf{x}_{k+1}^i$ for particle i depends on the current position $\mathbf{x}_k^i$ and velocity $\mathbf{v}_{k+1}^i$

$$\mathbf{x}_{k+1}^i = \mathbf{x}_k^i + \mathbf{v}_{k+1}^i \tag{12}$$

where the velocity is calculated as follows

$$\mathbf{v}_{k+1}^i = w\mathbf{v}_k^i + c_1 r_1\left(\mathbf{p}_k^i - \mathbf{x}_k^i\right) + c_2 r_2\left(\mathbf{p}_k^g - \mathbf{x}_k^i\right). \tag{13}$$

$\mathbf{p}_k^i$ is the best ever position for particle i and $\mathbf{p}_k^g$ is the best ever position for the whole swarm. w is so called inertia, r_1 and r_2 are uniform random numbers $r_1, r_2 \in [0,1]$ and c_1 and c_2 are the scaling parameters. The value of w controls how widely the search process is done in the search space. The value of c_1 indicates how much a particle trusts on itself and c_2 how much on the swarm. The idea of the last two terms connected to c_1 and c_2 in the Eq. (13) is to direct the optimization process towards good potential areas in the search space. Usually $0{,}8 \leq w \leq 1{,}4$ and $c_1 = c_2 = 2$ are selected. The value of w can be changed dynamically so that it is bigger during early iteration rounds and becomes smaller later when it is time to focus on the promising areas.

Basically PSO is an algorithm for continuous unconstrained optimization problems. Discrete design variables can be taken into account simply by rounding each design variable to closest allowed value in Eg. (12) and constraints can be handled by penalizing unfeasible solutions according to the unfeasibility. The standard form of constrained optimization problem

$$\begin{aligned} &\min f(\mathbf{x}) \\ &g_i(\mathbf{x}) \le 0 \qquad i = 1,\ldots,n \end{aligned} \tag{14}$$

is replaced with a new unconstrained minimization problem in which the object function is

$$\bar{f}(\mathbf{x}) = f(\mathbf{x})\left[1 + \sum_{g_i(\mathbf{x})>0} R\, g_i(\mathbf{x})\right] \tag{15}$$

and R is the penalty parameter. Penalizing can lead to such situation that solution $\mathbf{p}_k^g$ is no longer feasible. To avoid this the best ever found feasible solution in PSO should be kept in memory.

The suitable size of the swarm depends on the amount of design variables so that the more variables the bigger swarm. If there are 10-20 design variables in the optimization problem then roughly speaking 20-50 might be the proper amount of particles. Usually the initial swarm is chosen randomly. As a terminating criteria the fixed iteration round amount can be used. Also the best known feasible object function value can be observed and if there is no improvement during last few rounds the optimization is terminated.

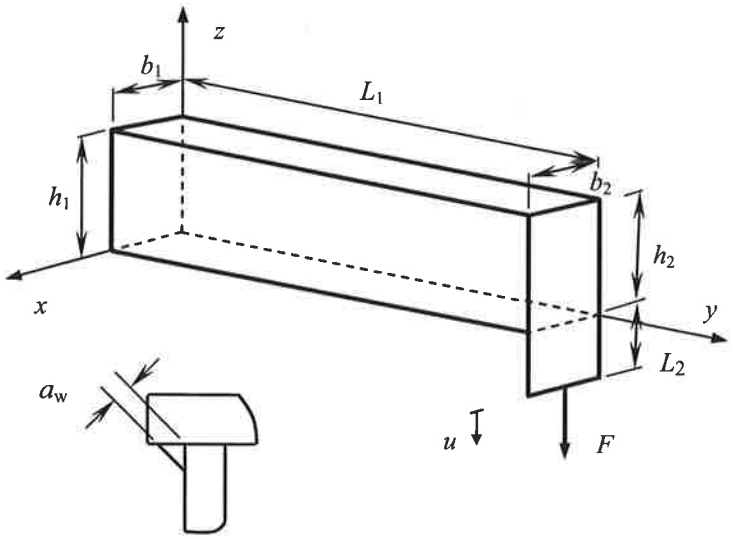
In discrete structural optimization the structure has to be analyzed hundreds or thousands of times during the optimization. It is useful to keep in memory some time the values of the object function and constraints after they have been calculated. Before a new analysis the memory is checked and if the solution is not there, the values of the object function and the constraints are calculated. It is typical for heuristic methods that later in the optimization process most of the needed values of the object function and constraints have been already calculated.

COST MINIMIZATION OF WELDED BOX BEAM

The first example problem handles the cost minimization of a welded box beam (Fig. 1). The beam is supported from one end and there is a point force as a load in the other end. The idea is to choose values for design variables h_1, b_1, h_2, b_2, t_1, t_2, t_3 and t_4 so that the cost of the structure is minimized and all constraints are fulfilled. Continuous design variables h_1, b_1, h_2 and b_2 are connected to the shape of the box beam with lower and upper bounds $h_1^{\min} = h_2^{\min} = 0{,}1\ \text{m}$, $h_1^{\max} = h_2^{\max} = 0{,}5\ \text{m}$, $b_1^{\min} = b_2^{\min} = 0{,}05\ \text{m}$ and $b_1^{\max} = b_2^{\max} = 0{,}2\ \text{m}$. Discrete design variables t_1, t_2, t_3 and t_4 mean the thicknesses of plates (t_1 bottom plate, t_2 side plates, t_3 top plate and t_4 end plate) and their values have to be chosen from set {3, 5, 7, 10, 12, 15, 20, 25, 30} mm. Constraints are such that the vertical displacement u has to be less than $u^{\max} = 5$ mm at the end of the beam, the von Mises stress σ_{mises} is less than $\sigma^{\max} = 237$ MPa everywhere in the structure and the critical load factor λ_{cr} according to linear buckling theory has to be at least 3.

All the welds of the box beam are fillet welds. The size of the weld a_w is $a_w = 0{,}7\, t_{\min}$ where $t_{\min}$ means the thickness of thinner plate. The side plates are welded to top and bottom plates by using SAW welding line and the end plate is welded by using manual SMAW welding.

Both presented cost functions (Jármai & Farkas and Pavlovčič, Krajnc & Beg) have been used as an object function. The material cost factor (the price of steel) is assumed to be $k_m = 0{,}6$ \$/kg in both cases. In order to compare the results the fabrication cost factor k_f in the cost function of Jármai and Farkas should correspond to the price level in Slovenia. The value $k_f = 0{,}75$ \$/min is used which means that ratio k_f/k_m is 1,25 kg/min. Tables 1 and 2 show all needed values for the different parameters in the object functions.



$F = 50$ kN
$L_1 = 2,0$ m
$L_2 = 0,2$ m
$E = 210$ GPa
$\nu = 0,3$
$\rho = 7850 \frac{\text{kg}}{\text{m}^3}$

Figure 1. Design variables in the cost minimization of the welded box beam and a fillet weld. The bottom surface remains on the *xy*-plane during the optimization.

Table 1. Parameter values for manufacturing costs according to Jármai and Farkas in the welded box beam example.

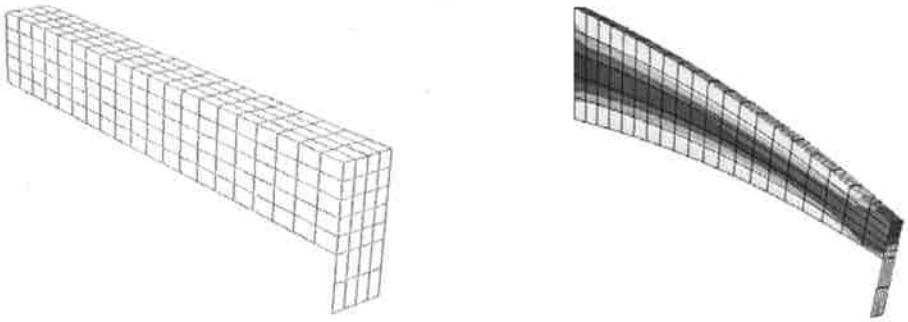
Preparation, assembly and tacking	$C_1 = 1$, $\Theta_d = 2$ and $\kappa = 5$
Welding and additional fabrication costs	$C_2 = 0,2349$ and $n = 2$ (SAW longitudinal fillet welds downhand position) $C_2 = 0,7889$ and $n = 2$ (SMAW longitudinal fillet welds downhand position)
Surface preparation	$\Theta_{ds} = 1$ and $a_{sp} = 3 \cdot 10^{-6}$
Painting	$\Theta_{dp} = 1$, $a_{gc} = 3 \cdot 10^{-6}$ and $a_{tc} = 4,15 \cdot 10^{-6}$
Cutting	$C_6 = 1,1051$ and $n = 0,25$ (high speed propane)

In the mathematical form the mixed integer optimization problem is

$$\min K(\mathbf{x})$$

$$\begin{aligned} & u(\mathbf{x}) \le u^{\max} \\ & \sigma_{\text{mises}}(\mathbf{x}) \le \sigma^{\max} \\ & \lambda_{\text{cr}}(\mathbf{x}) \ge n_{\text{cr}} \\ & h_1^{\min} \le h_1 \le h_1^{\max} \qquad b_1^{\min} \le b_1 \le b_1^{\max} \\ & h_2^{\min} \le h_2 \le h_2^{\max} \qquad b_2^{\min} \le b_2 \le b_2^{\max} \\ & t_1, t_2, t_3, t_4 \in \left\{ t^1, t^2, \ldots, t^n \right\} \\ & \mathbf{x} = \left[h_1 \; b_1 \; h_2 \; b_2 \; t_1 \; t_2 \; t_3 \; t_4 \right]^{\mathrm{T}} \end{aligned} \tag{16}$$

The structural analysis of the box beam is done by using commercial ABAQUS finite element method program. The FEM-model includes 388 S4 type shell elements and the mesh is shown in Fig. 2 a).



a) b)

Figure 2. a) The mesh of the welded box beam. b) The deformed shape and the von Mises stress distribution for the minimum cost structure (Jármai & Farkas).

The cost minimization problem of welded box beam is solved 10 times using both cost functions and PSO. Also the simple mass minimization problem is solved 10 times in order to find out how far such structure is from the minimum cost structure. In all optimization runs the size of the swarm is 15 particles but it will be increased by one randomly chosen particle every time the best known feasible object function value has not improved during 5 previous iteration rounds. However, if the best known object function value stays the same 20 iteration rounds the increase of swarm stops. The idea is to spread out the search up to a certain point if the progress of the object function seems to fade. The initial inertia is $w_0 = 1{,}4$ and the new inertia for the next iteration round is calculated from previous one by multiplying with factor 0,8. The values of scaling parameters are $c_1 = c_2 = 2$. The number of iteration rounds is 40, the initial swarm is chosen once randomly and the penalty for unfeasible constraints is 2. The amount of solutions is 500 in the memory. For the best found solutions the values of cost, displacement u, maximum von Mises stress and critical load factor λ_{cr} have been presented in the table 3. Figure 3 shows the cost distribution between material and different production stages.

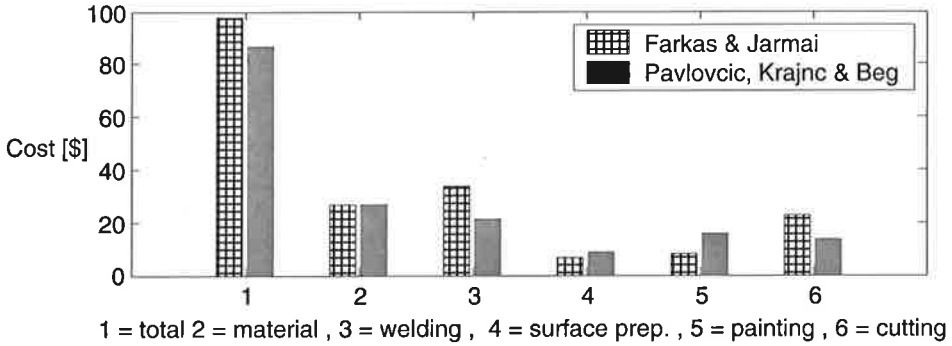


Figure 3. The distribution of costs for the minimum mass structure in the welded box beam example.

Table 2. Parameter values for manufacturing costs according to Pavlovčič, Krajnc and Beg in the welded box beam example (1 EUR = 1,18 $).

Welding manufacturing cost	$T_{\text{weld}} = 2,62a_{\text{w}}^2 + 1,37a_{\text{w}} + 0,09$ [min/m], $T_{\text{weld.extra}} = 5,0$ [EUR/h], $f_{\text{w}} = 0,625$ and $k_{\text{weld}} = 69,7$ [EUR/h]. (Very automatic SAW welding line.) $T_{\text{weld}} = 9,03a_{\text{w}}^2 + 4,68a_{\text{w}} - 0,82$ [min/m], $T_{\text{weld.extra}} = 0,3$ [EUR/h], $f_{\text{w}} = 1,40$, $k_{\text{weld}} = 7,4$ [EUR/h]. (Manual metal arc welding, downhand position)
Welding material cost	$M_{\text{weld.wire}} = 0,97a_{\text{w}}^2 - 0,01a_{\text{w}} + 0,001$ [kg/m], $M_{\text{weld.flux}} = 0,51a_{\text{w}}^2 + 0,29a_{\text{w}} - 0,044$ [kg/m], $k_{\text{m.weld.wire}} = 1,92$ [EUR/kg] and $k_{\text{m.weld.flux}} = 1,56$ [EUR/kg]. (Very automatic SAW welding line.) $M_{\text{weld.electrodes}} = 0,66a_{\text{w}}^2 + 0,18a_{\text{w}} - 0,10$ [kg/m], $M_{\text{weld.power}} = 1,22a_{\text{w}}^2 + 3,24a_{\text{w}} - 1,83$ [kWh/m], $k_{\text{m.weld.electrodes}} = 1,4$ [EUR/kg] and $k_{\text{m.weld.power}} = 1,4$ [EUR/kWh]. (Manual metal arc welding, downhand position)
Assembly and tacking	$T_{\text{handling}} = -8 \cdot 10^{-8}(\rho V)^2 + 0,001\rho V + 4,52$ [min], $T_{\text{tack}} = 15,0$ [min], $T_{\text{tack.prep}} = 45,0$ [min] and $k_{\text{assembly}} = 69,7$ [EUR/h].
Cutting	$T_{\text{cut}} = -0,015t^2 + 0,421t + 1,43$ [min/m], $M_{\text{cut.propane}} = 2,171t + 7,87$ [l/m], $M_{\text{cut.oxygen}} = 1,645t^2 + 56,644t - 6,73$ [l/m], $T_{\text{handling.pl}} = -4 \cdot 10^{-8}(\rho V)^2 + 0,001\rho V + 3,72$ [min], $f_{\text{cut}} = 1,03$, $T_{\text{cut.extra}} = 2,0$ [EUR/h], $k_{\text{cut}} = 18,4$ [EUR/h], $k_{\text{m.cut.propane}} = 0,002$ [EUR/l], $k_{\text{m.cut.oxygen}} = 0,0016$ [EUR/l] and $k_{\text{m.handling.pl}} = 11,0$ [EUR/h].
Painting	$T_{\text{paint}} = 7,0$ [min/m^2], $k_{\text{paint}} = 25,8$ [EUR/h], $M_{\text{paint,1}} = 0,13$ [l/m^2], $M_{\text{paint,2}} = 0,173$ [l/m^2], $M_{\text{paint,3}} = 0,15$ [l/m^2], $k_{\text{m.paint.1}} = 4,5$ [EUR/l], $k_{\text{m.paint.2}} = 3,8$ [EUR/l] and $k_{\text{m.paint.3}} = 3,8$ [EUR/l].
Surface prep.	$L_{\text{blast}} = 300$ [cm], $T_{\text{blast}} = 2,2$ [min/m] and $k_{\text{surf.prep}} = 39,4$ [EUR/h].

Based on the table 3 it can be seen that the minimum cost structure depends on the chosen cost function. The cost function of Jármai and Farkas gives higher price for the box beam than the alternative approach. The cost minimization by using the cost function of Jármai and Farkas leads to the same result as the mass minimization and this structure is slightly lighter than the one which comes from the cost minimization by using the cost function of Pavlovčič, Krajnc and Beg. By comparing the material and the manufacturing costs between the minimum cost and the minimum mass structures it can be noticed that they are almost the same. The displacement constraint is the most restrictive constraint in all cases.

Table 3. Optimization results in the welded box beam example.

	Cost minimization Jármai & Farkas	Cost minimization Pavlovčič, Krajnc & Beg	Mass minimization (J&F / P, K&B)
K_m [\$]	26,98	27,69	26,98
K_f [\$]	70,58	58,67	70,58 / 59,43
K [\$]	97,57	86,36	97,57 / 86,41
h_1^* [mm]	499,96	466,95	500,00
b_1^* [mm]	50,00	50,00	50,00
h_2^* [mm]	126,75	103,55	126,75
b_2^* [mm]	50,00	50,00	50,00
t_1^* [mm]	3	3	3
t_2^* [mm]	3	3	3
t_3^* [mm]	15	20	15
t_4^* [mm]	10	10	10
u [mm]	5,00	5,00	5,00
σ_{mises} [MPa]	167,36	167,86	167,36
λ_{cr}	18,60	22,26	18,97

COST MINIMIZATION OF TUBULAR PLANE TRUSS

The second example problem deals with the tubular plane truss presented in Fig. 4. The cost of the structure should be minimized so that the vertical displacements in joints 4 and 6 are less than $v^{max} = 75$ mm and Eurocode 3 strength and buckling requirements for beams and strength requirements for welded joints (except joints 1 and 11) presented in [9] are fulfilled. The topology and the shape of the structure are constant and the task is to choose profiles from given set of 53 different kind of recommended RHS-profiles which all belong to the cross section class 1 or 2 [9]. The cross section of upper flange is constant as well as the cross section of lower flange. Web bars can be different but the structure has to be symmetrical around vertical center line. Thus the number of possibly different kind of profiles is 7 in the truss.

The analysis of truss is done by using simple linear FEM with the mesh of 19 beam elements (5 in upper flange, 4 in lower flange and one per each web bar). It is assumed that flanges are continuous beams and they both consist of three pieces welded together. Joints between web bars and flanges are hinges and the eccentricity is zero. The compressed upper flange is supported in out of plane direction in joints 1, 3, 5, 7, 9 and 11. In the truss the alignment of RHS-profiles is such that the heigh of the profile cross section is parallel to the xy-plane.

Possible set of 53 RHS-profiles is arranged in the order of magnitude. The design variable $x_i \in \{1,2,\ldots,53\}$ represents the ordinal number of profile which is chosen for element i or the group of elements i ($i = 1,2,\ldots,7$) All the needed cross-section properties for element (the group of elements) i can be picked up from manufacturer's table [9].

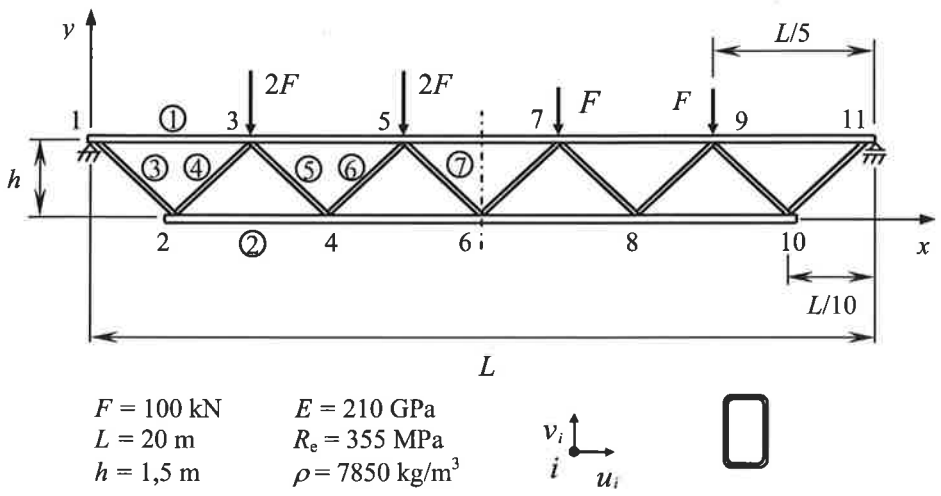


Figure 4. Symmetrical tubular plane K-truss made of RHS-profiles, different cross sections (1, …, 7), joints (1, …, 11) and displacements u_i and v_i connected to joint i.

The current optimization problem can be presented into following mathematical form

$$\begin{aligned}
&\min K(\mathbf{x}) \\
&|v_4(\mathbf{x})|, |v_6(\mathbf{x})| \le v^{\max} \\
&g_i^{s}(\mathbf{x}) \le 0 \qquad i = 1, \ldots, 19 \\
&g_i^{bl}(\mathbf{x}) \le 0 \qquad i = 1, \ldots, 19 \\
&g_i^{j}(\mathbf{x}) \le 0 \qquad i = 1, \ldots, 9 \\
&\mathbf{x} \in \{\mathbf{x}_1, \mathbf{x}_2, \ldots, \mathbf{x}_{\bar{n}}\}
\end{aligned} \tag{17}$$

The displacement constraints limit the desired node displacements v_4 and v_6 to be less than the maximum allowed value. The strength constraints $g_i^{s}(\mathbf{x}) \le 0$ take care that all 19 beams fulfill the strength requirements of Eurocode 3. The buckling constraints for individual beams $g_i^{bl}(\mathbf{x}) \le 0$ prevent beams from loosing their stability according to Eurocode 3. $g_i^{j}(\mathbf{x}) \le 0$ are the strength constraints for welded joints between tubular members (except joints 1 and 11). Connections can be either gap or overlap joints. $\bar{n} = 53^7$ is the number of possible candidate solutions in the current pure discrete optimization problem. It is, as usually, a huge number and it is not possible to check all the candidate solutions one by one and choose the best feasible solution.

The cost function of Jármai and Farkas is chosen as the object function and the values of needed parameters are presented in the table 4. The cost minimization problem is solved 100 times using the same version of PSO as in the first example problem. However this time the size of the swarm is 70 particles and the number of iteration rounds is 300. The initial swarm includes 10 feasible particles. In addition to the cost minimization also the mass minimization is done. The best found solution (i.e. at the same time the most economic and the lightest structure) is presented in the table 5.

Table 4. Parameter values for the manufacturing cost in the tubular truss example.

Preparation, assembly and tacking	$C_1 = 1$, $\Theta_d = 3$ and $\kappa = 16$
Welding and additional fabrication costs	$C_2 = 0,3394$ and $n = 2$ (GMAW-C longitudinal fillet welds downhand position)
Surface preparation	$\Theta_{ds} = 2$ and $a_{sp} = 3 \cdot 10^{-6}$
Painting	$\Theta_{dp} = 2$, $a_{gc} = 3 \cdot 10^{-6}$ and $a_{tc} = 4,15 \cdot 10^{-6}$
Cutting	$\Theta_{dc} = 2$

Table 5. The best found solution in the tubular truss example.

K_m [\$]	K_f [\$]	K [\$]	
195,03	606,02	801,05	
Design variable	h [mm]	b [mm]	t [mm]
$x_1 = 21$	100	80	3
$x_2 = 3$	60	40	2,5
$x_3 = x_5 = 2$	60	40	2
$x_4 = x_6 = x_7 = 6$	70	50	3

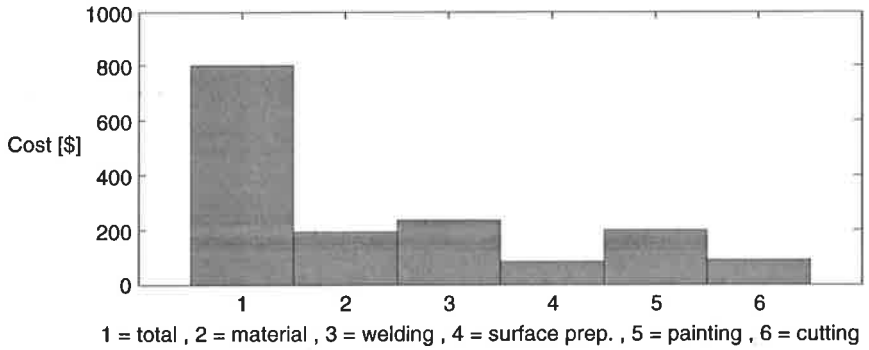


Figure 5. The distribution of costs for the minimum cost and the minimum mass structure in the tubular truss example.

One of the mass minimization runs gave the solution in the table 5 and the best result from the cost minimization runs was more expensive. Thus there was no use to take the cost function as the object function in tubular truss example. Probably the minimum cost and the minimum mass structure are the same or almost the same and stochastic PSO found the most economic structure by chance during the mass minimization.

CONCLUSION

There is no need to be limited to the mass minimization in case of the optimum design of welded steel structures. The manufacturing cost can be taken into account considering different manufacturing stages. There are several ways to calculate the manufacturing costs and these methods are always in some sense case-specific due to the varying of the level of technology.

Particle swarm optimization is a suitable algorithm for optimization problems in which a commercial FEM-code is used for the structural analysis. The idea of algorithm is rather simple and it is easy to implement as a computer program. Heuristic PSO can not guarantee the global optimum but it can be used to find good solutions that are relatively close to the global optimum. Such solutions are good enough in many applications and there is no need to find the best solution. The big amount of FEM-analysis is the major drawback of PSO in structural optimization.

Based on previous experience it is known that the manufacturing cost is higher than the material cost in many welded steel structures. This suggests that the cost optimized structure might be different than the mass optimized structure. However according to presented example problems the cost minimum and the mass minimum structures are close to each other and the total cost of the structure is almost the same in both cases. The type of the cost function does not substantially affect on this result. Pavlovčič, Krajnc and Beg have been also noticed the adjacency of costs between mass and cost minimized structures in their paper [8].

The connection between the manufacturing cost and the mass, area and plate thicknesses of the structure is probably the reason why different optimizations lead to the same result. If the area or the plate thickness increase the relation between the cost of the structure and the mass of the structure remains roughly speaking the same and thus optimization leads to same result in both cases. The situation might be different if the topology of the structure may change during the optimization as in the example problem in Ref. [2].

Despite the fact that the cost optimization does not necessary offer benefit compared to the traditional mass minimization the manufacturing cost should be included to object function. The manufacturing cost can be calculated rather simply and in some cases the difference between the mass minimized and the cost minimized structure might be significant.

REFERENCES

[1] Farkas J. and Jármai K. 1997. *Analysis and Optimum Design of Metal Structures.* A. A. Balkama.

[2] Farkas J., Simões L.M.C. & Jármai. K. 2005. Minimum cost design of a welded stiffened square plate loaded by biaxial compression. *Structural and Multidisciplinary Optimization* 29, 298-303.

[3] Fourie P.C. and Groenwold A. A. 2002. The particle swarm optimization algorithm in size and shape optimization. *Structural and Multidisciplinary Optimization*, 23, 259-267.

[4] Jármai K. & Farkas J. 1999. Cost calculation and optimisation of welded steel structures. *Journal of Constructional Steel Research* 50, 115-135.

[5] Jármai. K. & Farkas J. 2001. Optimum Cost Design of Welded Box Beams with Longitudinal Stiffeners Using Advanced Backtrack Method. *Structural and Multidisciplinary Optimization* 21, 52-59.

[6] Jármai K. 2002. Design, Fabrication and Economy. *European Integration Studies, Miskolc* Vol.1, No. 2, 91-107.

[7] Kennedy J., Eberhart R. 1995. Particle Swarm Optimization. *Proceedings of the IEEE International Conference on Neural Networks*, Perth, Australia.

[8] Pavlovčič L., Kranjc A. & Beg D. 2004. Cost function analysis in the structural optimization of steel frames. *Structural and Multidisciplinary Optimization* 28, 286-295.

[9] Rautaruukki Metform. 1997. *Rautaruukin putkipalkkikäsikirja.* (Design Handbook for Rautaruukki Structural Hollow Sections).

[10] Vartiainen M. 2000. *Welding Time Models for Cost Calculations in the Early Stages of the Design Process.* Dissertation. Lappeenranta University of Technology.

[11] Venter G., and Sobieszczanski-Sobieski J. 2003. Particle Swarm Optimization. *AIAA Journal*, Vol. 41, No 8, 1583-1589.

MODELLING OF BEAMS IN DISCRETE ELEMENT SIMULATIONS

Jani Paavilainen

Helsinki University of Technology
Department of Mechanical Engineering, Laboratory for Mechanics of Materials
P.O. Box 4300, 02015 TKK, Finland
e-mail: jani.paavilainen@tkk.fi

ABSTRACT

Discrete element method (DEM) is a numerical tool used to simulate the nonlinear dynamics of a system of particles. DEM is also useful in analysis of fragmentation of solids as well as structural failure and collapse. In such studies, in addition to modelling fracture, also the behavior of the structure before fracture must be modelled with DEM.

In discrete element simulation a plane beam is composed of discrete particles which are joined together. In this paper, the joining of discrete particles together and calculation of forces between joined discrete particles is presented and implementation into a DEM code is verified through examples.

1 INTRODUCTION

In many fields of mechanics, such as rock and ice mechanics, several problems are characterized by a transition from a continuous to a discontinuous state. Initially these problems are presented by a small number of continuous regions. These regions then divide into many smaller bodies through fracture processes. To be able to simulate such a process, both the continuous and the discontinuous phenomena must be modelled in addition to modelling of fracture.

One way of modelling problems involving discontinuous processes is the discrete element method (DEM). It is a technique for modelling the nonlinear dynamics of systems consisting of granular and particulate materials [1]. DEM can also be used for modelling the fragmentation of solids as well as structural failure and collapse [2], [3]. In such studies, in addition to modelling fracture, also the behavior of the structure before fracture must be modelled with DEM.

In 2D-DEM, a plane beam can be modelled with discrete particles that are joined together with beam elements. The approach to use beam elements to combine discrete particles has been used e.g. [4], [5]. In this work, the joining of discrete particles together with beam elements and calculation of forces between joined discrete particles is presented and implementation into a DEM code is verified through simulation examples.

2 DISCRETE ELEMENT METHOD

Discrete element method is based on Newtonian mechanics. In traditional DEM, individual material particles, discrete elements, can interact with each other only through

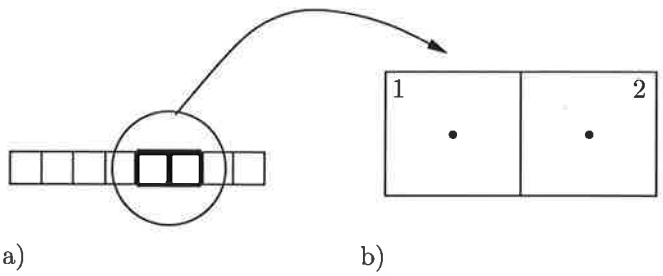


Figure 1: a) A continuum body formed of discrete particles. b) Two joined discrete particles.

pairwise contacts. The forces exerted from the contacts on individual particles are derived from the chosen interaction laws. Each individual particle is considered to be rigid and is represented by geometries such as disks, spheres, ellipsoids and polygons. The main parts of the discrete element simulation are: i) Contact detection, ii) calculation of the forces for contacting particles and iii) solving the new particle positions.

The position, $\mathbf{x}$ and $\boldsymbol{\theta}$, of each particle is determined in some frame of reference. According to Newton's second law of motion, the position of a rigid particle is described by the following differential equations

$$m_i \frac{\mathrm{d}^2 \mathbf{x}_i}{\mathrm{d}t^2} = \mathbf{F}_i \quad \text{and} \quad I_i \frac{\mathrm{d}^2 \boldsymbol{\theta}_i}{\mathrm{d}t^2} = \mathbf{M}_i \tag{1}$$

for each particle i. In Equation (1) m_i, $\mathbf{F}_i$, I_i and $\mathbf{M}_i$ are the mass, force, moment of inertia and moment respectively. The equations of motion (1) are solved with some explicit difference scheme. In this context the contact detection and calculating the contact forces is not studied further. For more details of that subject see e.g. [6], [7].

The forces $\mathbf{F}_i$ and moments $\mathbf{M}_i$ in equation (1) can contain both internal and external forces. Internal forces in DEM are present only when two or more particles are joined together by some manner to form a continuum body, see Figure 1. Internal forces are defined by the relative movement between two joined adjacent particles. In a continuum body two adjacent particles cannot collide and so the collision detection is not performed. The external forces are due to sources such as gravity, buoyancy and collisions. The collisions are defined between two particles, particle and a continuum body formed of individual particles or two continuum bodies.

3 INTERNAL FORCES

A two dimensional DEM with rectangular particles is studied. When two such particles are joined together internal forces are present. The joining of the particles can be done with a finite element type beam element. In two dimensions the beam element node and the center of mass of a particle have the same degrees of freedom, two displacements and a rotation, see Figure 2. In addition, nodes of the beam element unite with the center of masses of the combined discrete particles. Thus, one beam element can be used to combine two adjacent discrete particles as shown in Figure 2.

For the beam element the non-linear Timoshenko plane beam model is used, for details see e.g. [8], [9]. The Lagrangian kinematics of the C^0 beam element is shown in Figure 3. Let $X = \left[\begin{smallmatrix} X_p \\ Y_p \end{smallmatrix}\right]$ denote the position vector of a material point in reference configuration and x in deformed configuration. The displacement of the neutral axis of the beam is denoted as $\mathbf{u}_c = \left[\begin{smallmatrix} u_X \\ u_Y \end{smallmatrix}\right]$ and $\overline{\gamma}$ is the mean shear deformation.

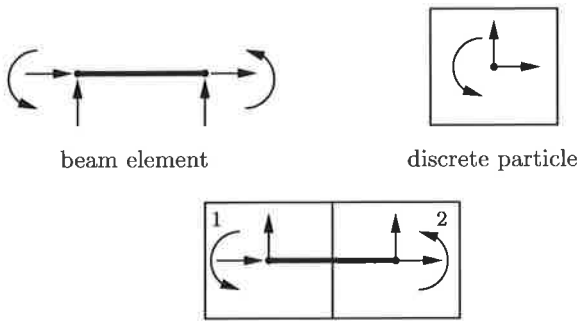


Figure 2: Combining discrete particles with a beam element.

The Lagrangian representation of the motion is

$$\mathbf{f}(\mathbf{X}) = \mathbf{X} + \mathbf{u}(\mathbf{X}) = \begin{bmatrix} X_p + u_X - Y_p \sin\theta \\ u_Y + Y_p \cos\theta \end{bmatrix}. \tag{2}$$

Thus, the deformation gradient is

$$\nabla\mathbf{f}(\mathbf{X}) = \begin{bmatrix} 1 + u'_X - Y_p\kappa\cos\theta & -\sin\theta \\ u'_Y - Y_p\kappa\sin\theta & \cos\theta \end{bmatrix}, \tag{3}$$

where $\kappa = \theta'$.

The Green-Lagrange strain tensor is defined as

$$\mathbf{E} = \frac{1}{2}(\nabla\mathbf{u}^T + \nabla\mathbf{u} + \nabla\mathbf{u}^T\nabla\mathbf{u}) = \begin{bmatrix} \epsilon_{XX} & \epsilon_{XY} \\ \epsilon_{YX} & \epsilon_{YY} \end{bmatrix}. \tag{4}$$

The nonzero strains are the axial strain ϵ_{XX} and the shear strain $\epsilon_{XY} + \epsilon_{YX} = 2\epsilon_{XY}$. For the axial strain ϵ_{XX}, consistent linearization with small-strain assumption is performed and the strain vector

$$\mathbf{e} = \begin{bmatrix} \epsilon_{XX} \\ 2\epsilon_{XY} \end{bmatrix} = \begin{bmatrix} (1 + u'_X)\cos\theta + u'_Y \sin\theta - Y_p\theta' - 1 \\ -(1 + u'_X)\sin\theta + u'_Y \cos\theta \end{bmatrix} = \begin{bmatrix} \varepsilon - Y\kappa \\ \gamma \end{bmatrix} \tag{5}$$

is obtained. Here the three strain quantities $\mathbf{h} = \begin{bmatrix} \varepsilon & \gamma & \kappa \end{bmatrix}^T$ characterize axial strains, shear strains and curvatures, respectively. For linear beam element ε and γ depend only on θ and κ is constant over the element, thus relations $1 + u'_X = L\cos\Psi/L_0$ and $u'_Y = L\sin\Psi/L_0$ hold. The strains ε and γ can then be expressed in the geometrically invariant form as

$$\varepsilon = \frac{L\cos\overline{\gamma}}{L_0} - 1 \tag{6}$$

$$\gamma = \frac{L\sin\overline{\gamma}}{L_0}. \tag{7}$$

When beam material is assumed to be homogeneous and isotropic, the only nonzero stresses are the axial stress and the shear stress. The stress resultants are defined in terms of second Piola–Kirchhoff stresses as follows

$$N = EA_0\varepsilon, \qquad Q = GA_0\gamma, \qquad M = EI_0\kappa, \tag{8}$$

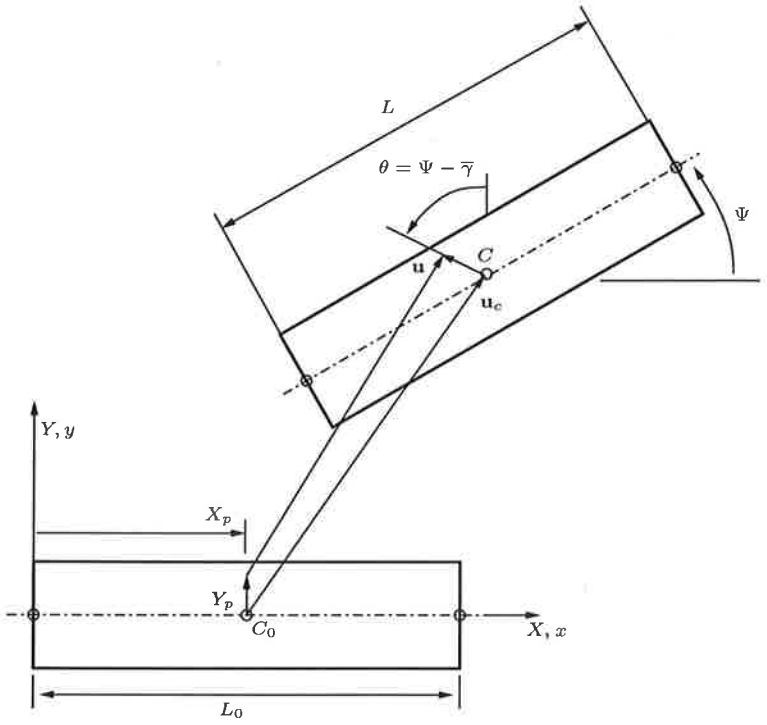


Figure 3: Lagrangian kinematics of the C^0 beam element.

where E is the Young's modulus, A_0 is the cross sectional area in the reference configuration, G is the shear modulus and I_0 moment of inertia of the cross section. The stress resultants N, Q and M represent axial force, transverse shear force and bending moment in the current configuration respectively.

The internal force $\mathbf{p}$ is obtained by variating the strain energy U with respect to the node displacements $\mathbf{u}$

$$\delta U = \int_{L_0} \mathbf{z}^T \mathbf{B} \, \mathrm{d}X \, \delta\mathbf{u}, \tag{9}$$

where $\mathbf{z} = \begin{bmatrix} N & Q & M \end{bmatrix}^T$ is stress resultant vector and $\mathbf{B}$ is defined by the strain displacement relation $\delta\mathbf{h} = \mathbf{B}\,\delta\mathbf{u}$. Because $\delta U = \mathbf{p}^T \delta\mathbf{u}$, the internal force

$$\mathbf{p} = \int_{L_0} \mathbf{B}^T \mathbf{z} \, \mathrm{d}X \tag{10}$$

is obtained. At the midpoint of the beam $\theta_m = (\theta_1 + \theta_2)/2$, $\varepsilon_m = L\cos(\theta_m - \Psi)/L_0 - 1$ and $\gamma_m = L\sin(\Psi - \theta_m)/L_0$. When evaluated at the midpoint, the equation (10) takes the form

$$\begin{aligned} \mathbf{p} &= L_0 \mathbf{B}_m^T \mathbf{z} \\ &= \begin{bmatrix} -c_m & -s_m & \frac{1}{2}L_0\gamma_m & c_m & s_m & \frac{1}{2}L_0\gamma_m \\ s_m & -c_m & -\frac{1}{2}L_0(1+\varepsilon_m) & -s_m & c_m & -\frac{1}{2}L_0(1+\varepsilon_m) \\ 0 & 0 & -1 & 0 & 0 & 1 \end{bmatrix}^T \begin{bmatrix} N \\ Q \\ M \end{bmatrix}, \end{aligned} \tag{11}$$

where $c_m = \cos\theta_m$, $s_m = \sin\theta_m$ and subscript m stands for the midpoint of the beam.

Because DEM analysis is dynamic, damping is introduced for the beam element. A viscous damping model is used to dissipate energy during the simulation. The viscous forces N_d, Q_d and M_d present axial damping, shear damping and damping moment respectively. They are proportional to the strain rates $\dot{\varepsilon}$, $\dot{\gamma}$ and $\dot{\kappa}$ of the beam.

The strain rates are defined by taking the time derivative of the strains, Equations (6), (7) and equality $\kappa = \theta'$. The viscous forces are then defined by equations

$$N_d = c_n A_0 \dot{\varepsilon}, \qquad Q_d = c_Q A_0 \dot{\gamma}, \qquad M_d = c_M I_0 \dot{\kappa}, \tag{12}$$

where c_N, c_Q and c_M are the damping coefficients. These viscous forces are then added to the stress resultants $\mathbf{z}$.

Now from the position $\mathbf{x} = \begin{bmatrix} x \\ y \end{bmatrix}$ and orientation θ of two adjacent particles, the strains $\mathbf{h}$ of the beam element combining the particles are calculated using Equations (6), (7) and equality $\kappa = \theta'$. In addition, the strain rates $\dot{\mathbf{h}}$ are defined from the particle positions and velocities. Next the stress resultants $\mathbf{z}$ using Equation (8) and damping forces $\begin{bmatrix} N_d & Q_d & M_d \end{bmatrix}$ using Equation (12) are calculated. After the stress resultant and damping forces are added, the internal forces $\mathbf{p}$ of the beam element are defined from Equation (11). Internal forces are then added to the corresponding particle forces.

4 EXAMPLES

4.1 Bending of a beam

As a first example bending of a beam was simulated with DEM. The beam was modelled with different boundary conditions and the displacement of the beam was compared to the displacement given by a nonlinear FEM analysis done with Ansys.

The modelled beam had length $L = 4.0$ m and rectangular cross section with dimensions $H = 0.5$ m and $B = 1.0$ m, see Figure 4 for the different arrangements. Material parameters used were Young's modulus $E = 1.0 \cdot 10^9$ N/m^2 and Poisson ratio $\nu = 0.3$. Two different values $F_1 = 5.0 \cdot 10^6$ N and $F_2 = 1.0 \cdot 10^7$ N for the force was used. In FEM analysis, the BEAM3 element of Ansys was used. For both models, large displacements and linear Hookean material model were considered.

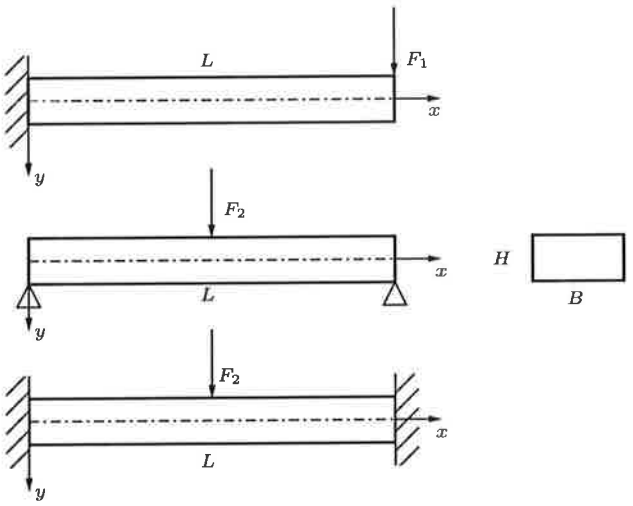
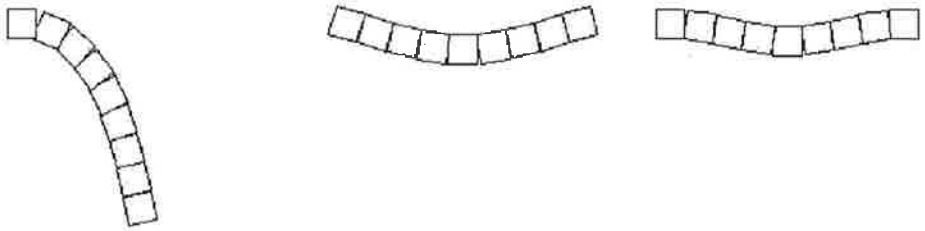


Figure 4: Different boundary conditions for the beam bending simulations.



(a) (b) (c)

Figure 5: Beam displacements with different boundary conditions.

Figure 5 shows the displacement of the beam with different boundary conditions obtained with DEM using 9 particles. The maximum displacements u_y calculated with both DEM and FEM for the different boundary conditions are given in Table 1.

Table 1: Maximum displacement u_y of a beam with different boundary conditions.

boundary conditions	u_y [m] (DEM)	u_y [m] (FEM)
clamped–free	3.147	3.157
supported–supported	0.440	0.454
clamped–clamped	0.289	0.316

No significant differences in the displacements with the first two boundary condition cases can be observed. The maximum difference obtained with the clamped–clamped boundary conditions was reduced when the number of particles in DEM and the number of elements in FEM was increased. The displacements u_y with 33 DEM particles and 30 FEM element were 0.298 m and 0.312 m respectively. The influence of the discrete particle size to the displacement was also studied. In Table 2 the displacement u_y of the clamped–free beam with different number of particles are given.

Table 2: The effect of the discrete particle size on the displacement u_y.

number of particles	particle edge length [m]	u_y [m]
9	0.500	3.147
17	0.250	3.154
33	0.125	3.175

For comparison, the displacement u_y was 3.188 m when calculated with FEM and 40 elements.

4.2 Beam on an elastic foundation

As a second example a beam on an elastic foundation was simulated with DEM. The results obtained were compared to the analytical solutions presented in [10]. The simulated

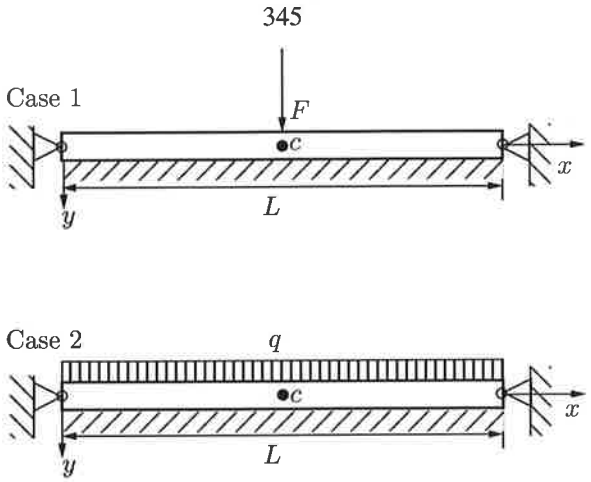


Figure 6: Simulated cases of the beam on an elastic foundation example.

cases are presented in Figure 6. The beam length L and cross sectional dimensions H and B were the same as in previous example. Young's modulus in case 1 was $E = 1.0 \cdot 10^7$ N/m^2 and in case 2 $E = 5.0 \cdot 10^7$ N/m^2. The Poisson ratio was $\nu = 0.3$ in both cases. In case 1 a force $F = 5.0 \cdot 10^3$ N was applied in the midpoint c of the beam and in case 2 the beam weight was used as a loading. Beam material density was $\rho_b = 930$ kg/m^3. Water was used as an elastic foundation.

In Table 3 the displacement of the midpoint of the beam obtained from analytical solution and DEM simulation with 51 particles is given for both studied cases. The maximum difference between analytical and DEM solutions of the displacement is about 3.0%.

Table 3: Displacement of the midpoint of the beam.

Case	u_c [mm] (DEM)	u_c [mm] ([10])
1	52.1	51.5
2	27.0	27.8

5 CONCLUSIONS

In this work combining of discrete particles together with a beam elements in two a dimensional DEM was studied. A nonlinear Timoshenko beam model was presented and used for combining the discrete particles. The implementation of the method into a DEM program was verified through two simple examples. The examples showed a good correspondence of the DEM simulation results to both analytical and nonlinear FEM solutions.

ACKNOWLEDGEMENTS

The financial support from the Academy of Finland, the Finnish Cultural Foundation, and Heikki and Hilma Honkanen Foundation is gratefully acknowledged.

REFERENCES

[1] Cundall, P.A. and Strack, O.D.L. 1979. *A discrete numerical model for granular assemblies.* Géotechnique. 29, 47-65.

[2] Kun, F. and Herrmann, H.J. 1996. *A study of fragmentation processes using a discrete element method.* Comput. Methods Appl. Mech. Engrg. 138, 3-18.

[3] Owen, D.R.J et al. 2004. *The modelling of multi-fracturing solids and particulate media.* Int. J. for Numerical Methods in Engineering. 60, 317-339.

[4] Ibrahimbegovic, A. and Delaplece, A. 2003. *Microscale and mesoscale discrete models for dynamic fracture of structures built of brittle materials.* Computers and Structures. 81, 1255-1265.

[5] Griffiths, D.V and Mustoe G.G.W. 2001. *Modelling of elastic continua using a grillage of structural elements based on discrete element concepts.* Int. J. for Numerical Methods in Engineering. 50, 1759-1775.

[6] Munjiza, A. 2004. *The combined finite-discrete element method.* Chichester, England. John Wiley & Sons Ltd. 333 p. ISBN 0-470-84199-0.

[7] Hopkins, M.A. 1992. *Numerical Simulation of Systems of Multitudinous Polygonal Blocks.* CRREL Report. 92-22.

[8] Felippa, C.A. *Nonlinear Finite Element Methods.* University of Colorado (Online) 2001. [Referenced 25.4.2006]. Material assembled from lecture notes for the course Nonlinear Finite Elements Methods. Available: http://www.colorado.edu/engineering/CAS/courses.d/NFEM.d/.

[9] Crisfield, M.A. 1991. *Non-linear Finite Element Analysis of Solid and Structures, Volume 1: Essentials.* Chichester, England. John Wiley & Sons Ltd. 345 p. ISBN 0-471-97059-X

[10] Ylinen, A. 1976. *Kimmo- ja lujuusoppi I.* Second ed. Porvoo, Finland. WSOY. 476 p. ISBN 951-0-05358-9.

FATIGUE STRENGTH ANALYSIS OF A CRANKSHAFT BY USING MULTIBODY DYNAMIC SIMULATION

M. SAVOLAINEN, B.R. RABB

Calculation & Simulation
Engine Technology Development
Engine Division
Wärtsilä Finland Oy, Vaasa

Abstract

More effective engines have to be developed due to ever increasing competition between large and medium-size diesel engine manufacturers. This basically means a reduction in fuel consumption and air emissions. A simultaneous challenge is to maintain the required output power level and durability of engine components. Therefore, accurate calculation methods are needed from the mechanical perspective.

This paper presents a method for calculating crankshaft fatigue strength by evaluating the stresses during an engine cycle using a combination of multibody dynamic simulations and FE-calculations. The stresses are then used to define the fatigue strength of the component as a multiaxial case.

Safety against fatigue is considered as a statistical concept in many senses. This concept includes the use of used material values, the size effect of the critical area and the effect of surface roughness. Eventually, the lifetime of the crankshaft is calculated at a certain probability of failure.

The vibration torques from measurements and simulations are compared to reality.

Keywords: *Fatigue, crankshaft, multiaxial, multibody dynamics, Findley, size effect.*

1. INTRODUCTION

From a mechanical perspective, improvements to combustion engine efficiency can be mainly made by increasing component strength and reducing the mass of moving parts. Therefore, accurate calculation methods are needed. Due to the development of computers, it has now become possible to simulate the behaviour of engine components with realistic constraints within a reasonable time range, also when using multibody dynamic simulations. This makes it possible to obtain accurate engine-component load data without making measurements.

The lifetime of Wärtsilä engines is very long. Since difficult to replace components, like the crankshaft for example, can see billions of load cycles during engine usage, high strength against fatigue is demanded. According to mathematicians, the world is statistically distributed, which

leads to a concept of estimating component lifetime also using a statistical approach. At Wärtsilä, the statistics are present in the fatigue analysis in many ways: material strength is defined from a distribution of tests; the effect of component size is related to a distribution of surface stresses and scatter of strength; the effect of surface roughness is taken into account by considering the material strength data; and the long engine usage time has been included as a result of using a long life factor.

Finally, all the above is used to calculate a component safety value at a certain probability of failure.

New crankshaft designs in marine installations have to be accepted by a classification society chosen by the customer. The appropriate classification society's requirements are more or less based on tests, which have lead to simplified calculation rules according to geometric parameters. This paper shows a method to make a crankshaft fatigue analysis using numerical computerized tools aiming for better accuracy.

2. SAFETY CALCULATION PROCEDURE

The analysis procedure can be divided into three stages. During the first stage, the material parameters are defined. The second stage deals with pre-processing, whereby all the needed models for FE-calculations, simulations and the simulation model itself are made. This is the most labour intensive stage. In the third stage, the simulation results are used in the fatigue analysis and the safety for the component is defined.

2.1. Tensile strength and the Haigh diagram

The tensile strength for quenched and tempered high-grade steels, for example, is defined as a range in the material standards. It is quite common to use the minimum value of the range to be on the safe side in fatigue analysis. On the other hand, steel companies make tensile strength tests for batches they deliver. According to the test data, a distribution was produced for 42 CrMo4 in size class of 100<diameter<160 mm as shown in Figure 2.1.

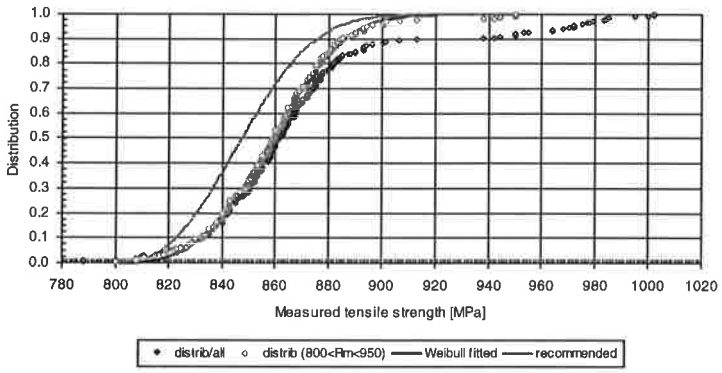


Figure 2.1. Measured tensile strength distribution for 42 CrMo4 (100<d<160 mm).

A Weibull distribution was fitted to the test data and a safer recommended line was produced according to this. The mean value of the line is then used as the tensile strength. In Figure 2.1, the recommended tensile strength value is 845 MPa, which is about 6 % higher than the minimum value from the standards.

It is known that the fatigue ratio, i.e. the ratio of the fatigue limit in fully reversed tension compression and the ultimate tensile strength, is fairly constant for a given material type. Therefore, the tensile strength can be used in a first analytical determination of the fatigue limits $\sigma_{aR=-1}$ and $\sigma_{aR=0}$. The first ratio shows the value in a fully reversed uniaxial tension compression and the second ratio shows the stress pulsating from 0 to its maximum value. Obviously, an accurate method for determining the two different stress ratios requires tests of the particular material. However, the Haigh diagram can be constructed according to these fatigue limits.

The Haigh diagram used in the example analysis shown later in this paper is in Figure 2.2. The diagram is constructed by using the value of 750 MPa for the tensile strength. This is the minimum tensile strength in the largest size class (160<diameter<250 mm) available in the standards /1/. However, even though the crankshaft diameter is larger, there is a reason to believe that the crankshaft meets this above value due to high quality requirements at Wärtsilä.

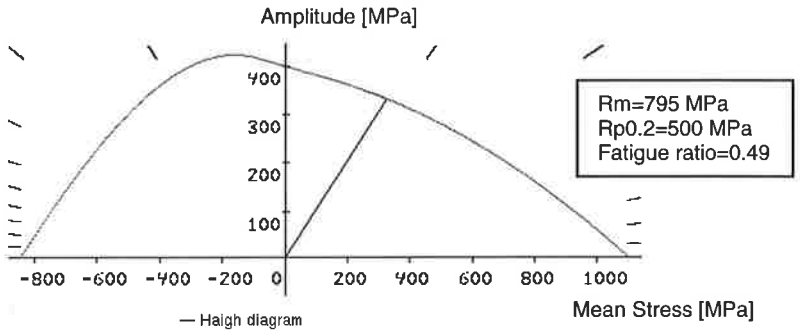


Figure 2.2. The Haigh diagram of the 42 CrMo4. This diagram is used in the example analysis in this paper.

The goal of the tensile strength manipulation is to reduce over-dimensioning from the material perspective.

2.2. Surface roughness, life and size effect factors

The low surface quality is considered to provide a higher probability of failure for the component since the majority of failures start from the surface. The surface factor K_r uses a ten point height of irregularities and tensile strength as follows /2, p. 140/:

$$K_r = \frac{1}{1 - 0.22 \cdot (\lg R_z)^{0.64} \cdot \lg R_{mMedian} + 0.45 \cdot (\lg R_z)^{0.53}} \tag{2.1}$$

According to relatively recent studies, it has been shown that the horizontal part of the Wöhler-curve is falling slowly at a higher number of load cycles /3, p. 273/. This is considered by reducing the fatigue limit of steels and cast irons with life factor K_N for 5 % per decade of cycles N /4, p. 14/.

$$K_N = 1 - \left[\lg N - \lg\left(2 \cdot 10^6\right)\right] \cdot 0.05 \qquad (2 \cdot 10^6 \le N \le 2 \cdot 10^{10}) \tag{2.2}$$

Since Wärtsilä diesel engine components are relatively large, size also has to be taken into consideration. The idea is that the larger the component, the larger the probability of possible material or surface defects in the critical area, where the failure can start. The definition of the statistical size effect is derived by using the theory of the weakest link, where the number of links

is determined by comparing the effective stress areas of the examined part and a test specimen. The effective area is calculated using the expectation value for the standard deviation and it is formed by dividing the critical surface area into sub areas A_i /5, p. 2, 3/.

$$A_{eff} = \sum_i \frac{\log R_i}{\log 0.5} \cdot A_i \tag{2.3}$$

Where reliability R_i at the average stress σ_i in area i is determined with equations

$$R_i = \frac{1}{\sqrt{2\pi}} \cdot \int_{\lambda_i}^{\infty} e^{\frac{x^2}{2}} dx \tag{2.4}$$

Where the standard normal variable λ_i is as follows

$$\lambda_i = \frac{1}{s_{rC50}} \cdot \left(\frac{\sigma_i}{\sigma_{\max}} - 1 \right) \tag{2.5}$$

The maximum stress σ_{max} at the critical point is assumed to correspond to a reliability of 0.5. The number of links can then be evaluated with the following equations.

$$n = \frac{A_{eff}}{A_{ref}}, A_{eff} > A_{ref} \tag{2.6}$$

$$n = \frac{A_{ref}}{A_{eff}}, A_{ref} > A_{eff}$$

Finally, the size factor K_{size} can be calculated. The used confidence limit of 90 % was applied on the standard deviation s_{rC} when the effective stress area of the part is larger than the area of the specimen. A relative standard deviation s_{rC} of 0.09 is then used respectively for steels.

$$K_{size} = \frac{1}{1 + \lambda s_{rC90}} \tag{2.7}$$

Where the standard normal variable λ is found by using the number of links from Equation

$$R = \sqrt[n]{0.5} = \frac{1}{\sqrt{2\pi}} \cdot \int_{\lambda}^{\infty} e^{\frac{-x^2}{2}} dx \tag{2.8}$$

2.3. Multiaxial failure criterion and safety factor

The utilized multiaxial criterion in this paper is the Findley criterion. The basic idea is to find a plane in the stress space, where the sum of the shear stress range and the normal stress obtains its maximum value. According to Wärtsilä experience, it has been noted that the Findley criterion can handle anisotropy, provides realistic results even for cast iron, and is usually slightly conservative in comparison to other criteria like McDiarmid, Dang Van or Papadopoulos. The Findley damage D is

$$D=\left(\frac{\Delta\tau}{2}+k\cdot\sigma_n\right)_{\max}\leq f \tag{2.9}$$

Where the constant k can be extracted from

$$\frac{k+\sqrt{1+k^2}}{2k+\sqrt{1+4k^2}}=\frac{\sigma_{aR=0}}{\sigma_{aR=-1}} \tag{2.10}$$

And the fatigue limit in shear f

$$f=\frac{\sigma_{aR=-1}}{2}\left(k+\sqrt{1+k^2}\right) \tag{2.11}$$

The evaluated factors are considered in the safety factor calculation with Findley variables

$$S_F=\frac{K_N\cdot K_R\cdot f}{K_{size}\cdot D} \qquad \text{when } A_{eff}\geq A_{ref} \tag{2.12}$$

$$S_F=\frac{K_{size}\cdot K_N\cdot K_R\cdot f}{D} \qquad \text{when } A_{eff}\leq A_{ref}$$

One difficulty in the use of the Haigh diagram is how to determine the safety factor. This can be made in different ways either by considering the maximum stress, the mean stress or the stress ratio as constant. The general assumption in this paper is the latter, meaning that the shear stress amplitude and the normal stress vary in the same way in an overloading situation.

To overcome the above difficulties, a uniaxial stress state change has been taken into use. It is possible to change a multiaxial state to an equivalent uniaxial stress state with the same safety factor by transforming the damage D to the following form

$$D=\frac{\sigma_{r,\max}-\sigma_{x,\min}}{4}\sin(2\alpha)+k\sigma_{x,\max}\cos^2\alpha \tag{2.13}$$

The direction of the critical plane α can be solved with derivation

$$\frac{dD}{d\alpha}=0 \tag{2.14}$$

When the direction of the critical plane and the maximum and minimum stress values in the plane are determined, the equivalent mean stress and amplitude can be extracted and the safety calculation can be continued.

2.4. Probability of failure

Basically, safety is tied to a probability of failure. This means that there are always some parts of the manufactured design, which will fail. For example, if the safety analysis for the crankshaft shows 1.29, statistically 1 out of 1000 pieces will fail before the desired lifetime at a confidence level of 90 %. Figure 2.3 lists some recommended safety factors at Wärtsilä.

Material and surface	Relative standard deviation s_{rC} at confidence limit C_a		Safety factor S_F at probability of failure P	
	$C_a = 0.1$	$C_a = 0.9$	$P = 10^{-3}$ and $\lambda = -3.09$	$P = 10^{-4}$ and $\lambda = -3.72$
Machined steel surface with parallel grain flow	0.05	0.08	1.29	1.36
Machined steel surface with perpendicular grain flow	0.085	0.12	1.48	1.61

Figure 2.3. Recommended safety factors at Wärtsilä.

One problem is to define the grain flow direction. The initial assumption is that the grain flow is considered to be parallel with the damage. However, the grain flow direction of deep machined fillets might not be ideal in comparison to the loading situation. Therefore, at least the probability of failure $P=10^{-4}$ should be used to be on the safe side.

3. STRESS CALCULATION PROCEDURE

The stress calculation starts from the simulation. The engine assembly is constructed out of different relatively rough FE-models and used in the simulation. The resulting displacements at the examined part are used in a separate stress calculation. The simulation presented in this paper was made with AVL's Excite and the FE-calculations with Abaqus.

The simulation model consists of a crankshaft, connection rods with pistons, an engine block, a generator and a common base frame on which the parts are assembled. Figure 3.1 shows an example of a real engine assembly using a 6-cylinder Wärtsilä 32 engine and a generator. An analysis performed for this type of engine assembly is used as an example in this paper. The crankshaft of the Wärtsilä 32 was obviously designed according to the IACS rules to meet the safety requirements and to be as efficient as possible in other matters i.e. weight and bearing load.

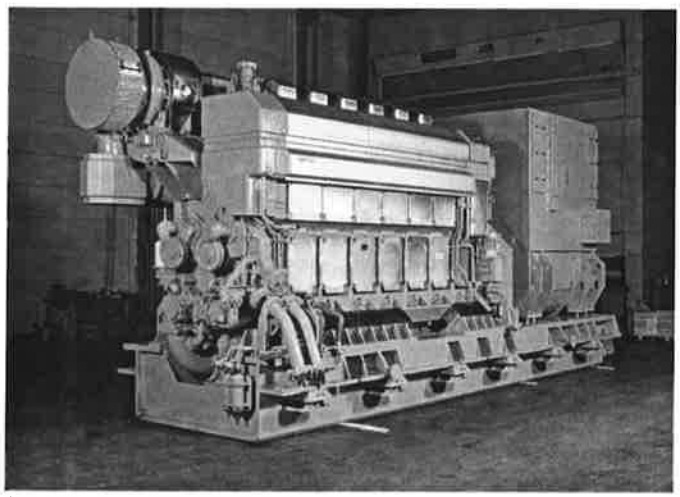


Figure 3.1. Wärtsilä 32 connected to a generator.

3.1. The simulation

There are two type of movement in the multibody simulation. The global motion is handled by solving the theorem of momentum for translation and angular movement for all the bodies in the model. The connection elements transfer forces and moments between adjacent elastic bodies in a mechanically realistic way. Mathematically, they supply the constraints forces and moments to the equations of motion and vibration.

The small movement, local deformation, can be governed by Newton's equation for a linear elastic system

$$M_i \cdot \ddot{q} + D_i \cdot \dot{q} + K_i \cdot q = f_i^a + f_i^* + p_i \qquad (3.1)$$

Where q is a generalized displacement vector for a sub-body i (an element) in a model, M, D and K represent mass, damping and stiffness matrixes respectively. The f^a is known forces and moments, f^* is external unknown constraint forces/moments and p is a nonlinear term originating from coordinate transformations /6, p. 3-2/.

The building of a simulation model starts from making the necessary FE-models of the parts. The parts can be divided into two categories

- Parts with large movement e.g. crankshaft and connection rod with pistons
- Parts with small movement e.g. engine, generator and base frame

The masses/moments of inertia and stiffness data of the parts are needed in the simulation. Therefore, the FE-models of the parts were made and an eigen value analysis was performed to verify the models to the measurements when available. Due to the large number of degrees of freedom (DOF), the FE-models cannot be used in the simulation directly. Substructuring is used for a dynamic reduction of the engine block and the generator assembly.

A dynamic reduction has to be made for the crankshaft and connection rod as well. This is made by dividing the crankshaft into small sections, where mass/moments of inertia and stiffness are known. Then a beam-mass model is gathered out of these sections. Figure 3.2 shows the FE-model, the divided crankshaft model and then the beam-mass model as well as a comparison of eigen values between the FE-model and the reduced model, which shows that the stiffness-mass distribution is similar. The generator rotor is directly connected to the flywheel.

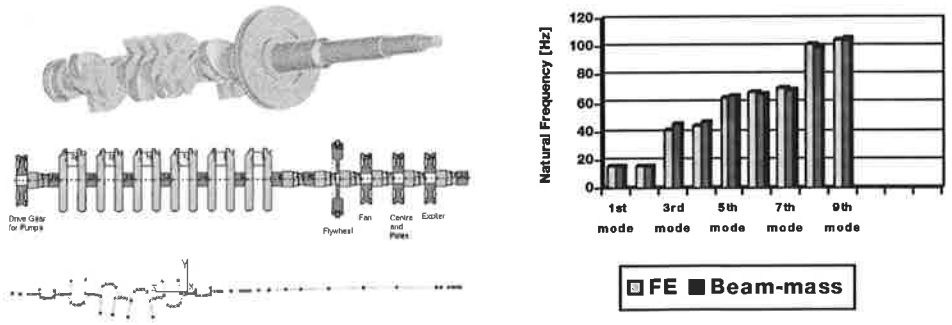


Figure 3.2. Reduction of the crankshaft model from an FE-model to a beam-mass model via dividing the crankshaft to smaller sections with mass/moments of inertia and stiffness data in between. An eigen value comparison of the FE and beam-mass models is shown on the right.

The gas pressures are applied on the connecting rods and a resisting moment is added on the generator axis in the simulation model as loads. Nonlinear spring elements with damping are used as connection elements between parts. An example of the main bearings is shown in Figure 3.3 as well as the simulation model.

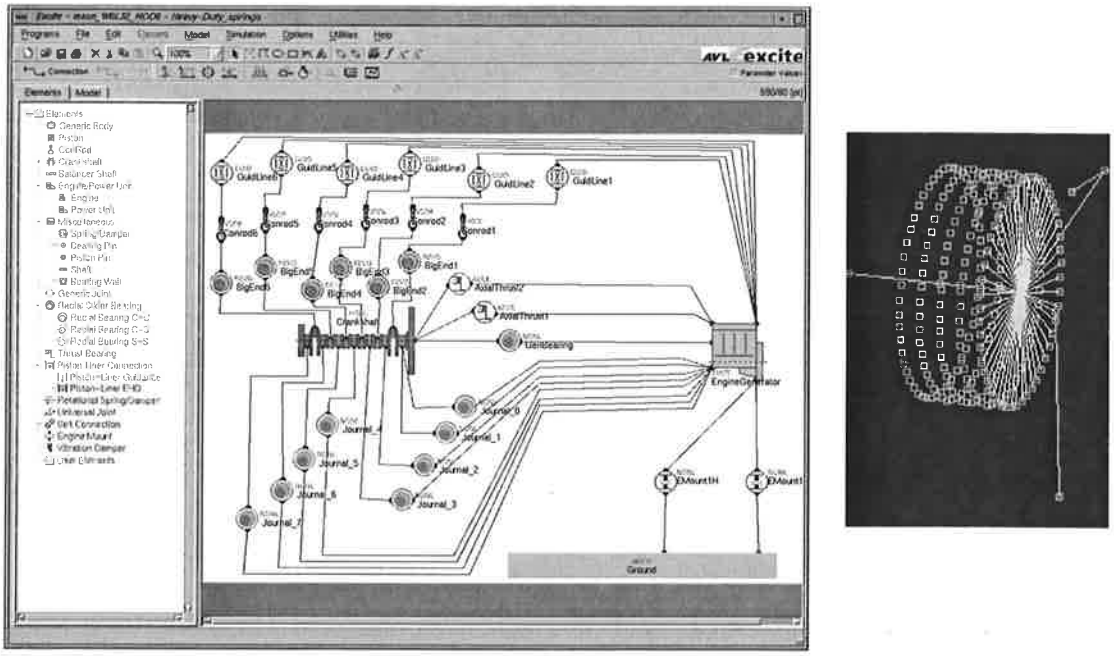


Figure 3.3. The simulation model of a Wärtsilä 32 generating set and a visualization of a main bearing model. Yellow lines in the bearing figure are presenting the springs with damping, which are connecting the crankshaft to the main bearing housing nodes.

3.2. Stress calculation

The displacement data from the crankshaft nodes from the simulation results are used as forced displacement loading in the stress analysis. First the analysis is made for a relatively rough crankshaft model shown in Figure 3.2. For necessary accuracy, sub-models of the interesting locations have to be used. The interesting locations are usually the crank and the journal fillets as well as the outlet of the oil bore. Furthermore, certain other locations related to the oil borings are usually checked.

The properties of the linear elastic material model were used. The models were made out of second order tetrahedron elements. When the stresses are known, the safety calculation can then be carried out as shown in Chapter 2.

4. RESULTS

The simulation was made at the highest loaded working situation of the engine. The parameters were 750 RPM and 110 % load, which is also possible to run in the Wärtsilä Vaasa laboratory environment. Naturally, a 110 % load is not permissible with a normal production engine. Another difference is that normally there is a vibration damper assembled on the crankshaft, which was taken off during the measurements in this case.

Basically, there are displacement results available for every DOF in the simulation model. The displacements data was taken into the stress calculation. The difficulty is that the measurements at the critical locations are quite demanding to do even in this size class of engine. The vibration torque on the other hand can be measured relatively easily to verify the simulation results to reality.

4.1. Measurement comparison

The vibration torque was measured with a strain gauge in a laboratory engine at Wärtsilä Vaasa. The sensor location is shown in Figure 4.1. The simulation result was taken at the same location in the model. The measured and simulated results are compared in Figure 4.2.

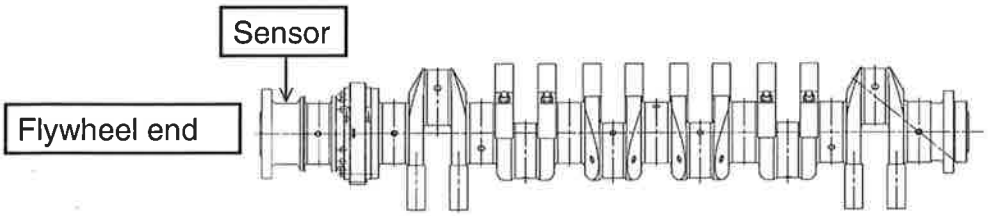


Figure 4.1. The sensor location in the crankshaft measurement.

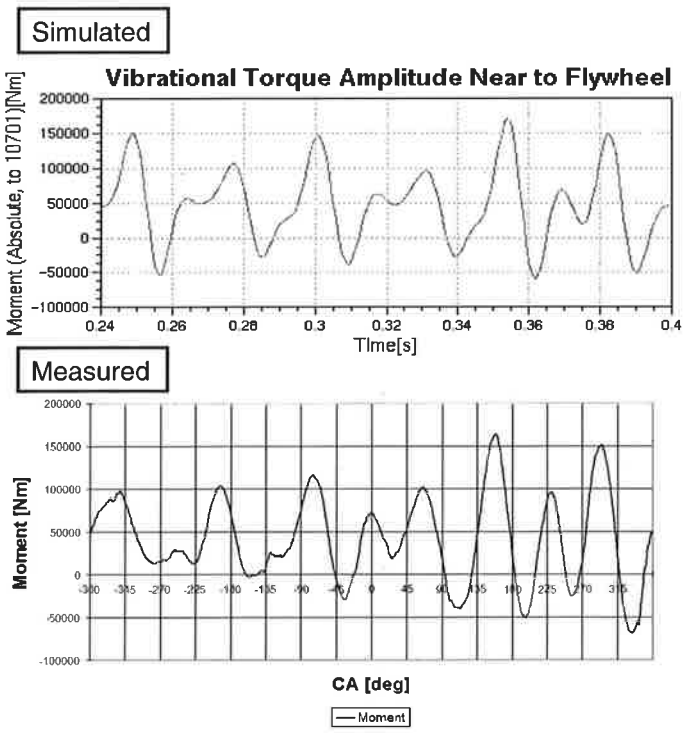


Figure 4.2. Simulated and measured vibration amplitudes compared.

The results in Figure 4.2 include the torque during one engine cycle. The profiles of the curves follow each other quite well. Peaks are at the same locations. The overall maximum and minimum values are practically the same.

However, there appear to be differences in the damping of the system. The oscillation between two high peaks to the right of Figure 4.2, for example, is smaller in the simulated curve. One source of inaccuracy is the gear wheels, which are in contact to the crankshaft. Those were not modelled in the simulation.

4.2. Stress results

The interesting location in the crankshaft was found to be the 3rd web as shown in Figure 4.3. The stresses were extracted by using sub-models of the critical locations.

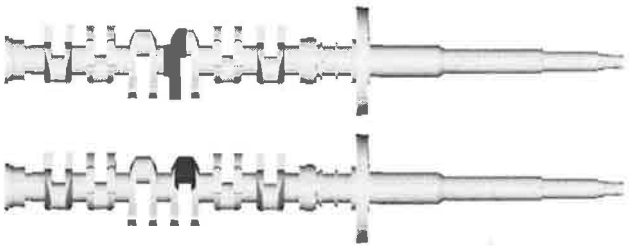


Figure 4.3. The critical crank web.

In this paper, the journal pin fillet is shown as an example. The safety calculation procedure is implemented in the Abaqus environment at Wärtsilä as an automatic process. This speeds up the analysis significantly. The stress history is collected automatically from the result database of the sub-model calculation and the safety is then extracted according to Chapter 2. The resulting data at the chosen nodes are written into another result database file, which can then be examined as a normal result database file.

Figure 4.4 shows the safety factor calculation results for the journal fillet. The results show the safety without the effect of the size factor, because the use of it will lead to only one value for the examined location (the safety with certain probability) and cannot be shown as a contour plot.

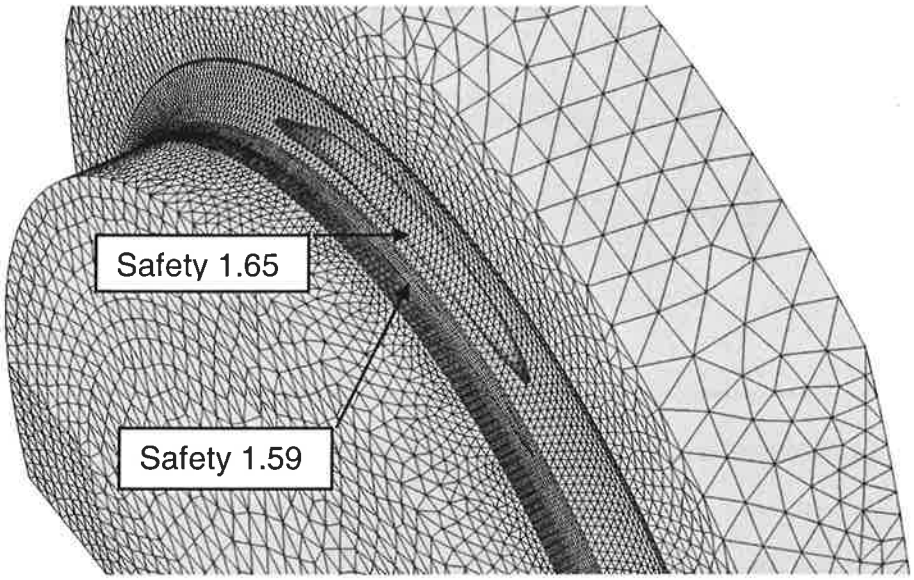


Figure 4.4. The journal fillet safety without the size effect factor.

When the size effect is also taken into account the safety will drop from 1.59 to 1.51, because the effective area is larger than the reference area. The calculated factors are shown in Table 4.1.

Table 4.1.The calculated factors for the journal fillet.

Surface factor	K_r	0.9
Life factor	K_N	0.82
Size factor	K_{size}	1.05
Safety factor without Ksize	$S_{F,\,pre}$	1.59
Safety factor	S_F	1.51

The recommended safety is 1.36 with the probability of failure being 10^{-4}. Hence, the assumption is that the grain flow is parallel with the stresses.

5. CONCLUSIONS AND DISCUSSION

A crankshaft fatigue analysis method is presented in this paper. Classification societies necessitate the diesel engine's crankshaft to meet certain requirements. The presumption was that the requirements lead to over-dimensioning. The goal of the research shown in this paper aims to introduce another analysis procedure with better accuracy by combining a fatigue calculation method used at Wärtsilä with a multibody dynamic simulation and FE-calculation.

The introduced procedure takes loading from the simulation instead of an analytical approach, whereby the loads are extracted from the gas and mass forces subjected to the crankshaft. This certainly lowers the stresses in the crankshaft in a more realistic direction, since the elasticity of the surrounding structures and the real shape of the crankshaft are also considered. The simulated and the measured results show clear equivalence in the torsion vibration curves. However, it can be seen from the comparison that the responses are not exact. This can be due to the fact that the dynamics of the gearwheels, which are rotated by the crankshaft, were not modelled. Nevertheless, the accuracy of the simulation model can be enhanced especially due to an increase of computing power.

The extraction of the loads by multibody dynamic simulation is labour intensive. To gain the full benefit, this kind of simulation should be utilized to provide realistic loading for analysis of several parts in the engine.

The example crankshaft was designed to meet the IACS rules and dimensioned with a very small margin. The resulting safety with the new method, 1.51 in the example analysis, is clearly higher than the required 1.36 (probability of failure 10^{-4}). However, the assumption is then that the grain flow is parallel with the stress field. It can be noted that with deep machined fillets there can be a risk that the directions of the grain flow and the stress field are not ideally parallel at the critical location.

One reason for the higher safety factor is the global load distribution in the structure as mentioned above. Another noticeable issue is the statistical approach to manipulate the tensile strength. A large margin against the material property variation has been used by accepting the lowest required value for the tensile strength according to the standards. In reality, the tensile strength is distributed and in this paper a 6 % higher value was used in comparison to the minimum in standards, when safety is considered as a statistical variable.

It can be seen from Table 4.1 that the effect of the size factor is relatively low, i.e. about 5 %. On the other hand the life factor has a significant effect on safety. This is depending on the predicted lifetime for the component. This time, the used value was $8 \cdot 10^9$ cycles, which generally speaking is very long. The surface factor also has a large effect despite the fact that the surface quality requirement is high ($R_a = 0.8$). The material characteristics also have an effect on this, meaning the higher the strength of the material, the lower the factor. It has been discussed at Wärtsilä that multiplying the life and the surface factors with each other will lead to an unrealistically low safety factor. Then the assumption is that these are more or less undependable on each other. This would basically mean that the surface factor considers the possible failures starting from the surface and the long life factor respectively takes into account the possibility of a crack nucleation from underneath the surface. One approach could be to use either one of the factors, whichever has the larger effect to the safety factor. Nevertheless, this is still under research and in this paper the most conservative method was used by considering both factors.

There has also been a discussion at Wärtsilä about the safety factor extraction from the Haigh diagram recently. The starting point was that there are several ways to define safety from the Haigh diagram depending on the case. This can be somehow circumvented by using uniaxial stresses. Nevertheless, an explicit method would be needed. It is obvious that when the loading situation point is near the limiting line, the methods provide relatively similar safety values. Therefore, perhaps the Haigh diagram limiting line should be transformed to cross the examined point and the safety should be calculated from the magnitude of the transformation. This kind of proceeding on the other hand could provide more reliable results regarding the magnitude of potential over-dimensioning.

ACKNOWLEDGEMENTS

The authors would like to thank Mr. Magnus Lassus at Wärtsilä for the good advice and fruitful conversations during the making of the analysis related to this paper and the paper itself.

REFERENCES

1 FINNISH STANDARDS ASSOCIATION SFS, SFS-EN 10083-1. Quenched and Tempered Steels. Part 1. Technical Delivery Conditions for Special Steels, Helsinki 1997.
2 Gudehus, H. Zenner, H. Leitfaden für eine Betriebsfestigkeitsrechnung, 3. Auflage. Verlag Stahleisen mbH, Düsseldorf, Germany 1995. 309 p. ISBN 3-514-00445-5.
3 Murakami, Y. Metal Fatigue: Effect of Small Defects and Nonmetallic Inclusions. ELSEVIER SCIENCE Ltd. 2002. 369 p. ISBN 0-08-044064-9.
4 Kaufmann, H. Wolters, D. B. Zyklische Beanspruchbarkeit disckwandiger Bauteile aus ferritischem Gußeisen mit Kugelgraphit. Konstruieren + gießen 27, Nr. 1, 2002.
5 Rabb, B. R. Interpretation and evaluation of the statistical size effect. CIMAC paper.
6 AVL List GmbH, Excite Base Module Reference Manual v5.1, 2000.

EFFECT OF LOCAL GEOMETRICAL VARIATIONS ON THE FATIGUE STRENGTH OF FILLET WELDED JOINTS

T. NYKÄNEN, G. MARQUIS, T. BJÖRK
Laboratory of Fatigue and Strength
Lappeenranta University of Technology
P.O.Box 20, FIN-53851 LUT, FINLAND
e-mail: timo.nykanen@lut.fi; gary.marquis@lut.fi; timo.bjork@lut.fi

ABSTRACT

The goal of this investigation was to study the effect of local geometrical variations of the weld on the fatigue strength. Therefore the fatigue behaviour of non-load-carrying cruciform fillet welded joint under tensile loading has been studied parametrically. Several two-dimensional (2D) finite element models of the joint were analyzed using plane strain linear elastic fracture mechanics (LEFM) calculations in order to get the magnification function M_k. A maximum tangential stress criterion was used to predict the crack growth direction under mixed mode K_I - K_{II} conditions. The derived M_k solution was then applied both for continuous weld toe cracks and also for semi-elliptical toe cracks at the deepest point of the crack front. An experimental crack aspect ratio development curve was used for propagating semi-elliptical cracks. The as-welded condition was assumed with the result that no crack initiation period was considered and stress ranges were fully effective. The Paris crack growth law was used to predict the growth rate. The effects of weld toe radius, flank angle and weld size on the fatigue strength were systematically studied. Finally, predicted fatigue strength values corresponding to different assumed crack sizes were compared with the available test results.

1. INTRODUCTION

In current industrial practice, welds and welded joints are an integral part of many complex load-carrying structures. Unfortunately, welds are often the weakest portions of these structures and their quality directly affects the integrity of the structure. Fatigue strength is known to be closely related to the precise geometrical discontinuity of the welded joint. Welding imperfections that may be introduced during fabrication are only partially considered in the conventional fatigue design rules for welded joints that are based primarily on S-N curves. In most cases the S-N curves in design guidance documents are based on laboratory tests of "normal" quality welds, even though the precise definition of normal quality is not always clearly defined. There is a need to better understand the fatigue behaviour of welded joints with consideration of the geometrical factors that produce locally high stresses. The goal of this study is to quantify the link between weld quality and fatigue strength. Some fabricators of fatigue loaded structures are able to produce and are willing to invest in welds with consistently higher fatigue strength. The ultimate goal, therefore, is to produce welds of suitable strength at reasonable cost.

The existence of crack-like imperfections in the welded joint is normally considered to eliminate the so-called crack initiation stage of fatigue life. Therefore, the emphasis of the fatigue assessment is focused on the crack growth stage of the fatigue life. In a wide variety of cases, crack growth can be evaluated within the framework of linear elastic fracture mechanics (LEFM). This is the case when the yield zone at the crack tip is small with respect to both the crack size and

the remaining ligament. By characterizing stable macroscopic crack growth using the stress intensity factor range ΔK, it is possible to predict crack growth rate of a weld under cyclic loading, and hence the number of cycles necessary for a crack to extend from some initial size, i.e. the size of pre-existing crack or crack-like defects, to a maximum permissible size to avoid catastrophic failures.

This work is concerned with the fatigue behaviour of cruciform fillet welded joints in the as-welded condition and under cyclic tensile loading. In the as-welded condition the fatigue crack initiation period was considered non-existent and LEFM was used to calculate fatigue strength for a range of weld geometries. The curved crack growth paths of continuous toe cracks were taken into account. Normally this kind of non-load-carrying welded attachment always fails at the weld toe. By systematically altering weld throat size, weld toe radius and weld flank angle, parametric relationships between these different factors could be formulated. In this study the crack path was not pre-selected, but crack direction was allowed to change according to the maximum tangential stress criterion.

Fracture mechanics assessment of these weld toe cracks requires accurate stress intensity factor solutions. A particular feature of such solutions is the stress concentration magnification function M_k which takes into account the stress concentration due to the welded joint geometry. In this study M_k factors were calculated using the stress intensity factors obtained directly from the 2D finite element crack growth simulation programme.

2. FRACTURE MECHANICS ANALYSIS

2.1 Introduction

Numerous 2D finite element (FE) analyses were performed in order to study the effect of local geometrical variables parametrically. When appropriate, weld toe radius, weld flank angle and weld size were altered and tensile cyclic loading was applied at the end of the main plate. This required the creation of 128 different FE models.

In engineering structures, welded joints are normally elements of a complex structure having boundary conditions that may vary from those used in this study. Because the boundary conditions affect the results, the joint was modelled as restrained so that the crack propagated under force control. This is considered to provide conservative fatigue strength estimates.

2.2 Stress intensity factor calculation

The FE crack growth simulation programme FRANC2D/L [1] was used in the analysis. The opening mode and sliding mode stress intensity factors K_I and K_{II} were calculated using the J-integral approach by Dodds and Vargas [2]. The influence of K_I and K_{II} on fatigue crack growth was based on the maximum tangential stress criterion by Erdogan and Sih [3]. This criterion assumes that the predicted propagation path of the fatigue crack is perpendicular to the maximum principal stress and the crack grows under opening mode. The equivalent opening mode stress intensity factor, which is used in crack growth predictions, is calculated according to the same criterion.

2.3 Stress concentration magnification factor, M_k

For an elliptical crack at the toe of a fillet welded joint, the range of the stress intensity factor, ΔK, can be written as [4]:

$$\Delta K = \frac{M_k Y_u}{\phi_0} \Delta\sigma\sqrt{x} \tag{1}$$

In Eq. (1) M_k is the stress concentration magnification factor which is defined as the ratio of the stress intensity factor of a cracked plate with a stress concentration to the stress intensity factor with the same cracked plate without the stress concentration. $\Delta\sigma$ is the nominal tensile stress range in the plate and x is the crack depth. The correction factor, $Y_u = M_s M_t$ is the product of the free surface correction factor, M_s, and depends on the crack aspect ratio and position around the crack front and M_t is a correction to allow for the presence of a free surface ahead of the crack and depends on the crack depth to plate thickness ratio and the crack front shape. ϕ_0 is a correction term given by the complete elliptic integral of the second kind and depends on the crack front shape.
In this analysis the M_k-factor functions are based on continuous edge cracks, hence, the crack aspect ratio is zero, $x/2c = 0$, and $\phi_0 = 1$. The correction term Y_u for a double-edge crack in a plate under tensile loading, Eq. (2), given by Brown and Srawley [5] was applied.

$$Y_u = 1.98 + 0.36\left(\frac{2x}{T}\right) - 2.12\left(\frac{2x}{T}\right)^2 + 3.42\left(\frac{2x}{T}\right)^3, \qquad 0 < \frac{2x}{T} < 0.95 \tag{2}$$

In those cases when a correction for the semi-elliptical crack was used, the value of Y_u defined by Newman and Raju [6] was used. This formulation is presented in the Appendix. The derived M_k solution was assumed to apply also at the deepest point of the semi-elliptical crack front.

2.4 Calculation of fatigue life

In order to predict fatigue crack propagation, numerous empirical or semi-empirical equations have been proposed to relate fatigue crack growth rate data to the parameter ΔK. Among the proposed equations, the Paris-Erdogan relationship [7] is commonly accepted and used in practice for a wide range of mode I cracks. This relationship is given as

$$\frac{dx}{dN} = C\Delta K^m, \tag{3}$$

where dx/dN is the crack growth rate per cycle, C and m are material constants, and ΔK is the range of the stress intensity factor for the opening mode. Eq. (3) is also recommended by the International Institute of Welding (IIW) [8] for calculating the fatigue crack propagation rate of welded joints made of steel or aluminium. The constants $m = 3$, $C_{char} = 3\times10^{-13}$, and $C_{mean} = 1.7\times10^{-13}$ (dx/dN in mm/cycle and ΔK in $\mathrm{Nmm}^{-3/2}$) are recommended by IIW [8] for the assessment of ferrite-pearlite steel welded joints in the as-welded condition and are used in this study. C_{mean} is considered to be the mean fatigue crack growth rate coefficient and C_{char} is the characteristic value corresponding to 95% survival probability value. The threshold value of the stress intensity factor was not used in this study. If the crack length is normalised by the plate thickness, $2x/T$, Eq. (1) and Eq. (3) can be combined and integrated to give the expected number of cycles to failure.

$$N = \int_{\frac{2x_i}{T}}^{\frac{2x_f}{T}} \frac{1}{C}\Delta K^{-m}\frac{T}{2}d\left(\frac{2x}{T}\right) = \int_{\frac{2x_i}{T}}^{\frac{2x_f}{T}} \frac{1}{C}\left(M_k Y_u \Delta\sigma\sqrt{\frac{T}{2}\left(\frac{2x}{T}\right)}\right)^{-m}\frac{T}{2}d\left(\frac{2x}{T}\right) \tag{4}$$

By separating the constants from the integration

$$N\Delta\sigma^m = \frac{I}{C\,T^{m/2-1}}, \quad \text{where } I = \int_{\frac{2x_i}{T}}^{\frac{2x_f}{T}} \left(M_k Y_u \sqrt{\left(\frac{2x}{T}\right)} \right)^{-m} d\left(\frac{2x}{T}\right) \tag{5}$$

This leads to

$$N\left(\Delta\sigma^*\right)^m = \frac{1}{C}, \quad \text{where } \Delta\sigma^* = \left(\frac{T^{m/2-1}}{I}\right)^{1/m} \Delta\sigma \tag{6}$$

The term $\Delta\sigma^*$ is the equivalent structural stress range [9] or the generalized stress parameter [7]. This modified stress parameter takes into account the applied stress and the stress gradient resulting from alternate specimen geometries. The initial and final crack lengths are x_i and x_f, respectively. The value of crack growth integral, I, depends on x_i and x_f. For semi-elliptical cracks, the same M_k-factors were used to model crack growth in the thickness direction as were used for edge cracks. This is expected to give conservative results, because the M_k-factors based on 2D analysis are slightly higher than those based on 3D analysis [10].
The experimental crack aspect ratio curve proposed by Engesvik and Moan [11] is used for the growing semi-elliptical surface cracks to take into account the random coalescence of cracks at the weld toe:

$$\frac{x}{2c} = \begin{cases} 0.5 & x < 0.062 \text{ mm} \\ 1/(6.43 - 0.27/x) & 0.062 \le x \le 3 \text{ mm} \\ 0 & x > 3 \text{ mm} \end{cases} \tag{7}$$

In principle, we need only one on the equivalent stress range based *S-N* curve in cases, where the above fatigue assessment procedure is valid, that is the first Eq. (6).

2.5 Fatigue strength

The fatigue strength of a welded joint is normally characterised by its fatigue class, *FAT*, which identifies the range of stress corresponding to 2×10^6 cycles to failure with a 95% survival probability [8]. Using the values, $m = 3$, and $C_{char} = 3\times10^{-13}$, the cyclic life corresponding to any stress range can be evaluated. The theoretical *FAT* can then be determined by adjusting the result according to the *S-N* curve, Eq. (5), so as to give the stress range corresponding to the fatigue life of two million cycles.
On the basis of Eq. (5) the corresponding mean fatigue strength is:

$$\Delta\sigma_{mean} = \sqrt[3]{\frac{C_{char}}{C_{mean}}}\, FAT = 1.208 FAT \tag{8}$$

2.6 Models

The investigated non-load carrying fillet welded cruciform joint is shown in Fig. 1.

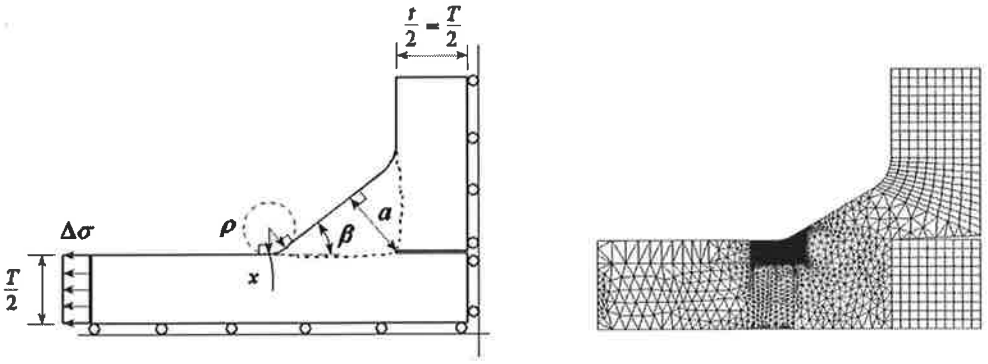


Fig. 1. Basic joint geometry and a typical mesh used in finite element analysis.

Finite element analyses were performed with an attachment plate thickness equal to the base plate thickness $T = 10$ mm. The weld throat, a, weld flank angle, β, and weld toe radius, ρ, were varied. The analysis was carried out for a/T ratios 0.1, 0.3, 0.65 and 1.0, weld flank angles β of 15°, 30°, 45° and 60° and ρ/T ratios 0.0, 0.01, 0.02, 0.05, 0.1, 0.2, 0.4 and 1.0.

For each case the stress concentration factor K_t was determined first using element sizes, which were smaller than half of the shortest crack length in the high stress region. A typical mesh used in the FE analysis is also shown in Fig. 1. Gap elements were not used.

Next a continuous crack, which is perpendicular to the main plate surface, with length x of 0.01 mm was assumed and the stress intensity factors K_I and K_{II} were calculated. Then the crack length was increased with increments 0.01, 0.01, 0.01, 0.02, 0.02, 0.02, 0.05, 0.05, 0.05, 0.1, 0.1, 0.1, 0.2, 0.2, 0.2, 0.5, 0.5, 0.5, 0.5 and 0.5 mm. For each new crack length, x, the opening and sliding mode stress intensity factors and growth direction were calculated. The final crack length was 3.65 mm, which corresponds to 73% of plate thickness in the symmetric model. Finally, in each case the equivalent opening mode stress intensity factor were computed and the corresponding M_k-factors were calculated using Eq. (1).

2.7 Analysis of results

For each a/T-ratio, the corresponding M_k-factors (704 data points) were curve fitted as a function of $2x/T$, ρ/T and β using nonlinear regression analysis [12]. For very small cracks $M_k \approx K_t$. The M_k-factors were therefore set equal to K_t when $2x/T = 0$. The fitted M_k-function is presented by Eq. (9) and the parameters $a_{i,j}$, $b_{i,j}$, $c_{i,j}$, and $d_{i,j}$ are presented in Tables 1 - 4 for $\beta = 15° - 60°$ and $\rho/T = 0 - 1.0$.

$$M_k = \frac{1 + s_1\left(\frac{2x}{T}\right)}{s_2 + s_3\left(\frac{2x}{T}\right)^{s_4}}, \quad \text{where} \quad s_i = \frac{r_{1,i} + r_{2,i}\left(\frac{\rho}{T}\right)^{r_{3,i}}}{r_{4,i} + \left(\frac{\rho}{T}\right)^{r_{3,i}}} \quad \text{and} \quad r_{i,j} = \frac{a_{i,j} + b_{i,j}\left(\frac{\pi}{180}\beta\right)^{c_{i,j}}}{d_{i,j} + \left(\frac{\pi}{180}\beta\right)^{c_{i,j}}}, \quad i,j = 1...4 \tag{9}$$

Table 1. Parameters for $a/T = 0.1$. Maximum deviation for any data point = 0.102 and avg. deviation = 0.018.

	j	1	2	3	4	1	2	3	4
i	$a_{i,j}$				$b_{i,j}$				
1		-0.0374	0.0289	1.3337	-0.1795	1.6434	0.0123	0.7060	0.3101
2		1.5269	0.9857	1.5614	1.1726	5.0884	1.4754	1.8828	1.1936
3		0.5293	1.7912	0.7091	0.8202	-0.3439	0.0930	-0.6775	-0.0765
4		1.0137	0.4586	1.1969	0.0503	-0.2177	0.6150	-0.3387	0.0829
	$c_{i,j}$				$d_{i,j}$				
1		0.8340	-8.8873	1.1405	0.1593	1.1991	2.3480	0.7419	1.6016
2		-1.1373	5.9377	-0.4673	2.1911	-0.4851	0.7346	-0.7391	1.0216
3		0.7790	-0.9384	0.9881	1.7714	1.5089	3.3838	1.4001	1.4180
4		2.0148	2.5641	1.2647	0.9201	0.5366	0.7456	0.6643	0.0966

Table 2. Parameters for $a/T = 0.3$. Maximum deviation for any data point = 0.172 and avg. deviation = 0.015.

	j	1	2	3	4	1	2	3	4
i	$a_{i,j}$				$b_{i,j}$				
1		0.06299	0.0485	1.6428	0.0924	1.8252	0.01454	0.6781	0.0233
2		0.8792	1.0190	0.7627	1.3618	1.1063	1.5602	2.7588	1.2413
3		-1.1096	2.1771	-0.000098	0.5707	1.2164	0.1257	0.000125	0.1938
4		-0.1504	0.3881	1.5385	0.0737	1.7204	0.7261	-0.3522	0.0648
	$c_{i,j}$				$d_{i,j}$				
1		0.9385	-0.5946	1.3202	0.5450	1.8145	3.3400	-0.1263	1.0936
2		-0.4621	10.2607	-0.5464	5.0486	-0.7984	0.7010	-0.7484	1.1514
3		-0.3035	-1.1654	-5.4198	2.9705	2.5792	4.2679	1.1226	1.2295
4		-2.2122	5.2328	1.3858	1.3235	1.4680	0.5343	-0.1132	0.0234

Table 3. Parameters for $a/T = 0.65$. Maximum deviation for any data point = 0.19 and avg. deviation = 0.018.

	j	1	2	3	4	1	2	3	4
i	$a_{i,j}$				$b_{i,j}$				
1		1.5625	0.05905	0.9922	-0.00639	0.0741	0.01570	0.6807	0.1690
2		2.3279	1.0478	2.101	1.4231	5.9185	1.6187	1.8392	1.1184
3		-0.1416	1.7082	0.5033	0.5701	0.4951	-0.2936	-0.4716	0.2430
4		1.2432	0.4139	1.3295	0.0531	0.5609	0.8525	-0.2178	0.1465
	$c_{i,j}$				$d_{i,j}$				
1		-1.5111	-0.8079	0.8640	0.3993	0.7043	3.8128	0.9454	1.1671
2		-4.3718	0.8426	-0.6901	9.2696	0.0941	0.6542	-0.2853	1.1092
3		-0.3989	-0.4339	1.4108	3.5264	3.0880	2.2291	1.6285	1.2543
4		2.0962	2.6229	1.2654	1.7109	0.5863	0.4831	1.3503	0.0869

Table 4. Parameters for $a/T = 1.0$. Maximum deviation for any data point = 0.18 and avg. deviation = 0.015.

	j	1	2	3	4	1	2	3	4
i	$a_{i,j}$				$b_{i,j}$				
1		0.7895	0.0115	0.4315	0.0640	0.9701	0.0151	0.2322	-0.00886
2		4.3057	0.3420	0.4481	1.1479	7.2975	1.4614	10.5044	0.8728
3		0.7453	2.0673	-1.9094	0.0540	-0.5478	0.2716	2.0890	0.4897
4		0.7627	0.7800	0.7646	0.0667	0.3925	0.6089	-0.2288	-0.00409
	$c_{i,j}$				$d_{i,j}$				
1		0.2242	-3.7736	1.1454	1.1104	1.3543	0.9466	1.0889	1.2440
2		-0.4701	2.8158	1.6045	0.2199	0.2448	0.2231	0.7981	0.7760
3		0.6263	-2.2588	-0.5329	5.2627	2.0248	3.9828	1.7797	0.0963
4		2.0902	3.8035	0.9644	1.2096	0.1057	1.0331	1.9074	0.0351

2.7.1 Comparison with some published results

Lie [13] investigated non-load-carrying fillet welded joints using boundary element analysis. The value of M_k for a crack at a stress concentration was computed based on the principle of superposition, which uses the stress distribution for an un-cracked body to determine the stress intensity factor of a crack located in the region of the stress concentration. The stress distribution on a plane perpendicular to the applied load and containing the weld toe was applied. This method does not take into account the curved crack front path of small cracks. Variations of attachment plate thickness and weld leg length were considered. A sharp weld toe was assumed as was a weld angle of 45° and T = 10 mm. Only one M_k-curve is appropriate for comparison with the current study and this is presented in Fig. 2 using both a linear and a logarithmic scale. The Y_u-function used by Lie, however, was different than that used in the present study. The M_k-curve of Lie was therefore modified based on Eq. (2). This modified curve is also shown in Fig. 2. As can be seen, both Y_u-functions are similar. Lie's M_k-curve gave lower values at small $2x/T$-ratios, 8.5% lower at $2x/T$ = 0.002 and 5.5% lower at $2x/T$ = 0.04 than Eq. (9). Lie's M_k-curve gives approx. 5% lower fatigue strengths for plate thicknesses 10 - 25 mm with 0.05 - 0.2 mm initial continuous cracks in this particular case.

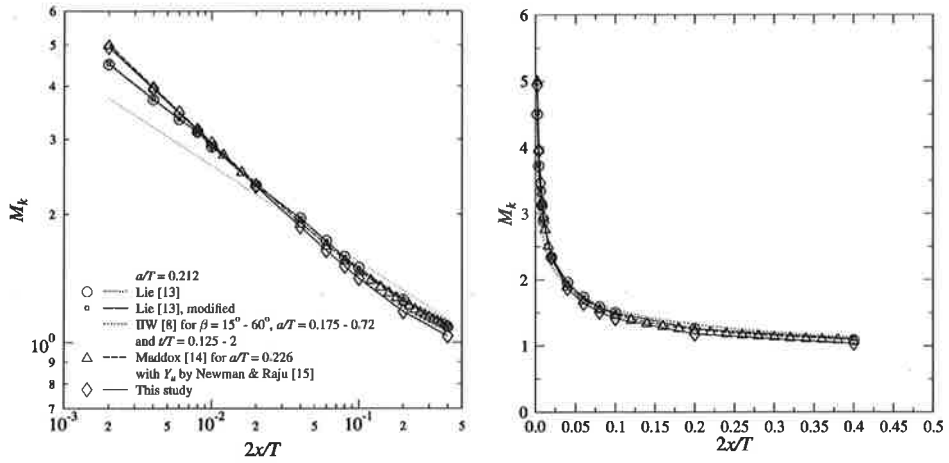


Fig. 2. Comparison of M_k-factors with published results.

The M_k-curve of IIW [8] is also drawn in Fig. 2, but this curve is only approximate because of its generality. The results of Maddox [14] are very similar to those in this study. Unfortunately, only one case from Maddox was comparable.

2.8 Predicted fatigue strengths

2.8.1 Continuous crack

Based on the above presented M_k-factor results for the toe crack, the Paris equation was integrated from three different initial continuous crack depths, x_i equal to 0.05, 0.2 and 0.8 mm. The final crack size was equal to $T/2$. The maximum effect of throat thickness is observed in the case of a small weld toe radius (ρ = 0), weld angle β = 45°, and the initial edge crack depth was 0.2 mm. In this case, FAT varied by only 11% over the entire range, $0.1 \le a/T \le 1$ and 5 mm $\le T \le$ 50 mm. For rounded weld toes the effect of throat thickness was even smaller. In general, as the throat thickness increases, the fatigue strength tends to decrease. The predicted fatigue strengths for the case T = 6 mm and a = 4 mm are presented in Fig. 3.

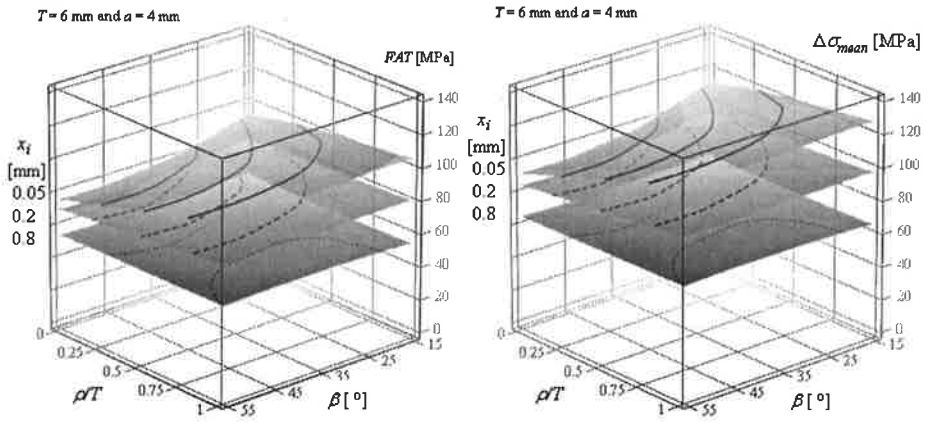


Fig. 3. Predicted fatigue strengths at $N_f = 2\times10^6$ cycles for continuous toe cracks.

For the 0.2 mm initial edge crack case in Fig. 3, the maximum difference between minimum and maximum predicted *FAT* is approximately 15% over the entire range of weld angles and weld toe radii studied. For a deeper initial edge crack, x_i = 0.8 mm, the effect of weld toe radius and weld flank angle vanishes. For a smaller initial edge crack size, the effect of weld toe radius and flank angle is more pronounced as is expected due to the local nature of the stress concentration.

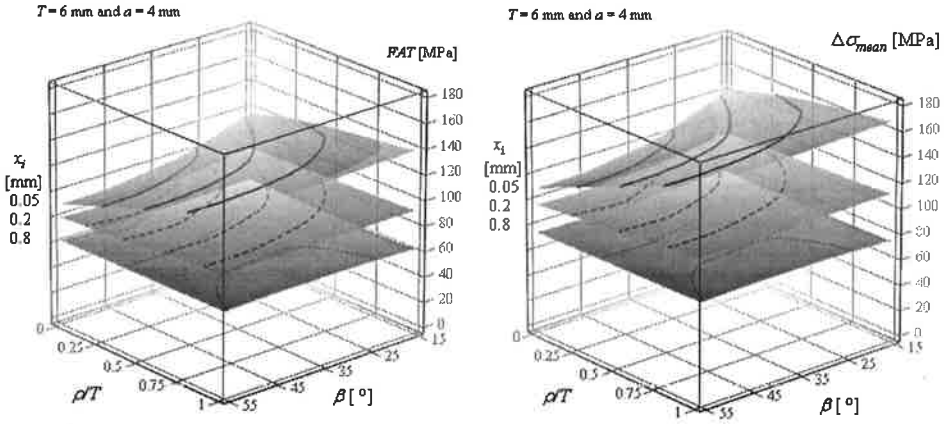


Fig. 4. Predicted fatigue strengths at $N_f = 2\times10^6$ cycles for semi-elliptical toe cracks.

2.8.2 Semi-elliptical and semi-elliptical versus continuous crack

Equation (3) was also integrated from three different initial crack depths, x_i equal to 0.05, 0.2 and 0.8 mm, to through the thickness for semi-elliptical surface crack at the weld toe using the above presented M_k-factor results. The predicted fatigue strengths are presented in Fig. 4.

A comparison of Figs. 3 and 4 reveals that the expected fatigue strength for a semi-elliptical crack is approximately14% higher than for the corresponding continuous crack, when x_i equals to 0.2 or 0.8 mm and 19 - 31% higher when x_i equals to 0.05 mm. For example, the computed fatigue strength for T = 25 mm and a/T = 0.3 in case of continuous crack with x_i = 0.2 mm (surface C0.2) is presented in Fig. 5. This same figure also shows the cases of a semi-elliptical crack with x_i = 0.2 mm (surface E0.2) and a semi-elliptical crack with x_i = 0.05 mm (surface E0.05). The IIW fatigue class *FAT* = 80 for non-load-carrying attachments [8] is also shown in Fig 5.

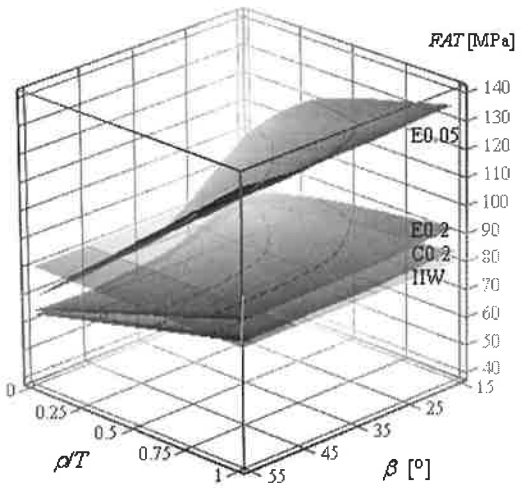


Fig. 5. Comparison of predicted fatigue strengths at $N_f = 2\times10^6$ cycles based on different crack shape and initial crack depth assumptions. $T = 25$ mm and $a/T = 0.3$.

3. COMPARISON OF THEORETICAL ANALYSIS AND PUBLISHED DATA

The theoretical calculations were compared with published experimental data generated from cruciform non-load-carrying joints failing from cracks at the weld toe [16-20].

3.1 Experimental data

Test specimens in Ref. [16] were fabricated from SM50B rolled steel plates (UTS = 570 MPa, σ_y = 485 MPa) with manual arc welding and with covered electrodes (SMAW) in flat position, PA [EN ISO 6947, EN 287-2]. Tests were carried out for joints with T equal to 9, 20 and 40 mm under load control and zero to tension loading (i.e. stress ratio $R = 0$). Similar tests were later done using SMAW and metal active gas welding (MAG) for joints with $T = 20$ mm [17]. Branco et al. [18] carried out tests on joints welded entirely by tungsten inert gas welding (TIG) or by plasma processes. Joints were fabricated from 3 mm thin Grade 50 C-Mn structural steel plate and fatigue tested with applied loading such that the maximum stress was maintained constant at 300 N/mm^2. Weld toe radius and tangent angle were measured with a video monitoring system and the data were treated by statistical analysis. Lindqvist [19] tested 12 mm thick non-load-carrying transverse fillet welded cruciform joints in pure tension. The joints were made of the steel DOMEX 550 MC. DOMEX 550 MC is high strength hot rolled steel with the minimum yield strength 550 MPa and minimum and maximum tensile strengths of 600 MPa and 760 MPa, respectively. MAG welding was used with shielding gas MISON 8 and the filler metal OK12.51. Before the welding the specimens were shot blasted to avoid cold laps. The effective throat thickness was nominally 6 mm. Measurements later showed that the effective throat thickness varied between 6 and 7 mm with an average of 6.5 mm. Altogether sixty measurements were made and the weld toe radius fluctuated between 0.15 and 2 mm. The average radius was 0.62 mm. The weld angle varied by only couple degrees, but since the reported precision of the measuring system was smaller than the measured variation; the weld angle was approximated as 45°. The original aim of the measurements was reportedly to locate the point of crack initiation and measure the initial crack and weld toe radius at this point. Neither initial points nor cracks could be found. So the weld toe radii were just measured at random points along the welds on the specimens. The fatigue

specimens were tested with constant amplitude loaded at a stress ratio $R = 0$ with the frequency 10 Hz. Kuhlmann et al. [20] tested joints in constant amplitude pulsating tension at $R = 0.1$. The specimens were fabricated from 12 mm thick S 460 steel plate using fully mechanized welding. The widths of the sawed small scale specimens were 40 mm. Manual TIG-dressing was performed on all specimens. All experimental data collected from the literature is presented in Fig. 6 and the corresponding average values of geometrical parameters are shown in Table 5.

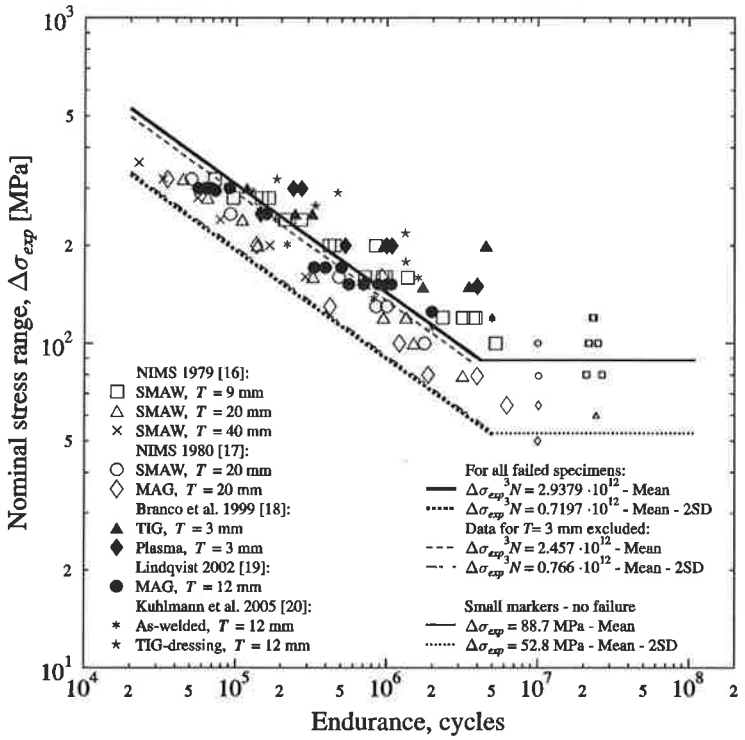


Fig. 6. Summary of test results for as-welded specimens.

Table 5. Average values of geometrical parameters used in this study.

		T [mm]	ρ [mm]	β [°]	a [mm]
NIMS 1979 [16]		9	0.465	39.2	4.59
		20	0.470	50.9	7.35
		40	0.546	37.4	8.45
NIMS 1980 [17]		20	0.650	35.0	6.93
		20	0.400	43.0	8.00
Branco et al. 1999 [18]	- TIG	3	6	10	2
	- Plasma	3	6	7	2
Lindqvist 2002 [19]		12	0.62	45	6.5
Kuhlmann 2005 [20]	- As-welded	12	1.1	41.0	4
	- TIG-dressing	12	7.0	41.0	4

3.2 Comparisons

3.2.1 Continuous crack

In Fig. 7 the experimental data collected from the literature, i.e., data from Fig. 6, is presented in terms of the equivalent structural stress range, $\Delta\sigma^*$. In this figure an initial continuous crack with depths x_i = 0.2 or 0.05 mm was assumed. The use of $\Delta\sigma^*$ in place of nominal stress reduced the scatter for the 90 failed specimens by 22.2% for a 0.2 mm assumed initial crack, i.e., the standard error in log(1/C), Eq. (6), when the slope of the curve was forced to be -1/3. If the assumed initial crack size is reduced to x_i = 0.05 mm, the scatter is reduced by 36.9% with respect to the scatter observed based on nominal stress. Secondary stresses due to misalignments were not considered in the calculations.

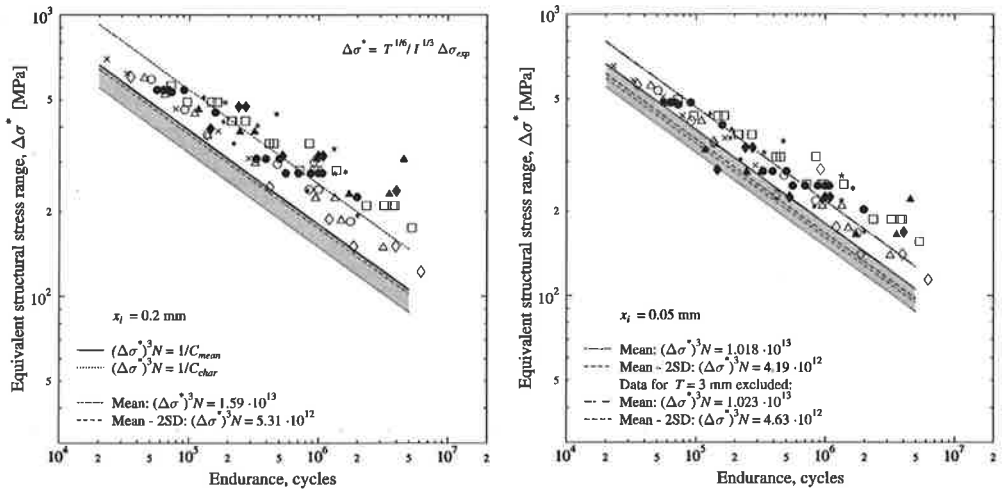


Fig. 8. Equivalent structural stress range versus N in continuous toe crack case, when x_i = 0.2 and 0.05 mm.

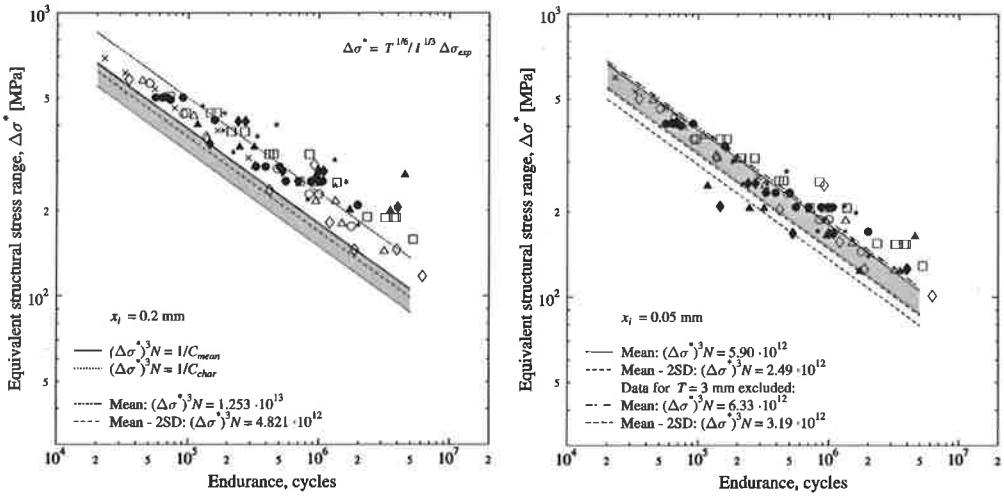


Fig. 7. Equivalent structural stress range versus N in semi-elliptical crack case, when x_i = 0.2 and 0.05 mm.

From Fig. 7 it can generally be observed that the scatter seems to be larger if specimens with $T = 3$ mm (15 specimens) are included. If these 15 specimens are excluded, the scatter for a 0.2 mm assumed initial crack is reduced by 20.8%, for a 0.05 mm assumed initial crack the respective reduction is 32.0%. Thus the exclusion did not reduce the scatter in this case.

3.2.2 Semi-elliptical crack

In Fig. 8 the experimental data collected from the literature, i.e., data from Fig. 6, is presented in terms of the equivalent structural stress range, $\Delta\sigma^*$. In this figure an initial semi-elliptical crack with depths $x_i = 0.2$ mm or $x_i = 0.05$ mm were assumed. In comparison with the scatter observed in Fig. 6, the scatter in Fig 8 is reduced by 32.1% for a 0.2 mm assumed initial crack and for a 0.05 mm assumed initial crack the respective reduction is 38.7%.

If data points with $T = 3$ mm are omitted, the scatter is reduced by 30.8% for the 0.2 mm assumed initial crack and by 41.2% for the 0.05 mm assumed initial crack. In later case the reduction in scatter is more than when all data in included.

It is interesting to note that when specimens for which $T = 3$ mm are omitted and the initial crack size of $x_i = 0.05$ mm is assumed, the mean and mean–2SD $\Delta\sigma^*$–N curves are nearly coincident with curves drawn on the basis of C_{mean}- and C_{char}- values given by IIW [8]. See Fig. 8. A summary of the statistical information from Figs. 6 - 8 is provided in Table 6.

Taulukko 6. Relative scatter in $\log(1/C)$, Eq. (6), as compared to the scatter 0.3215 for all failed specimens or scatter 0.2664 for specimens, for which the data for $T = 3$ mm is excluded in Fig. 6.

	Continuous initial crack		Elliptical initial crack	
x_i mm	All failed specimens	Data for $T = 3$ mm excluded	All failed specimens	Data for $T = 3$ mm excluded
0.05	0.631	0.680	0.613	<u>0.588</u>
0.075	-	-	<u>0.595</u>	0.615
0.09	-	-	0.600	0.629
0.2	0.778	0.792	0.679	0.692

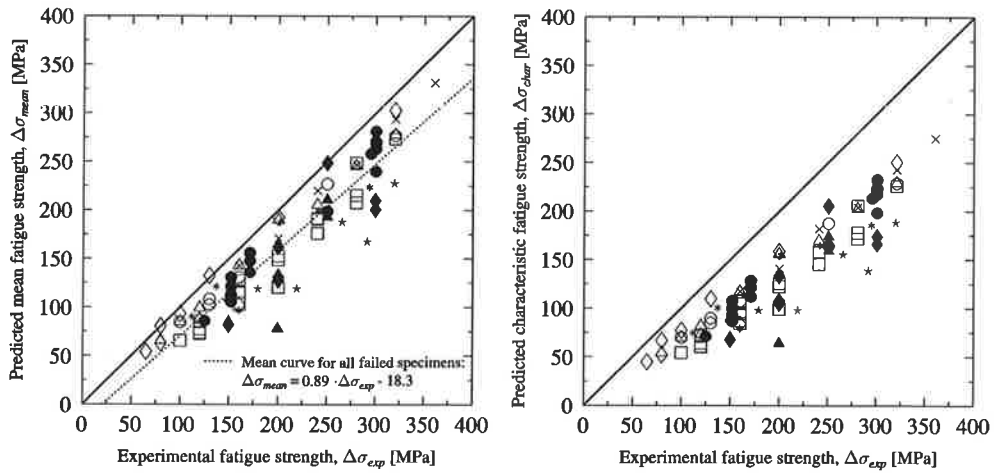


Fig. 9. Correlation between predicted and experimental fatigue strengths, if semi-elliptical toe crack with $x_i = 0.2$ mm is assumed.

In Figs. 9 and 10 the experimental and predicted strengths are compared based on nominal stress ranges in cases of x_i = 0.2 and 0.05 mm, respectively. The right hand figure in each case shows the comparison based on predicted characteristic fatigue strength while the left hand figure is based on predicted mean strength.

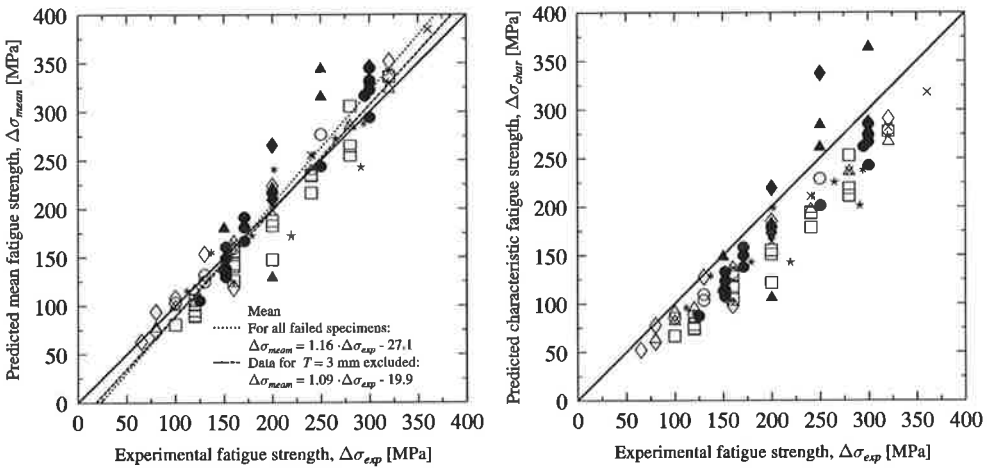


Fig. 10. Correlation between predicted and experimental fatigue strengths, if semi-elliptical toe crack with x_i = 0.05 mm is assumed.

The slope of the mean curve, as in Figs. 9 – 10, would be one, if semi-elliptical toe crack with x_i = 0.09 mm is assumed or x_i = 0.075 mm, when data for T = 3 mm is excluded, i.e., $\Delta\sigma_{mean} = \Delta\sigma_{exp} -$ 22.0 MPa or $\Delta\sigma_{mean} = \Delta\sigma_{exp} -$ 17.3 MPa, respectively.

3.3 Initial stress intensity factor range, ΔK_i

If the data in Fig. 6 is presented using initial stress intensity factor range, ΔK_i, instead of nominal stress range, we get the results presented in Figs. 11-12.
All, except the thin plate results are quite nicely around the mean curve. The fatigue assessment could then be based also on the ΔK_i-N curve.
If we calculate the threshold stress intensity factor range on the basis of experimental data using different initial crack depth assumptions, we get the results presented in Fig.13. For an assumed semi-elliptical crack with depth of 0.05 mm $\Delta K_{th\ mean}$ = 47.7 Nmm$^{-3/2}$ and $\Delta K_{th\ char}$ = 31.6 Nmm$^{-3/2}$ and for 0.2 mm crack 117.9 Nmm$^{-3/2}$ and 82.5 Nmm$^{-3/2}$, respectively.

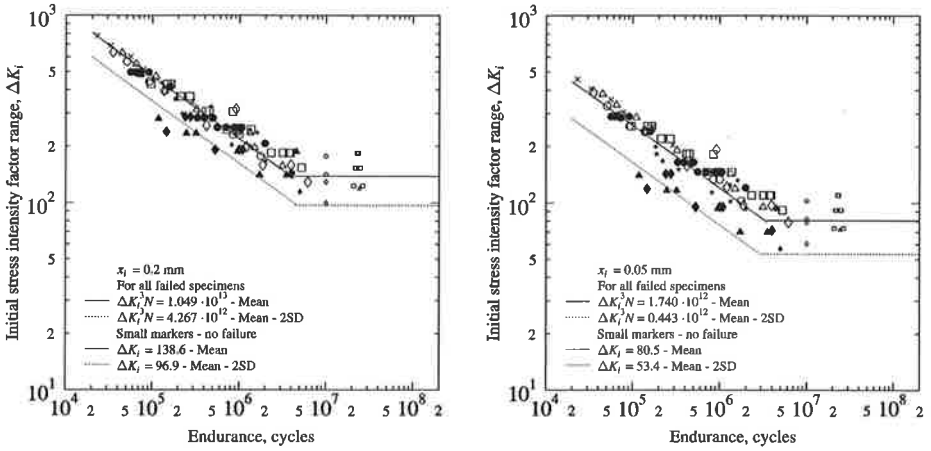


Fig. 12. Initial stress intensity factor range versus N for continuous toe cracks with $x_i = 0.2$ and 0.05 mm.

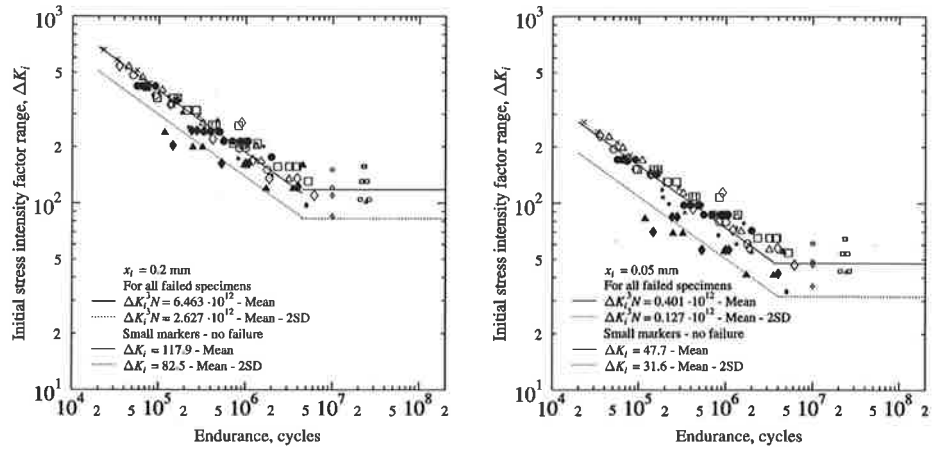


Fig. 11. Initial stress intensity factor range versus N for semi-elliptical toe cracks with $x_i = 0.2$ and 0.05 mm.

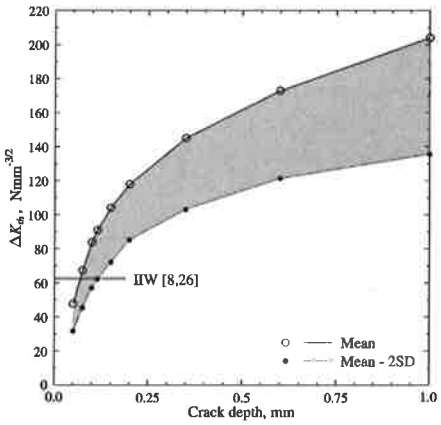


Fig. 13. Threshold stress intensity factor range, ΔK_{th}, as a function of assumed initial crack depth.

The initial crack depth for normal quality welds is usually assumed to be 0.1– 0.2 mm. For example British Standard BS 7910:1999 [21] recommend an initial flaw size x_i between 0.1 and 0.25 mm. IIW-recommendations [8] gives characteristic threshold value of 62 Nmm$^{-3/2}$ for welds with high tensile residual stresses. If the stress intensity factor is smaller than 62 Nmm$^{-3/2}$, the crack does not propagate. In this study the threshold level 62 Nmm$^{-3/2}$ corresponds to an elliptical crack with depth of 0.115 mm. For smaller cracks the calculated threshold level is well below that value. It is known [22] that cracks will grow at stress intensities below the so called long crack threshold [23, 24]. This short crack behaviour can be explained with Kitagawa-Takahashi diagram [25]. According to the well-known El Haddad model [26], the Kitagawa-Takahashi diagram is described by the following empirical relationship:

$$\Delta K_{th} = \frac{\Delta K_{th0}}{\sqrt{1+\frac{x_0}{x}}}, \tag{10}$$

where ΔK_{th0} is the crack-size independent threshold stress intensity range for long cracks, x_0 is an intrinsic crack length defined as follows

$$x_0 = \frac{1}{\pi}\left(\frac{\Delta K_{th0}}{\Delta \sigma_{th0}}\right)^2 \tag{11}$$

and $\Delta\sigma_{th0}$ is the fatigue limit for smooth specimens. For instance, the intrinsic crack length x_0 ranges from 0.001 – 0.01 mm for very high strength steels (yield stress σ_y up to 2000 MPa) to 0.1 – 1 mm for very low strength steels (σ_y as low as 200 MPa) [27].

In order to estimate the characteristic ΔK_{th} for a short crack, we may choose ΔK_{th0} = 62 Nmm$^{-3/2}$ and $\Delta\sigma_{th0}$ = 116 MPa. $\Delta\sigma_{th0}$ = 116 MPa is the constant amplitude fatigue limit at $N = 10^7$ cycles for *FAT* 160, which is the fatigue class for unwelded parts of a component [28]. Eq. (11) gives then x_0 = 0.091 mm and Eq. (10) ΔK_{th} = 36.9 Nmm$^{-3/2}$, when x = 0.05 mm. This is 17% higher than ΔK_{thchar} = 31.6 Nmm$^{-3/2}$, which was calculated above on the basis of experimental data. Fatigue limit at $N = 10^8$ or 10^9 cycles would give ΔK_{th} = 34.4 and 31.9 Nmm$^{-3/2}$, respectively. After IIW [28] the constant amplitude knee point is at 10^7 cycles in standard applications.

The crack length of 0.05 mm is very small and these kind of microstructurally small cracks (if length comparable to the grain size) grow in a complicated manner that is affected by the crack closure and microstructure in addition to crack size. The crack may grow slower or faster than a long crack or may even stop. This makes the direct analysis with linear elastic fracture mechanics difficult. However, it is known, that when crack size is several times larger than the grain size, typically around 10 grain sizes, microstructurally small crack growth curve generally merges with the physically small and then long crack curve. Then, the engineering approximation might be to extrapolate the long crack behaviour to the short crack region, at least for small-grain size steels [29].

4. DISCUSSIONS

The predicted *FAT* classes, Fig. 5, which are based on the M_k-factor equation derived in this work, are presented as contour plots in Fig. 14 for both 0.2 and 0.05 mm deep semi-elliptical toe cracks as a function of β and ρ/T, when a/T = 0.3 and T = 25 mm. It can be seen, that the effect of flank angle on the fatigue strength is small for rounded weld toes. For high quality welds the weld toe radii should be large and the initial crack depth should be much smaller than 0.2 mm as is frequently assumed for normal quality welds.

IIW 2004 [28] and British Standard 7910:1999 [21] recommend a slightly larger C_{char} when integrating the Paris-Erdogan relationship. If the value $C_{char} = 5\times10^{-13}$ [28] or $C_{char} = 5.21\times10^{-13}$ [21] are used in place of $C_{char} = 3\times10^{-13}$ recommended by IIW 1996 [8], the predicted FAT classes are reduced by 15.6% and 16.8%, respectively.

In the studied cases, for $\Delta\sigma$ corresponding to 50% failure probability at two million cycles, the plane strain cyclic plastic zone radius, r_y', was computed to be smaller than one-quarter of the crack depth (0.05 mm) and thus the basic assumption of LEFM is satisfied [29]. At higher stress levels in some thick specimen, excessive plasticity may occur for small cracks. The notch tip plasticity caused by the weld was not considered.

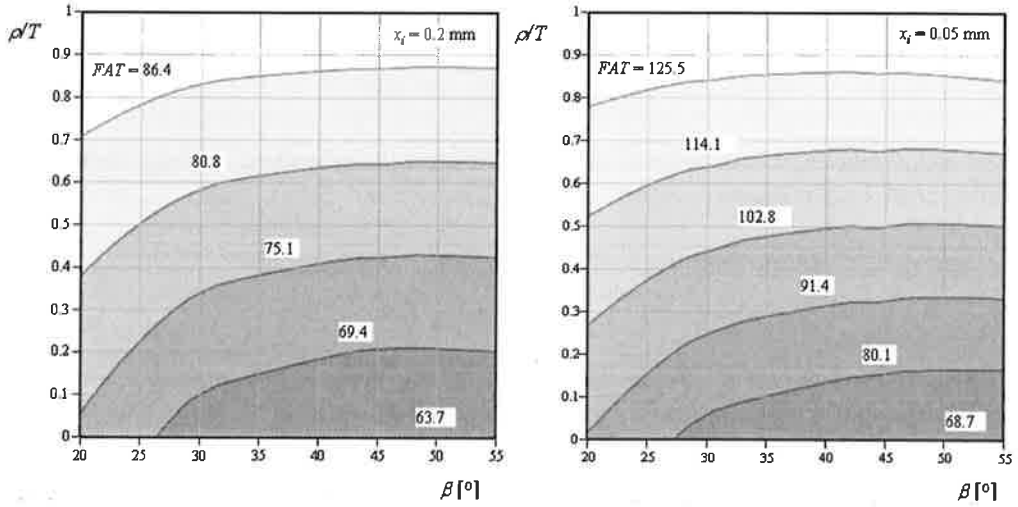


Fig. 14. Predicted fatigue classes, when semi-elliptical toe cracks with initial depths x_i of 0.2 and 0.05 mm were assumed. $a/T = 0.3$ and $T = 25$ mm.

With Paris law parameters given by IIW [8] the mean value of the equivalent structural stress range (or the generalized stress parameter), $\Delta\sigma^*$, equals to143.3 MPa at two million cycles, first Eq. (6). This value is independent from the crack shape, depth or joint type. An assumed semi-elliptical toe crack with depth of 0.05 mm and second Eq. (6) and Fig. 8 gives a mean value of $\Delta\sigma^*$ =143.4 MPa for the published experimental data. If experimental data for which T = 3 mm is ignored in the analysis, experimental mean $\Delta\sigma^*$ increases to 146.8 MPa. This is 2.4% higher that the mean value 143.3 MPa. The scatter is still large, but the characteristic S-N line of the experimental data is in this case in good agreement with the characteristic S-N line obtained from Eq. (6) when C_{char} [8] is used.

The characteristic value of $\Delta\sigma^*$ equals to 118.6 MPa, which corresponds to the $\Delta\sigma^*_{mean}$ = 143.3 MPa. For comparison, by solving $\Delta\sigma$ from second Eq. (6) with $\Delta\sigma^*$ = 118.6 MPa and using the same aspect ratio development as before and assuming quarter-elliptical corner crack [6] with initial depth of 0.05 mm and M_k = 1 gives $FAT \approx 145$ MPa. This is quite near to 140 MPa as recommended by IIW [8] for machine gas cut plate strip. The thickness has only a small effect on the results in this case.

If the experimental data is presented using initial stress intensity factor range, ΔK_i, which is based on nominal stresses used in tests, we get the ΔK_i -N curve, which is comparable with S-N curve. The data points locate quite nicely around the curve, Figs. 11-12, except the thin plate results (total 15 data points for failed specimens, T = 3 mm), for those the ΔK_i-values should be higher.

On the basis of ΔK_i-N curve for non failed specimens it is possible to dry to estimate the threshold stress intensity factor range level, ΔK_{th}, Figs 11-12. The estimated ΔK_{th} value is expected to be a little smaller than that, for which the determination is done properly. The calculated $\Delta K_{th\ char}$-value based on experimental data is 31.6 Nmm$^{-3/2}$ for semi-elliptical crack, when $x_i = 0.05$ mm. Kitagawa diagram gives 1 - 17% higher values depending on the position of the knee point of S-N curve, which defines the fatigue limit.

5. CONCLUSIONS

The influence of local geometric parameters on the fatigue strength of welded joints has been studied using the finite element method and linear elastic fracture mechanics simulations. Parametric M_k-functions have been derived for non-load-carrying cruciform fillet welded joint under tensile loading. The weld throat, a, weld flank angle, β, and weld toe radius, ρ, were varied as follows: $a/T = 0.1 - 1.0$, $\beta = 15^o - 60^o$, $\rho/T = 0 - 1.0$, where T is the thickness of plates. The following conclusions can be made:

1) Local geometrical variations of the weld and weld throat size have only a small effect on the fatigue strength, if the depth of an initial toe crack is greater than 0.2 mm. As the depth of the initial toe crack increases, the local geometrical effects disappear.
2) The effect of weld angle on the fatigue strength is small when the toe radius is large. For high quality welds, the weld toe radii should be large and the initial crack depth should be very small. According to this study the fatigue strength of joints with large toe radii increases approximately 20-40% as the initial crack depth decreases from 0.2 mm to 0.05 mm.
3) Based on statistical analysis, the best fit between predicted and experimental fatigue strengths was achieved when an initial semi-elliptical toe crack with depth of 0.05 mm was assumed. Then, if the experimental data is presented using equivalent structural stress range, $\Delta\sigma^*$, the mean and mean–2SD $\Delta\sigma^*$–N curves almost coincide to the curves drawn on the basis of C_{mean}- and C_{char}-values of Paris law (first Eq. (6)) given by IIW [8], when $T = 9 - 40$ mm.
4) Based on quite limited statistical analysis (only 15 data points) the mean and characteristic threshold stress intensity factor ranges for semi-elliptical crack with depth of 0.05 mm are estimated to be: $\Delta K_{th\ mean} = 47.7$ Nmm$^{-3/2}$ and $\Delta K_{th\ char} = 31.6$ Nmm$^{-3/2}$, respectively.

Acknowledgements

This preliminary study is a part of the weld quality project "LAATU" which is ongoing in the Laboratory of Fatigue and Strength at Lappeenranta University of Technology. The support of Metso Paper Inc., Andritz Oy, KCI Konecranes Oyj, John Deere Forestry Oy, Ruukki, VR, Wärtsilä, Auramo, Ponsse, John Deere, Bronto Skylift Oy, Stalatube Oy and the National Technology Agency of Finland, are greatly appreciated.

References

[1] James M and Swenson D, FRANC2D/L: A Crack Propagation Simulator for Plane Layered Structures, available from http://www.mne.ksu.edu/~franc2d/.
[2] Dodds RH and Vargas PM, Numerical evaluation of domain and contour integral for non-linear fracture mechanics: formulation and implementation aspects. Report from University of Illinois at Urbana-Champaign, Dept. of Civil Engineering, 1988.
[3] Erdogan F and Sih GC, ASME J Basic Engng 1963; 85: 519-527.
[4] Maddox SJ, Int. J. Fract., 1975, 11, 221-243.
[5] Brown WF and Srawley JE, Plane strain crack toughness testing of high strength metallic materials, ASTM STP 410, ASTM, West Conshohocken, PA, 1966.

[6] Newman JC and Raju IS, Stress-intensity factor equations for cracks in three-dimensional finite bodies, Fracture Mechanics, ASTM STP 791, 1983.
[7] Gurney TR, Fatigue of welded structures. Cambridge: Cambridge University Press, 1979.
[8] Hobbacher A, IIW Doc. XIII-1539-96/XV-845-96, 1996.
[9] Dong P, Hong JK et al., Life predictions using mesh-insensitive structural stress method. Fatigue Design and Evaluation Committee of the SAE, Spring 2003 Meeting, April 15-16, 2003, hosted by Caterpillar in Peoria, Illinois. http://www.fatigue.org/Minutes/Spring-2003/contents.html
[10] Pang HLJ, A review of stress intensity factors for semi-elliptical surface crack in a plate and fillet welded joint, The Welding Institute 1990. Cambridge, England, Abington Publishing.
[11] Engesvik KM and Moan T, Probabilistic analysis of the uncertainty in the fatigue capacity of welded joints. Eng Frac Mech 1983 18 (4) 743-762.
[12] Sherrod PH, NLREG, Nonlinear regression analysis program. http://www.nlreg.com/
[13] Lie ST, Analysis of fatigue strength on non-load-carrying and load-carrying fillet welded joints, Journal of Strain Analysis, Vol. 29, No 4, 1994.
[14] Maddox SJ, The effect of plate thickness on the fatigue strength of fillet welded joints. The Welding Institute 1987. Cambridge, England, Abington Publishing.
[15] Newman JC and Raju IS, Analysis of surface cracks in finite plates under tension or bending loads, NASA Technical Paper 1578, 1979.
[16] NIMS 1979, Data sheets on fatigue properties of non-load-carrying cruciform welded joints of SM50B rolled steel for welded structure -Effect of Specimen Size-. http://tsuge.nims.go.jp/
[17] NIMS 1980, Data sheets on fatigue properties for non-load-carrying cruciform welded joints of SM50B rolled steel for welded structure -Effect of Welding procedure-. http://tsuge.nims.go.jp/
[18] Branco CM, Maddox SJ, Infante V and Gomes EC, Fatigue performance of tungsten inert gas (TIG) and plasma welds in thin sections, Int. J Fatigue 1999 21 587-601.
[19] Lindqvist J, Fatigue strengths thickness dependence in welded constructions, Master thesis, Borlänge, Sweden, 2002. http://hem.passagen.se/johanlindq/Exjobb.pdf
[20] Kuhlmann U, et al., Erhöhung der Ermüdungsfestigkeit von geschweißten höherfesten Baustählen durch Anwendung von Nachbehandlungsverfaren, Stahlbau, Stahlbau 74 (2005), H. 5, S. 358-365.
[21] Guide on methods for assessing the acceptability of flaws in metallic structures, British Standard BS 7910:1999, 1999.
[22] Socie DF and Marquis GB, Multiaxial Fatigue, Society of Automotive Engineers, Inc., Warrendale, PA, USA, 2000.
[23] Socie DF, Notches in Fatigue, Fatigue Seminar, University of Illinois at Urbana-Champaign, 2002. http://www.mie.uiuc.edu/content/files/FCP%202002%20Advance%20Short%20Course/2.0%20Notches.pdf
[24] Spagnoli A, Fractality in the threshold condition of fatigue crack growth: an interpretation of the Kitagawa diagram, Chaos, Solitons and Fractals 22 (2004) 589–598.
[25] Kitagawa H, Takahashi S, Applicability of fracture mechanics to very small cracks or cracks in the early stage. In: Proceedings of the second international conference on mech. behaviour of matls., ASM; 1976. p. 627-31.
[26] El Haddad MH, Topper TH and Smith KN, Prediction of nonpropagating cracks, Engineering Fracture Mechanics 1979; 11: 573–84.
[27] Taylor D, Fatigue thresholds. London: Butterworths; 1981.
[28] Hobbacher A, IIW Doc. XIII-1965-03/XV-1127-03, Update June 2005.
[29] Stephens RI, Fatemi A et al., Metal Fatigue in Engineering, John Wiley & Sons, Inc., USA,2001.

Appendix

Mode-I stress intensity factor solution for a semi-elliptical surface crack

The stress intensity factor for a semi-elliptical surface crack in a finite plate subjected to remote tension load presented by Newman and Raju [6] is given by

$$K = \sigma\left(\frac{\pi x}{Q}\right)^{\frac{1}{2}} F_s\left(\frac{x}{c}, \frac{x}{T}, \frac{c}{B}, \phi\right) = \frac{Y_u}{\phi_0}\sigma\sqrt{x} \quad \text{for} \quad \frac{c}{B} < 0.5 \quad \text{and} \quad 0^\circ \le \phi \le 180^\circ,$$

if x/T satisfies: $\frac{x}{T} < 1.25\left(\frac{x}{c} + 0.6\right)$ for $0 \le \frac{x}{c} \le 0.2$ and $\frac{x}{T} < 1$ for $0.2 \le \frac{x}{c} \le \infty$.

The correction factor F_s was chosen to be $F_s = \left[M_1 + M_2\left(\frac{x}{T}\right)^2 + M_3\left(\frac{x}{T}\right)^4\right] g f_\phi f_w$.

For $x/c \le 1$:

$$M_1 = 1.13 - 0.09\frac{x}{c}, \quad M_2 = -0.54 + \frac{0.89}{0.2 + \frac{x}{c}}, \quad M_3 = 0.5 - \frac{1}{0.65 + \frac{x}{c}} + 14\left(1 - \frac{x}{c}\right)^{24},$$

$$g = 1 + \left[0.1 + 0.35\left(\frac{x}{T}\right)^2\right](1 - \sin\phi)^2, \quad f_\phi = \left[\left(\frac{x}{c}\right)^2 \cos^2\phi + \sin^2\phi\right]^{\frac{1}{4}}, \quad f_w = \left[\sec\left(\frac{\pi c}{2B}\sqrt{\frac{x}{T}}\right)\right]^{\frac{1}{2}} \text{ and } Q = 1 + 1.464\left(\frac{x}{c}\right)^{1.65},$$

where

x	=	depth of surface crack
c	=	half length of surface crack
B	=	half width of plate
F_s	=	boundary correction factor
Q	=	shape factor for elliptical crack
T	=	plate thickness
g	=	fitting function
f_w	=	finite-width correction
f_ϕ	=	angular function derived from embedded elliptical crack solution
ϕ	=	parametric angle of ellipse, deg. $\phi = 0^\circ$ at surface intersection and 90° at deepest point.

COMPARISON OF LOCAL APPROACHES IN FATIGUE ANALYSIS OF WELDED STRUCTURES

I. POUTIAINEN and G. MARQUIS
Laboratory of Fatigue and Strength
Lappeenranta University of Technology
P.O. Box 20
FIN-53851 Lappeenranta, FINLAND

ABSTRACT

In this paper three fatigue assessment methods for the welded structures are compared. These are the effective notch method, a 1mm depth geometric stress method and a modified structural stress method. The object was to test how well these methods assess welded structures when the plate stiffness and stress distribution below the weld toe changes significantly. The traditional structural hot spot stress method is not suitable when the these conditions are present. The conclusion was that all of the methods produced similar results in predicting the failure location. Methods responded also to the weld size changes resulting lower fatigue strength to smaller weld size. The fatigue strength estimates between methods had some variation.

NOMENCLATURE

FAT	Fatigue strength of the joint
FAT_0	Fatigue strength of the joint with non-loaded weld (σ_{weld}=0)
FAT_{0B}	Fatigue strength of the joint with non-loaded weld (σ_{weld}=0) in bending mode
FAT_{0T}	Fatigue strength of the joint with non-loaded weld (σ_{weld}=0) in tension mode
K_{sa}	Local structural stress concentration factor caused by the loaded weld
K_t	Stress concentration factor
l_w	Weld leg length
N_f	Fatigue life [cycles]
T	Plate thickness
δ_b	Degree of bending
σ_{notch}	Notch stress
σ_{nom}	Nominal stress
σ_{weld}	Average weld stress in the weld throat (perpendicular to throat)

1. INTRODUCTION

Fatigue assessment of welded structures is always based on a specific well defined stress component (or stress intensity factor). An assessment procedure must ensure that actions on the structure, the fatigue resistance of the structure and the method for obtaining a stress value based on the load action are all consistent and well defined. The stress in the critical location of a fabricated structure can be partitioned, e. g., into nominal, structural and local notch stress. The

structural stress is frequently termed as *structural hot spot stress (SHS)* when the structural stress at a potential failure location is being assessed. Structural stress in plate-type structures is defined as the surface stress based on a linearized through thickness stress distribution. This stress value excludes the non-linear stress component caused by the notch in the weld toe. If the weld toe geometry is kept constant and, e.g., the weld size is varied, the total stress distribution also varies. The local notch geometry is not altered by weld size and the linear stress distribution also remains constant. This clearly indicates that the linear stress distribution cannot always correctly define the weld toe stress state.

Even though the structural hot spot stress is, by definition, a linear through the plate thickness, the true stress distribution will be nonlinear. It has been recognized that structural stress is not always appropriate for fatigue assessment and nonlinear stress extrapolations have been proposed for some types of welded details. The use of term *geometric stress* is more suitable in these cases. Niemi (2000) has defined some cases that required a parabolic surface extrapolation method for fatigue assessment and Niemi and Tanskanen (1999) have provided guidelines for stress extrapolation for plate edges that are not based on the thickness of the plate. These are examples of cases where the hot stress is not based on the linear stress distribution. However, in the majority of structural plate details the linear stress distribution assumption gives good results.

Structural stress based methods permit much larger mesh sizes and models normally have only a fraction of the degrees of freedom as compared to other local methods. Assuming only a linear stress distribution through thickness in front of the weld toe, the structural stress can be determined with fairly simple element meshes and therefore the method is widely used as a compromise between global and local approaches (Radaj 1990). The structural stress based method is included, e.g., in the recommendation of IIW (International Institute of Welding) (Hobbacher 2006),in European design guidance documents for steel structures (ENV 1993) and pressure vessels (EN 13445-3, 2002). Poutiainen and Marquis (2006) have presented a method to improve the accuracy of the structural hot spot method. The idea behind this modified structural stress method is to account for the local behaviour of the welded detail by assuming a mult-linear through-thickness stress distribution similar to the bi-linear stress distribution of Dong et al. (2003). The method modifies the structural stress based on the load passing through the weld and the weld size. Thus, the effects of weld load and the weld size can be accounted.

The effect of local weld toe geometry can be included in the analyses using notch stress or strain methods. Application of these methods to welded structures is presented by Radaj and Sonsino (1998). The effective notch stress method is included in the IIW recommendations (Hobbacher 2006).

A relatively new fatigue assessment procedure has been published by the Xiao and Yamada (2004). The method is based on the geometric stress at the depth of 1 mm from the surface. By selecting the below surface stress, the stress peak at the weld toe is excluded. This can not be measured experimentally and a finite element analysis is required. The required element mesh density is less than for the effective notch method since the smallest element is 1 mm in thickness direction. The stress to be determined is, in this method, unambiguous. In many respects the method is similar to that presented previously by Partanen (1991). Partanen suggested that the hot spot -stress could be determined at a depth of 1-2mm where the expected fatigue lives for a variety of joint types with different stress distributions could be correlated.

In this paper three local approaches are examined. Also, the traditional structural stress approach is applied. An I-beam cover plate detail was selected for the comparison. The structure was previously analysed by Poutiainen (2002) using structural hot spot method (SHS). The conclusion in this paper was that determination of the structural stress using surface stress extrapolation can

not represent the local behaviour the weld toe when the plate stiffness is varied and when the weld size is changed.

2. ANALYSIS METHODS

Three relatively new finite element method based fatigue analysis procedures are presented in this paper. All three methods have improved accuracy with respect the traditional structural stress method in that they, to some degree, consider the local stress distribution in the weld area. Yet, the three methods have been developed based on differing sets of assumptions. As a general rule, local methods require larger model sizes as compared to the traditional structural stress method. As a benefit, however, local methods are suitable for a wider variety of structural details with improved accuracy as compared to non-local methods.

Effective notch method

The effective notch stress method according Radaj (1990) introduces a fictitious 1 mm notch radius at the weld toe or weld root where a fatigue crack may occur. This is seen in Figure 1. The fictitious radius accounts for the microsupport effect of the sharp notch at the weld toe or the weld root (Radaj 1990). The analysis model must be constructed so that notch stress can be determined accurately, i.e. element sizes on the order of 0.2 mm or less are needed in the radius region. The maximum principal stress in the most highly stressed location is used during fatigue assessment. An example of the element mesh for the notch stress determination in the filled welded detail is presented in Figure 2.

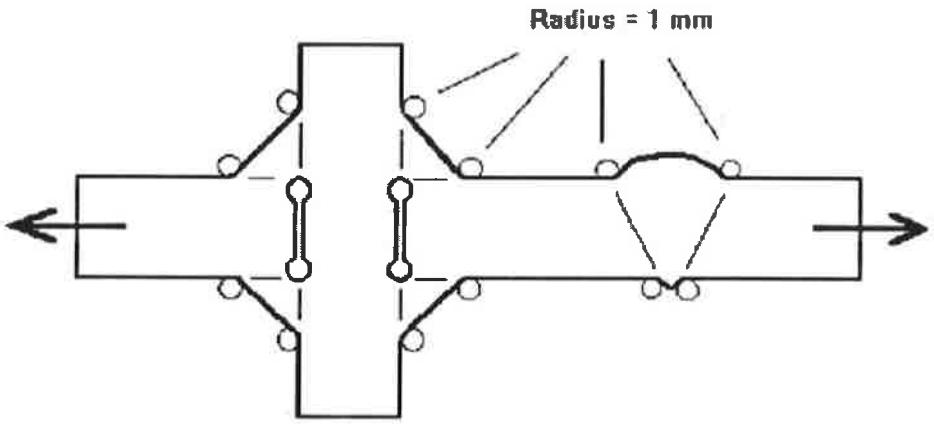


Figure. 1 Model configuration for the effective notch method (Hobbacher 2006).

According to the IIW recommendations the fatigue strength of a weld can be assessed using a fatigue class *FAT* 225 S-N curve when the effective notch method is applied (Hobbacher 2006). This fatigue class indicates that an effective notch stress of 225 MPa results a fatigue life of 2 million cycles at 95% survival probability. The fatigue strength (*FAT*) of the welded detail can then be determined using Eqs. (1) and (2).

$$FAT = \frac{225}{K_t}, \quad where \tag{1}$$

$$K_t = \frac{\sigma_{notch}}{\sigma_{nom}} \tag{2}$$

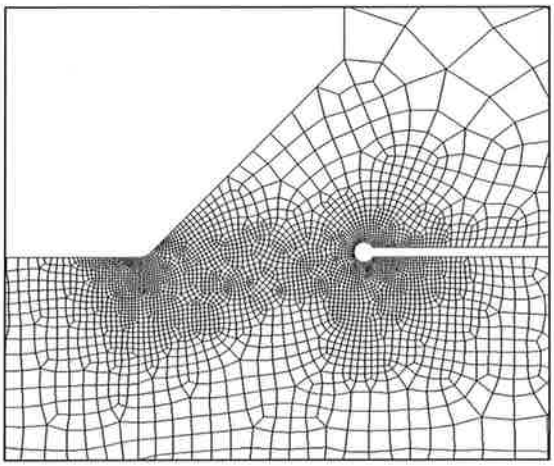


Figure. 2 An element mesh for the notch stress determination

Geometric stress at 1 mm depth

A relatively new method for determining the structural stress has been proposed by the Xiao and Yamada (2004). The method is based on the geometric stress at the depth of 1 mm from the surface. By selecting the stress at a depth of 1 mm, the structural stress concentration of the weld attachment can be determined while excluding the local effect of the weld toe. This method can be used to estimate the geometric stress in cases where the geometric and structural stresses deviate from one another. This is often a case in attachments in thick plates and in-plane gussets. The influence of weld toe radius and flank angle variation nearly vanishes as the depth of 1 mm. This can be seen in Figure 3.

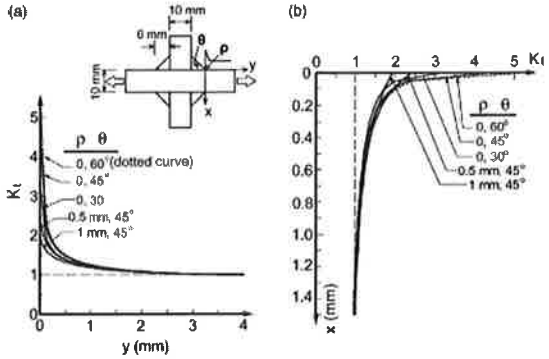


Figure. 3 Variation of the stress distribution in the surface (a) and in thickness direction (b) (Xiao and Yamada, 2004

The element mesh size has significant effect on the computed weld toe stress value, especially when the toe radius approaches zero. Any attempt to make use of the computed weld toe stress value in fatigue analysis would require strict guidelines regarding element size and element type in the weld toe area. Xiao and Yamada showed that the stress range at the depth of 1mm is relatively element mesh insensitive. By selecting an element size of 1 mm, the stress at this depth could be obtained from directly from the FE analysis as seen in Figure 4.

Xiao and Yamada selected a non-load carrying cruciform joint as a reference detail. Then, more complex details were modelled and it was discovered that the fatigue strength of a variety of details could be correlated when the stress at a depth of 1 mm was evaluated. A S-N curve plotted using this geometric stress showed that the fatigue test data are just above Japanese design curve (JSSC,1995) JSSC-D, which corresponds to fatigue class *FAT* 100. This *FAT* class was used for further comparison.

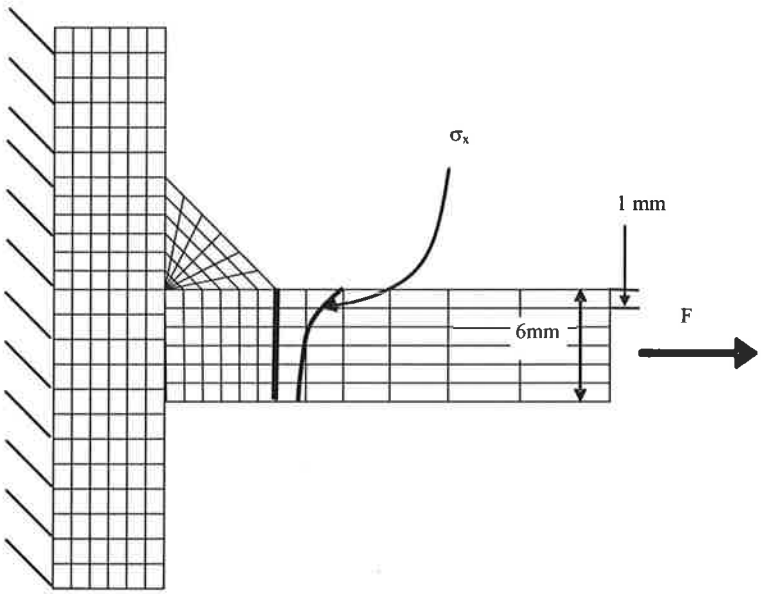


Figure. 4 Stress determination at a depth of 1mm directly from the FE model.

Modified structural stress

Poutiainen and Marquis (2004, 2006) have presented a modified structural stress method that takes into account the stress in the weld to determine a local concentration factor. The modified structural stress concentration factor, K_{sa}, is determined from Eqs. (3) and (4). The degree of concentration depends on weld size and weld stress. The local structural stress concentration is greatest for thick plates and small load-carrying welds.

$$K_{sa} = 1 + \frac{\sigma_{weld}}{\sigma_{nom}}\left(1 - \frac{l_w}{T}\right) \quad , \quad l_w \le \frac{T}{2} \tag{3}$$

$$K_{sa} = 1 + \frac{\sigma_{weld}}{\sigma_{nom}}\left(\frac{T}{4l_w}\right) \quad , \quad l_w \ge \frac{T}{2} \tag{4}$$

The advantage of this modified structural stress method is that the element model can be simple and the number of elements required is less that for the two previously presented methods. Only the structural stress and the weld stress (force) are needed from the FE model. Both can be determined reliable with coarse element mesh. Figure 5 shows an example of the method applied for a complex welded tubular structure.

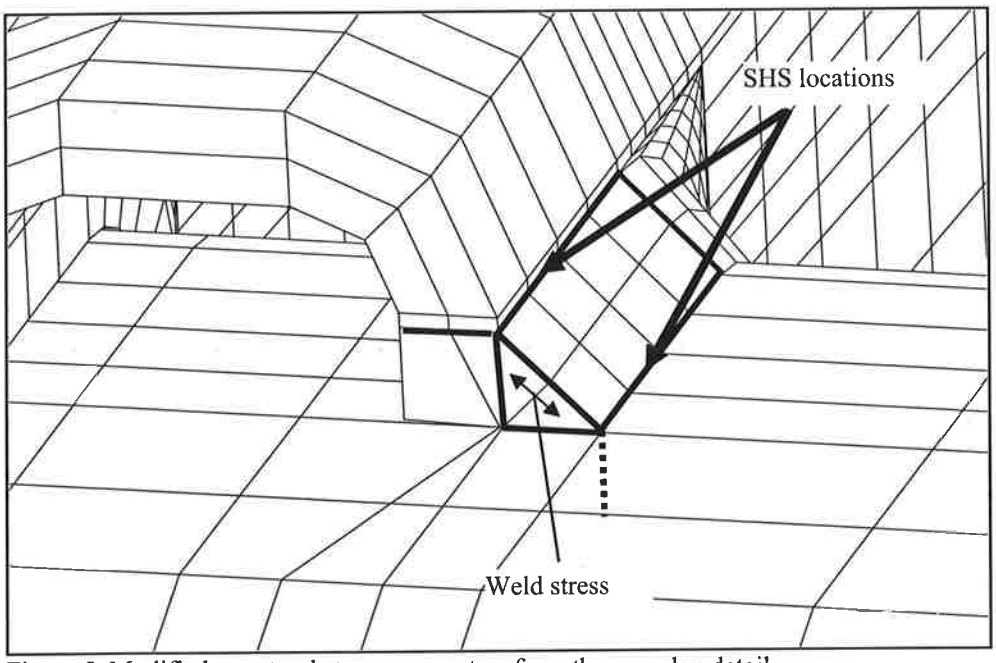


Figure 5. Modified structural stress parameters from the complex detail

The modified structural stress method takes into account both the weld size and the stress in the weld. If the weld is non-load carrying, the fatigue life is lower for larger welds. During fatigue assessment, the fatigue strength of the detail is first computed assuming that the weld is free of stress. The fatigue strength in the load-free case will vary depending on if the structure is loaded in tension or bending. Estimates for the load-free fatigue class can be determined from the Eq. (5) in the case of tension only loading, FAT_{0T}, and Eq. (6) for the case of bending only loading, FAT_{0B}. Equations (5) and (6) were derived from analysis results previously developed by Poutianen and Marquis (2006). These equations take into account the influence of stress gradient through the plate thickness as a function of weld size and plate thickness.

$$FAT_{0T} = 314,40 - 0,032 \cdot T + 1,43 \cdot \left[\frac{w}{T}\right]^{2} - 135,50 \cdot w^{0,06} - 77,93 \cdot \left[\frac{w}{t}\right]^{0,08} \quad (5)$$

$$FAT_{0B} = 1016 - 0,0078 \cdot T + 3,0 \cdot \left[\frac{w}{T}\right]^{1,90} - 899 \cdot w^{0,013} \quad (6)$$

Most welds are loaded with some combination of tension and bending loading, so the zero-load fatigue strength, FAT_0, is computed using Eq. (7). The degree of bending, δ_b, in Eq. (7) is expressed as the ratio of the structural stress due to bending divided by the total structural stress. If the structural stress is determined using surface extrapolation methods, the influence of bending stress will be exaggerated and may lead to an overly conservative fatigue life estimate in those structures where the structural stress is predominantly due to bending. This definition of degree of bending has been used, e.g., by Dong (2006). Surface extrapolation does not directly give indicate the portion of stress due to bending. If applicable, a through thickness determination procedure could be used (Poutiainen et al., 2004). Fatigue strength of a welded detail is calculated by dividing FAT_0 by the local stress concentration factor K_{sa} from Eqs. (3) and (4), see Eq. (8).

$$FAT_0 = FAT_{0T} \cdot (1 - \delta_b) + FAT_{0B} \cdot \delta_b \quad (7)$$

$$FAT = \frac{FAT_0}{K_{sa}} \quad (8)$$

3. STRUCTURAL DETAIL

The three previously described local methods were applied to the structural detail shown in Figure 6. This detail was chosen both because it is a common structural detail and because the web creates an interesting stress concentration for purposes of analysis. The same detail was previously analyzed by Poutiainen (2002). The objective of this previous study was to develop parametric equations for the structural stress as the geometry of the I-beam and cover plate were varied. One conclusion was that the conventional structural stress approach predicted the primary fatigue failure location to be approximately 40 mm from the centreline of the flange. Flange bending in the middle of the beam is restricted by the stiff web, thus, the computed structural stress in this region is less than at a distance of 40mm from the centreline. From the same model it was observed that, even though the structural stress is less near the beam centreline, the weld stresses near the beam centreline are higher.

Fatigue tests of similar cover plate structures are reported by Fisher (1971) and Miki et.al. (1992). Actual dimensions are not the same as used in this study, but the overall size is similar. Both test serie were done under the bending load. In Fisher's tests, cracks initiated the near the centre line of the beam in those cover plates with transverse fillet welds at the end of the cover plate. Miki observed that cracks initiation at many locations along the transverse cover plate end weld. The test specimens were little bit different indicating that the transverse weld can have quite constant fatigue strength along the weld toe line with some dimension combination.

A second observation from the previous study (Poutiainen 2002) was that the structural stress was nearly independent of weld size. In cases like the I-beam cover plate detail, the weld load remains relatively constant even if the throat thickness is varied. A smaller weld transmits the same force as a large weld, but the stress in a smaller weld is greater. Higher stresses in the weld will increase the local stress concentration which tends to reduce the fatigue strength. In contrast, for non-load

carrying welds a smaller weld has higher fatigue strength because of the stress gradient effect. This effect, however, is less pronounced and the net result is that a smaller weld throat thickness is expected to have lower fatigue strength as compared to a larger throat thickness weld. If an extrapolation method is used to assess the structural stress, the larger weld will indicate higher stresses at the extrapolation points with the result that the larger weld would be expected to have lower fatigue strength. To assess this behaviour, the detail in Figure 6 was analyzed with three weld sizes. The throat thicknesses were 3 mm, 5mm and 10mm.

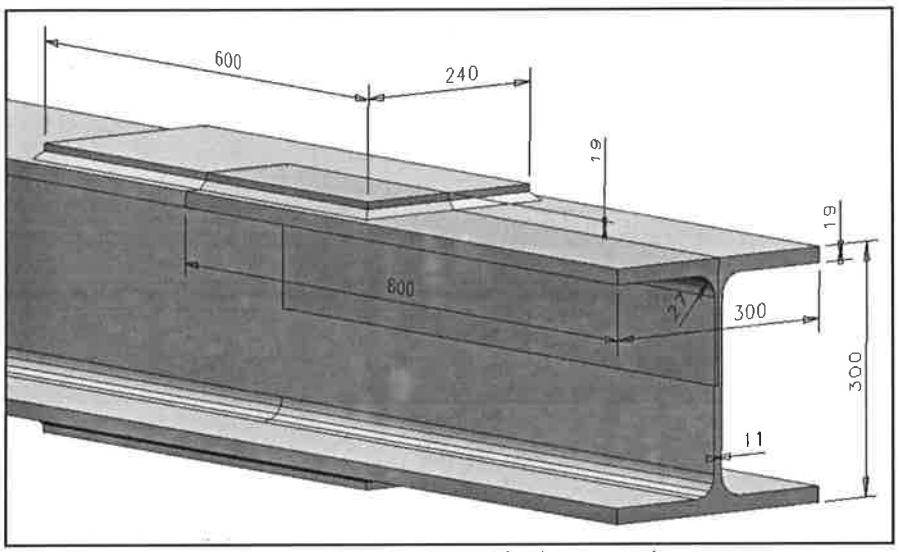


Figure 6 The structural cover plate detail used in the comparison.

4. FINITE ELEMENT MODELS

Finite element models for 1/8 of the structure were constructed for each of the three methods and weld sizes. Suitable symmetry restraints were used in all models. I-deas 9.0 was used for both modelling and analyzing of the details. Tension loading mode was assumed. Because weld size was varied and the weld stress was needed for the modified structural stress method, a gap between flange and cover was used and contact between plates was excluded.

Analysis of the local stresses in the weld toe region generally requires a dense element mesh in the weld toe area. Depending on the meshing strategy the local mesh size is also reflected in modelling of other portions of the structure. In this study, the structure was relatively simple and special measures were not used minimize the degrees of freedom (DOF) in the analysis models. The result was that relatively large models were needed for the effective notch and 1mm methods. The model used for fatigue assessment based on the effective notch method was constructed with parabolic isoparametric elements. The DOF was 554562 for the model with 5 mm throat thickness, see Figure 7. For the 1mm method, linear isoparametric elements were used and the DOF for the 5mm throat thickness model was 124026. Linear elements were also used for the model based on the modified structural stress method and DOF was 15066. The modified structural stress method model is shown in Figure 8. Figure 9 shows a two dimensional view of the models of the weld toe region for each of the three methods.

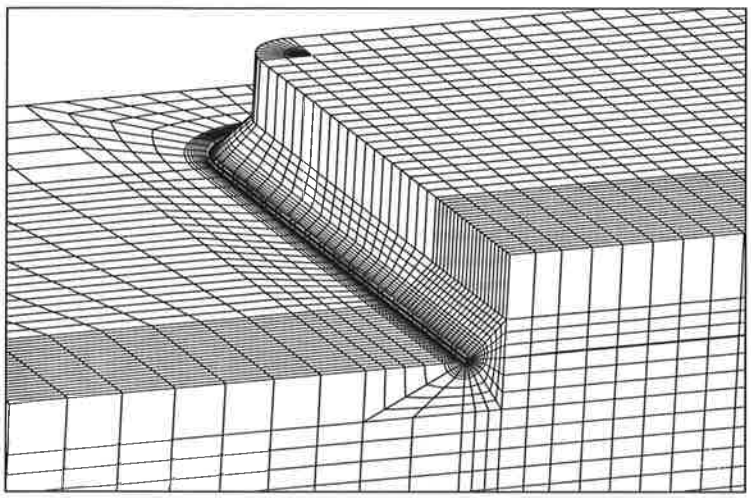


Figure 7 Model for the effective notch method with a5 weld size

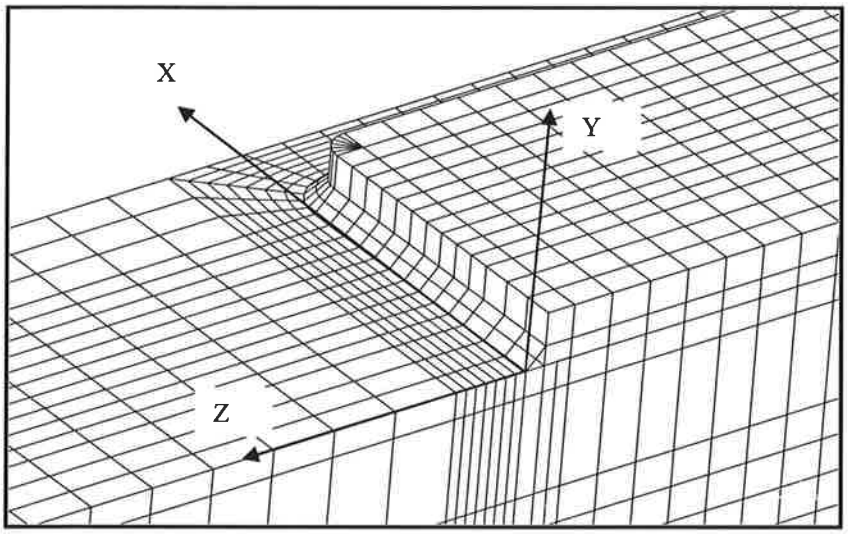


Figure 8 Model for modified structural hot stress method (a5).

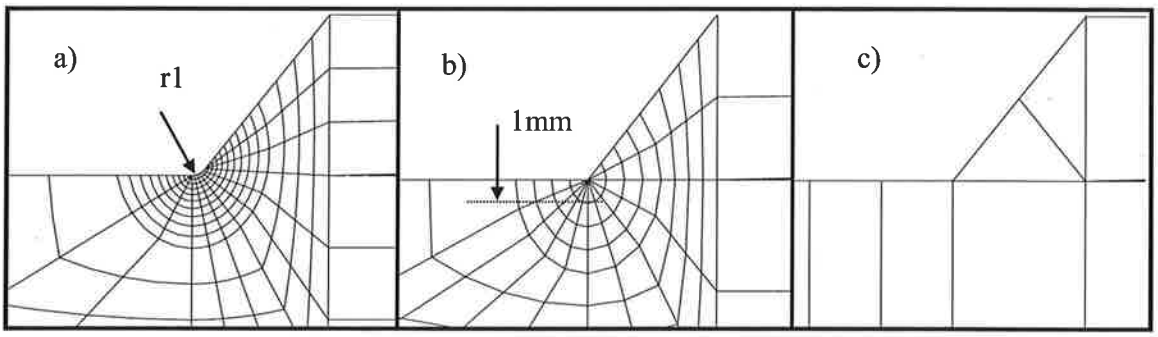


Figure 9. Element mesh in the weld zone. a) effective notch, b) 1mm depth stress range, c) modified S

5. RESULTS

Stresses along the weld toe at the end of the cover plate, i.e., along the x- axis shown in Figure 8, were computed for each of the three analysis methods. For the effective notch stress method, maximum principal stresses were plotted. The maximum principal stress distribution in the effective notch as a function of distance x is presented in Figure 10. For the 1 mm depth method, the σ_z stress distribution in the x-direction along the weld toe is plotted in Figure 11.

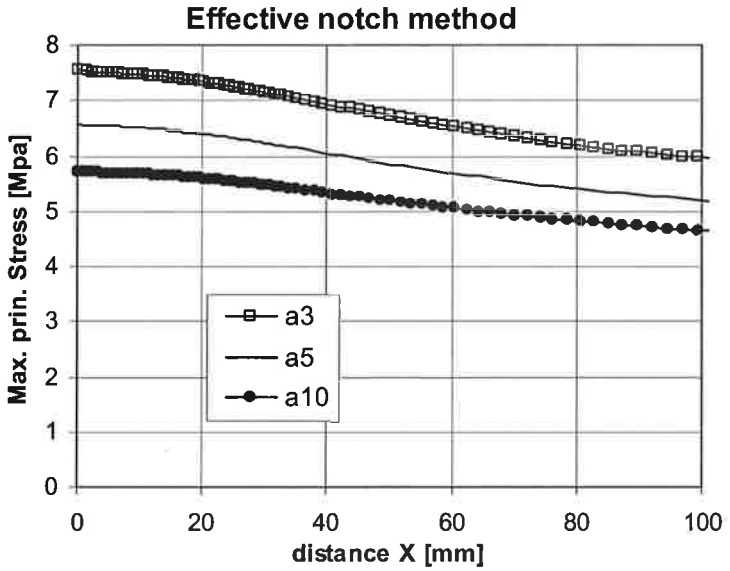


Figure 10 Maximum principal stress distribution in the 1 mm radius notch

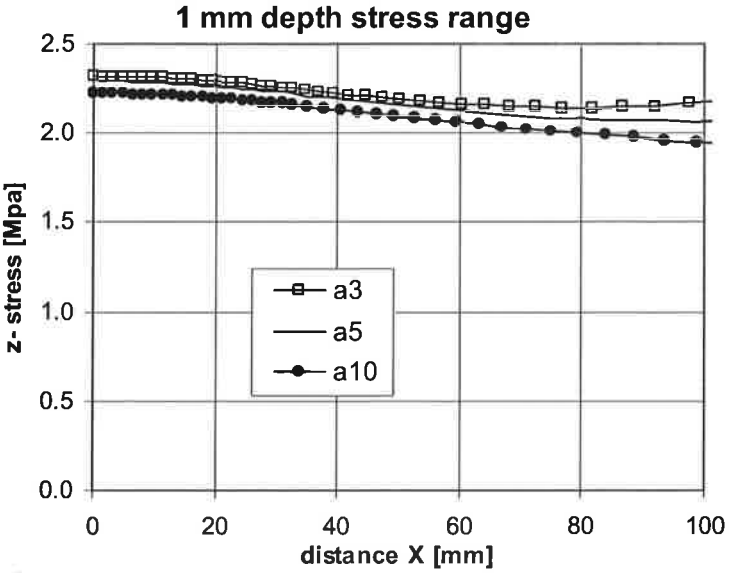


Figure 11. Stress distribution at the depth of 1 mm

The structural hot spot stress was determined from the extrapolation points away from the weld toe. Extrapolation distances were 0,4T and 1,0T and linear extrapolation was used. The weld stresses were calculated from the nodal forces at the edge of the cover plate. The structural stress distribution is presented in Figure 12 a) and the corresponding weld stresses in Figure 12 b). The structural stress distribution shows somewhat less variation along the weld toe than was found earlier (Poutiainen 2002) also the structural stress values are slightly higher. The mesh density in this study was lower in the thickness direction, which causes this small difference in structural stress estimate.

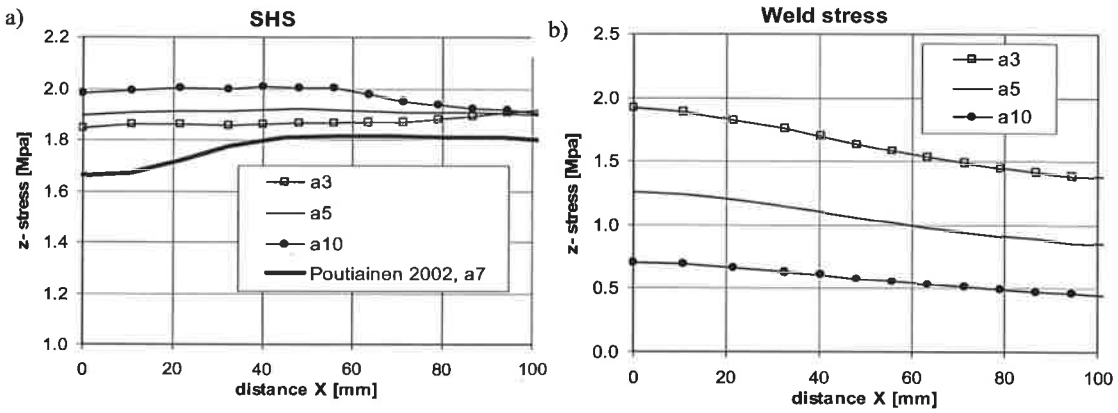


Figure 12 a) Structural hot spot stress distribution and b) weld stress distribution

The characteristic fatigue strength for the cover plate detail was calculated for each method to obtain the corresponding fatigue class (*FAT*). In the modified structural hot spot stress method, fatigue strength is obtained using the local stress concentration factor, Eqs. (3) and (4), and the zero load fatigue class, FAT_0 , determined from Eqs. (5) - (7). The use of surface extrapolation procedure in the SHS calculation does not provide the degree of bending, δ_b, value. The bending portion of total SHS was assumed as 0,4. Characteristic fatigue strengths along the cover plate end are presented in Figure 13. The characteristic fatigue strength based on the traditional structural stress methods were calculated using a fatigue class *FAT* 100 as per IIW recommendations (Hobbacher 2006).

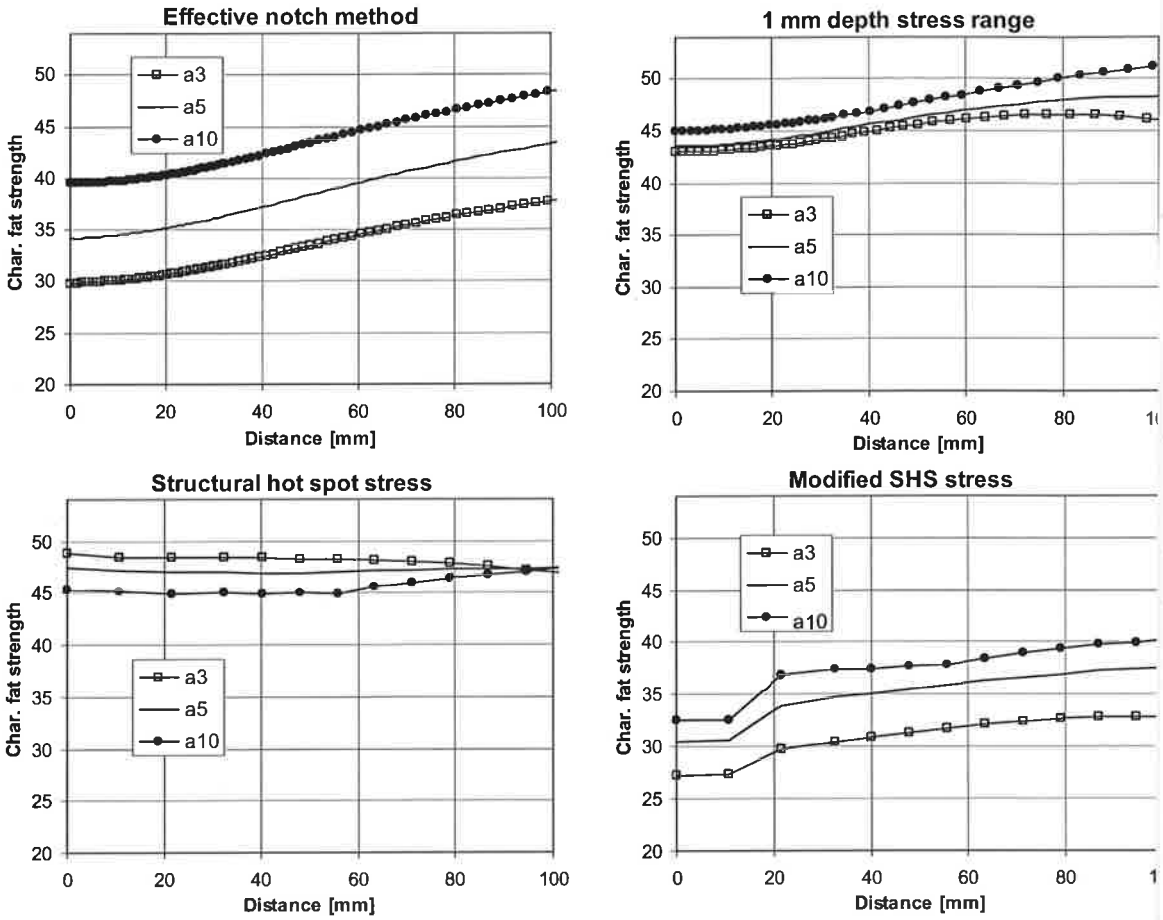


Figure 13 Characteristic fatigue strengths along the cover plate ends based on different assessment methods

6. DISCUSSION

Critical stress values used in each of the three assessment methods can be compared using Figs. 10-12. The effective notch stress method shows the clearest response to weld size variation. Also, the stress concentration at the centreline of the I-beam is obvious from this method. The stress at the depth of 1 mm also shows the maximum stress along the beam centreline, but the reduction in stress away from the centreline is less pronounced than for the effective notch stress method. Weld size does not show any significant influence on stress at a depth of 1 mm. This is due to the through thickness stress distribution at the weld toe. Figure 14 shows the through thickness stress distributions taken from the effective notch models. Weld size influences the stress at the surface, but all three curves intersect at a depth of about 1 mm. The small variation in stress for different weld sizes seen in Figure 11 for the 1mm depth model is most likely caused by a the coarser mesh which was used for this method. The convential structural hot spot stress at the weld toe, Figure 12 a), was nearly constant along the weld toe. Unlike the three more local methods the larger weld produces a higher stress than does a smaller weld. The weld stress distribution in Figure 12 b) shows significantly more variation along the weld toe.

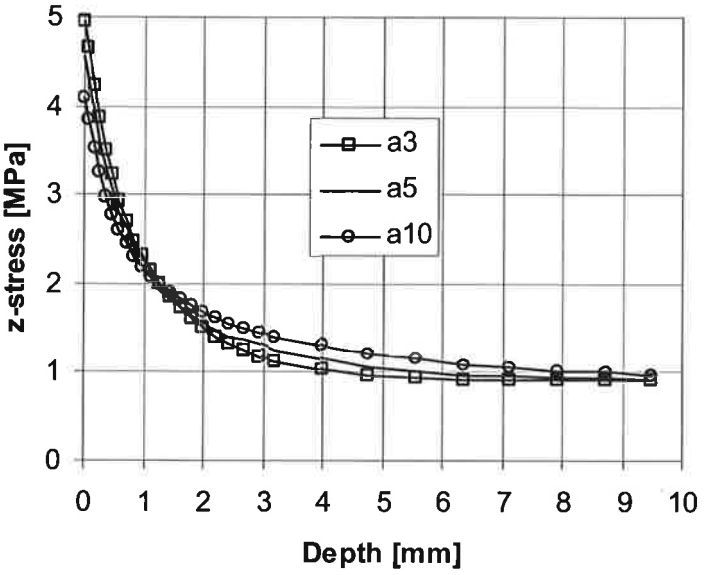


Figure 14 Through thickness stress distributions at the weld toe for the three weld sizes (Note: based on the effective notch stress models).

The characteristic fatigue curves in Figure 13 show that all methods except the structural hot spot stress method predict the most critical fatigue location for the cover plate to be at the centre line of the I-beam. The effective notch stress method shows the greatest variation in the fatigue strength between the beam centreline and flange ends. The effective notch, 1 mm depth and modified structural stress method all predict that fatigue strength increases with weld size while the structural stress methods predicts the opposite effect.

The modified structural stress method predicts the lowest fatigue strength for the cover plate structure. The FAT_0 classes calculated with Eqs. (5)-(7) are based on the LEFM calculations assuming a continuous crack along the weld toe. If semi-elliptical crack growth at the weld toe is assumed the resulting FAT_0 values would be greater. The increase would be in the range of 20 to 40% with the constant S-N curve slope m=3 (Gurney 1991). The modified structural stress method predicts a sudden drop in fatigue strength for that portion of the transverse cover plate weld directly on top of the web. This is partially the result that, in the local stress concentration factor calculation, the thickness T was set equal to the I-beam height, i.e. T = 300 mm in Eq. (3), for the two data points nearest the beam centreline.

The mesh densities and resulting DOF for the three local methods varied greatly. For the cover plate with a 5 mm throat thickness weld, DOF was 554562 for the effective notch stress model, 124026 for the 1mm depth method model and 15066 for the modified structural stress method model. While no two stress analysts would produce exactly identical meshes, the value obtained here could be considered as representative of good stress analysis practice. The DOF for the modified structural stress methods was more than one decade less than for the effective notch method. For large or complex structures this radically different modelling demand could be significant.

7. CONCLUSION

Three local approaches developed for the analysis of fatigue strength of welded structures were used to analyze a cover plate detail with varying weld throat thicknesses. All methods predicted approximately the same fatigue strength behaviour. The influence of weld size was most clearly seen when the effective notch method was used and least clearly when the 1 mm depth method was applied. The modified structural stress method also predicted a clear decrease in fatigue strength with decreasing weld size. For all the local method evaluated here the influence of weld size was opposite to that predicted using the conventional structural stress method. Modelling requirements for the three methods varied greatly with the effective notch method requiring more than one decade more DOF than the modified structural stress method.

REFERENCES

[1] Dong, P., Hong, J. K., Cao, Z., Stresses and stress intensities at notches: anomalous crack growth, Int. J Fatigue, 25; 811-825, 2003.

[2] Dong, P, Introduction to the Battelle structural stress analysis method, lecture notes 16.5.2006 Lappeentanta University of Technology, 2006.

[3] EN 13445-3, Unfired Pressure Vessels -Part 3: Design, CEN 2002.

[4] ENV 1993-1-1, Eurocode 3: Design of steel structures - Part 1-1. CEN 1992

[5] Fisher, J.W., Fatigue strength of welded A514 steel beams, Paper 9, Proceedings of the conference on fatigue of welded structures, The Welding Institute, Cambridge, 1971

[6] Gurney, T.R., The fatigue strength of transverse fillet welded joints, Abington publishing, 1991

[7] Hobbacher, A., Recommendations for fatigue design of welded joints and components, IIW doc. XIII-1965-03/XV-1127-03. International Institute of Welding, version March 2006

[8] JSSC, Fatigue Design Recommendations for steel structures, Japanese Society of Steel Construction,1995

[9] Miki, C., Toyoda, Y., Mori, T.,Enokido, N., Fatigue of large-scale welded girders under simulated highway loadings, IIW document XIII-1459-92, IIW, 1992

[10] Niemi, E., Structural hot spot stress approach to fatigue analysis of welded components, IIW-document XIII-1819-00/XV-1090-01, International Institute of Welding, 2000

[11] Niemi, E., Tanskanen, P., Hot spot stress determination for welded edge gussets, IIW-document XIII-1781-99/XV-1027-99, International Institute of Welding, 1999

[12] Partanen, T., On factors affecting the fatigue life of welded components using the hot-spot approach, Proc. of the 4th Finnish Mechanics Symposium, 1991, ISBN 951-763-663-6

[13] Poutiainen, I., Determination of parametric hot spot stress equation for the cover plate on an I-beam, Design and analysis of welded high strength steel structures, Fatigue 2002, EMAS, Stockholm, 2002

[14] Poutiainen, I., Marquis, G., A fatigue assessment method based on weld stress, Int J Fatigue, accepted for publication, 2006

[15] Poutiainen, I., Marquis, G., A Single-point structural stress assessment procedure for load-carrying fillet welds, IIW document XIII-2012-04/XV-1174-04, International Institute of Welding, 2004

[16] Poutiainen, I., Tanskanen, P., Marquis, G., Finite element methods for structural hot spot stress determination - a comparison of procedures. Int J Fatigue, 2004,26:1147-1157

[17] Radaj, D., Design and analysis of fatigue resistant welded structures, Abington publishing, Cambridge, 1990, ISBN 1-85573-004-9

[18] Radaj, D., Sonsino C.M., Fatigue assessment of welded joints by local approaches. Abington publishing, Cambridge, 1998

[19] Xiao, Z-G.,Yamada, K., A method of determining geometric stress for fatigue strength evaluation of steel welded joints, Int J Fatigue 2004;26:1277-1293

FATIGUE ASSESSMENT OF A NOTCHED NODULAR CAST IRON COMPONENT SUBJECTED TO MULTIAXIAL LOADING

J.S. LEPISTÖ
Laboratory of Fatigue and Strength
Lappeenranta University of Technology
P.O. Box 20
FI-53851 LAPPEENRANTA, FINLAND

ABSTRACT

In this paper, some results of fatigue tests carried out for a cast component are presented. The component is a large thick walled structure fabricated from nodular cast iron. In addition to fatigue tests, static measurements and FE-analyses were performed. The results from static measurements were also compared with the results obtained from FE-analysis. The FE-results were in good agreement with the static measurements. Several different load cases were studied. These involved bending-only, torsion-only, combinations of bending and torsion and constant and variable amplitude loading. In total, 10 fatigue tests were done. Based on these tests, a mean S–N curve was determined. For the two test cases in which variable amplitude loading was used, the fatigue strength was significantly lower than that observed in constant amplitude loading.

1. INTRODUCTION

Cast components are widely used in such applications, which require rather complex geometry. One of these applications is a cast axle studied in this paper. This component is typically subjected to quite complex loading. Usually the loading is alternating and can be either proportional or non-proportional. The presence of several load components makes the axle to be subjected to a multi-axial stress state.

The critical area regarding to fatigue is the shoulder made on it due to the bearing. The notch on the shoulder has rather tight radius, which causes, especially in bending loading, a significant stress concentration. The loading in question (torsion plus bending) makes the stress state to be bi-axial on the bottom of the notch.

Both static and fatigue tests were performed. In order to estimate and determine the stress level at the notch, also FE-analyses were carried out. This had to be done because of the fact that no strain gauges etc. could be attached on that region. The FE-analyses were made using a 2D-model utilising axisymmetric elements. Bending was analysed in 2D-models by means of Fourier series. This feature was included in software used (MSC Marc and ABAQUS). The results of the FE-analysis were compared with static test results.

Two different constructions were used in tests. The original structure had to be modified, since it appeared that a wrong part of the test system failed. The torsion axle of the test system was too weak. In total, ten fatigue tests were performed including the run-out tests. The studied cases were constant amplitude proportional bending, torsion and torsion-bending (two tests of each), constant amplitude non-proportional torsion-bending (two tests) and variable amplitude proportional torsion-bending (two tests). Most tests were carried out using a min-max stress ratio of R = 0, meaning that mean stress was included in results. The load spectrum in variable amplitude tests was very simple; one over- underload cycle in 10000 cycles.

2. FE-ANALYSES

FE-analyses were performed using MSC Marc and ABAQUS software. The original construction was analysed using Marc and the modified one with ABAQUS. A 2D-model was used with axisymmetric elements. This approach was chosen since the region of the notch wanted to have a fine element mesh enough. This goal in mind, a 3D-model would have become too large. The element size used in these models was approximately 0.2x0.2 mm at the vicinity of the notch. Element models consisted approximately of 3500 elements. When the loading is bending, axisymmetric elements normally cannot be used, because they require the load in addition to the geometry also to be axisymmetric. However, both of named softwares could use Fourier series when analysing a bending case. This was done by different means, though. This technique was utilised to solve the bending case and the combined torsion-bending case when using Marc software. ABAQUS does not allow the combined case, since it uses different elements for torsion type loading and bending type loading. In this case, the combined load case was calculated from separately analysed torsion and bending cases. Detailed explanations about using the Fourier series technique for bending load in axisymmetric models can be found from software manuals [1, 2].

2.1 Original construction

MSC Marc was used to analyse the original structure. Axisymmetric elements of type 62 in Marc element library were used. These elements have eight nodes. When analysing the bending case with axisymmetric elements in Marc, the FOURIER option must be used. By using this method, several load cases are solved. These are then combined using the superposition principle. Thus, only linear analysis is possible.

The bending load (100 kN) was given in a user subroutine and the torsion load (100 kNm) directly in the input file. Since the nodal load given for the axisymmetric element is either in radial, axial or tangential direction, one must consider that with a radial load, the bending force is its cosine component. The load given in the user subroutine was a cosine distributed pressure load to the range of $-\pi/2$ to $\pi/2$ of angle θ (Figure 1). By integrating its cosine component, the bending force is obtained, eq. (1). The user routine used the pressure term p solved from eq.(1).

$$F = \int_{-\pi/2}^{\pi/2} p\cos(\theta)\cos(\theta) r\, d\theta \Rightarrow F = \frac{\pi}{2} p r \tag{1}$$

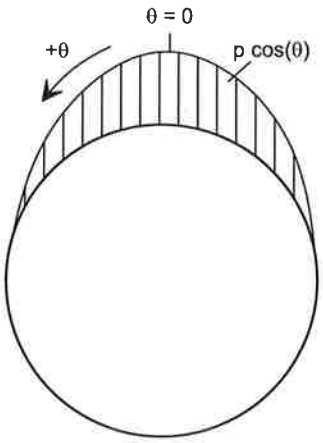


Figure 1. Load distribution given for the bending case in user subroutine.

2.2 Modified construction

The modified construction was analysed with ABAQUS software. In the model, the inner diameter of the cast axle was enlarged, thus the wall thickness was reduced. In addition, the bending arm length with respect to the notch differed from the original construction model. In ABAQUS, the bending case using axisymmetric elements can be also nonlinear. In this case, however, the analysis was linear.

Both bending case and torsion case were solved separately. A combined case can then be calculated afterwards using equations (2)–(4). In the bending case, an element of type CAXA8R2 was used. This is an eight-node element with Fourier series expansions. The torsion case was analysed using an element CGAX8R, which is also an eight-node element that includes a degree of freedom in circumferential direction. Both elements use reduced integration. The given loads were 100 kN in bending and 100 kNm in torsion.

$$\begin{cases} \sigma_1 = \frac{1}{2}\left(\sigma_x + \sigma_y + \sqrt{\left(\sigma_x - \sigma_y\right)^2 + 4\tau^2} \right) \\ \sigma_2 = \frac{1}{2}\left(\sigma_x + \sigma_y - \sqrt{\left(\sigma_x - \sigma_y\right)^2 + 4\tau^2} \right) \end{cases} \tag{2}$$

$$\sigma_{vm} = \sqrt{\sigma_x^2 + \sigma_y^2 - \sigma_x\sigma_y + 3\tau^2} \tag{3}$$

$$\sigma_x = F_b \frac{\sigma_{1b}}{F_{bFEA}}, \quad \sigma_y = F_b \frac{\sigma_{2b}}{F_{bFEA}}, \quad \tau = T \frac{\sigma_{1T}}{T_{FEA}} \tag{4}$$

In the equation (4), stresses σ_{1b} and σ_{2b} are principal stresses obtained from FE-analysis for the bending case and the force F_{bFEA} is the force used in the analysis. Accordingly, the stress σ_{1T} is the principal stress from torsion case and T_{FEA} is the torsion moment used in the analysis. F_b and T are the bending force and torsion moment of the combination in question.

3. LABORATORY TESTS

All tests were carried out in LUT laboratory of fatigue and strength. Test specimens were modified after few first tests since the torsion shaft of the test system was broken instead of the cast component itself. Consequently, the diameter of the torsion shaft was enlarged as well as the inner diameter of the cast component axle accordingly. By this means, the stress level at the cast component notch was increased and the critical area was moved at a location under investigation. The test arrangement is presented in Figure 2.

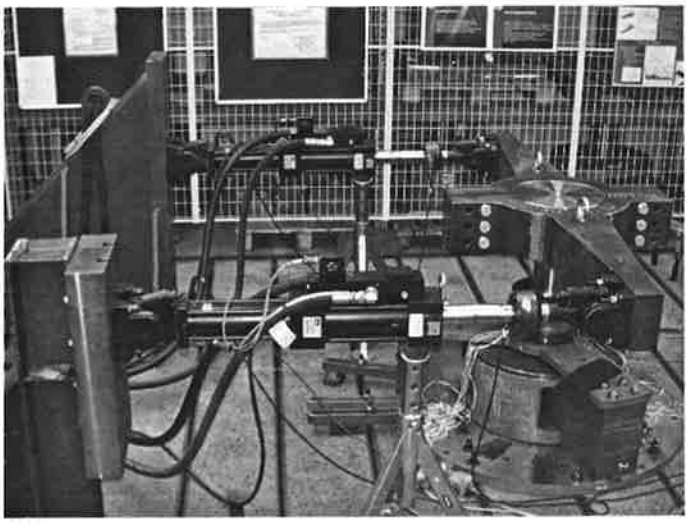


Figure 2. The test arrangement of the cast component fatigue tests.

3.1 Test material

Test specimens were fabricated from nodular cast iron. For each specimen, material properties of the casting were determined. These are presented elsewhere [3]. The modulus of the elasticity and the Poisson's ratio used in FE-analyses and stress calculations in static tests were $E = 175000$ MPa $\nu = 0.275$, respectively.

3.2 Test method

Test specimens were loaded using two hydraulic actuators shown in Figure 2. The bending arm was attached to the torsion shaft and the combination of these was inserted into the cast component axle and tightened by using a special tightening ring. The torsion moment was thus transmitted into the cast component via friction. The distance from the actuator to the centreline of the axle was 1000 mm, so each actuator produced a torsion moment of 1 kNm with a force of 1 kN in actuator. Both actuators were driven separately, if needed, thus enabling to produce a complex loading combination. This could be, for example, the combination of torsion and bending or a non-proportional loading. A torsion-bending loading is produced with this arrangement by setting a force of different magnitude on both sides. If the other force is tensile and the other compressive, a torsion moment is produced that is the sum of the absolute values of the forces (the sign for the load direction is then ignored). The bending force will be the difference of those.

3.2.1 Details

For each test specimen, some static tests were carried out before the fatigue test. Specimens were instrumented with strain gauge rosettes. The angle between the grids A and B as well as B and C was 45 degrees. One of the strain gauges was located as near the notch as possible, Figure 3. This means, that the gauge had to be placed under the bearing. Therefore, a space for the gauge was machined on the inner ring of the bearing. The orientation of the gauges with respect to the cast component axis was as shown in Figure 3. In the first tests, the orientation was like on the left of Fig. 3 and later, the orientation was like on the right of Fig. 3. The strain values were measured for each grid separately. Principal strains and stresses can then be calculated using equations (5)–(8). It must be noted, that the result of the angle of the principal strains (and stresses) will be in the coordinate system based on the gauge. In this system, the first axis is the direction of the grid A and the second axis in the direction of the grid C. If one is using Mathcad software for calculations, it is convenient to replace the equation (8) with the eq. (9), which gives the result measured from the first axis of the gauge coordinate system.

$$\begin{cases} \varepsilon_1 = \dfrac{1}{2}\left(\varepsilon_A + \varepsilon_C + \sqrt{(\varepsilon_A - \varepsilon_C)^2 + (2\varepsilon_B - \varepsilon_A - \varepsilon_C)^2}\right) \\ \varepsilon_2 = \dfrac{1}{2}\left(\varepsilon_A + \varepsilon_C - \sqrt{(\varepsilon_A - \varepsilon_C)^2 + (2\varepsilon_B - \varepsilon_A - \varepsilon_C)^2}\right) \end{cases} \tag{5}$$

$$\begin{cases} \sigma_1 = \dfrac{E}{2}\left(\dfrac{\varepsilon_A + \varepsilon_C}{1-\nu} + \dfrac{1}{1+\nu}\sqrt{(\varepsilon_A - \varepsilon_C)^2 + (2\varepsilon_B - \varepsilon_A - \varepsilon_C)^2}\right) \\ \sigma_2 = \dfrac{E}{2}\left(\dfrac{\varepsilon_A + \varepsilon_C}{1-\nu} - \dfrac{1}{1+\nu}\sqrt{(\varepsilon_A - \varepsilon_C)^2 + (2\varepsilon_B - \varepsilon_A - \varepsilon_C)^2}\right) \end{cases} \tag{6}$$

$$\tau_{max} = \frac{E}{2(1+\nu)}\sqrt{(\varepsilon_A - \varepsilon_C)^2 + (2\varepsilon_B - \varepsilon_A - \varepsilon_C)^2} = \frac{\sigma_1 - \sigma_2}{2} \tag{7}$$

$$\theta = \frac{1}{2}\arctan\left(\frac{2\varepsilon_B - \varepsilon_A - \varepsilon_C}{\varepsilon_A - \varepsilon_C}\right) \tag{8}$$

$$\theta = \frac{1}{2}\text{angle}[(\varepsilon_A - \varepsilon_C), (2\varepsilon_B - \varepsilon_A - \varepsilon_C)] \tag{9}$$

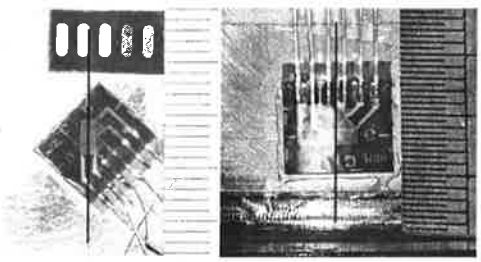


Figure 3. The orientation of the strain gauges on test specimens.

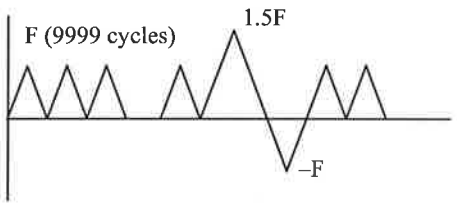


Figure 4. Load spectrum for variable amplitude fatigue tests.

Some of the fatigue tests were aborted before the cast axle totally broke. In those cases, however, the presence of a crack was obvious based on the output of the strain gauge. The occurrence of a crack on the cast axle was considered as a failure. The load level for the actuators was determined based on the FE-analysis results at the axle notch. Loading sequences for the non-proportional cases were simple. They are shown elsewhere [3]. The load spectrum for variable amplitude fatigue tests is presented in Figure 4. Here, F denotes the loading combination (torsion with slight bending).

4. RESULTS

4.1 FE-analysis

Figure 5 show the distribution of the largest principal stress at the notch for bending and torsion case for the original model and Figure 6 for the modified model, respectively. Calculated principal stresses and von Mises stress at the most critical spot at the notch of the cast component for both original and modified model are presented in Table 1.

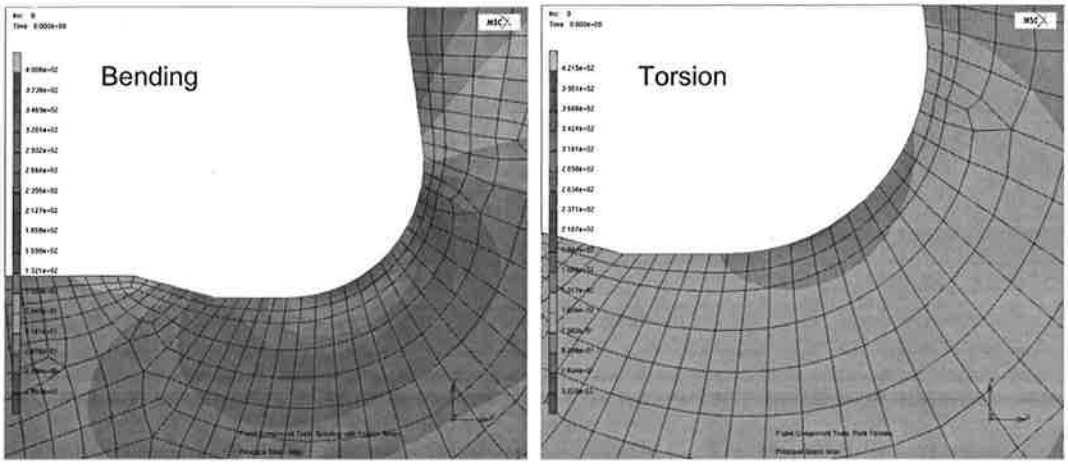


Figure 5. Maximum principal stress distribution at the notch for the original model.

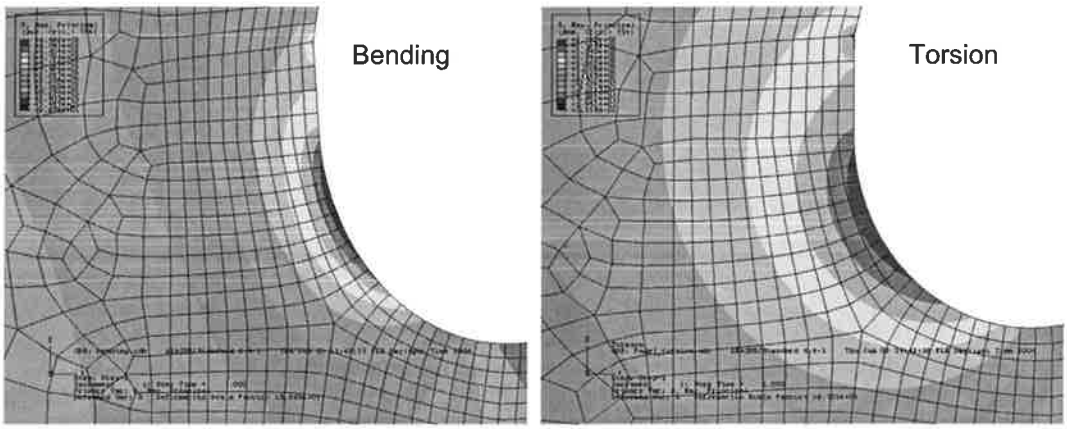


Figure 6. Maximum principal stress distribution at the notch for the modified model.

Table 1. Results from FE-analysis. Principal and von Mises stresses at notch.

	Loading	σ_1 [MPa]	σ_2 [MPa]	σ_{vm} [MPa]
Original	Bending 100 kN	401	120	354
	Torsion 100 kNm	162	–162	280
	Torsion 100 kN + Bending 100 kN	474	46	451
	Torsion 100 kN + Bending 10 kN	188	–136	282
Modified	Bending 100 kN	668	225	588
	Torsion 100 kNm	232	–232	402
	Torsion 100 kN + Bending 100 kN	767	125	713
	Torsion 100 kN + Bending 10 kN	278	–189	406

4.2 Static tests

Table 2 presents the results obtained from static measurements. In the table, the test results are compared with the results based on FE-analysis at strain gauge locations for same loads as in test. The strain gauge G2 was placed 49.5 mm above the gauge G1. This location does not have a deep stress gradient, and it was used for the comparison of the FE-analysis results.

Table 2. Static test results for both constructions and the comparison of the results with the FE-analysis results at same locations.

	Loading, gauge	σ_1 [MPa]	σ_2 [MPa]	τ_{max} [MPa]	σ_1 / $\sigma_{1,fea}$	σ_2 / $\sigma_{2,fea}$	τ_{max} / $\tau_{max,fea}$
Original	B, G1	102	34	34	0.94	1.06	0.89
	B, G2	70	6	32	1.00	0.86	1.00
	T, G2	85	–78	81	1.05	0.96	1.00
Modified	B, G1	119	61	29	1.05	1.28	0.88
	B, G2	44	2	21	1.01	–1.73	0.93
	T, G1	134	–110	122	1.14	0.93	1.04
	T, G2	119	–106	113	1.06	0.95	1.00

Original structure, bending case: F_b = 100 kN, T = 0 kNm
Original structure, torsion case: T = 99.8 kNm, F_b = –0.2 kN
Modified structure, bending case: F_b = 51.8 kN, T = 0 kNm
Modified structure, torsion case: T = 95.1 kNm, F_b = –0.1 kN

4.3 Fatigue tests

The numerical data for fatigue tests are presented in [3]. The specimens were considered as failed, when a crack was observed. The presence of the crack was judged based on the output of the strain gauge near the notch. When a change of approximately five to ten percent in maximum strain level of one grid was noticed, the breaking point was set on that cycle count.

Figure 7 shows a typical crack for the bending loading. Figure 8 presents a typical failure when the loading is fully reversed torsion. Finally, Figure 9 shows a typical crack for torsion-bending loading cases with $R = 0$. The direction of the crack is very close to the normal of the largest principal stress (usually approximately 50 degrees from the centreline of the cast component for these cases). Often several small cracks at the notch were observed. These were typically in a direction normal to the largest tensile principal stress.

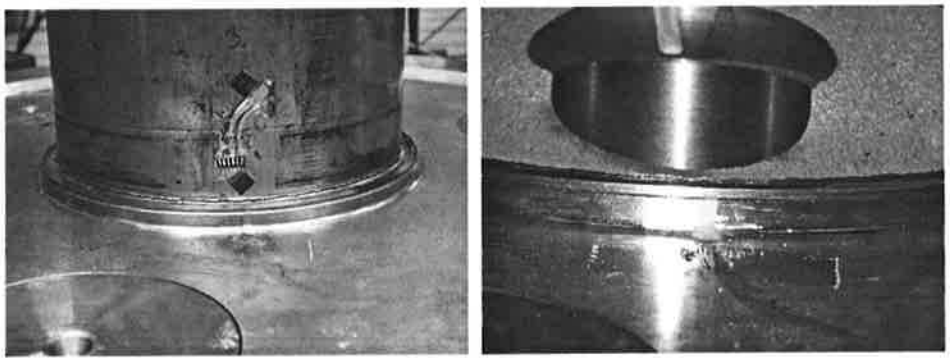


Figure 7. Failure of a test specimen subjected to a pure bending loading. The crack grows along the notch.

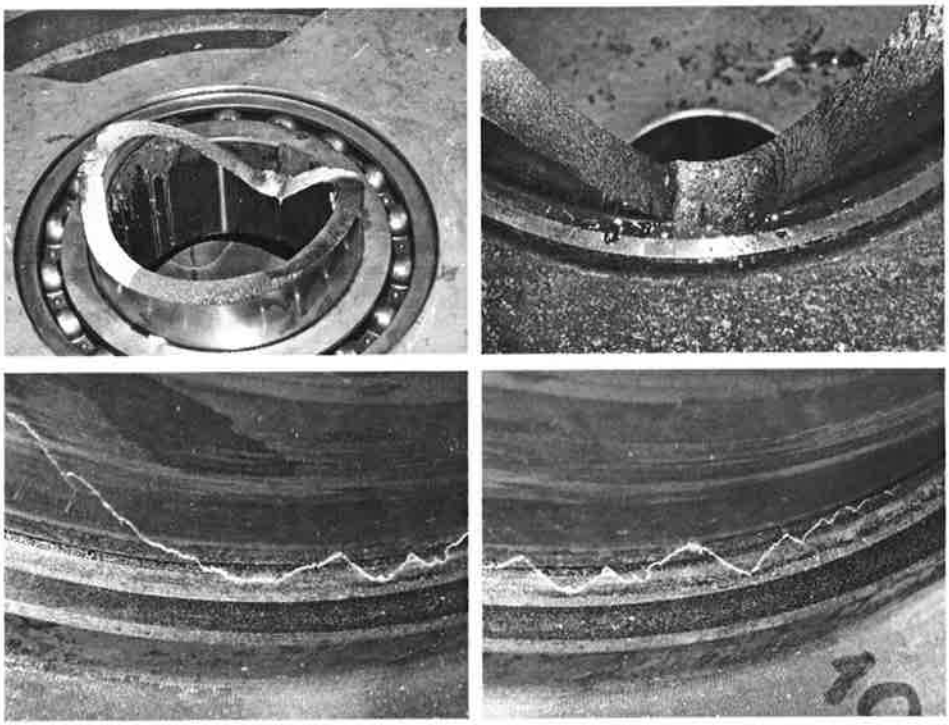


Figure 8. Failure of a test specimen subjected to fully reversed torsion loading. Two major cracks have led to a failure. Zigzag cracks along the notch were also observed (shown at lower part of the figure).



Figure 9. A typical failure of a test specimen subjected to torsion-bending loading (R=0). Often several small cracks were observed, too.

5. DISCUSSION

Finite element analysis results are in good agreement with the static measurements. For example in the bending load case, the difference between the results of the largest principal stress lies within six percent. For maximum shear stress in torsion case, the difference of the results lies within four percent. For the second principal stress, there are cases with a large percentage difference. One must remember, however, that the absolute values in these cases are small, meaning that a large percentage difference can arise due to rather small measurement error. On the other hand, the FE-model in this case is somewhat idealised, so it cannot always describe the real construction properly.

The occurrence of the crack could be observed relatively early in the fatigue tests from the output of the strain gauge placed near the notch. The gauge was usually placed near the expected site of the crack initiation. Even a rather small crack seemed to change the gauge output five to ten percent. However, even after the crack initiation was observed, the structure still had significant residual life being longer in the original construction than in modified one.

Since the fatigue tests varied from each other as regards the loading type as well as the mean stress, biaxial stress ratio and material strength, the results are not directly comparable with each other, e.g. by means of S–N curve. For that reason, they must be normalised somehow. This was done by using equation (10). A similar equation in slightly different form is presented in [4] and [5]. In eq. (10), the stress amplitude σ_{a0} represents a case with uniaxial, fully reversed loading (no mean stress).

$$\sigma_{a0} = \frac{\sigma_a}{\frac{1}{k_\lambda} - \frac{\sigma_m}{\sigma_{fl}}}, \text{ where}$$

$$\begin{aligned} k_\lambda &= 1 - 0.25\lambda \\ \lambda &= \sigma_2 / \sigma_1 \\ \sigma_{fl} &= \frac{1}{2}\left(R_{p0.2} + R_m\right) \end{aligned} \qquad (10)$$

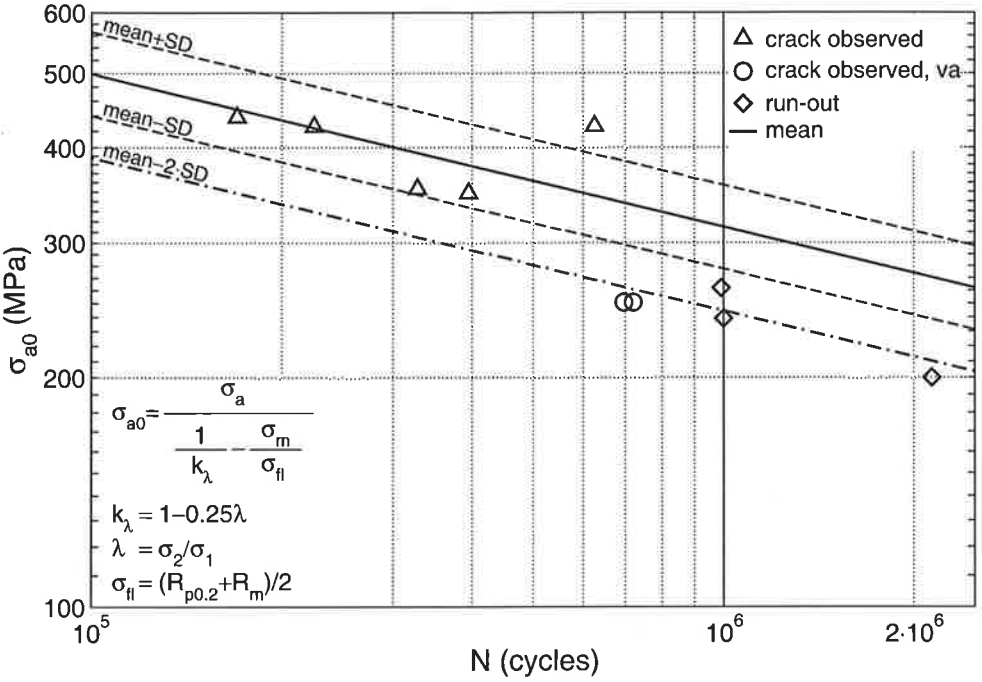


Figure 10. S–N curve for fatigue test results.

Figure 10 shows the normalised results of the fatigue tests in a form of an S–N curve. The solid line without any markings represent the mean fatigue capacity $C_{\mathrm{m}} = N\sigma_{\mathrm{a0}}^{b}$ of the results. The mean fatigue capacity, which is a geometric mean of the fatigue capacities of each test result, is calculated from eq. (11). Only results leading to a failure are included. The slope of the curve used here is $b = 5$. The line marked as "mean−2·SD" is calculated from the mean by subtracting two standard deviations. The standard deviation in log(C) is obtained from eq. (12). The calculated values for mean fatigue capacity and standard deviation are $C_{\mathrm{m}} = 3.089 \cdot 10^{18}$ and $SD = 0.27$, respectively.

$$C_{\mathrm{m}} = \sqrt[n]{\prod_{i=1}^{n} C_i} \qquad C_i = N_i \sigma_{a0i}^{b} \tag{11}$$

$$SD = \sqrt{\frac{\sum_{i=1}^{n} \left(\log(C_i) - \log(C_{\mathrm{m}})\right)^2}{n-1}} \tag{12}$$

The modified Haigh diagram in Figure 11 expresses the same results as Figure 10, but seen from different direction. This kind of presentation can be found from references [4, 5], too. The line drawn in figure cuts the ordinate axis at a point defined from the mean curve in Figure 10 at one million cycle endurance and average σ_{fl}. This diagram shows also the fact that the cases with occasional over- underload cycles were worse compared with the others.

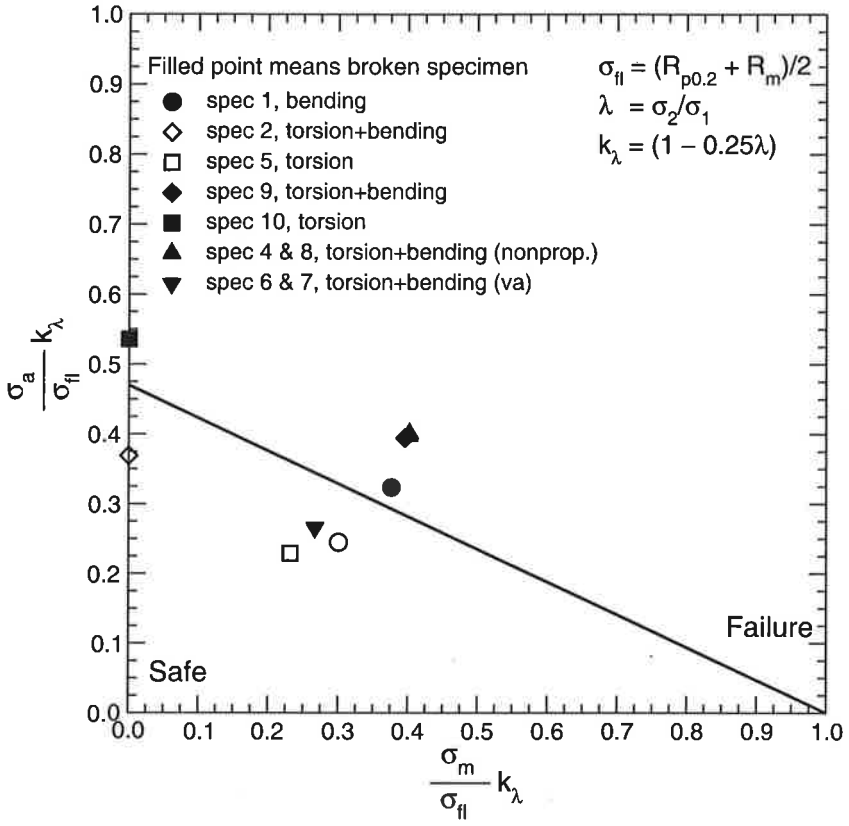


Figure 11. The fatigue test results presented in a modified Haigh diagram.

One of the test specimens lasted exceptional well. This was specimen 8, which had a non-proportional loading. The non-proportionality might have had an influence on the result, but since there is only one test like this, one cannot say it to be so for sure. The other non-proportional test gave an average result, however. On the other hand, the loading sequence for the second case was quite near the proportional one, because the direction of the largest principal stress changed only a little during the load cycle.

Figure 10 also shows clearly, that the test results for variable amplitude tests were significantly worse compared with those of constant amplitude tests. It can be concluded that an occasional over- underload cycle has a harmful influence on the fatigue strength. This is the case even though the extra damage produced by the overload cycles, when computed using a simple linear damage rule, is negligible. The larger over- underload cycle has no significant influence on the computed equivalent stress amplitude.

6. CONCLUSIONS

The FE-model calculated using axisymmetric elements gave good agreement with the static test results.

The occurrence of small cracks could be observed relatively early in the fatigue tests based on output of the strain gauge located near the expected site of crack initiation. By using the occurrence of the crack as a criterion for the failure, the fatigue strength of alternate cast component constructions could be compared to each other. However, even after crack initiation was observed, the structure still had significant residual life.

Usually several small cracks nucleated at the bottom of the notch in a direction normal to the largest principal stress (when $R = 0$). With torsion case ($R = -1$), also zigzag cracks along the notch were observed.

The test results for different loading cases could be reduced to a single design line using eq. (10) to normalise the principal stress amplitude. This takes into account different mean stresses, principal stress ratios and materials in each test.

The test results show clearly, that an occasional over- underload cycle is harmful and reduces the fatigue strength significantly. This is the case even though the extra damage produced by the overload cycles, when computed using a simple linear damage rule, is negligible. The larger over-underload cycle has no significant influence on the computed equivalent stress amplitude.

ACKNOWLEDGEMENTS

This work was partially supported through a grant from the Finnish Academy and the project Fadel/Gjutdesign, which is funded by the Nordic Industrial Fund, Wärtsilä Technology, Metso Corp. Componenta Corp. and VTT Industrial systems. All involved persons will also be gratefully acknowledged.

REFERENCES

1. MSC.Marc. Volume A: Theory and User Information, Version 2001. Revision April 2001. MSC.Software Corporation 2001.

2. ABAQUS Theory Manual, Version 6.4. ABAQUS inc. 2003.

3. Lepistö, J., Fatigue assesment of a cast axle. In: Samuelsson, J., Marquis, G., Solin, J. (eds.), Competent Design by Castings. Improvements in a Nordic project. Gjutdesign-2005 final seminar, Espoo 13.–14.6.2005. VTT Symposium 237, Helsinki 2005, p. 311–328. ISBN 951-38-6298-4, ISSN 0357-9387.

4. Marquis G.B., Karjalainen-Roikonen P., Long-life multiaxial fatigue of nodular graphite cast iron. In: Carpinteri A., Freitas M., Spagnoli A. (eds.), Biaxial/Multiaxial Fatigue and Fracture. ESIS Publication 31. Elsevier Science Ltd 2003, p. 105–122.

5. Marquis G:, Solin J., Long-life fatigue design of GRP 500 nodular cast iron components. Espoo 2000. Technical Research Centre of Finland, VTT Tiedotteita – Meddelanden – Research Notes 2043. 70 p.

FATIGUE STRENGTH OF COLD-FORMED TUBULAR X- AND T-JOINTS

L. HUHTALA, V.-M. LIHAVAINEN
Department of Mechanical Engineering, Lappeenranta University of Technology
P.O. BOX 20, FI-53851 Lappeenranta, Finland
Email: Lauri.Huhtala@lut.fi

ABSTRACT

In this paper, analytical and experimental fatigue strengths of welded stainless steel RHS joints are presented. The main objective of the research was to study the fatigue strength of cold-formed tubular X- and T-joints. Two alternate configurations were used for both joint types. The first configuration consisted of a conventional transverse fillet weld connection between the chord and brace members. The second joint had laser cut rectangular holes in the chord webs which allowed a continuous brace member to be used. Fatigue tests on RHS joints from a stainless steel, EN 1.4301, have been performed under constant amplitude axial tension or bending. The wall thicknesses used were mainly 4mm and two β-ratios (width of a brace/ width of a chord) were investigated. The finite element method was used to evaluate structural stress concentration factors (SCF) of the alternate connections. Calculated SCFs were found to be slightly higher than published values. The test results show that the configuration that employed a continuous brace member seems to have higher fatigue strength compared to joints fabricated using only fillet welds.

1. INTRODUCTION

Structural hollow sections are widely used in all kinds of structures under different types of loading. The support systems and undercarriages in many applications are subjected to static and fatigue loading during their expected lives. Enhanced mechanical properties of stainless steels have extended the use of stainless steels to structures under dynamic loads as well. Stainless steel has gained more and more market volume in the road transportation industry and agricultural industry for applications such as truck trailers and bus frames. Stainless steel grades offer optimized combinations of strength and toughness with excellent corrosion resistance against atmospheric conditions. Welding is a typical process constructing these structures from cold-formed stainless steel tubular sections. Because appearing of discontinuation by welds the fatigue strength have a great importance and therefore the main criterion in design.

The fatigue life of welded joints depends on the joint type, joint loading and structural detailing of the joint. The loading in the joint depends on the type of structure and the fatigue actions. In welded tubular joints the stiffness around the intersection is not uniform, resulting in a geometrical non-uniform stress distribution.

The hot spot stress method relates the fatigue life of a joint to the so-called hot spot stress at the joint rather than the nominal stress. In the hot spot stress method, the nominal stress range is converted to the hot spot stress range using SCFs. It takes the uneven stress distribution around the perimeter of the joint into account directly. The hot spot stress range includes the influences of the geometry and type of load but excludes the effects related to fabrication such as the configuration of the weld and the local condition of the weld. The hot spot stress is the maximum geometrical stress occurring in the joint where the cracks are usually initiated. In the case of welded joints, this generally occurs at the weld toe.

Because strain gauges on test specimens or FE-analysis are typically not feasible for designers, stress concentration factors (SCFs) are used as simple multiplication factors on the nominal stress range. The SCF is the ratio between the hot spot stress at the joint and the nominal stress in the member due to a basic member load which causes this hot spot stress. It may vary around the perimeter of the joint. Several fixed lines can be chosen for a joint, along which the SCFs are determined. The SCfs can be determined by experimental testing or FE simulation, by using detailed formulae or simplified parametric formulae or graphs.

This paper deals with the testing of tube-to-tube X- and T-connections made up of rectangular hollow sections under constant amplitude axial tension or out-of-plane bending. Welded connection tests were performed on cold-formed RHS sections of austenitic stainless steel type EN 1.4301 (304). Two alternate configurations are used. The rectangular hollow sections have tube wall thickness 4mm and 3mm and two β-ratios were investigated. A total of 34 connections were tested. The welded connections revealed different failure modes under axial tension and out-of-plane bending. The evaluated SCFs by using FE-analysis are compared to SCFs from parametric equation in current fatigue design guide such as CIDECT Design Guide No. 8 (Zhao et al. 2001). The evaluated SCFs were found to be slightly lower than the SCFs from parametric equations. Since differences have been found between SCFs by FEA and parametric equation determined hot spot stresses with help of both SCFs are expressed. Mean fatigue classes for each joint type were determined. The test results are compared with existing European design formulae Eurocode 3 and IIW recommendations for fatigue design of welded joints and components.

2. TEST PROGRAMME

The gas metal-arc welding process was used in joining the braces to the chords. Test welds were produced in two locations by various welders, also the welding equipment varied at different places. Shielding gases and material remained unaltered between the different welding locations. Starting and finishing points of welding were located in the middle of the flat part of the branch member as is recommended for connections under fatigue loading, to avoid discontinuities at the corners. The effective throat thickness of a fillet weld was chosen to be $1.25t$. The filler metals were austenitic steels of a composition that matched closely to the base metal under investigation. Prior to fatigue testing, all the specimens were measured to find out angular misalignment.

Fatigue tests on RHS joints from a stainless steel, EN 1.4301, have been performed under constant amplitude axial tension or bending. Axially loaded tension tests were performed for X-joints and bending tests for T-joints. Test arrangement for static and dynamic tests of X-and T-joints is shown in Figs. 1 and 2. Strain gauges were mounted on the top flange of the brace at the distance of 4mm and 50 mm from the weld toe. However, the results of measurements were not utilized at this stage of study. Table 1 shows the details of the connection series tested including series name, nominal rectangular hollow section sizes, type of joint, fabrication method of joint, loading type,

and the corresponding joint parameters ($2\gamma = b_0 / t_0$, $\beta = b_1 / b_0$ and $\tau = t_1 / t_0$). The sections are labelled from 1 to 34.

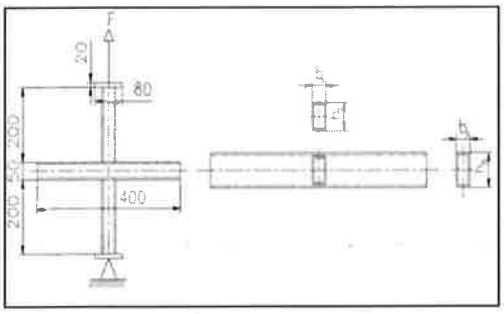
Table 1. X-and T-joints for static and fatigue tests.

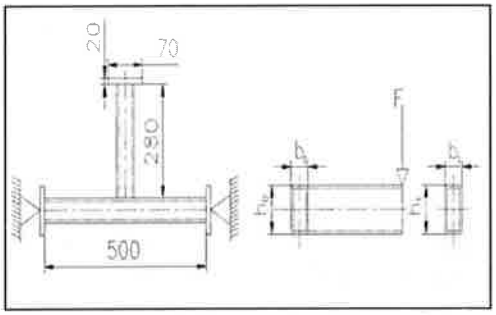
Label	Chord member	Brace member	Type of joint/load	Detail	Material	Load/ stress range	2γ	β	τ
1	100x50x4	100x50x4	X/tension	Conv.	304/304	fatigue	25	1.0	1.0
2	100x50x4	100x50x4	X/tension	Conv.	304/304	fatigue	25	1.0	1.0
3	100x50x4	80x50x4	X/tension	Conv.	304/304	fatigue	25	0.8	1.0
4	100x50x4	80x50x4	X/tension	Conv.	304/304	fatigue	25	0.8	1.0
5	100x50x4	80x50x4	X/tension	Conv.	304/304	fatigue	25	0.8	1.0
6	100x50x4	100x50x4	X/tension	Conv.	304/304	fatigue	25	1.0	1.0
7	100x50x4	100x50x4	X/tension	Conv.	304/304	fatigue	25	1.0	1.0
8	100x50x4	80x40x4	X/tension	Conv.	304/355	fatigue	25	0.8	1.0
9	100x50x4	100x50x4	X/tension	Conv.	304/355	fatigue	25	1.0	1.0
10	100x50x4	100x50x4	X/tension	Conv.	304/304	fatigue	25	1.0	1.0
11	100x50x4	100x50x4	X/tension	Conv.	304/304	fatigue	25	1.0	1.0
12	100x50x4	100x50x4	X/tension	Conv.	304/304	fatigue	25	1.0	1.0
13	100x50x4	100x50x4	X/tension	Conv.	304/304	fatigue	25	1.0	1.0
14	100x50x4	100x50x4	X/tension	Conv.	304/304	fatigue	25	1.0	1.0
15	100x50x4	80x50x3	X/tension	Cont. brace	304/304	fatigue	25	0.8	0.75
16	100x50x4	80x50x4	X/tension	Cont. brace.	304/304	fatigue	25	0.8	1.0
17	100x50x4	100x50x4	T/bending	Conv.	304/304	fatigue	25	1.0	1.0
18	100x50x4	80x40x4	T/bending	Cont. brace.	304/304	fatigue	25	0.8	1.0
19	100x50x4	100x50x4	T/bending	Conv.	304/304	fatigue	25	1.0	1.0
20	100x50x4	100x50x4	T/bending	Conv.	304/304	fatigue	25	1.0	1.0
21	100x50x4	100x50x4	T/bending	Conv.	304/304	fatigue	25	1.0	1.0
22	100x50x4	100x50x4	T/bending	Conv.	304/304	static	25	1.0	1.0
23	100x50x4	80x40x4	T/bending	Conv.	304/304	fatigue	25	0.8	1.0
24	100x50x4	80x40x4	T/bending	Conv.	304/304	fatigue	25	0.8	1.0
25	100x50x4	80x40x4	T/bending	Conv.	304/304	static	25	0.8	1.0
26	100x50x4	100x50x3	T/bending	Conv.	304/304	fatigue	25	1.0	0.75
27	100x50x4	80x40x3	T/bending	Cont. brace	304/304	fatigue	25	0.8	0.75
28	100x50x4	80x40x3	T/bending	Cont. brace	304/304	fatigue	25	0.8	0.75
29	100x50x4	80x40x3	T/bending	Cont. brace	304/304	static	25	0.8	0.75
30	100x50x3	80x40x3	T/bending	Cont. brace	304/304	fatigue	25	0.8	1.0
31	100x50x4	80x40x4	T/bending	Cont. brace	304/304	static	25	0.8	1.0
32	100x50x4	80x40x4	T/tension	Conv.	304/304	static	25	0.8	1.0
33	100x50x4	100x50x4	T/tension	Conv.	304/304	static	25	1.0	1.0
34	100x50x4	80x40x4	T/tension	Cont. brace.	304/304	static	25	0.8	1.0

In all tests, the chord consisted of an 100x50x4 mm RHS. Loading was applied as brace load in the case of bending test as well. The thickness of sections tested ranged from 3 mm to 4 mm and two β-ratios (width of a brace/ width of a chord) were investigated. Two alternate configurations were used for both joint types. The first configuration consisted of a conventional transverse fillet weld connection between the chord and brace members. The second joint had laser cut rectangular holes in the chord webs which allowed a continuous brace member to be used.

A total of 34 tests were performed on RHS of austenitic stainless steel of type 1.4301 (AISI 304). The other material tested was RHS of grade 355 that was applied in two tests as a brace. The stress-strain characteristics vary around the tube, because the plastic deformation of the section during rolling is non-uniform. Generally the strength values are lowest in the wall perpendicular to the wall containing the weld. Three tensile tests were performed on X-joints and four for T-joints. A servo-hydraulic testing machines with capacity of 5 MN and 400 kN were used for producing the brace axial tension load.

The static 0.2 % tensile proof stress and the tensile strength were measured as $\sigma_{0.2}$ = 422 MPa and σ_u = 648 MPa on section 100x50x4 and $\sigma_{0.2}$ = 464 MPa and σ_u = 673 MPa on section 80x50x4, respectively, and the elongation after fracture was measured as 50 % and 47.5 %. Gage length of 250 mm was used for both joint types.





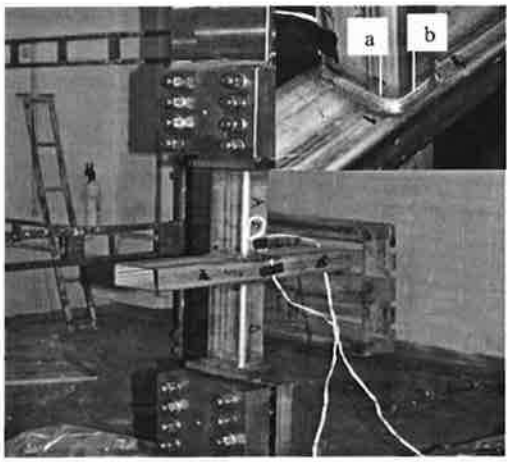


Fig. 1. Test arrangement for static and dynamic tests of X-joints.

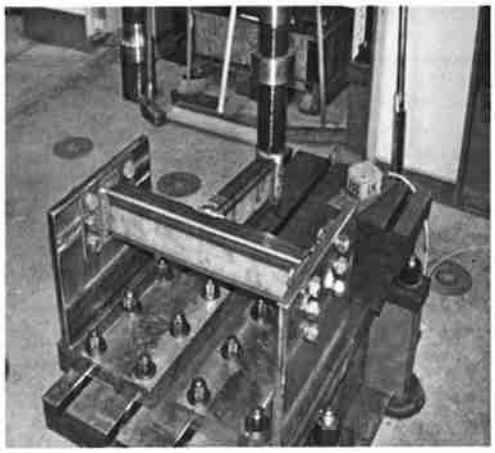


Fig. 2. Test arrangement for static and dynamic tests of T-joints.

3. FAILURE MODES

Different modes of failure have been observed during the fatigue testing of connections. These failures occurred due to the initiation and propagation of cracks resulting in the separation of the brace from the chord along the weld toe in either the chord or the brace. Most cracks initiated at the weld toe in the brace and chord of the brace junction. Root side failure and weld toe failure were observed to be modes of failure for X-joints. Root side failure occurred with β-value 1.0, Fig. 3. The crack initiated at the root side of a weld and propagated towards the weld metal of the brace. Weld toe failure was current failure mode in X-joints despite β-value of 0.8 or 1.0, Fig. 4. Failure in X-joints with continuous brace member occurred at the weld toe as well.

Most mode of failure of T-joints occurred in base material at the opposite side of the brace in the corner area of the chord, Fig. 5. This might result from distortion of a chord. This mode of failure was observed with β-value of 1.0 that is more vulnerable to this phenomenon compared to β-value of 0.8. At the rest of T-joints (β-value of 0.8) cracks initiated at the weld toe of the chord or the brace. Depending on a location of initiation the crack propagated in the chord or brace and in two cases propagation of crack in base material was observed, Figs. 6 and 7. The highest SCF for X-joints occurs in the chord (line b, Fig. 8) with β-value of 0.8 according to parametric equations. On the contrary the highest SCF according to FEA were located in the brace (β-value of 0.8, line a) and in the chord (β-value of 1.0, line c). However, all the specimens of X-joints fractured in the brace.

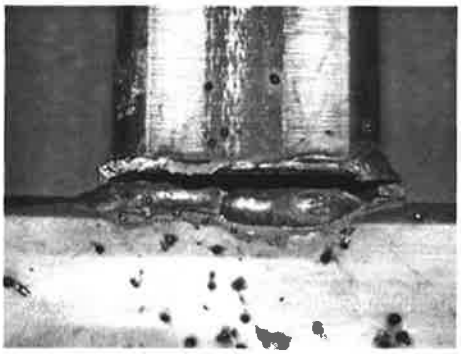


Fig. 3. Root side failure (brace-side failure) of X-joint.



Fig.4. Weld toe failure (brace-side failure) of X-joint.

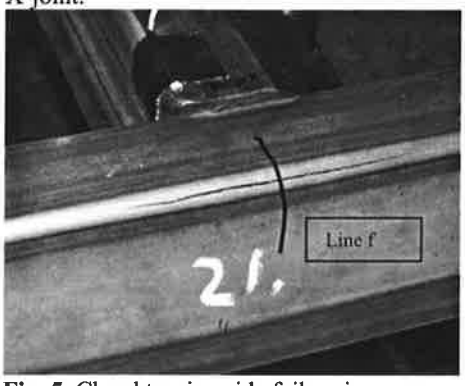


Fig. 5. Chord tension side failure in a corner area (CTSC) of T-joint.

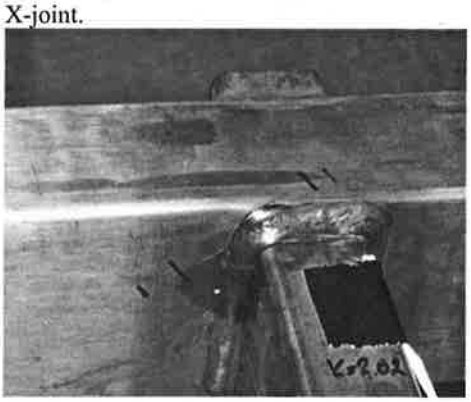


Fig. 6. Chord tension side failure from weld toe to base material (CTSB) of T-joint.



Fig. 7. Chord tension side failure in weld toe (CTSW) of T-joint.

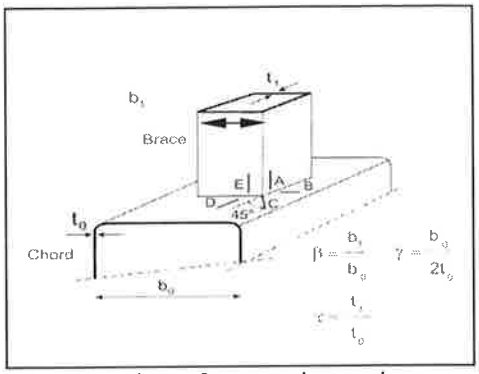


Fig. 8. Locations of parametric equations.

4. FINITE-ELEMENT ANALYSIS AND PARAMETRIC EQUATIONS

In this study the commercial software package I-DEAS 9.0 was used in modelling tubular joints. The aim of FEA is to localize stress concentration and confirm it's magnitude in addition to parametric equations as a reference value. By using of symmetry in loading and geometry, only a half of the joint needs to be modelled for T-joints and 1/8-joint for X-joints. The nodal displacement perpendicular to the plane of symmetry is restrained while two remaining transitional degrees of freedom are free. Solid linear brick elements, solid parabolic tetrahedron elements and rigid elements were used. The material properties of the brace and the chord are taken as 200 GPa for modulus of elasticity (E) and 0.28 for Poisson's ratio (υ). For both type of joints three different models were used. In all cases dimensions of 100x50x4 for chord were applied. The brace dimension was 100x50x4 (β = 1.0) or 80x40x4 (β = 0.8) depending on the case. Typical FE meshing of with conventional fillet weld and continuous brace for X-joint and extrapolation region for different lines are shown in Figs. 9-12.

The fatigue life of tubular joints is normally determined by use of the empirical stress concentration factor method. Based on a large number of experiments and numerical simulations, formulae have been determined, from which the hot spot stresses can be estimated. The stress concentration factor (SCF) is defined from the following equation (1):

$$\sigma_{hs} = SCF \cdot \sigma_{nom} \tag{1}$$

Values of the stress concentration factors for uniplanar RHS T- and X-joints in the case of axial force on the brace can be estimated as follows (Table 2):

Table 2. Equations for SCFs (CIDECT, 2001).

	Equations
Line a, e	$SCF = (0.013 + 0.693 \cdot \beta - 0.278 \cdot \beta^2) \cdot (2 \cdot \gamma)^{(0.790 + 1.898 \cdot \beta - 2.109 \cdot \beta^2)}$ (2)
Line b	$SCF = (0.143 - 0.204 \cdot \beta - 0.064 \cdot \beta^2) \cdot (2 \cdot \gamma)^{(1.377 + 1.715 \cdot \beta - 1.103 \cdot \beta^2)} \cdot \tau^{0.75}$ (3)
Line c	$SCF = (0.077 - 0.129 \cdot \beta - 0.061 \cdot \beta^2 - 0.0003 \cdot 2\gamma) \cdot (2 \cdot \gamma)^{(1.565 + 1.874 \cdot \beta - 1.028 \cdot \beta^2)} \cdot \tau^{0.75}$ (4)
Line d	$SCF = (0.208 - 0.387 \cdot \beta - 0.209 \cdot \beta^2) \cdot (2 \cdot \gamma)^{(0.925 + 2.389 \cdot \beta - 1.881 \cdot \beta^2)} \cdot \tau^{0.75}$ (5)

The SCFs given are valid for square hollow section braces and rectangular hollow section chords with h_0/b_0 between 0.75 and 1.5. The SCFs are determined along limited fixed lines or location of interest, Fig. 8. For joints with fillet welds brace SCFs will be multiplied by 1.40 for brace side of weld in designing. Evaluated values based on equations (2)-(5) and FEA are presented in Table 3. Because the failure occurred at the weld or root side of the brace for X-joints SCFs evaluated by using FEA are expressed along lines a and e. These values are the highest found in modelling as well. It was observed that a location of the highest stress peak not results essentially the highest structural stress. Stress concentration factors for T-joints are shown Table 4, correspondingly. Because the load condition out-of-plane bending is not included in CIDECT (2001) SCFs based on equations are not presented for T-joints. As in the case of X-joint the highest SCFs values were determined at the location of failure or initiation of the crack expected.

Table 3. Stress concentration factors on the brace according to FEM-analysis and equations (2) – (5) for X-joints.

	X-joint, β=0.8, conv.	X-joint, β=1.0, conv.	X-joint, β=0.8, cont. brace
SCF - FEM	8.9 (line a)	3.5 (line e)	1.8 (line a)
Equations (2)-(5)			
Line a, e	8.52	2.76	-
Line b	14.90	1.81	-
Line c	10.60	2.77	-
Line d	6.16	3.02	-

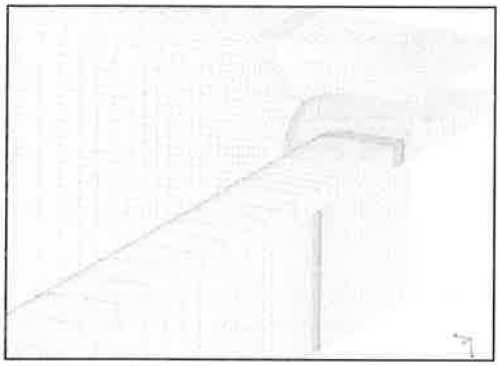


Fig. 9. Typical FE meshing for 1/8-model of X-joint with continuous brace.

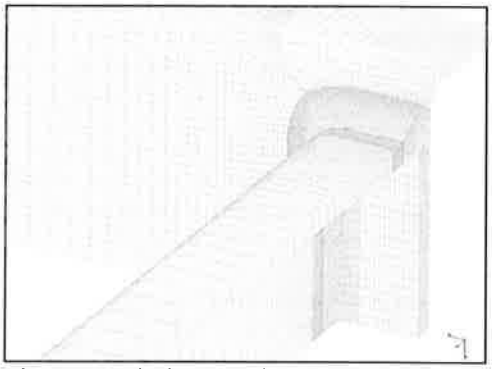


Fig. 10. Typical FE meshing for 1/8-model of X-joint with conventional fillet weld.

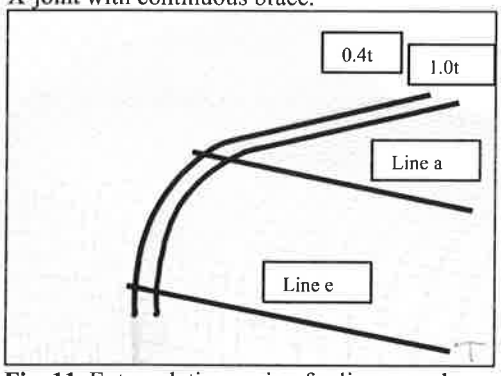


Fig. 11. Extrapolation region for lines a and e.

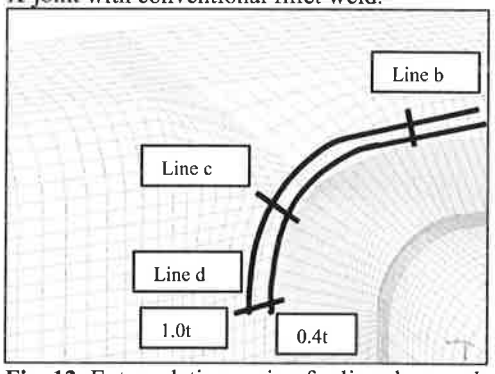


Fig. 12. Extrapolation region for lines b, c, and d.

Table 4. Stress concentration factors according to FEM-analysis for T-joints.

	T-joint, $\beta = 0.8$, conv.		T-joint, $\beta = 1.0$, conv.			T-joint, $\beta = 0.8$, cont. brace	
	chord	brace	chord	chord, fig. 5	brace	chord	brace
SCF-FEM	6.9, line c	6.1, line a	5.7, line c	3.5, line f	6.6, line a	1.2, line c	2.2, line a

The hot spot stress has to be determined at the weld toe position from the stress field outside the region influenced by the local weld toe geometry. The location from which the stresses have to be extrapolated depends on the dimensions of the joint and the position around intersection. According to CIDECT (2001) boundaries of extrapolation region for RHS joints are $L_{r,min} = 0.4t_0$ (chord), $0.4t_1$ (brace) and $L_{r,max} = L_{r,min} + t_0$, (chord), $L_{r,min} + t_1$, (brace) correspondingly. However minimum value for $L_{r,min}$ is 4 mm. In this context extrapolation points 0.4t and 1.0t were used. This might be one reason for higher values of SCFs.

5. RESULTS AND DISCUSSION

Obtained tensile test results for X-joints and T-joints are presented in Figs. 13 and 14. The mode of failure was observed to occur in weld metal for X-joints using conventional transverse fillet weld connection. The ultimate capacity of the specimen with β-value of 1.0 was nearly double compared to the specimen with β-value of 0.8. Chord webs which allow a continuous brace member to be used, the ultimate strength was 1.34 times higher than the specimen with β-value of 1.0, even the failure occurred in the heat affected zone of brace near the attachment plate.

Obtained bending test results are similar to X-joints. Higher β-value results 1.19 higher bending capacity using conventional transverse fillet weld connection. As in the case of X-joint the use of continuous brace member gives the highest bending capacity. However, significant difference can be observed between wall thicknesses of 3mm and 4mm, being 1.37 higher with thicker one. Web failure in the chord was observed with β-value of 0.8 and a distortion of the chord with β-value of 1.0. Brace-side failure in the heat affected zone of the brace-chord junction was observed in connections T29 and T31.

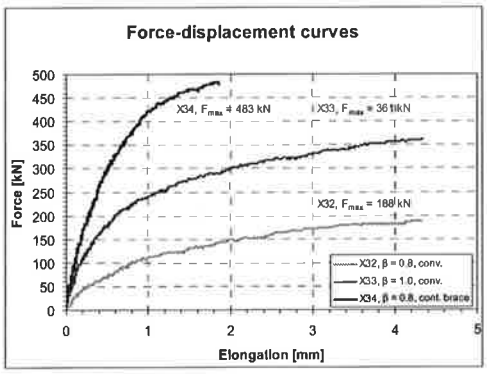


Fig. 13. Load-displacement curves for static tests of X-joints.

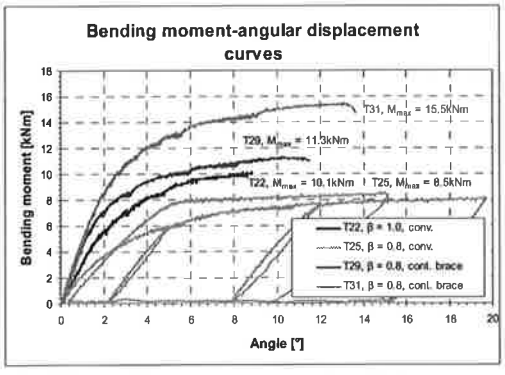


Fig. 14. Bending moment–angular displacement curves for static tests of T-joints.

The data obtained from the fatigue tests of X-joints is presented in Table 5. Tests were carried out at a stress ratio 0.1. The following were tested: (1) 16 connections under constant amplitude axial tension made of steel grade EN 1.4301 (304), (2) 11 connections under constant amplitude out-of-plane bending load made of steel grade EN 1.4301 (304). Table 5 shows the list of connections tested, number of cycles to failure, nominal stress range, SCFs based on CIDECT (2001) and FE simulations, hot spot stress ranges and failure mode. Stress concentration factors from the hot spot locations, A and E, are given despite the fact that higher values of SCFs can be assigned. This is because of similarity of failure mode. However, in test specimens failed at the root side of the weld, given SCFs are inappropriate. Table 6 shows the test results obtained from the fatigue tests of T-joints: the list of connections tested, number of cycles to failure, nominal stress range, hot spot stress range and SCFs based on FE simulations and failure mode. The nominal stress is obtained by using the simple beam theory $\sigma = M/W$. Nominal bending stress value at the weld toe of the brace is used.

Table 5. Results of fatigue tension tests for X-joints.

Label	$\Delta\sigma_{nom}$	N	SCF Eq. (2)	$\Delta\sigma_{hseq}$	SCF FEM	$\Delta\sigma_{hsfem}$	Failure mode
1*	98	53700	2.76	270	3.5	343	RSF
2*	98	45267	2.76	270	3.5	343	RSF
3***	181	765	8.52	1542	8.9	1611	WTF
4	61	50460	8.52	520	8.9	543	WTF
5	34	381311	8.52	290	8.9	303	WTF
6**	98	9848	2.76	270	3.5	343	RSF
7**	98	21754	2.76	270	3.5	343	RSF
8	34	1122000	8.52	290	8.9	303	WTF
9	120	14577	2.76	331	3.5	420	RSF
10	103	209983	2.76	284	3.5	361	WTF
11	104	157479	2.76	287	3.5	364	WTF
12	64	1672722	2.76	177	3.5	224	WTF
13	137	48098	2.76	378	3.5	480	WTF
14	40	7589632	2.76	-	3.5	-	Run-out
14 re- test	78	316709	2.76	215	3.5	273	WTF
15	209	383900	-	-	1.8	376	WTF
16	149	1475959	-	-	1.8	268	WTF

Note: RSF=root side failure (brace-side failure), WTF=weld toe failure (brace-side failure) *Starting and finishing point of a weld locates in a corner (excluded in statistical analysis)
**Cold lap was observed (excluded in statistical analysis)
***Result is not reliable because of $\Delta\sigma_{hs} > 2f_y$ (excluded in statistical analysis)

S_{hs}-N data shown in Fig. 15 is based on the hot spot ranges determined from parametric formula or FE simulation. Fatigue strength curve (*FAT100*) for RHS joints according to the hot spot stress method is represented as a reference curve (IIW 2004). This curve describes the characteristic fatigue class ($FAT_{95\%}$). The statistical analysis of test series has been calculated according to equations (5) - (7). Fatigue class (*FAT*) can be presented as follows (5):

$$\Delta\sigma_i^m \cdot N_i = C_i = FAT_i^m \cdot 2000000. \tag{5}$$

Mean value of fatigue capacity is computed by equation (6)

$$\log C_{50\%} = \frac{\Sigma \log C_i}{n}, \tag{6}$$

where n is the number of test specimens in the sample. The standard deviation, s, of the fatigue capacity of the sample can be computed as following (7):

$$s = \sqrt{\frac{\Sigma(\log C_i - \log C_{50\%})^2}{n-1}}. \quad (7)$$

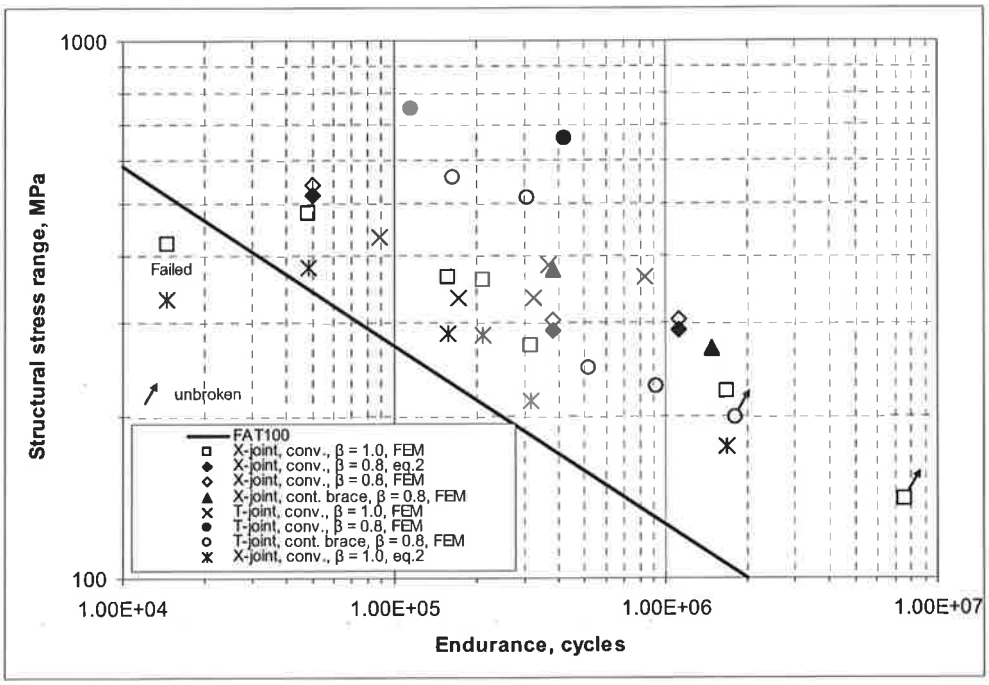


Fig. 15. Comparison of fatigue test results with S-N curve given IIW (2004).

Table 6. Results of fatigue bending tests for T-joints.

Label	$\Delta\sigma_{nom}$	N	SCF FEM	$\Delta\sigma_{hsfem}$	Failure mode
17	64	838,800	5.7	365	CTSW
18	166	1,797,190	1.2	199	run-out
18 re-test	206	515,364	1.2	247	CTSB
19	95	172,685	3.5	542	CTSC
20	95	324,427	3.5	542	CTSC
21	124	88,777	3.5	707	CTSC
23	96	424,309	6.9	662	CTSW
24	123	114,966	6.1	750	BTSW
26	110	367,000	3.5	627	CTSC
27	255	164,710	2.2	561	BTSW
28	232	306,900	2.2	510	BTSW
30	190	927,000	1.2	228	CTSB

Note: CTSW=chord tension side failure in weld toe, CTSB = chord tension side failure from weld toe to base material, BTSW = brace tension side failure in weld toe, CTSC = chord tension side failure in the corner area

Evaluated fatigue classes ($FAT_{50\%}$) of tested X- and T-joint are shown in Table 7. Fatigue classes were determined by setting the slope m = 3. Test specimens included in statistical analysis and

basis of SCF are shown inside brackets. The standard deviation for X-joint is 0.36 (12 test specimens) and T-joints 0.53 (11 test specimens. The results show that the configuration that employed a continuous brace member had higher fatigue strength compared to joints fabricated using only fillet welds. However, in the case of T-joint (β = 0.8) higher fatigue class was established. This is due to high nominal stress of joints as evaluated SCfs can be expected to be the order of magnitude of current joint type. Higher values of SCFs were observed as evaluating in plane bending on the brace based on CIDECT (2001). In any case this result should be discounted.

Table 7. Mean fatigue classes according to type of joint and β - value.

		$\beta = 0.8$	$\beta = 1.0$	Cont. brace
X/tension	$FAT_{nom50\%}$	22 (4,5,8)	41 (9,10,11,12,13,14)	127 (15,16)
	$FAT_{hs50\%}$	182 (eq.)/190 (FEM)	114 (eq.) /145 (FEM)	229 (FEM)
T/bending	$FAT_{nom50\%}$	52 (23,24)	49 (17,19,20,21,26)	127 (18,27,28,30)
	$FAT_{hs50\%}$	338 (FEM)	189 (FEM)	207 (FEM)

6. CONCLUSIONS

In this paper, the fatigue strength and the stress concentration factors of tubular X- and T-joints are investigated. Two alternate configurations were used for both joint types. A total of 27 fatigue tests were performed under constant amplitude axial tension or bending. The hot spot stress range was determined by using the numerical stress concentration factors and the factors based on design formula. Fatigue classes were evaluated for different joint types.

The ultimate load capacity of chord webs which allowed a continuous brace member to be used was considerably higher than conventional transverse fillet weld connection between the chord and brace members. Furthermore, for β-value of 1.0, the load capacity of X- and T-joints is higher than those of β-value of 0.8 with conventional connection. There are differences between the predicted SCFs from the parametric equations and evaluated by FEA, with the evaluated SCFs being slightly higher at the location of failure. The failure of location, SCFs based on FE simulation and SCFs based on equations were not consistent. The highest SCFs were found for β-value of 0.8 ratios. The location of the highest stress concentration does not guarantee the highest hot spot stress. The mean fatigue class evaluated were mainly quite high, especially case of bending ($\beta = 0.8$).

This result should be discounted. However, results of continuous brace member look hopeful. The intention of tests and FE simulations was not to determine final conclusions of the test results of studied joint types, but rather be a launch of further study. The fatigue strength of both conventional transverse fillet weld connections in out-of-plane bending load on the brace needs to be studied with extra tests and FE simulations. The SCFs based on measured experimental strain need to be checked as well.

NOTATION

The following symbols are used in this paper:

A = design throat thickness
BTS = brace tension side failure
B =section width of member
b_0 = external width of hollow section chord member
b_1 = external width of hollow section brace member

C_i = fatigue capacity
CTSB = chord tension side failure from weld toe to base material
CTSC = chord tension side failure in the corner area
CTSW = chord tension side failure in weld toe
E = modulus of elasticity
F_{max} = maximum force of tensile test
FAT = fatigue class
FAT_{hseq} = fatigue class based on hot spot stresses using SCFs from parametric equation
FAT_{hsfem} =fatigue class based on hot spot stresses using SCFs determined by FEA equation
FAT_{nom} = fatigue class based on nominal stresses
f_y = nominal yield stress of material
h_0 = external depth of hollow section chord member
h_1 = external depth of hollow section brace member
N = number of cycles to failure
m = the slope of the S-N curve
R = stress ratio, ratio of minimum to maximum algebraic stress in cycle
RSF = root side failure (brace-side failure)
S_{hs} = the hot spot range
SCF = stress concentration factor
s = standard deviation
t = wall thickness of member
t_0 = wall thickness of chord member
t_1 = wall thickness of brace member
WTF = weld toe failure (brace-side failure)
β = ratio of brace width to chord width = b_1/b_0
γ = half width to thickness ratio of the chord = $b_0/2t_0$
σ = stress
σ_{hs} = the hot spot stress = the maximum stress at the weld toe
$\Delta\sigma_{hseq}$ = the hot spot stress range based on SCF by equation
$\Delta\sigma_{hsfem}$ = the hot spot stress range based on SCF by FEM
$\Delta\sigma_{nom}$ = nominal stress range
τ = brace wall thickness to chord wall thickness ratio
υ = Poisson's ratio

REFERENCES

ENV 1993-1-1:1992. *Eurocode 3: Design of steel structures, Part 1.1: General rules and rules for buildings*, Brussels: European Committee for Standardization (CEN).

CIDECT, 2001, Design Guide for circular and rectangular hollow section welded joints under fatigue loading. X.-L. Zhao, S. Herion, J.A. Packer, R.S. Puthli, G. Sedlacek, J. Wardenier, A.M. van wingerde, N.F. Yeomans. Comité International pour de Développement et l'Etude de la Construction Tubulaire. TÜV-Verlag GmbH, Köln.

International Institute of Welding (IIW), (2004). *Recommendations for fatigue design of welded joints and components,* IIW Doc. XIII-1965-03/XV-1127-03, Joint Working Group XIII-XV(Hobbacher, A.), Paris, France.

Mashiri, F. R., Zhao, X. L., and Grundy, P. (2002). "Fatigue tests and design of welded T connections in thin cold-formed square hollow sections under in-plane bending." Journal of Structural Engineering, 128(11), 1413-1422.



Lappeenrannan teknillinen yliopisto
Digipaino 2006

ISBN 952-214-227-1
ISSN 1459-2924